JAERI-M
7479

ANNUAL REPORT OF DIVISION OF THERMONUCLEAR FUSION RESEARCH AND DIVISION OF LARGE TOKAMAK DEVELOPMENT, FOR THE PERIOD OF APRIL 1, 1976 TO MARCH 31, 1977

February 1978

Division of Thermonuclear Fusion Research and
Division of Large Tokamak Development

日本原子力研究所
Japan Atomic Energy Research Institute

JAERI-M 7479

Annual Report of Division of Thermonuclear Fusion Research and Division of Large Tokamak Development for the period of April 1, 1976 to March 31, 1977

Division of Thermonuclear Fusion Research
and Division of Large Tokamak Development,
Tokai Research Establishment, JAERI

(Received December 16, 1977)

Research and development activities in fiscal year 1976 of Division of Thermonuclear Fusion Research and Division of Large Tokamak Development are described; works in the two divisions are closely related.

1) Theoretical and computational studies continued on tokamak confinement and heating related to experimental problems.
Studies on NBI heating in JT-60 were completed.

2) Experimental studies on impurities, density control and effects of density fluctuations were made in JFT-2. Neutral beams up to 30 keV and 8 A were injected into JFT-2 plasma perpendicularly. The ion temperature was increased by 10% - 15%, which is in agreement with the prediction by classical Fokker-Planck theory.
In JFT-2a(DIVA), plasma-wall interaction (behavior of heavy and light impurities) was studied. The divertor of DIVA reduced the plasma-wall interaction and hence the radiation loss due to heavy impurities by a factor of 3.
A grazing-incidence vacuum monochromator was first used in impurity studies in JFT-2 and JFT-2a.

3) Technological improvements were made raising efficiencies of operation, maintenance and plasma research.

4) Neutral beam injector test stand ITS-2 of 100 keV was completed.
Construction of a 200 kW, 650 MHz radiofrequency heating system for JFT-2 was started.

5) In surface phenomena, sputterings of molybdenum and pyrolytic graphite by low-energy protons and chemical reaction rates of pyrolytic graphite with protons were measured. Honeycomb structure greatly reduced the sputtered particles.

6) the superconducting magnet development group made the design of cluster test apparatus and the development of large current superconductor.

7) Phase-I preliminary design of experimental fusion reactor JXFR was completed and preliminary safety evaluation of JXFR was made.

8) Detailed (pre-construction) design of JT-60 was completed in November 1976. The engineering development of the major components was made by five industrial groups. Engineering development contracts were all completed by March 1977.

9) Engineering studies and tests on critical components of JT-4 with non-circular plasma cross section and divertors were made, after the preliminary design in fiscal year 1975.

Key words : Annual Report, Plasma Confinement, Plasma Physics, Tokamak, JFT-2, JFT-2a(DIVA), Diagnostics, Neutral Beam Injector, RF Heating, Surface Study, Superconducting Magnet, Reactor Design, JT-60, JT-4

核融合研究部および大型トカマク開発部年報
（昭和５１年度）

日本原子力研究所東海研究所
核融合研究部・大型トカマク開発部

（1977年12月16日受理）

核融合研究部と大型トカマク開発部の昭和51年度における研究開発の現況とその成果をとりまとめたものである。その概要は次のとおりである。

1) 理論的研究においては，実験上の問題と密接に関連したプラズマの閉込めと加熱の解析が続けられた。ＪＴ−６０用に開発した中性粒子加熱の解析コードは完成した。

2) ＪＦＴ−２では，不純物，密度制御および密度の揺らぎの効果が調べられた。中性粒子入射による加熱実験では１０〜１５％のイオン温度の上昇が得られた。

ＪＦＴ−２ａではプラズマと壁の相互作用が調べられ，そのダイバータは重金属による放射損失を３分の１に減らす効果があることが分かった。

プラズマ計測では，斜入射域真空分光計がＪＦＴ−２およびＪＦＴ−２ａにおける不純物の研究に用いられた。

3) 装置運転の効率の上昇およびその保守維持のための技術的改良を行なった。

4) プラズマ加熱に関しては，１００kVの中性粒子入射のテスト・スタンドＩＴＳ−２が完成した。ＪＦＴ−２用の２００kW，６５０MHzの高周波加熱システムの建設が始まった。

5) 表面現象の研究に関しては，低エネルギー水素によるモリブデンとグラファイトのスパッタリング，およびグラファイトの水素による化学的スパッタリングが測定された。多孔構造は大巾にスパッタリングを減少することが見出された。

6) 超電導開発グループにおいては，クラスターテスト装置の基本設計を行なう一方大電流の超電導導体の開発を進めている。

7) 炉設計研究では，１００ＭＷのトカマク実験炉の第１次予備設計が終了しその安全性評価の解析も行なわれた。

8) ＪＴ−６０の詳細設計および主要コンポーネットの試作開発が実施されいずれも完了した。

9) ＪＴ−４（非円形プラズマ断面のダイバータ付きトカマク）については，前年度の予備設計に引き続き，主要コンポーネントの技術的検討を行なった。

Contents

PREFACE

I. PLASMA THEORY AND COMPUTATION 1

1. Introduction 1

2. MHD Stability 3

2.1 Two-dimensional MHD stability analysis by the finite element method 3

2.2 Two-dimensional MHD stability analysis as an initial-boundary value problem 3

2.3 Numerical study of tearing instability 7

3. Transport and Impurity 9

3.1 Equilibrium radial electric field in a tokamak 9

3.2 Temperature gradient effect on impurity-ion transport .. 9

3.3 Numerical investigation of the time evolution of impurity concentration in a tokamak 9

3.4 Impurity drift instability of dissipative type 10

3.5 Nonlinear saturation of dissipative trapped ion instability and anomalous transport 10

3.6 Analysis of the breakdown threshold in a tokamak discharge 10

3.7 Computer simulation of the initial stage of tokamak discharge 11

4. Heating 13

4.1 Theoretical investigations of lower hybrid resonance heating in a tokamak 13

4.2 Propagation of lower hybrid wave 13

4.3 Stochastic acceleration by an electrostatic wave near ion cyclotron harmonics 14

5. Numerical Analysis and Computing 16

5.1 Two-dimensional tokamak transport analysis 16

5.2 Computer simulation on plasma confinement in a divertor tokamak 17

5.3 A new interative method for a large-scale general eigenvalue problem 17

5.4 A method to solve impurity diffusion equation with ionization and recombination source terms 18
5.5 Development of a pre-processor for effective use of COMMON statements and its useage 18
5.6 Pre-processor for the use of the OLYMPUS SYSTEM 18
5.7 Application of REDUCE-2 to the computations in CTR ... 19

II. TOROIDAL CONFINEMENT EXPERIMENTS

1. JFT-2 24
1.1 Introduction 24
1.2 Confinement experiments at toroidal field 18 kG 26
1.2.1 Experimental results on impurity contamination 26
1.2.2 Particle balance 27
1.2.3 Density fluctuations 28
1.2.4 Simulation 30
1.2.5 Z_{eff} profile 30
1.2.6 Electron temperature profile from soft X-ray 32
1.2.7 Radiation loss profile 33
1.3 Neutral beam injection heating experiment 44
1.4 Miscellaneous topics 48
1.4.1 High density discharges 48
1.4.2 Partial pressure measurement at plasma boundary ... 48
1.4.3 Breakdown in JFT-2 49
1.4.4 Remodeling the JFT-2 device for impurity and heating studies 53

2. JFT-2a(DIVA) 62
2.1 Introduction 62
2.2 Radiation loss 63
2.3 Heavy impurities 63
2.3.1 Two-dimensional measurement of heat flux 64
2.3.2 Origin of heavy impurities 64
2.3.3 Heat transmission rate to a floating plate in the scrape-off layer 66
2.4 Light impurities 67

3. Diagnostics 75
3.1 Time history method of electron temperature 75

3.2 Local counting efficiency of a Ceratron multiplier for plasma diagnoses on charge-exchanged fast atoms ... 78
3.3 Impurity estimation with K X-ray lines 80

III. OPERATION AND MAINTENANCE

1. Introduction 91
2. Operation and Maintenance of JFT-2 Tokamak 91
3. Operation and Maintenance of JFT-2a Tokamak 92
4. Development of Equipment and Instrument 92
5. Constant Plasma Current Operation 92

IV. DEVELOPMENT OF PLASMA HEATING SYSTEM

1. Introduction 100
2. Neutral Beam Injection System 100
   2.1 Ion source development 100
   2.2 Beam line studies 105
   2.3 Neutral beam injector for JFT-2 107
   2.4 Design study of the neutral beam injector for JT-60 ... 109
3. Radiofrequency Heating System 132
   3.1 Characteristics of lower hybrid wave in JFT-2 plasma ... 132
   3.2 Radiofrequency heating system for JFT-2 133
   3.3 Design study of radiofrequency heating system for JT-60. 135

V. SURFACE SCIENCE AND VACUUM TECHNOLOGY

1. Introduction 144
2. Interaction of Energetic Particles with Wall Materials 145
   2.1 Experimental facility 145
   2.2 Sputtering by hydrogen 147
   2.3 Blistering and grain ejection by helium and hydrogen .. 149
3. Vacuum Science and Technology for Fusion Device 151

VI. SUPERCONDUCTING MAGNETIC DEVELOPMENT

1. Introduction 162

2. Design of Cluster Test Apparatus 162

3. Development of Three Dimensional Stress Analysis for Toroidal Coil 164

4. Development of Large Current Superconductors 165

VII. REACTOR DESIGN STUDY

1. Introduction 178

2. General Description of the First Preliminary Design of the JAERI Experimental Fusion Reactor (JXFR) 178

3. Design Studies for JXFR 182

3.1 Plasma characteristics 182

3.2 Blanket and shield neutronics 184

3.3 Reactor structure 186

3.4 Major components 187

3.5 Major systems 189

4. Design Related Studies 199

4.1 Effects of neutron streaming through injection ports on neutronic characteristics of a fusion reactor 199

4.2 Neutronics design of fusion reactors and application of blanket neutronics experiment to the design 199

5. Design Study of a Power Reactor 199

6. Safety Analysis 200

VIII. DEVELOPMENT OF A LARGE TOKAMAK --- JT-60

1. Introduction 202

2. Outline of the Progress in JT-60 Program 202

3. Design of Machine 209

3.1 Review of machine design 209

3.1.1 System design 209

3.1.2 Vacuum vessel and its auxiliary components 209

3.1.3 Toroidal field coils 212

3.1.4 Poloidal field coils 214

3.1.5 Primary cooling system 216

3.1.6 Support structures 217

3.1.7 Fast movable limiter 217
3.2 Development of components 220
3.2.1 Vacuum vessel 220
3.2.2 Toroidal field coils 225
3.2.3 Poloidal field coils 228
3.2.4 Fast movable limiter 231

4. Design of Power Supplies 241
4.1 Review of power supply deisgn 241
4.1.1 Toroidal field power supply 241
4.1.2 Poloidal field power supply with vacuum circuit breakers 241
4.1.3 Poloidal field power supply with thyristor circuit breakers 243
4.1.4 Power supply for supplementary heating systems ... 243
4.2 Development of high current circuit breakers 245
4.2.1 Development of vacuum circuit breakers and related engineering studies 245
4.2.2 Development of thyrister circuit breakers and related engineering studies 247
4.3 Studies related to the design of power supplies 252
4.3.1 Analysis of high frequency transient voltage oscillations in the poloidal field coils 252
4.3.2 Three-dimensional analysis of eddy currents 252
4.3.3 Design of inductive energy storage coils 252
4.3.4 Circuit analysis of poloidal field power supply .. 253
4.3.5 Computer design of trigger gap shapes 253
4.3.6 Some considerations on multistage inductive energy storage systems 254
4.3.7 Design of vertical field excitation circuit 255
4.3.8 Studies of interaction between the poloidal field coils and the plasma 255

5. Design of Control and Diagnostic Systems 259
5.1 Review of control system design 259
5.1.1 System design 259
5.1.2 Plasma position and shape control 263
5.2 Planning of diagnostic system 274

6. Design of Auxiliary Systems 281
6.1 Review of auxiliary systems design 281
6.1.1 Vacuum pumping system 281
6.1.2 Secondary cooling system 281
6.1.3 Power distribution system 282
6.1.4 Gas supply system 282
6.1.5 Preionization system 283

7. Studies on Plasma Physics and Elementary Processes Relevant to JT-60 Program 285
7.1 Studies related to magnetohydrodynamic behaviors 285
7.1.1 Plasma equilibria during the current build-up with dynamic magnetic limiter 285
7.1.2 Positional instabilities in a tokamak with magnetic limiter 285
7.1.3 Computer code for determination of poloidal field coil positions 286
7.2 Studies related to particle and energy balances 288
7.2.1 Breakdown processes of toroidal discharges 288
7.2.2 Effect of minor-radius expansion in the current build-up phase 289
7.2.3 Impurity analysis 289
7.2.4 Studies of neutral beam injection heating 291
7.3 Experimental studies of surface-related problems 293
7.3.1 Outgassing rates of first wall materials 293
7.3.2 Cleaning of molybdenum surfaces by chemical treatment 293
7.3.3 Surface damage energetic ion bombardment 294

IX. DEVELOPMENT OF A NONCIRCULAR TOKAMAK --- JT-4

1. Introduction 299

2. Purposes and Schedule 299

3. Design of JT-4 302
3.1 Development of noncircular welded bellows 302
3.2 Development of TF coil joints 303
3.3 Experiments on in-situ coating of molibdenum 304
3.4 Experiments on Ti-getter pump 305
3.5 Design study of poloidal field system 306

4. Plasma Physical Studies Relevant to JT-4 Program 313
4.1 Study on the positional instability of JT-4 plasma ... 313
4.2 Behavior of particles near the separatrix magnetic surface 313
4.3 Destruction of magnetic surfaces in a divertor region attributed to a discrete structure of magnetic coils .. 314

APPENDIXES

A1. Publication List 318
A1.1 List of JAERI-M Report 318
A1.2 List of Papers Published in Journals 322
A1.3 List of Papers Published in Conference Proceedings ... 324
A2. Personnel of the Divisions 326
A2.1 Number of the Staff of the Divisions 326
A2.2 List of Scientific Staffs and Officers 327
A3. Budget of the Divisions 334

目　　次

まえがき…… 1
Ⅰ 理論および計算…… 1
1 はじめに…… 1
2 MHD安定性…… 3
2.1 有限要素法による2次元MHD安定性解析…… 3
2.2 初期値問題としての2次元MHD安定性解析…… 3
2.3 テァリング不安定性の数値計算…… 7
3 輸送現象および不純物の問題…… 9
3.1 トカマクにおける径方向平衡電場…… 9
3.2 不純物イオン輸送に対する温度勾配効果…… 9
3.3 トカマクにおける不純物密度の時間変化の数値計算…… 9
3.4 散逸型不純物ドリフト不安定性…… 10
3.5 散逸型捕捉粒子不安定性の非線形飽和と異常輸送現象…… 10
3.6 トカマクにおける放電開始条件の解析…… 10
3.7 トカマク放電の初期段階の計算機シミュレーション…… 11
4 加　熱…… 13
4.1 トカマクにおける低減混合波共鳴加熱の理論的研究…… 13
4.2 低域混合波の伝播…… 13
4.3 イオン・サイクロトロン高周波近傍の静電波による統計加速…… 14
5 数値解析および計算…… 16
5.1 トカマク・プラズマの輸送現象の2次元解析…… 16
5.2 ダイバータ付トカマクにおけるプラズマ閉じ込めの計算機シミュレーション…… 17
5.3 大型一般固有値問題の新しい遂次近似解法…… 17
5.4 電離および再結合項を含む不純物拡散方程式の解法…… 18
5.5 OLYMPUSシステムの導入とプリ・プロセッサの開発…… 18
5.6 OLYMPUSシステムのプリ・プロセッサ…… 18
5.7 REDUCE－2の核融合計算への応用…… 19
Ⅱ プラズマ実験…… 24
1 JFT－2…… 24
1.1 はじめに…… 24
1.2 トロイダル磁場18kGの閉込め実験…… 26
1.2.1 不純物についての結果…… 26
1.2.2 粒子バランス…… 27
1.2.3 密度揺動…… 28
1.2.4 シミュレーション…… 30
1.2.5 Z_{eff}分布…… 30

1.2.6 軟X線による温度分布…… 32
1.2.7 放射損失分布…… 33
1.3 中性粒子入射実験…… 44
1.4 トピックス…… 48
1.4.1 高密度放電…… 48
1.4.2 プラズマ周囲の分圧測定…… 48
1.4.3 JFT－2での気体の破壊…… 49
1.4.4 不純物と加熱を目的としたJFT－2改造…… 53
2 JFT-2a (DIVA) …… 62
2.1 はじめに…… 62
2.2 輻射損失…… 63
2.3 重元素不純物…… 63
2.3.1 熱束の2次元測定…… 64
2.3.2 重元素不純物の源…… 64
2.3.3 スクレイプ層中の板への熱伝達率…… 66
2.4 軽元素不純物…… 67
3 診　　断…… 75
3.1 スペクトル線時間経過法による電子温度…… 75
3.2 荷電交換高速粒子計測のためのセラトロン増倍管の局所計数効率…… 78
3.3 K－X線を用いた不純物評価…… 80
Ⅲ 装置の運転・保守と技術開発…… 91
1 はじめに…… 91
2 JFT－2の運転と保守…… 91
3 JFT－2aの運転と保守…… 91
4 装置の技術開発…… 92
5 プラズマ電流の定電流化…… 92
Ⅳ プラズマ加熱装置の開発研究…… 100
1 はじめに…… 100
2 中性粒子入射加熱装置…… 100
2.1 イオン源の開発…… 100
2.2 ビームライン系の研究…… 105
2.3 JFT－2用中性粒子入射加熱装置…… 107
2.4 JT－60用中性粒子入射加熱装置の設計研究…… 109
3 高周波加熱装置…… 132
3.1 JFT－2プラズマの低域ハイブリッド波の特性…… 132
3.2 JFT－2用高周波加熱装置…… 133
3.3 JT－60用高周波加熱装置の設計研究…… 135

Ⅴ 表面科学と真空工学…… 144
1 はじめに…… 144
2 壁材料とエネルギー粒子の相互作用…… 145
2.1 実験装置…… 145
2.2 水素によるスパッタリング…… 157
2.3 ヘリウム及び水素によるブリスタリングと結晶粒子放出…… 151
3 核融合装置における真空工学…… 151
Ⅵ 超電導磁石開発…… 162
1 はじめに…… 162
2 クラスター・テスト装置の設計…… 162
3 トロイダル・コイルの3次元応力解析コードの開発…… 164
4 大電流超電導体の開発…… 165
Ⅶ 核融合炉の設計研究…… 178
1 はじめに…… 178
2 核融合実験炉（JXFR）第1次予備設計の概要…… 178
3 JXERの設計研究…… 182
3.1 プラズマ特性…… 182
3.2 ブランケットと遮蔽の核特性…… 184
3.3 炉構造…… 186
3.4 主要コンポーネント…… 187
3.5 主要システム…… 189
4 設計に関連した研究…… 199
4.1 中性粒子入射孔からの中性子ストリーミング効果…… 199
4.2 炉の核設計とブランケット炉物理実験の核設計への応力…… 199
5 動力炉の設計研究…… 199
6 安全性解析…… 200
Ⅷ 大型トカマク装置の開発……JT−60…… 202
1 はじめに…… 202
2 JT−60計画の概況…… 202
3 本体の設計…… 209
3.1 本体設計概要…… 209
3.1.1 システム設計…… 209
3.1.2 真空容器およびその付属機器…… 209
3.1.3 トロイダル磁場コイル…… 212
3.1.4 ポロイダル磁場コイル…… 214
3.1.5 一次冷却系…… 216
3.1.6 架台…… 217
3.1.7 高速可動リミタ…… 217

3.2 各構成機器の試作開発…… 220
3.2.1 真空容器…… 220
3.2.2 トロイダル磁場コイル…… 225
3.2.3 ポロイダル磁場コイル…… 228
3.2.4 高速可動リミタ…… 231
4 電源設計…… 241
4.1 電源設計の概要…… 241
4.1.1 トロイダル磁場電源…… 241
4.1.2 真空しゃ断器を用いたポロイダル磁場電源…… 241
4.1.3 サイリスタしゃ断器を用いたポロイダル磁場電源…… 243
4.1.4 第二段加熱設備用電源…… 243
4.2 大電流直流しゃ断器の開発…… 245
4.2.1 真空しゃ断器の開発と関連検討…… 245
4.2.2 サイリスタしゃ断器の関連検討…… 247
4.3 電源設計に関連した諸検討…… 252
4.3.1 ポロイダル磁場コイル中の過渡電圧振動解析…… 252
4.3.2 3次元電源解析…… 252
4.3.3 誘導性エネルギー蓄積コイルの設計…… 252
4.3.4 ポロイダル磁場コイル電源の回路解析…… 253
4.3.5 計算機によるトリガーギャップ電極形状の決定…… 253
4.3.6 誘導性エネルギーによる電源システムの検討…… 254
4.3.7 垂直磁場コイル電流励起用電源回路の設計…… 255
4.3.8 ポロイダル磁場コイルとプラズマの相互作用に関する検討…… 255
5 制御系および計測系の設計…… 259
5.1 制御系の設計概要…… 259
5.1.1 システム設計…… 259
5.1.2 プラズマ位置形状制御…… 263
5.2 計測系の計画…… 274
6 付属設備の設計…… 281
6.1 付属設備の設計概要…… 281
6.1.1 真空排気系…… 281
6.1.2 二次冷却系…… 281
6.1.3 配電系…… 282
6.1.4 ガス導入系…… 282
6.1.5 予備電離系…… 283
7 JT-60に関するプラズマ物理と素過程の研究…… 285
7.1 磁気流体力学的研究…… 285
7.1.1 可動磁気リミタを使った電流立上げ時のプラズマ平衡…… 285

7.1.2 磁気リミタ付トカマクの位置不安定性…… 285
7.1.3 ポロイダル磁場コイルの位置決定用計算機コード…… 286
7.2 粒子・エネルギーバランスに関する研究…… 288
7.2.1 トロイダル放電の形成過程…… 288
7.2.2 プラズマ電流立上げ過程におけるプラズマ副半径膨張効果…… 289
7.2.3 不純物解析…… 289
7.2.4 中性粒子入射加熱の検討…… 291
7.3 プラズマー壁面相互作用に関連した基礎実験…… 293
7.3.1 第1壁材料の放出ガス量…… 293
7.3.2 ガスによるモリブデンの化学的表面処理 …… 293
7.3.3 高エネルギーイオン照射による表面損傷…… 294
K 非円形断面トーラス試験装置（JT−4）の設計研究…… 299
1 はじめに…… 299
2 研究目標と計画…… 299
3 JT−4の装置設計…… 302
3.1 非円形溶接ベローズの開発…… 302
3.2 分割型トロイダル磁場コイル接続部の開発…… 303
3.3 装置内モリブデン蒸着法の実験 …… 304
3.4 Ti ゲッターポンプの実験…… 305
3.5 ポロイダル磁場系の設計検討…… 306
4 JT−4計画の科学的検討…… 313
4.1 JT−4プラズマの位置不安定性の検討…… 313
4.2 セパラトリックス磁気面付近における粒子のふるまい…… 313
4.3 磁場コイルの不連続性による磁気面の破壊…… 314

Preface

A brief summary of activities in the fiscal year 1976, ending March 1977, is as follows.[1]

JT-60: Development and tests of the major components of JT-60, and integrated pre-construction design were finished; these tasks were performed by Japanese five major nuclear industry groups under the contracts with JAERI. For the tests, some components in full scale were manufactured; e.g. a full scale sector of the vacuum chamber and the toroidal coil. Thus we were fully prepared for the construction of JF-60. As a first step of JT-60 construction, a contract for manufacturing the whole toroidal coils will be made in late 1977.

JT-4: It is a tokamak with non-circular cross section and divertors, to study high beta limit and impurity control of a tokamak. Its preliminary design had been finished in FY 1975. On the basis of the design, necessary component tests were performed in this fiscal year; such as a joint section in toroidal coil windings and non-circular bellows of the vacuum chamber.

JFT-2: Density was controlled by a puff technology. As a engineering test, two neutral beams of 25∿30 kV and 6-8 A equivalent was injected almost perpendicularly to the toroidal axis (85°). The temperature increase of ions was 10-15 % and was in agreement with a theoretical calculation.

JFT-2a (DIVA): Reduction of metal impurities by the divertor and screening effect of scape-off layer were studied. In order to install new toroidal coils, capable of producing 20 kG, and to remodel a control system of a power supply for its alternate use of JFT-2 and 2a, they were shut down in December 1976 for four months.

Surface Study: Two new ion accelerators went into full operation from the begining of this fiscal year. Sputtering yield of 0.1-6 keV regime and effect of honey comb structure were measured.

Superconducting Magnet: A new activity of this important technology was begun at March 1976. A preliminary design study and planing of the

(1) The preceding annual reports are JAERI-M 4654 (FY 1970), 5029, 5564, 5888, 6359 and 6926 (FY 1975).

development were performed with emphasis on SC toroidal coils in a D-T burning tokamak (Mock Up Test Facility), next to the JT-60.

Reactor Design Study: A phase-I preliminary design of EPR was completed and its safety was studied.

At June 1, 1976 the Large Tokamak Laboratory became a new Division of Large Tokamak Development. (S. Mori)

I. PLASMA THEORY AND COMPUTATION

1. Introduction

We have continued theoretical and computational studies on tokamak confinement and heating in close connection with experimental programs. Throughout the period under review computational efforts have been steadily increasing.

Numerical calculation of the nonlinear evolution of tearing instability revealed the formation of magnetic islands, whose saturated width amounts to about 20% of the column radius, and flattening of current profile inside the $q = 1$ surface. A two-dimensional MHD stability code by finite element method was rewritten using the cylindrical coordinates system in order to avoid the singular behavior of the Jacobian near the magnetic axis. Complication in the matrix element calculation was settled by use of REDUCE-2 (a symbol manipulating language). Another code, which solves 2D stability as an initial value problem, is modified also by using this language to take account of higher order terms in equilibrium solution.

We have made a study on the LHRH of the JT-60 plasma in collaboration with Kyoto University. By taking account of the toroidal curvature we found a strong damping of hot plasma waves (ion Bernstein waves) takes place at resonant layers corresponding to the ion cyclotron harmonics. Parametric decay process of LHW for the pump of finite wavelength was studied. Also we made a simulation of stochastic acceleration of ions by electrostatic waves near the ion cyclotron harmonics. A good agreement with theoretical prediction was obtained on the formation of high energy tail of ion distribution function. A two-fluids code has been applied to the propagation of LHW in slab geometry. Study on NBI heating in JT-60, which had been pursued during preceding years, was completed. The computer codes so far developed was handed over to the JT-60 group.

As for the transport process in tokamak we reexamined impurity transport in the presence of radial electric field by taking account of temperature gradient. Strong temperature equilibration between ions nullifies the term proportional to ∇T in the expression of the diffusion flux of light impurity ions. While heavy impurity ions are inhibited to penetrate deep into the plasma even when $d\log T/d\log n > 0$. We also studied in some detail dissipative impurity drift instabilities. Nonlinear saturation of dissipative trapped ion instability was considered by taking account of

the effect of turbulent collisions, which is evaluated by retaining dominant terms in the perturbation series. Numerical evaluation yielded the diffusion coefficient in agreement with the estimate due to Kadomtsev and Pogutse.

A preliminary version of 2D tokamak transport code has been written on the basis of the Grad-Hogan model. Application of particle codes has been made on 2D simulation of the plasma in the scrape-off layer of JFT-2a, and of the breakdown process in the JFT-2 discharge. A collision model described in the previous annual report was applied to estimate the width of the scrape-off layer. Computation yielded the width in agreement with the neoclassical theory (Diffusion coefficient obtained in the experiment, however, is about 1/10 of the Bohm). The code for the breakdown process was completed on the basis of electromagnetic PIC (particle in cell) method, guiding center motion, and various atomic processes. Preliminary computation was made using a simplified model, i.e. assuming an extremely strong toroidal magnetic field (inhibition of the cross-field motion), which yields the breakdown threshold similar to that obtained in the experiment if one chose an appropriate electron multiplication factor at a prescribed instant after the application of accelerating electric field.

We had developed a preprocessor to make easier access to the Olympus System which was installed in the JAERI computer system in 1974 through the courtesy of Prof. K. V. Roberts of Culham Laboratory. Also we have conveniently made use of HLISP REDUCE provided by the courtesy of Prof. E. Goto of the University of Tokyo.

2. MHD Stability

2.1 Two-dimensional MHD stability analysis by the finite element method

Two dimensional stability analysis codes by the variational method are developed by Grimm et al.[1],[2] and Gruber et al.[3],[4] and successfully used to analyze MHD behaviours of toroidal plasmas. Grimm et al. used the mixed Fourier-finite element method, and Gruber et al. used the fully two-dimensional finite element method in a poloidal plane. Both of them adopted a nonorthogonal coordinate system (ψ,θ,ϕ), where ψ,θ, and ϕ are the flux function, azimuthal coordinate, and toroidal one, respectively.

We have also developed a two-dimensional code of the same kind. In our code we adopted the cylindrical coordinate system (R,Z,ϕ) instead of the above mentioned nonorthogonal coordinate system. In the above nonorthogonal coordinate system there are singularities at stagnation points of a poloidal magnetic field (at the points where $\Delta\psi = 0$), whereas we have no singularities. Therefore, our choice of the coordinate system will make it easier to analyze the stability of multi-magnetic-axis configurations such as the doublet equilibria.

By using our code we calculated the stability of a fixed boundary cylindrical plasma in order to study the features of our numerical model. Figure I.2.1-1 shows the calculated growth rates. The small circles(o) are the growth rates obtained by Takeda et al.[5], by using the one dimensional code. Though they are smaller than our results for the $m = 2$ mode, it can be explained by the inadequate choice of the basis functions in the one-dimensional code[3]. The triangles are the growth rates obtained by Kurita and Amano[6] by solving an initial value problem. Our results agree with their results very well.

2.2 Two-dimensional MHD stability analysis as an initial-boundary problem

The growth rate and eigen-function of the MHD instability of a toroidal plasma are calculated numerically as an initial-boundary problem[6],[7].

The results are summarized as follows: when the conducting shell is placed far from the plasma, toroidicity scarcely effects the growth rate of external kink modes for a slender tokamak, but it stabilizes the modes for a fat tokamak, on the other hand when the shell is placed near the plasma, unstable external modes are stabilized by both the toroidicity and effect of the shell (Figs. I.2.2-1 and -2).

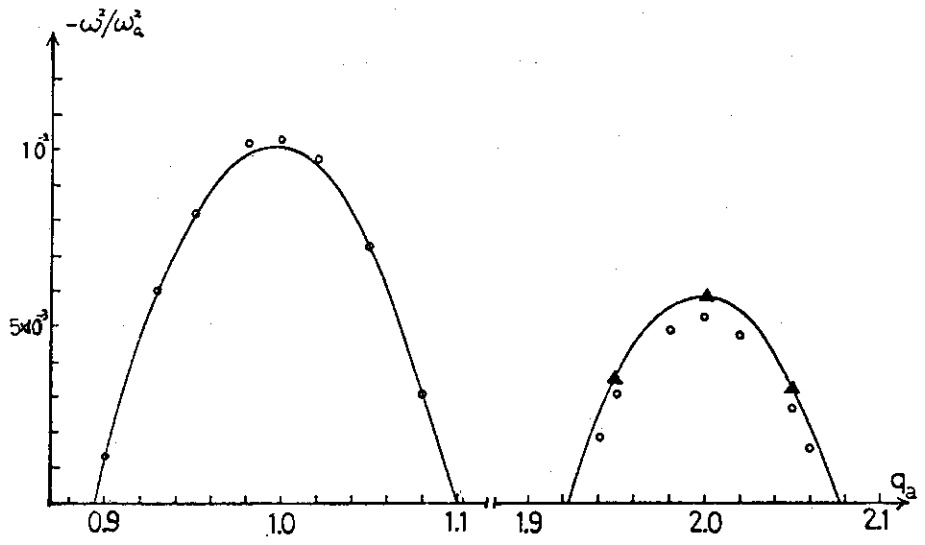

Fig.I.2.1-1 Growth rates of a fixed boundary cylindrical plasma Solid lines denote the results of the two dimensional code. Circles and triangles show the results of Takeda et al.[5] and Kurita and Amano[6], respectively.

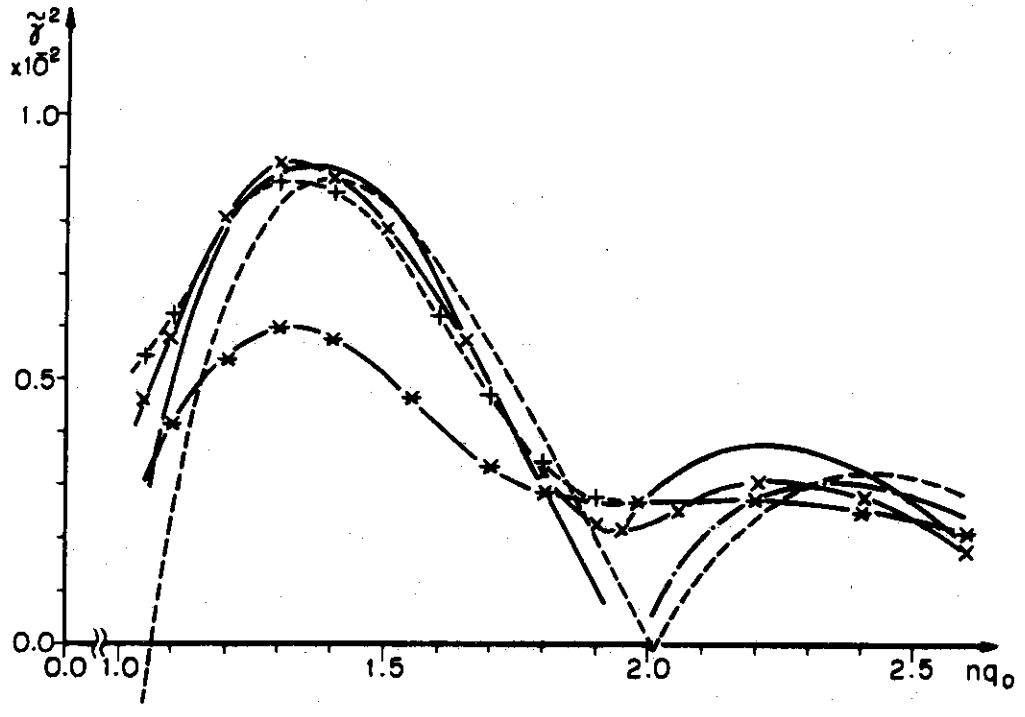

Fig.I.2.2-1 Normalized growth rate versus safety factor at magnetic axis (r=0) multiplied by toroidal wave number n. Solid dotted and dotted solid lines with no mark are the growth rate in cylindrical case and other curves show toroidal one, in which the solid curve with mark x, the dotted curve with mark + and the solid curve with mark * denote the cases of ε^{-1}=15, ε^{-1}=10 and ε^{-1}=5, respectively, for β_p=1, b=2a and uniform current distribution.

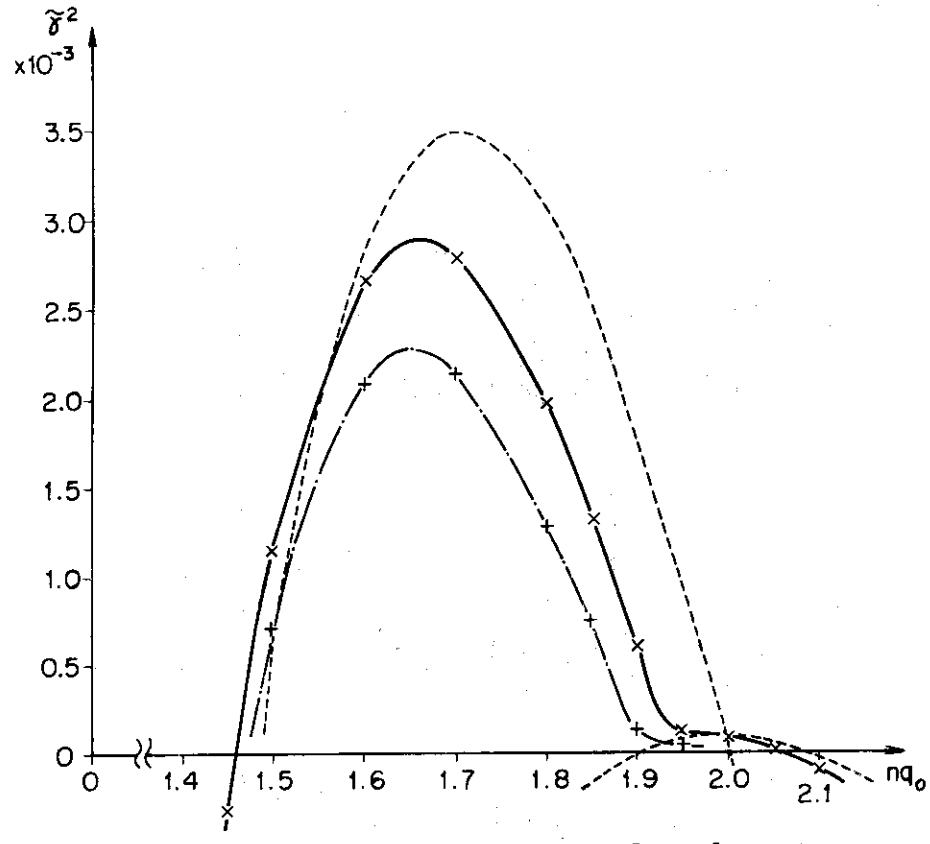

Fig.I.2.2-2 Normalized growth rate versus safety factor at magnetic axis (r=0) multiplied by toroidal wave number n. Dotted lines show cylindrical growth rate and other curves show toroidal one, in which solid curve with mark x, dotted curve with mark + and solid curve with mark * denote the cases of ε^{-1}=15, ε^{-1}=10 and ε^{-1}=7, respectively, for β_p=1, b=2a and uniform current distribution.

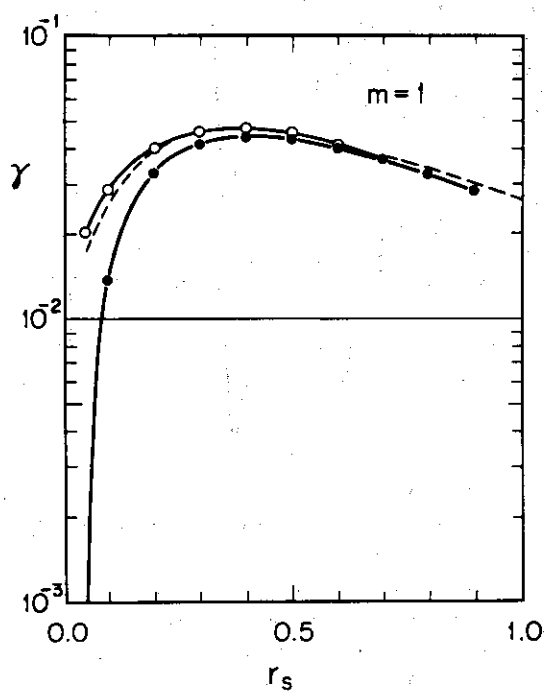

Fig.I.2.3-1 Linear growth rates of m=1,2 resistive modes for s=10^5 and a peaked current profile. Here r_s denotes the position of singular surface. ●—● for $\tilde{\eta}=0$, ○—○ $d\tilde{\eta}/dt=0$, Dotted lines show the growth rates predicted by theory.

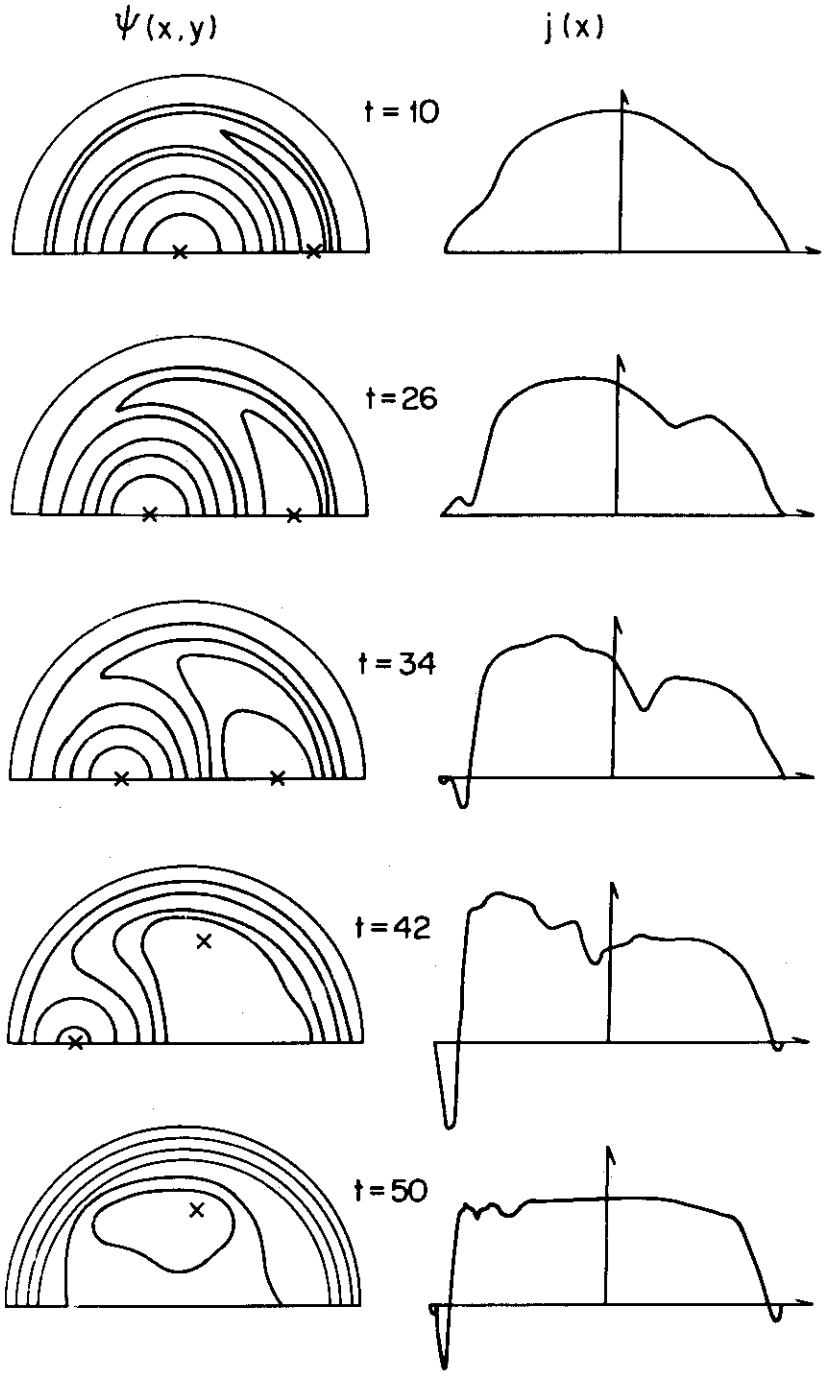

Fig.I.2.3-2 Temporal variations of flux surface ($\psi(x,y) = \text{const}$) and current profile ($j(x)$) due to the unstable resistive internal mode. Initially the current profile is parabolic and $q = 1$ surface locates at $r = 0.75$. After $50\tau_{pA}$ (poloidal Alfven time), the current density becomes nearly uniform within the initial $q = 1$ surface, and the field configuration remains almost unchanged.

2.3 Numerical study of tearing instability[8]

Resistive instabilities play an important role in the confinement of a tokamak plasma because of the magnetic island formation and the resultant enhancement of the cross-field diffusion of the plasma. Presently it is widely believed that they provide a probable mechanism for disruptive instability[9] as well as the anomalous penetration of the skin current[10].

We have studied linear and nonlinear evolutions of resistive modes on the basis of a simplified set of MHD equations. In the lowest order of small parameters β, B_p/B_t, and ka/m, we obtain simultaneous equations for flux function ψ, stream function ϕ, and resistivity. After expanding these variables into the Fourier harmonics, the equations are integrated by the predictor-corrector method. This method of solution has several advantages, especially we can chose a rather long time step by ignoring higher harmonics near the magnetic axis.

Brief summary of the computational results is given below.

1) linear growth: The growth rates of $m = 2$ and 3 modes are in good agreement with theoretical prediction for large S(ratio of poloidal Alfven time to skin time) and large r_s (position of singular surface). When the singular surface falls near the magnetic axis deviation from the theoretical values becomes significant even for large S, and tearing modes become stable near the magnetic axis in contrast with theory. The perturbation of the resistivity due to convection is destabilizing, i.e. the growth rate increases and unstable region widens. For $m = 1$ internal mode the growth rate agrees well with theory and also the effect of convective perturbation is insignificant except close to the axis.

2) nonlinear evolution: For $m = 2$ we observed that the magnetic island of $m = 2$ grows in proportion to the time after the initial exponential growth. The saturation amplitude of the island width is about 0.2 a when $\tilde{\eta} = 0$ is assumed, $\tilde{\eta}$ being the perturbation of the resistivity. The resistive internal mode continues rapid exponential growth untill a flat current profile is realized within the $q = 1$ surface. During this period reverse current flows just outside the layer where the field reconnection takes place. This current decays as the instability saturates. The saturation takes place after the time about 50 times the poloidal Alfven time, and the kinetic energy is about 10^{-3} times the magnetic energy of the poloidal field.

More detailed study is in progress.

References

(1) Grimm R.C. and Johnson J.L.: "Recent developments in the computational aspects of mhd stability" in Computing in Plasma Physics and Astrophysics p.45 (North-Holland Publishing Co., N.Y., 1977).

(2) Grimm R.C., Greene J.M. and Johnson J.L.: "Computation of the magnetohydrodynamic spectrum in axisymmetric toroidal confinement systems" in Methods in Computational Physics vol.16, p.253 (Academic Press, N.Y., 1976).

(3) Gruber R.: "Numerical computations of the magnetohydrodynamic spectrum for one and two dimensional equilibria using regular finite elements and finite hybrid elements", These no.249, Ecole Polytechnique Federale de Lausanne (1976).

(4) Berger D., Gruber R. and Troyon F.: "A two-dimensional mhd stability code with a finite hybrid expansion in both direction" in Computing in Plasma Physics and Astrophysics, Proceedings of the 2nd European Conference on Computational Plasma Physics, April 27-30, 1976, Garching, IPP 6/147.

(5) Takeda T., Shimomura Y., Ohta M. and Yoshikawa M.: Phys. Fluids 15 (1972) 2193.

(6) Kurita G. and Amano T.: "Two-dimensional simulation of the MHD stability (I)" JAERI-M 6474 (1976).

(7) Kurita G. and Amano T.: "Two-dimensional simulation of the MHD stability (II)" JAERI-M 7310 (1977).

(8) Azumi M.: "Nonlinear evolution of tearing modes in a tokamak" unpublished. Azumi M.: in preparation.

(9) Kadomtsev B.B.: Fiz. Plsamy 5 (1975) 710.

(10) Stix T.H.: Phys. Rev. Letters 36 (1976) 521.

3. Transport and Impurity

3.1 Equilibrium radial electric field in a tokamak

Effects of the equilibrium ion temperature gradient and the perturbation of the ion temperature were considered on the decay of poloidal rotation and equilibrium radial electric field in the MHD regime[1].

The temperature gradient does not influence the value of the decay time,

$$\tau_{MHD} = 0.39 \frac{R^2}{v_{Ti}^2 \tau_i} ,$$

where $v_{Ti} = \sqrt{T_i/m_i}$ is the ion thermal velocity and τ_i the ion-ion collision time by Braginskii.

3.2 Temperature gradient effect on impurity-ion transport[2]

Effects of temperature gradient on the impurity transport are considered in MHD regime, taking account of the effects of the inertia of impurity ion and temperature equipartition between ions.

For light impurities, the temperature equipartition effect nullifies the temperature screening term.

The diffusion flux of heavy impurities largely varied in considering the ion inertia. When the host ion has a long mean free path, the impurity diffusion flux is outward when $\eta = d\,\ell n\, T_i / d\,\ell n\, n_i > 0$ with T_i the ion temperature and n_i the ion density.

3.3 Numerical investigation of the time evolution of impurity concentration in a tokamak[3]

Numerical analysis has been made of the time evolution in density profiles of the impurities in a Tokamak. The diffusion and atomic processes of impurities are treated simultaneously. Two different numerical methods were used; the results are in good agreement between the two. Calculations are made in the case of a constant spatial distribution of the plasma. The impurity concentration in the plasma is revealed. The procedure may be useful for analysis of the time evolution of a Tokamak plasma in computer simulation and for the analysis of the impurities by optical measurement.

3.4 Impurity drift instability of dissipative type[4]

A new type of impurity drift instability is studied in the limit of short mean free path. The mode is driven by the ion parallel viscosity, and is stabilized by the collisional diffusion across the magnetic field when the impurity concentration is less than a certain value. This condition is also applied for the collisionless impurity drift mode.

3.5 Nonlinear saturation of dissipative trapped ion instability and anomalous transport[5]

An expression for the turbulent collision frequency is derived by summing up the most dominant terms from each order in the perturbation expansion in order to obtain the nonlinear saturation level of the dissipative trapped ion instability. Numerical calculation shows that the anomalous diffusion coefficient at the saturated state is in good agreement with the result of Kadomtsev and Pogutse when the effect of the magnetic shear is taken into account.

3.6 Analysis of the breakdown threshold in a tokamak discharge[6]

The initial phase of tokamak discharge was investigated by numerical calculations, and the breakdown threshold was obtained by a simple analysis Papoular made an analysis in a zero-dimensional geometry by introducing some particle loss mechanisms, and obtained fair agreement with TFR's data.[7] He applied Townsend's first coefficient proportional to the filling pressure. This is inappropriate, however, when $p \geq 2\times10^{-4}$ torr and $E \leq 0.05$ V/cm ($\simeq$30 V/turn in TFR). Further Townsend's coefficient in the high E/p is not authorized.

In the present calculation the electronic cross-sections are directly used to compute the time evolution of the electron density n, mean velocity v and mean energy w in a one-dimensional geometry. Particle losses are neglected in this simple analysis. Figure I.3.6-1a shows the breakdown threshold, in which, we assume tentatively, n becomes 10^3 times the initial electron density during 500 μsec. This time τ_0 is determined by the duration of the external circuit. From the results of numerical calculation one can approximate the ionization frequency as

$$\nu \propto w^2 \qquad \text{for} \quad w \leq 13.6 \text{ eV},$$
$$\nu \propto w^{-1/2} \log (w/80) \qquad \text{for} \quad w \geq 200 \text{ eV}.$$

It is noted that ν becomes small in the high energy region with the increase in w.

Taking account of particle losses due to the toroidal drift (life time for a particle of 13.6 eV is denoted by τ_T) and also due to the error field (life time for a particle with parallel velocity of 13.6 eV is τ_B), one can obtain the breakdown threshold in O-D geometry. It is approximately given by

$$n_{f\,min} \simeq 4\times10^{13}(\tau_o^{-1} + \tau_B^{-1} + 4\tau_T^{-1}) \quad m^{-3}$$

$$E_L \propto n_f^{1/2} \quad \text{for } n_f > 2.5\times10^{12}\ \tau_o(2\tau_o^{-1} + \tau_B^{-1} + 8\tau_T^{-1})^2\ m^{-3}$$

$$E_H/\ell nE_H \propto n_f \quad \text{for } \tau_o \ll \tau_B,\ \tau_T$$

where τ's are in second. This result agrees well with that of the numerical calculation (Fig. I.3.6-1a) and also with the experimental data in JFT-2 (Fig. I.3.6-1b)[7].

3.7 Computer simulation of the initial stage of tokamak discharge

A particle code has been developed to study the initial stage of tokamak discharge[8]. We assume initially a small number of seed electrons in a vessel filled with hydrogen molecules. Immediately after the application of an accelerating electric field the electrons begin to be accelerated along the vacuum toroidal magnetic field. The multiplication of the number of electrons takes place by the collisions with hydrogen atoms or molecules in parallel with the modification of the magnetic field due to the induced current. During these processes some of the electrons are guided to the wall and lost therein.

These phenomena are simulated by the use of a two-dimensional electromagnetic PIC (particle in cell) method. The effects of elastic and inelastic collisions are described by the Monte Carlo method.

Detailed analysis is now under way.

References

(1) Tuda T.: to be published. Detailed analysis in the banana regime was given in Tuda T., J. Phys. Soc. Japan, 39 (1975) 1358.

(2) Tuda T.: JAERI-M 6965 (1977) (in Japanese), also presented at the Third International Conference on Plasma Theory, (Apr. 4-9, 1977, Trieste, Italy).

(3) Amano T. and Okamoto M.: J. Phys. Soc. Japan 42 (1977) 1019.
(4) Tuda T. and Tanaka M.: J. Phys. Soc. Japan 43 (1977) 1407.
(5) Sugihara M. and Ogasawara M.: JAERI-M 7050, (1977).
(6) Takizuka T.: to be published in JAERI-M.
Takizuka T.: Hohden Kenkyu 69 (1977) 31 (in Japanese).
(7) Sometani T. et al.: ibid 69 (1977) 20 (in Japanese).
(8) Takizuka T.: to be published.

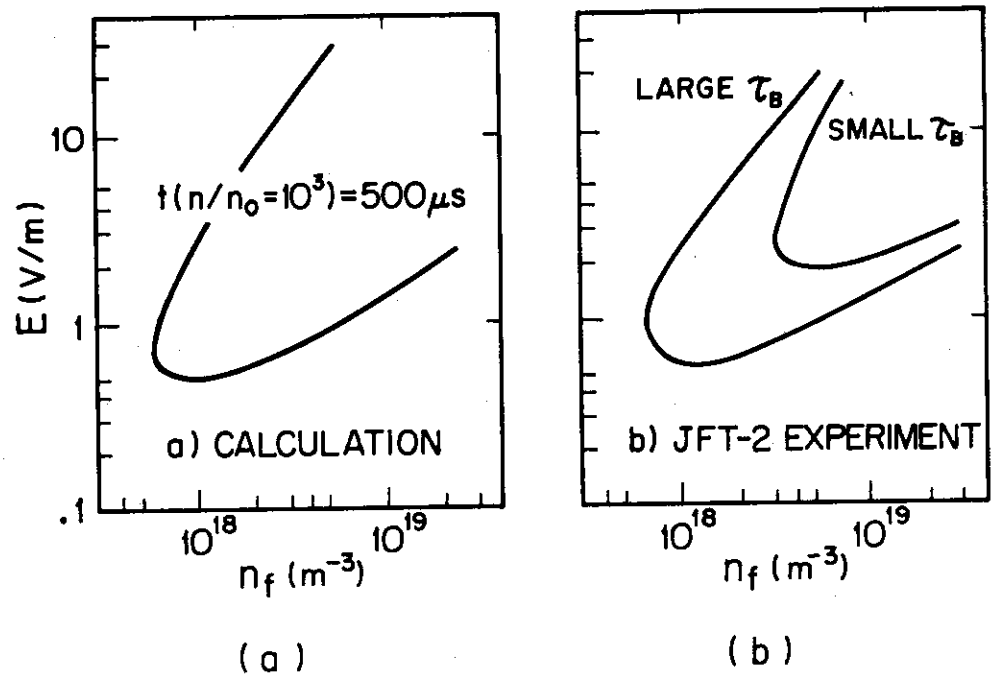

Fig.I.3.6-1 Breakdown threshold in JFT-2 obtained by numerical calculation (a) and by the experiment (b)

4. Heating

4.1 Theoretical investigations of lower hybrid resonance heating in a tokamak[1]

Theoretical investigations of the lower hybrid wave heating in a tokamak have been performed systematically. The requisite power for the supplementary heating of a large scale tokamak, JT-60, is estimated to be about 10 MW. Linear behaviour of an incident wave is extensively examined and its physical picture is clarified. The effect of toroidicity on propagation and dispersion of a lower hybrid wave is also studied. Parametric phenomena are treated without dipole approximation and the threshold in JT-60 is also examined. The formation of the high energy ion tail attributed to a high power wave is shown by theory and a good agreement with numerical calculation is obtained.

4.2 Propagation of lower hybrid wave

Lower hybrid resonance heating (LHRH) is one of the promising methods of supplementary heating of tokamaks. In order to investigate the lower hybrid wave propagation, a computer code based on the fluid model is developed[1]. The computer code solves the two-fluid equations for ions and electrons in the x-z plane, where the density varies in the x-direction and an external magnetic field is applied in the z-direction. A lower hybrid wave is excited at the boundary in the form; $\phi(x = x_L, z, t) = \phi_0 \cos(k_z z - \omega_0 t)$, where ω_0 is the lower hybrid frequency at a prescribed point inside the plasma (near the plasma center) and the parallel wave number k_z satisfies the accessibility condition. The excited wave propagates towards the center of the plasma and the ray trajectory forms a cone. An example of the lower hybrid cone is shown in Fig. I.4.2-1 for the case in the presence of a drift wave. Further investigations, which are in progress, are as follows;

1) to study and check the linear theory of the lower hybrid wave propagation.
2) to examine the nonlinear distortion of the cone due to the self-focussing.
3) to examine the nonlinear distortion of the cone in the presence of drift wave density fluctuations.

4.3 Stochastic acceleration by an electrostatic wave near ion cyclotron harmonics[3]

We studied a nonlinear effect on ion motion in an electrostatic wave propagating perpendicularly to a uniform magnetic field. When the wave near the ion cyclotron harmonics has sufficiently large amplitude, the trapped motion of hot ions ($v_\perp > \omega/k_\perp$) becomes stochastic in the region of appreciable width near the separatrix. Numerical calculation shows the formation of tail in the $v_\perp$ distribution function. The upper limit of accelerated ion energy agrees between theory and computation.

References

(1) Momota, H., Fukuyama, A., Azumi, M., Okamoto, M. and Takizuka, T.: JAERI-M 6964 (1972).

(2) Okamoto, M.: To be published.

(3) Fukuyama, A., Momota, H., Itatani, R. and Takizuka, T.: Phys. Rev. Letters 38 (1977) 701, see also Sect. 4.1.

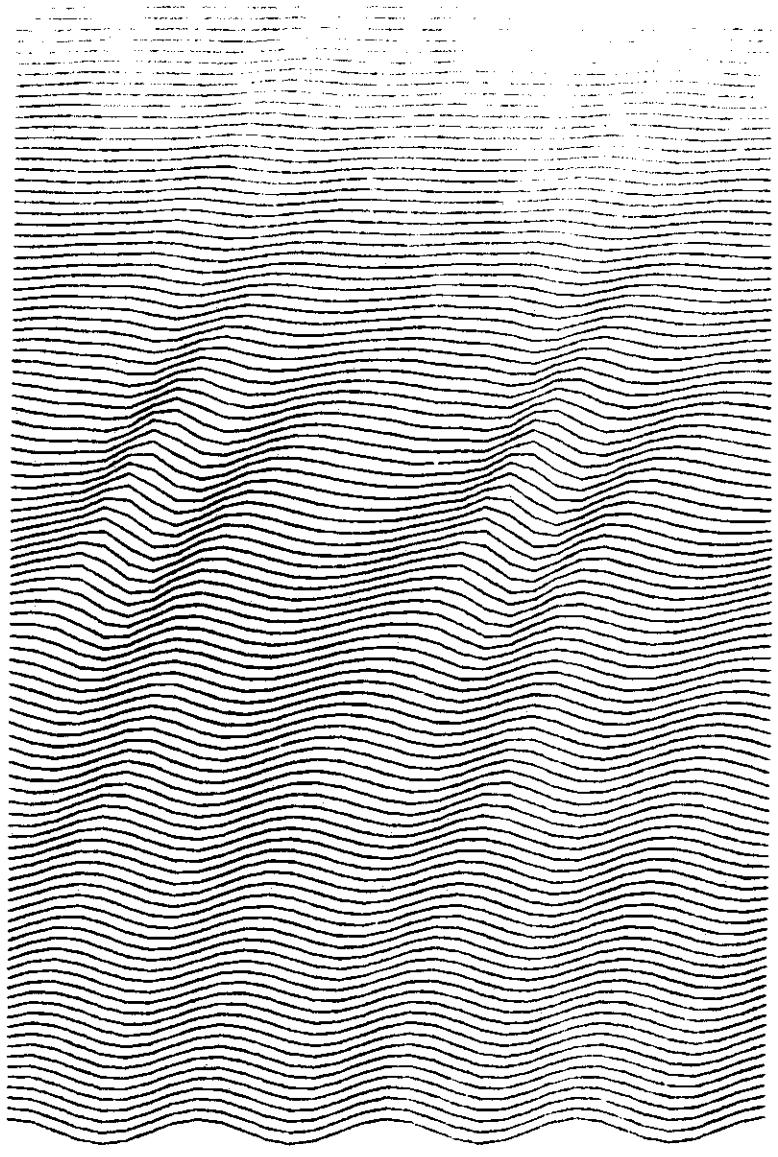

Fig.I.4.2-1 An example of lower hybrid cone obtained by the two-fluids simulation.

5. Numerical Analysis and Computing

5.1 Two-dimensional tokamak transport analysis

Many kinds of radial transport codes for tokamak plasma[1] were developed and used to analyze experimental data and to estimate plasma parameters when designing a new device. However it is needed to write a 2D (two-dimensional) transport code because an actual tokamak plasma is not cylindrical but toroidal and recently the analysis of tokamak transport of a noncircular cross-section becomes important as the high beta tokamak plasma is studied intensively.

One of the difficulties in 2D fluid model plasma simulation codes is the wide range of time scales appearing in solutions of the set of equations. Though the Alfven time, skin time, and diffusion time are concerned in the solutions of the equations, in our problem we are mainly interested in phenomena concerning the skin time and diffusion time. Therefore it is desirable to suppress phenomena of Alfven time scale and we chose the Grad-Hogan model[2] for the 2D simulation code. The equations based on this model consist of the 2D MHD equilibrium equation, 1D transport equations, and diffusion equations of the magnetic fields. Such 2D codes are being studied by several authors[3][4] but there are still many problems to be solved to operate the 2D transport codes successfully.

The basic idea of this model is to reduce the 2D time-dependent transport phenomena into a sequence of 2D equilibrium calculation and 1D transport calculation. Therefore, if the toroidal magnetic flux is time-independent (f = const.) the equations to be solved are given as follows,

$$\Delta^*\psi \equiv r\frac{\partial}{\partial r}\left(\frac{1}{r}\frac{\partial\psi}{\partial r}\right)+\frac{\partial^2\psi}{\partial z^2} = -f\frac{df}{d\psi} - \mu_o r^2\frac{dp}{d\psi} \tag{1}$$

$$\frac{\partial}{\partial t}\left(\frac{dv}{d\rho}\, n_e\right) + \frac{\partial}{\partial\rho}\left\{\frac{dv}{d\rho} < n_e(u-u_\rho)\cdot\nabla\rho>\right\} = (\text{source}), \tag{2}$$

$$\frac{3}{2}\frac{\partial}{\partial t}\left\{P_e\left(\frac{dv}{d\rho}\right)^{5/3}\right\} + \left(\frac{dv}{d\rho}\right)^{2/3}\frac{\partial}{\partial\rho}\left\{\left(\frac{dv}{d\rho}\right)\left[q_e+\frac{5}{2}T_e\Gamma_e\right]\right\}$$

$$= \left(\frac{dv}{d\rho}\right)^{5/3}\left\{-Q_i + \frac{<j\cdot\nabla\zeta><E_{11}\cdot B>}{f<\frac{1}{r^2}>} - \frac{\Gamma_e}{n_e}\frac{\partial P_i}{\partial\rho} + \mu_i T_i A_{1i}\right\}, \tag{3}$$

$$\frac{3}{2}\frac{\partial}{\partial t}\left\{P_i\left(\frac{dv}{d\rho}\right)^{5/3}\right\} + \left(\frac{dv}{d\rho}\right)^{2/3}\frac{\partial}{\partial\rho}\left\{\left(\frac{dv}{d\rho}\right)\left[q_i+\frac{5}{2}T_i\Gamma_i\right]\right\}$$

$$= \left(\frac{dv}{d\rho}\right)^{5/3}\left\{Q_i + \frac{\Gamma_i}{n_e}\frac{\partial P_i}{\partial\rho} - \mu_i T_i A_{1i}\right\}, \tag{4}$$

where n_e, p_e and p_i are electron density, electron pressure, and ion pressure, respectively, $V(\psi)$ is the volume within a flux surface ψ, ρ is the mean radius of the flux surface, and the functional dependence of transport quantities such as q_e are given theoretically[5].

The time-dependent equations (Eqs. 2-4) are integrated with respect to the shorter time step (Δt_s) whereas the equilibrium is calculated every longer time step (Δt_L) (Fig. I.5.1-1). The flow chart for the whole 2D transport code is presented in Fig. I.5.1-2. Presently coding is finished and test calculations are being carried out for equilibrium of a cylindrical plasma.

5.2 Computer simulation on plasma confinement in a divertor tokamak

The property of a collisional plasma near the separatrix in a tokamak with a poloidal divertor (e.g. JFT-2a) has been investigated by the use of a particle simulation[6]. The model is as follows:[7] i) two-dimensional cylindrical geometry, ii) electrostatic PIC method with a fixed magnetic field configuration, iii) guiding center approximation for particle motion, iv) the Monte Carlo method to describe the effect of binary collisions.[8]

We have carried out a simulation run with following parameters; $a = 0.23$ m, $B_z = (1+\varepsilon(r/a)\cos\theta)$ Wb/m^2, $\varepsilon = 0.38$, $r_s = 0.08$ m, $B_\theta/B_z|_{r_s} = 0.075$, $m_i/m_e = 100$ (m_i: real mass), $T_i = T_e = 100$ eV, $\lambda_D = 0.01$ m, and $\tau_{be} = 6$ μsec. The effects of binary collisions are artificially enhanced so that the collision time is comparable to the bounce time. Particles diffuse out across the magnetic field from the inner region of the separatrix to the outer region, and escape to the divertor along the field. It can be seen from Fig. I.5.2-1 that the loss of particles to the divertor is dominated by the ion behavior. The width of the scrape-off layer is approximately given by $\ell \simeq (D_\perp L/v_{Ti})^{1/2}$, where $L = 2\pi r_s B_z/B_\theta$. The neoclassical diffusion coefficient in the plateau regime gives $\ell \simeq 2$ mm. Figure I.5.2-2 shows the e-folding length of the density profile to be about 3.5 mm. We may conclude that reasonable results are obtained by the particle simulation on the plasma confinement in a divertor tokamak.

5.3 A new inerative method for a large-scale general eigenvalue problem[9]

A new method for solving a large-scale general eigenvalue problem is devised. In this method the general eigenvalue problem of matrices ($AX = \lambda BX$) is reduced to a standard one by introducing a new matrix $U_n^j = A - \lambda_n^j B$,

where λ_n^j is an approximate value of the j-th eigenvalue at the n-th iteration step. The solution of the original problem is obtained by solving the new standard problem $U_n^j Y = \Delta\lambda_n^j Y$ and correcting the eigenvalue as $\lambda_{n+1}^j = \lambda_n^j + \Delta\lambda_n^j$. In order to investigate the accuracy and convergence of the procedure, we solved a general eigenvalue problem which appears in the analysis of the MHD spectra of a current carrying cylindrical plasma[10]. To compare the results by our method with the one obtained by the conventional method, we prepared rather small scale matrices (N = 41). Figures I.5.3-1(a) and (b) show squares of frequencies of MHD oscillations corresponding to the five lowest eigenvalues. It is easily seen from these figures that the accuracy of 10^{-3} are obtained within several iterations and the stopping criterion ($|\Delta\lambda_n^j|/|\lambda_n^j| < \varepsilon$; $\varepsilon = 10^{-4}$) is satisfied within about ten iterations.

5.4 A method to solve impurity diffusion equation with ionization and recombination source terms[11]

Diffusion equations of impurities with ionization and recombination source terms are solved numerically by the splitting and fractional-step method for non-commutative operators. Diffusion equations and rate equations are solved successively and the very small time step for calculation determined by ionization process can be avoided by solving the rate equation as an eigenvalue problem. The time step is determined by the diffusion process and it is possible to follow the time evolution of impurities for a long time.

5.5 Development of a pre-processor for effective use of COMMON statements and its usage

A pre-processor is developed, which generates COMMON statements automatically. The pre-processor is written by FORTRAN language and contains new versions which remove restrictions of previously developed pre-processor. The present pre-processor is very useful when the sizes of arrays in COMMON statements are changed. The usage of this pre-processor is also presented.

5.6 Pre-processor for the use of the OLYMPUS SYSTEM[12]

OLYMPUS SYSTEM, which was developed by K. V. Roberts et al., was converted and introduced into the computer system, FACOM 230/75, of JAERI

data processing center. Also, a pre-processor was developed for the OLYMPUS SYSTEM. The OLYMPUS SYSTEM is very useful for the development, standardization and exchanges of programms in the field of nuclear fusion research and plasma physics. The pre-processor developed by the present authors is not only indispensable fot the JAERI OLYMPUS SYSTEM, but also useful to manipulate, create and correct program files.

5.7 Application of REDUCE-2 to the computations in CTR[13]

Complicated analytical calculations in CTR were carried out by using the algebraic manipulation language REDUCE-2[14][15]. They are the calculation of coefficient matrix in the MHD stability analysis by a variational method, the calculation of metrics and the equilibrium quantities in the stability analysis as an initial value problem, and the calculation of equilibrium magnetic field for the positional control of a toroidal plasma. It was shown that the application of algebraic manipulations by computers are very useful in the CTR computations.

References

(1) Hogan J.T.: "Multi-fluid tokamak transport models" in Methods in Computational Physics vol.16, p.131, (Academic Press, N.Y., 1976).
(2) Grad H. and Hogan J.T.: Phys. Rev. Letters 24 (1970) 1337.
(3) Grad H., Hu P.N., Stevens D.C. and Turkel E.: "Diffusive transition from belt pinch to doublet" in Computing in Plasma Physics and Astrophysics, April 27-30, 1976, Garching, IPP 6/147.
(4) Helton F.J., Miller R.L. and Rawls J.M.: "Two-dimensional multi-fluid tokamak transport code", GA-A13799 (1975).
(5) Hinton F.L. and Hazeltine R.D.: Rev. of Mod. Phys. 48 (1976) 239.
(6) Takizuka T.: to be published.
(7) Takizuka T. and Wakatani M.: JAERI-M 6926 (1977) p.139.
(8) Takizuka T. and Abe H.: to be published in J. Comp. Phys.
(9) Tsunematsu T. and Takeda T.: submitted for publication in J. Comp. Phys.
(10) Takeda T., Shimomura Y., Ohta M. and Yoshikawa M.: Phys. Fluids 15 (1972) 2193.
(11) Okamoto M. and Amano T.: to be publihsed in the J. Compt. Phys.
(12) Okamoto M., et al.: to be published in JAERI-M report.

(13) Tsunematsu T., Kurita G., Ninomiya H. and Takeda T.: JAERI-M 7179 (1977) (in Japanese).

(14) Hearn A.C.: "REDUCE-2 user's manual", Univ. of Utah (1973).

(15) Kanada Y.: "Implementation of HLISP and Algebraic Manipulation Language REDUCE-2", Technical Report 75-01, ISD Univ. of Tokyo (1975).

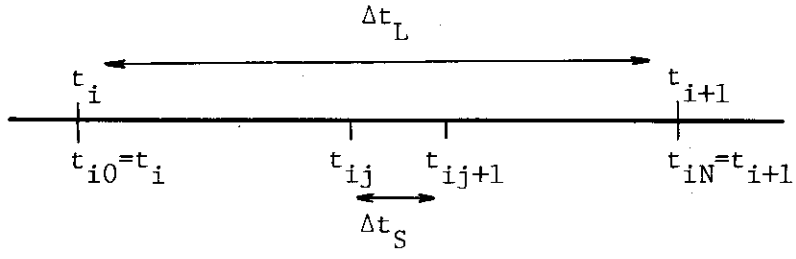

Fig.I.5.1-1 Time steps for the 2D tokamak transport code.

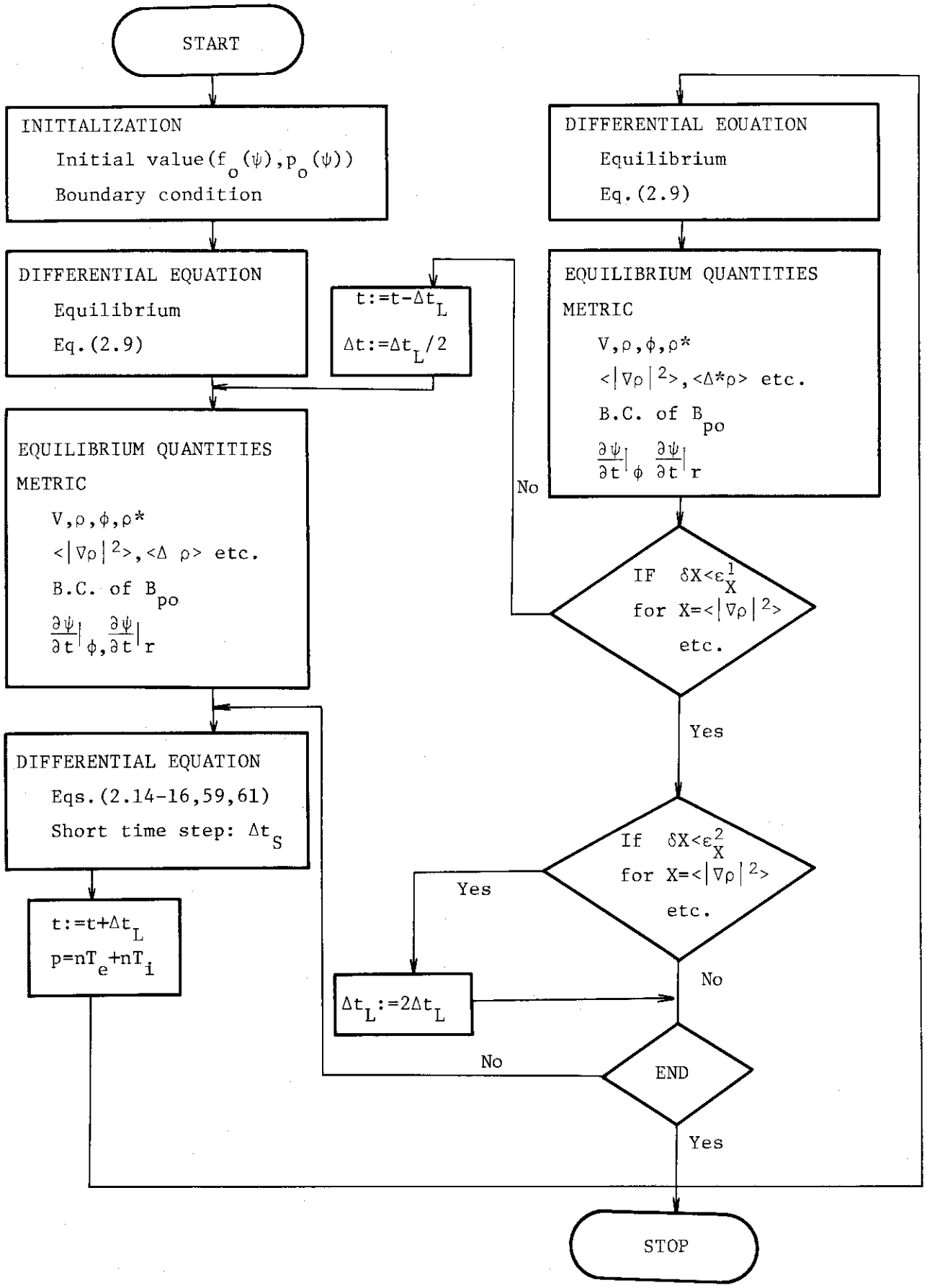

Fig.I.5.1-2 Flow diagram of the 2D tokamak transport code.

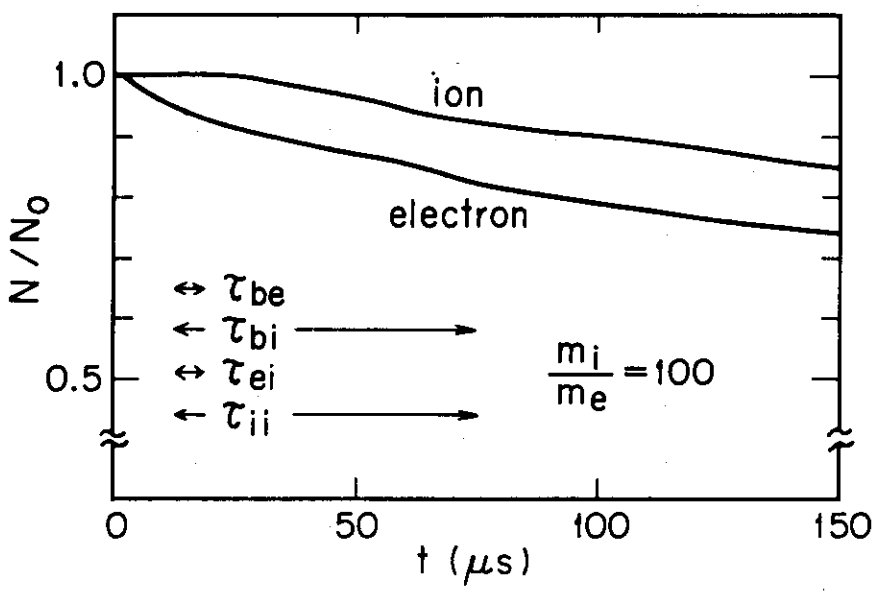

Fig.I.5.2.1 Decay of particle density.
The loss of particles to the divertor along the magnetic field is dominated by ions.

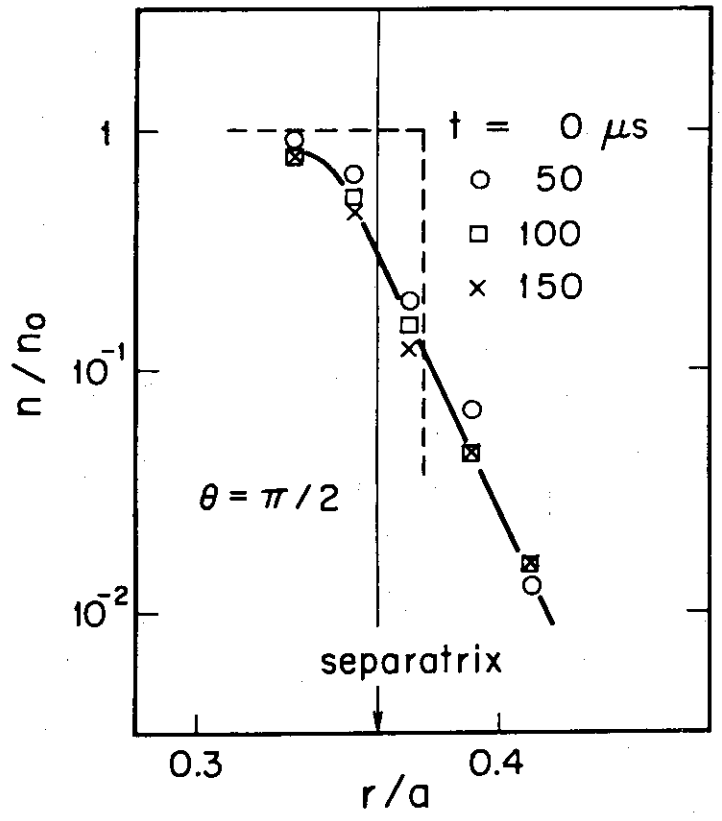

Fig.I.5.2-2 Density profile near the separatrix at $\theta = \pi/2$.
The e-folding length is about 0.015a.

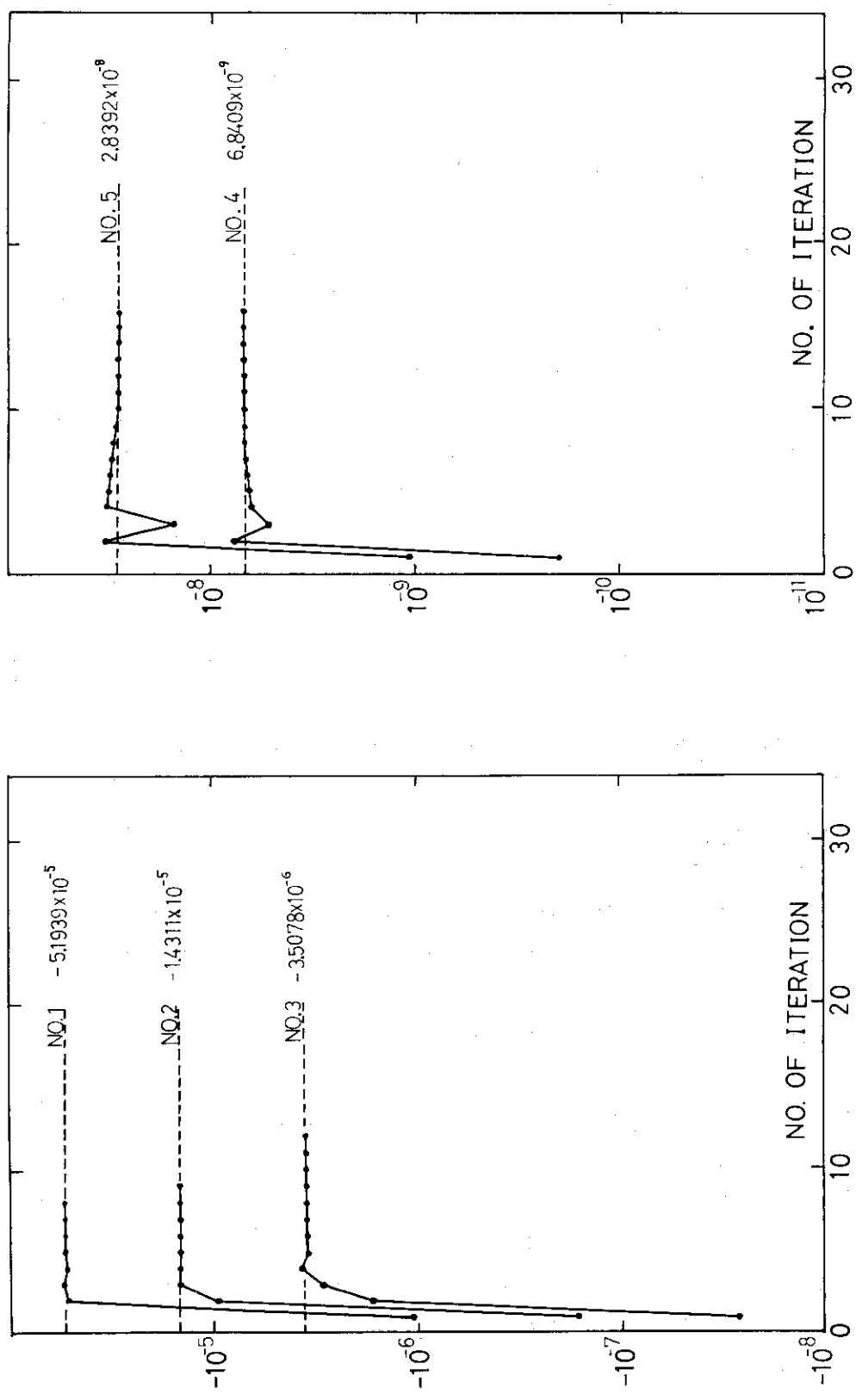

Fig.I.5.3-1 Squares of frequencies of MHD oscillations of a current carrying cylindrical plasma.

II. TOROIDAL CONFINEMENT EXPERIMENTS

1. JFT-2

1.1 Introduction

In the first half of this reporting period, the confinement studies have concentrated on the effects of impurities (radiation loss and Z_{eff} profile), the density control (particle balance and the maximum density) and the effects of fluctuations (density). The heating experiments by neutral beam injection have been carried out in the period from September 1976 to March 1977. The main results are as follows:

(1) a constant plasma current operation improved the efficiency of confinement studies,

(2) a controllable neutral gas feed enabled the density to be the desired and constant value,

(3) the main impurity is oxygen. Metal impurities (iron and molybdenum) are less than 1/100 of the oxygen density which is (5∿7)% of the electron density,

(4) the radiation loss due to the oxygen impurity is about one fourth of the joule input,

(5) the Z_{eff} at the plasma center is ∿5, and in the middle region it decreases to ∿3,

(6) the peaking of Z_{eff} on axis leads to q(o)>1, which is in agreement with no appearance of m=1 soft X-ray fluctuations,

(7) the density fluctuation amplitudes are (1∿0.1)% of the electron densities, and the density dependence of diffusion coefficient is consistent with the empirical scaling law,

(8) the soft X-ray measurement determines the radial profile of the electron temperature,

(9) the maximum electron density in JFT-2 scales as $\bar{n}_e$ $(10^{13}cm^{-3})$ = $2\ B_t(T)/R(m)$,

(10) a pyroelectric detector indicates that the large radiation loss comes mainly from the outer part of the plasma,

(11) studies on the neutral beam injection heating show that the rise in the ion temperature can be explained by the neoclassical ion energy balance, and that the energy spectrum of the fast ion is in agreement with the prediction of the classical Fokker-Planck theory,

(12) the temporal behaviour of gaseous impurities during discharges is

observed using mass spectroscopy,

(13) the electrical breakdown of hydrogen gas in the initial stage of a discharge has been studied experimentally,

(14) remodeling plan of JFT-2 for impurity and heating studies has been established.

1.2 Confinement experiments at toroidal field 18 kG

1.2.1 Experimental results on impurity contamination

Impurity study was extensively performed in this period, using mainly a 3 m grazing incidence UV monochromator and a Si(Li) soft X-ray detector. In this subsection, several characteristic features of impurity behaviour and the influences on the plasma energy confinement are described.[1] (Detailed discussion will be given in refs.[2],[3].)

(a) Impurity behaviour

In normal operation of the JFT-2 discharges (A typical 160 kA, MHD stable (q = 4) discharge is shown in Figs. II.1.2-1, II.1.2-2), the main impurity is oxygen. The ground state population density of the oxygen ion amounts to 5∿7% of the electron density in the quasi-steady state. Other light (carbon and nitrogen) and heavy (molybdenum, iron, chromium and nickel) elements are estimated to be less than 1/100 of oxygen. In the steady state, nearly equilibrium distribution of the impurity ions are established (Fig. II.1.2-3). The structures are largely different from the predicted ionization-recombination balance for a given temperature profile. Interpretation with the collisional impurity diffusion theory[4] clarifies this discrepancy.

Examples of the absolute radiation intensities of ions are shown in Fig. II.1.2-4. Besides the dominant resonance line emission, the intensities of so-called 'group of many lines' and their integration over the wavelength region from 50 Å to 120 Å are also shown.

(b) Resistance anomaly

Resistances of the JFT-2 plasma are greatly affected by the oxygen concentration. Radial profile of the effective ionic charge Z_{eff} indicates that Z_{eff} in the central region ($r \lesssim 6$ cm) is slightly (factor of ∿2) higher than in the outer region within ambiguities estimated. (Detailed discussion on the enhanced bremsstrahlung radiation is given in § 1.2.5)

A calculated profile of the safety factor q(r) is shown in Fig. II.1.2-5, assuming that the current density is determined only by T_e and Z_{eff}. In the figure, it is seen that the plasma is expected to be free from m = 1 internal kink instability in this case. Experimental results with PIN junction diode array support this calculation.

(c) Energy balance

(i) Joule heating power (P_{IN})

Total resistive input power in the steady state is about 320 kW

(I_p=160 kA, V_L=2 V). Assuming the toroidal electric field ($V_L/2\pi R$) to be constant along a minor radius (i.e. $P_{IN}(r) \propto T_e^{3/2}(r)/Z_{eff}(r)$), the radial profile of the input power can be calculated from T_e and Z_{eff} profiles (Figs. II.1.2-2 and II.1.2-18). With electron kinetic energy $W_e(r)$, the electron energy containment time $\tau_{Ee}(r)$ ($=3/2\ W_e/P_{IN}$) is estimated to be 5∿6 msec and is nearly constant over the minor radius within the experimental error. Figure II.1.2-6 shows these quantities (X) included in a unit shell ($2\pi R \cdot 2\pi r \cdot X$), where R and r are the major and minor radii, respectively.

(ii) Radiation power (P_{rad})

In the central hot region, radiation loss is mainly due to the emission lines from O VII and O VIII ions. The summation (ΣP_{rad}) of dominant resonance line radiation is shown in Fig. II.1.2-6; it amounts to 25% of the total input power.

On the other hand, radiation measurements (including particle flux) with a pyro electric detector indicate that the radiation profile has a peak at the edge of the plasma ($r \gtrsim 15$ cm).

The emission from group of many lines will be a plausible candidate of the main component of the edge radiation. Assuming the radiation profile of group of many lines is the same as that of pyro-electric detector, the power lost by the radiation is calculated to be about 160∿200 kW.

(iii) Ion heating and others

Total power transfer from electron to ion is calculated to be roughly 40∿50 kW from radial profiles of T_e and T_i, which is expected to be balanced with charge-exchange loss (∿20 kW) and neo-classical heat loss (See Sect. 3.3). The resultant heat load to a limiter will be 10∿20 % of the total input.

1.2.2 Particle balance[5]

Particle balance of the JFT-2 plasma is evaluated in ref. (6) from spectroscopic measurement of the radial profile of the H_α intensity. However the recycling of particles at a limiter localized in a narrow region is not taken into account, so the estimated particle confinement time is the maximum. Here, the particle balance is studied by other method with a simple model such as $dN_e/dt = -\frac{N_e}{\tau_n} + \gamma\frac{N_e}{\tau_n} + \alpha Q$, where N_e is the total number of electrons, τ_n is the particle confinement time, γ is the recycling coefficient, Q is a controllable influx of hydrogen atoms through a control puff described in § 1.4.1 and α is the effective ionization rate.

This simple model is supported by experimental results as follows.

(a) The electron density increases linearly with time through the constant gas feeding by control puff and decreases monotonically after stop of the gas feed. These phenomena are observed in discharges with various rates of gas influx. So, γ is constant during discharges, independent of the electron density. The particle balance can be evaluated with a simple model such as $dN_e/dt = -\frac{N_e}{\tau_n} + \gamma \frac{N_e}{\tau_n} + \alpha Q$. The recycling coefficient γ is $0<\gamma<1$. Under certain wall conditions the model indicates $\tau_n \sim \frac{N_e}{5\times10^{20}} \cdot (1-\gamma)$ sec. Therefore $\tau_n \propto N_e$. If τ_n is determined from a toroidal distribution of the H_α intensity, the recycling coefficient may be estimated.

(b) The radial profile of electron density keeps constant during the discharge whether the density increases or decreases. Therefore, the total number of electrons Ne can easily be calculated from the line-averaged density $\bar{n}$.

(c) The time derivative of the total density increases linearly with the gas influx, so the effective ionization rate is constant.

(d) Since oxygen is a dominant impurity and roughly constant during a discharge, the electron source from impurities can be ignored.

These results in different days are shown in Fig. II.1.2-7. Scattering of the data possibly depends on the uncontrollable wall conditions.

1.2.3 Density fluctuations

Fluctuations may be closely related to the anomalous transport of the Tokamak plasma. Therefore, density fluctuations due to micro-instability have been measured by two methods: interferometer, and scattering system of 4 mm microwave.

(a) Measurement by microwave interferometer[7]

The high frequency components of the detected signal are proportional to phase change $\tilde{\phi}_1$ due to density fluctuations $\tilde{n}_1$[8]. In the case of instabilities with wave length λ smaller than the horn width λ_H, $\tilde{\phi}_1$ is represented by the relation; $\tilde{\phi}_1 \sim \int \tilde{n}_1 \lambda/\lambda_H \, d\ell$. By rotating a tephlon sheet (specific permittivity $\varepsilon_s=2$) of 2mm thickness with comb-tooth of $\lambda=2\sim130$mm between two horns, this phase shift dependence on wave length which saturates at $\lambda \gtrsim \lambda_H$ was studied experimentally. The detected signals are processed by auto-correlation and Fourier transformation, and are averaged

statistically over several shots. The power spectra obtained in typical three discharge conditions have a frequency dependence of $f^{-2.5}$. The spatial distribution of total power density in three cases are shown in Fig. II.1.2-8. Considerable asymmetry between outside and inside of the torus is observed. A possible explanation of this asymmetry is the ballooning effect of dissipative trapped electron mode[9]. The calculated results with this effect are also shown by dotted lines in Fig. II.1.2-8. The maximum amplitude of the density fluctuations in case B in Fig. II.1.2-8 is estimated to be 10^{-2} of the mean electron density. The density dependence of the fluctuation powers is shown in Fig. II.1.2-9. From these results, the maximum fluctuation powers are nearly independent of the mean electron density, that is, $\langle S^2 \rangle \sim (\tilde{n}_{max}/K_\perp)^2 \sim$ constant. The width of localization has a tendency to decrease with increasing the density.

(b) Measurement by microwave scattering method[10]

The observed spectra of fluctuations have two components of azimuthal and radial wave numbers. Frequency spectra have the form of $f^{-(1.8\sim2.5)}$, which is the power law dependence of the turbulent fluctuations. The amplitude of the density fluctuations, $\langle|\tilde{n}_e(k)/n_e|^2\rangle^{1/2}$ is shown in Fig. II.1.2-10 for the different scattering positions. The measured level of fluctuations is of the order of 10^{-3}, which is somewhat less than that predicted by the strong turbulent theory[11], i.e. the order of $(L_n k_r)^{-1}$ where $L_n = d\ln n_e/dr$ (Fig. II.1.2-10).

(c) Discussions

The range of observed frequency is approximately that of drift waves. The order of diffusion coefficient is possibly explainable (in case B in Fig. II.1.2-8). The particle diffusion by electrostatic density fluctuations can be derived by using the relations,[12] $\tilde{D} = \Sigma\gamma/L_n(\tilde{n}_e/n_e)^2$ where $\gamma = \varepsilon^{1/2}\,\omega_e^* \eta\, \nu_{eff}/(\omega_e^{*2} + \nu_{eff}^2)$, $\eta = d\ln T_e/d\ln n_e$, $\nu_{eff} = \nu_{ei}/\varepsilon$ and ω_e^* is the drift frequency. In the present case, $\tilde{n}_{max}/\bar{n} \sim L_n/k_\perp \sim 10^{-2}$, $\omega^{EXP} \sim \omega_e^* \sim 10^6$ ($k_\perp \rho_i = 0.5$), $L_n \sim 10^{-1}$, $\eta \sim 2$, $\gamma \sim 10^5$, $k_\perp \sim 5$ and $\tilde{D} \approx 10^{+4}\,cm^2/s$ (Fig. II.1.2-11). This value of diffusion coefficient is of the same order as that obtained by the spectroscopic measurements. In order that the density dependence of the fluctuation amplitudes $(\tilde{n}/\bar{n} \sim k_\perp/\bar{n})$ is compatible with the relation of the saturation level $(\tilde{n}/\bar{n} \sim L_n/k_\perp)$, the wave number must be proportional to the square root of the mean electron density, that is, $k_\perp \sim \sqrt{L_n \bar{n}} \sim \sqrt{\bar{n}}$. Therefore, $\tilde{D} \sim \bar{n}^{-1}$, and this dependence is consistent with the empirical scaling.

1.2.4 Simulation

Simulations of the JFT-2 tokamak plasmas have been made with a one-dimensional transport code[13], assuming $Z_{eff} \propto 1/\bar{n}_e$, which means that the impurity concentration is constant in a plasma during a discharge. Results in the case of 160 KA, 18 KG discharge with gas puffing are presented below.

The time evolution of the total plasma current and the one turn voltage of the discharge are shown in Fig. II.1.2-12. Figure II.1.2-13 shows the evolutions of the electron density, the electron temperature, and the ion temperature at the plasma center. The recycling ratio γ of the plasma particles is introduced to explain the evolution of the electron density with gas puffing. Then the particle flux is represented as (in-flux)=γ·(out flux) + (puffing gas flux), where the value of puffing gas flux is measured experimentally. Simulation results are in good agreement with experimental ones when γ is 0.9.

Experimental results show that most of the energy is lost from the bulk plasma as radiation loss by impurities at the plasma boundary. The energy banalce in the peripheral region as well as in the hot central region can be simulated by the effective conduction loss including the radiation loss.

Figure II.1.2-14 and -15 show the profiles of electron density and electron temperature. The anomalous diffusion without Ware pinch[14], which is about 200 times the classical one, gives a non-inverted density profile in the simulation. The time-space evolution of electron temperature can be explained when the anomalous electron conduction is assumed to be 700 times the classical one.

Figure II.1.2-16 shows energy confinement time τ_E, particle confinement time τ_n, beta poloidal $\beta_p = 8\pi n_p (T_e + T_i)/B_\theta^2(a)$, and internal inductance $l_i = \overline{B_\theta^2}/B_\theta^2(a)$. These results agree with the JFT-2 experimental ones.

1.2.5 Z_{eff} profile

An enhancement factor of a soft x-ray intensity provides important information on Z_{eff}. Here, the Z_{eff} profile is evaluated with the soft x-ray and the spectroscopic measurements.

The soft x-ray apparatus is described in § 1.2.6. The formula for hydrogenic bremsstrahlung for a maxwellian plasma is well known.

$$\left(\frac{\Delta W}{\Delta k}\right)_{ff} = 3\times 10^{11} \frac{n_e \sum n_i Z_i^2}{10^{26}\,\mathrm{cm}^{-3}} \left(\frac{T_e}{\mathrm{keV}}\right)^{-1/2} \bar{g}_{ff}(T_e, k) \exp(-k/T_e) \quad \mathrm{cm}^{-3}\cdot\mathrm{sec}^{-1}$$

Symbols have the usual significances. A comparison between a measured spectrum and the bremsstrahlung formula involves an integration of this formula over the measured area of the plasma which is determined by the geometrical configuration of the apparatus. A cylindrical plasma is assumed for simplicity. Necessary information for the calculation is as follows: distance between a plasma center and a first collimator, distance between the first and the second collimators, apperture radius of collimators, distance from the horizontal midplane, calibration curve, thickness of Be absorber, and profiles of electron density and temperature. The distribution of the energy spectrum and of the total counting rate along the Z axis can be calculated. Here $n_e(r)$ from the 4 mm microwave interferometer and Te(r) approximated by soft x-ray spectrum measurement were used.

The soft x-ray intensity was measured in two manners in § 1.2.6; one is the total counting rate, and the other is the time-resolved spectrum. The former data have many points along the Z axis because many discharges are not necessary to measure it, and include both continuum and line radiation. The latter data have opposite characteristics. The total counting rate data was used, refering to the spectrum data. The counting loss is taken into account and the Be thickness is experimentally determined because of large deviation (30%) from a nominal value. By the two methods, the enhancement factor ζ was obtained for the hydrogen bremsstrahlung.

The continuum radiation consists of hydrogen bremsstrahlung, impurity bremsstrahlung and impurity radiative recombination. Then the measured enhancement factor is represented as

$$\zeta = Z_p^2 \cdot n_p/n_e + \sum_i \gamma_i \cdot Z_i^2 \cdot n_i/n_e$$

Here γ_i is the ratio of the continuum over the bremsstrahlung for a considering charge-state of an impurity[5]. On the other hand, the effective ionic charge and the neutrality of the plasma are represented as

$$Z_{eff} = \frac{\sum_i n_i Z_i^2 + n_p Z_p^2}{n_e} \quad , \quad n_e = n_p Z_p + \sum_i n_i Z_i \ .$$

Then, if a main impurity and its ionization state are known, Z_{eff} can be estimated. Spectroscopically, a main impurity in the JFT-2 is oxygen and its radial profiles of density of various ionization states are derived. The Z_{eff} profiles are shown in Fig. II.1.2-17. The minimum and maximum values estimated from the enhancement factor depend on whether the fully

stripped oxygen is taken into account or not.

Conclusions are as follows.

(a) A main impurity is oxygen in the JFT-2 plasma and the value of Z_{eff} has been determined mainly by oxygen.

(b) The Z_{eff} profile estimated by soft x-ray measurement is in good agreement with that by spectroscopic measurement. The effect of the fully stripped oxygen is taken into account.

(c) The Z_{eff} profile is slightly peaked in the JFT-2 plasma. It explains the reason why a sawtooth oscillation on the PIN diode is not observed for the measured plasma in spite of $q(0)<1$ which is calculated from $Te(r)$ assuming the uniform profile of Z_{eff}.

1.2.6 Electron temperature profile from soft X-ray

Radial profiles of electron temperatures derived from a vertical distribution of soft x-ray spectra will be described. The electron temperatures determined from the soft x-ray spectra with a Si(Li) detector are in agreement with those by laser scattering measurement within an observation error of about 10%. A combination of the time resolved soft x-ray spectra with the total counting rates gives a time evolution of electron temperatures.

In order to treat successfully the large variation of the soft x-ray intensity along a plasma radius, the attachment consisting of double collimators and absorber foils was improved. The improved soft x-ray measurement apparatus is shown in Fig. II.1.2-18. The vertical scan box is movable to cover all plasma region from +25 cm to -25 cm. The first and second collimators have 12 apertures ranging from 0.2 mm to 6.5 mm in the manner of geometric progression by double in steradian, which are changable in vacuum. The absorber foils of Beryllium (0∿500 μm) can be inserted into the optical path to cut off the low energy photons. These functions enable adjustment of the incoming soft x-ray photons to the optimum counting rate. The soft x-ray data are collected in three ways as follows.

(a) The time evolution of the total counting rate of the soft x-ray photons is measured by single channel energy analyzer and multi-channel scaler. These data are used not only to adjust the collimators, but also to support other data with the good time resolution $\Delta t \sim$ ms.

(b) The energy spectrum summed over the plasma duration is processed with a multi-channel pulse height analyser (512 or 1024 chs.). These data have

a comparatively small statistical error because total counts are large, so it is easy to know the existence of the characteristic line radiation from metal impurities and to estimate the maximum electron temperature or the effect of the runaway electron.

(c) The time resolved energy spectrum is obtained with the multi-channel pulse height analyser and its memory controller (256 chs.× 16). The measuring time is divided into 16 intervals, normally 10 ms. A reasonable spectrum is obtained by summing up data over 20∿50 shots of the same discharges. A time evolution of a electron temperature is evaluated from these data and other data above mentioned; these data are shown in Fig. II.1.2-19.

A radial profile of electron temperatures is determined as follows. The measured spectrum is transformed to a power spectrum and corrected for the absorption of Beryllium. Then, the first estimate of the electron temperature is derived by the semi-log-fitting method in a energy region of the continuum, E/Te>2∿3. This temperature is 20∿30 % lower than the temperature at the chord center because of the spatial profile effect. Next, we calculate the dremsstrahlung spectrum integrated along the chord with the approximate temperature profile and the measured density profile, assuming the uniform enhancement factor for a hydrogen plasma. The correction factor for the profile effect is evaluated by this calculation. The radial profile of electron temperatures thus can be determined from the vertically scanned soft x-ray spectra. A part of the results of the measurements are presented in Fig. II.1.2-2(b).

1.2.7 Radiation loss profile

By space-time resolved bolometry, a preliminary study on the radiative power profile including charge-exchange neutral particle loss in the JFT-2 tokamak was made.

We have used a pyroelectric device, or a pyrometer as a bolometer, whose applicability to radiation power measurement is guaranteed by our previous results. We compared its time-integrated signal to Silicon thermister output to prove a proportionality between them.

Figure II.1.2-20 shows a time evolution of the radiation power profile after Abel-inversion procedure. The discharge parameters are as follows: B_t=18kG, I_p=160kA, a_L=25cm, $\bar{n}_e=1.3\times10^{13}cm^{-3}$. Assuming roughly flat spectral response in the vacuum-ultraviolet region, the conclusion is derived that the radiation loss profile is hollow in the steady state. The radiation peak, which is located at around 15cm from

the plasma core, moves outward, then inward, following constant electron temperature (∿200eV). The joule input power which concentrates at the central hot region is transferred to the periphery, and dissipated by impurity radiation.

What is the main source of this hollow radiation? The contribution of charge-exchange neutral is small. It shares only a small fraction (less then 10%) of joule input power, and its profile is peaked at the centre (see § 3.3) The radiation power profile estimated from the first resonant lines of highly ionized oxygen ions is rather broad with a peak at the centre. The pseudo-continuum, or group of many lines of metal impurities is the most probable candidate. (see § 1.2.1)

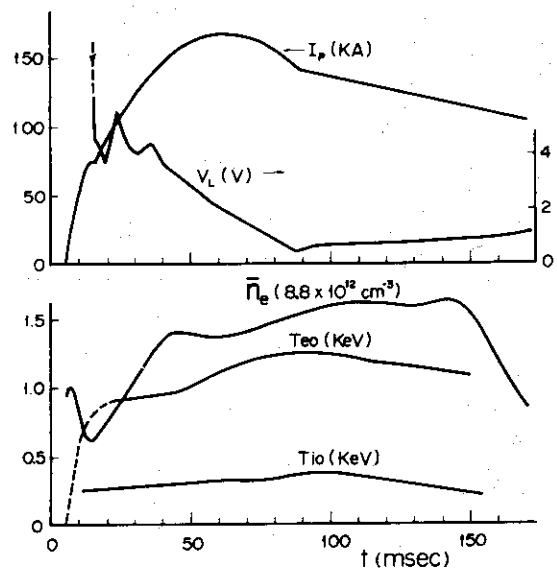

Fig.II.1.2-1 Time evolution of plasma current I_p, one-turn loop voltage V_L, chord averaged electron density $\bar{n}_e$ and central electron and ion temperature T_{e0} and T_{i0} under a typical $q = 4$ discharge. Initial rise of T_e is obtained both from time-history method of impurity radiation and time variation of soft X-ray counts.

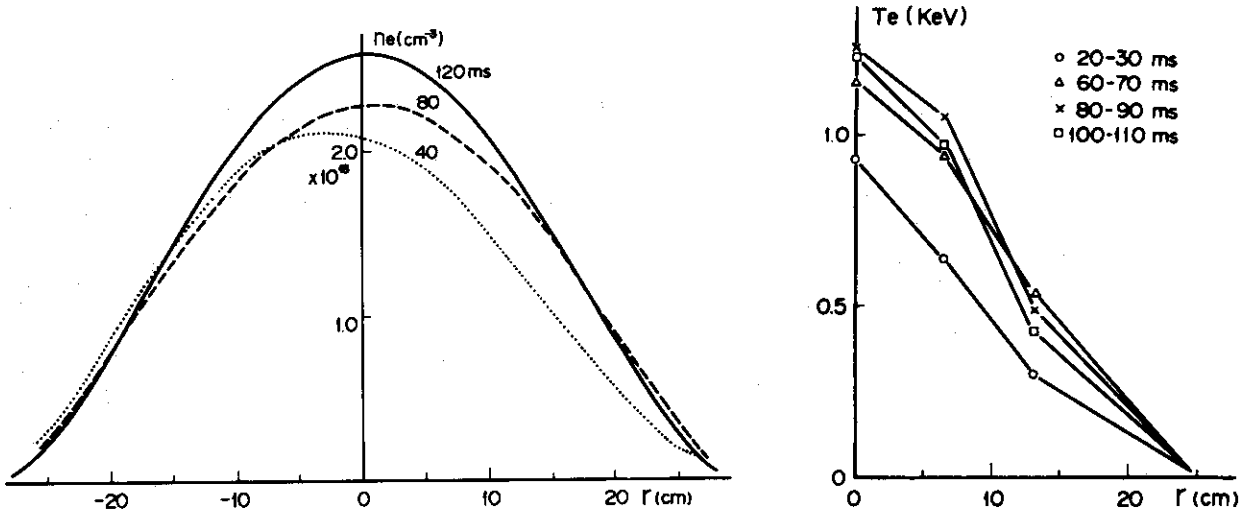

Fig.II.1.2-2 Radial profiles of electron density (a) and electron temperature (b).

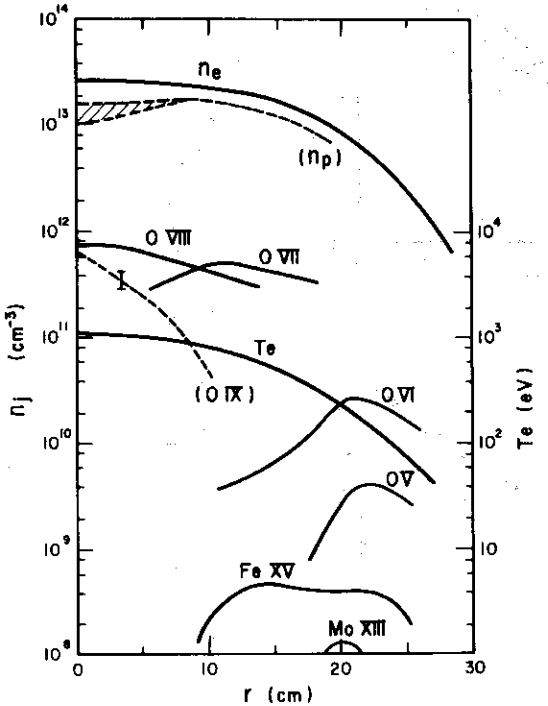

Fig.II.1.2-3

Radial profiles of the ground state population density of typical ions in the steady state of the discharge.

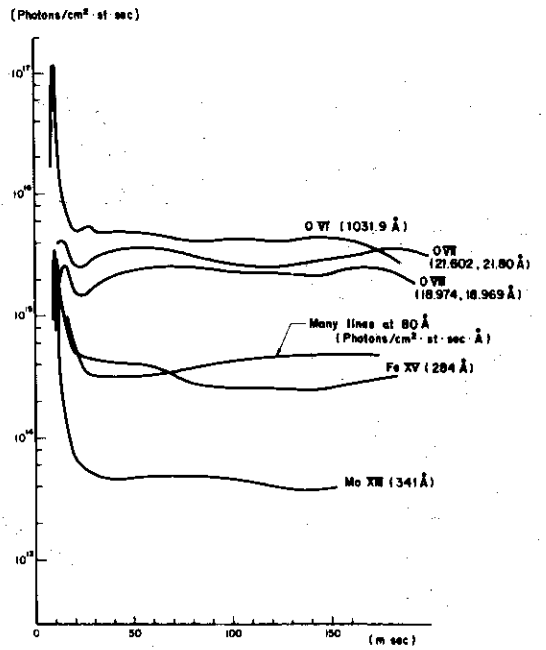

Fig.II.1.2-4

Time behaviour of the intensities from impurity ions (OVI∿OVIII, MoXIII and FeXV), group of many lines at 80Å.

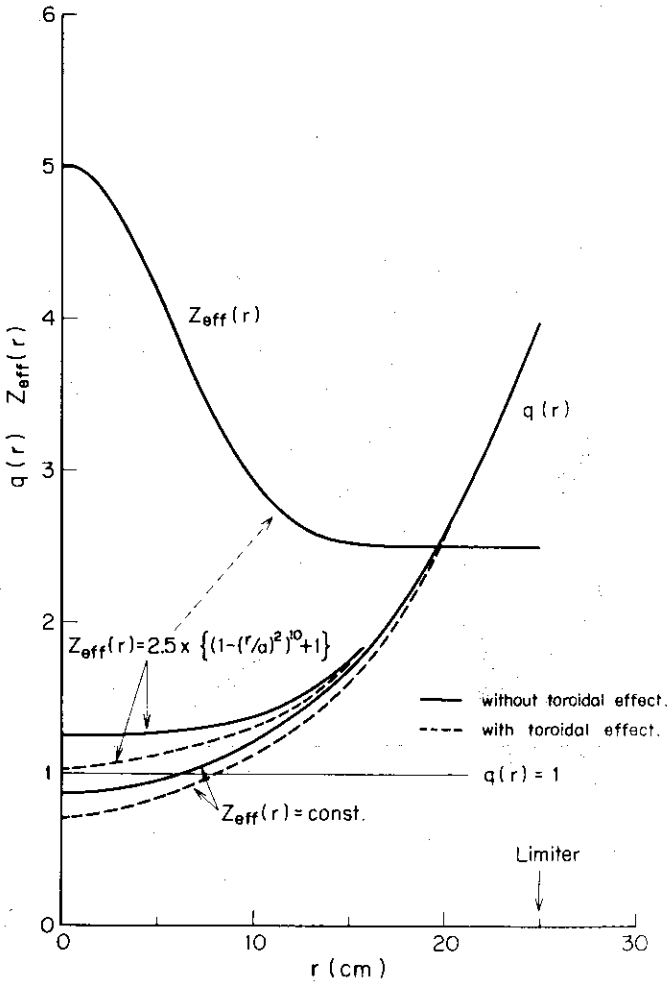

Fig.II.1.2-5

Estimated profiles of safety factor q(r) for the variation of Z_{eff}.

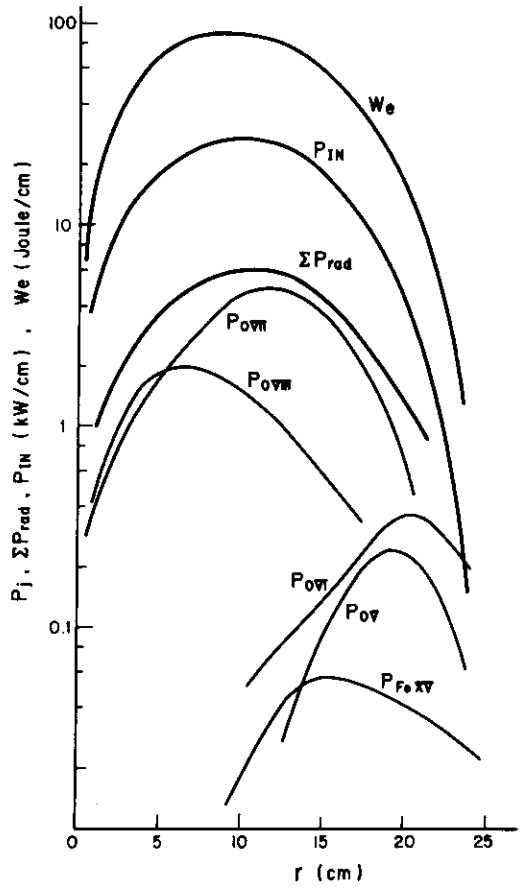

Fig.II.1.2-6 Radial profiles of joule heating power P_{IN}, electron kinetic energy W_e and radiation power of typical lines and their summation ΣP_{rad}.

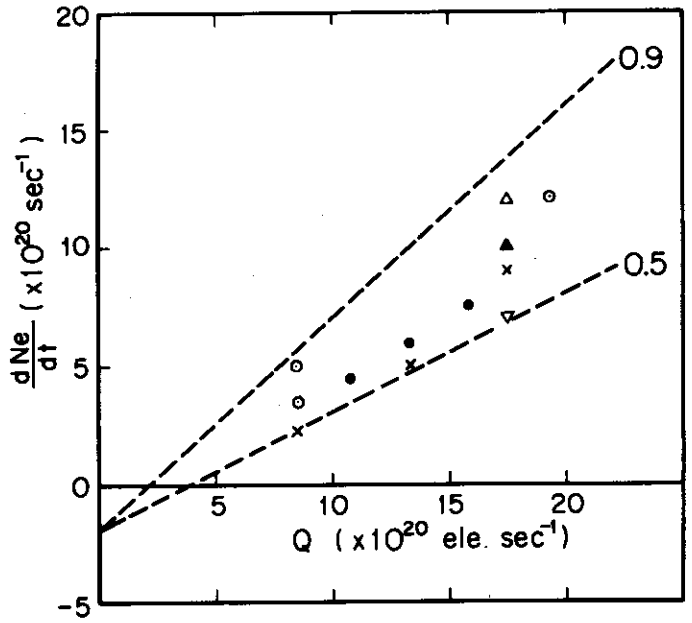

Fig.II.1.2-7 Time derivative of total electron number Ne versus gas influx from the control puff. $B_t = 18$ kG, $I_p = 160$ kA. These data are obtained in different days and symbols correspond to individual days.

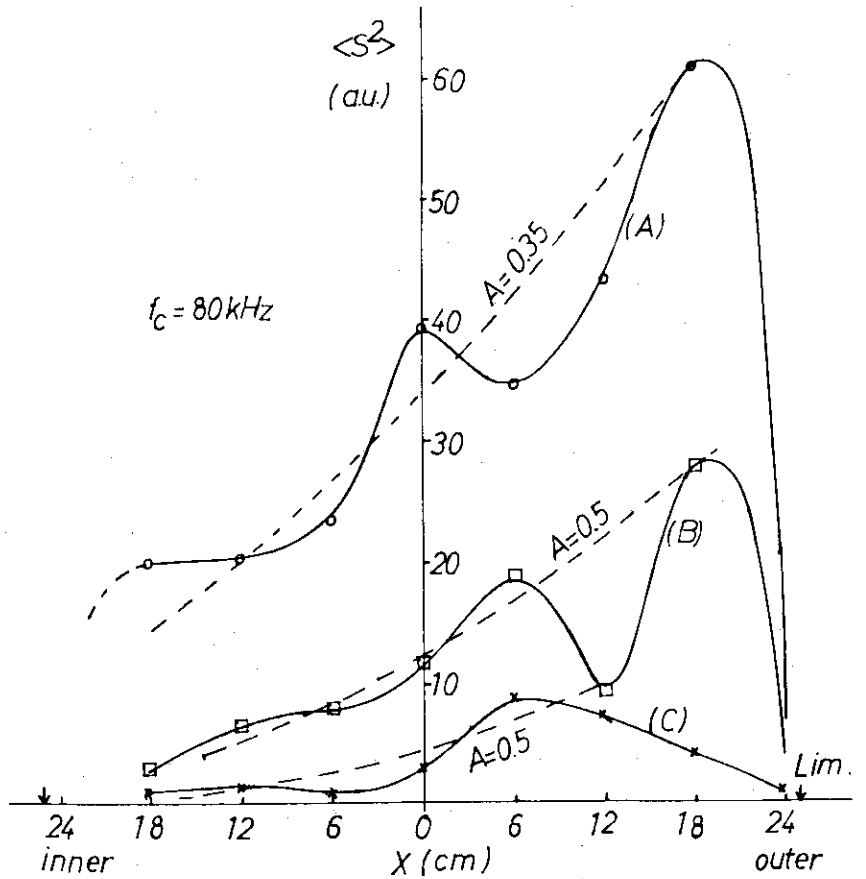

Fig.II.1.2-8 The spatial distributions of the total power density in typical three discharges; $n_e(0)=2\times10^{13}$ cm^{-3}, (A) B_T=9 kG, a=25 cm, (B) B_T=18 kG, a=25 cm, (C) B_T=18 kG, a=17 cm. Dotted curves show the calculated results with the ballooning effect.

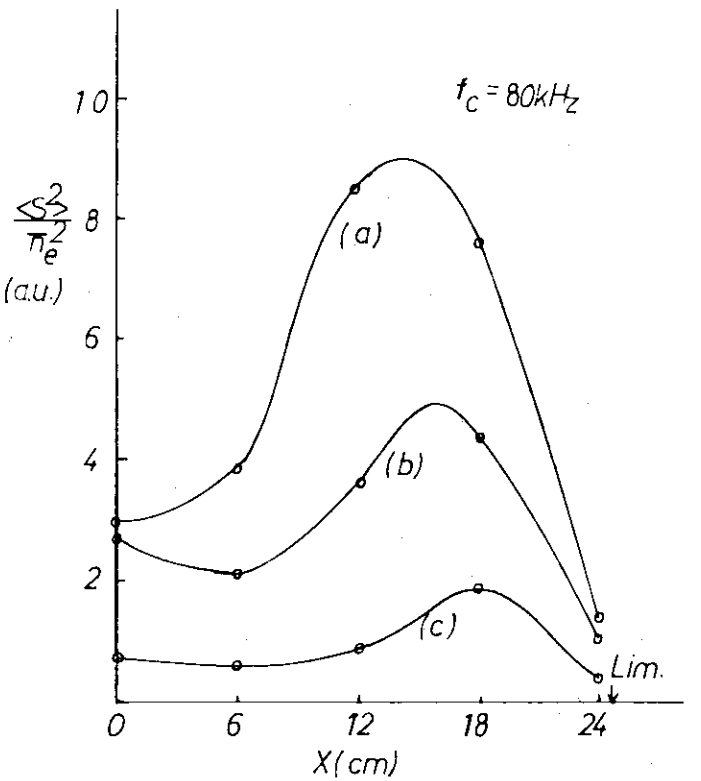

Fig.II.1.2-9 The density dependence of power distributions of fluctuations in discharge conditions; B_T=14 kG, a=25 cm, (a) $n_e(0)=2\times10^{13}$ cm^{-3}, (b) $n_e(0)=2.8\times10^{13}$ cm^{-3}, (c) $n_e(0)=4\times10^{13}$ cm^{-3}.

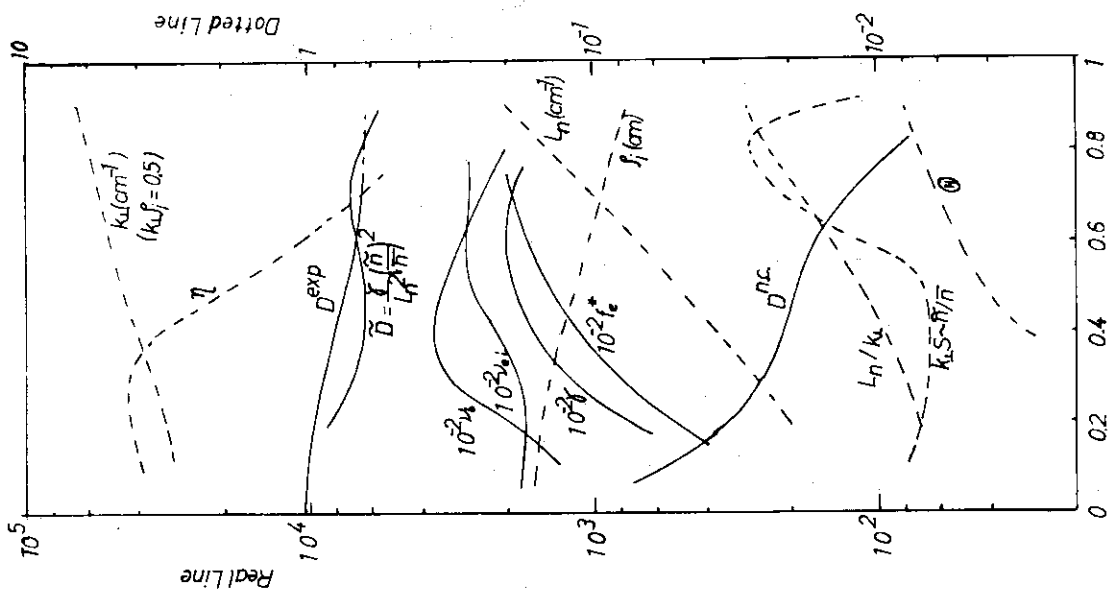

Fig.II.1.2-11 The various parameters relating to the transport coefficient in the case B.

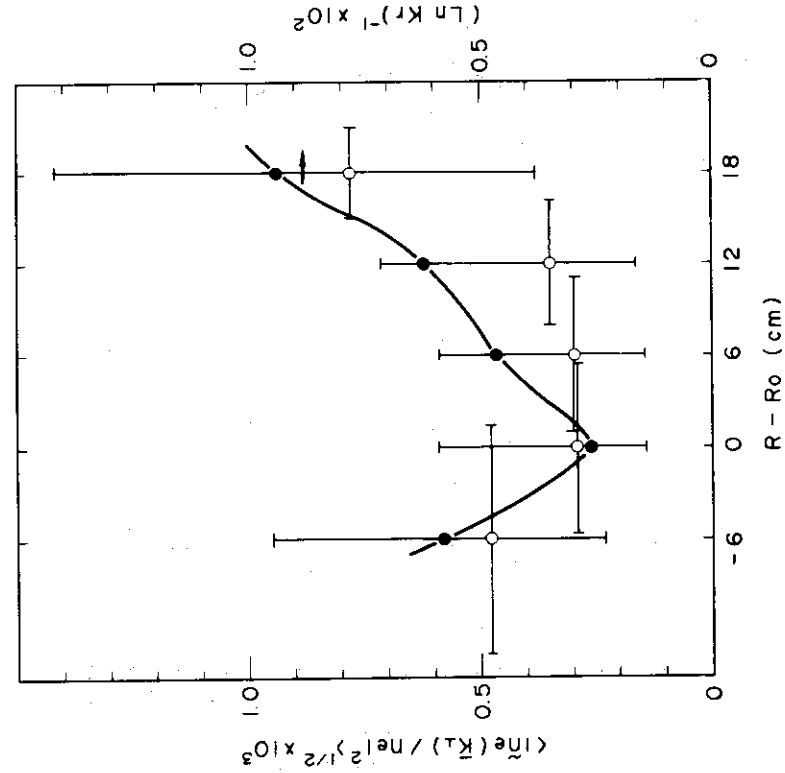

Fig.II.1.2-10 The amplitude of density fluctuations at the different scattering regions. The open circle indicates the measured value and the solid circle indicates the value of $(L_n k_r)^{-1}$ where $L_n = d\ln n_e/dr$.

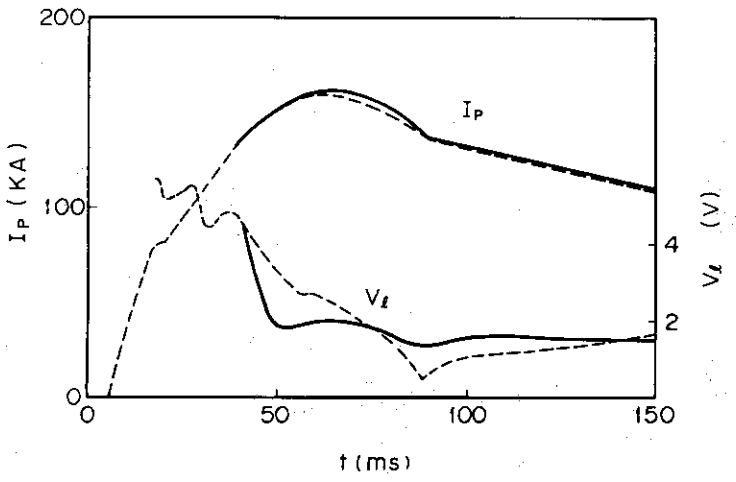

Fig.II.1.2-12 Time evolution of the total plasma current I_p, one-turn loop voltage V_l, and the plasma voltage V_p.

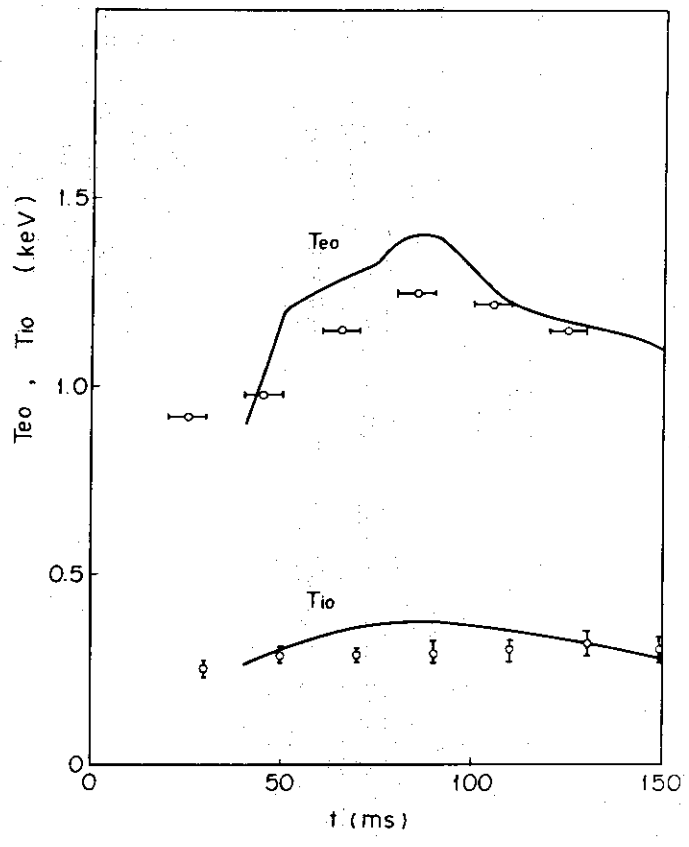

Fig.II.1.2-13 Time evolution of the central values of electron density n_e and temperature T_e, and ion temperature T_i.
The electron densities strongly depend on the recycling ratio.

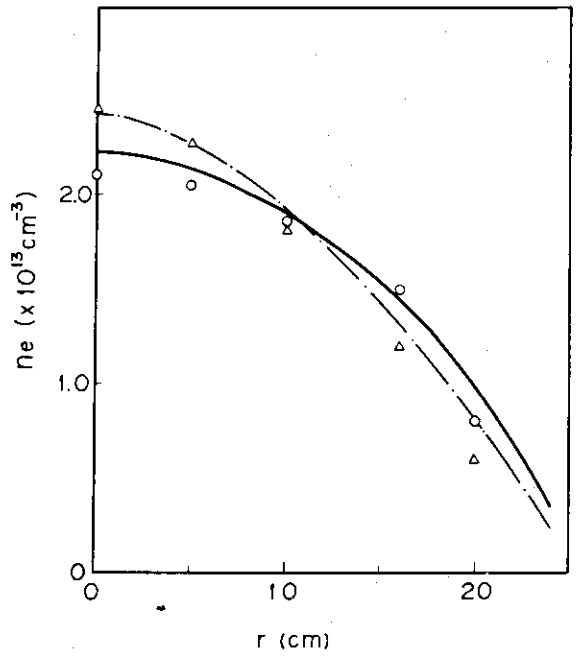

Fig.II.1.2-14 Radial distributions of the electron densities at selected time.

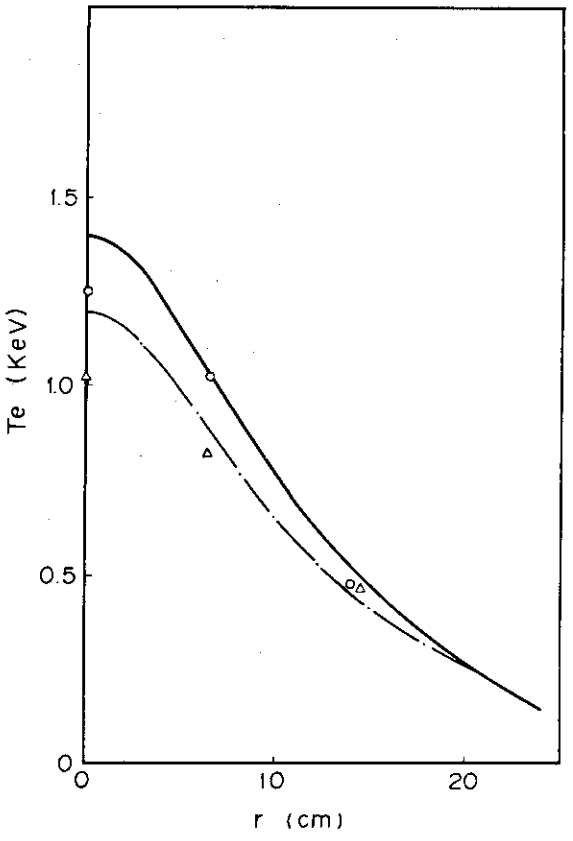

Fig.II.1.2-15 Radial distributions of the electron temperature at selected time.

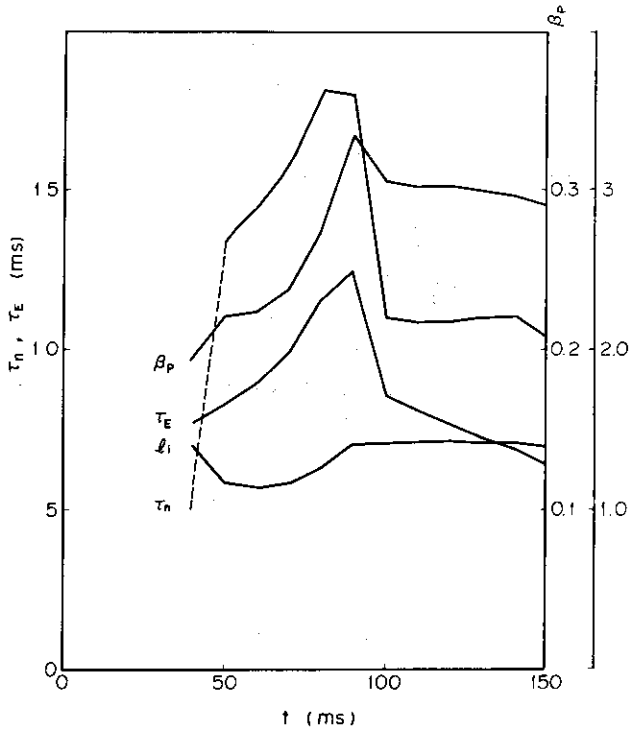

Fig.II.1.2-16 The computed time evolution of the energy confinement time τ_E, the particle confinement time τ_n, the beta poloidal β_p, and the internal inductance l_i.

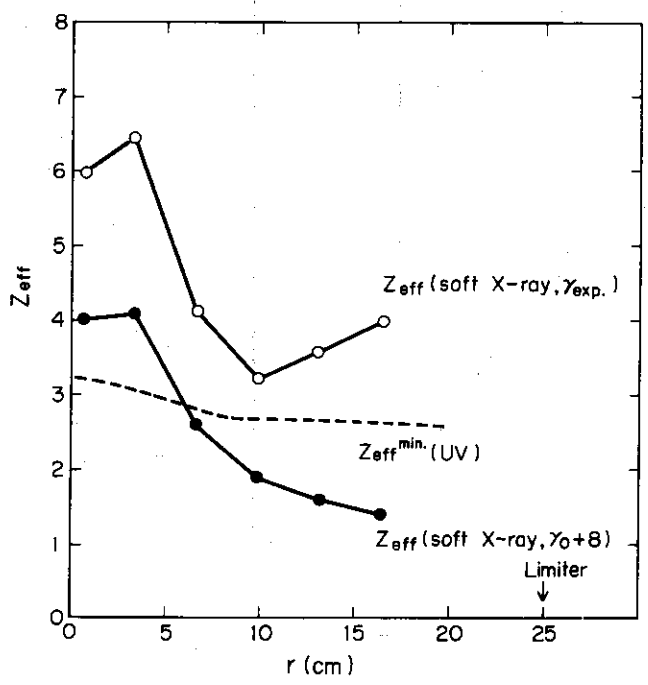

Fig.II.1.2-17 Z_{eff} profiles from the soft x-ray measurement. They are derived with and without the effect of the fully stripped oxygen. The Z_{eff} profile from the spectroscopic measurement gives the minimum value because the fully ionized oxygen is not taken into account.

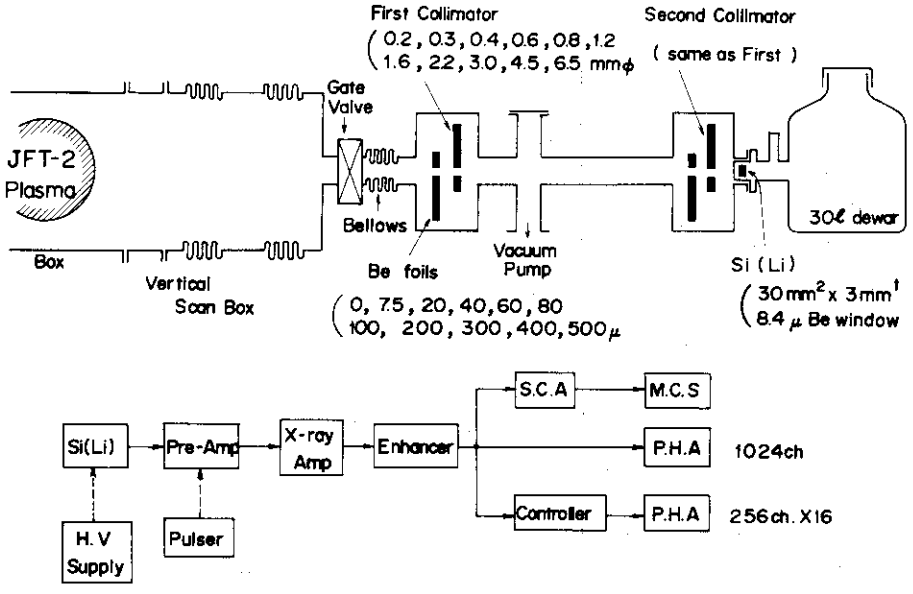

Fig.II.1.2-18 Schematic diagram of the soft x-ray measurement apparatus to obtain a vertical distribution of the soft x-ray radiation.

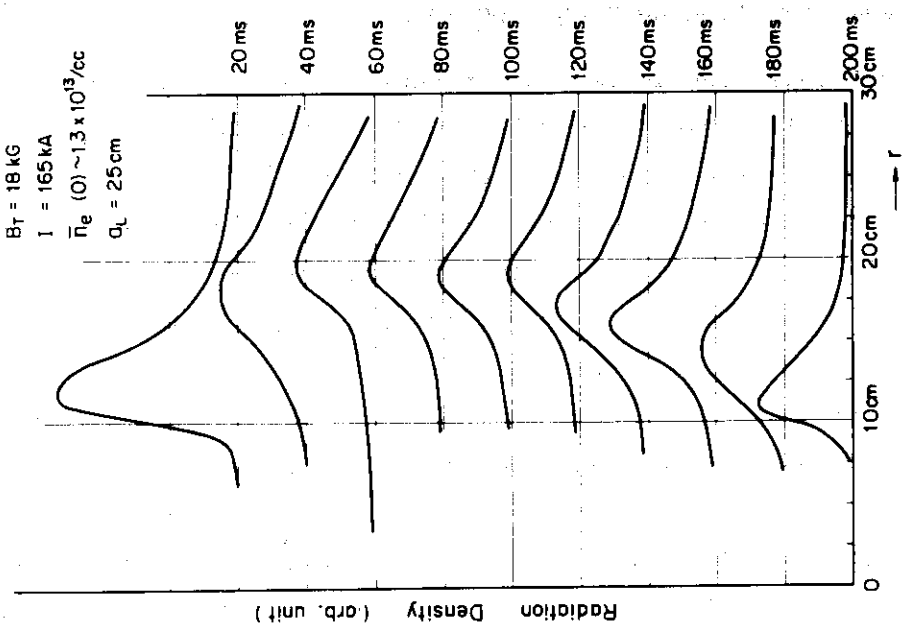

Fig.II.1.2-20 Time evolution of radiation power profile

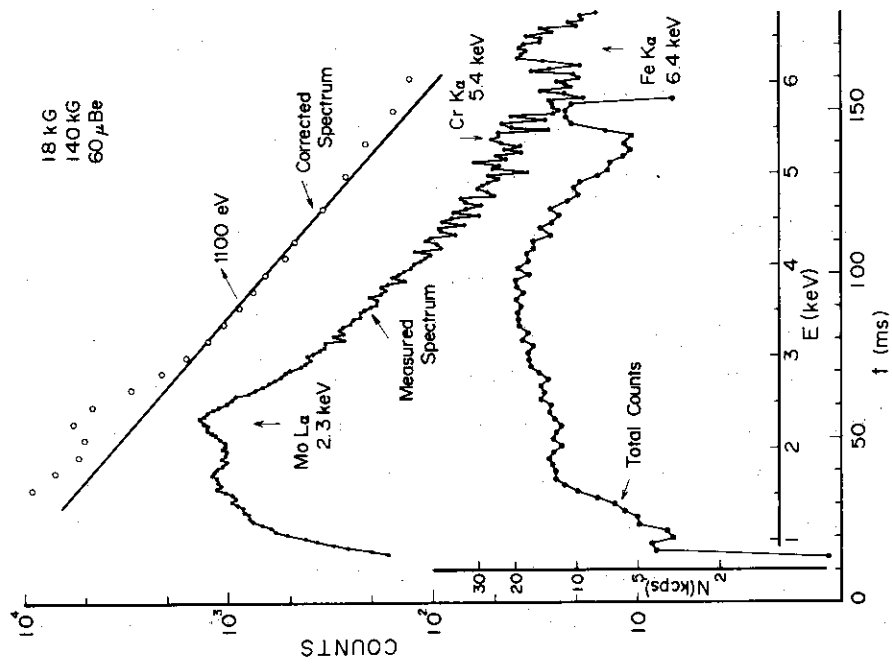

Fig.II.1.2-19 Examples of the time evolution of the total counting rate and the energy spectrum summed over the plasma duration.

1.3 Neutral beam injection heating experiment

Neutral beam injection is made at an angle of 85 degrees to a plasma current. The complete lines are capable of delivering the beam power of up to 85 kW at 30 kV extraction. Heating experiment is made for hydrogen target plasma under the conditions; toroidal magnetic field 18 kG, aperture limiter radius 25 cm, plasma current 160 kA, central chord averaged electron density (0.5-2.5) $\times 10^{13}$ cm^{-3}, one-turn loop voltage 1.6 V, electron temperature 1.0-1.2 keV, ion temperature 0.2-0.4 keV and effective charge 4-5. A main feature of the target plasma is that the neutral hydrogen density derived from charge exchange neutral analyzer is inversely proportional to the electron density.

Injection did not almost disturb the macroscopic plasma parameters. No effects on the loop voltage and the plasma current could be detected Appreiable change in the line radiations of visible and vacuum ultraviolet region from carbon, oxygen, iron, nickel and molybdenum could not be found. The electron density was found to increase by several per cent, roughly corresponding to trapped beam current.

The rise in ion temperature is derived from the ratio of the charge exchanged neutral counts during the injection to those in the absence of injection in the range of thermal energy ($E<7\ T_i$). Results of ion temperature rise are shown in Fig. II.1.3-1. In the lower electron density region, the temperature rise increases with the density. On the other hand, the rise decreases with electron density in the higher density region. The former phenomenon is mainly due to the decrease of the charge exchange loss of beam power with the increase of electron density. The latter is due to the increase of electron-ion energy transfer with plasma density. A maximum ion temperature rise of about 15 % was obtained for $\bar{n}_e=1.1\times10^{13}$ cm^{-3} discharge. The power flow is given in Table II.1.3-1. The range of the ratio of charge exchange rate to slowing-down rate is obtained by fitting the experimentally measured energy spectrum of fast ion to the calculated spectrum based on the homogeneous classical Fokker-Planck code. The expected $\delta T_i/T_i$ value in the table is calculated by applying the scaling law of $\delta T_i/T_i=2P_i^{NBI}/3P_{ei}$. The experimental value of ion temperature rise agrees with the expected value.

Build-up and decay of fast ion energy spectra were measured. The fast neutral analyzer faces the toroidal plasma current. The sampling time is 2 msec. Build-up time is confirmed to be shorter than the above sampling

time, so that attention is given to the decay processes. Typical time behaviour of the fast ion spectrum after turn-off of the beam pulse is shown in Fig. II.1.3-2, where the electron density is $\bar{n}_e = 2.0 \times 10^{13}$ cm^{-3}. Under the condition of large plasma current such as in TFR, the fast ion stays in a narrow region around the birth drift surface for slowing-down to thermal energy. Therefore, in the analysis of chord-averaged fast neutral spectra, it is necessary to take into account the plasma inhomogeneity. Actually it is reported in TFR experiment that the measured decay time of fast ion signal for a certain energy does not agree with the calculated one, assuming a homogeneous target of mean plasma parameters. In the case of relatively small plasma current, however, the spread of drift surfaces become wide, so that it is reasonable to presume that an uniform plasma of mean values represents a non-uniform target plasma for analyzing the slowing-down process of fast ions. Solid lines in Fig. II.1.3-2 are the calculated spectra based on the homogeneous code. Upper and lower curves denote the spectra at the initial and final time of the sampling duration, respectively. The plasma parameters used are $n_e = 3 \times 10^{13}$ cm^{-3}, $n_o = 1 \times 10^{9}$ cm^{-3}, $T_e = 1.0$ keV, $T_i = 0.3$ keV, $Z_{eff} = 4$ and $V_{loop} = 1.6$ V. The spectrum agrees satisfactorily with the measured one.

Table II.1.3-1 Calculated power flow and ion temperature rise

ION SOURCE OUTPUT	H^+	H_2^+	H_3^+	
30 kV - 6 A	2.4 A	0.96 A	0.64 A	4 A
	1.0 A	0.48 A	0.52 A	2 A
NEUTRAL BEAM CURRENT THROUGH THE PORT	0.93 A	1.02 A	1.24 A	3.19 A
NEUTRAL POWER TRANSFERRED TO PLASMA	11.74kW	6.43kW	5.27kW	23.44kW
TRANSFERRED POWER TO IONS	0.86kW*	1.63kW*	2.37kW*	4.86kW*
	0.49kW**	1.05kW**	1.70kW**	3.24kW**
TRANSFERRED POWER FROM ELECTRONS TO IONS				30.8 kW
EXPECTED $\delta T_i/T_i$			7 %** -	10.5 %*

*) $\nu_{cx}/\nu_s = 4$

**) $\nu_{cx}/\nu_s = 8$

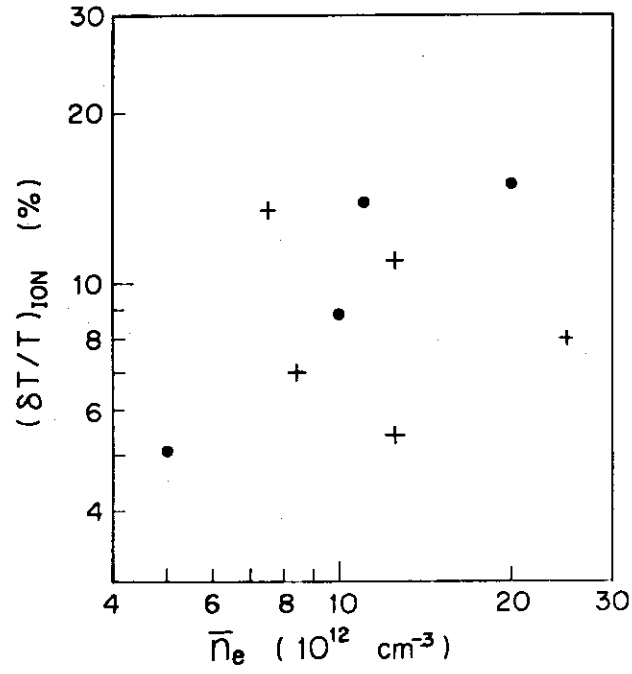

Fig.II.1.3-1 Ion temperature rise versus electron density. The solid circles and crosses indicate 30kV - 6A and 25kV - 8A injection, respectively.

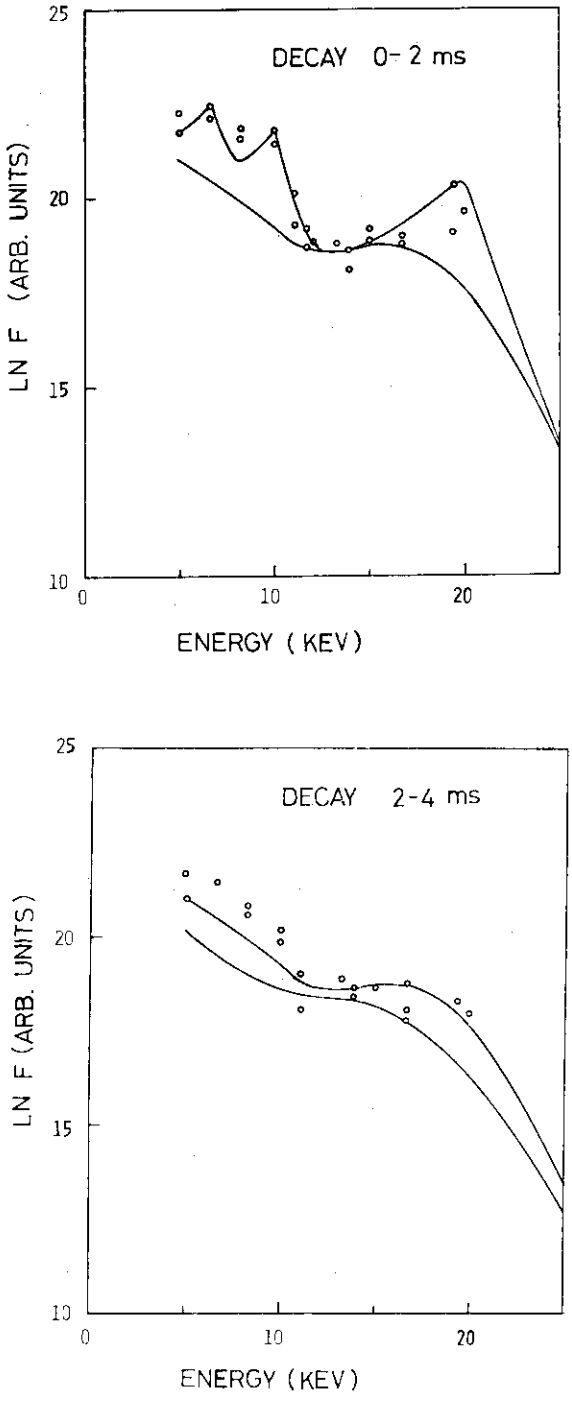

Fig.II.1.3-2 Slowing down process of fast ions. Solid, lines are the calculated spectra based on the homogeneous classical Fokker-Planck code.

1.4 Miscellaneous topics

1.4.1 High density discharge

The cold gas injection system is as follows. A piezoelectric gas valve with response time 2 ms is controlled by independent three square pulsers. A gas flow Q is measured by a fast manometer from the relation $V \cdot \frac{dp}{dt} = Q$, where V is the volume of vacuum vessel and P the pressure. The delay time of a gas influx after start of an applied voltage is 7∿15 ms due to the time constant of a piping in the gas injection system. The gas flow rates of individual elements range from 5 to 30 Torr. l/sec. Controllable parameters of the square pulsers are delay time, pulse width and pulse height. Time behaviour of the density is shown in Fig. II.1.4-1, where only one pulser is operated by changing the delay time. The high density discharges obtained with the cold gas injection are described in the following.

Firstly, the density increases linearly with time for a constant gas flow and, then a disruptive instability occurs. The maximum density is defined as the value achieved just before the disruption. In this experiment a safety factor q(a)=4 is chosen, because a plasma is unstable in q(a)=3. Figure II.1.4-2 shows that the maximum density is given as $\bar{n}_e(\times 10^{13}\mathrm{cm}^{-3}) = 2 \cdot B_T(T)/R(m)$.

Secondly, the electron temperature and the effective ionic charge Z_{eff} in high density discharges are studied. Figure II.1.4-3 shows time evolutions of plasma parameters in low and high density discharges. The electron temperature in the high density discharge decreases by only 10∿20 % that of the low density discharge. The profile of soft x-ray intensity obtained with PIN diode keeps its shape during the density increase, so $n_e(r)$ and $T_e(r)$ seem to keep their profiles. The enhancement factor for the hydrogen bremsstrahlung is also shown in Fig. II.1.4-3. The relation $Z_{eff} \propto 1/\bar{n}_e$ is established. In other words the density of the impurity is constant whether the electron density is high or low. As a result, the one-turn voltage slightly decreases for high density discharges. The scaling $\tau_E \propto \bar{n}_e$ is concluded. The maximum attainable density in experiment is related also to cleanliness of the wall, because a high density discharge is not achieved in poor wall conditions. A Titanium coating system is being prepared for obtaining a clean wall surface.

1.4.2 Partial pressure measurement at plasma boundary

A quadrupole mass spectrometer has been used to analyze neutral gas

species outside a plasma during a discharge. The quadrupole mass spectrometer is mounted 1.2m away from the vacuum vessel of the JFT-2. The vacuum time constant of the tubulation is ∿20msec. The bend in the pipe prevents energetic particles from directly entering the spectrometer from the plasma. The mass spectrometer is pumped directly through the torus. Thin iron plates covering the spectrometer are used as a magnetic shield, and thereby the effect was reduced by a factor 1/10. A spurious signal, so called a dark current, appears at all mases, which is proportional to the base pressure. The neutral gas pressure[19] outside the plasma decreases rapidly from $\sim 10^{-4}$ to 10^{-5}-10^{-6} Torr during a discharge. If the mass peak signal is as high as the dark current, the mass peak signal can not be found out from the spurious signal. Using the data processing system, the mass peak signal can be distinguished from the measured signal which contains the effect of the magnetic field and the dark current. Figure II.1.4-4 shows the procedure. The mass peak signal and the dark current are S(t) and D respectively. The magnetic effects on S(t) and D are $G_s(t)$ and $G_d(t)$. The pressure dependence of the dark current is represented as $G_p(t)$. Then the measured signal can be written as $S(t)\cdot G_s(t) + D\cdot G_d(t)\cdot G_p(t)$. Following the flow chart in Fig. II.1.4-4, the real mass peak signal $S_2(t)$ can be easily found as shown in Fig. II.1.4-5. Figure II.1.4-5 shows the time evolution of the partial pressure corresponding to the carbon of mass 12. It is seen that the gas production begins at the initial stage of the discharge and increases steadily to its maximum at the end of the discharge. The same evolution is observed for other gas species except hydrogen, the pressure of which decreases during a discharge. As described in § 1.2.1, low Z impurity stays the same during the discharge period. Thus, it suggests that all of the impurities at the plasma boundary do not penetrate into the plasma body. Further discussion on this point is now continuing. For the pressure dependence on the sensitivity, we have been developing the special type of spectrometer which secures the linearity of the sensitivity in the pressure range from 1×10^{-4} to 1×10^{-8} Torr.

1.4.3 Breakdown in JFT-2

The electrical breakdown of hydrogen gas in the JFT-2 apparatus has been studied experimentally as the first step of the initial phase research of a Tokamak plasma. The purpose of the study is to clearify the effects of the toroidal drift and various vertical magnetic fields on the breakdown voltage.

(a) Effects of vertical and horizontal fields

The vertical field for plasma equilibrium and the horizontal field to cancel the stray field will enhance the loss of electrons. Variation of the following quantities was examined by changing strength of the external vertical field B_{vd}:

V_p: breakdown voltage observed on the loop voltage trace,

t_o: the time when the microwave density of electrons exhibits an increase first,

t_1: the time when the microwave density of electrons increases by the first fringe ($0.9\times10^{12}cm^{-1}$) from zero,

t_β: the time of the peak of H_β line,

t_p: the time of breakdown.

The values of toroidal field B_t and external horizontal field B_h are adjusted to be 14 kG and 5 G, respectively. This is because it is known empirically that excellent plasma confinement can be obtained under these conditions. Figure II.1.4-6 shows variation of the above quantities versus B_{vd}. Small values of these quantities mean that a situation favourable for breakdown is established. When B_{vd} is about 15 G an optimum condition for breakdown results. The value of t_0, as well as of other quantities takes minimum, when B_t takes another value. The value of B_h is changed in proportion to the value of B_t. Figure II.1.4-7 shows variation of the quantities such as t_0 vs. B_h with B_t=14 kG and B_{vd}=15 G. An optimum condition for breakdown is attained when B_h is about 5 G. An optimum condition for breakdown results still at the value of 5 G of B_h even if the values of B_t and B_{vd} are different from those for Fig. II.1.4-7. This suggests that the value of B_h for the optimum condition is dependent only on the value of B_t regardless of B_{vd}. The quantities such as V_p and t_0 response very sensitively to the variation of the vertical field. There is possibility that the small vertical field can be detected in the presence of a strong toroidal field by observing the minimum breakdown voltage.

(b) Pressure dependence of breakdown voltage

The optimum condition for breakdown is obtained under constant pressure (1.35×10^{-4}Torr, H_2). It will change if the pressure varies. However, breakdown voltage (V_p)-pressure (p) curves have been obtained under the optimum condition for this pressure, because the filling pressure in plasma confinement experiments lies around this pressure. Figure II.1.4-8 shows one of V_p-p curves. If the applied loop voltage is too high, the gas fails to breakdown especially at lower pressure. This phenomenon is attributed

to the toroidal drift of electrons, and is not observed in a usual bredk-down in a linear geometry without strong longitudinal magnetic field. The V_p-p curve in Fig. II.1.4-8 is obtained by varying the peak value of the applied loop voltage without changing its wave form. Thus, the gas is subjected at each shot to different values of dV/dt (rise rate of voltage at breakdown) and of $\int Vdt$ (time integral of the loop voltage from its application to breakdown). The plots of dV/dt and $\int Vdt$ vs. pressure exhibit a two-value chracteristic similar to the plot of V_p. The breakdown voltage V_p increases with increasing value of dV/dt. However, the time integrals of the loop voltages with different values of dV/dt remain unchanged if the pressure is constant. This indicates that the balance between loss and generation of electrons does not occur in a time interval much shorter than the rise time of the loop voltage. The V_p-p obtained under another optimum condition exhibits the effect of the toroidal drift. However, under a condition very different from the optimum one, the effect of the toroidal drift is less noticeable on the V_p-p curve.

(c) Separation of factors influencing breakdown

The loss of electrons in the vertical direction of Tokamak apparatus is brought about by the following vertical fields:

x: effective vertical field equivalent to the toroidal drift,

y: vertical field proper to the apparatus,

z: net vertical field produced by the liner current and the shell current,

B_{vd}: externally applied vertical field.

The values of x, y, and B_{vd} are positive if they are directed upward. The value of z is positive if it is directed upward when the plasma current is parallel to the toroidal field. When direction of the plasma current with respect to the toroidal field is reversed, the direction of the drift due to the vertical fields B_{vd} and y is reversed, and that due to the other vertical fields remains unchanged. It is reasonably assumed that the optimum condition for breakdown is established when various vertical fields reponsible for the loss of electrons are cancelled. Thus, two relations

$$x - B_{vd} - y - z = 0 \text{ and } x + B'_{vd} + y - z = 0$$

hold in the parallel case and in the antiparallel case, respectively, where B'_{vd} is the external vertical field in the antiparallel case. The values of x and y can be determined by

$x = 1/2(B_{vd} - B'_{vd}) + z$ and $y = -1/2(B_{vd} + B'_{vd})$.

Figure II.1.4-9 shows that the value of y is nearly proportional to B_t. The results of Fig. II.1.4-9 were obtained in the later experiment after the previous one for obtaining the results of Fig. II.1.4-6, the apparatus was reassembled in the later experiment. In order to obtain the value of the effective vertical field equivalent to the toroidal drift, it is necessary to evaluate the net vertical field produced by the liner current and the shell current. By calculating the vertical field due to the liner current and measuring the magnetic field near the internal surface of the shell it is found that the field due to the liner current is cancelled by the field due to the shell current except for several gausses. Thus, the major portion of $1/2(B_{vd} - B'_{vd})$ consists of the net vertical field. The calculated value of the effective vertical field equivalent to the toroidal drift is about 0.5 G under the conditions of $B_t=10^4$ G, $V_p=53$ V and $p=1.35\times10^{-4}$ Torr.

(d) Discussion on the experimental results

The breakdown voltage V_{pm} under the optimum condition is plotted against B_t in Fig. II.1.4-10 together with the results of Fig. II.1.4-9. So long as the optimum condition exists for each value of B_t, the breakdown voltage is unchanged for a wide variation of the toroidal field regardless of parallel or antiparallel direction of the plasma current. If the various vertical fields responsible for the drift of electrons are cancelled completely by the externally applied vertical field, the electrical bredkdown in the toroidal geometry takes place as if it were a breakdwon in a linear geometry without longitudinal magnetic field. In order to interpret the breakdwon under the optimum condition phenomenologically, models A and B are tried. In model A, the life time of electrons contributing to breakdown is not restricted, but the number of electrons is assumed to decrease by a factor γ after every complete round of electrons along the major circumference of the apparatus. The factor γ is equivalent to the coefficient of secondary emission if an imaginary electrode is disposed in the toroidal path of electrons. In model B, it is assumed that electrons do not decrease after each complete round of them, but instead the life time of electrons contributing to breakdown is restricted in effect. The length of that path is considered as an interelectrode distance which is followed by an electron during its life time. Figure II.1.4-11 shows a plot of t_{0m} (the value of t_0 under the optimum condition) and V_o (the voltage at t_{0m}) vs. pressure with $B_t=10$ kG and $B_h=3.5$ G. The factor γ of model A and the life time of model B are determined from Fig. II.1.4-11.

The minimum breakdown voltage obtained with models A and B agree, but are smaller than the minimum breakdown voltage of Fig. II.1.4-11. This is possibly because the loop voltage is raised too steeply to establish the characteristic between breakdwon voltage and pressure.

1.4.4 Remodeling the JFT-2 device for impurity and heating studies

JFT-2 is a moderate size tokamak, which was constructed in the spring of 1972.[20] The main subject of research on JFT-2 is to realize a stable high temperature plasma above several hundreds eV, and to study plasma confinement in tokamak configuration. Experiences in design and manifacturing of the device, and in diagnostics of high temperature plasmas are also important objects of the JFT-2 project. Features of the device are small aspect ratio, a dynamic limiter retractable at a speed of 10 m/s, and good axisymmetry.

The confinement experiments at a toroidal field of 9 kG were made.[21] In the autumn of 1975 the toroidal field was increased up to 18 kG. Now the typical plasma parameters of a 160 kA discharge are $T_e(0) \simeq 1.2$ keV and $T_i(0) \simeq 0.35$ keV for $\bar{n}_e = (1\text{-}2) \times 10^{13}$ cm^{-3}. The main impurity is oxygen and the effective ionic charge 3-5.[16]

As a next step of the JFT-2 project, we have made a choice to place emphasis on the plasma wall interaction and furhter heating of the tokamak plasma. The experiment is scheduled to begin in the Autumn of 1978.

(a) Fundamental concepts

Tokamak experiments have made remarkable advances over the world in understanding plasma confinement and heating in tokamak devices, which encourages big tokamak projects aiming at the ignition experiment. In JAERI the JT-60 project has been started, and now design of the device as well as technological development of the major components is at the final stage. There remain, however, numerous problems to be clarified. Among them the influence of impurity ions on the tokamak discharge has been recognized as one of the most serious problems. For JT-60 several methods are studied reducing the impurity flux into the plasma. They are a magnetic limiter, special processing of the first wall, etc.. Also, construction of JT-4, a medium size tokamak with elliptic plasma cross section and with an axisymmetric divertor, is projected, which will be operated togehter with JT-60.

Under the circumstances, the next phase of the JFT-2 project has been discussed. Emphasis will be placed on the plasma wall interaction and the

supplementary heating of the tokamak plasma. There exist several restrictions in remodeling the existing JFT-2 device, i.e., limited fund, limited power supply for toroidal field, etc.. We must proceed with the design with minimum modification on the existing device. In the remodeling design, the following conditions are taken into consideration:

(1) light impurities (oxygen and carbon) contamination of the liner is minimized by several cleaning techniques,

(2) the ultra-high vacuum as high as 10^{-9} Torr is aimed at,

(3) emphasis is placed on the plasma wall interaction study,

(4) RF plasma heating is studied,

(5) the dimensions of JFT-2 are retained as they are,

(6) as many diagnostics and pumps as possible are provided,

(7) large spaces for observations are ensured.

(b) Vacuum chamber

The vacuum chamber consists of 14 box-shaped sections and 14 bellows sections. The box-shaped sections are used for diagnostics and pumps, and connected with each other by the bellows of an inner diameter of 60 cm. Tangential ports are also provided.

Three kinds of limiter are applicable. The first is an aperture limiter of 50 cm diameter, the second a dynamic rail limiter with speed 10 m/s, and the third a rotating rod limiter. All limiters are made of molybdenum.

The vacuum chamber and the limiters are bakable up to 450°C. Ultra-high vacuum seals should be used. The vacuum chamber is pumped by turbomolecular pumps, now used for JFT-2.

(c) Toroidal magnetic fields

The present toroidal magnetic fields of JFT-2 are produced by sixteen fan-shaped coils. The gap between the toroidal coils is narrow (about 130 mm), which ensures uniformity of the toroidal field (the maximum field ripple<1%), however, this leads to difficulty in access to the ports for diagnostics and pumps. In order to ensure enough space for easy access to a plasma, the toroidal coils will be converted into those with gaps of 250-300 mm.

(d) Vertical magnetic fields

Sufficient space for diagnostics results in difficult installation of the shell. Giving up the merits of the shell, a feedback control system is thus provided for active vertical control of a plasma.

The vertical magnetic fields consist of three components. The first

is a constant vertical field ($\lesssim$0.4 kG) produced by coils placed outside the toroidal winding. The second is a pulsed vertical field ($\lesssim$0.4 kG), which is applied in start-up of a discharge. The third is a vertical field ($\lesssim$0.1 kG), which controls the plasma position in the intermediate stage of a discharge. The latter two fields are generated by coils inside the toroidal winding.

(e) Wall cleaning

In order to minimize the contamination of the molybdenum liner of the first wall by light impurities (oxygen and carbon), the following methods are tested. The liner is baked up to 450°C.

The molybdenum coating is also applied over the liner wall. This technique is under development.

A few methods of discharge cleaning are tested. The first is a 50-80 kA discharge per minute, as used in JFT-2. The second is a 60 Hz cathodeless discharge, and the third is a glow discharge. Characteristics of these discharge cleanings are studied through surface observation with AES and SIMS.

References

(1) Annual Report of JAERI Thermonuclear Fusion Laboratory JAERI-M 6926 (1977) 3.
(2) Shiho M., et al. : to be published.
(3) Suzuki N., et al. : to be published.
(4) Tsuda T. and Tanaka M. : J. Phys. Soc. Japan 38 (1975) 1228.
(5) Suzuki N. : to be published.
(6) Fujisawa N., et al. : Proc. of Fifth International Conference on Plasma Physics and Controlled Nuclear Fusion Research, November 1974, Tokyo (IAEA, Vienna, 1975) Vol.1, p.3.
(7) Shoji T., et al. : to be published.
(8) Pawer E.J., et al. : Journal of Appl. Phys. 47, 9 (1976) 3911.
(9) Liewer P.C., et al. : Phys. Fluids 19, (1976) 276.
(10) Yamamoto T., et al. : to be published.
(11) Kadomtsev B.B. : Plasma Turbulence, (Academic Press, New York 1965), Chap. 4.
(12) Kadomtsev B.B., et al. : Nucl. Fusion 11, (1971) 67.
(13) Kobayashi T., et al. : JAERI-M 7014 (1977), (in Japanese).
(14) Berry L.A., et al. : IAEA-CN35/A4-1 (1976).
(15) Goeler S. von, et al. : Nuclear Fusion 15 301 (1975).
(16) Maeda H., et al. : 6 th International Conference on Plasma Physics and Controlled Nuclear Fusion Research(Berchtesgarden, Federal Republic of Germany, 1976) IAEA CN-35/A-18.
(17) Odajima K., et al. : to be published.
(18) Goeler S. von, et al. Phys. Rev. Lett. 33, (1974) 1201.
(19) Maeno M., et al. : JAERI-M 6712 (1976) (in Japanese).
(20) Itoh S., et al., in Toroidal Plasma Confinement (Proc. 3rd Int. Symp., Garching, March, 1973) B-4.
(21) Fujisawa N., et al., Plasma Physics and Controlled Nuclear Fusion Research, Vol. 1 (IAEA, Vienna, 1975) p.3.

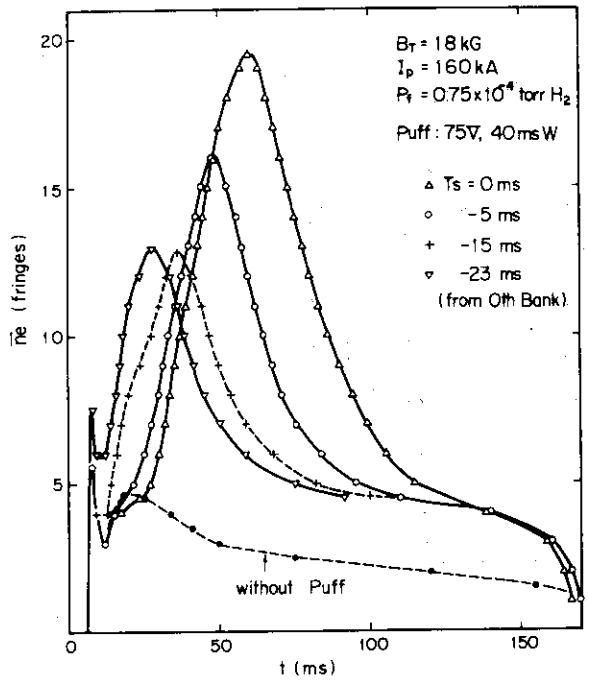

Fig.II.1.4-1 Time evolution of the electron density for one pulse operation of the control puff. The timing of the cold gas ingection is changed with the delay time of the pulser. In the figure 1 fringe corresponds 1.0×10^{13} cm^{-3}.

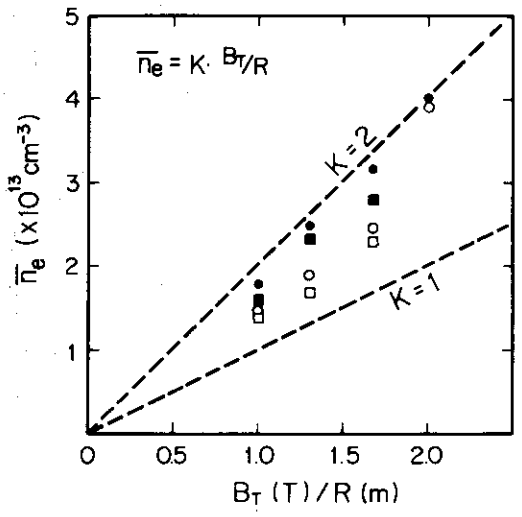

Fig.II.1.4-2 The maximum density versus B_t/R according to the Murakami scaling. The timing and the pulse height of the pulser are changed. B_t = 18 kG, I_p = 160 kA and q(a) = 4.

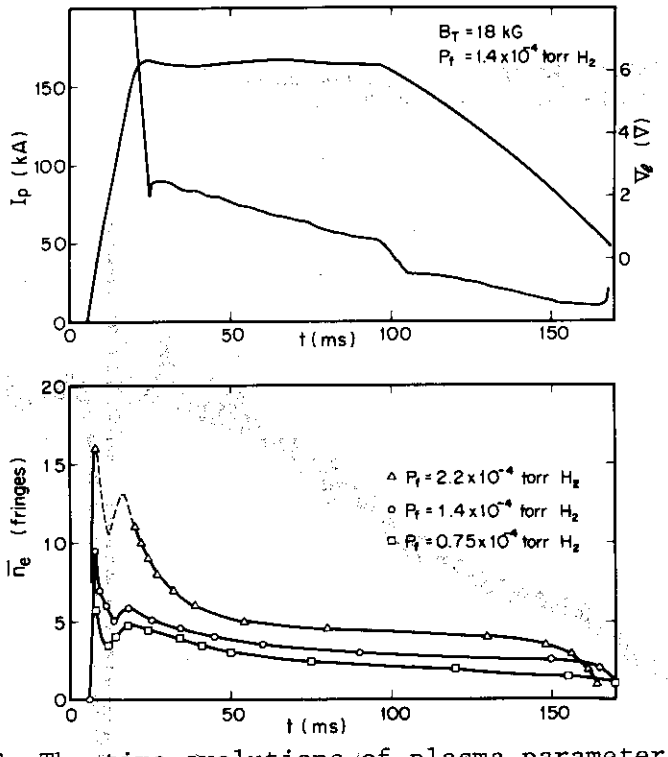

Fig.II.1.4-3 The time evolutions of plasma parameters for the low (solid line) and the high (dotted line) density discharges. The electron temperatures at the plasma center are estimated from the soft x-ray spectra and the relative value of Z_{eff} is evaluated from the soft x-ray intensity.

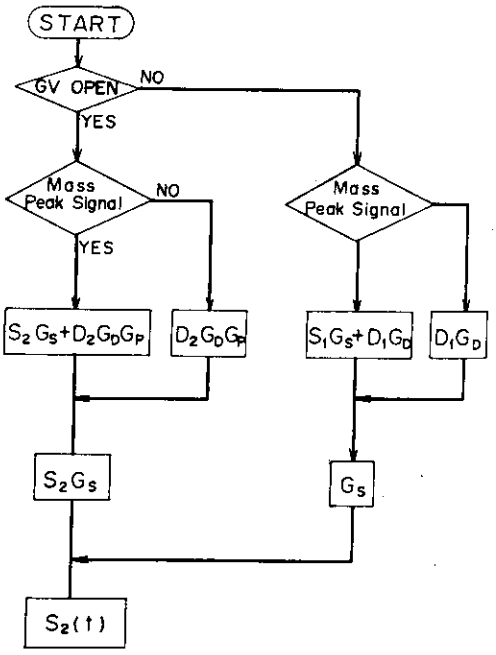

Fig.II.1.4-4 Flow chart of the data processing program

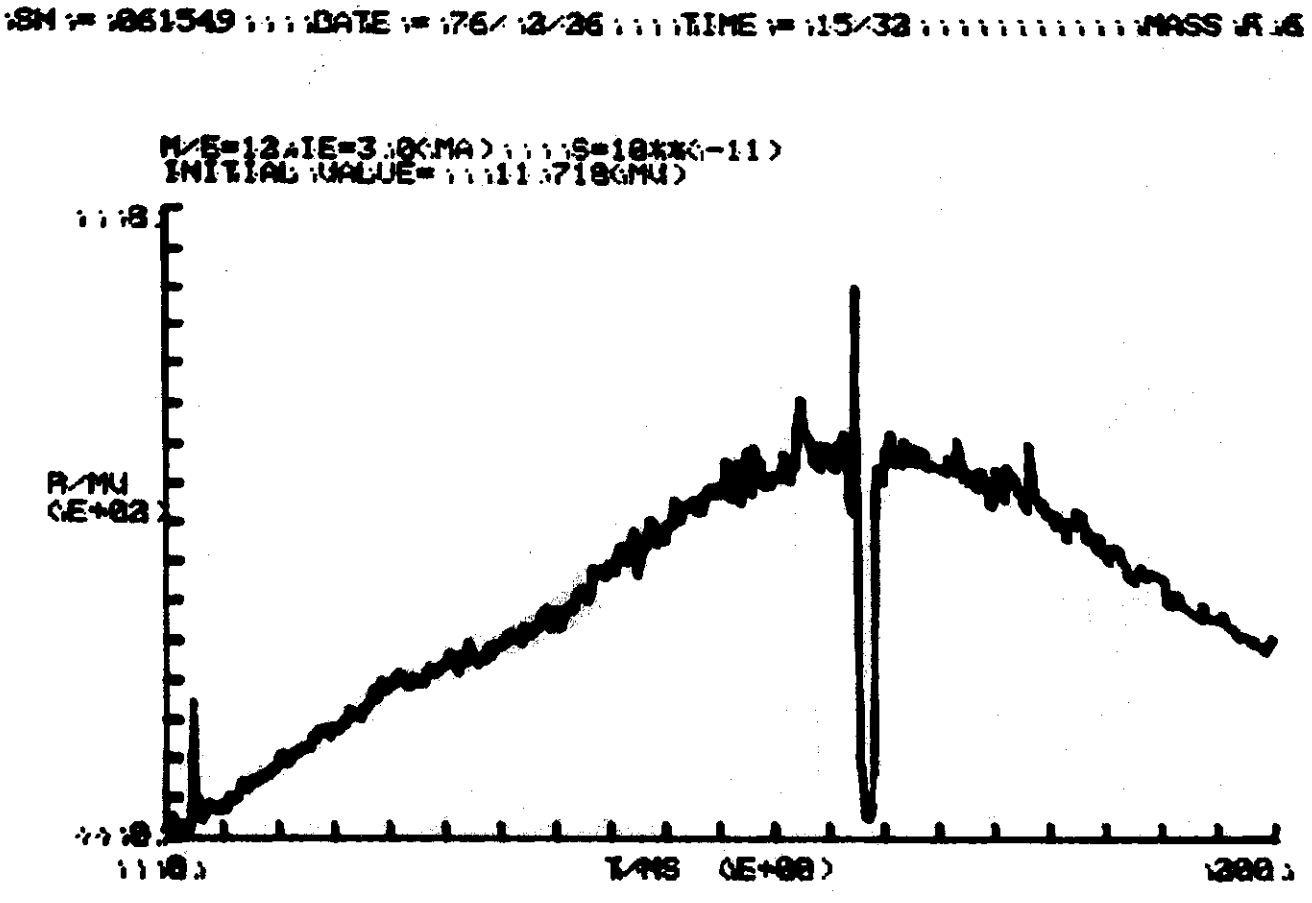

Fig.II.1.4-5 Real mass peak signal $S_2(t)$.
The mass number is 12 which corresponds to carbon.

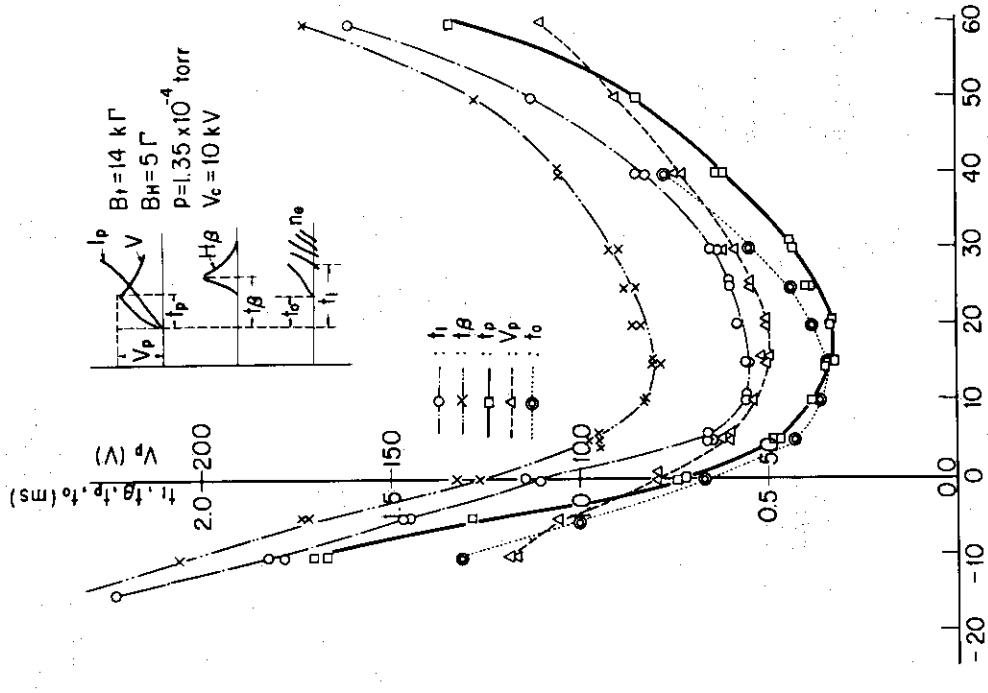

Fig.II.1.4-6 Plots of various quantities such as breakdown voltage versus the external vertical field.

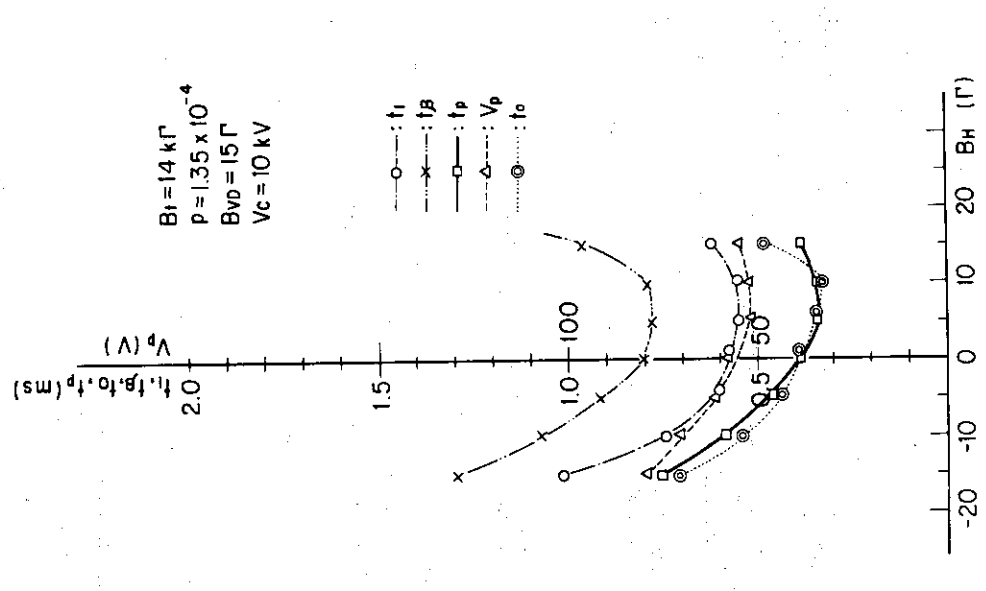

Fig.II.1.4-7 Plots of various quantities such as breakdown voltage versus the external horizontal field.

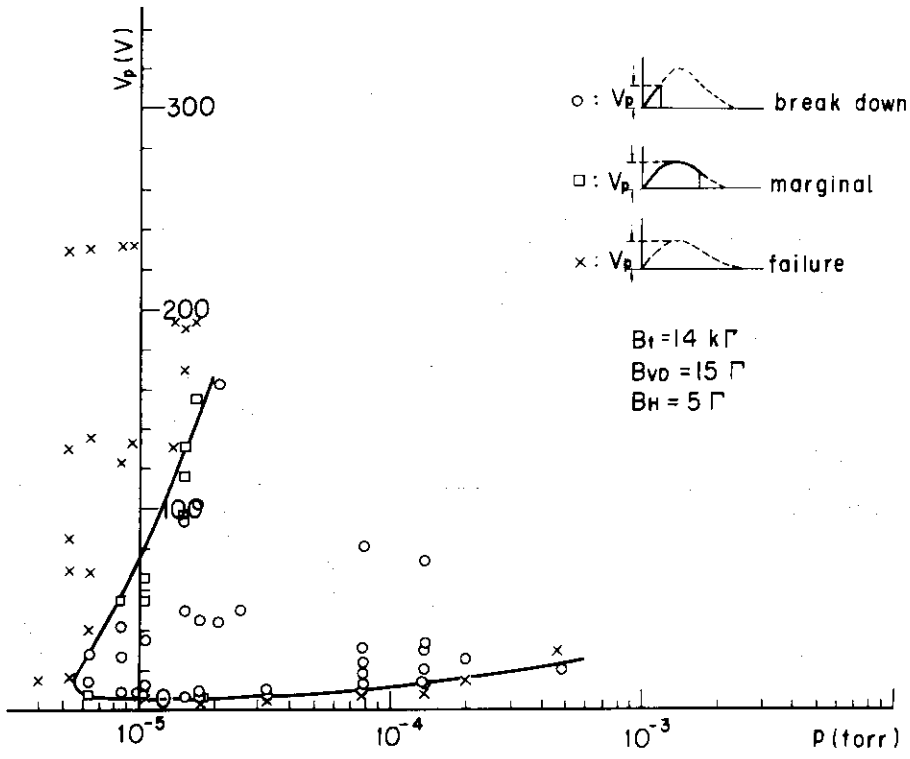

Fig.II.1.4-8 Breakdown voltage-pressure curve under an optimum condition.

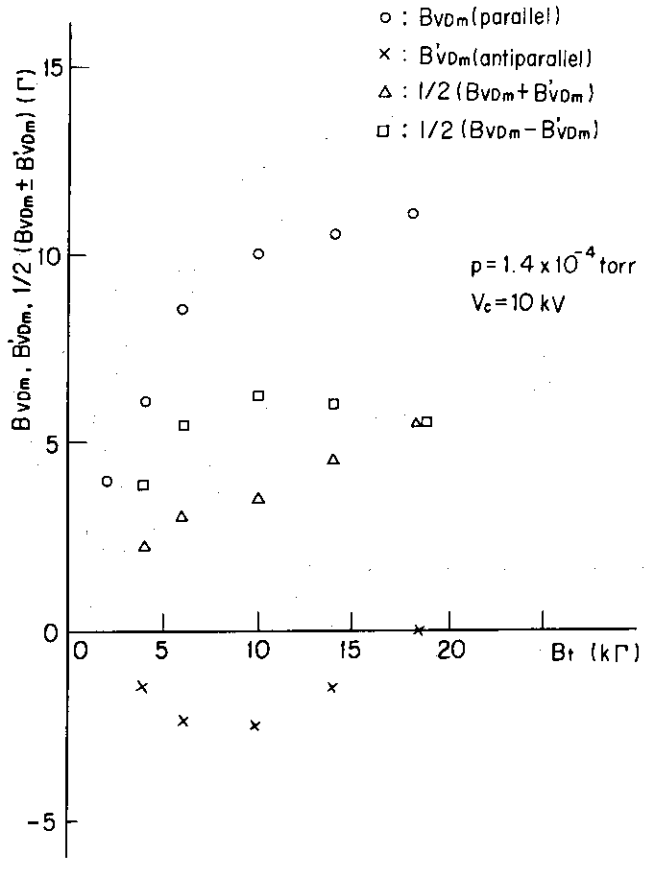

Fig.II.1.4-9 Plots of the external vertical field giving optimum conditions versus toroidal field in the parallel and the antiparallel cases.

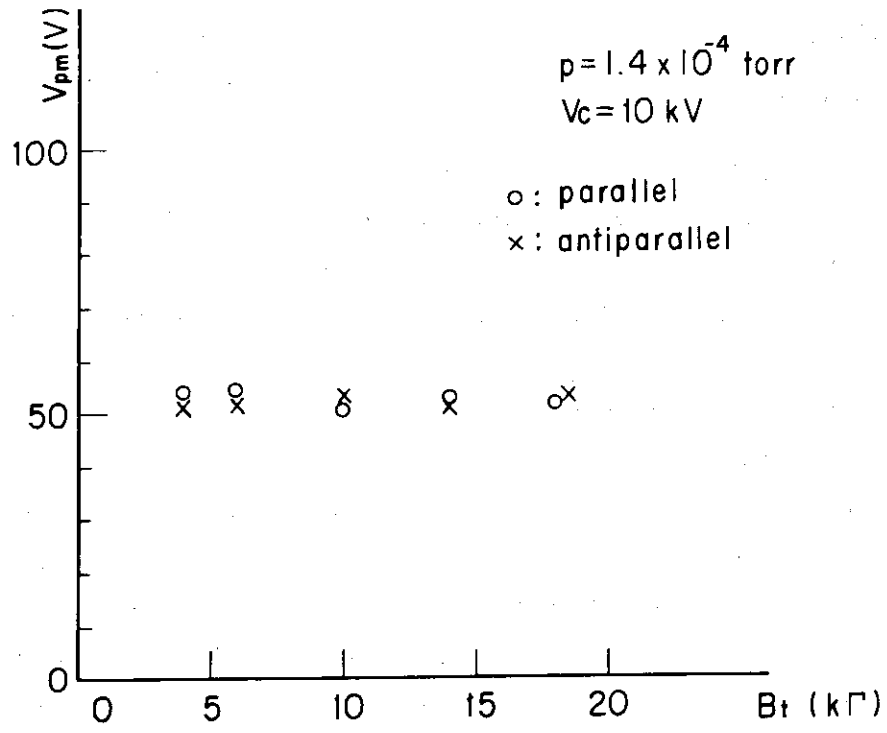

Fig.II.1.4-10 Plots of breakdown voltages under optimum conditions versus toroidal field.

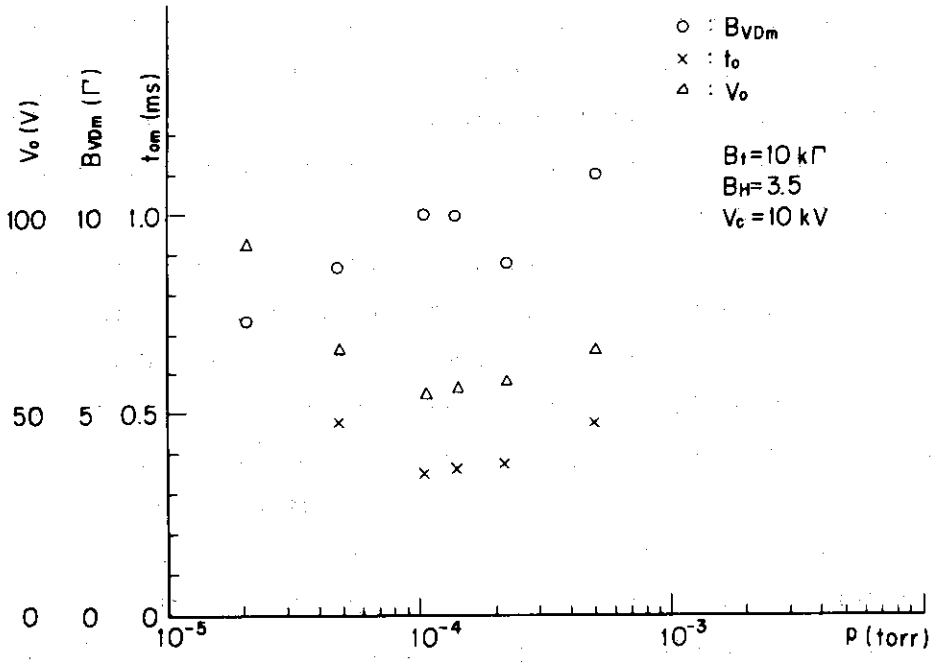

Fig.II.1.4-11 Plots of t_{0m} (the value of t_0 under the optimum condition) V_0 (the voltage at t_{0m}) versus pressure. The external vertical field giving optimum conditions is also plotted versus pressure.

2. JFT-2a(DIVA)

2.1 Introduction

DIVA had completed 10 kG divertor experiments in December, 1976 and has been put reconstructed for increasing toroidal field up to 20 kG. The 20 kG divertor experiments will start in June, 1977.

Plasma-wall interactions namely, the behavior of heavy impurities in light-impurity free plasma and the behavior of light impurities were investigated in the period of April 1, 1976 to March 31, 1977 in DIVA (JFT-2a). The main results are as follows:

(1) Particles diffusing from the main plasma are reflected at the gold surface of the metal shell.

(2) Relatively high energy electrons exist in the scrape-off layer and these cause a large heat transmission rate to a floating plate.

(3) The light impurities (C, N, O) are not influential in DIVA and they come from the burial chamber, and not from the gold surface of the metal shell.

(4) The heavy impurities are influential in DIVA and responsible for the radiation loss from the main plasma. The contamination is caused by evaporation due to the heat flux on the copper rods supporting titanium wires in the burial chamber and presumably the heat flux on the movable shells. The molybdenum target employed to intercept particle and heat flux to the burial chamber furhter reduces the radiation loss to less than 30% of the ohmic dissipation (P_{ohm}).

Thermal insulation by the plasma sheath is effective with respect to the metal contamination due to the heat flux from the plasma flow.

(5) The divertor reduces the plasma-wall interaction and consequently reduces the radiation loss due to heavy impurities by a factor of 3. The radiation power from the plasma due to heavy impurities (pressuremably gold and/or copper) concentrates in the wavelength 123 Å - 243 Å.

Plasma wall interactions were summarized in ref. (1) and the behavior of heavy impurities in light-impurity free plasma was given in Refs. (1) (2) and (3). The behavior of light impurities was given in Refs. (4) and (5).

The following sections describe the summaries of the above-mentioned works performed during the period under the review.

2.2 Radiation loss

Heavy impurities are influential in DIVA experiments, especially regarding to radiation loss from the main plasma. Because of the lack of knowledge about spectroscopic properties of gold and copper, wall materials used in DIVA, it is difficult to estimate the amount of them in the plasma. However, power spectrum emitted from the main plasma are measured with a grazing incidence vacuum UV monochrometer calibrated by a branching method.

Figure II.2.2-1 shows the power spectrum vs. wavelength in the range 123 Å - 243 Å. The spectrograph of the range 20 Å - 1300 Å shows that radiation power from the plasma concentrates in this range. Comparative study is performed with respect to the power spectrum in the wavelength 123 - 243 Å on various discharge conditions. Unfortunately it is quite difficult to identify what species this pseudo continum is due to, however, the profile of the spectrum is almost the same on various discharge conditions except its magnitude.

Figure II.2.2-2 shows the relationship between the total radiation power measured with pyroelectric detector (P_{py}) and that measured with the VUV monochrometer (P_{vuv}). Closed circles represent the relationship in the case without the divertor and triangles in the various discharge conditions with the divertor reported in Ref. (1). An open circle represents that in the optimum condition, that is, in the case with the divertor and the Mo target in the divertor region. The results show that radiation loss due to heavy impurities is comparable with power loss due to charge-exchange hot neutrals in the optimum condition. The radiation loss in this optimum case is less than 30% of the ohmic dissipation (Pohm). The detailed description is found in Ref. (6).

2.3 Heavy impurities

Impurities observed with vacuum UV spectroscopy are grouped into light elements (C, N, O) and heavy elements (Au etc.). The light elements can be reduced to half by flushing titanium on about half of the divertor chamber surface and their concentrations are less than 1 % of the plasma. This suggests that the light elements come from the surfaces of the burial chamber and not from the surface of copper shells covered with gold films, i.e., the clean surfaces in the DIVA device decrease contamination of the plasma due to light elements. The resistivity and the radiation loss are not changed when the amount of light elements is reduced to half.

Therefore the heavy elements (Au etc.) are more influential in DIVA experiments. The DIVA device uses various materials which can be the source for impurity contamination of the plasma. The surfaces of the copper shells are covered with gold films and the protection plates are made of gold. Materials used in the burial chamber are copper, titanium and stainless steel. Supports for titanium wire are made of copper rods and the surfaces of which are covered with titanium and gold. It is difficult to estimate the amount of these heavy elements in the plasma spectroscopically, especially the amount of gold and copper. Qualitative investigations on the cause of the contamination of the plasma by heavy elements and the impurity behaviours are performed.

2.3.1 Two-dimensional measurement of heat flux

Two-dimensional measurements of orbits of high energy electrons (10 - 100 keV) and of the heat flux to the burial chamber were performed across the plasma with an axisymetric divertor. Figure II.2.3-1 shows the orbits of high energy electrons (10 - 100 keV). The results show that the high energy electrons are well-guided to the burial chamber and collide with the copper rods supporting titanium wire. The behavior of high energy electrons is governed by magnetic field configurations and gives the information about the equilibrium configuration with a magnetic separatrix surface. These will be discussed in Ref. (7).

Figure II.2.3-2 shows the heat flux to the burial chamber. The heat flux to the burial chamber disappears beyond the copper rods. About 30% of the heat flux measured at R=40 cm is missing between R=40 cm and R=43 cm. The lost heat flux is presumably deposited to the movable shells.

2.3.2 Origin of heavy impurities

The cause of the contamination of the plasma by heavy elements is investigated qualitatively[1][2].

Figure II.2.3-3 shows the typical waveforms of loop voltage V_L, radiation losses P_R, time evolution of total particles N_e, ion saturation current to the copper shells I_s, heat flux q to the divertor at Z=4.5 cm and R=40 cm and charge-exchange neutral flux whose energy is above 250 eV. Solid and broken lines represent the variation of plasma parameters during the discharge with an additional gas injection of $4.5\times10^{19}H_2/s$ (Case A) and $1.7\times10^{19}H_2/s$ (Case B), respectively. The figure shows that the charge-

exchange neutral flux has no correlation with the increase of P_R in the later phase of the discharges and also shows there is not correlation between ion flux incident on the shell surface and the increase of P_R. These results suggest the heat flux density in the scrape-off at R=40 cm has the correlation with the increase of P_R.

Figures II.2.3-1 and 2.3-2 show the results of two dimensional measurements of orbits of high energy electrons (10-100 keV) and the heat flux to the burial chamber. The heat flux to the burial chamber disapears beyond the copper rods supporting titanium wire and the heat flux density at the surface of the rods is almost the same as the one at R=40 cm both in Case A and B. It should be noted here that all of the high energy electrons and the whole of the heat flux to the burial chamber are intercepted by these rods due to the rotational transform of the magnetic field.

The results show that the copper rods supporting titanium wire are exposed to the heat fluxes of 430 watts/cm^2 (Case B) and 180 watts/cm^2 (Case A) at 15 ms. The difference between two cases are due to the amount of high energy electrons in the scrape-off plasma. High energy electrons cause a large heat transmission rate to electrically insulated conducting rods and cause the evaporation of the material from the rods' surfaces. When the copper rods are positively biased to collect electron saturation currents on the supports in Case A, the radiation loss P_R and loop voltage V_L increase and become the same as in Case B. This indicates that the violation of thermal insulation of the copper rods from the plasma also leads to the increase of the radiation loss and the resistivity.

Above mentioned results show that the increase of the radiation loss from the plasma in the later phase of the discharge is due to the plasma contamination by heavy elements, a part of which come from copper rods supporting titanium wire and the release of the metals is caused by evaporation due to heat deposition on the surface of the rods. According to the heat flux measurements (Fig. II.2.3-2), about 30 % of the heat flux measured at R=40 cm is missing between R=40 cm and R=43 cm. The lost heat flux is presumably deposited to the movable shells. The experimental results show that the resistivity and radiation loss are actually very sensitive to the opening width d of the movable shells. When the opening width d is changed form 9.5 cm to 5 cm, the loop voltage, the radiation loss and the intensity of Au II line (1800 Å) increase by a factor of 1.4, 1.4 and 1.5 respectively, while the ion saturation current falling on the surface of the movable shell increases by a factor of 2.

Particle flux to the movable shells amounts about half of that, guided to the burial chamber even with the opening width d of the movable shells kept at 9.5 cm. Therefore, according to the following discussions (section 2.3.3) the lost heat flux is presumably accounted for by this particle flux to the movable shells if we assume heat transmission rate $F\gamma$ for ion flux to the movable shells is about half of that for ion flux to the burial chamber. The results show that there exists also a possibility of impurity contamination caused from the edge of the movable shells.

2.3.3 Heat transmission rate to a floating plate in the scrape-off layer

Heat which diffuses from the main plasma flows in the scrape-off layer and reaches the surfaces of the materials placed in the scrape-off layer. An electrostatic sheath potential is built up in front of an electrically insulated conducting plate and takes various values accordingly with plasma species and electron temperature. The magnitude of an electrostatic sheath potential plays an important role for thermal insulation of the floading plate from the plasma flow incidence and several authors have investigated heat transmission rate in view of these respects[8]~[10]. As noted in previous experiments[11][12], heat fluxes in the scrape-off layer are highly asymmetric as to the median plane and high energy electrons escaping from the main plasma cause this asymmetry. In that case heat transmission rate to an insulated conducting plate placed at R=40 cm is a few to 10 times as large as the one expected from the hydrogen plasma flow when a normal plasma sheath is assumed with parameters of the bulk plasma in the scrape-off layer.

Figure II.2.3-4 shows profiles of heat fluxes q, electron temperature T_e and ion saturation currents at R=40 cm and t=20 ms in Case B. Figure II.2.3-5 shows time variations of the heat fluxes at various vertical positions at R=40 cm in Case B. The results show the profile of the heat flux transmitted to the floating plate have a sharp peak and time variation of the flux is very sensitive to the Z-position in the scrape-off layer.

Figure II.2.3-6 shows energy spectrums of electrons in the scrape-off plasma measured with a Faraday cup. The results show relatively high energy electrons exist in the scrape-off plasma and the amount of them is varied with the time during the discharge. We assume that distribution function of electrons in the scrape-off layer in these experiments is described as two component Maxwellian. According to the simple calculation similar to

one by Lovberg[9], heat transmission rate ($\equiv q/i_s T_e$) is described $F\gamma$ where F is a correction factor for a two component model. Here the case with F=1 and γ=7.8 corresponds to Lovberg's expression for hydrogen plasma of $T_e=T_i$ and the case with F=1 and γ=4.8 corresponds to Hobbs' expression with no secondary emission and $T_i=0$.

Figure II.2.3-7 shows the relationship between q and $i_s T_e$ measured in the scrape-off layer at R=40 cm. Solid and broken lines represent the case of $q=7.8\ i_s T_e$ and $q=4.8\ i_s T_e$, respectively. The experimental results are plotted with no bracket and the corresponding corrected values q vs. $Fi_s T_e$ are shown with brackets. F is calculated by determing distribution function of electrons with a Faraday cup of each corresponding time and position. The results show that heat transmission rate to the floating plate is relatively large, and the two component model presumably accounts for these large transmission rates at various positions and times, however secondary electron emission effects can not be excluded experimentally, which effects are pointed out in Ref. (8). The detailed discussions will be given in Ref. (13).

2.4 Light impurities

Discharge characteristics concerning light impurities were investigated (Refs. (4) and (5)). DIVA is designed specially to reduce the contamination by light-impurities usually found in ordinary tokamaks; (1) the plasma is surrounded by a gold plated (20 μm in thickness) copper shells which has an opening towards the burial chamber, (2) on the burial chamber which is made of stainless steel, a divertor coil which carries a current parallel to the plasma current and titanium evaporation sources are set. More detailed description of the device and recent experimental result on the divertor action are found in Refs. (2), (3) and (11) respectively.

The titanium is evaporated from 16 ULVAC Ti-wire sources which are set to turn around the inner side of the torus. Evaporation is made with closing the movable shells not to contaminate the gold surface with titanium. The amount of sublimation is set to 0.1 gm and the area of approximately 3×10^4 cm^2 is exposed to the sources. This corresponds to about 50 monolayers.

Before gettering the burial chamber with titanium, the base pressure in the torus is 1×10^{-7} Torr. With gettering, base pressure as low as 3.5×10^{-8} Torr have been obtained. After the gettering, VUV measurement

shows that the gettered surface remains clean over a hundred shots and it remaines some pumping capacity over a few days.

To avoid saturating the surface before the discharge, the inside of the shell is filled via a fast pulsed gas valve, 500 μsec before the start of discharge. A second slower pulsed valve is used to inject additional gas into the plasma.

The operational conditions and typical plasma parameters are as follows; toroidal field is 10 KG, peak plasma current is 14 KA, the ratio of divertor hoop current to the plasma current is 1.2, peak-electron temperature is 200 eV, peak ion temperature of 75 eV and energy confinement time is 0.7 msec.

The VUV measurement for before-gettered discharge shows the following result on impurity concentrations at middle stage of the discharge with $\bar{n}_e \sim 1 \times 10^{13}$; OVI $\sim 4 \times 10^{10}$, NIV $\sim 6 \times 10^{8}$, CIII $\sim 5 \times 10^{9}$ (all in cm^{-3}).

Intensity profile of CV is measured along the chords across the minor radius using calibrated visible monochromator, and its accumulation is calculated by assuming a modified coronal model for the helium-like ions[14]. The calculated intensity ratio of CV 40.27 and 40.73 Å lines is found to agree with the measured value. The carbon is dominatly in helium-like (CV) state in this discharge and its accumulation appears to be 1×10^{11} cm^3.

As is deduce from the wave form of OVI 1032 Å intensity and its ionization potential (138 eV), the oxygen is thought to be dominantly in OVI and OVII (helium-like state). Although we cannot evaluate the exact oxygen accumulation in this discharge, it is sufficient for power loss considerations since 2S-2P transition (1032 Å) is most strongly excited. Apparently the accumulation of the nitrogen is negligible compared with oxygen and carbon impurities.

Figure II.2.4-1 shows the discharge chracteristics of before and after the gettering. The measurements for after-gettered discharge are made within 15 shots after the gettering.

After gettering, light intensities of OVI 1032 Å, NIV 765 Å and CIII 977 Å decreases by a factor of 2-3 in whole period through the discharge. It is clear that the impurity flux from the burial chamber is important from the discharge start-up, and that the fresh titanium surface decrease low-Z impurities.

As can be seen in the figure, however, appreciable reduction of the plasma resistivity is not observed. Also the reduction of total radiation power is much small compared with that of the line radiation from low-Z impurities.

Thus it can be recognized that, including even without gettered case, the low-Z impurities are not important in DIVA plasma.

References

(1) Maeda, H., et al., Proc. Int. Symp. on Plasma Wall Interaction, Jülich, Germany, (1976) 537.

(2) Maeda, H., et al., 6th IAEA Conf. on Plasma Physics and Controlled Nuclear Fusion Research, Berchtesgaden, paper IAEA-CN-35/A18 (1976).

(3) Yamamoto, S., et al., to be presented at 8th European Conference on Controlled Fusion and Plasma Physics, Prague.

(4) Nagami, N., et al., to be published in Nuclear Fusion.

(5) Nagami, N., et al., to be published in Nuclear Fusion.

(6) Odajima, K., et al., to be published in Nuclear Fusion.

(7) Yamamoto, S., et al., to be published in Nuclear Fusion.

(8) Hobbs, G.D., et al., Plasma Physics 9 (1967) 85.

(9) Lovberg, R.H., "Plasma Diagnostic Techniques" (R.H. Huddlestone and S.L. Leonard, ed.) Chap. 3 Academic Press New York (1965).

(10) Feinberg, B., Plasma Physics 18 (1976) 265.

(11) Shimomura, Y., et al., Proc. 7th Europ. Conf. on Controlled Fusion and Plasma Physics, Lausanne, 2 (1975) 81.
Shimomura, Y., et al., Phys. Fluids 19 (1976) 1635.

(12) Maeda, H., et al., Nucl. Fusion 16 (1976) 148.

(13) Kimura, H., et al., to be published.

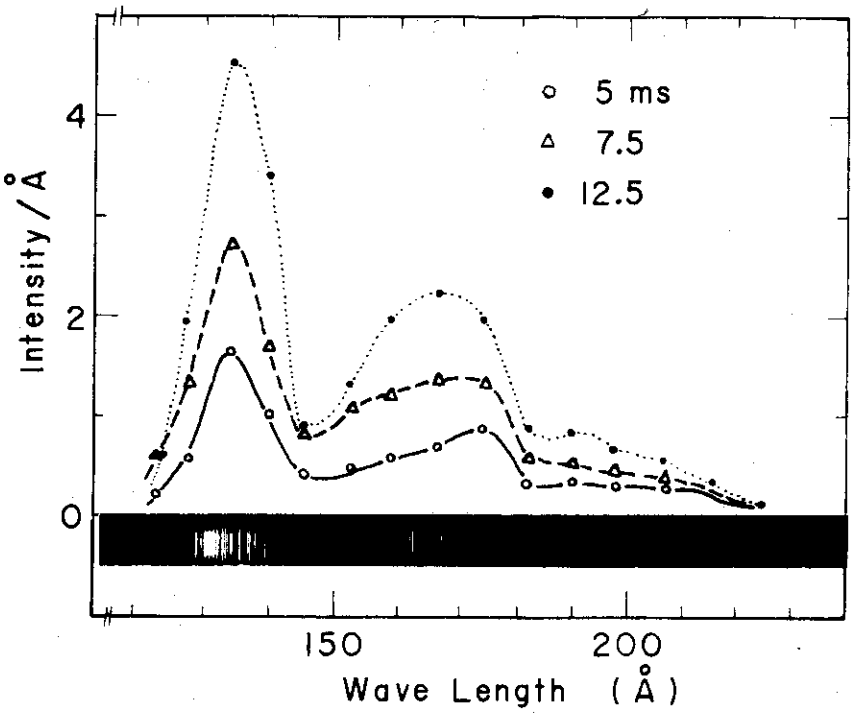

Fig.II.2.2-1 Power spectrum vs. wavelength in the range 123-243 Å.

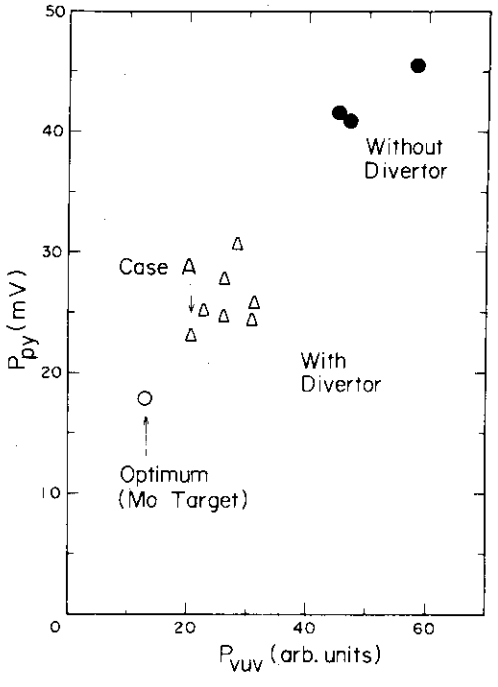

Fig.II.2.2-2 Relationship between the total radiation power including hot neutral outflux (P_{py}) and the radiation power measured with the VUV monochrometer (P_{VUV}).

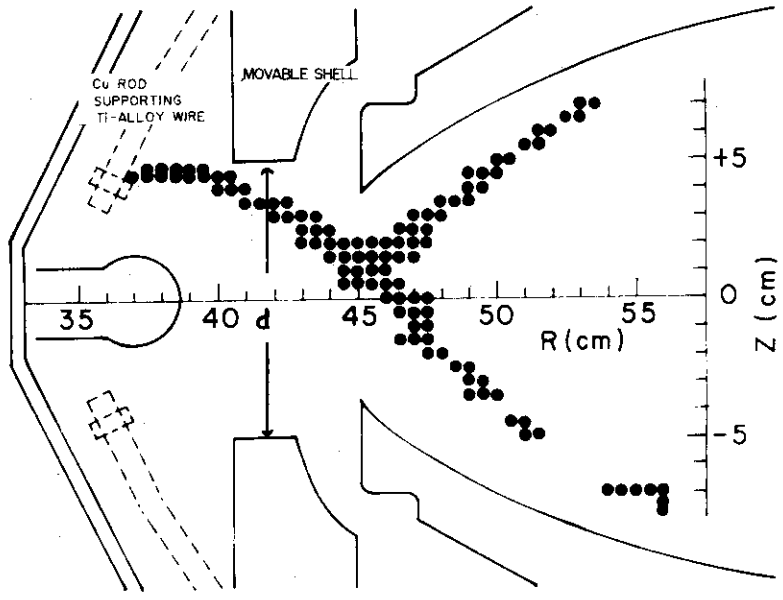

Fig.II.2.3-1 Two dimensional measurements of orbits of high energy electrons (10-100 keV). These are well-guided to the burial chamber and collide with the copper rods supporting titanium wire.

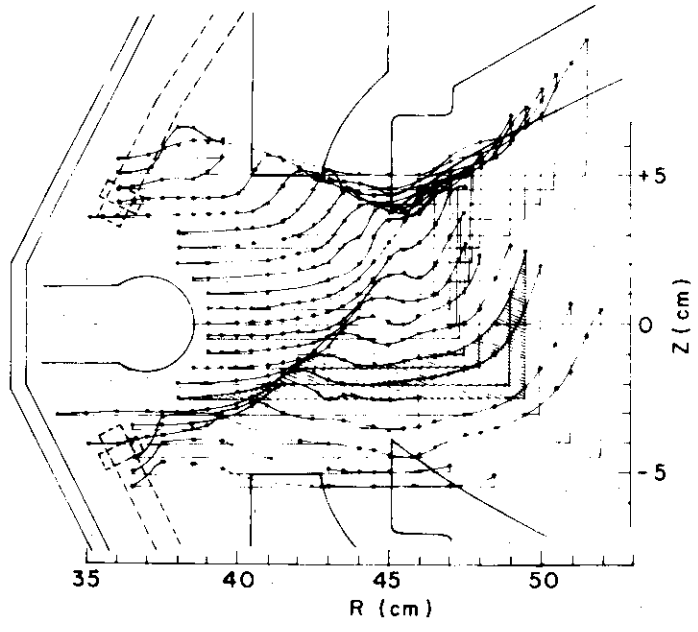

Fig.II.2.3-2 Two dimensional measurements of the heat flux to the burial chamber. The heat flux to the burial chamber disappears beyond the copper rods. About 30% of the heat flux measured at R=40 cm is missing between R=40 cm and R=43 cm. The lost heat flux is presumably deposited to the movable shells.

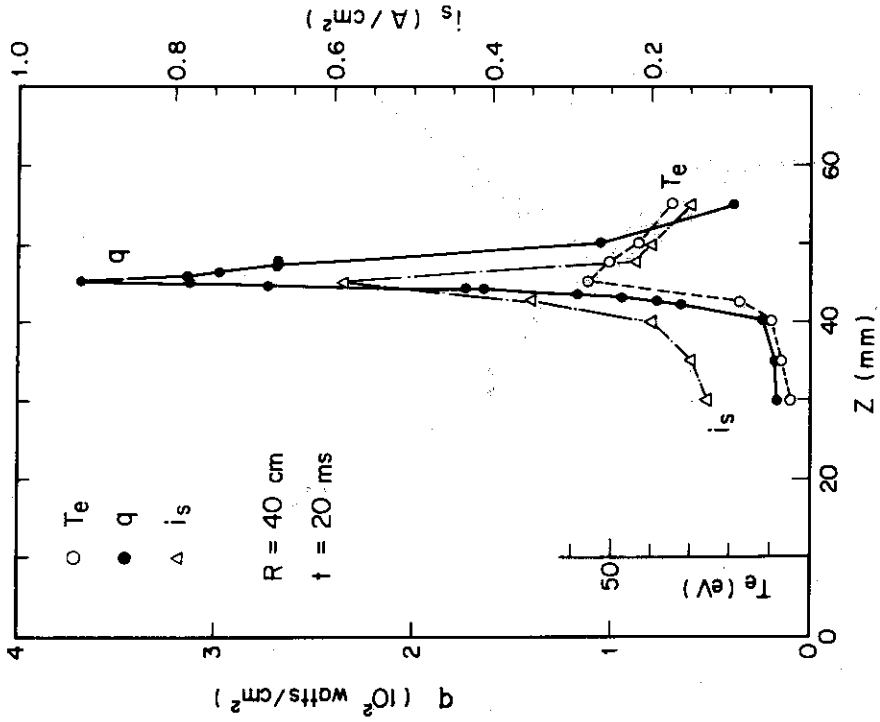

Fig.II.2.3-4 Profiles of heat fluxes, electron temperature T_e and ion saturation currents at R=40 cm and t=20 msec in Case B.

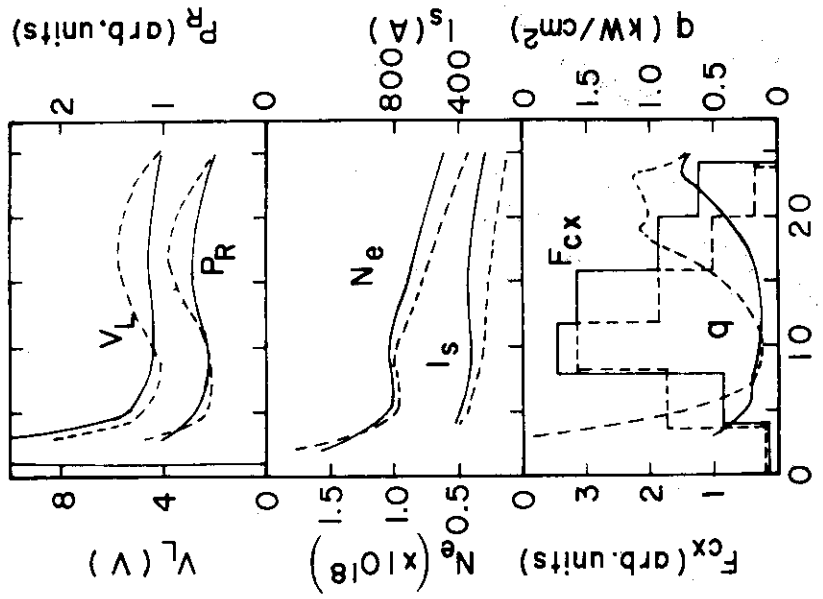

Fig.II.2.3-3 Typical waveforms of loop voltage V_L, radiation losses P_R, time evolution of total particles Ne, ion saturation current to the copper shells Is, heat flux q to the divertor at Z=4.5 cm and R=40 cm, and charge-exchange neutral particle flux in the energy above 250 eV. Solid and boken lines represent the variation of plasma parameters during the discharge with an additional gas injection of 4.5×10^{19} H_2/s (Case A) and 1.7×10^{19} H_2/s (Case B), respectively. The heat flux density in the scrape-off layer has the correlation with the increase of P_R.

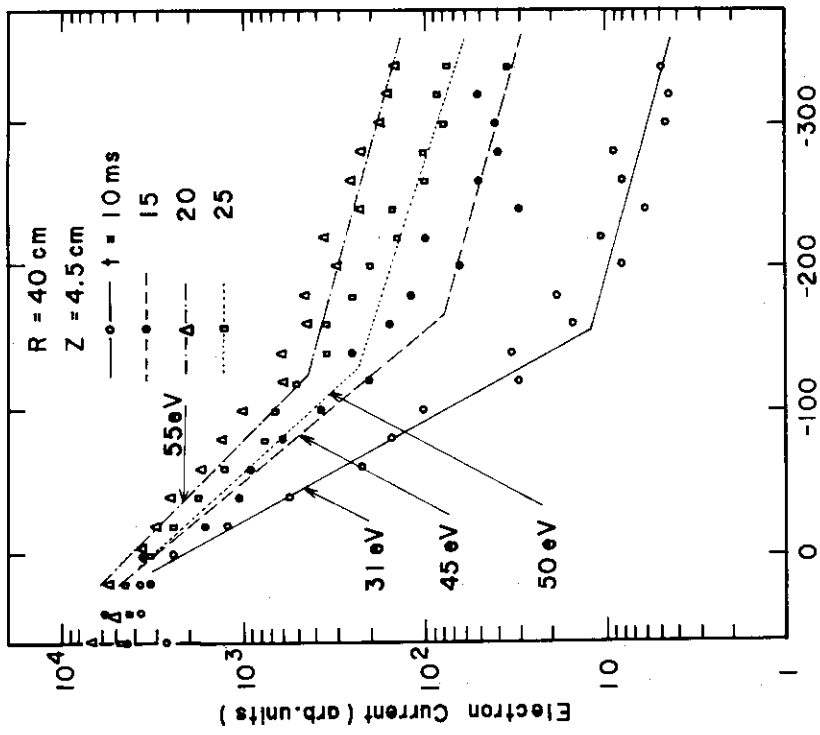

Fig.II.2.3-6 Energy spectrums of electrons in the scrape-off plasma measured by a Farady cup. Relatively high energy electrons are contained in the scrape-off plasma.

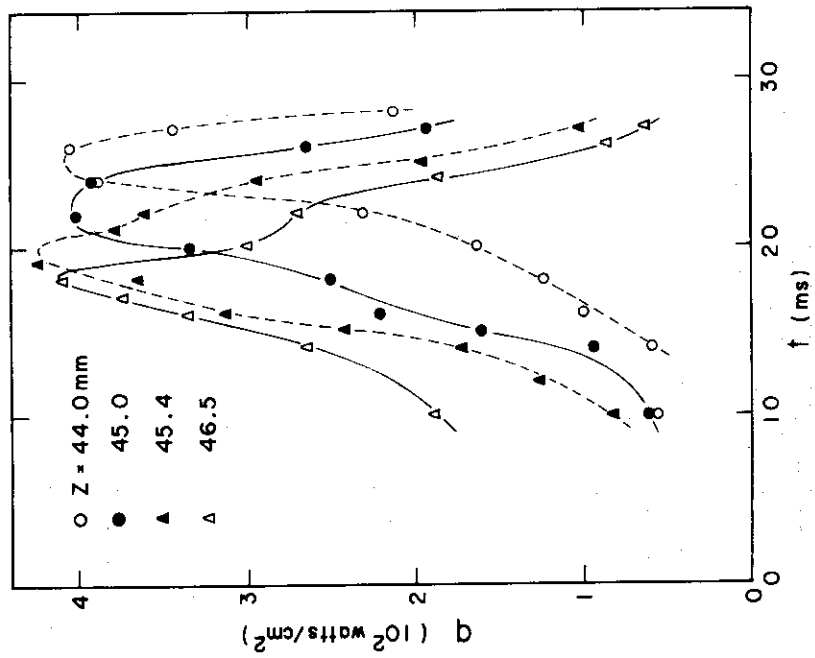

Fig.II.2.3-5 Time variations of the heat fluxes at various vertical positions at R=40 cm in Case B. The profile of the heat flux transmitted to the floating plate have a sharp peak.

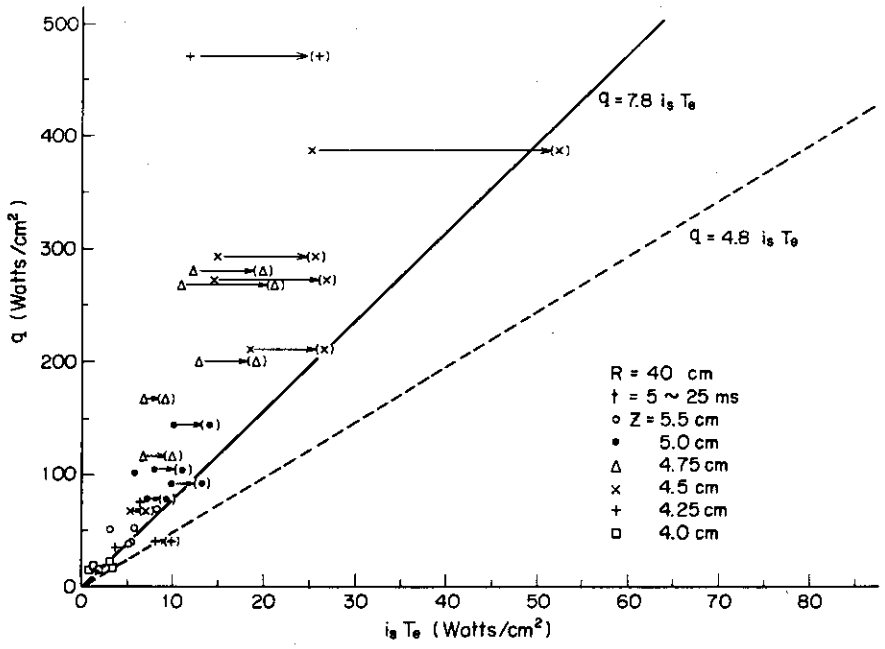

Fig.II.2.3-7 Relationship between heat flux q and i_sT_e measured in the scrape-off layer at R=40 cm. Solid and dashed lines represent the case of $q=7.8\ i_sT_e$ and $q=4.8\ i_sT_e$, respectively. Experimental results are plotted with no bracket and the corresponding corrected values are shown with brackets. The two component model presumably accounts for large transmission rates.

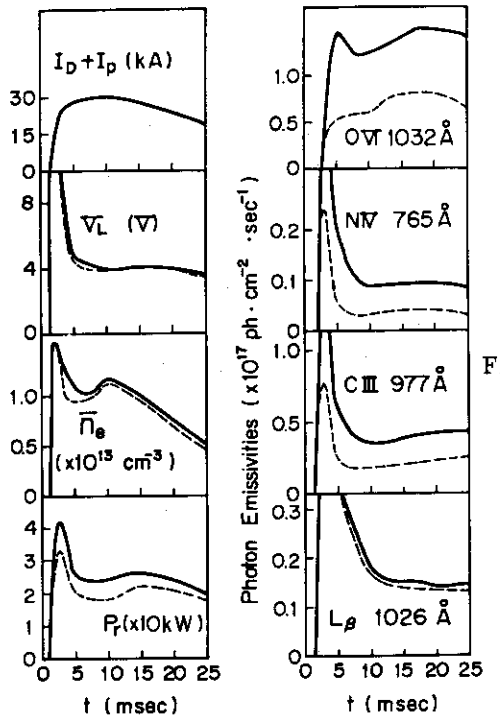

Fig.II.2.4-1 Discharge characteristics before (solid lines) and after (dotted lines) the gettering the burial chamber with titatnium. Plasma current I_p, divertor hoop current I_D, average electron density $\bar{n}_e$, total radiation loss P_r and line emission intensities of L_β, OVI 1032 Å, NIV 765 Å, CIII 977 Å vs time.

3. Diagnostics

3.1 Time-history method of electron temperature

The estimations of electron temperatures from time-histories of impurity-lines were attempted in some plasma devices, for example θ-pinch[1] or Zeta[2] devices. For the purpose of extending the time-history method to a tokamak plasmas, the present section describes the summary[3] of some improvements in which not only ionization and radiative recombination but also finite confinement time of impurity-particles and their influxes from the limiter and the wall of the vacuum chamber are considered. An improved time-history method developed here also includes contributions from the dielectronic recombination process. Recently a method similar to the present one has been used to determine initial electron temperatures for the TFR tokamak plasma.[4] Ohasa et al.[5] have also evaluated electron temperature in the JIPP-Ib stellarator device from the times of appearance of impurity-lines.

The number density of impurity-ions in individual ionization states is determined by solving the following rate equations

$$\frac{dn_k}{dt} = n_e[S_{k-1}\, n_{k-1} + (\alpha^R_{k+1} + \alpha^D_{K+1})n_{k+1}]$$

$$-n_e[S_k n_k + (\alpha^R_k + \alpha^D_k)n_k] - \frac{n_k}{\tau_k} \quad .$$

$$(k=2,3, \ldots., Z) \qquad (1)$$

Here n_k represents the number density of ions with ionic charge (k-1), n_e electron density, τ_k confinement time and Z atomic number of the impurity in question. S_{k-1} and S_k are rate coefficients for the collisional ionization of ions with ionic charge (k-2) and (k-1) to the next ionization states, and α^R_{k+1}, α^R_k and α^D_{k+1}, α^D_k, radiative and dielectronic recombination coefficients of ions with ionic charge k and (k-1) to the descending ionization states. Equations for neutral atoms and fully-stripped ions are written by

$$\frac{dn_1}{dt} = n_e[(\alpha^R_2 + \alpha^D_2)n_2 - S_1 n_1] + \Phi \qquad (2)$$

and

$$\frac{dn_{Z+1}}{dt} = n_e(S_Z n_Z - \alpha^R_{Z+1}\, n_{Z+1}) - \frac{n_{Z+1}}{\tau_{Z+1}} \quad , \tag{3}$$

respectively. In Eq.(2) Φ indicates a source term of impurity atoms from outside to the plasma and is taken to be given by the equation

$$\Phi = \sum_{k=2}^{Z+1} \frac{n_k}{\tau_k} \quad . \tag{4}$$

This equation implies that the total amount of the impurity in a plasma is held to be constant during the discharge. Numerical expressions of S_k and α^R_k used in the present calculations are ones given by Hinnov.[6] The dielectronic recombination coefficient α^D_k is given by Burgess's semi-empirical formula.[7] The intensity I(p,q) of a spectral line arising from a transition between levels p and q is given by

$$I(p,q) = h\nu(p,q) n_e n_k(g) X_k(g,p) \frac{A(p,q)}{\sum_{r<p} A(p,r)} \tag{5}$$

where $h\nu(p,q)$ is the photon energy corresponding to the transition, and $n_k(g)$ represents ion density in the ground level. $X_k(g,p)$ is the rate coefficient of collisional excitation from g-level to p-level and Seaton's expression[8] of $X_k(g,p)$ is adopted here. Values of A(p,r) and oscillator strength used in the present calculations are those given in tables by Wiese et al.[9]

The plasma is assumed to be uniform over a minor cross-section. The electron density and temperature are respectively taken to be the average value, $\bar{n}_e(t)$ measured along the central vertical chord and the average one $\bar{T}_e(t)$ defined as

$$\bar{T}_e = \int_o^a T_e(r) n_e(r) r dr \Big/ \int_o^a n_e(r) r dr, \tag{6}$$

in order to consider particularly the effects of distributions of the temperature. If the electron temperature and density have squared-distributions which are very close to experimental results, Eq. (6) becomes to

$$\bar{T}_e = \frac{2}{3} T_e(0) \tag{7}$$

The central electron temperature $T_e(0)$ can be estimated by adjusting so that the peak-times for the different lines may coincide in both the experimental

and numerically calculated results. The impurities from the limiter and the wall of the vacuum chamber are assumed to be initially neutral atoms and to be uniformly distributed at the beginning of the discharges. Thus initial conditions for the impurities are written as follows

$$n_1 = N_0 \text{ (uniform in space)}, \tag{8a}$$

$$\text{and } n_k = 0 \quad (k = 1) . \tag{8b}$$

The confinement times τ_k are taken to be the same for all ionization states of impurities and equal to the mean global life-time for electrons τ_e, i.e.,

$$\tau_k = \tau_e \quad (k=2,3, \text{ ---- }, Z+1) . \tag{9}$$

The justification of this assumption has been confirmed approximately in the ST device.[10]

We estimate electron temperatures during the initial phase of the JFT-2a plasma for the toroidal magnetic field of 10 KG, the peak plasma current of 15 KA and the ratio of divertor current to plasma current of 1.1. For the JFT-2a plasma the time-evolution of plasma current (I_p) and loop voltage (V_L) is shown in Fig. II.3.1-1(a), and the average electron density along central vertical chords is given in Fig. II.3.1-1(b). Figure II.3.1-2 shows the time-histories of observed spectral lines normalized to their peak values. The numerical values in the figure indicate wavelengths and ionization potentials of the spectral lines. Figure II.3.1-3 shows the time-evolution of electron life-time in the JFT-2a plasma.

Experimental results are compared with theoretical values. Figure II.3.1-4 shows time-histories for carbon (dotted curve) and oxygen ions (solid curve) in the JFT-2a plasma. Those are calculated with use of the experimental values of τ_e given in Fig. II.3.1-3 by assuming a time-variation of electron temperature indicated by a solid line of Fig. II.3.1-5. A good agreement between calculations and experiments is obtained within about 0.3 msec at peak intensities of all spectral lines. In order to examine the influence of particle confinement time on the electron temperature, numerical calculations have been performed for both cases of τ_k=1 and 0.5 msec. An assumed time-variation of electron temperature is shown by a dotted line in Fig. II.3.1-5. To examine effects due to ambiguities of electron densities during the initial phase, numerical

calculations are performed for the variations of 30 percents in electron densities from 1 to 7 msec. The calculation results yield only slight differences peak-times.

With use of the above results, it is possible to estimate the central electron temperatures during the initial phase of the JFT-2a discharge, whose time-variation is shown in Fig. II.3.1-6. The width of these temperatures are originated from some ambiguities of τ_k-values. The estimated electron temperatures are (70∿90)eV and (190∿215)eV at 3 and 8 msec, respectively. These values are consistent with the results obtained from measurements of ruby-laser light scattering, which yield the central electron temperature of (220±25)eV at 8 msec.

3.2 Local counting efficiency of a Ceratron multiplier for plasma diagnoses on charge-exchanged fast atoms

In researches on the tokamak devices JFT-2 and JFT-2a at Japan Atomic Energy Research Institute, a neutral particle energy analyser[11] with ten detectors has been used to analyse charge-exchanged fast hydrogen-atoms emitted from the tokamaks and to determine ion temperatures. In the analyser Ceratron multipliers have been adopted as the detectors for protons which are converted from the fast atoms in a chrage-stripping cell. A Ceratron is made of ceramic materials and a secondary electron multiplier similar to Channeltron.[12] Up to now an absolute efficiency of Ceratron for protons has not been examined in any laboratories, although accurate knowledges on the efficiency are necessary to obtain quantitative information on cold atom densities and charge-exchanged losses or fast neutral fluxes leakaged from hot plasmas. In the present investigation, local measurements on the absolute efficiency of a Ceratron multiplier were performed for the purpose of quantitative analyses on charge-exchanged hydrogen-atoms emitted from JFT-2 and JFT-2a tokamaks.

In Fig. II.3.2-1 is shown the schematic diagram of experimental setup. Protons were selected with a 60-degrees momentum analyser from hydrogen-ions which were generated in an electron-impact ion source and accelerated by a static electric field. They entered a 127-degreees cylindrical electrostatic energy analyser which permitted one to measure accurately the proton energy. An exit slit in the energy analyser defined a diameter of proton beam, which was beforehand confirmed to be 2 mm by scanning a small Faraday cup installed behind the slit at a position of the entrance aperture

of Ceratron (see Fig. II.3.2-1). The pressure in the experimental setup was maintained below 8×10^{-6} Torr by a 200 ℓ/sec turbomolecular pump. An oil-diffusion pump was not here used to avoid the deterioration on the Ceratron due to oil-vapors. The absolute value of Ceratron local efficiency was determined from a counting rate on the Ceratron N_c and a total current I_t which entered a Faraday cup in Fig. II.3.2-1 when the Ceratron was removed not to interrupt an orbit of the beam. The Ceratron was able to be scanned along the beam diameter with an accuracy of 0.1 mm. The values of N_c and I_t were measured with a pulse counting circuit and a vibrating reed electrometer, and were typically (10^2 -- 10^4) cps and about 10^{-15}A respectively. The Ceratron which was of a MURATA EMW-1081B type had a funnel openning with an aperture 10 mm in diameter and a waved multiplication channel of 1.2 mm in bore and 80 mm in length. The Ceratron was operated under the condition where a high voltage (- 4.5 kV) and a low voltage (- 200 V) were applied to its entrance aperture and exit end, respectively, and its collector was an earth-potential. Thus the energy of protons impinging on a surface of the entrance aperture always exceeded 4.5 keV. A gain of the Ceratron was an order of 10^8 under the operating condition.

The local counting efficiency was measured on the proton beam with its energy of 600 eV by moving the Ceratron at an interval of 0.2 mm along the beam diameter. In Fig. II.3.2-2 is shown an experimental result of local counting efficiency (eN_c/I_t) against the position of proton beam across the entrance aperture with the charge of proton $e = 1.6 \times 10^{-19}$ Coulomb. Since the result shown in the figure was obtained with a good reproducibility, it was confirmed that the observed shape of local efficiency did not result from (various) electric noises. The hollows near the center may be due to the fact that the Ceratron does not operate in a complete saturation-mode. The decrease of counting efficiency in outer regions are coming from leakages of secondary electrons produced by impacts of protons at an edge of the funnel. A local counting efficiency similar to the result presented in Fig. II.3.2-2 was observed on another Ceratron multiplier. For quantitative arguments on charge-exchanged fast atoms, the local efficiency must be averaged over an area of the entrance aperture. An over-all efficiency averaged over the aperture was determined to be 0.20 from the result in Fig. II.3.2-2. The value of the over-all efficiency accorded with that of another Ceratron within 10 percents. The over-all efficiency had been examined to have an approximately constant value within 90 percents

for the proton energy to 1.5 keV in a preliminary measurement.[14] By using the efficiency and from 10-channel energy analyses on fast neutrals the central densities of cold hydrogen-atom are found to be typically (1 -- 3) $\times 10^8$ and about 10^9 cm^{-3} on JFT-2 and JFT-2a tokamaks respectively. These values are in good agreements with atom densities determined from measurements of absolute intensities on the H_α-line.

Furthermore, the total charge-exchange loss is measured to be 15∿20 kW for the standard operation of JFT-2 (B_t:18 kG, I_p:160 kA Pohm≃330 kW). The thermal loss of proton is approximately equal to the value estimated by the neoclassical theory with this charge-exchange loss. The details on the proton behavior due to exchange fast atoms in the JFT-2 plasma will be given in Ref. (13).

3.3 Impurity estimation with K X-ray lines

We have been studied a diagnostic method for impurity content in high temperature plasmas[15]. A photon number of K X-rays emitted from impurity atoms or ions, of which density is n_{imp} (cm^{-3}), per cubic centimeter and per second is

$$\Phi_k = \int_{E_k}^{\infty} \sigma_k \, v \, n_e \, n_{imp} \, F(E)dE \qquad \left(\frac{1}{cm^3 \cdot sec}\right) , \tag{1}$$

where n_e is the electron density (cm^{-3}), E the electron kinetic potential, E_K the K-shell ionization potential, σ_K (cm^2) the cross section of K X-ray emission, v (cm/sec) the colliding speed between impurity and electron, and F(E) the velocity distribution function of electrons. When the electron kinetic energy is larger than the impurity kinetic energy, v is expressed by a relativistic relation

$$v = c \sqrt{1 - \left(\frac{mc^2}{eE+mC^2}\right)^2} , \tag{2}$$

where c is the light speed, m the electron mass and e the electric charge. If F(E) is the single component Maxwell distribution function at electron temperature T_e (eV), F(E) is approximately expressed by a nonrelativistic relation

$$F(E) = \frac{2}{\sqrt{\pi}\, T_e^{3/2}} \sqrt{E} \exp\left[-E/T_e\right] . \tag{3}$$

A emission rate of K X-rays is defined as

$$\langle \sigma_k \, v \rangle = \int_{E_k}^{\infty} \sigma_k \, v \, F(E) dE \qquad (\frac{cm^3}{sec}) \ . \tag{4}$$

Thus, using numerical values for σ_K, Eq. (2) for v and Eq. (3) for F(E), the emission rate can be calculated numerically as a function of electron temperature T_e. Substituting Eq. (4) for Eq. (1) gives

$$\Phi_k = n_e n_{imp} \langle \sigma_k \, v \rangle \qquad (\frac{1}{cm^3 \cdot sec}) \tag{5}$$

Therefore the impurity density n_{imp} can be experimentally estimated from Eq. (5) by using the measured values of Φ_K, n_e and T_e.

Since experimental values of σ_K were determined only at several discrete energies of colliding electrons, we must evaluate σ_K from numerical calculations. Three different methods of numerical calculations are as follows :

(1) Empirical method

σ_K can be evaluated from the experimental values of K X-ray emitted from solid target bombarded with electron beam.

(2) Non-relativistic theory

We use a modified formula[16] for total K-shell ionization cross section Q_K given by Mott and Massey. Then σ_K is obtained from following relation

$$\sigma_K = Q_K \cdot \omega_K \tag{6}$$

where ω_K is the fluorescence yield of the K shell.

(3) Relativistic theory

Arthurs and Moiseiwitsch give a discussion of relativistic formula for Q_K in Ref. (7). Comparisons between calculated cross sections and experimental ones for nickel (Ni), silver (Ag), tin (Sn), and gold (Au) are shown in Fig. II.3.3-1-a, 1-b, 1-c, and 1-d, respectively. The cross sections calculated by A&M theory are in good agreement with the experimental ones at electron energies below 500 keV. The K X-ray emission rates calculated by Eq. (4) for atomic numbers of 13 to 82 is shown in Fig. II.3.3-2. The abscissa is the atomic number and the ordinate is the emission rate. Errors in the impurity density measurement are critical when the electron temperature is as low as the emission rate below 10^{-15} (cm^3/sec), because the emission rate decreases steeply as electron temper-

ature decreases. Therefore, in impurity measurement we should choose light metals, such as Al, Si and Ti, at T_e below 1 keV, or normal metals, such as Fe, Cu and Mo, at T_e of several keV, or heavy metals, such as W and Au, at T_e above 10 keV. It is concluded that the impurity estimation with K X-ray lines is one of the important methods for impurity density measurements in high-temperature plasmas.

Some problems to be examined hereafter are as follows :

(1) Relativistic distribution function of electron should be considered.

(2) Feasibility of measuring a radial distribution of the impurity density should be studied, considering spatial variations of electron temperature and density. Detailed discussions will be given in Ref. (15).

References

(1) Goldman L.M. and Kilb R.W. : Plasma Phys. 6 (1964) 217.

(2) Hobbs G.D., et al. : Proceedings of the Fifth International Conference on Ionization Phenomena in Gases August 1961, Munich (North-Holland, Amsterdam, 1962) Vol. II, p, 1965.

(3) Kasai S. et al. : J. Phys. Soc. of Japan 43 (1977) 2061.

(4) TFR Group : Nuclear Fusion 15 (1975) 1053.

(5) Ohasa K., et al. : Japan J. appl. Phys. 15 (1976) 2403.

(6) Hinnov E. : MATT-777 (September 1970).

(7) Burgess A. : Astrophys. J. 139 (1964) 776, 141 (1964) 776, 141 (1965) 1588.

(8) Seaton M.J. : The Theory of Excutation and Ionization by Electron Impact, in Atomic and Molecular Processes edited by D.R. Bates (Academic Press, New York and London, 1962) Chap. 11, p.374.

(9) Wiese W.L., et al. : Atomic Transition Probabilities (National Bureau of Standards, Washington, 1966) Vol. 1.

(10) Hinnov E. : MATT-1240 (May 1976), Phys. Rev. A14 (1976) 1533.

(11) Takeuchi H., Funahashi A., Takahashi K., Shirakata H. and Yano S. : Japan J. appl. Phys. 16 (1977) 139.

(12) Ray J.A. and Barnett C.F. : IEEE Trans. Nucl. Sci. NS-17 (1) (1970) 44.

(13) Takeuchi, H. et al. to be published.

(14) Takahashi K., Shirakata H. and Yano S. : private communication.

(15) Matoba T., Kumagai K., Funahashi A. and Kawakami T. : JAERI-M 7196, "Evaluation of Radiation Cross Sections of K X-rays and Application to Measurement of Metal Impurity Densities in High-Temperature Plasma" (1977) (in Japanese).

(16) Worthington C.R. and Tomlin S.G. : Proc. Phys. Soc., 69 (1956) 401.

(17) Arthurs A.M. and Moiseiwitsch B.L. : Proc. Roy. Soc., A247 (1958) 550.

(18) Pockman L.T., Webster D.L., Kirkpatrick P. and Harworth K. : Phys. Rev., 71 (1947) 330.

(19) Clark J.C. : Phys. Rev. 48 (1935) 30.

(20) Motz J.W. and Placious R.C. : Phys. Rev., 136 (1964) A662.

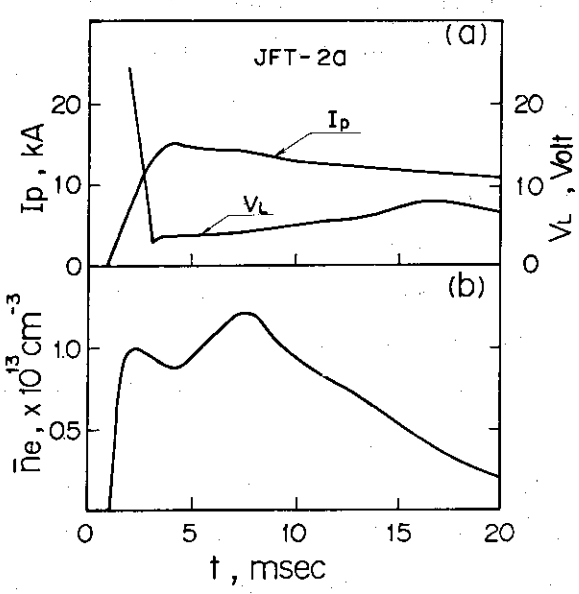

Fig.II.3.1-1 Time evolutions of plasma current I_p and loop voltage V (a) and averaged central electron density $\bar{n}_e$ (b).

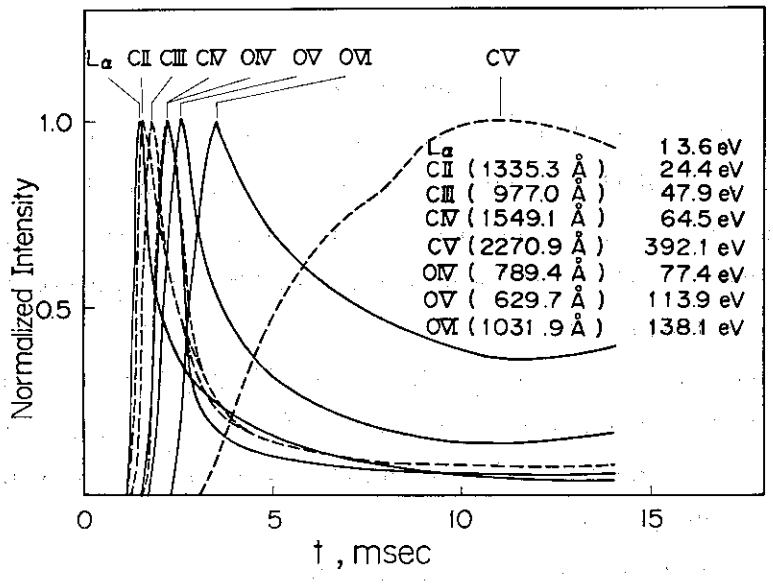

Fig.II.3.1-2 Observed time-histories of L_α, oxygen and carbon lines on the JFT-2a plasma.

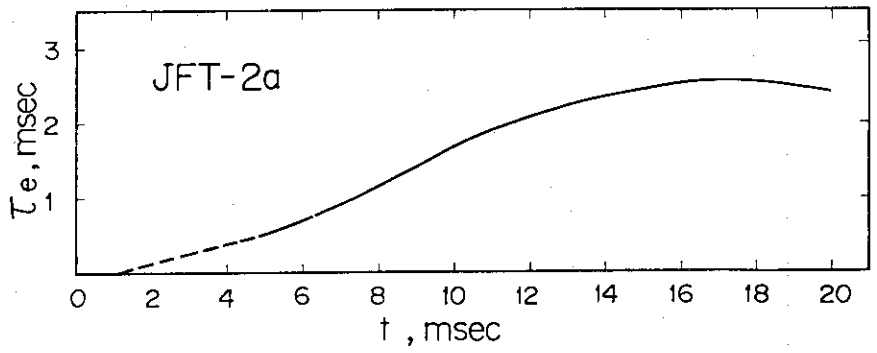

Fig.II.3.1-3 Electron life-time τ_e on the JFT-2a plasma.

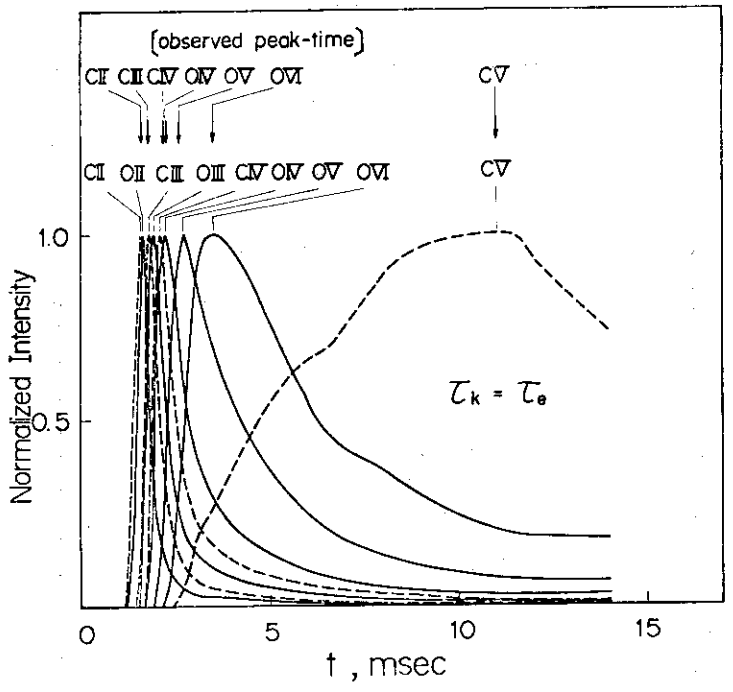

Fig.II.3.1-4 Time-histories of oxygen and carbon lines numerically calculated from time-variations of electron temperature indicated in Fig.5 for $\tau_k = \tau_e$.

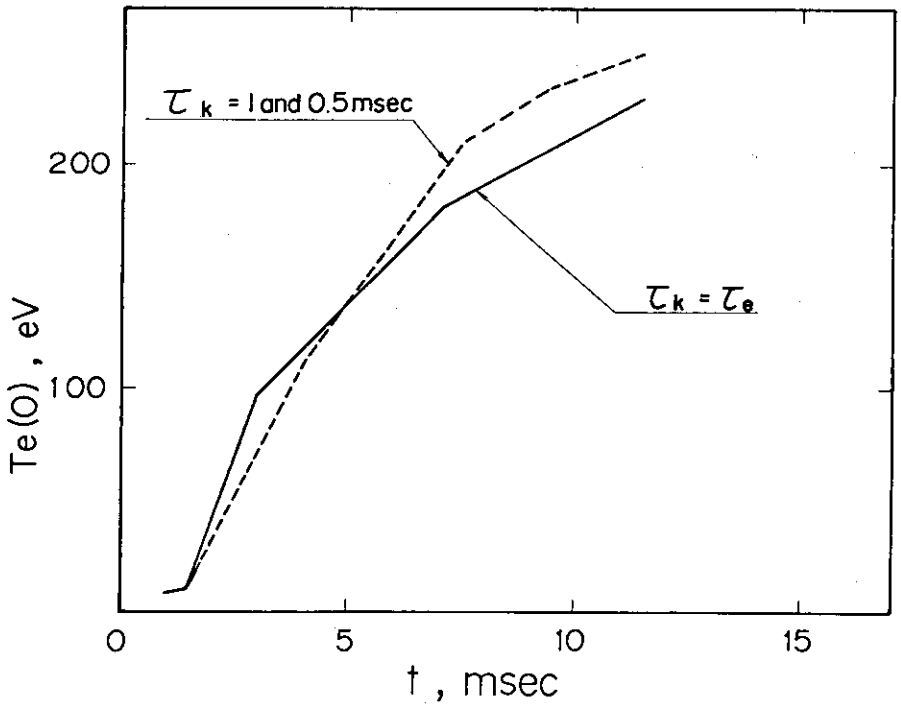

Fig.II.3.1-5 Assumed time-variations of central electron temperature.

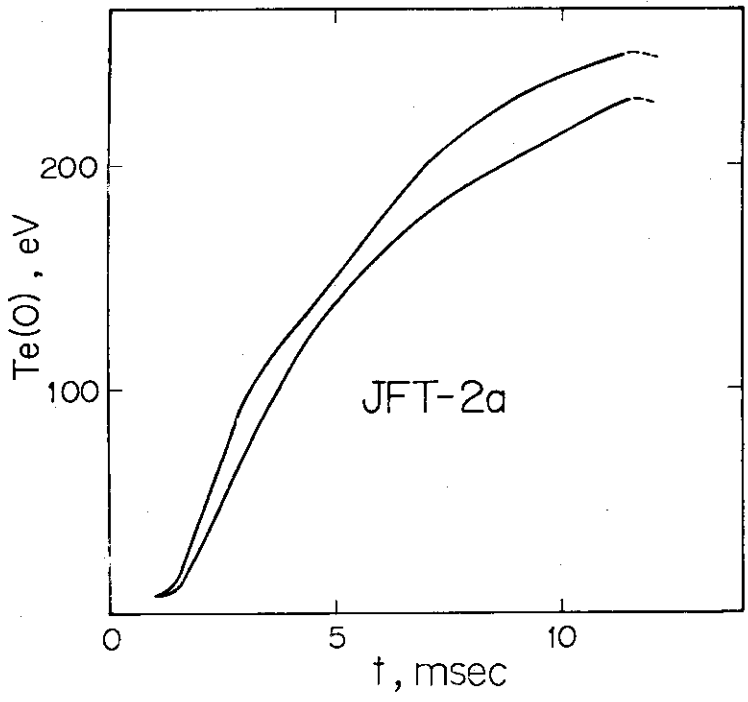

Fig.II.3.1-6 Initial rise of central electron temperature estimated on the JFT-2a plasma.

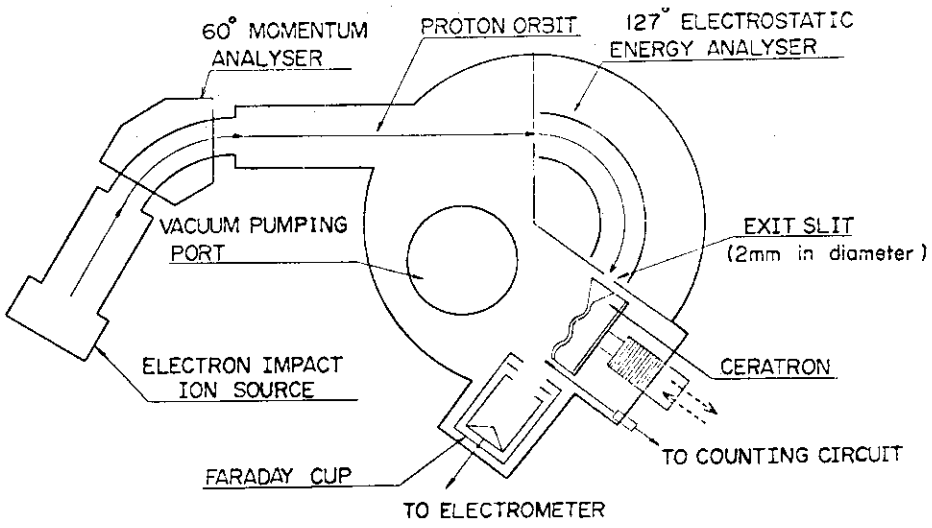

Fig.II.3.2-1 Schematic diagram of an experimental setup to examine the local efficiency of a Ceratron multiplier.

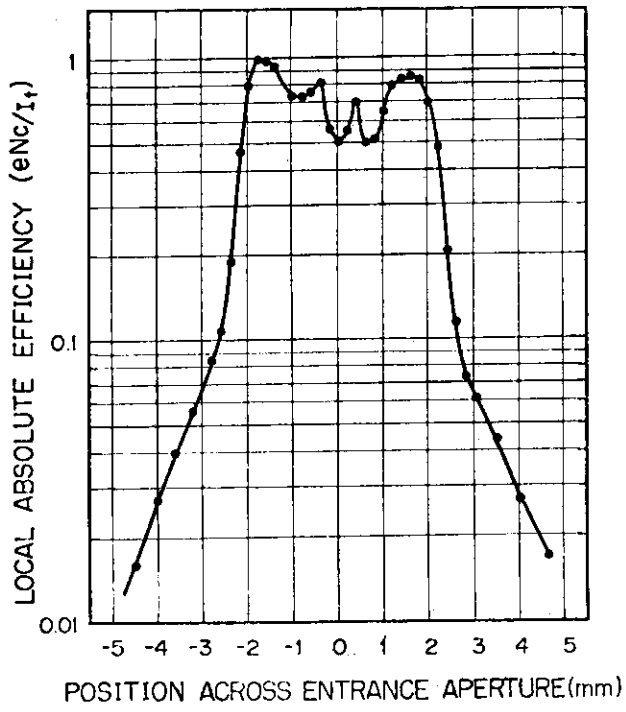

Fig.II.3.2-2 Local absolute efficiency of a Ceratron multiplier for protons. The abscissa is the position of proton beam from the center of an entrance aperture of Ceratron.

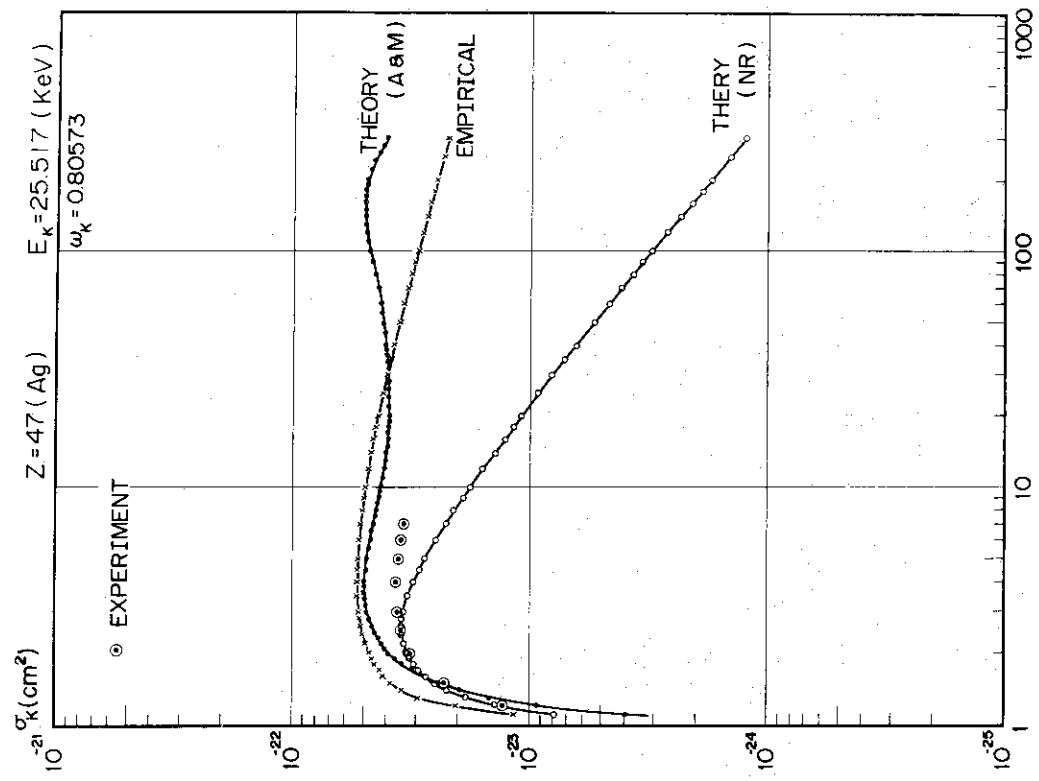

Fig.II.3.3-1 Energy dependence of the cross section of K X-ray emission.
(b) Silver (Ag); experimental values are quoted from ref. (19).

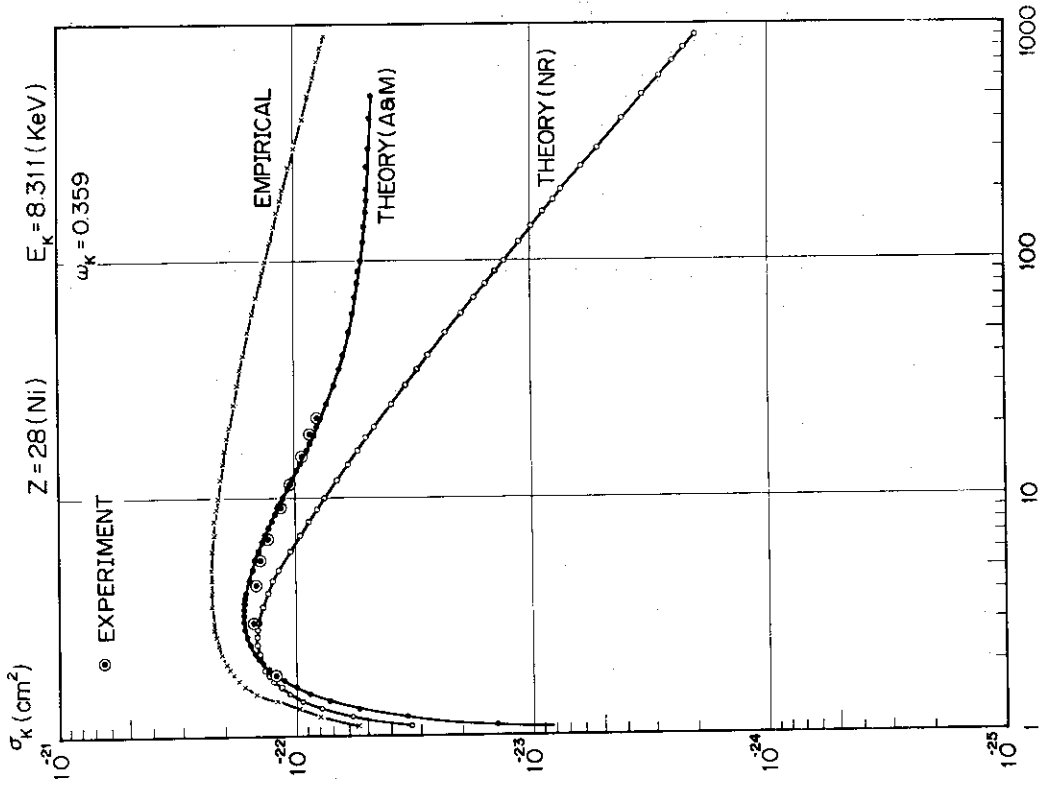

Fig.II.3.3-1 Energy dependence of the cross section of K X-ray emission.
(a) Nickel (Ni); experimental values are quoted from ref. (18).

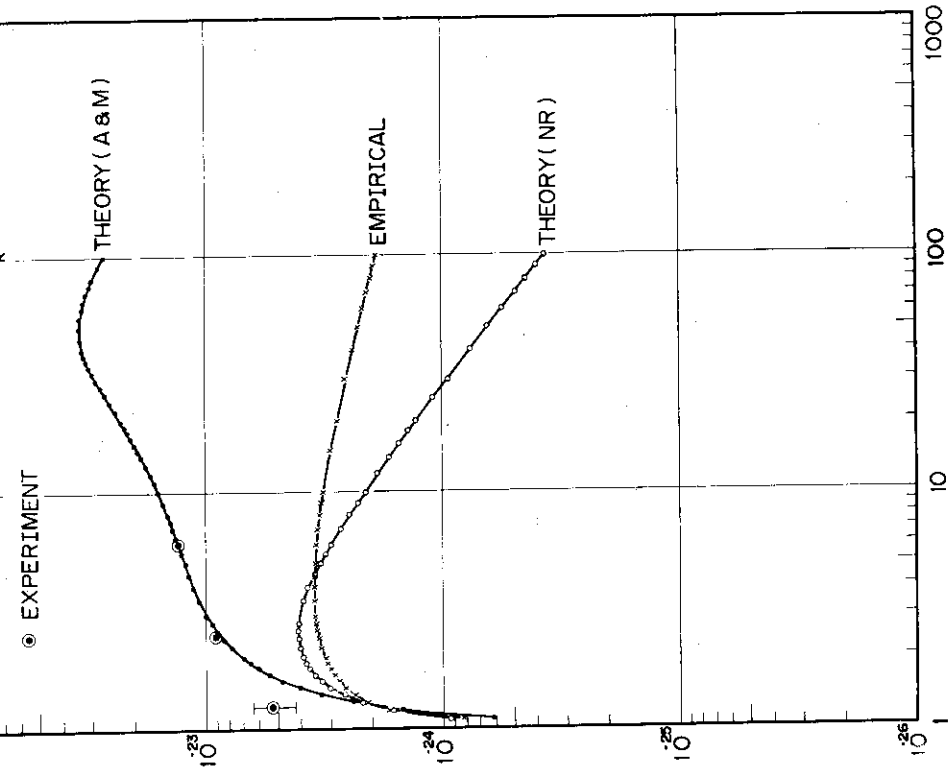

Fig.II.3.3-1 Energy dependence of the cross section of K X-ray emission.
(d) Gold (Au); experimental values are quoted from ref. (20).

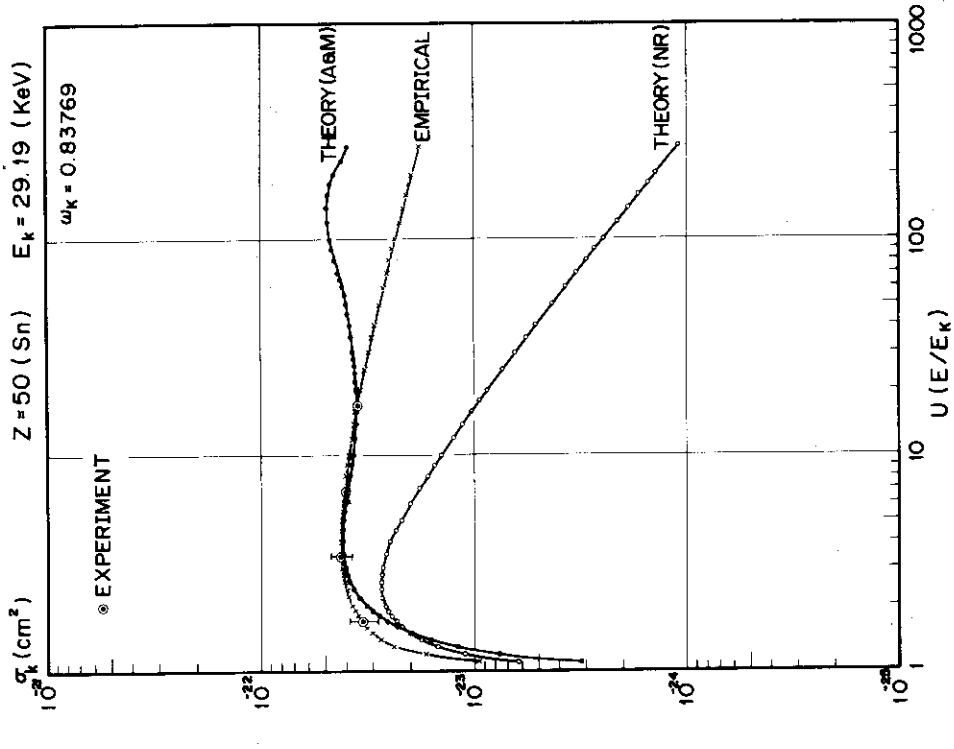

Fig.II.3.3-1 Energy dependence of the cross section of K X-ray emission.
(c) Tin (Sn); experimental values are quoted from ref. (20).

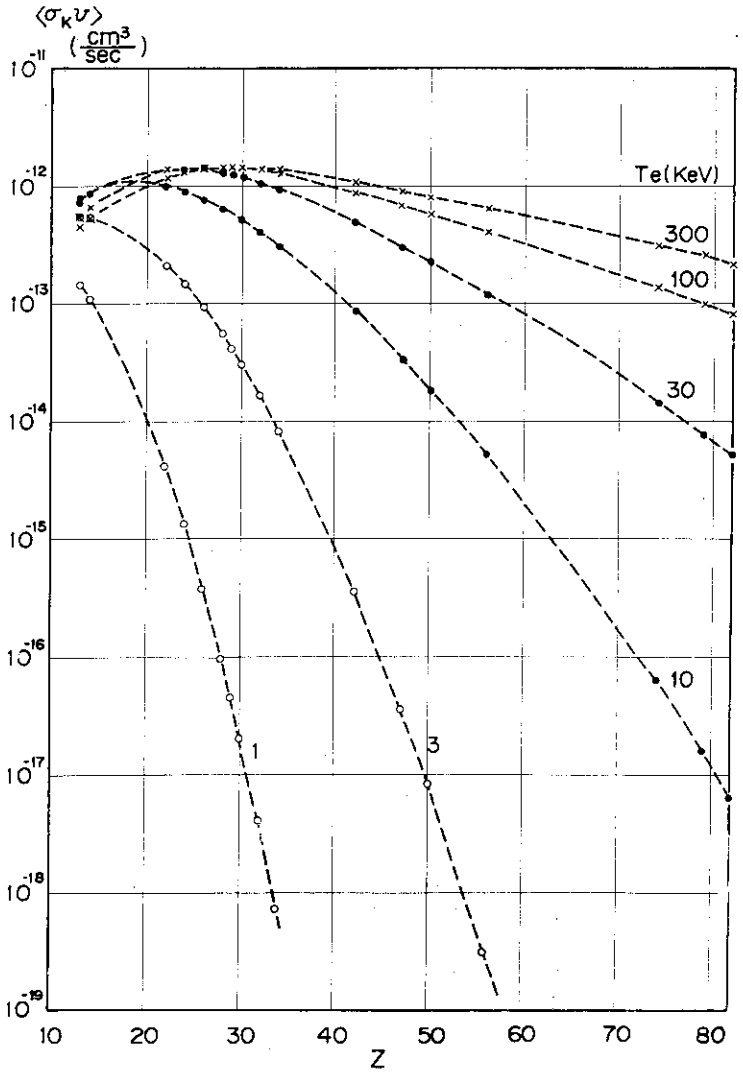

Fig.II.3.3-2 Dependence of the emission rate of K X-rays on the atomic number.

III. OPERATION AND MAINTENANCE

1. Introduction

In JAERI there are now tokamak fusion research devices; JFT-2, first operated in 1972; JFT-2a, first operated in 1974. Facility operation and Engineering Section contributed to experimental research on plasma confinement and heating through operation, maintenance and development of auxiliary equipments and instruments.

In fiscal 1976 the two machines have operated on schedule. Several technical improvements were made to improve efficiency of operation, maintenance and means of plasma research. These works are summarized as following subsections.

2. Operation and Maintenance of JFT-2

JFT-2 operated satisfactorily with a total of 31,981 discharges for substantial 29 weeks. The detail of operation for each quarter is shown in Table III.2-1. Operation was suspended from June 18 to July 29 to install Neutral Beam Injection system, and from December 3 to February 7 to arrange for the motor-generator in common to JFT-2 and JFT-2a by the change of sequence control. A ground accident of a toroidal coil occurred on February 14. However it gave only slight damage to the machine, so the operation was resumed in March 1977.

During the suspension of operation, careful maintenance of the device and equipment were carried out. Gas injection system was largely rebuilt to operate easily and control plasma density. 40/5 ton crane were adjusted to facilitate their operation. The B_2 box, one of the observation box, was replaced with a new one owing to minor vacuum trouble.

3. Operation and Maintenance of JFT-2a

JFT-2a operated satisfactorily with a total of 32,072 shots for substantial 122 days. The detail of operation for each quarter is shown in Table III.3-1. Operation was suspended from December 1976 to reinforce the toroidal field 20 kG from 10 kG.

During the suspension of operation, careful check and test of machine was carried out. To increase the current duration, the number of turns of primary winding was changed to 24 from 48, and a 7 mH coil was inserted in current transformer circuit.

4. Development of Equipment and Instrument

4.1 JFT-2

(1) Reptition rate of JFT-2 discharge was limited mainly by the capacity of cooling system of toroidal coils. To raise the rate, the system was reinforced by installation of a chill unit with capacity 116,000 kcal/h cooling. The improved cooling system is shown in Fig. III.4-1. As the result, the reptition rate could be increased to 1 shot per 5 minutes from per 10 minutes.

(2) An automatic CO_2 fire extinguisher system was installed with the capacitor banks. A reactor was inserted between "zero" bank and "first" bank of the current transformer circuit to operate with miss fire of ignitrons.

(3) The sequence control of toroidal field was adjusted to provide a constant toroidal field of 2 kG steadily. This was the first step for improvement of discharge cleaning with higher reptition.

4.2 JFT-2a

(1) An Auger Electron Spectroscope was applied to on JFT-2a for monitoring in the wall condition of discharge cleaning. Preliminary results obtained are shown in Fig.III.4.2-1 and III.4.2-2. In discharge cleaning of JFT-2a, it was seen that oxygen and carbon deposited on the surface of Au sample, JFT-2a vacuum wall material, decreases faster than the case of 304 SS by a factor 3.

(2) Three years passed from first Au plating, so Au was again evaporated onto the shell surface to thickness about 10 μm. The atomic profile of the depth is shown Fig. III.4-3.

5. Constant Plasma Current Operation

A constant plasma current operation is necessary to facilitate analysis and to decrease horizontal movement of plasma column. This was achieved by delay circuit. An ordinary delay circuit consists of many equal coils and capacitors, but in the delay circuit used in JFT-2 the last element is JFT-2 primary winding itself, of which inductance is much larger than those of the preceding coils. From calculations, nine coils of inductance 4 mH were used. And the "second" bank of current transformer

circuit was converted to ten capacitor banks of 2,800 μF (Fig.III.5-1).

In ordinary pre- conditioning consisting of baking the vacuum wall about a week and about 3,000 shots discharge cleaning, constant plasma current was obtained with flat-top duration. As an example, the wave forms of primary current and plasma current are shown in Fig.III.5-2(a), (b). Then parameter survey was made by changing the number of turns of primary winding and the inductance of coils. The results are shown in Table III.5-3. As the result, flat-top duration τ_{fe} becomes $2n\sqrt{LC}$ which is the duration of the ordinary delay circuit, almost independent of the number of turns of primary winding.

Reference

(1) Maeno M., Matsuzaki Y. and Fuzisawa N.: JAERI-M 6762 (in Japanese) (October 1976).

Table III.2-1 Operation of JFT-2

	First Quarter	Second Quarter	Third Quarter	Forth Quarter	Total
Discharge Shots	12,491	9,960	6,853	2,677	31,981
Operation Cycle(week)	9.25	9	8	3	29.25
Baking Operation	1	1	0	1	3
Discharge Cleaning(week)	1	1	0	1	3
Breaking of Vacuum Chamber	1	1	1	1	4

Table III.3-1 Operation of JFT-2a

	First Quarter	Second Quarter	Third Quarter	Forth Quarter	Total
Discharge Shots	9,560	13,728	8,783	0	32,072
Operation Cycle(day)	39	48	35	0	122
Baking Operation	1	0	0	0	1
Breaking of Vacuum Chamber	6	9	11	0	26

Table III.5-3 Flat-top duration of constant plasma current: $T=2n\sqrt{LC}$, duration of the ordinary delay circuit, where the last inductance L_n equals L. τ_{fe}, duration of the experimental data.

L \ W / L_n		52 Turns	116 Turns	180 Turns
		~21 mH	~100 mH	~250 mH
0.917 mH	T	33.1 m sec		
	τ_{fe}	~40 m sec		
2.28 mH	T	52.1 m sec		
	τ_{fe}	~57 m sec		
3.91 mH	T	68.3 m sec		
	τ_{fe}	~72 m sec	~72 m sec	~72 m sec

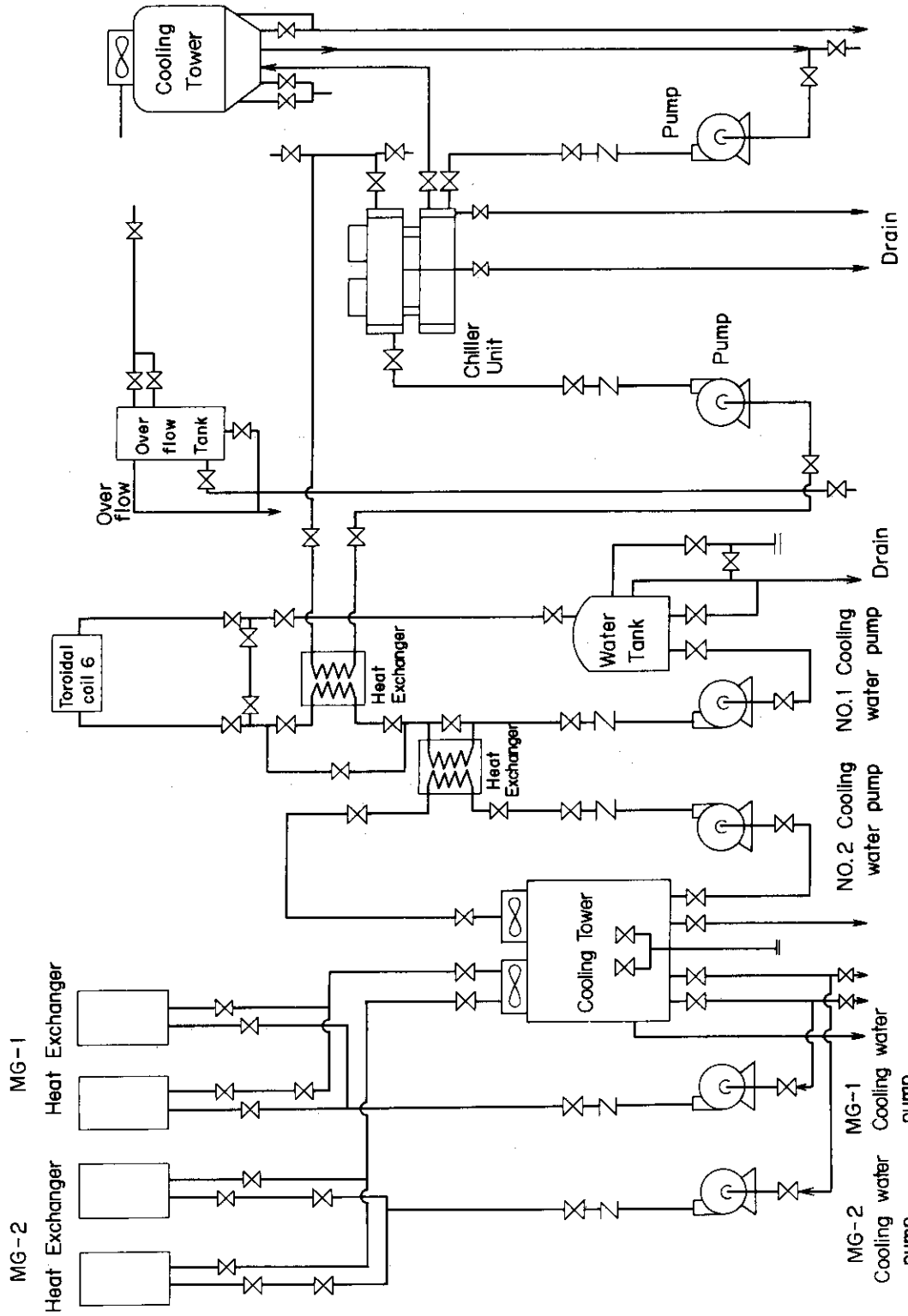

Fig.III.4-1 Cooling system of toroidal coils of JFT-2

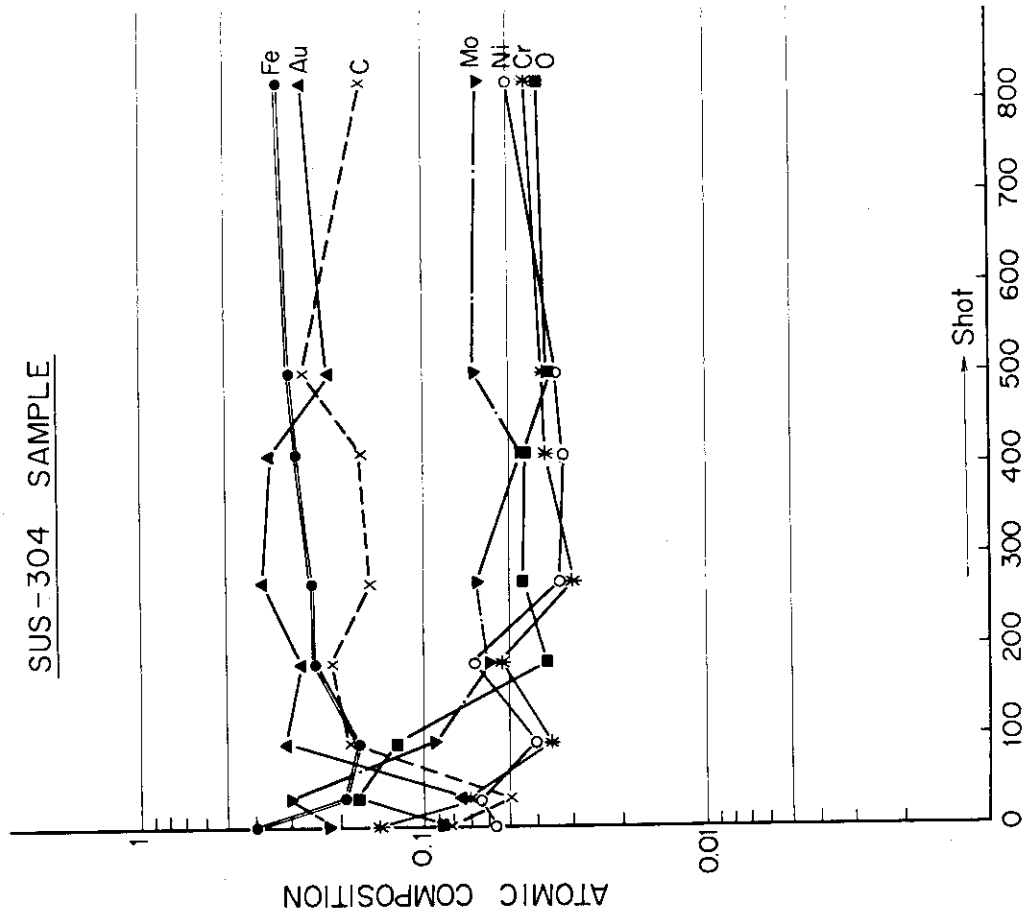

Fig.III.4.2-2 The change of the surface composition of SS. sample with discharge cleaning of JFT-2a

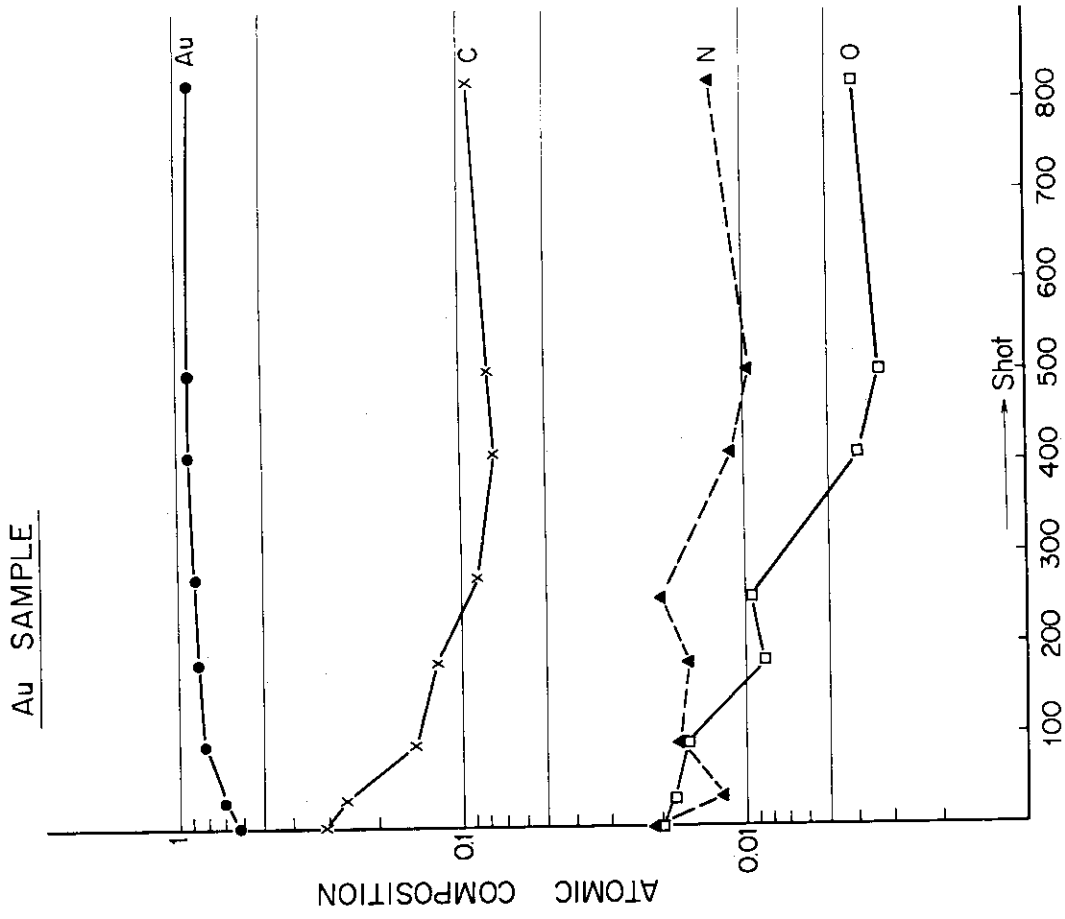

Fig.III.4.2-1 The change of the surface composition of Au sample with discharge cleaning of JFT-2a

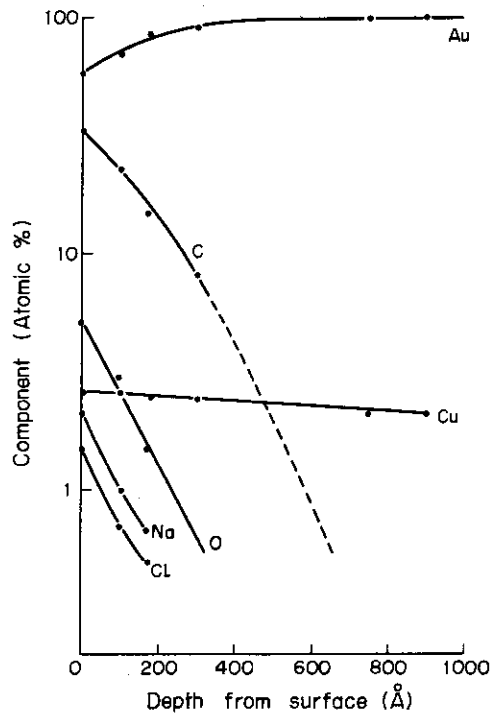

Fig.III.4-3 An evaporation in JFT-2a shell

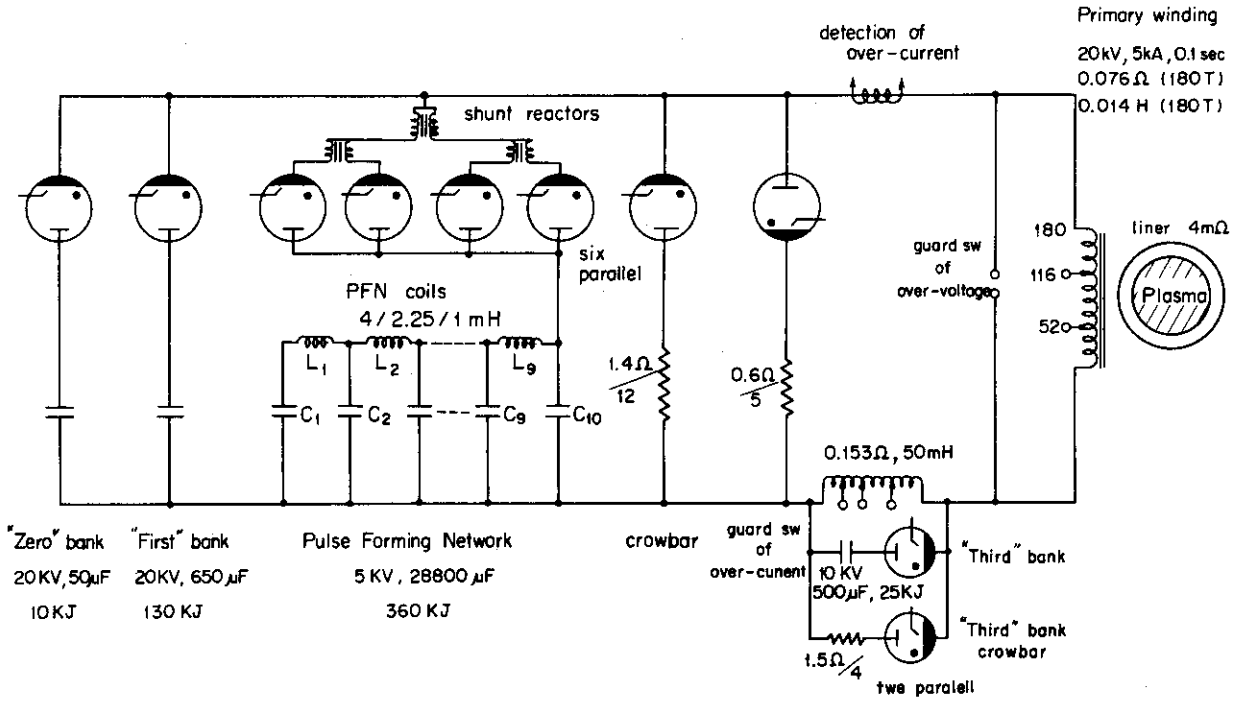

Fig.III.5-1 Current transformer circuit of JFT-2 with delay circuit

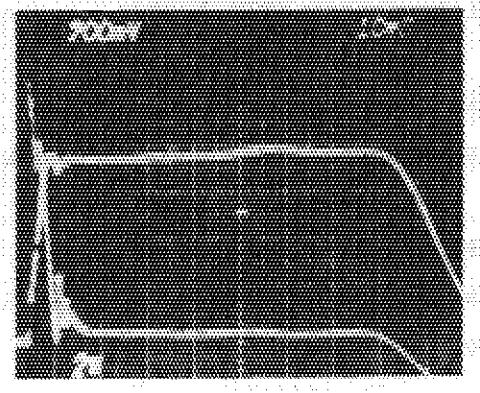

(a)

I_n 0.4 kA/div

V_1 2 kV/div

10 m sec/div

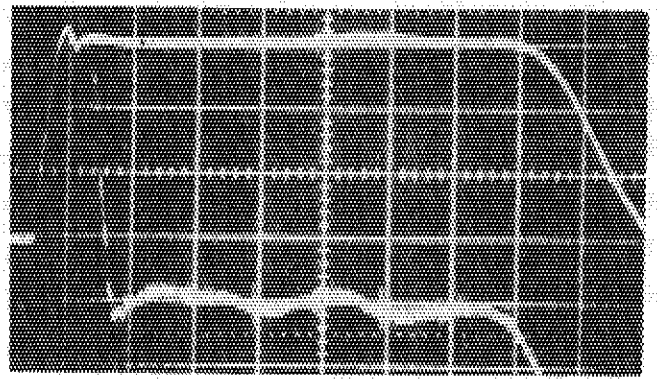

(b)

I_p 27 kA/div

V_L 2V/div

10 m sec/div

Fig. III.5-2 Results of constant plasma current operation

IV. DEVELOPMENT OF PLASMA HEATING SYSTEM

1. Introduction

For supplementary heating of the JT-60 and JFT-2 plasmas, neutral beam injection and radiofrequency (RF) heating systems are under development.

In the neutral beam injection, major events of fiscal 1976 are completion of the 100 kV test stand ITS-2 and the neutral beam injector for JFT-2.

The test stand ITS-2 is used to develop a high energy ion source for the JT-60 injectors. By useing ITS-2, we have developed a two-stage ion source of diameter 5 cm, and obtained a beam of 1.2 A at 70 keV with divergence of 1.34 degree. In addition, ion source improvements and beam line studies have continued with ITS-1.

A neutral beam injector with two beam lines for JFT-2 was completed, and the experiment on nearly perpendicular injection was started in September 1976. During the experiment, the injector has operated satisfactorily. The ion temperature thus rose by a maximum of about 15 %.

In the RF heating, following on the design of a 200 kW RF power source for JFT-2 in 1975, we have studied the lower hybrid wave propagation in JFT-2 and coupling features of phased waveguides array. Consequently, we selected 650 MHz as the optimum frequency. Construction of the 200 kW, 650 MHz RF heating system for JFT-2 was started in the middle of 1976. This system will be completed in the autumn of 1977.

2. Neutral Beam Injection System

2.1 Ion source development

For the neutral beam research and development at JAERI, we built an ion source test stand ITS-1 in Feb., 1975[1]. Using this test stand we have developed and tested the ion source for the JFT-2 neutral beam injector. We also built an ion source test stand ITS-2 in Dec., 1976, to develop the higher energy ion source for the JT-60 injectors. By making use of these test stands, we are required to develop a 75 kV - 35 A, 10 sec ion source for the JT-60 injectors by the end of FY 1978. In particular, our efforts must be concentrated on beam optics, source plasma production and cooling of the extraction grids which appear to be the

basic problems involved in the high power and long duration ion source development.

2.1.1 ITS-2 test stand

To develop the higher energy ion source for the JT-60 injectors, we have constructed a 100 kV test stand. It is primarily responsible for developing a 75 kV - 35 A ion source by the end of FY 1978. The main specifications are listed in Table IV.2.1-1.

The two-stage series power supplies are capable of delivering ion beams up to 40 A at 100 kV level. The voltage up to 80 kV is regulated by the series tubes, EIMAC Y676 (for the accelerator P.S.), and Y546s (for the extractor and decelerator P.S.). They also serve to modulate the current in the case of breakdowns within 20 μsec. The system can provide the pulsed arc power either followed by the pulsed acceleration voltage, or under the continuous acceleration voltage. The beam line vacuum tank is equipped with three turbo molecular pumps with the total pumping speed of 7000 ℓ/s. The beam dump inside the vacuum tank as well as the electrodes of ion sources and diagnostic elements are cooled by the pressurelized, demineralized water cooling system. It is capable of removing about 800 kW continuous or 4000 kW pulsed (1 sec) heat lord. Figure IV.2.1-1 shows the two-stage ion source with 5 cm diam. electrodes. These electrodes can be replaced by up to 15 cm diam. electrodes after the performance of the source is confirmed satisfactorily. The test stand was accomplished in December 1976.

2.1.2 Source plasma study

Our prototype ion source was geometrically almost the same as Oak Ridge 7 cm diam. duopigatron[2]. We reconfirmed with this source that the hydrogen beam can be extracted up to 5.5 A at 25 kV. The first modification of this prototype ion source is the geometrical scale up of the extraction electrodes to 10 cm diam. together with a larger target chamber. By improving the uniformity of the source plasma, we can obtain a beam with the drain current of 8 - 9 A at 25 - 27 kV. The second modification is the further geometrical scale up of the extraction electrodes to 15 cm diam. together with the larger electrodes for source plasma production. We first tried to improve the uniformity of the source plasma.

Figure IV.2.1-2 shows the schematic of the duopigatron ion source

with a 15 cm grid diameter. We have measured the ion saturation current, the electron temperature and the space potential by Langmuir probes. Typical radial profiles of the ion saturation current is shown by the broken line in Fig. IV.2.1-3. Improved plasma uniformity shown by the solid line in the same figure has been obtained by the use of an axial button of the proper size located at 2.5 cm downstream of the intermediate electrode.

To obtain a more uniform dense plasma, it is necessary to reduce the diffusion loss of ions across the magnetic field lines. For this purpose, we have made the duopigatron with the line cusp added as shown in Fig. IV.2.1-4. The line cusp field configuration is made by 16 columns of permanent magnets about 12 cm long, magnetized radially with opposite polarity of the adjacent columns. The magnets (1 cm diameter, 3 cm long; maximum magnetic field B = 4 kG) have been set in the slots on the walls of the arc chamber. Although the plasma uniformity is not good enough as expected so far[3], it will be improved by enlarging the anode diameter or by increasing the arc power supply.

2.1.3 Small aperture extractor[4]

For the extraction electrode of the fixed area and transparency, a higher extraction current can be expected by employing smaller apertures on the basis of the scaling law of the beam extraction. In order to confirm the scaling, two sets of electrodes are tested. Their diameter is 7 cm each. The model-I has 221 holes of 3.75 mm diam. each, and the model-II 693 holes of 2.2 mm diam. each. The results are shown in Fig. IV.2.1-5, where the equivalent beamlet divergence and the fraction of the beam power impinging on the grounded electrode are plotted against the perveance per hole. We are interested in the optimum perveance value p_c, where the divergence becomes minimum. In the model-I electrode, p_c is about 5 micro-perves and is insensitive to the aspect ratio. Unlike our expectation, p_c in the model-II electrode is too small, around 1 micro-perves for the decel gap $z_d = 2$ mm. We suspect that the decel gap has a comparable importance with the accel gap. If we reduce the decel gap in keeping the aspect ratio constant, we find that p_c increases significantly (see the data for $z_a = 3.0$ mm, $z_d = 1.2$ mm), although there still remains a difference by a factor of two. This difference is conceivably due to the unscaled electrode thickness; both electrodes of the model-I and II are

made of copper disks of 1.6 mm thick.

These works have been made in the last fiscal year, and the continueing effort has been made by the use of model-III electrode with the scaled thickness in accordance with the aspect ratio. Due to the machining difficulty, the aperture diameter is chosen to be 3.0 mm in this case. The optimum perveance value is increased and is close to those of the model-I electrode. Thus one can see that the scaling of the beam extraction is roughly hold with respect to the fixed aspect ratio.

2.1.4 Focusing by curved electrode

In order to increase the injection power to the torus, it is effective to focus each beamlet to the injection port. There are two methods for the focusing; one is by aperture displacement, the other is by electrode curving. The effectiveness of aperture displacement is already reported[5]. Here, the other method is examined. The center of curvature of each extraction electrode corresponds to the desired focal point. The electrodes are curved spherically so that the focal length is 1.0 m. The beam divergences are measured calorimetrically at the focal point. Dependences of the beam divergence on the perveance per hole are measured as the parameter of beam extraction voltage as shown in Fig. IV.2.1-6, where the extraction gap distance is 5 mm. The minimum beam divergences obtained at each extraction voltage are reduced appreciably in comparison with those obtained by the plane extraction electrodes, and are almost equal to those obtained by aperture displacement method. Therefore, we conclude that the focusing by electrode curving is as effective as that by aperture displacement.

2.1.5 Graphite grids[6]

To remove the high heat loading into the extraction grids, we have chosen a radiation cooling method as one of the candidates next to the forced water cooling method. We use a set of multiaperture grids made of graphite with 7 cm in diam., transparency of 70 %. Temperature rise in the edge of the exit electrode is measured with the thermocouple. The beam current has been extracted up to 3 A at 25 kV for 0.1 sec. A great number of breakdowns have occurred, especially above this power level. Maximum temperature rise is estimated to be about 800°C based upon the temperature rise measurement of about 100°C at the edge. Beam composition

has been measured by the mass analyzer installed in the ITS-1. The dominant impurities in this source are carbon and hydro-carbons. The amount is 2-15 % of the total ion current, and is too large to be used for the JT-60 NBI system. However, this approach cannot be discarded completely if one uses other materials such as Tungsten rather than graphite.

2.1.6 Two-stage acceleration

The design work of the JT-60 neutral beam injection system requires two ion sources in each beam line. A low divergent ion beam of 35 A at 75 keV shall be extracted for several to ten seconds through 12 cm × 27 cm extraction grid. The corresponding ion current density is about 0.27 A/cm^2 with 40 % transparency.

To develop ion sources of these specifications, we investigate the beam optics of the ion source with two-stage acceleration system numerically[7][8] and esperimentally[9] using the ITS-2 test stand (See Fig. IV.2.1-7). The extraction grid is made of copper disk with 83 apertures over 5 cm diam. area. The aperture diameter is 3.5 mm in the source and the gradient grid, while it is 4.0 mm in the suppressor and the exit grid. The e-folding beam divergence is measured by the scanning calorimeter set 1.0 m apart from the extractor. The total acceleration energy ranges from 50 keV to 70 keV, the extraction and acceleration gap distances are changed in the range of 6-8 mm. The beam divergence is plotted as a function of perveance for a set of these parameters. We find the tendency that the minimum beam divergence is improved with the decrease of field intensity ratio f, defined by the ratio of electric field intensities in the extraction to the acceleration gap, while one must allow the decrease of optimum perveance, the perveance at which the beam divergence is minimum (See Fig. IV.2.1-8). When f is smaller than 0.25, where the strong lens effect is expected, we obtain the smallest beam divergence of one degree, but the heat load to the source and the gradient grid increases significantly. Chamfering of the aperture edge in the source and gradient grids improves beam optics appreciably. Typical current density and the beam divergence are 0.15 A/cm^2 and 1.34 degree at 70 keV, respectively.

2.2 Beam line studies

Cryogenic pumping system may be one of the most important components in the neutral beam injection system for the JT-60. In order to confirm its performance, we are now testing a small scale cryogenic pump with a pumping speed of 6×10^4 ℓ/s. Energetic particles reflected from the structural materials of the injector will result in a heat input to the cryopanels. To know their influence, we have measured the energy-reflection coefficients for hydrogen ions impinging on different metals[10]. Blistering studies[11] are also in progress in our laboratory so as to estimate wall erosion and impurity concentration in the tokamak plasma associated with beam injection. In future, an energy recovery system should be introduced to improve the power efficiency of the neutral beam injector. We have begun a computer simulation study[12] of the system and are now on the search for the optimum configurations.

2.2.1 Cryopump

In the neutral beam injector for the JT-60, cryogenic pumps that have pumping speed of 10^6 ℓ/s for hydrogen will be installed in beam lines. To develop these cryopumps we have built two small scale pumps of 10^4 ℓ/s and 6×10^4 ℓ/s and have measured the fundamental pumping characteristics[13][14]. Both cryopumps have liquid helium cooled cryopanels, liquid nitrogen tanks. The temperature of cryopanels can be lowered to 3.6 °K by evacuating the vapor of the helium. The shevrons blackened by oxidization have a trasparency of 0.25. Figure IV.2.2-1 shows a schematic view of the pump of 10^4 ℓ/s and a system of measurement of the pumping speed. The cryopanel has a cylindrical shape and the shevron is arranged concentrically inside the cryopanel. The reason of the cylindrical shape is that cylindrical pumps are proposed in the first design of injectors and in the drift pumping region of the present design. The pumping speed S shown in Fig. IV.2.2-2 is obtained by the relation, $S = C_1 (P_1 - P_2)/P_3$, where P_1, P_2 and P_3 are the pressures measured by ionization gauges in Fig. IV.2.2-1 and C_1 is the conductance of a hole of 1 cm diam. Constant pumping speed at the temperature lower than 4.2 °K is 7500 ℓ/s and agrees with the design value considering the geometric structure of the pump. It is also certified that the pumping speed does not change after condensing 23.8 Torr.ℓ/cm^2 on the cryopanel. Fig. IV.2.2-3 shows a bird's-eye view of the cryopump of 6×10^4 ℓ/s with a pair of cryopanels. Each

cryopanel is 50 cm × 60 cm wide. The pumping speed obtained by measuring the pressure in the cryopump and the flow rate of hydrogen agrees well with the design value assuming a sticking probability of 0.5 to 0.8. The equiliblium pressure also agrees with the results in the literature. The rate of liquid helium consumption is obtained by the measurement of the boil-off helium when the hydrogen is being pumped. This result shows that the heat load caused by the condensing hydrogen molecules is about 0.1 J/Torr.ℓ. This value agrees well with internal energy difference of the normal hydrogen between 77°K and 4°K. The pump is being connected with the ITS-2 test stand beam line to investigate the pumping and heat loading problems associated with thermal radiation, backscattered hydrogens, physical and chemical damages of the oxidized shevrons in the presence of the beam dump.

2.2.2 Total backscattering[10]

The energy-reflection coefficient is defined as the fraction of incident energy carried away by reflected particles. The coefficients for 10 to 30 keV hydrogen ions bombarding Mo, Cu, stainless steel and Al have been measured calorimetrically in an explicit manner with a broad beam, a small thermocouple and large target plates (see Fig. IV.2.2-4). The energy flux sensor consists of an Alumel-Cromel thermocouple of 1.6 mm in diam., a copper cover, a ceramic tube and copper cooling pipes. The cover and the ceramic tube prevent the primary beam from directly hitting the thermocouple when we want to measure the reflected energy. The incident energy can be measured by rotating the sensor by 180° around an axis perpendicular to the beam axis without changing the operating conditions for the ion source. After corrections due to geometrical configuration of the apparatus and due to mixed beam composition of the source, the energy-reflection coefficients for protons normally incident on metals have been obtained as seen in Fig. IV.2.2-5. The figure shows that the coefficient decreases with increasing incident energy for a given target material and it decreases with decreasing mass number of the target material for a given energy. Introducing the Linhard's reduced energy ε makes the results more general as shown in Fig. IV.2.2-6, and enables us to estimate the energy-reflection coefficients at lower or higher energies for different target materials.

2.2.3 Blistering[11]

As surface problems associated with beam injection, surface damage is our great concern because it causes migration of impurities into the torus plasma. Molybdenum used for limiters of the JT-60 torus, and the beam limiters in the beam drift tube will be subject to the bombardment of fast hydrogen atom beam. To investigate the damage of Mo, polycrystalline molybdenum is bombarded with H^+ and H_2^+ ion beam of 25 keV, 30 mA/cm^2, 90 msec pulse at 9 % duty cycle, at the temperature from 20°C to 500°C. The surface damage strongly depends on the target temperature. Only near the temperature of 200°C, a new type surface damage "grain ejection" is observed. Numerous blisters at room temperature and no blisters or no traces of grain ejection at 500°C are observed. Details of this study are described in section V.2.3.

2.2.4 Energy converter[12]

In the neutral beam injector, neutral equilibrium fraction of the extracted beam falls off rapidly with the energy and the power efficiency decreases correspondingly. On the other hand, collecting the unneutralized fraction of the beam at full energy would produce high wall loading on the ion beam dump. It is thus necessary to recover the energy efficiently from high energy ions by decelerating and collecting them after the neutralizer exit. As the first step, we have performed computer simulation of an "in-line" type electrostatic energy converter. Figure IV.2.2-7 is one of the results obtained for monoenergetic 75 keV, 9 A proton beam. In this example, 98 % of the ions are collected at the recovery electrode and energy recovery efficiency is 85 %. The space charge neutralization by neutralizer beam plasma is included but the effect of secondary particles produced by charge exchange and ionization and of secondary electrons from the electrode surface are not included.

2.3 Neutral beam injector for JFT-2[15]

Neutral beam injector was installed in the JFT-2 Tokamak in July 1976. Two weeks were necessary to adjust the power supply and the control system. After that, an operational test of each elements of the beam line and the coolant system has been carried out by investigating the beam profile, the extraction power and the drain current of the ion source. Subsequently, improvements have been made on magnetic shield of the ion

source, switching system of the arc current and absorption of the surge voltage in the case of breakdowns of the ion source.

A side view of two beam lines is shown in Fig. IV.2.3-1. The main elements of the line are the ion source(1), neutralizer(2), magnetic shield(3), flashing target(4), drift tube(5), titanium sublimeters(6), molybdenum target(7) and isolation valves. A diagram of the time sequence is given in Fig. IV.2.3-2. Hydrogen gas to the ion source is supplied by a pulsed gas feed system. The neutral beam can be injected at desirable time with the pulse width of 10-60 msec. In Fig. IV.2.3-2, for instance, it is injected between 40 msec and 100 msec after the initiation of the discharge.

There has been no serious trouble in the ion source. The ion source is magnetically shielded against a stray poloidal field. At first, the accel gap is shield by the short coaxial shield materials. The drain current, in this case, is considerably disturbed by the presence of stray magnetic field as shown in case (a) of Fig. IV.2.3-3. Therefore, a long mild steel of 10 mm thick is lapped over the shorter shield as illustrated in case (b) in the same figure, so that the whole body of the ion source is covered except for the zwischen region. As a result, good shield is attained.

In the neutralizer, the working gas of the ion source is used as target gas. The thickness is 0.3 Torr.cm, and is sufficient for equilibrium. The neutralizer is also shielded from a stray magnetic field. The magnetic shield consists of coaxial multiple cylinders; inner cylinder of Mu metal, second cylinder of permalloy and outer cylinder of mild steel. At the exit of the neutralizer, the beam power on and off the poloidal field is measured by calorimeter (called as a flashing target in this system). A fact that the difference of the beam power between these two cases is negligibly small indicates that effective magnetic shield is fulfilled. The radial plofiles of the beam flux are measured by movable calorimeter installed between neutralizer and flashing target. An example is given in Fig. IV.2.3-4. The beam axis almost coincides with the axis of the beam line.

Since it is required that the gas influx into the JFT-2 should be less than 0.7 Torr.ℓ/sec from the constraint of the target plasma, the gas feed system is pulsed and the size of the drift tube is designed in a way that its conductance is below 410 ℓ/sec. The differential pumping between the neutralizer and the drift tube is performed by two turbo-

moleculer pumps of 1000 ℓ/sec each and a bulk getter pump of 2000 ℓ/sec. Throughput characteristics of these pumps are shown in Fig. IV.2.3-5. The ultimate peressure obtained is 4.7×10^{-7} Torr. The maximum gas flow rate from each source is 4.0 Torr.ℓ/sec during 0.2 sec in the heating experiment.

The accel, decel power supplies are common to two ion sources, and the independent set of PIG power supplies is connected to each of them. The extraction voltages are applied continuously, while pulsed arc voltages are applied for the source plasma production. The accel, decel supplies are regulated and modulated by the high power tetrodes, EIMAC Y676 and NEC 8T43R, respectively. The regulation of the voltage across the extraction gap is achieved within ±5 % between on and off the beam, and the current turn off time in the case of breakdown is less than 200 μsec. In this power supply system, the maximum extracted beam power is 240 kW (8 A, 30 kV). To make faster the rise time and decay time of the beam, the switching system of the arc current has been modified by using DC thyristor switch. The rise time and decay time of the beam have been changed to be less than 200 μsec. This modification has made it possible to investigate the slowing down of fasions by use of the charge exchange analyzer. In the initial period of experiments, the JFT-2 Tokamak and diagnostic apparatus were often triggered by noises associated with breakdowns of the ion source. Several improvements have been made on the ground system, voltage insulation and surge suppressors, and consequently misoperation has occurred less frequently.

To cool the ion source, beam dumpers and other parts exposed to high heat fluxes, a closed-loop water cooling system is employed. The maximum heat load in this coolant system during a 60 msec is about 240 kW. For a maximum duty cycle of 1/20, the average heat load is about 10 kW.

2.4 Design study of the neutral beam injector for JT-60[17][18]

Conceptual design study has been made of the neutral beam injection system that will be applied to the JT-60 tokamak. In order to achieve the fusion-like plasma, it is required to inject 15-20 MW neutral hydrogen atom beam into the torus. The beam energy should be about 75 keV to provide enough penetration deep into the dense plasma, while keeping the adequate efficiency of the neutral beam production. The other main restriction imposed on the injection system is a very low permissible cold gas flux into the torus. This flux should be less than 10 % of the

energetic neutral beam flux. These requirements together with geometrical accessibility of the torus, essentially determine the overall system scale.

The NBI system for JT-60 consists of 16 injector units, each of which includes all hardware items needed to produce and transport neutral beams to each of the sixteen injection ports, e.g., ion sources, four extractors, four neutralizers, bending magnet, ion beam dump, calorimeter, isolation valves beam limiters, pumping system, power supplies and auxiliary systems (See Fig. IV.2.4-1). The ion sources will have to be the subject of a research task, but is required to produce a quiescent, uniform source plasma with an ion saturation current density of 0.3-0.45 mA/cm^2 over the 12 cm diam. extraction area. The ion extraction grids will be the multi-aperture type with forced water cooling pipes arranged alternatively with the array of apertures. Extremely good beam optics (less than 1.0 degree) are required not only to meet injection power requirement but to eliminate problems caused by the impinging beam fraction, such as gas load problem, heat load problem, and impurity problems. The accelerated ions then pass through the neutralizer cell and are converted to neutral atom beam by electron capture in a gas. To effectively shield the stray magnetic field from the control coils of the JT-60 tokamak, the ion sources, extractors and neutralizers are arranged vertically on one azimuthal plane.

Most part of the neutral beams ejected from the neutralizer pass through three aperture limiters, and drift tube and then are injected into the torus. Unneutralized energetic ions as well as the secondarily produced positive and negative ions are swept by the reflecting magnet and are led into the ion beam dump.

The gas flow into the pumping system in each injector unit is estimated to be about 14 Torr.ℓ/sec, whereas the maximum allowable gas flow into the torus is 0.246 Torr.ℓ/sec. Furthermore, the pressure in the neutral beam drift region should be kept low to suppress reionization loss of neutral beams less than 2 %. To satisfy these requirements, we adopt cryogenic differential pumping system with a total pumping speed of 8×10^5 ℓ/sec per injector unit.

Due to the geometrical restriction imposed on the JT-60 neutral beam injectors, a couple of injector units are placed at an azimuthal position stacked vertically one over the other. Therefore, the vacuum tank of the lower injector unit should have a role of supporting framework of the upper tank. The injection port is limited by the control field coils and

toroidal field coils and is 40 cm in diameter. Although the neutral beam power into the torus appreciably depends on the distance between extractors and the injection port, enclosure of those hardware items requires about 8 meter length for the beam line (Fig. IV.2.4-2).

2.4.1 Power efficiency

Using the ion simulation code, that is extensively applied to the two-stage acceleration system, the beamlet divergence and the extraction current are investigated in detail. By adjusting the source plasma density, the minimum beamlet divergence is obtained for each aperture geometry. Taking into account the aberration due to machining inaccuracy, setting error, thermal distortion, density gradient and fluctuations of the source plasma, and other unknown factors, the effective beam divergence ω_{eff} may be given by the relation,

$$\omega_{eff}^2 = \omega_{min}^2 + \omega_m^2 + \omega_s^2 + \omega_t^2 + \omega_g^2 + \omega_f^2 + \omega_u^2 \ ,$$

where ω_{min} is the minimum beamlet divergence, and ω_m are the beam aberration caused by those factors, respectively. Assmuing the machining inaccuracy of ±0.1 mm, setting error within ±0.1 mm and 10 % of the spatial nonuniformity, 10 % of fluctuations in the source plasma, and some safety factor amounts to 0.15° equivalent, we estimate the effective beam divergence to be about 1.0 degree with the total ion current of 15 A from the 12 cm diam. grids. Four extractor grids are assembled in one injector unit with the total ion drain current of 60 A at 75 kV (4.5 MW). Since the neutralization efficiency is 38 %, divergence loss is 18.3 %, reionization loss is 2 %, and the interception loss of ion beams by the grids is 5 %, the resulting overall power efficiency is about 29 %. Thus, the neutral beam power injected into the torus is estimated to be 1.3 MW per injector unit, and hence 20.8 MW in total with 16 injector units.

2.4.2 Gas efficiency

To consider the gas handling problem more generally, we propose to introduce a concept of the neutral beam gas efficiency defined by the ratio of energetic neutral beam flux to the rest of all other fluxes to be evacuated. These fluxes are given by

$$\Gamma_n \simeq \eta_G \Gamma_{ion}$$

$$\Gamma_c \simeq (1 - \eta_G) \Gamma_{ion} + Q_c \quad ,$$

respectively, where Γ_{ion} is the ion beam flux extracted from the grids, Q_c is the thermal gas flux from the neutralizer, and η_G is the neutralization efficiency of the ion beam (See Fig. IV.2.4-3). An inverse of the neutral beam gas efficiency is then given by

$$\frac{\Gamma_c}{\Gamma_n} = \frac{1 - \eta_G}{\eta_G} + \frac{Q_c}{\Gamma_n} \quad ,$$

where the first term in the right hand side represents the contribution from the unneutralized ions and the second term from the cold gas flow through the neutralizer. Since the first term is determined only by the beam energy, and there is no room to decrease this value, Q_c/Γ_n should be decreased to reduce the total amount of the cold gas. However, since $\Gamma_G < 0.4$, $Q_c/\Gamma_n \sim 2\text{-}3$ we find $\Gamma_c/\Gamma_n \sim 4.0$ provided the cold gas flow is not pumped out. Since Γ_c/Γ_n should be less than 0.1 at the injection port, almost 98 % of the cold gas flux shall be pumped out in the beam lines.

To reduce Q_c/Γ_n, we have to consider the cold gas flow by coupling the neutralizer cell and the ion source extractor. The line density necessary for neutralizer, about 0.32 Torr. cm to establish 90 % conversion efficiency of the equilibrium cell, can be obtained mainly by the thermal gas flow from the ion source. Assuming the fixed extraction current density from the ion extraction grid, and also assuming that the beam divergence is small enough so that the diameter of the neutralizer is chosen to match the extractor grid, the energetic neutral beam flux out of the cell Γ_n is eventually proportional to the diameter D of the grids.

$$\Gamma_n \propto \Gamma_{ion} \propto D^2$$

On the other hand, we obtain the cold gas flow determined by the conductance of the cell taking into account the required line density.

$$Q_c \propto D^3/\ell^2$$

where ℓ is the length of the gas cell. Combining these relations we obtain

$$\frac{Q_c}{\Gamma_n} \propto \frac{D}{\ell^2}$$

Namely, the neutralizer with small diameter and large length is effective in reducing relative fraction of the cold gas. The neutralizer with large length may be more effective than that of the smaller diameter, but when the beam divergence is taken into consideration, the injection power efficiency simultaneously decreases with the neutralizer length because the total beam line length is increased. The neutralizer is 180 cm long, 12.5 cm diameter with a slight taper toward injection port.

2.4.3 Pumping system

To effectively pump out the cold gas, a differential pumping system are adopted. The cryogenic pumping room is divided into three sections and they are connected each other by the small conductance apertures along the beam line. These rooms have the pumping speed of 3.9×10^5 ℓ/sec at 3.0×10^{-5} Torr, 3.4×10^5 ℓ/sec at 7.2×10^{-6} Torr, and 5.0×10^4 ℓ/sec at 3.4×10^{-6} Torr, respectively. Thus the total pumping speed is about 7.8×10^5 ℓ/sec for each injector unit. The cryopanels should be cooled by the liquid helium below 3.6°K. They must be shielded against thermal radiation and heat conduction due to hydrogen gas by putting liquid nitrogen shevrons with appropriate geometries.

2.4.4 Mile stones and R&D items

Prior to the construction of the 16 injectors for the JT-60 neutral beam system, we will build a prototype injector unit to confirm the system performance. Although the former scale is far larger than the latter, there seems no intrinsic difference from the engineering point of view. For instance, the power convertion system for the prototype injector unit will be the same as that of the JT-60 injector unit except for the absence of the fly-wheel AC generator system. The liquid helium circulation system for the cryogenic pump in both cases are equipped with helium recovery loops and decompression loops for cooling the liquid helium temperature down to 3.6°K, although the system scales are quite different. Therefore, the most important mile stone in the JT-60 injector development is the construction and successful tests of the ptototype injector unit.

In order to construct the prototype injector unit, following R*D works should be made.

(a) Ion source development

In the injector unit, four ion sources are stacked. Each ion source can provide ion beams of 15 A at 75 kV for 10 sec. The ITS-1, ITS-2 and ITS-3 (being constructed in FY 77) test stands are primarily oriented to develop this ion source.

(b) Cryogenic pump

We have built small scale cryogenic pumps which have pumping speeds of 1×10^4 ℓ/sec and 5×10^4 ℓ/sec, respectively. These pumps have been tested already and the results are satisfactory. Heat loading to the criopanel due to thermal radiation and backscattered particles is being made by connecting the latter pump to the ITS-2 beam line.

(c) Hard seal gate valve

To disconnect the NBI vacuum system for JT-60 vacuum chamber, a large diam. hard seal vacuum valve is necessary. Since the presently available hard seal valves have openings less han 30 cm diam., extensive effort would be necessary to develop the 60 cm diam. valve.

Finally Table IV.2.4-1 shows the typical performance of the NBI system for JT-60.

Recently, we have modified our design. Major points are: (1) Injector units are reduced in number from 16 to 14 to serve more accessibility for diagnostics ports, while maintaining the same injection power. (2) This requires an increase of the packing factor of ion extractor grids. For this reason, the number of ion sources stacked in each injector units is reduced from four axisymmetric sources to two rectangular sources, hence, the ion beam current per source is increased from 15 A to 35 A.

These modifications may permit more reliability of operation, more simplicity of connecting cables, while they cause larger gas flow rate into the vacuum tank and require longer development period of ion sources. However, these technical problems will be solved within the margin of the design and development.

References

(1) Matsuda, et al.: JAERI-M 6431 (1976) (in Japanese).
(2) Davis, R.C. et al.: ORNL-TM 4675 (1974).
(3) Stirling, W.L. et al.: ORNL-TM 5662 (1976).
(4) Matsuda, S. et al.: to be submitted for publication.
(5) Ohara, Y. et al.: JAERI-M 6438 (1976).
(6) Kondoh, U. et al.: to be submitted for publication.
(7) Ohara, Y.: JAERI-M 6757 (1976) (in Japanese).
(8) Ohara, Y.: JAERI-M 6813 (1976).
(9) Ohara, Y. et al.: to be submitted for publication.
(10) Tanaka, S. et al.: submitted to JJAP for publication.
(11) Nakamura, Y. et al.: to be published in J. of Nuclear Materials.
(12) Horiike, H. and Ohara, Y.: to be submitted for publication.
(13) Shibata, T. et al.: to be submitted for publication.
(14) Shibata, T. et al.: to be submitted for publication.
(15) Sugawara, T. et al.: JAERI-M 7043.
(16) Itoh, T. et al.: to be published in JAERI-M (in Japanese).
(17) Shirakata, H.: "Additional Heating in the Japanese Tokamak JT-60", a paper presented at the third Int. Meeting on Theoretical and Experimental Aspect of Heating of Toroidal Plasmas, June, 1976, Grenoble.
(18) Matsuda, S. et al.: "Conceptual design of the neutral beam injector for JT-60", Section 6.2 of the paper "Status of JT-60" presented at the 2nd IAEA Technical Committee Meeting on Large Tokamak Experiment, Nov., 1976, Princeton.

Table IV.2.1-1 Typical performance of the ITS-2

Beam Specifications	
beam species	Hydrogen
injection power (neutral)	15 MW(phase 1) 20 MW(phase 11)
beam energy	75 keV (main component)
Beam Lines	
number of beam lines	16
injection port	40 cm diam.
injection angle	36° against median plen 13° against radial direction
Gas Input to Torus	
permissible cold gas flux	less than $(2\text{-}3)\times10^{20}$ particles/s ($\Gamma_c/\Gamma_n \lesssim 0.1$)
Injector Unit	
ion beam output	60 A at 75 kV (4.5 MW)
extractor	water cooled multi-aperture
diameter	12 cm
number of apertures	470 each aperture is 3.5 mm
extraction current density	0.3-0.45 A/cm^2
beam composition	75% H^+, 20% H_2^+, 5% H_3^+
neutralizer	12.5 cm-15 cm, 180 cm long
reflecting magnet	4 kG
pole distance	20 cm
pole area	20 cm × 140 cm
power to the beam dump	2800 kW
power to the calorimeter	1700 kW
maximum heat loading	0.3 kW/cm^2
surface temperature	300°C
cryogenic pump	
pumping speed	7.8×10^5 1/sec
effective pumping speed	7-10 1/s·cm^2
cryo panel temperature	3.6° K
shevron temperature	77° K
hard seal gate valve	
diameter	24"
Power Supplies	
number of power supply unit	16
output power	100 kV, 80 A
AC power supply	156 MW fly-wheel generator

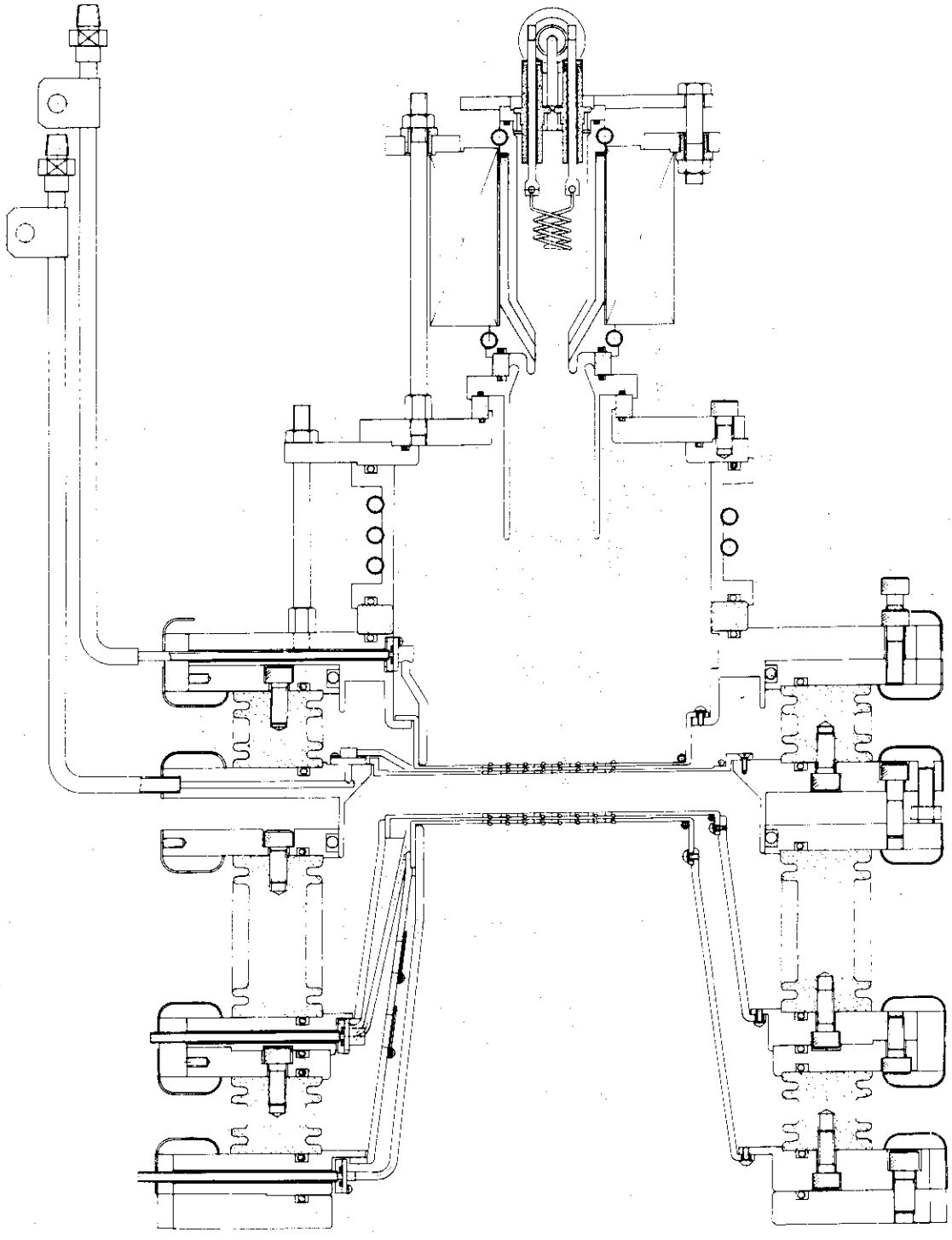

Fig.IV.2.1-1 Two-stage ion source with 5 cm diam. extractor grids.

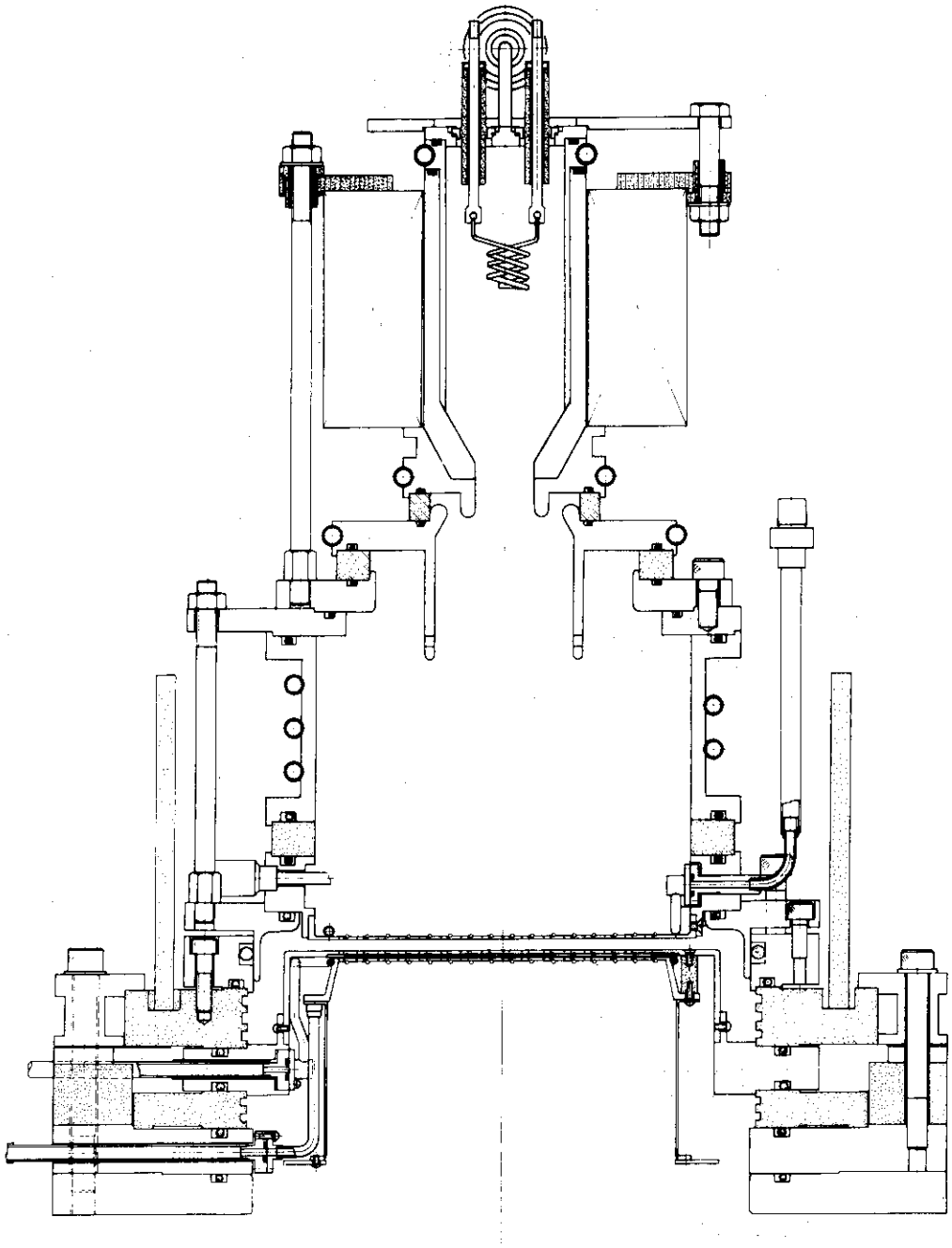

Fig.IV.2.1-2 Single stage ion source with 15 cm diam. extractor.

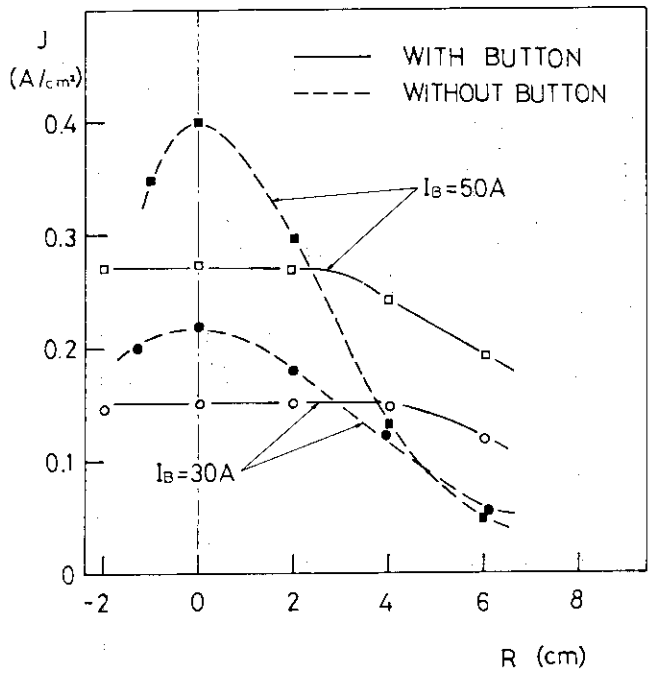

Fig.IV.2.1-3 Radial profiles of the ion saturation current density of the source plasma.

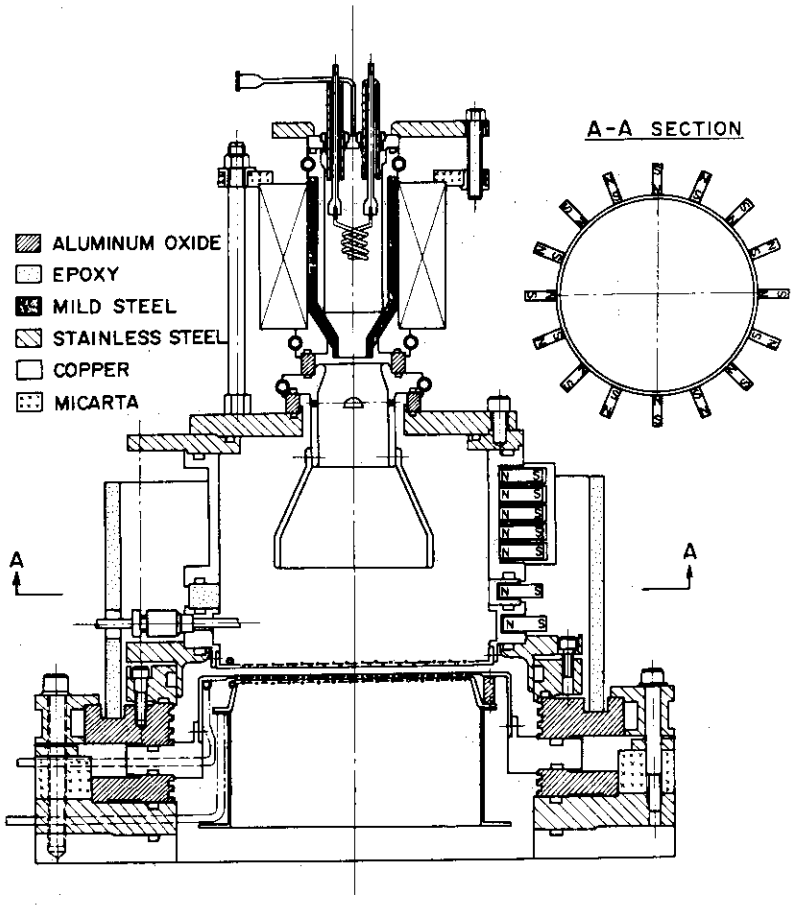

Fig.IV.2.1-4 Duopigatron with line cusp field added.

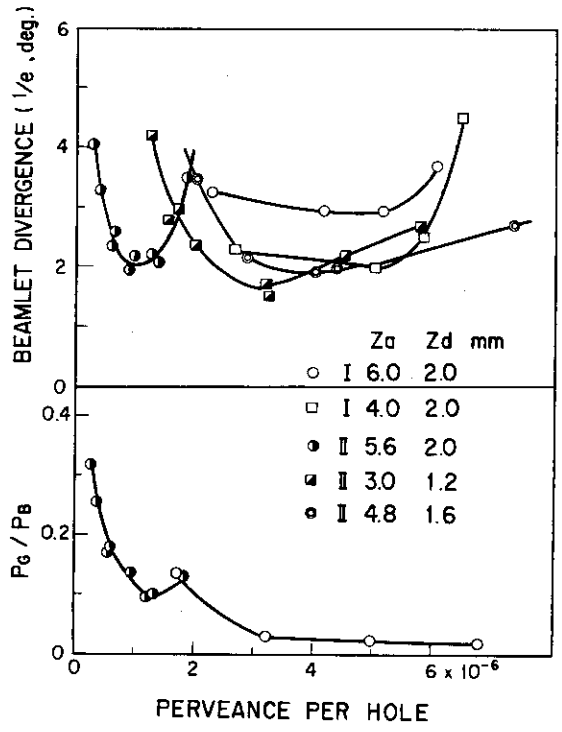

Fig.IV.2.1-5 Beamlet divergence and power loading on the grounded electrode, where z_a and z_d are the accel and decel gaps, respectively.

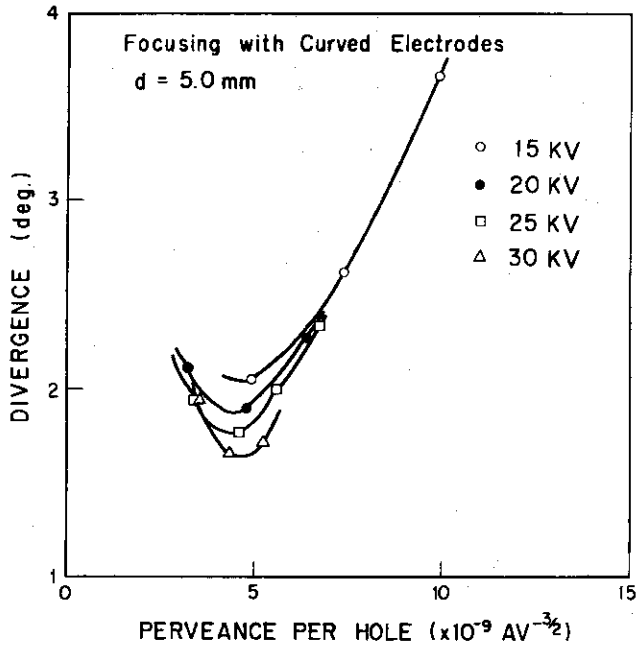

Fig.IV.2.1-6 Beam divergence v.s. perveance per hole. The accel voltage is chosen as a parameter.

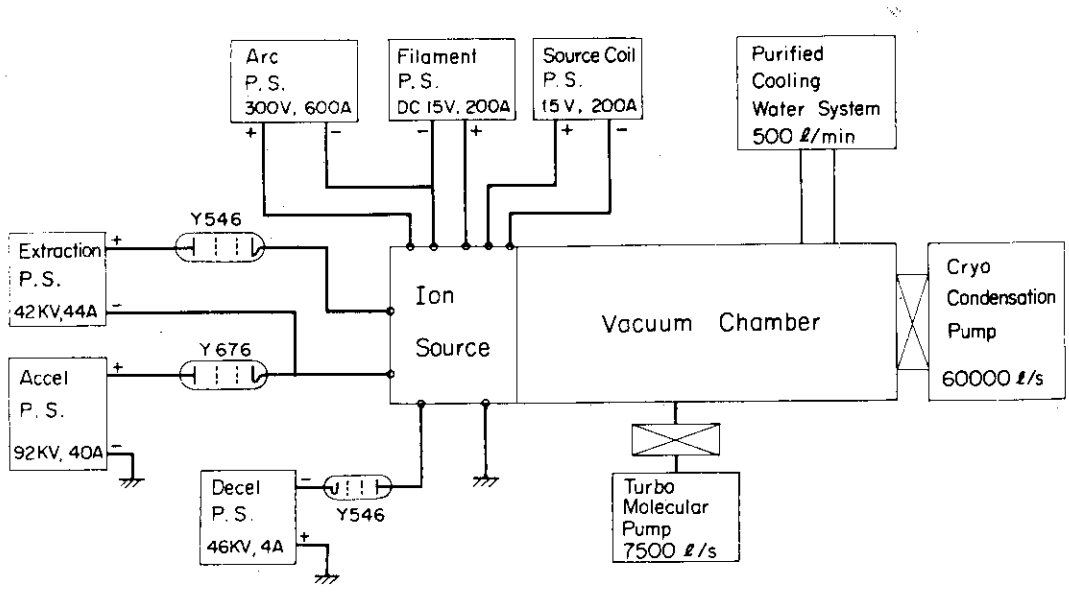

Fig.IV.2.1-7 Configuration of the two-stage injector test stand ITS-2.

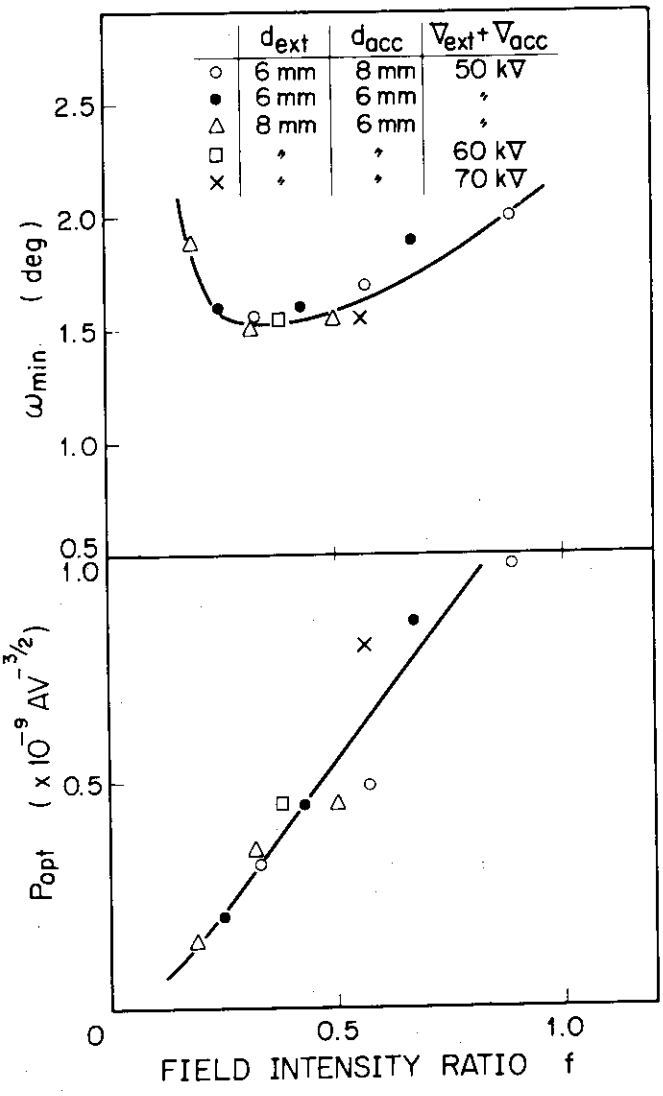

Fig.IV.2.1-8 Optimum beam divergence and perveance as a function of the field intensity ratio f.

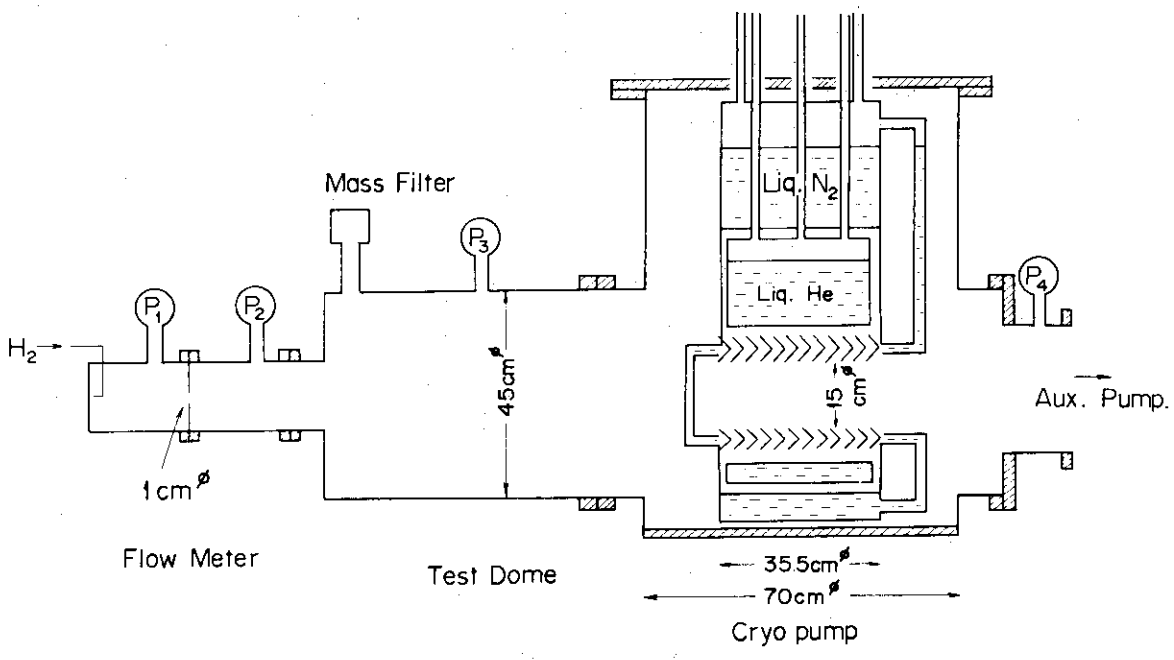

Fig.IV.2.2-1 A schematic view of the 10^4 1/s cryopump.

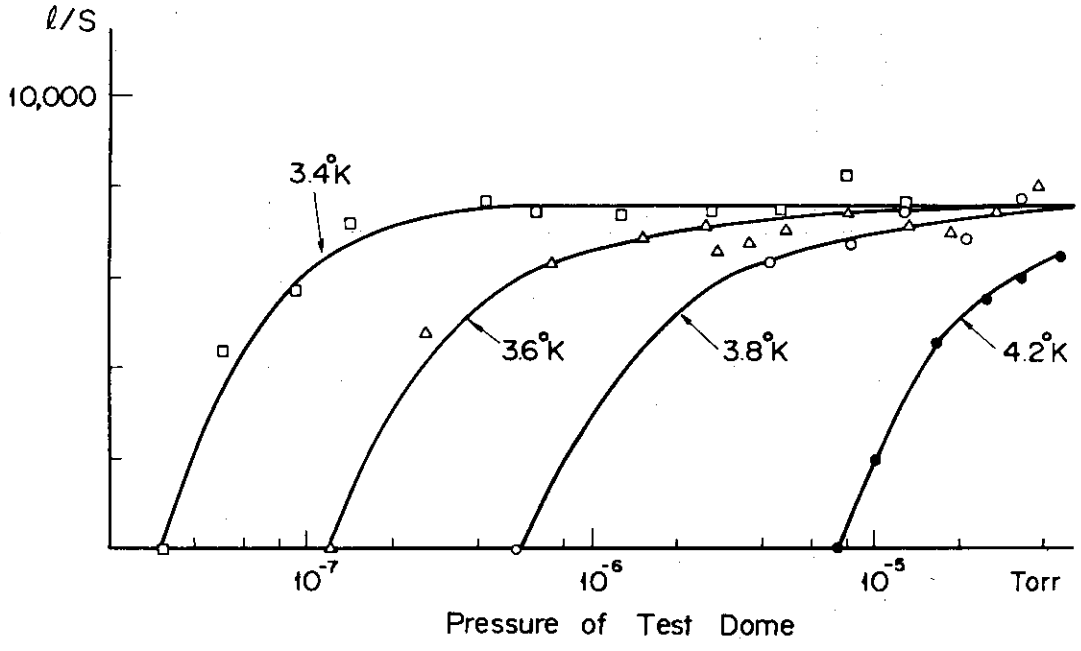

Fig.IV.2.2-2 Pumping characteristics of the 10^4 1/s cryopump.

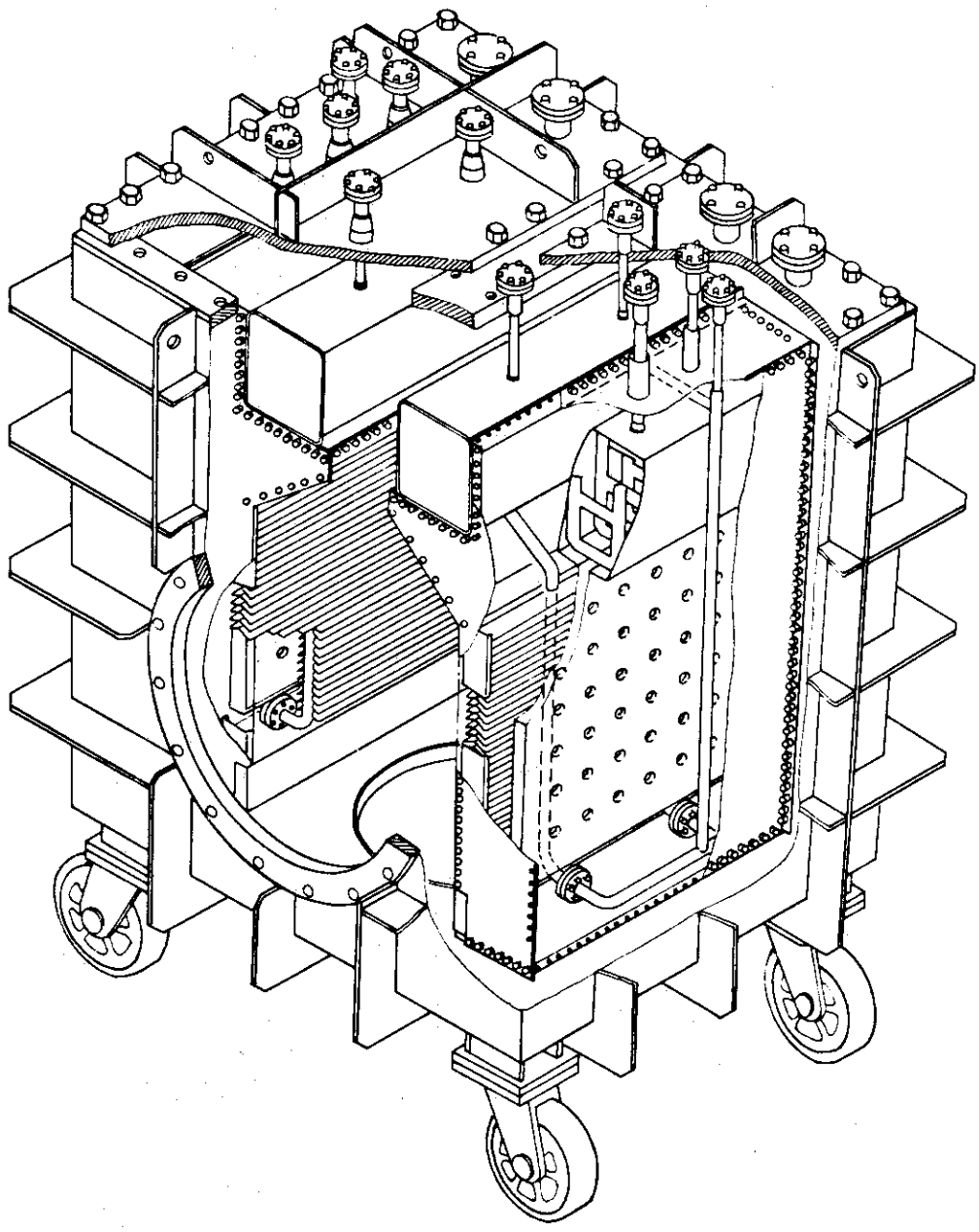

Fig.IV.2.2-3 Bird's-eye view of the 6×10^4 1/s cryopump.

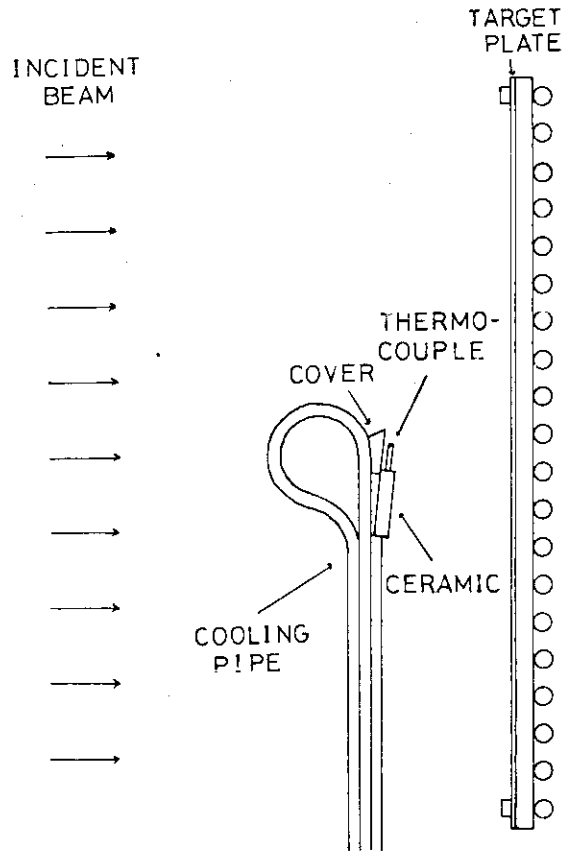

Fig.IV.2.2-4 Schematic view indicating the principle of measurement.

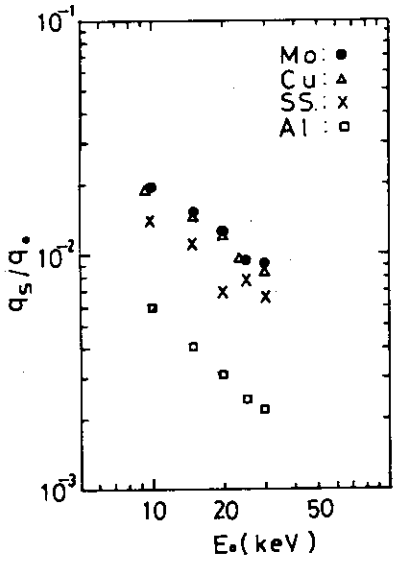

Fig.IV.2.2-5 Energy reflection q_s/q_0 as a function of the incident beam energy E_0.

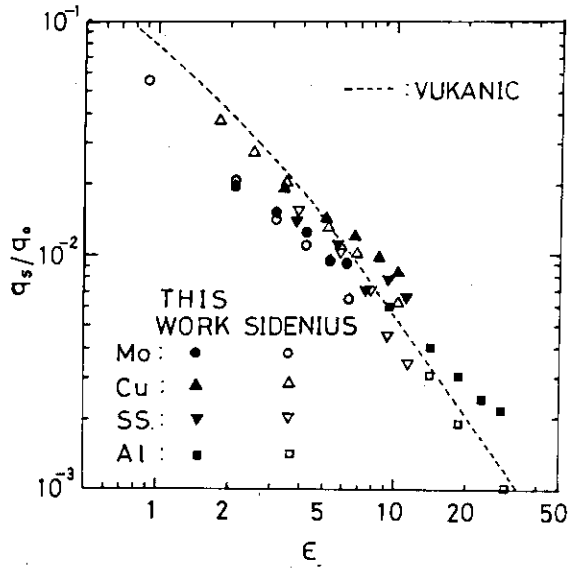

Fig.IV.2.2-6 Energy reflection coefficient γ as a function of the reduced energy, E. Also shown are the experimental and theoretical results of other authors.

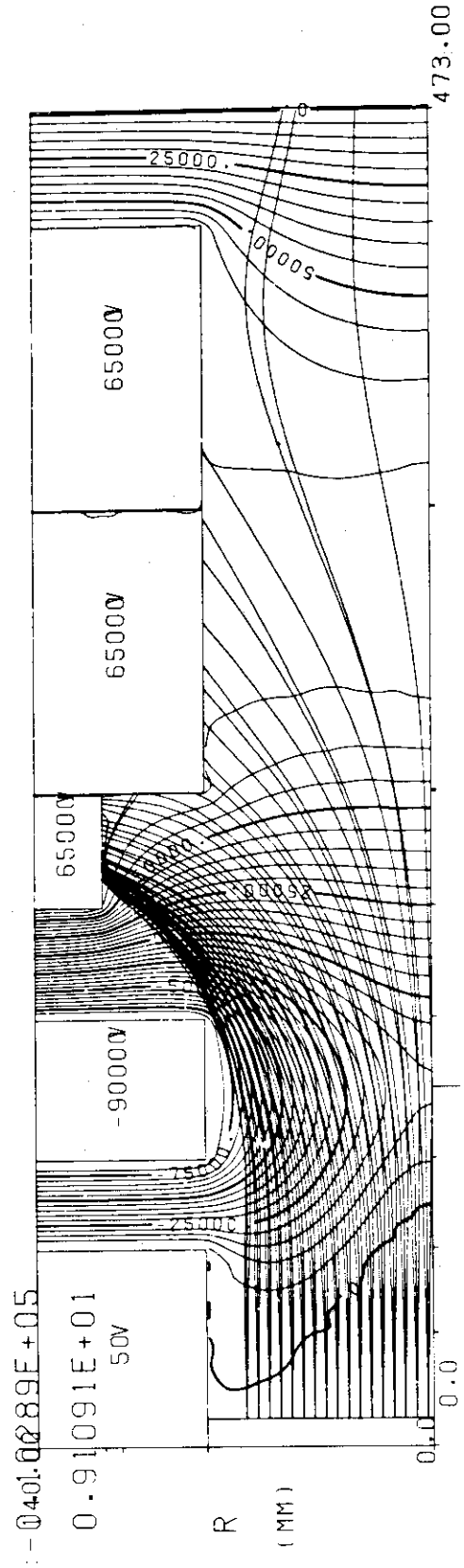

Fig.IV.2.2-7 An example of the computed beam trajectories in the energy converter.

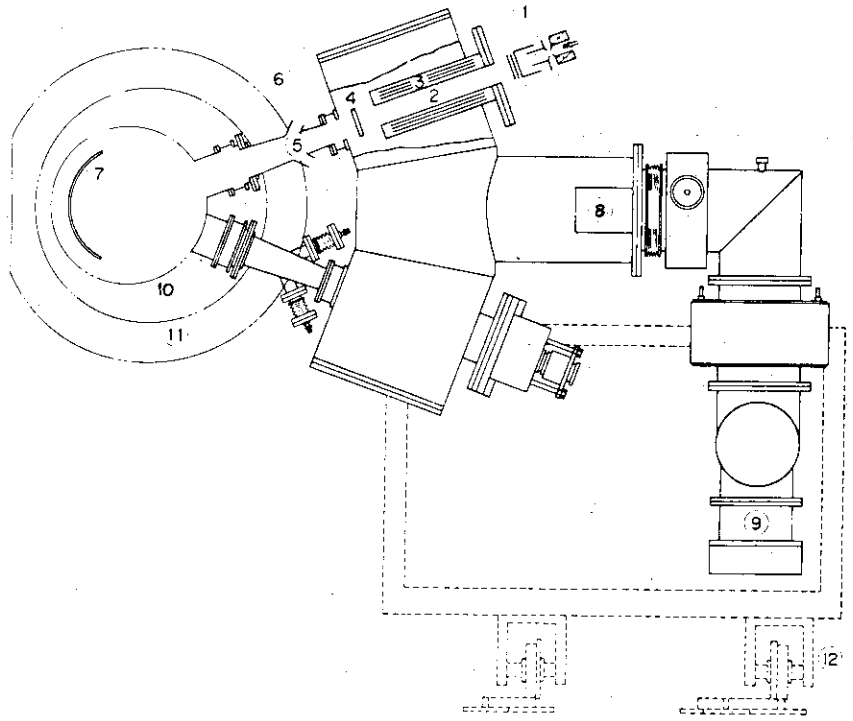

Fig.IV.2.3-1 A side view of the JFT-2 neutral beam injector.

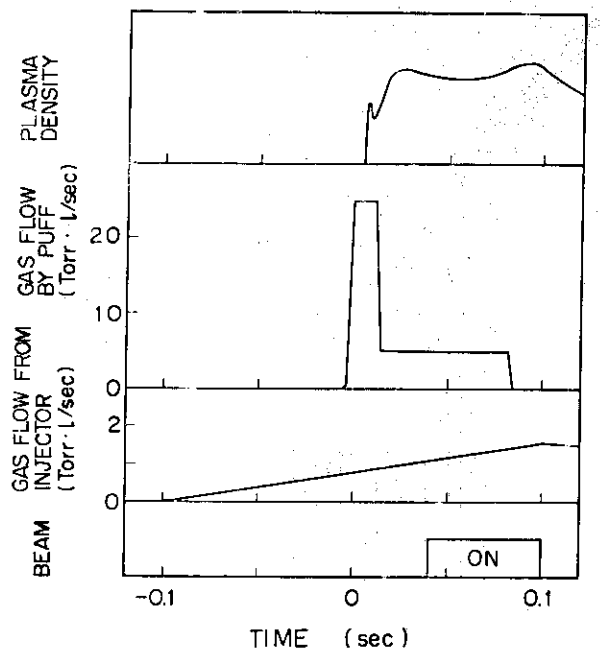

Fig.IV.2.3-2 Time sequence diagram of the gas feed and beam pulse.

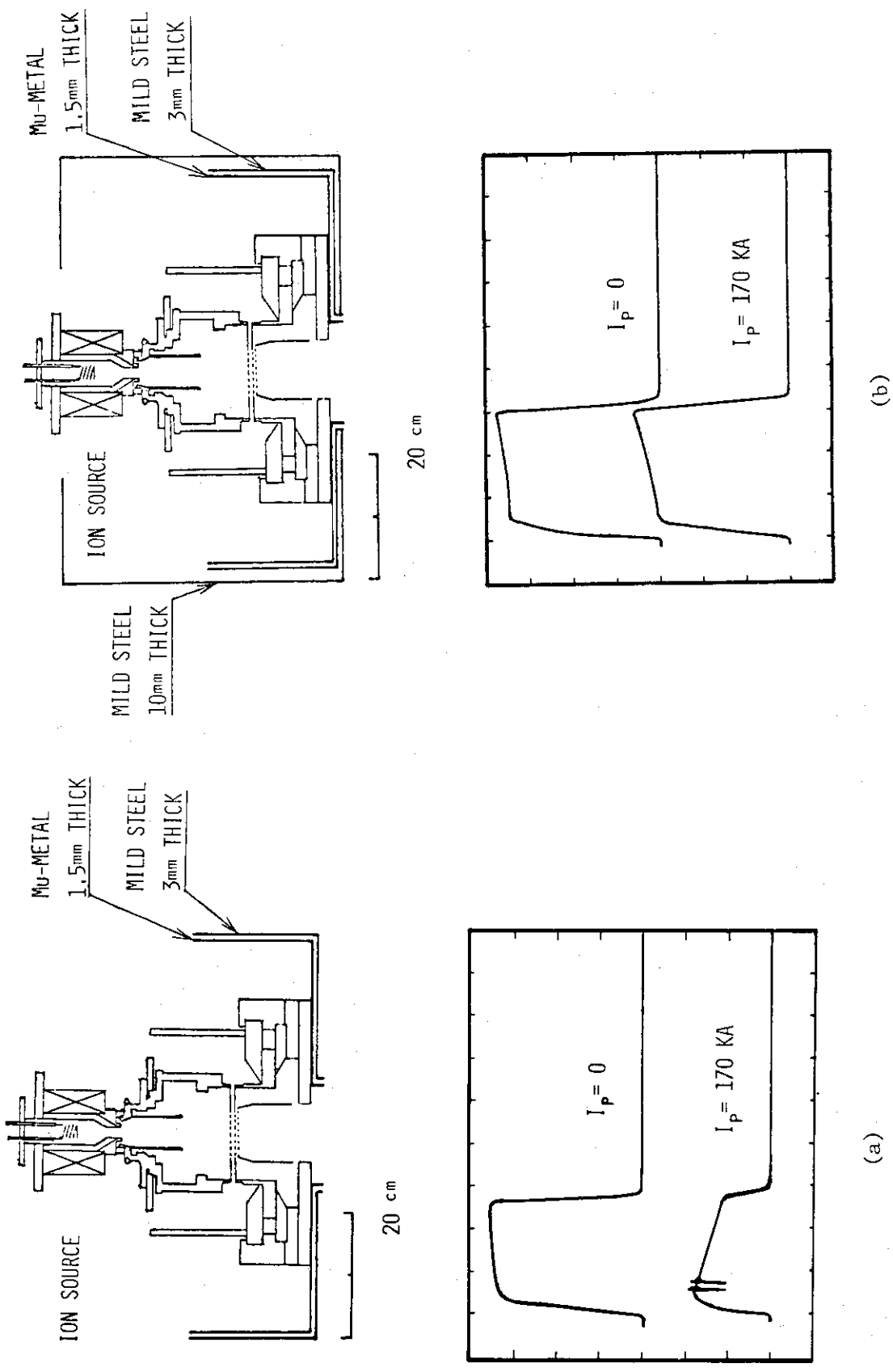

Fig.IV.2.3-3 Effect of the magnetic shield on the drain current, (a) for short magnetic shield and (b) for pile up magnetic shield. The upper and lower oscillogram traces give the drain currents for $I_p = 0$, and $I_p = 170$ kA, respectively

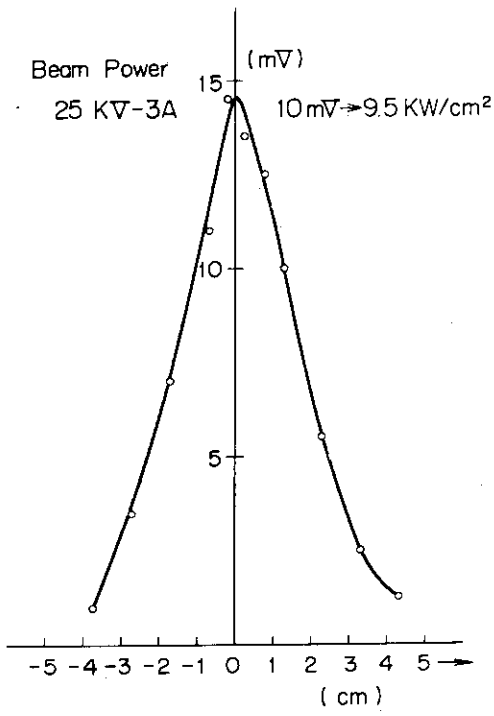

Fig.IV.2.3-4 Beam profiles measured by the movable calorimeter at 1.0 m apart from the extractor.

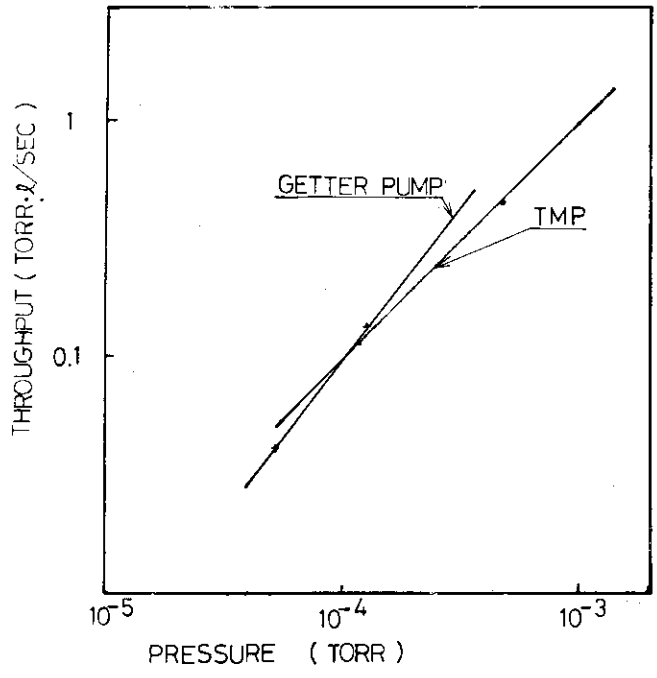

Fig.IV.2.3-5 Throughput characteristics of the pumping system of the JFT-2 neutral beam injection system.

Table IV.2.4-1 Dimensions of the JT-60 neutral beam injector unit

Typical Performance of the ITS-2

Power Supply

Accel. A: DC 10-50 kV (regulated/modulated), 20 A
DC 50-80 kV (unregulated), 20 A
Accel. B: DC 10-35 kV (regulated/modulated), 22 A
Decel : DC-(1-40) kV (regulated/modulated), 2 A

for the maximum pulse length of 1 sec at 10 % duty cycle. The current rating is doubled for 0.5 sec pulse at 2 % duty cycle. Continuous operation is also possible at the current rating of 30%.

Vacuum Chamber

Stainless steel
Size: Diam. 60 cm, Length, 3.2 m

Vacuum Pumping System

Turbo molecular pump	2500 1/s for H_2	3 sets
Mechanical booster pump	500 m^3/hr	2 sets
Cryogenic pump	10000 1/s for H_2	1 set
	50000 1/s for H_2	1 set

Demineralized Water Cooling System

Cooling capacity	400 kW continuous
	7800 kW 1 sec pulse
Flow rate	500 1/min
Pressure	10 kg/cm^2
Resistivity	> 1ΩM•cm

Diagnostics

Calorimeter, Faraday Cup, Mass Analyzer

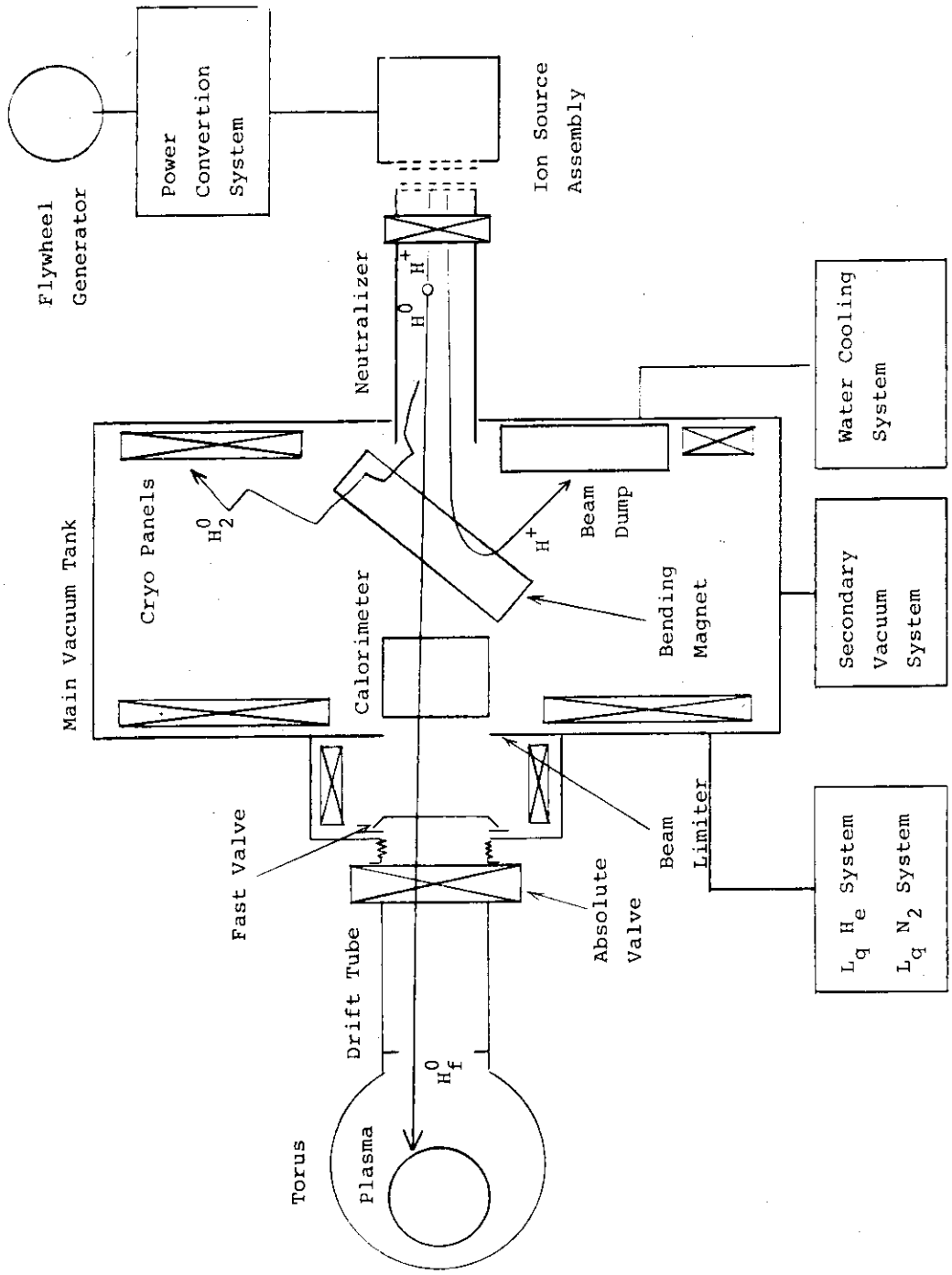

Fig.IV.2.4-1 Beam line components and functions.

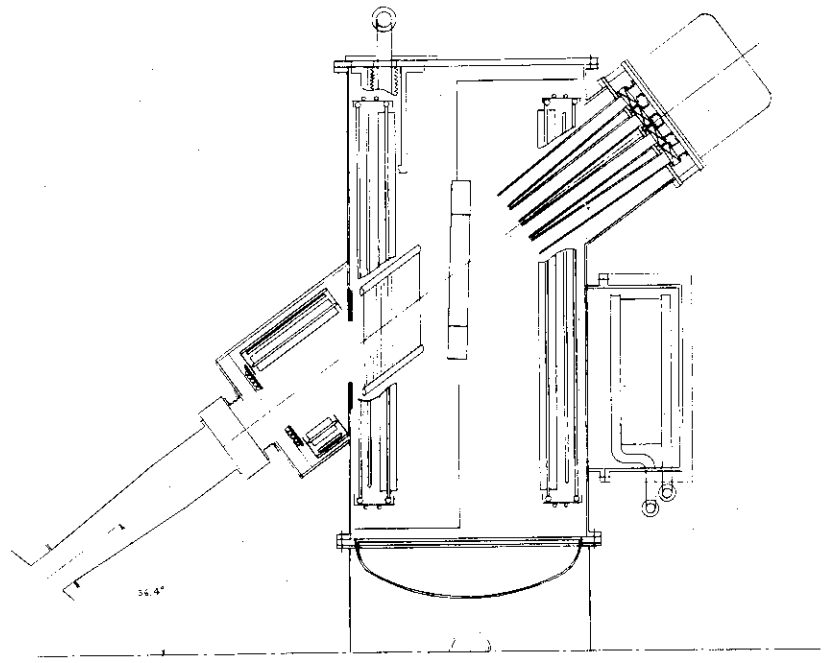

Fig.IV.2.4-2 JT-60 neutral beam injector unit.

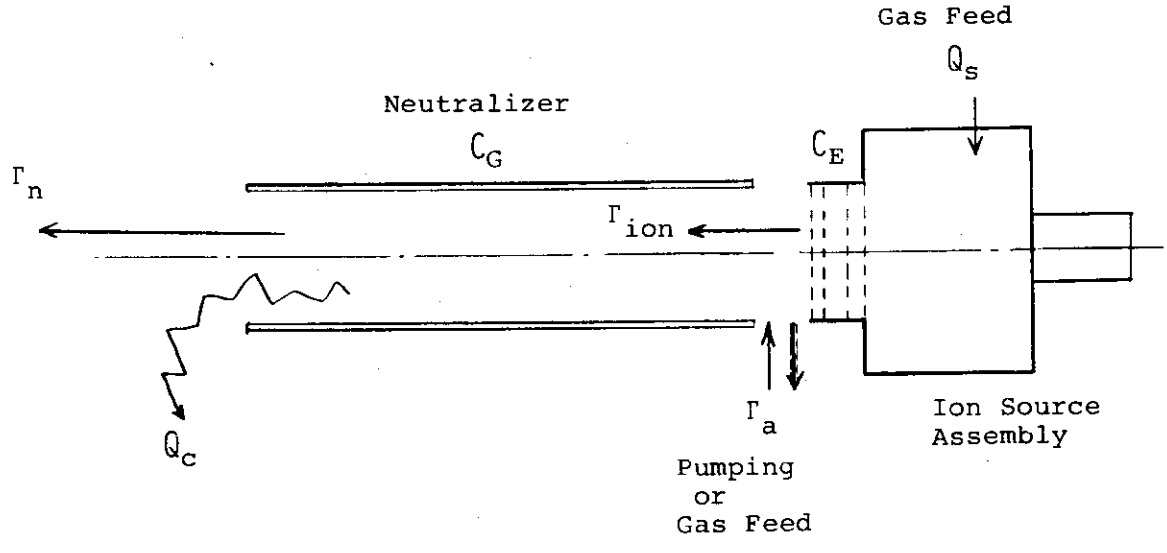

Fig.IV.2.4-3 Gas flow diagram.

3. Radiofrequency Heating System

3.1 Characteristics of lower hybrid wave and phased multi-waveguides array in JFT-2

Wave characteristics of lower hybrid wave (LHW) in JFT-2 and coupling features of phased waveguides array have been studied in order to optimize the frequency of the RF heating system. The lower hybrid resonance frequency is written in the following form:

$$\omega_{LH}^2 = \omega_{pi}^2/(1+\omega_{pe}^2/\omega_{ce}^2) \ . \qquad (1)$$

Wave behavior near the LHRF has been extensively studied by many authors since it is not only the object of plasma physics but also the heating mechanism of fusion plasmas. There are many theoretical and experimental works on it[1]~[5]. We have investigated numerically the wave propagation and wave coupling efficiency near the LHRF[5].

Electromagnetic wave near the LHRF launched by slow wave structure satisfies accessibility condition and can penetrate deep inside a plasma. The accessibility condition is given as $N_z > 1+\omega_{pe}^2/\omega_{ce}^2$, where N_z is the refractive index parallel to the external magnetic field. In the extent of linear theory, there are three stages of wave property during wave penetration in an inhomogeneous plasma (see Fig. IV.3.1-1). The first stage (1 in Fig. IV.3.1-1) is cold oblique electron plasma wave in outer plasma region. The second (2 in the figure) is warm ion plasma wave in the central part. The third (3 in the figure) is ion Bernstein wave. It is quite important for ion heating to see the location of the turning point (r_t in the figure), where cold plasma wave converts to warm ion plasma wave since wave energy comes to be absorved by ions via ion cyclotron damping when the thermal motion affects the wave. It is shown in Fig. IV.3.1-2 Fig. IV.3.1-4 that parametric dependence of the position of the turning point of the LHW in an electrostatic fluids approximation. Relations between the external magnetic field and electron density at the turning point (full lines) and cold lower hybrid resonance (dashed line) are shown in Fig. IV.3.1-2, where input frequency is 650 MHz and refractive index N_z parallel to the external magnetic field is indicated in the figure. The parabolic density profiles are also shown[1]~[4]. The position of the turning point vs. impurity (O^{+8} ions) concentration and input frequency is shown in Fig. IV.3.1-3 and Fig. IV.3.1-4, respectively, where peak electron density is 1.8×10^{19} m^{-3}, and the external toroidal magnetic

field is 1.2 Tesla. We can understand the position of the turning point r_t in a weakly inhomogeneous plasma depends on the input frequency, electron density and the external magnetic field. Impurity concentration and refractive index parallel to the magnetic field and temperature are also effective on r_t.

To summarize, if the refractive index parallel to the external magnetic field $N_z = 4 \sim 12$ and oxygen impurity (O^{+8}) is 4 %, we can see that the range of the appropriate frequency to heat ions may be from 600 MHz to 700 MHz.

Possibility of electron heating via electron Landau damping in the lower hybrid heating experiment of JFT-2 is also investigated. Electron Landau damping becomes effective when the relation between electron thermal velocity and phase velocity parallel to the external magnetic field v_{Te}/v_{phz} is larger than 1/3. The ratio corresponds to $N_z = 6$ at the electron temperature of 1 keV. Hence, we may expect the electron heating in JFT-2, as the parallel refractive index N_z is adequately large, namely, $N_z > 5$ as shown next.

Coupler of JFT-2 RF heating system is to be a set of phased four waveguides array (see Fig. IV.3.1-5). We calculated coupling feature of this type of wave launcher by the help of Brambilla's theory[6]. Reflection coefficient R vs. phase difference of adjacent waveguides $\Delta\phi$ and respective power spectra in refractive index N_z space are shown in Fig. IV.3.1-6 (a) and (b) respectively, where we restrict total width of waveguides to be 0.064 m because of the limit of the JFT-2 port width and input frequency 650 MHz and density gradient $\partial n/\partial x = 10^{20}$ m^{-4}. In the second phase of JFT-2 RF heating experiment from the autumn in 1978 the port width will be doubled or tripled to optimize the coupling feature of the array. Figure IV.3.1-8 shows that reflection coefficient R vs. phase difference of four waveguides array, where b indicates the height of each waveguide and the other parameters are the same as those of Fig. IV.3.1-6. If the height is larger than 0.03 m, the reflection is small. The power spectra are shown in Fig. IV.3.1-7 (b) in the case of b = 0.03 m. It is shown that the peak of power spectrum of parallel refractive index N_z is varied over the range from 2 to 7 corresponding to the variation in the phase difference $\Delta\phi$.

3.2 Lower hybrid RF heating system

In the summer of 1976, final work was begun on a RF heating system

to be used for lower hybrid heating experiment of JFT-2 tokamak. Study of lower hybrid wave propagation in a JFT-2 plasma and available high power RF sources in the UHF ranges led to the selection of 650 MHz as the optimum frequency. We could operate this system at the frequency of 750 MHz for a tokamak with a higher electron density. Summary of technical specifications is shown in Table IV.3.2-1.

Fabrication of the 650 MHz system and the preparation of experiments to attempt plasma heating by radio frequency power were important activities in 1976 and early 1977. Experiments will be started in the autumn of 1977 with 200 kW, 650 MHz source, to examine heating near the lower hybrid resonance.

3.2.1 RF system

A simple block diagram of the RF system is shown in Fig. IV.3.2-1. It shows a signal source which is a coaxial-line solid state exciter and a solid state power amplifier capable of a 80 W output. After a PIN modulator, signal is divided four ways by three hybrid power splitters and fed to each of four legs to provide the adjustments necessary for a set of four waveguides array in the output stage of this system.

The main part of the RF system is an E 3765 klystron amplifier. This tube is a 5 cavity, electromagnetically focused klystron, a modification of UHF TV klystron specifically designed for this project by Tokyo Shibaura Electric Co., Ltd. This tube is rated at approximately 60 kW of RF output. Four klystrons are utilized in this system and installed inside the high power amplifier cabinets.

The mode of operation would be to gate the beam current on and off by switching beam voltage with two vacuum contactors and inject the RF drive pulse within the pulse as shown in Fig. IV.3.2-2.

3.2.2 Control system

This system consists of four control cabinets. The first two of them are for control of four klystrons on the first floor. This control pertains to the application of high voltage and lower level voltages. It also includes fault sensing. The second two cabinets are for the operation and RF controls and placed in the JFT-2 control room on the 2nd floor. These include monitoring of relevant functions, proper sequence of events, interlock system for protection of personnel and equipment, status

indication, high voltage metering, on-off and raise and/or lower control for remote operation.

3.2.3 Coolant system

The cooling system is to be used for klystrons. Flow rate of the cooling water is 40 ℓ/min.

3.2.4 Transmission system

The transmission system is composed of 77 mm - 50 ohms (WX-77D) rigid coaxial lines and non-standard 95 mm × 340 mm rectangular waveguide.

3.2.5 Coupling system

A phased waveguide array (the Grill) has been selected for the coupling system employed on JFT-2. It is the most advanced theoretically and experimentally[6][7]. The launcher is shown in Fig. IV.3.2-3. It consists of four E-plane parallel waveguides adjacent to one another and positioned so that E is parallel to B_t in JFT-2. The size of each open waveguide is 14 mm × 340 mm. In front of the coupler molybdenum plate shutter is installed to protect the surface of a vacuum window inside the waveguide from metal sputtering on it. The distance between plasma edge and waveguide launcher is variable up to 100 mm by moving the whole coupling system.

In order to reduce the possibility of RF breakdown in the waveguide feed section and separate the high power klystron feed section from the launcher, two kinds of ceramic dielectric vacuum window (Al_2O_3) are to be placed and tested, as shown in Fig. IV.3.2-3 (vacuum seal 1 and 2) between the high power klystron and the launcher. To assure adequate reduction of pressure within the waveguide pumping will be done through holes in the waveguide sectors. A manifold will be built for the pumping system.

3.3 Design study of RF heating system for JT-60

We have a program to develop a high power 1 MW-10 sec klystron at 1∿2 GHz for LHRH in JT-60. The conceptual design of 1 MW-10 sec klystron at 1.2 GHz and the survey of technological requirements for the JT-60 RF heating system have been made by Nippon Electric Co., Ltd. under the contact with JAERI. Table IV.3.3-1 shows the electrical specifications of

the high power klystron.

References

(1) Stix, T.H.: Phys. Rev. Lett. 15 (1965) 878.

(2) Golant, V.E.: Soviet Phys. Tech. Phys. 16 (1972) 1980.

(3) Pesic, S.S.: Plasma Phys. 15 (1973) 193.

(4) Bellan, P.M., Porkolab, M.: Phys. Fluids 19 (1976) 995.

(5) Imai, T., Nagashima, T. and Azumi, M.: Numerical Studies of Lower Hybrid Wave Propagation in JFT-2, JAERI-M 6902, (February 1977), 39 pp. (in Japanese).

(6) Brambilla, M.: Nuclear Fusion 16 (1976) 47.

(7) Bernabei, S., Heald, M.A., Hooke, W.M. and Paoloni, F.J.: Phys. Rev. Lett. 34 (1975) 866.

Table IV.3.2-1 Summary of JFT-2 lower hybrid heating system.

RF Source	
Frequency	650 MHz
RF power output	200 kW
Pulse width	1 msec 100 msec
Pulse repetition frequency	1 pulse/2 min
Power droop during pulse	5 %
Coupling System	
A phased array of four waveguides	

Table IV.3.3-1 Summary of electrical specification of 1 MW-10 sec klystron.

Electrical	
Body voltage	80 kVdc
Collector voltage	80 kVdc
Anode voltage	80 kVdc
Cathode current	27.15 Adc
Body current	500 mAdc
Anode current	10 mAdc
DC input	2172 kW
Perveance	1.2×10^{6} A/V$^{3/2}$
Typical Operation	
Frequency	1200 MHz
Driving power	50 W
Saturated output power	1100 kW
Band width (instantaneous -3 dB)	80 MHz
Power gain	43.4 dB
Efficiency	50.6 %

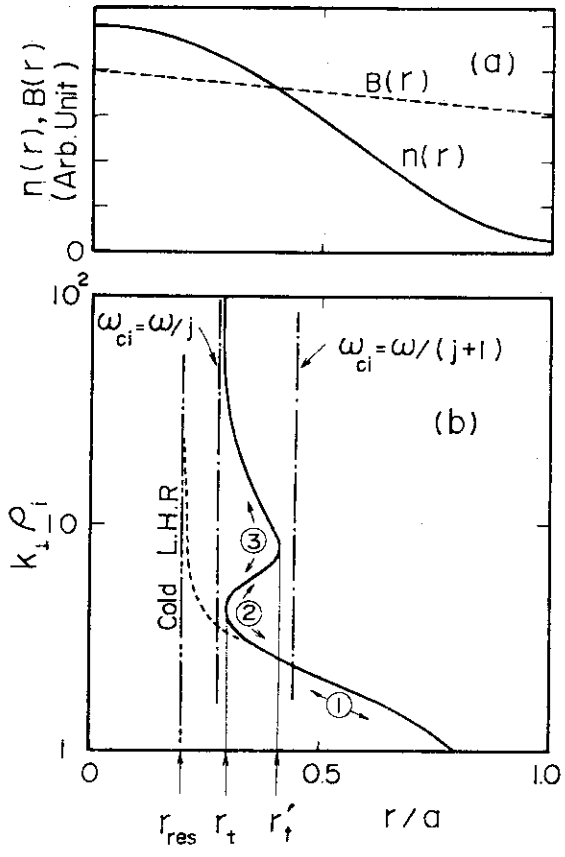

Fig.IV.3.1-1 (a) Radial distributions of density n(r) and external magnetic field B(r), and (b) schematic representation of wave number during the penetration in an inhomogeneous plasma.

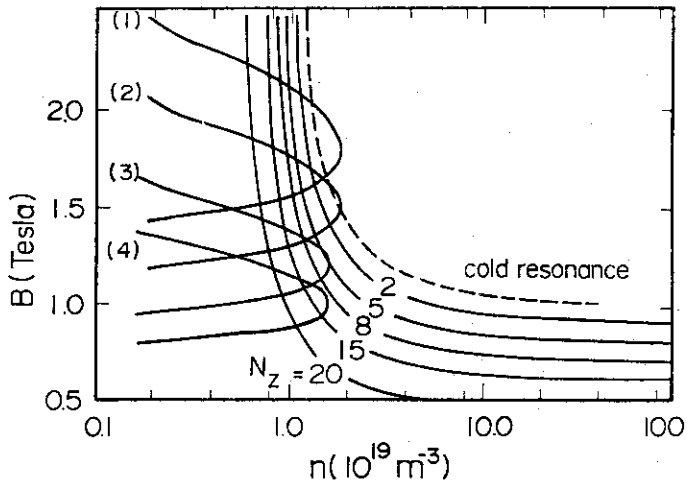

Fig.IV.3.1-2 Parametric dependence of turning point (full line and cold lower hybrid resonance (dashed line), (1)∿(4) indicate the density profiles. Input frequency is f=650 MHz and ion temperature T_i=0.25 keV.

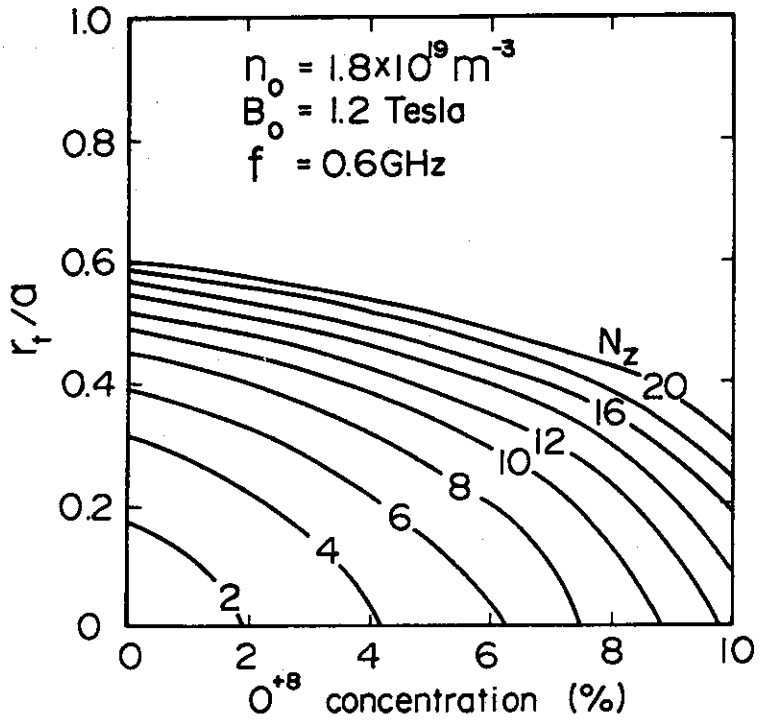

Fig.IV.3.1-3 Dependence of the position of turning point on impurity concentration. Ion temperature at the center T_{i0}=0.25 keV and a is the plasma radius.

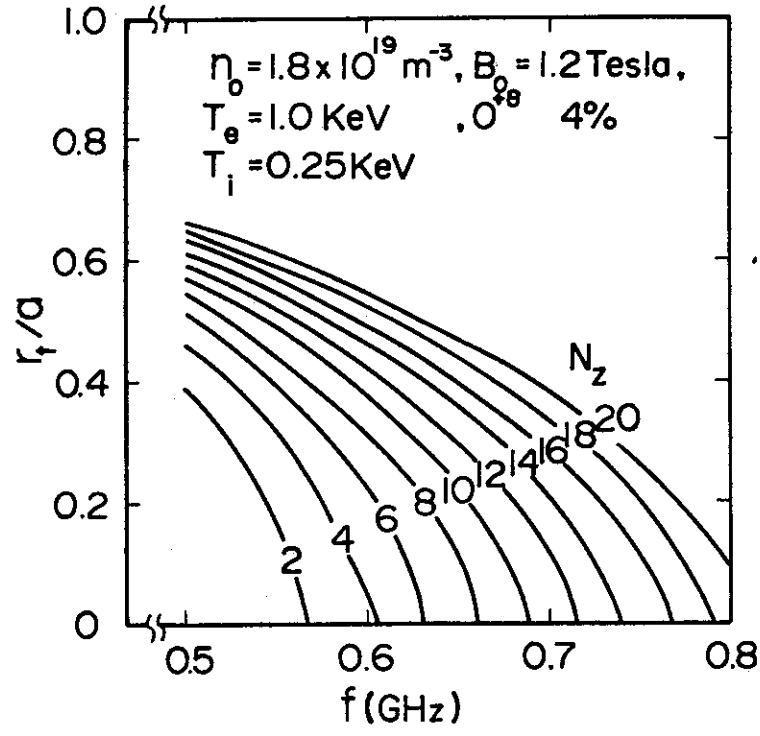

Fig.IV.3.1-4 Dependence of the position of turning point on input frequency.

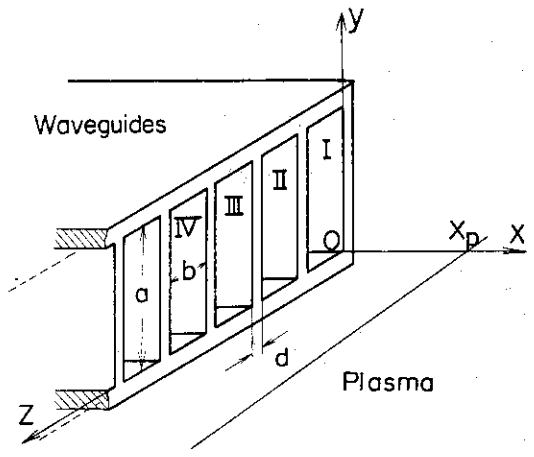

Fig.IV.3.1-5 Sketch of phased multi-waveguide array. Plasma region is $x \geq x_p$. Electric field of TE_{01} mode is in z direction.

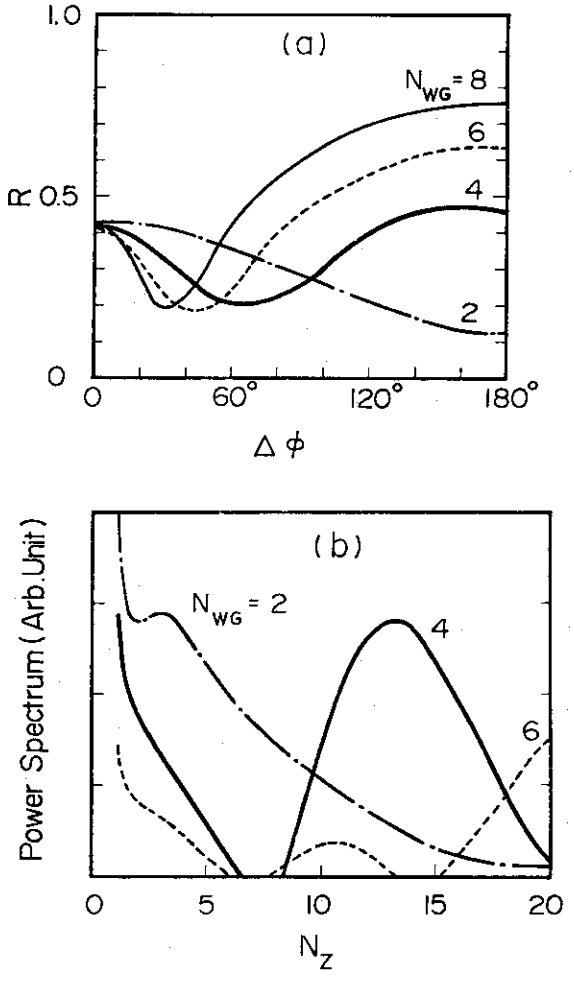

Fig.IV.3.1-6 (a) Reflection coefficient R vs phase difference $\Delta\phi$ between adjacent waveguides with the restriction of the total width of 0.064 m, $d \simeq 0.002$ m, $f = 650$ MHz, $x_p = 0$ and $\partial n/\partial x = 10^{20}$ m^{-4}. N_{WG} is the number of waveguides.

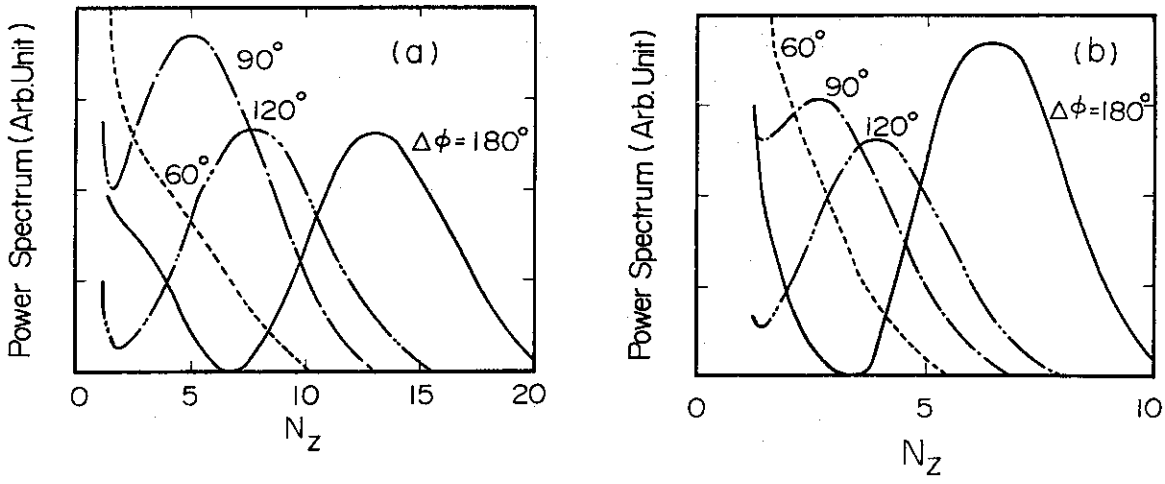

Fig.IV.3.1-7 (a) Power spectra for $N_{WG} = 4$, b = 0.014 m and f = 650 MHz in the case of $\Delta\phi = 60°$, 90°, 120°, 180°.
(b) Power spectra for b = 0.03 m. The others are similar to those of (a).

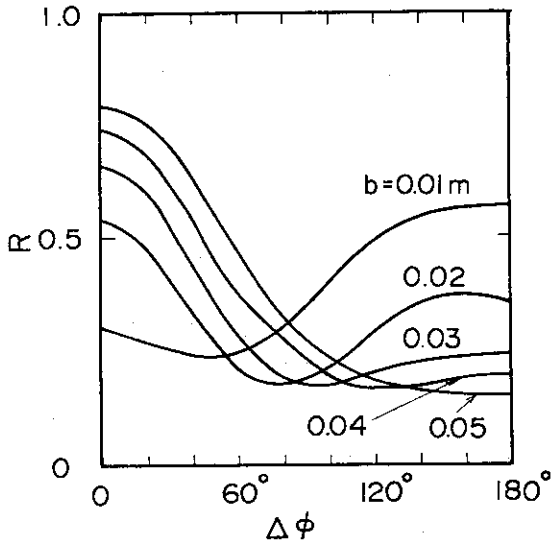

Fig.IV.3.1.8 Reflection coefficient R vs phase difference for $N_{WG} = 4$. The width of waveguide is varied from 0.01 m to 0.05 m. The other parameters are similar to those in Fig. IV.3.1-7.

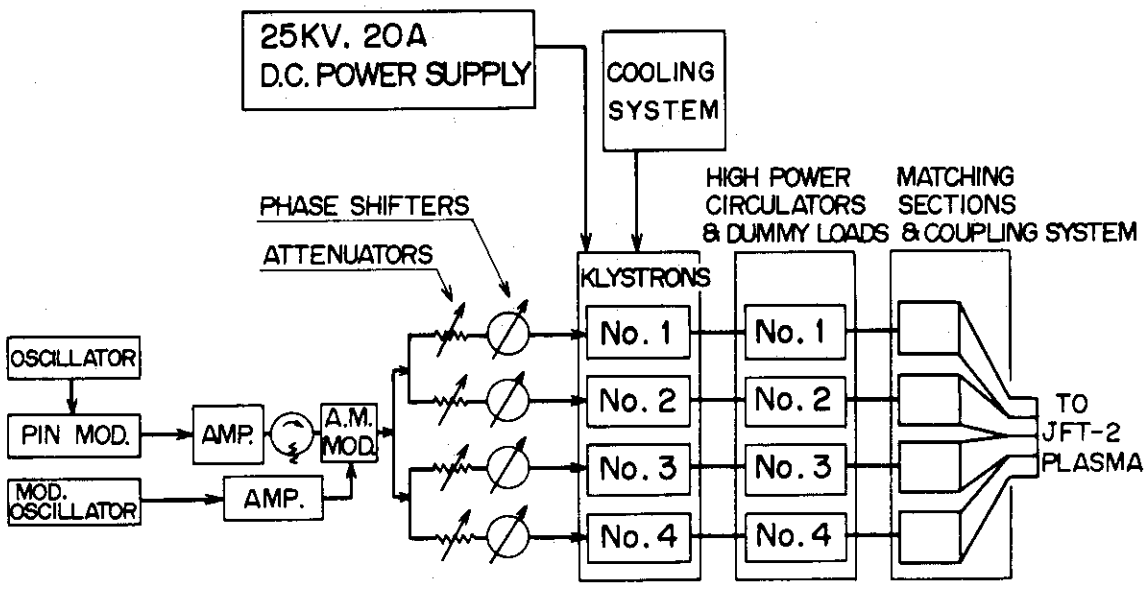

Fig.IV.3.2.1 Simple block diagram of lower hybrid heating system for JFT-2.

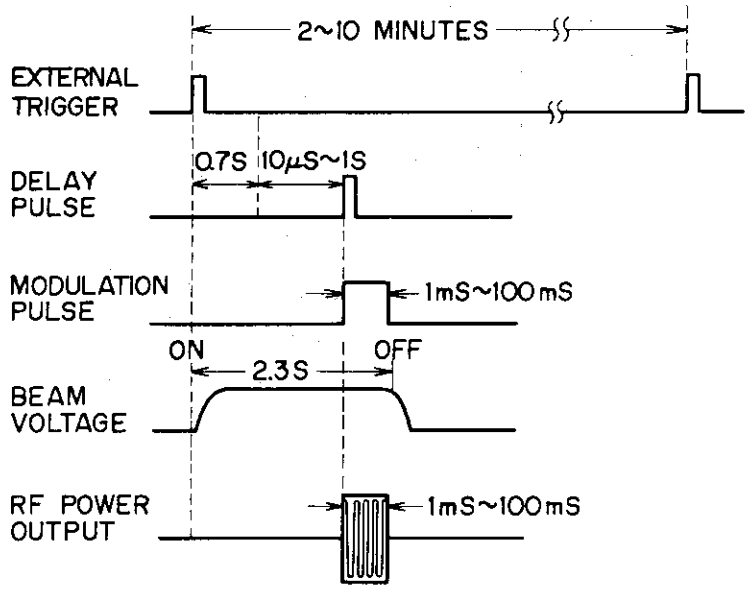

Fig.IV.3.2-2 Time sequence of JFT-2 lower hybrid heating system

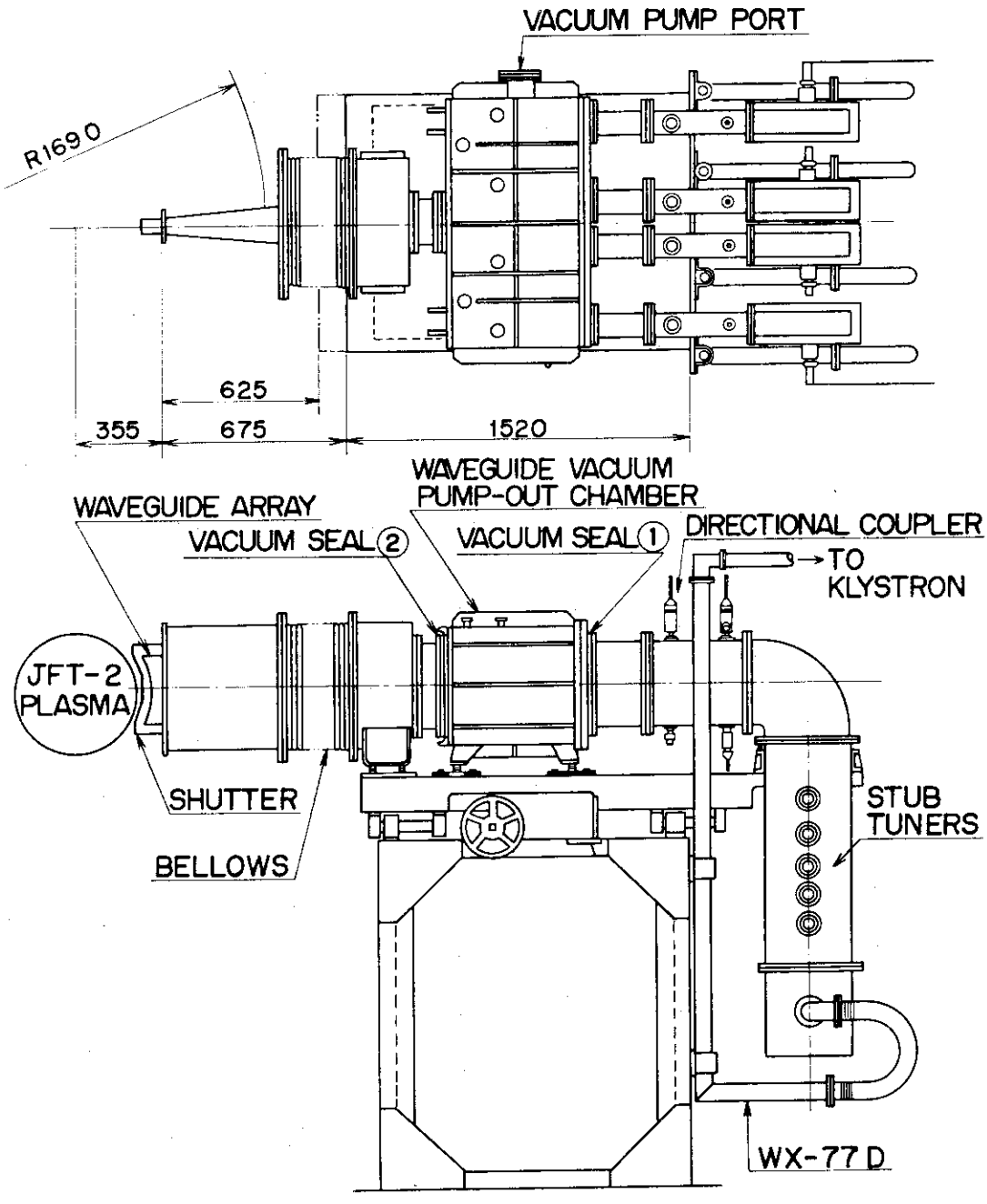

Fig.IV.3.2-3 Waveguide coupler for LHRH heating.

V. SURFACE SCIENCE AND VACUUM TECHNOLOGY

1. Introduction

Impurities entering the plasma from the walls of experimental tokamaks strongly influence plasma behavior and are a major problem for both present and future machines. Impurity atoms are mainly released from the first wall which is bombarded by energetic particles leaking from tokamak plasma through complicated processes including sputtering, blistering, local evaporation, chemical reaction, and desorption of adsorbed and occluded gases. On the other hand, particle-surface interactions such as backscattering, trapping, and reemission or desorption of trapped particles are also great concerns for the investigation of the recycling in plasma-wall systems.

The objective of the particle-surface interaction program in Division of Thermonuclear Fusion Research, JAERI, is to study the individual effects in plasma-wall interaciton. This program was started in April, 1975, and the main effort was directed to the design and construction of the experimental facility in FY 1975[1],[2]. In the following FY 1976, experiments were started by using a low energy sputtering testing accelerator (LSP) and a high energy sputtering testing accelerator (HSP). The sputtering yield of molybdenum and pyrolytic graphite bombarded by low energy protons was measured as a function of incident proton energy[3]. The chemical reaction rate of pyrolytic graphite with protons was measured at various temperatures[3]. The usefulness of a honeycomb structure which was proposed as a simple means of reducing the number of sputtered particles was also tested in an argon glow discharge[4],[5]. In the HSP experiments, observation was made on detailed processes of surface erosion in pyrolytic graphite bombarded with 100 keV He^+ and 200 keV H_2^+ ions[6]. On the other hand, a new type of surface damage "grain ejection" was found on molybdenum surface by using an intense hydrogen beam from a duoPIGatron source[7].

Late in FY 1976, one of the staff members began to study vacuum pumping and wall cleaning problems which are important to the design and manufacture of the actual machine and which are also very much concerned with the particle-surface interaction. Some of these are in progress or planned for the next few years.

2. Interaction of Energetic Particles with Wall Materials

2.1 Experimental facility

The two experimental apparatus, LSP and HSP, were designed and manufactured in FY 1975, and have been installed in JAERI in FY 1976.

The low energy sputtering testing accelerator (LSP) has several features to enable the measurement of a low level sputtering yield or a small amount of gas evolution from the target being bombarded[1],[8]. In this apparatus, a proton beam with energy ranging from 100 eV to 6 keV extracted from a duoplasmatron is finally focused on a target which is held at the ground potential. In order to avoid the beam spread caused by the space charge effect, the proton beam is transported with energies between 1 keV and 12 keV from the ion source to the final electrode which is located in front of the target (see Fig. V.2-1). Focusing of proton beam to the orifice S2 is made by a cylindrical lens (EL2, EL3) and to the point I by a magnetic sector type mass analyzer. Mass separation is indispensable since the sputtering yields for H_1^+ and H_2^+ differ approximately by a factor of 2, and furthermore, heavier impurity ions would cause serious errors. The focusing in and vertical to the median plane is attained by the sector magnet and the two-dimensional lenses (EL5-9). The ion beam is then transported through two stages of cylindrical lenses (EL10-12, EL14-16) and a diaphragm lens (EL16, 17) to the target. The electrode EL17 is kept at the ground potential. The ion beam transport system was designed by computer simulation. The energy spread measured at the target is 28 eV at half peak height with proton energy of 500 eV. When proton energies are 6 keV and 100 eV, the spot sizes on the target are 1 mm and 8 mm in diameter, respectively. A typical mass spectrum of the ions produced in the duoplasmatron is shown in Fig. V.2-2. Protons can be perfectly separated from other molecular ions.

One of the most important problems in these kinds of experimental apparatus is to maintain surface cleanliness of the targets. Especially, adsorption of residual gases on the target to be examined must be minimized during the measurement. It leads to a criterion of a partial pressure of 10^{-10} Torr for residual impurity gases. On the other hand, both the proton beam current and its density as large as possible are required to achieve reliable experiments. From these considerations, the vacuum system is built bakable including the ion source and target chamber, and oil-free uhv differential pumping systems are equipped. Three pumping

lines consist of a turbomolecular pump (250 ℓ/sec), two sputter ion pumps (128 ℓ/sec), two pool type cryopumps (1,000 ℓ/sec) and auxiliary mechanical pumps. An ultimate pressure of 5×10^{-9} Torr or lower is attained in the target chamber after a mild bake-out at around 150°C. Total pressure up to middle 10^{-7} Torr range is recorded during the proton bombardment. However, more than 99 % of the total pressure is due to hydrogen which does not mean any obstacles in most of the experiments.

Other instruments include two sets of manipulators with a vacuum lock, an Auger electron spectrometer (AES), an electro-microbalance, a quadrupole mass spectrometer and their calibration systems. These were described in the previous report of this series with the experimental procedures[2].

The high energy sputtering testing accelerator (HSP) is a 400 kV Cockcroft-Walton accelerator, which is designed to investigate in detail processes leading to surface erosion. The ion species can be selected from a wide range of gaseous and solid elements. A mass analyzing section with a 90° double focusing magnet is provided between an extraction electrode and an acceleration tube where masses from 1 to 260 amu are analyzed with mass resolution of 500. Ion beam energy and current to the target surface are 50-400 keV and 10-100 μA, respectively. The ion beam whose spot size is 5-7 mm in diameter is scanned by two sets of electrostatic deflection plates, if necessary. The beam transport line and target chamber are evacuated with an oil-free differential pumping system consisting of three turbomolecular pumps (200 and 400 ℓ/sec) and a sputter ion pump (400 ℓ/sec). An ultimate pressure of 5×10^{-8} Torr is attained in the target chamber. The temperature of the target can be continuously varied from room temperature to 800°C.

One of the features of HSP is to produce different ion species from H^+ to heavy metal ions by using an electron bombardment type ion source with a high temperature oven. This type was originally developed by Sidenius[9] and was improved in Danfysik Co. and High Voltage Co. as shown in Fig. V.2-3(a). However, it was difficult to obtain the ion beam of refractory metals such as Mo, Nb and V at a considerable rate. This is because the vaporization temperature of Mo and Nb is too high and the vapor pressure of V at its melting point is too low to obtain a sufficient vapor density of these elements in the discharge space. This implies that these refractory metals should be placed close to the discharge space and directly heated. In this fiscal year the effort has been directed to

the increment of the ion beam current. After some experiments in co-operation with Nissin-High Voltage Co., the ion source has been modified to use a molybdenum or niobium filament as a vapor and electron emitter and to ream the orifice of the outlet plate from 0.5 mm to 1.2 mm in diameter (see Fig. V.2-3(b)). This results in the extraction of an ion current of 3-6 μA with a life time of 1-3 hrs. In case of V, on the other hand, an ion current of about 2 μA has been obtained by inserting a small piece of vanadium in the tungsten coil (see Fig. V.2-3(c)).

2.2 Sputtering by hydrogen

Late in 1976, the sputtering yields of molybdenum and pyrolytic graphite were measured by using LSP[3]. Sputtered atoms from the target were received on a tungsten substrate surface located apart 20 mm from the target. After an appropriate duration of accumulation, the target was drawn back downward and the substrate was carried in front of the AES. The coverage of deposited molybdenum layer on the substrate was analyzed by the AES, and the sputtering yield was estimated from the calibration curve obtained by an electro-microbalance experiment carried out in advance. Figure V.2-4 shows the proton sputtering yield of polycrystalline molybdenum as a function of incident energy. The measured sputtering yield at above 1 keV is about three times larger than the values obtained by Finfgeld[10]. In the energy range below 1 keV, the yield decreases rapidly with decreasing energy and it reaches a low value of 1.9×10^{-4} atoms/ion at 150 eV. Although this energy range is most important in the plasma-wall interaction study, there had been no experimental data reported before.

The same technique was adopted to measure the sputtering yield for pyrolytic graphite by proton bombardment. The graphite samples were supplied by Nippon Carbon Co., whose density was 2.23 g/cm^3. Figure V.2-5 shows the measured sputtering yield of the pyrolytic graphite as a function of incident energy. The result has yet some ambiguities caused by, for example, inevitable residual carbon deposition, although the effect was minimized by heating the substrate, and zero drift of the microbalance during the course of a long time measurement. In spite of the error bars in the figure, it is worth-while to mention that this will be the first result of the physical sputtering yield in which the effect of chemical sputtering is excluded. The figure indicates that the yield is about an

order of magnitude larger than that of molybdenum. On the other hand, the present result shows an energy dependence which is different from that of the calculated values from the transport theory of Weissmann and Sigmund[11]. The energy dependence of the theoretical yield shows a monotonical decrease with increasing energy above 150 eV, whereas the experimental yield shows a monotonical increase with increasing energy up to 3 keV.

In addition to the experiments of proton physical sputtering, the chemical sputtering of pyrolytic graphite, which is due to the chemical reaction of hydrogen with graphite, was investigated under 1 keV proton bombardment. The temperature of the target was varied from 300 to 1,000 K. Methane molecules released from the target were accumulated in a hemispherical volume of 30 mm in diameter and measured by the quadrupole mass spectrometer equipped with an enclosed ion source. Methane generation was evidently observed. The temperature dependence of the chemical sputtering yield showed a maximum yield of about 0.1 molecules/ion at around 800 K as shown in Fig. V.2-6. Open and closed circles in the figure indicate the yields obtained in the heating and cooling processes of temperature, respectively. This result agrees well with that of Feinberg and Post[12], as shown with dashed bars in the fiture.

A honeycomb wall design was proposed as a simple means of reducing the number of sputtered particles which enter the plasma. A preliminary evaluation of the feasibility of such a honeycomb wall concept was pefformed theoretically by Cramer and Oblow for cylindrical cells[13] and by Yoshikawa for rectangular cells[14]. In order to make sure of the concept experimentally, a measurement has been made on the ratios of the sputtering yield of molybdenum honeycomb walls to that of a flat wall[4],[5]. The weight losses of the two targets were compared after the bombardment of argon ions in a d.c. diode sputtering system. In this experimental arrangement, the mean energy of the incident ions was found to be about 1 keV and its angle of incidence was distributed around normal. Figure V.2-7 shows the sputtering ratio of the honeycomb wall with rectangular cells (see Fig. V.2-8) to the flat wall as a function of the depth-to-width ratio (L/D) of the cells. It is clear that the sputtering ratio decreases drastically with increasing depth-to-width ratio and reaches an asymptotic value of 1/20-1/30 when L/D = 1 or larger.

2.3 Blistering and grain ejection by helium and hydrogen

It is well known that implantation of gaseous ions into wall materials to high fluence can result in surface erosion. Surface erosion in graphite targets by energetic helium bombardment was reported by several authors. Flaking was observed on graphite fibers after bombardment with 100 keV helium ions at a dose of 3.1×10^{18} ions/cm^2[15]. Many spheroidal blisters were seen on a low density carbon target irradiated with 0.6 MeV helium ions to a fluence of about 10^{19} ions/cm^2[16]. Surface deformation like blistering was observed on a graphite cloth target exposed in a 580 eV helium ion beam to a fluence of about 10^{20} ions/cm^2[12].

Recently in JAERI, surface erosion in pyrolytic graphite has been investigated under 100 keV He^+ and 200 keV H_2^+ (equivalent to two 100 keV H^+) bombardment by using HSP[6]. The graphite samples were supplied by Nippon Carbon Co. Prior to bombardment, the target samples were mechanically polished by buffing. Then they were irradiated by ion beams with a current density of 20-50 μA/cm^2 at room temperature. The fluence of helium ions ranged from 1×10^{17} to 5×10^{18} ions/cm^2 and that of molecular hydrogen ions from 5×10^{16} to 2.5×10^{18} ions/cm^2. The beam hit the target at normal incidence. The irradiated surfaces were observed by a scanning electron microscope.

In case of helium bombardment, many ridges are formed at a fluence of 1×10^{17} ions/cm^2. The surface is significantly eroded after the bombardment to a fluence exceeding 5×10^{17} ions/cm^2 (Photo. V.2-1(a)). Flaking of the first cover begins to occur at a critical fluence of 1×10^{18} ions/cm^2 (Photo. V.2-1(b)) and a cone structure appears after the first cover flakes off completely (Photo. V.2-1(c)). From a surface micrograph taken at the edge of the bombarded area (not shown), it seems that the cones stand out from the unbombarded surface level, which suggests that they are filled with pressurized helium gas. In case of hydrogen bombardment, on the other hand, no drastic surface deformation occurs up to a dose of 2.5×10^{17} ions/cm^2. But blisters begin to occur at a fluence of a little bit lower than 5×10^{17} ions/cm^2 and many circular blisters are seen at 5×10^{17} ions/cm^2 (Photo. V.2-2(a)). By continuing the bombardment up to 2.5×10^{18} ions/cm^2, the blister covers are sputtered off completely, whose remains are clearly seen in Photo. V.2-2(b).

In this connection, structural changes of the eroded surfaces have been observed after six months from ion bombardment[17]. As seen in Photo. V.2-3(a), the cones once produced by helium bombardment are partly

destroyed. This kind of destruction may be due to the burst of the accumulated gas. A large number of cracks are also observed in the whole bombarded area (Photo. V.2-3(b)). Since the fracture strength of pyrolytic graphite is approximately 3,500 kg/cm^2, the gas pressure in the cones would be nearly equal to this value. On hydrogen bombarded surfaces, the blisters seem to have sunk from the initial level in six months after bombardment (Photo. V.2-3(c)). It is a serious problem that surface erosion advances by mechanical fatigue with the time elapsed.

Recently, a new type of surface damage "GRAIN EJECTION" was found especially near the temperature of 200°C on the surface of molybdenum after the bombardment of intense hydrogen ion beam[17]. Intense ion beam was supplied by duoPIGatron ion source in the injection test stand ITS-1 in JAERI[18]. Pulsed ion beam irradiated at the energy of 25 keV with the dose rate of 30 mA/cm^2 for 100 msec with the duty cycle of 9 %. Experiments were performed with the doses from 1 C/cm^2 to 20 C/cm^2. Major compositions of the typical ion beam were 50 % H^+, 40 % H_2^+ and 10 % H_3^+. The dominant impurities were oxygen and its hydrides whose amount was about 2 %[19]. Base pressure in a stainless steel vacuum chamber, which was evacuated by diffusion pumps with 2000 ℓ/sec pumping speed, was 1×10^{-6} Torr. Target temperature ranged from room temperature to 500°C. The molybdenum used in this study was 99.9 % purity obtained by the process of powder metallurgy. The specimens were annealed for one hour at 1400°C in a vacuum lower than 1×10^{-7} Torr and had an average grain size of 25 μm after the heat treatment. Before the bombardment, they were mechanically polished and also electrolytically polished by the solution of 30 % H_2SO_4 in methanol and had a surface roughness within 1 μm. The radiation damage was observed by sanning electron microscope (SEM) and microstylus techniques.

Within the temperature range from 150°C to 250°C, the surface was significantly ravaged after the bombardment of the fluence exceeding 3 C/cm^2 (Photo. V.2-4(a) and (b)). One can see this signs of ravage and havoc with the unaided eyes. On the surface, there were numerous craters with a diameter of some tens of micrometers and a depth of a few tens of micrometers which were believed to be traces of "GRAIN EJECTION" and the numerous bending ups of the surface layer which were believed to be the portents of "GRAIN EJECTION". The size of craters was within 200 μm in diameter and within 30 μm in depth fathomed by means of microstylus techniques (Fig. V.2-9). The extent of damages increased with the amount

of fluence within a dose of 20 C/cm^2. At the temperatures except for above range, no grain ejection was observed.

Grain ejection is a new type of the surface damage which is quite different from blister. The thickness of the covers of blisters is approximately equal to the mean projected range[20], in our experiment, which is estimated to be only 10^3 Å. The crater of grain ejection is approximately equal to grain size of 30 μm. One can explain the temperature dependence of grain ejection in consideration of hydrogen diffusion in molybdenum. At room temperature, implanted hydrogen atom can not diffuse to the grain boundary for their low diffusivity. On the other hand, they can easily diffuse to the grain boundary at higher temperature. But they don't accumulate at the temperatures of 250°C for their high diffusivity and rapidly release from the molybdenum surface. Optimum temperature for hydrogen atom to accumulate in molybdenum will be from 150°C to 250°C. For example, at the temperature of 200°C hydrogen concentration near the grain boundary provides the gas bubble to its pressure exceeding the yield stress of molybdenum.

3. Vacuum Science and Technology for Fusion Devices

Thermonuclear fusion devices impose unique vacuum pumping problems involving extreme cleanliness requirements and very high pumping speeds[21]. It is worth noting that these problems are also very much concerned with the particle-surface interaction. Two principal pumping systems are required for a fusion device, a main pumping system for evacuating the torus and a vacuum system for removing unaccelerated hydrogen from neutral beam injectors.

The main vacuum system is that which removes impurities such as H_2O, CO and CH_4 from the torus between pulses as well as during discharge cleaning processes and maintains the first wall in the vacuum vessel as clean as possible. One crucial requirement to be imposed on this system is to get an information on the ultimate cleanness which can be expected on the first wall in the actual machine.

In neutral beam injectors, pumping of unaccelerated gas from the charge-exchange region of the beam and from the beam dump for deflected beams requires vacuum systems capable of handling large gas fluxes of hydrogen while maintaining pressures in the 10^{-4} to 10^{-6} Torr ranges. The most promising technique appears at present to be the cryopumping, but

special problems such as energetic particle and magnetic flux compatibility must be considered.

Vacuum pumping and cleaning studies in JAERI are to find an answer to the questions just mentioned, and some of which are in progress or planned for the next few years.

References

(1) Tsukakoshi, O. et al.: Experimental Apparatus to Investigate Interactions of Low Energy Ions with Solid Surfaces, JAERI-M 6331 (1975).

(2) Annual Report of the Division of Thermonuclear Fusion Research, JAERI, JAERI-M 6926 (1977) p.109.

(3) Sone, K. et al.: Sputtering Yields for 0.1-6 keV Protons Incident onto Molybdenum and Graphite Targets, Proc. Intern. Symp. Plasma Wall Interaction (Jülich, 1976) p.323.

(4) Abe, T. et al.: Reduction of Effective Sputtering Yield by Honeycomb Structure, to be published in J. Nucl. Sci. Technol.

(5) Obara, K., Abe, T. and Nakamura, H.: Sputtering Yield Measurement and Surface Observation of Molybdenum Honeycomb Walls, JAERI-M 7216 (1977).

(6) Sone, K. et al.: Graphite Surface Erosions by 100 keV Helium and Hydrogen Bombardment, J. Nucl. Materials, 71 (1977) 82.

(7) Nakamura, Y., Shibata, T. and Tanaka, M.: Grain Ejection from the Surface of the Polycrystalline Molybdenum Irradiated by Intense H^+ H_2^+ Ion beam, J. Nucl. Materials, 68 (1977) 253.

(8) Narusawa, T. et al.: An Experimental uhv Apparatus to Investigate Interactions of Low Energy Light Ions with Solid Surfaces, to be published in Proc. 7th Intern. Vac. Congr. & 3rd. Intern. Conf. Solid Surfaces (Vienna, 1977).

(9) Sidenius, G.: Proc. Intern. Conf. Ion Sources (Saclay, 1969).

(10) Finfgeld, C.R.: ORO-3557-15 (1975).

(11) Weissmann, R. and Sigmund, P.: Rad. Effects 19 (1973) 7.

(12) Feinberg, B. and Post, R.S.: J. Vac. Sci. Technol. 13 (1976) 443.

(13) Cramer, S.N. and Oblow, E.M.: ORNL-TM 4708 (1974); Nucl. Fusion 15 (1975) 339.

(14) Yoshikawa, M.: JAERI-M 5849 (1974).

(15) Ekern, R., Das, S.K. and Kaminsky, M.: Trans. 6th Symp. Engineering Problems of Fusion Research (San Diege, 1975).

(16) Rovner, L.H. and Chen, K.Y.: GA-A13812 (1976).

(17) Sone, K. et al.: Surface Erosions by Energetic Helium and Hydrogen Bombardment of Molybdenum and Pyrolytic Graphite, to be published in Proc. 7th Intern. Vac. Congr. & 3rd Intern. Conf. Solid Surfaces (Vienna, 1977).

(18) Matsuda, S., Itoh, T., Kondoh, U., Ohara, Y., Ohga, T., Shibata, T., Shirakata, H., Sugawara, T. and Tanaka, S.: JAERI-M 6431 (1976).

(19) Shibata, T., Itoh, T., Shirakata, H. and Sugawara, T.: JAERI-M 6990 (1977).

(20) Lindhard, J., Scharff, M. and Schøtt, H.E.: Mat. Fys. Medd. Dan. Div. Selsk. 33 No. 14 (1963).

(21) Murakami, Y.: internal memo (1977).

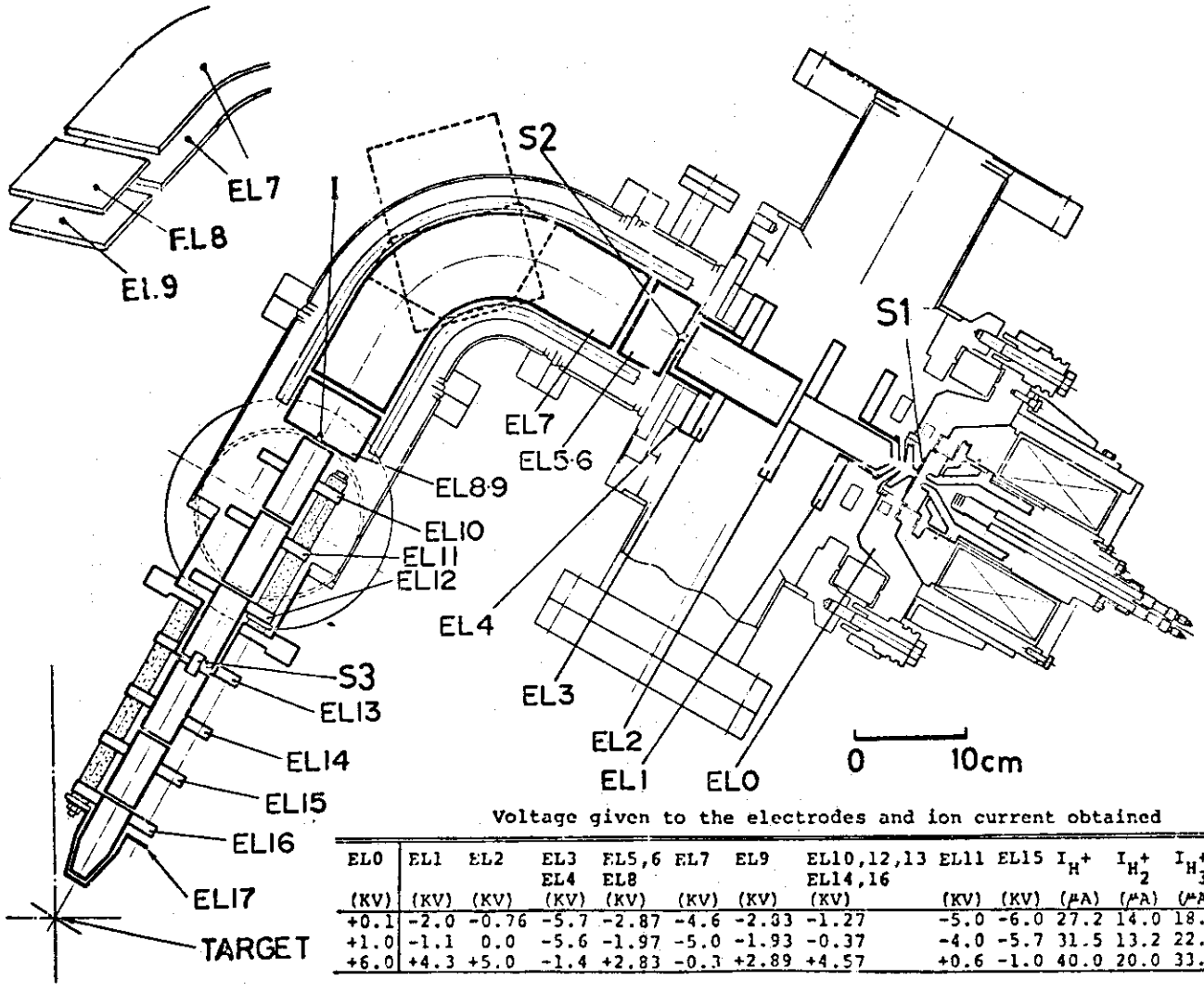

Voltage given to the electrodes and ion current obtained

EL0 (KV)	EL1 (KV)	EL2 (KV)	EL3 EL4 (KV)	EL5,6 EL8 (KV)	EL7 (KV)	EL9 (KV)	EL10,12,13 EL14,16 (KV)	EL11 (KV)	EL15 (KV)	I_{H^+} (μA)	$I_{H_2^+}$ (μA)	$I_{H_3^+}$ (μA)
+0.1	-2.0	-0.76	-5.7	-2.87	-4.6	-2.03	-1.27	-5.0	-6.0	27.2	14.0	18.4
+1.0	-1.1	0.0	-5.6	-1.97	-5.0	-1.93	-0.37	-4.0	-5.7	31.5	13.2	22.1
+6.0	+4.3	+5.0	-1.4	+2.83	-0.3	+2.89	+4.57	+0.6	-1.0	40.0	20.0	33.0

Fig.V.2-1 Duoplasmatron type ion source and beam transport system.

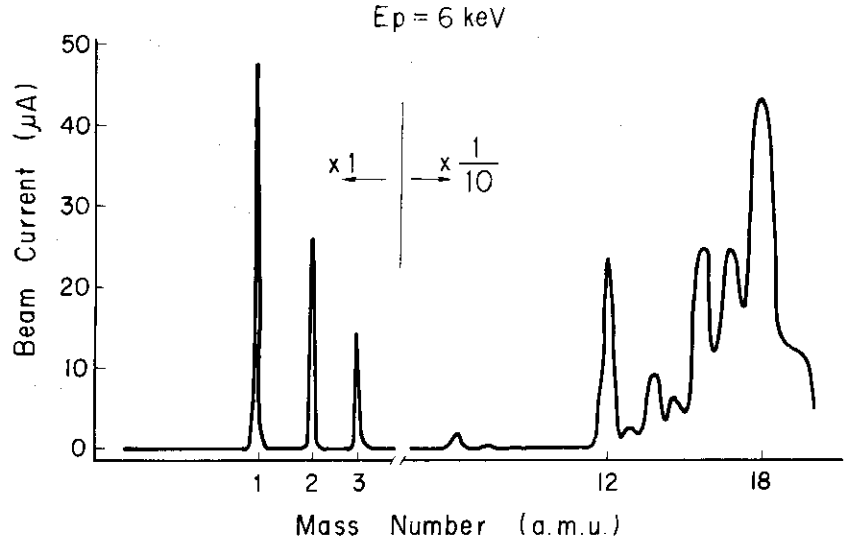

Fig.V.2-2 Typical mass spectrum of ions produced in the duoplasmatron source.

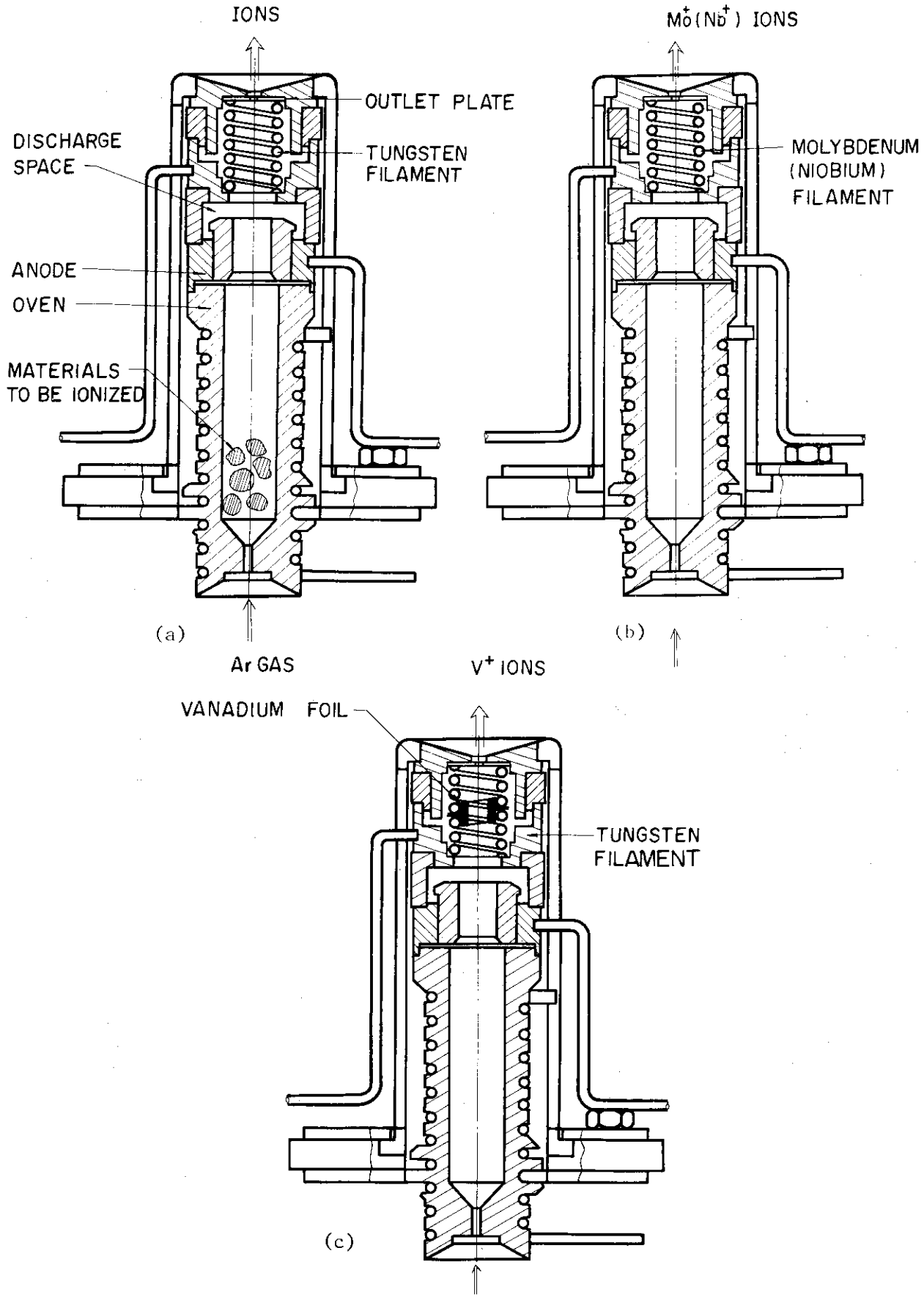

Fig.V.2-3 Electron bombardment type ion sources (a) original, and two modified versions (b) for Mo and Nb and (c) for V.

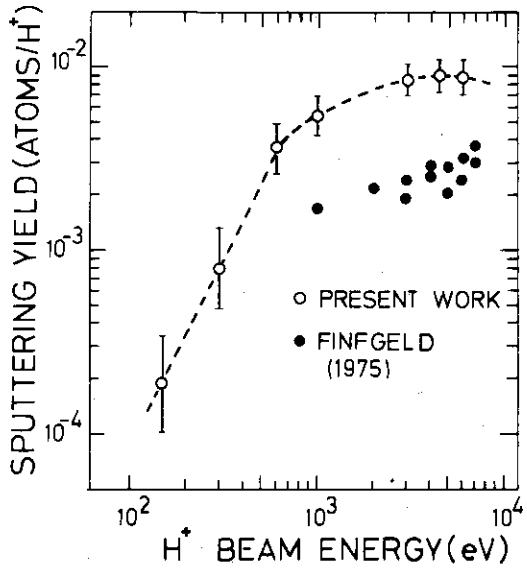

Fig.V.2-4 Proton sputtering yield of polycrystalline molybdenum as a function of incident energy.

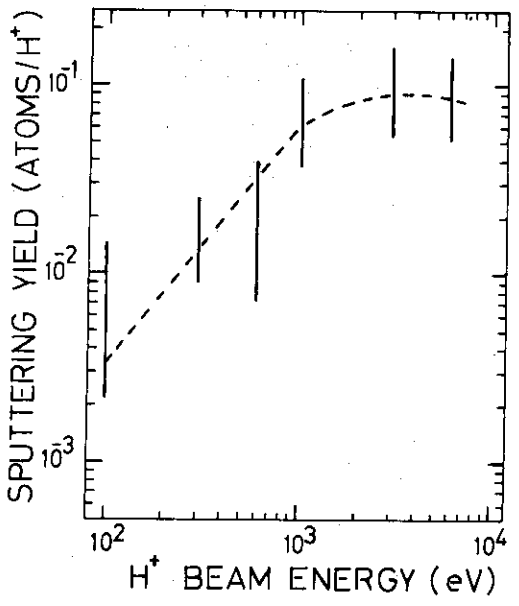

Fig.V.2-5 Proton sputtering yield of pyrolytic graphite as a function of incident energy.

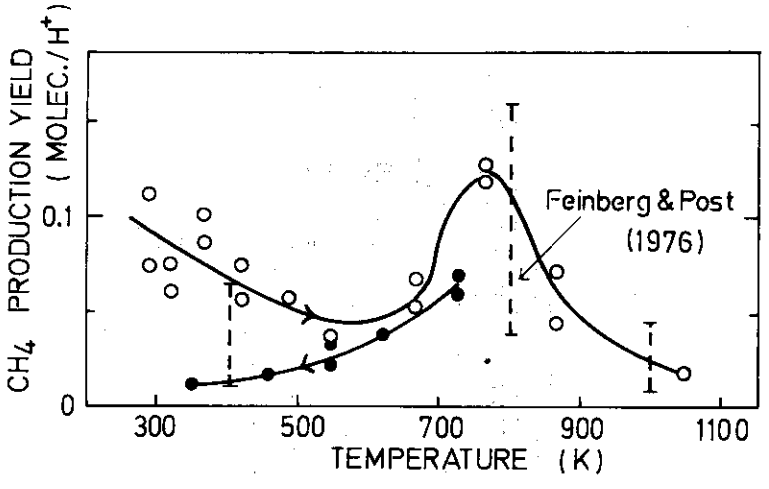

Fig.V.2-6 Temperature dependence of chemical sputtering yield of pyrolytic graphite.

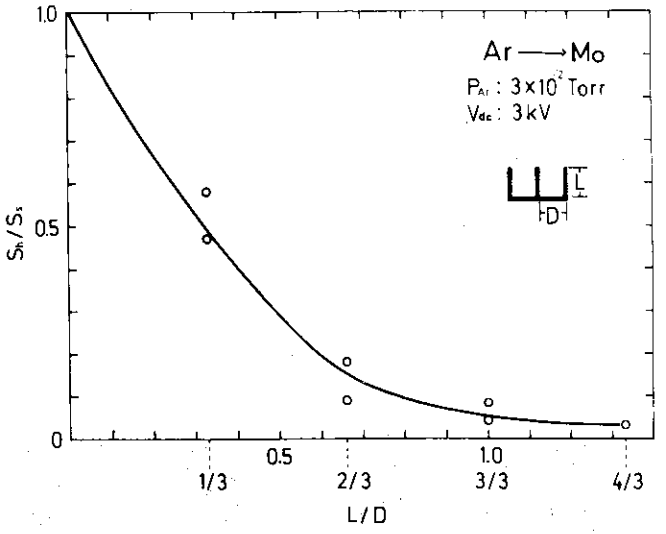

Fig.V.2-7 Sputtering ratio of honeycomb wall with rectangular cells to flat wall as a function of depth-to-width ratio (L/D) of the cells.

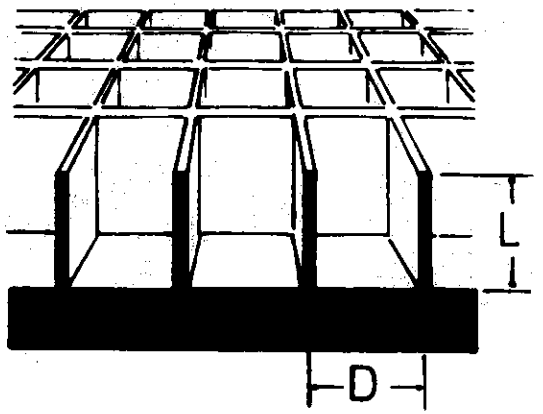

Fig.V.2-8 Honeycomb structure with rectangular cells.

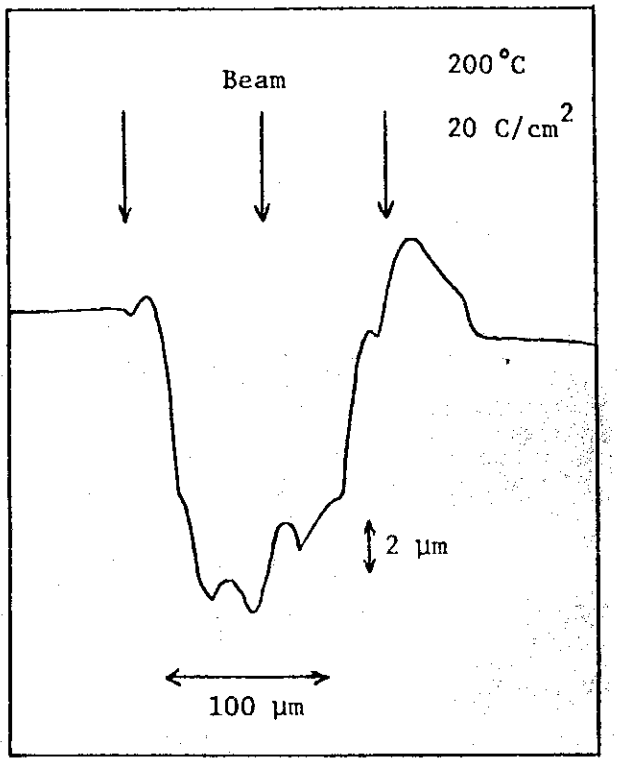

Fig.V.2-9 The roughness of plycrystalline molybdenum surface by means of microstylus techniques.

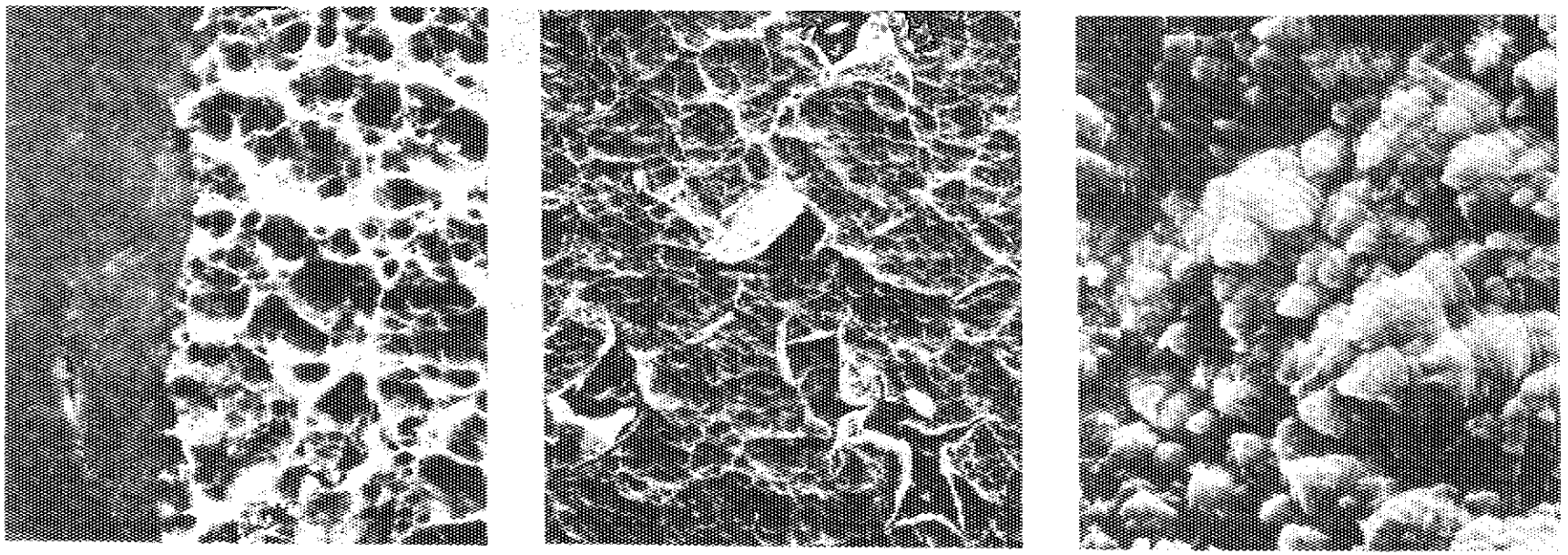

Photo V.2-1 Scanning electron micrographs of pyrolytic graphite surface bombarded with 100 keV He^+ ions
(a) 5×10^{17} ions/cm^2, (b) 1×10^{18} ions/cm^2,
(c) 5×10^{18} ions/cm^2.

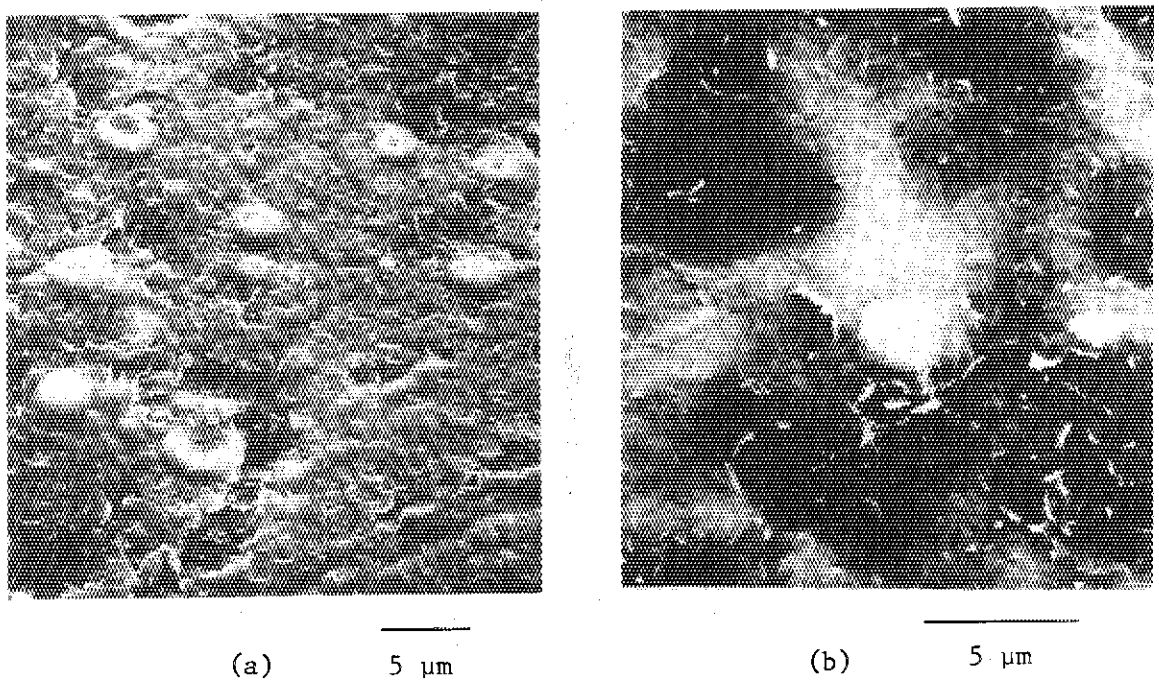

Photo V.2-2 Scanning electron micrographs of pyrolytic graphite surface bombarded with 200 keV H_2^+ ions (a) 5×10^{17} ions/cm^2, (b) 2.5×10^{18} ions/cm^2.

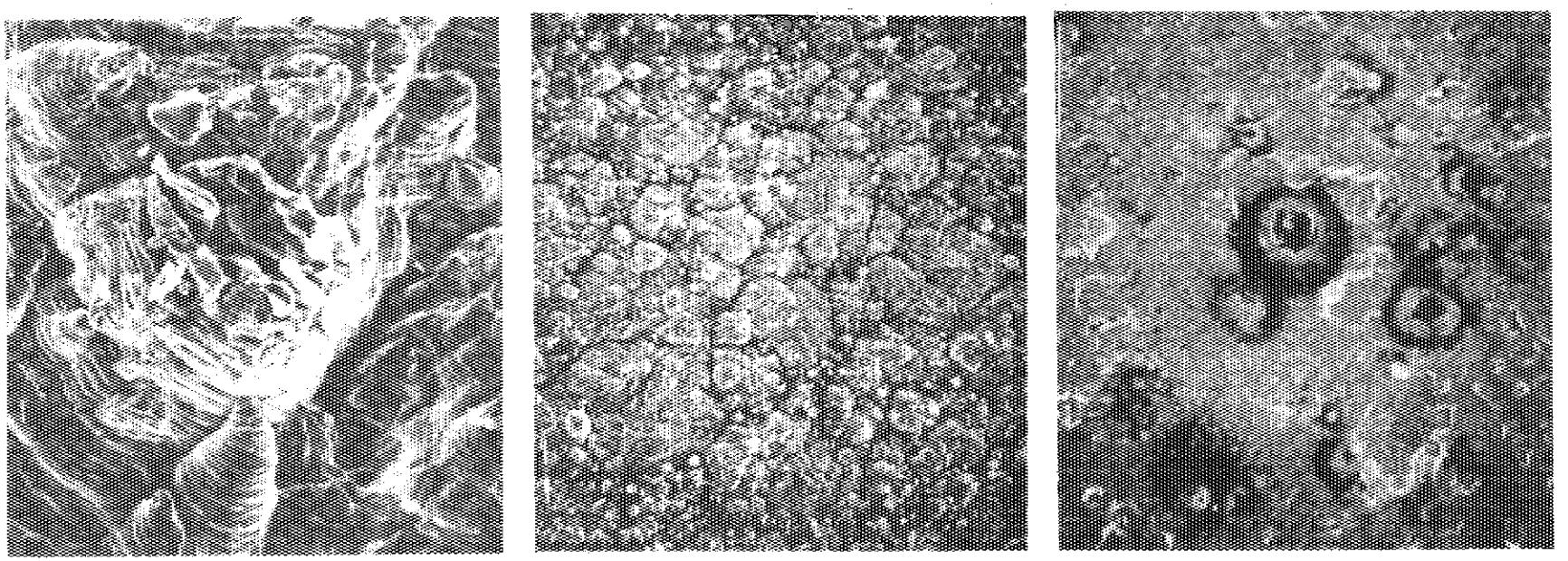

Photo V.2-3 Surface structures altered in six months after bombardment by mechanical fatigue
(a) and (b) 5×10^{18} ions/cm^2 (He), (c) 5×10^{17} ions/cm^2 (H_2).

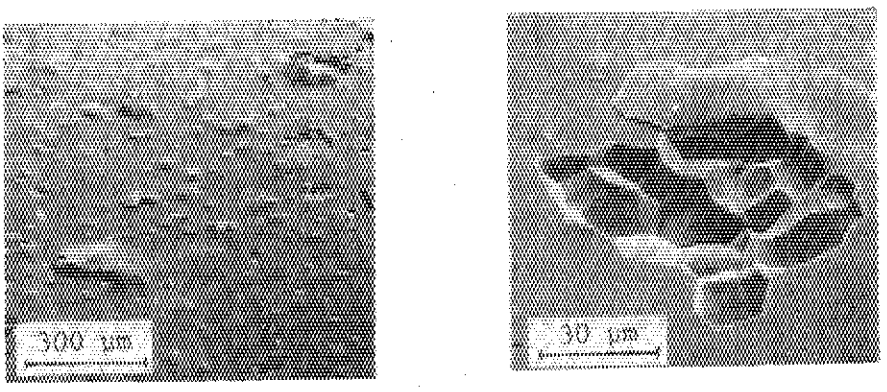

(a) (b)

Photo V.2-4 SEM-micrographs of polycrystalline molybdenum surface at the temperature of 200°C.

VI. SUPERCONDUCTING MAGNET DEVELOPMENT

1. Introduction

The working subject of superconducting magnet (SCM) development for fusion research was officially settled in the plasma engineering laboratory in the fiscal year of 1976. Then, the superconducting magnet laboratory was established on the 1st, July 1977.

The main purpose of the development of SCM for fusion research in JAERI is the construction of superconducting toroidal system for a device coming after JT-60 machine, named Mock-Up Experimental Power Reactor. The strategy for this purpose was fully discussed in the division of thermonuclear fusion research in connection with the SCM subcommittee in the Fusion Council of the Japanese Atomic Energy Commission. The conclusion is that the evolution of the development must be the scaling up of superconducting toroidal coil from a size of coil bore ∿1m to the post-JT-60 machine approximately by four stages, as cluster test, compact torus test, superconducting tokamak test assembly and Mock-Up prototype coil test.

The staff members in the laboratory participated in the activities of SCM Subcommittee, Fusion Power Coordinating Committee, International Energy Agency. They attended at the meetings and the workshops arranged by the subcommittee in order to prepare the implementing agreement for the international cooperations on SCM development for fusion research.

As scientific activities on SCM in the fiscal year of 1976, the design of cluster test apparatus, the three dimensional stress analysis for toroidal coil and the development of large current superconductor were evolved partially in corporation with industries. The details on each subject are explained in the followings.

2. Design of Cluster Test Apparatus

As the first step of toroidal coil development, we are planning to carry out the element coil test in which a coil structure will be selected for future toroidal magnet.

The purpose of the element coil test are the followings.

----experiment of a large current conductor of 10,000 A class in a magnetic field of 7.5T-8.0T

----experiment of practical operation of a coil in high and non-uniform

stress

----experiment of practical operation of a coil in a poloidal field

effect such as pulse field and out of plane force

----experience of fabrication and operation

After the selection of cluster test as element coil test, a preliminary design of cluster test apparatus[1] was carried out in the fiscal year of 1976. The mean diameter of the circular cluster test coil, which generates a back ground field to a test module coil, was decided as 1.5 m. The mean diameter of a circular test module coil was decided as 1.0 m. The fabrication of several module coils with different structure is planned in a few years and they will be tested in turn in cluster test apparatus.

The coil disposition and the dimension of the cluster test apparatus are shown in Fig. VI.2-1. In order to simulate the poloidal field effect, we chose a separated system as pulse poloidal coil and static poloidal coil. These two coils are also super conducting. The purpose of the static poloidal coil is to test out of plane force effect. And the purpose of the pulse poloidal coil is to test varying magnetic field effect on a test module coil.

The principal designed values of the cluster test apparatus are shown in Table VI.2-1. The nominal current of the cluster test coil is chosen as 1,200 A and the operational maximum magnetic field is chosen as about 5T, so that it should operate without any difficulty. The nominal current of a test module coil is determined as 10,000 A. The magnetic field on the axis of a test module coil is shown in Fig. VI.2-2. The distribution is similar to that of toroidal field of tokamak device.

It is revealed by calculation of electromagnetic force that the centering force on a test module coil increases up to 486 tons at the maximum operation of the system. It is also revealed that the out of plane force on a test module coil become 44 tons-m. These values are small comparing with those in a tokamak experimental power reactor. The maximum principal stress on the inner side of a test module coil is presented in Fig. VI.2-3. The maximum value is around 5 kg/mm^2, which is not so high as that in an experimental power reactor.

Fig. VI.2-4 shows the refrigeration system for the cluster test coil system. The first cooling down from room temperature coil is carried out by suppling 20K helium gas from refrigerator and after that, the second cooling down until 4.2K begins by transfer of liquid helium. The total

cooling weight is approximately 18 kg. It is calculated that the time for the first cooling down is approximately 75 hours and that the time for the second cooling down is about 4 hours. The mean temperature decrease with time is shown in Fig. VI.2-5.

This cluster test apparatus can be used as eccentric coil test apparatus with displacement of a pair of cluster test coils in parallel position.

As test module stracture, there are three types proposed actually; pancake winding type, disk winding type and hollow conductor winding type.

It is concluded that the principal experimental simulation of toroidal coil can be carried out with the cluster test apparatus on conductor, stability, insulator, mechanical reinforcement, cooling system and varying field effect except the stress due to electromagnetic force. In order to generate a high stress in a test module coil, a high current density coil may be constructed and tested with a fixed ampere turns.

The design is now being modified during the fiscal year of 1977 in order to get 8.0T on the test module coil and to have an oval type coil as a test module.

3. Development of Three Dimensional Stress Analysis for Toroidal Coil

One of the major problems in construction of large tokamak toroidal coils is the mechanical stress generated by electromagnetic force[2][3]. In order to estimate the stress values in a toroidal coil, finite element method computer code, named JAFUSAC (JAERI Fusion Structure Analysis on Coil), was developed[4][5]. This code which is able to calculate not only the electromagnetic force but also gravitational and seismic force, consists of three independent computer program groups, which are auto-mesh generator, stiffness matrix solver, and outputter. They are structured to be compatible with respect to input and output. Each of the three groups has a separate identity and can be run independently. Each group is set up so that, when applicable, it can also be run with edited output data generated by one of the other groups. In the auto-mesh generator program group, a toroidal coil of circular, oval, or D-sape, is divided into hexahedron elements, and be added fixed boundary condition. The other group, stiffness matrix solver program uses wave front method to solve the giantic size stiffness matrix which is 6000×6000 at maximum.

In the last group, outputter prints and plots the stress, displacement and reaction force of a toroidal coil, as illustrated in Fig. VI.3-1.

It was shown that fixed boundary condition has a severe influence upon the stress distribution in a toroidal coil.

4. Development of Large Current Superconductors

The nominal operating current in superconducting tokamak toroidal coil should be high value because with low current conductor there are several technical disadvantages such as high winding cost, wiere movement and high voltage between windings. An operational current of 10,000 A is considered in JAERI for a test module coil of the cluster test, mentioned above, and also for a future compact torus test coil. As the maximum value of a practical high current superconductor in Japan to date is 1,400A at 7T, studies of large current superconductor development of both NbTi and Nb_3Sn were begun by JAERI through tight contracts with industries.

In order to have an operational current of 10,000 A at 8T with NbTi conductor, a critical current of short sample conductor should be 12,000 A at 8T. Two kinds of conductors, solid type and transposed type were proposed as trial manufacturing of large current conductor[6]. Because of fabrication capacity of transposition, the quantity of element wire of transposed type was limited at the value which corresponds to 6,000 A at 8T. In these two type conductors the current capacity can be increased as a function of number of element superconducting wire. This is an advantage in comparison with monolithic conductor, in which the variation of current capacity is fixed. The details of the parameters of two conductors are shown in Table VI.4-1. Aluminum stabilizer is partially applied on both conductors in order to decrease magneto-resistance effect in comparison with copper.

Through fabrication of these conductors, the following techniques were obtained.

a. In solid type

--- a fabrication of 2,400 A conductor at 8T as an element conductor was succeeded.

--- a technique of assembly of several conductors with soldering was established.

b. In transposed type

--- a technique of formation of transposed wire was established.
--- a technique of soldering on aluminum through nickel plating was established.

Photo. VI.4-1 shows cross sectional views of each conductor. The critical current of each conductors can be 12,000 A and 6,000 A at 8 T by the extrapolation of data of element superconducting wires between 5 T and 8 T.

It is known that Nb_3Sn is superior to Nb-Ti on the superconducting properties (Tc, Hc, Jc). However, because Nb_3Sn material is brittle, Nb_3Sn conductors in tape have been used in small coils. This tape structure has the disadvantage of flux jump instability in perpendicular field and very high aspect ratio. Recently, as to remove this problem, multi-filamentary (MF) structure has been considered.

Thus, in JAERI in collaboration with industries, the fabrication of large current MF Nb_3Sn[8] conducter having current carrying capacity of 10 kA at 13 T was tried for the application of superconducting toroidal field coil in future.

In the several approaches to MF Nb_3Sn conductor fabrication the internal diffusion method was selected. This method is as follows. Nb rod and Sn rod (or bronze rod of Sn-10 at% Cu) are located into Cu tube and drawn into wire without annealing. And it is heat-treated on final size. This method has three advantages; (1) the drawing is done with cold work, (2) the matrix/superconductor ratio is large due to increase solid solubility of Sn in Cu, (3) the mass-production is possible.

A large current conductor and a testing conductor can be achieved by cabling a basic conductor and soldering it in stabilized Cu. Table VI.4-2 shows the parameters of the MF Nb_3Sn conductor fabricated by internal diffusion method. Photo. VI.4-2 shows the cross section of strand cable conductor. Fig. VI.4-1 shows a view of large current capacity conductor (10 kA at 13 T).

From the processing of conductor fabrication and the experimence of testing conductor, the following results were obtained.

(1) By internal diffusion method, the fabrication of multi-filamentary Nb_3Sn conductor having 504 filaments of 3.2 μm in diameter in Cu-Sn matrix was developed.
(2) It was observed that Nb_3Sn conductor was not damaged up to 0.6 % of strain, by the scanning electron micrograph. (Photo. VI.4-3)

(3) It was defined that the minimum bending radias without degradation of current was 60 times of conductor diameter.

References

(1) Shimamoto, S. et al.: to be presented at the 6th International Conference on Magnet Technology.
(2) Shimamoto, S. et al.: ibid.
(3) Nishimura, H. and Shimamoto, S.: JAERI-M 6865 (1977).
(4) Nishimura, H. and Shimamoto, S.: Internal memo (1977).
(5) Nishimura, H. and Shimamoto, S.: Internal memo (1977).
(6) Shimamoto, S. et al.: to be presented at the 6th International Conference on Magnet Technology.
(7) Shimamoto, S. et al.: ibid.

Table VI.2-1 Designed values of cluster test apparatus

	Cluster Test Coil (CTC)	Test Module Coil (TMC)
Magetomotive force	3,000X2KAT	2,000KAT
Nominal Current	1,200A	10,000A
Total magnetic energy	24.1MJ(all coils charged in cluster position)	
Mean current density	3,000A/cm^2	3,000A/cm^2
Total weight	52tons	
Peak magnetic field on TMC	3.37T from CTC	4.23T from TMC total 7.6T
liquifier of He	100l/h	

Table VI.4-1 Parameters of NbTi conductors

		solid type	transposed type
whole conductor	size (mm)	10×30	6.6×26.5
	cross section (mm^2)	300	175
	aspect ratio	3.00	4.00
super-conducting wire	size (mm)	2.6×6.0, 0.3R	1.60 ϕ
	cross section (mm^2)	15.5	2.01
	copper ratio	2.9	2.3
	NbTi filament	100μϕ×510	60μϕ×220
	Twist pitch (mm^2)	100	30
	quantity	5	15
	J_c (A/cm^2 at 8T)	0.6×10^5	0.65×10^5
	I_c (A at 8T)	5×2400	6000
stabilizer	material	OFHC/Al	Al
	size	6.5×7.9 (Al 60%) OFHC/Al/ OFHC 3.3×30 (Al 40%)	12ϕ×7×15
cooling method		edge face cooling channel 10wx0.5t	edge

Table VI.4-2 Parameter of MF_3Nb Sn conductor fabricated by internal diffusion method.

A) Multifilamentary conductor

Item	Value or Description
No. of filaments	87
Filament diam.	7.5um
Matrix material	Bronze (Cu-Sn)
Electrical-resistivity of matrix	10^5 -cm
Twist pitch	20mm
Conductor diam.	0.189mm
Overall current densities	6.3 10^4 A/cm^2 at 8 T

B) Testing conposite conductor

Item	Value or Description
Basic conductor	
No. of filaments	504
Filament diam.	3.26um
Conductor diam.	0.187 mm
Twist pitch	20 mm
Compleate conductor	
Conductor shape	Rectangular
Dimension of conductor	1.0 0.14 cm^2
Bonding methord	Solder
Bonding material	Pb-Sn
Cu area	1.04 cm^2
Critical current	1,000 A at 8 T
Current densities/ Cu area	9,600 A/ cm^2 at 8 T
Overall current densities	7,000 A/ cm^2 at 8 T

C) Large current conductor

Item	Value or description
Basic conductor	
No. of filaments	504
Filament diam.	4.77 um
Conductor diam.	0.187 mm
Twist pitch	20 mm
Complete conductor	
Conductor shape	Rectangular
Dimension of conductor	5.0 0.6 cm^2
Bonding methord	Solder
Bonding material	Pb-Sn
Cu area	2.25 cm^2
Critical current	10,000 A at 13 T
Current densieties/ Cu area	4,400 A/ cm^2 at 13 T
Overall current densities	2,800 A/ cm^2 at 13 T

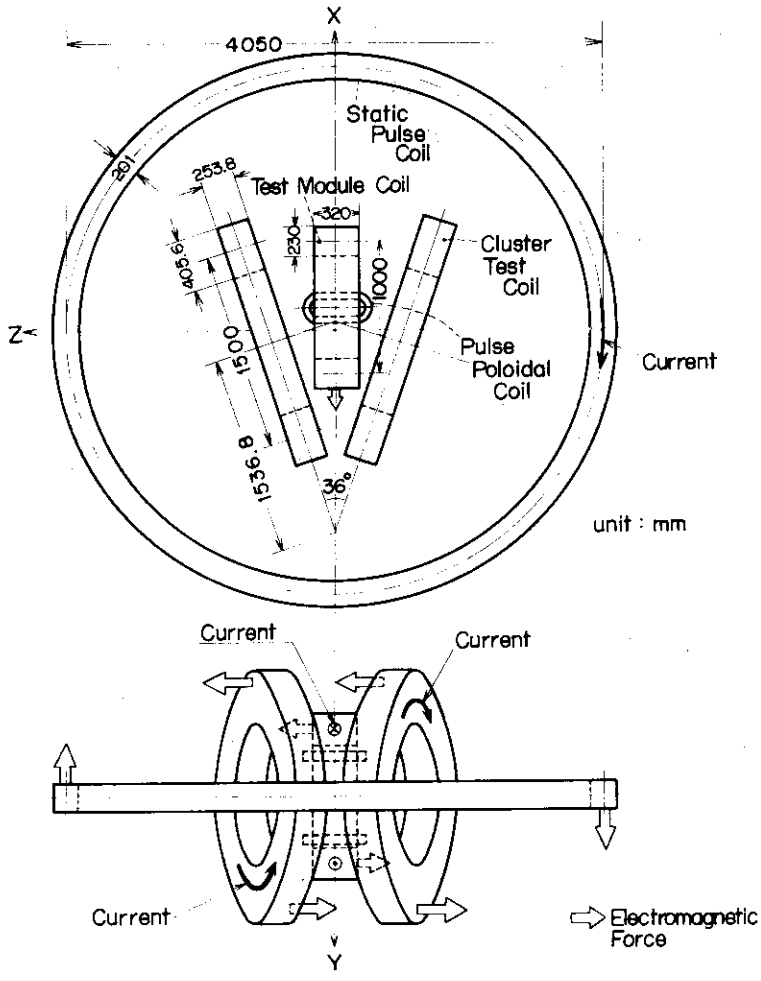

Fig.VI.2-1 Coil disposition of the cluster test apparatus

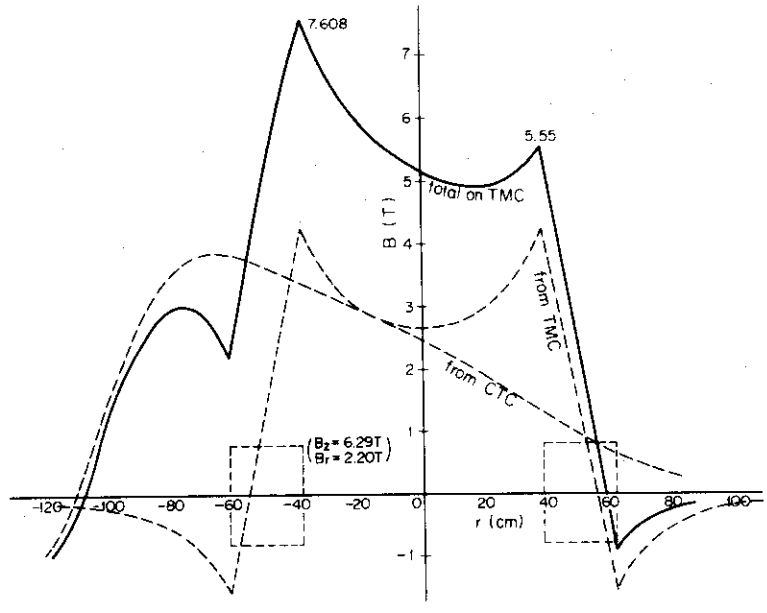

Fig.VI.2-2 Magnetic field distribution on the centerline of test module coil

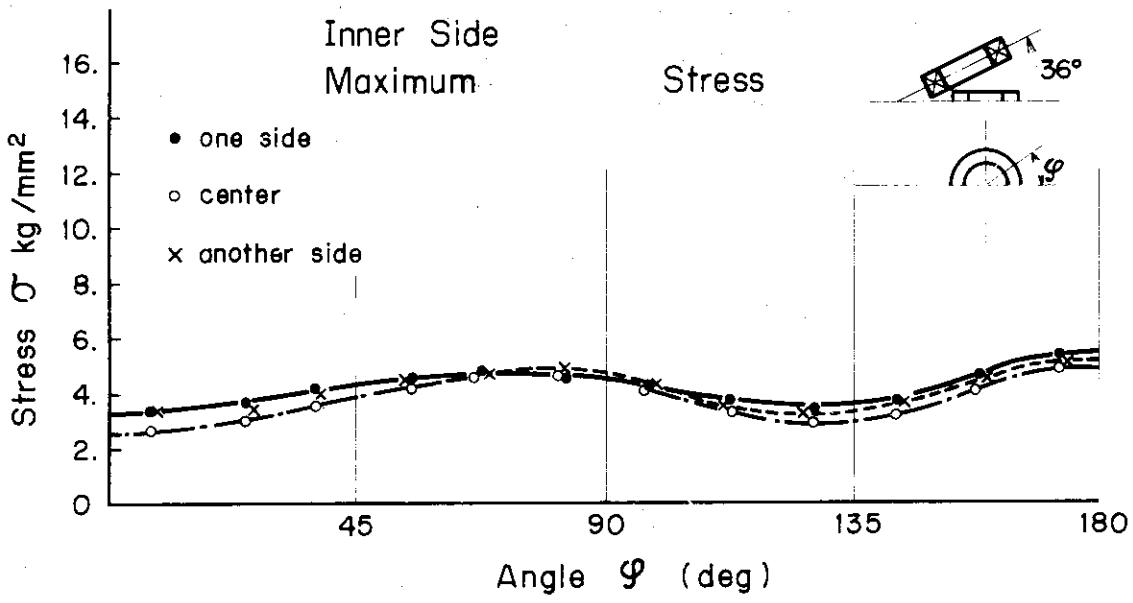

Fig.VI.2-3 Stress distribution on the inner surface of test module coil

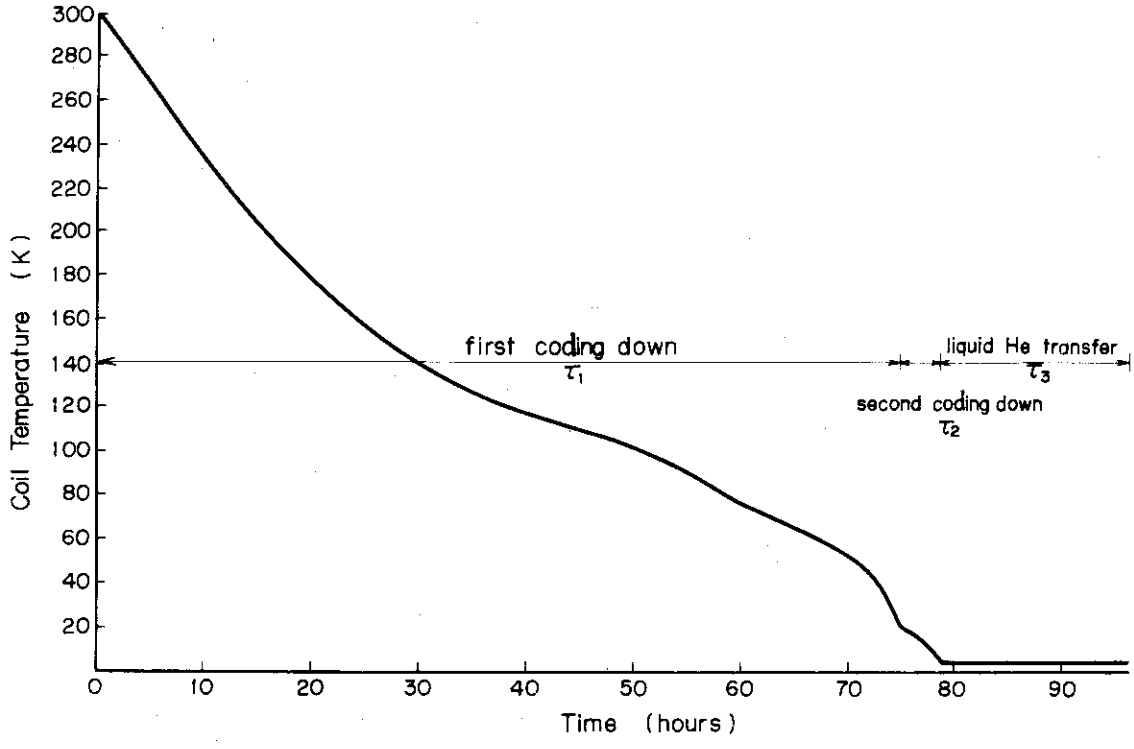

Fig.VI.2-5 Refrigeration system for the cluster test apparatus

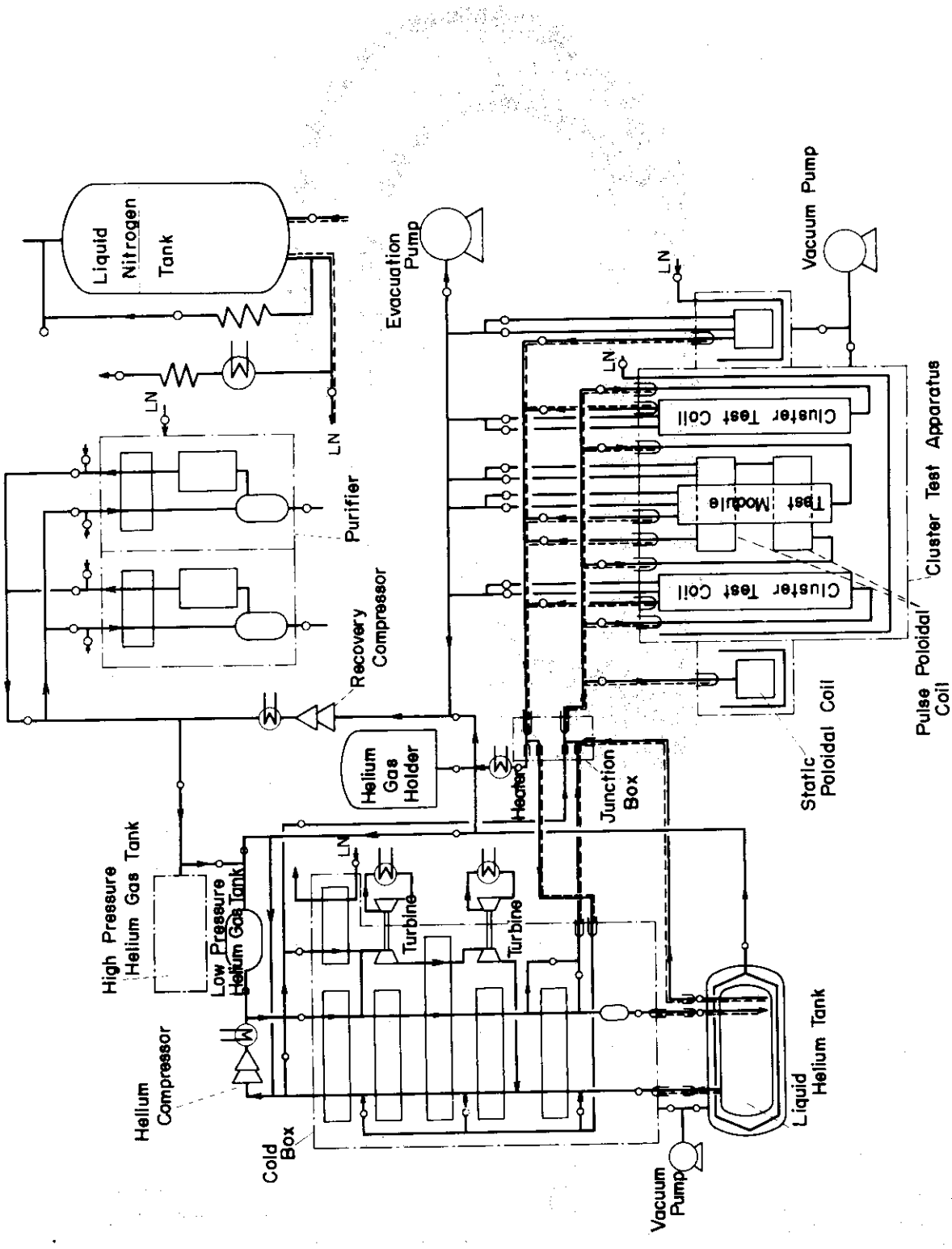

Fig.VI.2-4 Cooling down curve of the cluster system

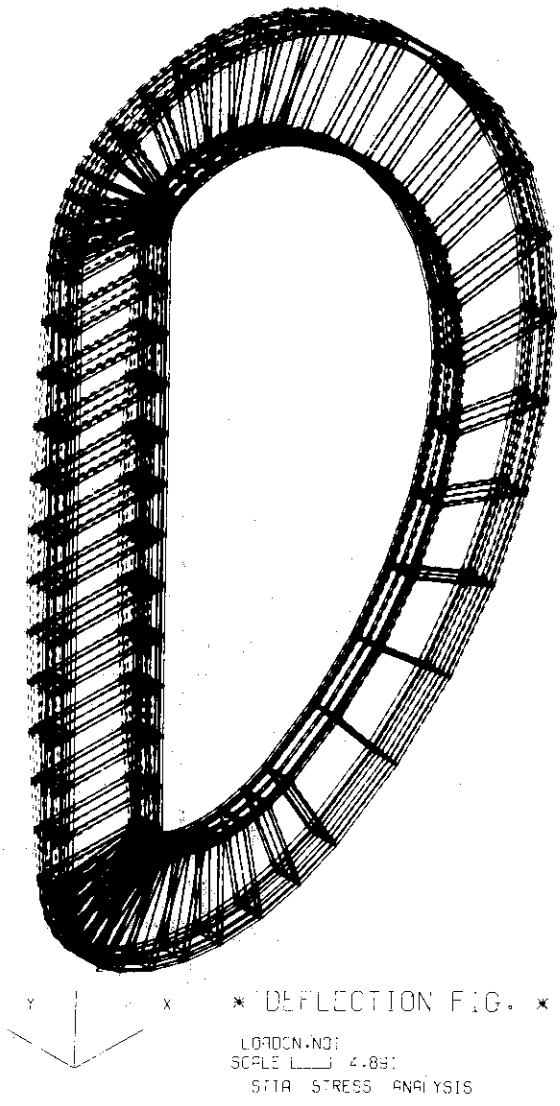

Fig.VI.3-1 Plot of displacement of a D type coil by outputter

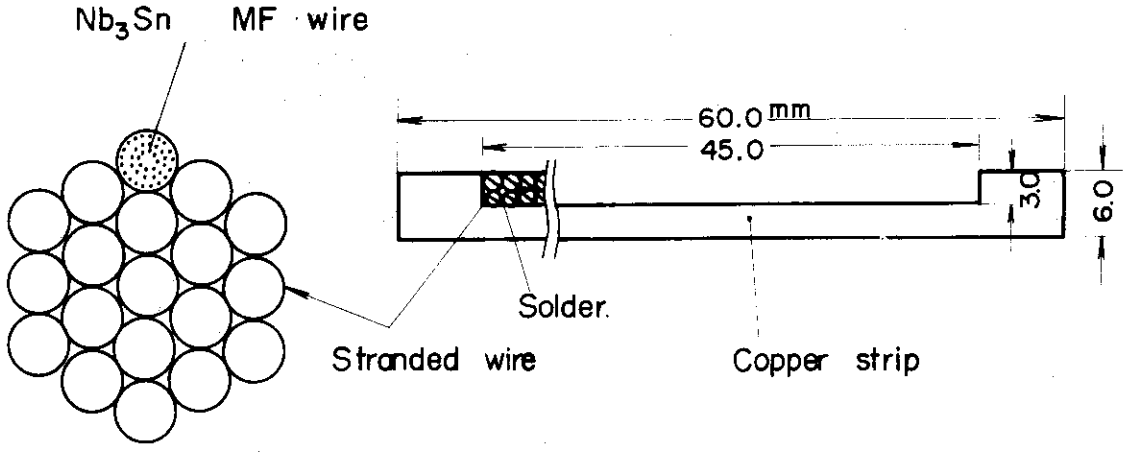

Fig.VI.4-1 Composition of large current Nb_3Sn conductor

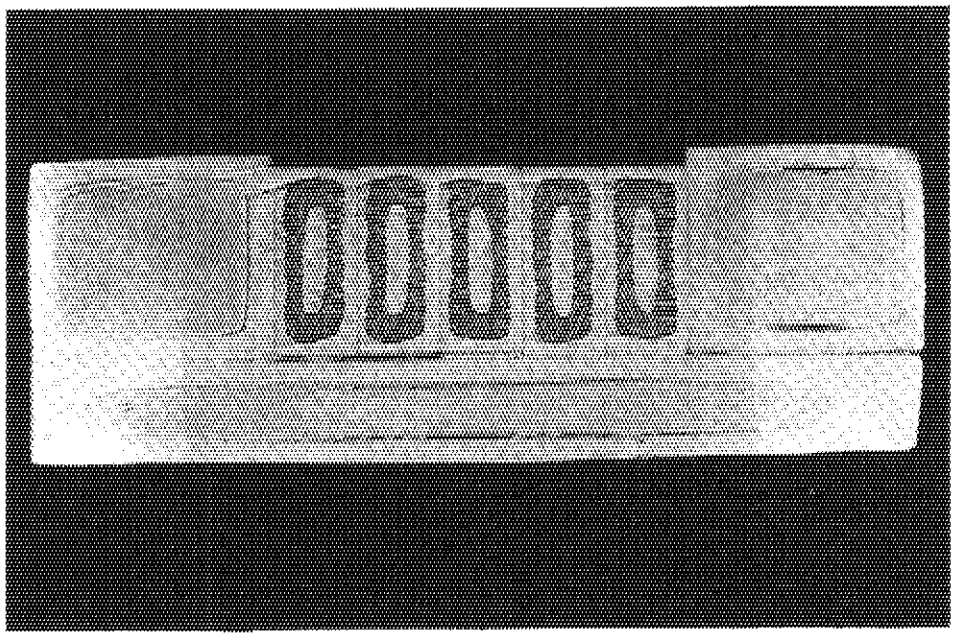

(a) solid type

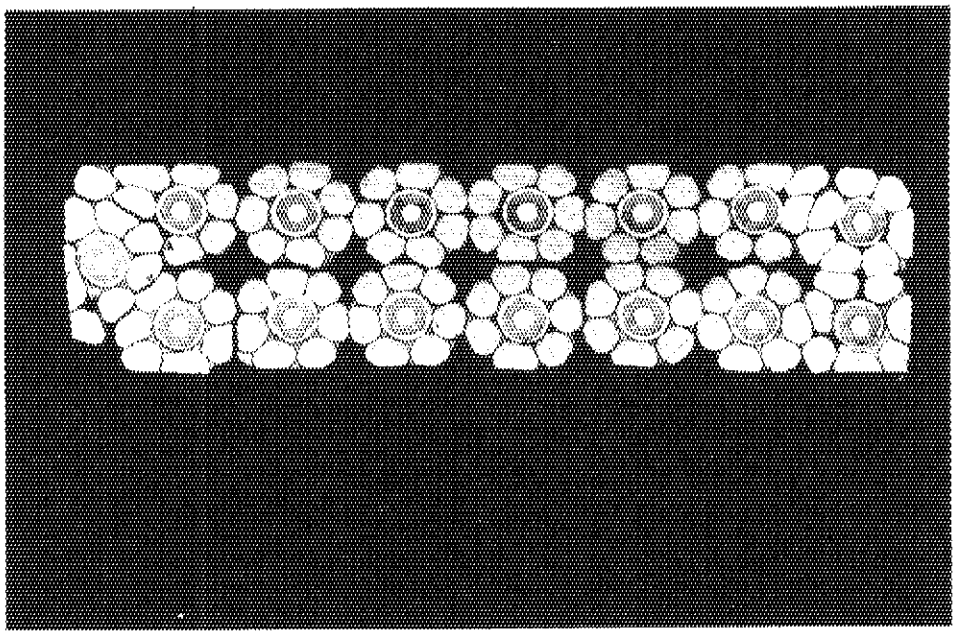

(b) transposed type

Photo VI.4-1 Cross section of the conductors

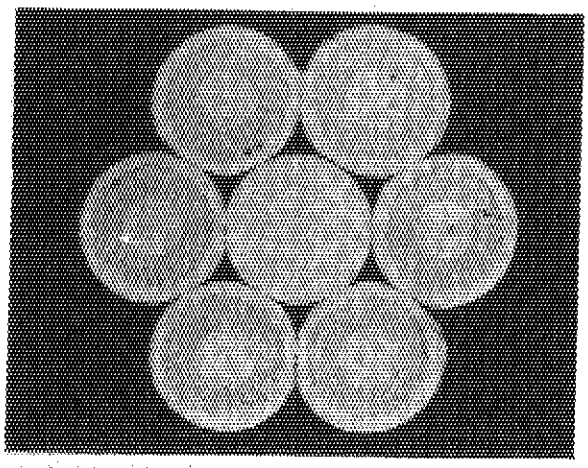

(a) before heat treatment

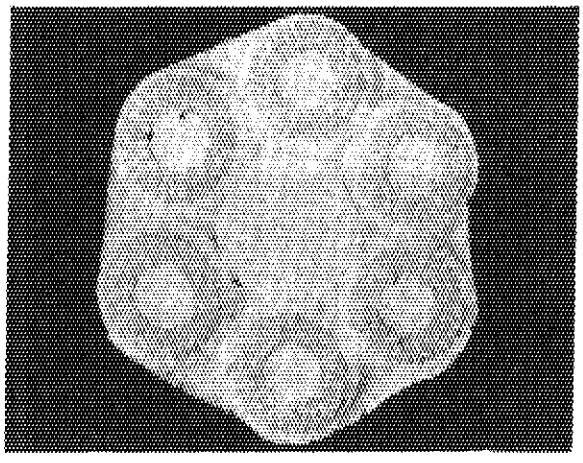

(b) after heat treatment

Photo VI.4-2 Multifilament Nb_3Sn strand cable having six basic conductor around a Cu core

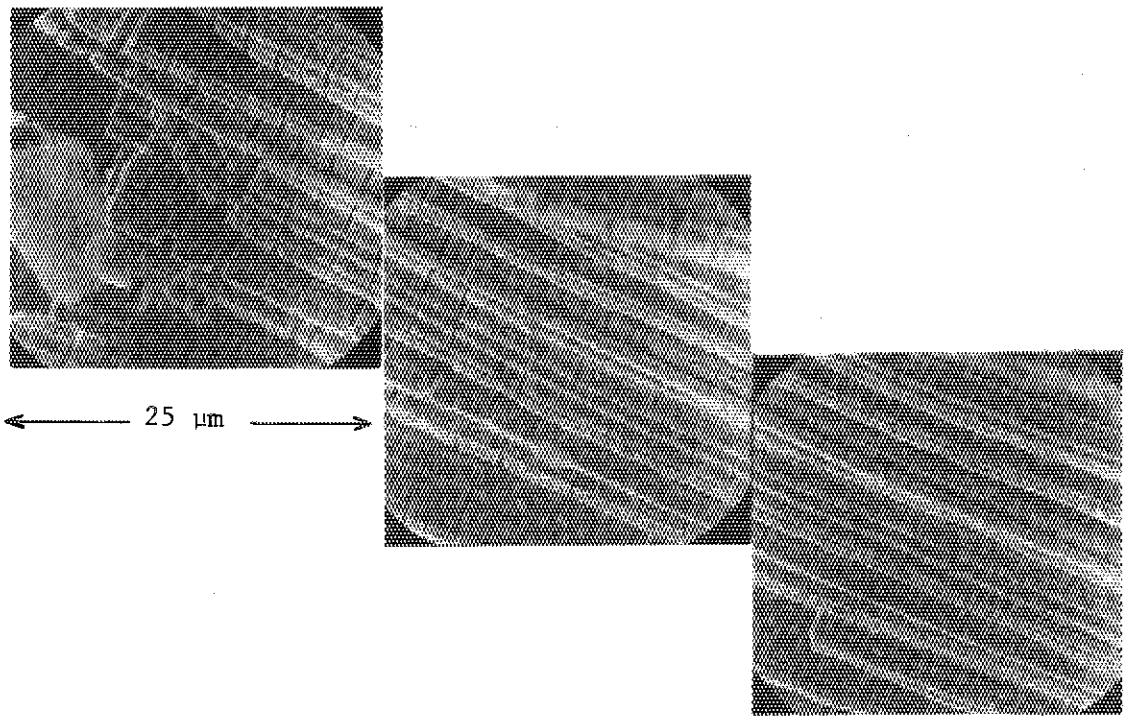

Photo VI.4-3 Scanning electron micrographs of cracks occurred in the MF_3Nb Sn at 1 % strain (×2000)

VII. REACTOR DESIGN STUDY

1. Introduction

First preliminary design of a tokamak experimental fusion reactor to be built in the near future has been completed in March 1976. The goals of the reactor are to achieve reactor-level plasma conditions for a sufficiently long operation period and to obtain design, construction and operational experiences for the main components of full scale power reactors. This design covers overall reactor system including plasma characteristics, reactor structure, blanket neutronics, shielding, superconducting magnets, neutral beam injector, electric power supply system, fuel recirculating system, reactor cooling and tritium recovery system and maintenance scheme.

Design of a power reactor is continued to supply the feedback informations to the design of the experimental reactor.

Preliminary safety evaluation of the experimental reactor is also carried out.

2. General Description of the First Preliminary Design of the JAERI Experimental Fusion Reactor (JXFR)[1],[2]

Main design paramters of the reactor are given in Table VII.2-1 and overview of the reactor is shown in Fig. VII.2-1.

Figure VII.2-2 shows the cross-sectional view of the reactor. The reactor consists of 8 reactor modules which may be withdrawn in the radial direction for repair. Each module has a blanket module which consists of blanket cells and a cell with a 1.2 meter dia. hole for the neutral beam injection and evacuation. Mechanical limiters employed are so designed that they may be withdrawn in case of failure. Four limiters and 4 injectors are alternately installed. Two vacuum pumps (cryo-pumps) are installed to every reactor module.

Table VII.2-1 Main design parameters of the JAERI Experimental Fusion Reactor (JXFR)

Operation Mode	
Fusion power (MW)	100
Operation period(s)	420
Burn time(s)	300
Load factor	0.5
Duty factor	0.7
Reactor dimensions	
Major radius (m)	6.75
Plasma radius (m)	1.5
First wall radius (m)	1.75
Plasma volume (m^3)	300
Plasma	
Mean temperature (keV)	7
Mean density (10^{14} cm^{-3})	1.1
Effective charge	1.6
Confinement time (s)	2.9
Injection power (MW)	27
Toroidal field (T)	6
Safety factor	2.5
Poloidal beta	2.2
Toroidal beta	0.017
Plasma current (MA)	4
Reactor Structure	
Reactor module/Reactor	8
Blanket cells/Reactor module	284
Injection and evacuation hole/Reactor module	1
Nominal max. 1st wall temp.(°C)	540
Materials	
Structural material	316SS
Blanket fertile material	Li_2O
Refrector material	Stainless steel
Neutronics	
Neutron current at 1st wall (n $cm^{-2}s^{-1}$)	7.6×10^{12}
Neutron wall loading (MW m^{-2})	0.17
First wall displacement damage rate (dpa y^{-1})	1.1
Max. helium production rate in 1st wall (appm y^{-1})	13
Max. hydrogen production rate in 1st wall (appm y^{-1})	38
Tritium breeding ratio	0.9
Nuclear heating per DT neutron (MeV n^{-1})	16.1
Total induced activity at one hour after shutdown (Ci) (after one year operation)	7.3×10^{7}
SCM irradiation effects	
Max. copper displacement (dpa y^{-1})	9.0×10^{-6}
Max. nuclear heating rate (W cm^{-3})	6.2×10^{-5}
Total nuclear heating in SCM (kW)	0.68
Toroidal field magnet	
Number of coils	16
Bore, Width/Height (m)	7/11
Magnetomotive force (MAT)	203
Max. field strength (T)	12
Stored energy (GJ)	60
SCM material	Nb_3Sn
Refrigerator capacity (MW)	5.4
Primary winding	
Number of coils	22
Magnetomotive force (MAT)	60
Maximum field intensity (T)	8
Stored energy (GJ)	2.1
Flux change (Wb)	140
SCM material	NbTi
Vertical field magnet	
Number of coils	12
Magnetomotive force (MAT)	±8
Maximum field intensity(T)	8
Field intensity (T) at plasma center	0.26
Stored energy (GJ)	0.5
SCM material	NbTi
Neutral beam injector	
Number of ion sources	48
Deuterium beam energy (keV)	200
Ion beam output (MW)	240
Injection power (MW)	33
Power efficiency	0.40
Power supply (MW)	
for Toroidal coils	0.6
for Poloidal coils	6
for Refrigerator of SCM (Toroidal, Poloidal, IES)	12
for Neutral beam injector	85
for Vacuum exhaust system (Main pump, NBI pump)	3
for Blanekt cooling system	40
for Auxiliary system	13
Total power	160
Fuel circulation system flow rate(mgs^{-1})	
Tritium insertion rate	17.5
Deuterium insertion rate	11.7
Herium exhaust rate	0.24
Cooling system	
Number of loops	4
Coolant, Pressure (kg cm^{-2})	He,10
Inlet/Outlet temp. (°C)	300/500
Flow rate (kg/s)	143
Secondary system	He, air-cooled
Tritium inventory (kg)	
Fuel recirculating system	0.3
Tritium recovery system including blanket	0.1
Total inventory including storage	0.5

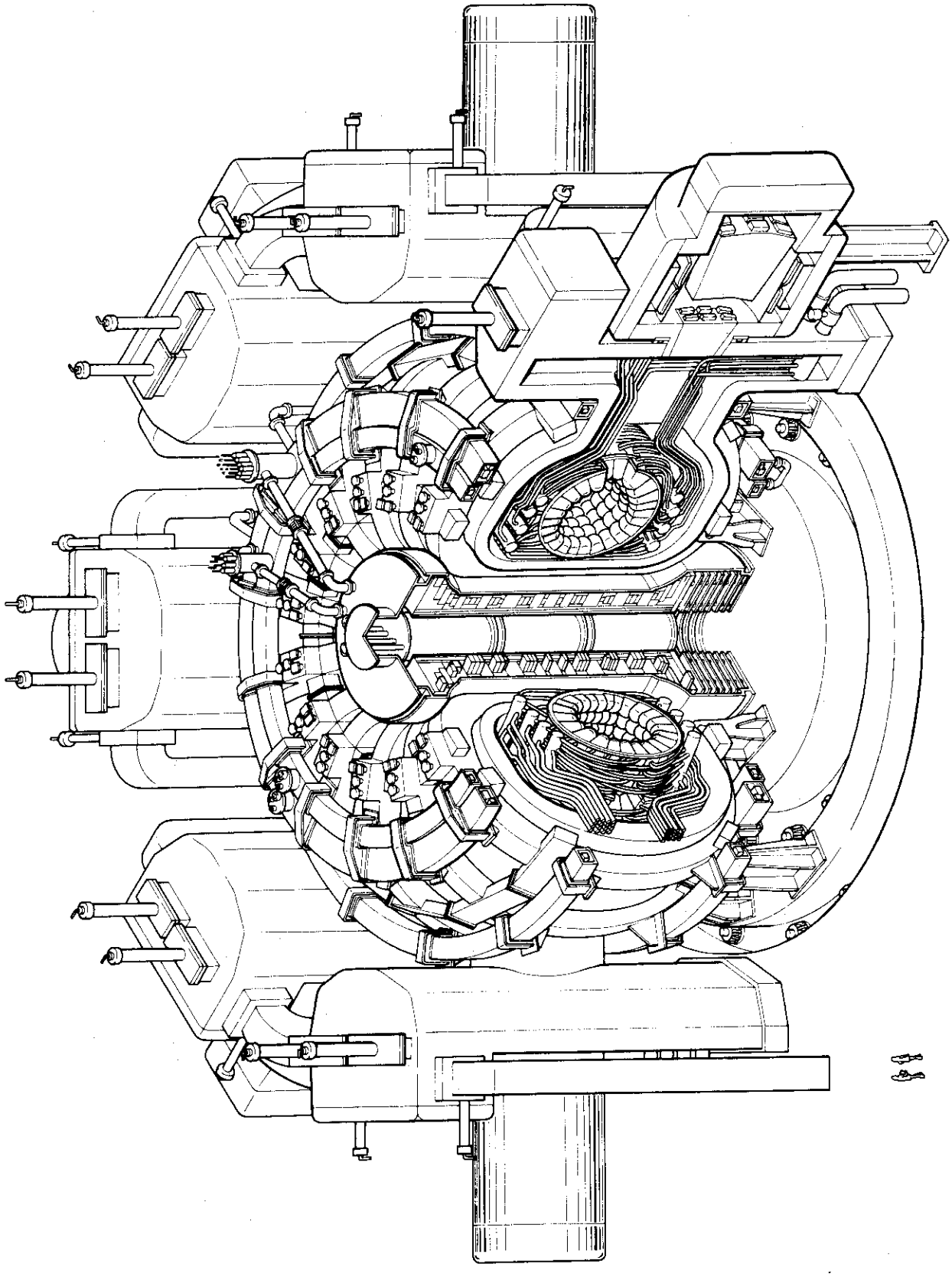

Fig.VII.2-1 Overview of the experimental reactor

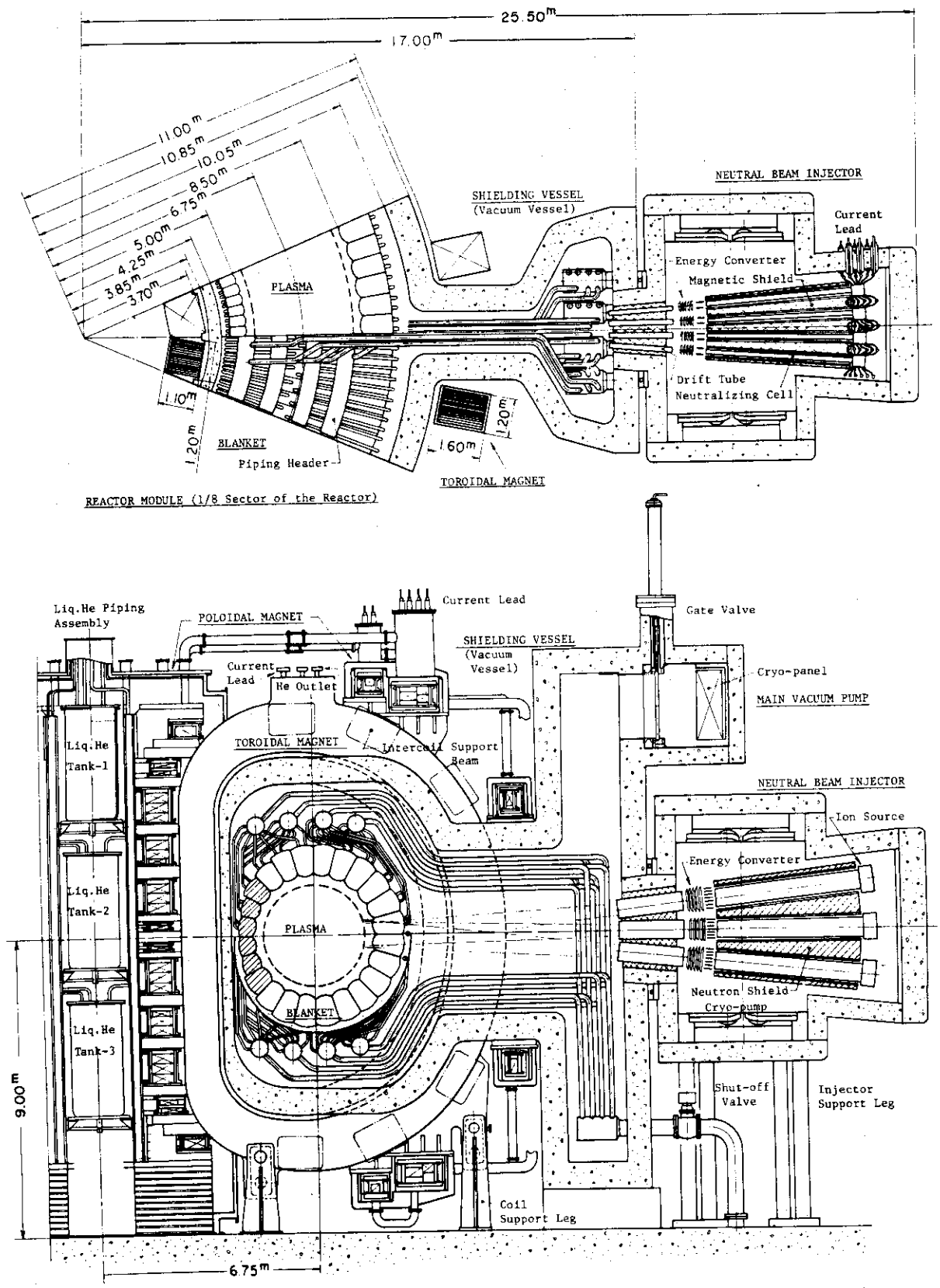

Fig.VII.2-2 Cross-sectional view of the reactor

3. Design Studies for JXFR

3.1 Plasma characteristics

3.1.1 Fuel supply and impurity problem

Further discussions of fueling were carried out. The rate of production of impurities seems to be suppressed to small value, since the surface region of the plasma becomes a rather thick cool plasma when fuel is supplied as cold neutral gas. An important problem is selection of material for the limiter and the first wall. An example of calculations is listed in Table VII.3-1. Graphite which is considered to be a promising material so far, may not be used because of the high chemical sputtering at around 500°C. (The chemical sputtering is neglected in the table.) Though it is a high Z material, molybdenum is a possible material because the surface temperature of the plasma may be made lower than the threshold of sputtering and then the production rate of impurities becomes smaller. One of the problems for molybdenum is whether impurities exhausted from the plasma can be evacuated with the fuel gas or stick to wall firmly so as not to be sputtered easily from the wall again by low energy particles. Another problem is that of self-sputtering because there may be multiplication of impurities as the sputtering ratio is greater than 1 if certain portion of impurities can not be evacuated. Other suitable materials are now under investigation.

3.1.2 Thermal instability and power dynamics with feedback[3]

The calculational model used for the analysis of the thermal instability and power dynamics with feedback is based on point-model equations for particle and energy balances. The thermal instabilities of equilibrium solutions are examined with the linear perturbation analysis. The growth rates against an injection power are depicted in Fig. VII.3-1. The sign on each curve indicates the solution obtained with the scaling laws used for confinement time[4]. The trapped ion mode (TI)[5], neo-Bohm (NB)[6] and pseudoclassical[7] diffusion scalings are considered. It should be noted that our scaling laws yield relatively short confinement time, for instance, about one-fifth of that in WASH-1295[8] for the trapped ion mode.

Particle and energy balance equations are given by

$$\frac{dn_i}{dt} = I_B + I_C - \frac{n_i}{\tau_p} - \frac{1}{2} n_i^2 \langle \sigma v \rangle - 2 I_B f_B$$

$$\frac{dn_\alpha}{dt} = \frac{1}{4} n_i^2 \langle\sigma v\rangle + I_B f_B - \frac{n_\alpha}{\tau_p}$$

$$\frac{3}{2}\frac{d(n_i T_i)}{dt} = [\frac{1}{4} n_i^2 \langle\sigma v\rangle + I_B f_B] E_\alpha f_{\alpha i} + I_B E_B f_{di} + \frac{3}{2} C_{ei} n_i n_e \frac{T_e - T_i}{T_e^{3/2}} - \frac{3}{2}[\frac{n_i}{\tau_E} + \frac{1}{2} n_i^2 \langle\sigma v\rangle - I_B(1-2f_B)] T_i$$

$$\frac{3}{2}\frac{d(n_e T_e)}{dt} = [\frac{1}{4} n_i^2 \langle\sigma v\rangle + I_B f_B] E_\alpha f_{\alpha e} + I_B E_B f_{de} - \frac{3}{2} C_{ie} n_i n_e \frac{T_e - T_i}{T_e^{3/2}} - P_{Br} - P_{cy} - \frac{3}{2}\frac{n_e}{\tau_E} T_e$$

where I_B is the injection rate of energetic deuterons, I_c the fueling rate of the neutral gas, P_{Br} the bremsstrahlung and P_{cy} the cyclotron radiation loss, respectively. The parameter f_B is the fraction of the beam undergoing fusion during the slowing down, and $f_{\alpha x}$ and f_{dx} are respectively the fraction of the 3.52 MeV alpha and injected deuteron energies given to particle x.

The feedback control applied with delay time Δt_d is based on the model used by Ohta et al.[9] which is given by

$$I_B = I_{B0} + \Delta I_B, \quad \Delta I_B = \alpha_B n_{i0} \Delta T_i / T_{i0}$$

$$I_c = I_{c0} + \Delta I_c, \quad \Delta I_c = \alpha_c n_{i0} \Delta T_i / T_{i0}$$

where $T_i = T_i(t - t_d) - T_{i0}$ and the subcript 0 indicates values at equilibrium.

The power transients with feedback control for the trapped ion scaling are presented in Figs. VII.3-2 and 3. The transients were initiated by a 0.5 keV perturbation in the ion and electron temperatures at equilibrium (T_i = 7 keV, 1 % SiC(Z_{eff} = 2.06)). The values of α_B, α_c and Δt_d in the figures are typical ones which stabilize the plasma, namely yield negative growth rates. The case of α_B = -0.03 and Δt_d = 1.0 results in a large amplitude of the oscillation in the initial state and in a long oscillation period. Increasing the feedback power to α_B = -0.1 (Δt_d = 1.0), the fusion power is stabilized in relatively short time, though the variation of the corresponding injection power is rapid. The delay time of 2.0

seconds for $\alpha_B = -0.1$ cannot stabilize the plasma (not shown).

The cold-fuel control with $\alpha_c = 0.6$ and $\Delta t_d = 1.0$ smoothly stabilizies the power. The lower feedback rate of $\alpha_c = 0.2$ and the case of $\alpha_c = 0.6$ and $\Delta t_d = 2.0$ cause undesirable oscillations in the power. At the equilibrium for $T_i = 9$ keV ($T_e = 8.53$ k3V) and 3 % SiC ($Z_{eff} = 4.18$) the controllable regime is narrower and it becomes more difficult to smoothly stabilize the power, though the figures are not shown.

Assuming the above perturbations for the present plasma conditions, the allowable delay time for smooth stabilization of the fusion power would be a degree of one second.

3.1.3 Shutdown analysis

Shutdown of plasma is discussed by using time dependent one point model. The pseudoclassical scaling law[7] plays the leading part of the plasma diffusion in the low energy region below several keV while the trapped ion scaling law[5] mainly applies in the higher region. In this shutdown model, heating power is not injected and only D is inserted during 20 second shutdown process. On the first 10 second stage, while plasma temperature, electron density and plasma current decrease from 7 keV to 1 keV, 1.1×10^{20} m^{-3} to 10^{19} m^{-3} and 4 MA to 1 MA, respectively, fusion power falls down. On the latter 10 second stage, while plasma temperature, electron density and plasma current decrease from 1 keV to 100 eV, 10^{19} m^{-3} to 10^{18} m^{-3} and 1 MA to 100 kA, respectively, plasma energy is removed. The typical results during the first and the latter stages are shown in Fig. VII.3-4 and VII.3-5, respectively. In these estimations, it is assumed that time constant of the change in D insertion rate from 1.5×10^{19} m^{-3} s^{-1} (during equilibrium operation) to 8×10^{18} m^{-3} s^{-1} is 4.2 s. Plasma one turn voltages are -4.0 volt and -0.5 volt which are surveyed to fall plasma current down to 1 MA and 100 kA during the first 10 seconds and the latter 10 seconds, respectively. Decrease of plasma current has a large effect on lowering plasma density and energy since particle and energy confinement times decrease as plasma current decreases.

3.2 Blanket and shield neutronics

3.2.1 Induced activity and dose rates[10]

Induced activity and biological dose rates around the reactor have been calculated by induced activity calculational code ACTIVE and one-

and two-dimensional transport codes. The biological dose rates during reactor operation were also calculated by the one-dimensional transport code. The results of calculations are as follows.

(1) The level of radioactivity in JXFR is about 10^8 Ci at shutdown after a year of operation.

(2) Dose rate at the outer surface of the shield for the super-conducting magnet (S.C.M) is 1 mrem/hr at a week after shutdown after a year of operation, when adequate shields are added to both sides of the S.C.M.

(3) When a reactor module is extracted for repair, the dose rates are on the order of 10^5 rem/hr at the surface of the first wall and $10^1 \sim 10^5$ rem/hr in the reactor room.

(4) Dose rate at the outer surface of the S.C.M shield is 10^5 rem/hr during reactor operation.

3.2.2 Evaluation of shielding design for superconducting magnets[11],[12]

Effect of the calculational conditions on accuracy of the shielding design for superconducting magnets has been studied by one-dimensional discrete-ordinate calculations.

The accuracy is found to be highly sensitive to the mesh interval spacing chosen. To meet the mesh spacing requirement in the calculation of the deeply penetrated neutrons, a method of connecting the neutron fluxes of two adjacent systems using a shell source is shown to be useful.

Shield for superconducting magnets has been evaluated. The preliminary shield design was modified so as to meet the design criteria.

Applicability of the one-dimensional calculation model for shielding design of the superconducting magnets was studied; the cylindrical model is found to be appropriate. As for the biological shield, a concrete layer 2 m thick is found to be sufficient for the secondary biological shield.

3.2.3 Calculation of the neutron radiation damage[13]

The methods of calculating the displacement damage in neutron irradiation have been studied comparatively. Effects of the secondary displacement model, treatment of nuclear reactions and nuclear data upon the neutron displacement cross sections were examined. High-energy neutrons are emitted in a fusion reactor, so it is important to calculate the displacement cross sections taking into consideration the electronic

energy loss, anisotropic elastic scattering and inelastic scattering.

Displacement and gas production rates in the first wall material (316 S.S.) were calculated. Displacement damage rate in the superconducting magnet stabilizer (Cu) was also calculated. The displacement rate in the first wall is smaller than in the fuel cladding of a fast fission reactor but the gas production rate is larger. Electric resistance of the copper stabilizer rises significantly, indicating the need for thicker shielding.

3.3 Reactor structure

3.3.1 Blanket structure

Blanket structure is in a vacuum vessel, its weight is about 2000 ton, and is linking with toroidal magnets as shown in Fig. VII.2-1 and VII.2-2. It consists of 8 blanket modules. As shown in Fig. VII.3-6, the module is formed with 12 blanket rings which consists of 24 blanket cells conjoined with two pieces of flanges.

The hatched portion of blanket in Fig. VII.2-2 serves exclusively for shielding purpose and the rest of the blanket includes Li_2O for tritium breeding. The unit blanket cell has a dual shell structure and cooled by helium gas at 10 ata.

Blanket cells for tritium breeding contain pebbles and blocks of Li_2O which are packed in the canning of stainless steel to prevent their deformation.

The volume fraction of the structural material in the blanket is limited from the requirement to obtain sufficient tritium breeding. There arise some difficult problems in the structural design of blanket cells such as reducing pressure stresses of wall to sufficiently low level. Sufficient consideration is also required on the fatigue of structural material under consideration, because the number of thermal stress (6 kg/mm^2) cycles on the first wall becomes 4×10^4 per year.

Following items are studied in this design; (1) pressure stress in a blanket cell which has a square cross section and the effect of adjacent cells, (2) change of temperature distribution in a blanket cell and effect of flow rate control, (3) electromagnetic force on a blanket cell, (4) change of first wall temperature during plasma burst and effect of protection wall, (5) effect of thermal cycles on the structural design of blanket cell, and (6) integrity of a blanket module.

3.4 Major components

3.4.1 Toroidal field magnet

The maximum toroidal field at the coil is 12.0 T, providing 6.0 T at the plasma center (R = 6.75 m). The total ampere-turns is 202.5 MAT, while the ampere-turns per coil is 12.66 MAT. The inner bore of the coil is 7.3×11.2 m, and the coil shape is constant-tension D-shape (Fig. VII.3-7). 16 coil design was chosen, considering the necessity for good access for the evacuation port or support structure of blanket and shield. The field ripple obtained at the design point is 0.47 %. The coil cross section is about 0.865 m^2, resulting in an average current density of 15 ampere/mm^2. The operational current is 25,100 amperes, and cryogenic stabilization is fulfilled.

Nb_3Sn superconductor was chosen in spite of its brittleness, to attain a toroidal field of 12 T which is higher than the practical limit for NbTi superconductor. The development of large Nb_3Sn coil technology may take a large amount of money and a long time, but high field superconducting magnet would be necessary to realize a economic fusion power reactor. Type 310S stainless steel is used as the disc supporting hoop force[14]. Even at the cryogenic temperature under 4°K austenite of type 310S stainless steel is stable. Epoxy fibreglass insulator is inserted between the conductor and stainless steel structure material.

The straight section length of the coil is about 8.1 m, and the inward centering force is 64,000 ton/coil. The centering force is supported by the wedged inner portions of the 16 coils and center cylinder. The compression stress of the wedged portion or the cylinder is 23-21 kg/mm^2. 62 % of the centering force is supported by the wedged portions. The total hoop force is about 166,000 ton/coil. The force is supported by stainless steel disc. The two dimensional and three dimensional structure analysis was performed. The maximum stress is approximately 40 kg/mm^2.

The time dependent field of the ohmic-heating coil, vertical field coil and plasma current generate eddy current loss in the conductors and stainless steel structure. A typical operation cycle consists of about 10 sec start-up time, 300 sec burn time, 10 sec shutdown time and 80 sec preparation time. The magnitude and direction of the superimposing poloidal field were computed at many points of the magnet. The result of computation gives 0.2 kW eddy current heating in the magnet. Total heat load including eddy current loss, neutron and gamma-ray radiation heating

and cryostat loss is 8.0 kW. The required liquefaction rate is 16,000 ℓ/h.

Coil protection and safety problems are examined on the 60 GJ magnet design. 18 disc power supply system (as shown in reference[15]) is used so that the induced voltage is low enough and generated magnetic force is negligibly small. The way of assembly and disassembly of the magnet was also discussed.

3.4.2 Poloidal magnet design

The superconducting poloidal magnets were designed. The arrangement of the coils are shown in Fig. VII.2-2. It is assumed that the plasma current of 4 MA is raised in 10s and sustained for 300s by the primary winding. The maximum rate of current change in the primary winding is 250 kA/s. The magnetomotive force and the maximum field intensity of the magnet are 60 MAT and 8.1 T respectively. The stored energy is 2.2 GJ and the current in the wire is 250 kA. The magnetomotive force of the vertical field magnet is 8 MAT and the stored energy is 0.5 GJ.

The superconducting material is copper-stabilized NbTi stranded wire. Wires are placed in a case of 304SS and electromagnetic force is mainly supported by this case. The maximum stress in the case is 46 kg/mm^2 which seems too high to withstand the repeated force. In order to prevent heating due to the eddy current, the liquid helium chambers are made of FRP. Because of difficulty in the removal of bubbles horizontally between pancakes in the coolant, forced cooling is applied, though consumption of coolant becomes larger. Insulation and high current feeders are also difficult problems in the design of the poloidal magnets.

3.4.3 Neutral beam injection system

The neutral beam injection system was designed, which consists of ion sources, neutralizing cells, direct converters, evacuation systems and drift tubes shown in Fig. VII.2-2. In this reactor 200 keV D^0 beam of 33 MW is injected to heat the plasma from about 1 keV to operating temperature of typically 7 keV and also to keep this temperature for 300 s.

Some optimizations and parameter studies of neutralizing cell length, gas flow rate, operating pressure of ion sources, total pumping speed and pressure at energy converters were carried out. Four injection ports are used and each port has 12 ion sources of about 32 A. It is proposed to apply a hollow cathode discharge to the ion source because longer life and

higher efficiency compared with ordinary hot filament discharges may be expected at a low gas pressure. Each port has a cryocondensation pump with pumping speed of about 10^6 ℓ/s. In-line direct converters are mounted in order to recover residual ion beam energy and as a result the overall efficiency of 40 % may be expected.

3.5 Major systems

3.5.1 Power supply system

It will be necessary to store energy on some energy storage device because of the large peak power demand for the poloidal field coil systems at the tokamak discharge. A superconducting inductive energy storage is used as this energy storage device. In order to cancel the outer leakage magnetic field, double solenoid coil shape is chosen for this energy storage coil. The main characteristics of this superconducting inductive energy storage are shown in Table VII.3-2. The energy transfer system between the poloidal field coils and the inductive energy storage is based on a thyristorized dc-to-dc converter. The necessary power input from the power grid is only to compensate the joule loss power that is dissipated in the plasma and the circuit resistance.

3.5.2 Fuel circulating system

The fuel circulating system (FCS) consists of vacuum system, fuel gas refiner, isotope separator, neutral beam injector and fuel feed system. The design performed is based on the previous study[1],[2]. The main parameters of the key components are given in Table VII.3-3.

The vacuum system is compoed of 16 cryosorption pumps, 8 auxiliary vacuum systems, 8 fuel recovery systems and 8 rough-pumping systems. 8 cryosorption pumps are alternately operated at an interval of 2 hr.

In the fuel gas refiner systems, impurities are effectively removed by using Pd-alloy membranes. The system consists of twelve 360 mm^D × 1300 mm^L separators, each has effective surface area of 820 cm^2. The impure gas flows at 1 kg/cm^2 to the inside of the Pd-alloy tubes. The pressure are kept to be less han 1 Torr within the shell side.

For the isotope separation system, the diffusion method through Pd-alloy membrane was adopted. This method can separate hydrogen isotopes in their atomic states. The system consists of 1st and 2nd cascades for removing protium and separating deuterium, respectively. The numbers of

separators are 47 for 1st cascade and 46 for 2nd cascade. The effective surface area for 1st and 2nd cascades are 2.541 and 2.617 cm^2, respectively. The primary and secondary pressure are maintained at 6 and 1 kg/cm^2, respectively. Tritium inventory of the FCS is approximatel7 270 g.

Preliminary study on the tritium safety and containment has been also performed.

3.5.3 Reactor cooling and tritium recovery system

Flow diagram of this system is shown in Fig. VII.3.1-8.

Because the reactor is operated periodically, temperature changes of the blanket structures become very rapid when the flow rate of the primary coolant is kept constant. Therefore control valves should be installed in the primary cooling system to keep the flow rate proportional to the reactor power. Flow bypass line and a heat reservoir which consists of stainless tube bundle in a pressure vessel are also required in the system to stabilize the temperature and flow rate. A catalytic oxidizer is installed at the entrance of a heat exchanger in order to supress the permeation of tritium to the secondary system through the heat exchanger tubes. By installing this oxydyzer, a partial pressure of tritium in molecular form may be reduced to the level of about 1.6×10^{-9} torr at the inlet of the heat exchanger. Most of the tritium produced through nuclear reactions between neutrons and lithium in Li_2O in the blanket is emerged into helium coolant in the form of T_2O.

Even if all of tritium are in the form of molecule, partial pressure of T_2 is estimated to be about 4×10^{-6} torr at the blanket outlet. The total inventory of helium coolant is about 1 ton. The tritium is recovered at the low temperature side of the primary cooling system by installing a bypass circuit with molecular sieves, where 1 % of primary flow is circulated.

Dual tube structure was chosen for the pipings from the reactor outlet to the catalytic oxidizer outlet. Tritium leak into a annular space of dual tubes is sweeped out by purified helium gas and returned into the primary cooling flow.

Table VII.3-1 Fuel flux hitting the first wall and the limiter and impurity flux into the plasma when C, Fe, and Mo are used for the first wall and the limiter. The neutral temperature of 0.1 eV and diffusion coefficient of fuel ions of 2×10^4 cm^2/s are assumed.

Flux / Energy	Fuel (s^{-1})	Impurity (s^{-1})		
		C	Fe	Mo
10 eV	3.1×10^{25}	3.4×10^{19}		
50 eV	5.7×10^{24}	1.7×10^{20}	1.3×10^{20}	
500 eV	5.5×10^{21}	5.5×10^{18}	8.8×10^{18}	1.7×10^{18}
2 keV	3.6×10^{17}	2.3×10^{15}	3.6×10^{15}	7.6×10^{14}
7 keV	4.8×10^{13}	5.3×10^{11}	8.2×10^{11}	1.7×10^{11}
Total	3.7×10^{25}	2.0×10^{20}	1.4×10^{20}	1.7×10^{18}

Table VII.3-2 Main parameter of energy storage

Stored Energy	10 GJ
Operation Period	420 s
Maximum Operating Current	270 kA
Coil Shape	Double Solenoid
Main Coil Radius	4.15 m
Shield Coil Radius	6.43 m
Coil Length	5.5 m
Maximum Field Strength	8.0 T
Current Density	90 MA/m^2
Conductor	NbTi/Cu/CuNi/Al/SUS
Cooling	Li He Forced Cooling at 4.2K
Average Heat Load	2.0 kW
Total Weight	3200 t

Table VII.3-3 Summary of fuel circulation system

Main Vacuum System		
Gas Lord (at 300°K)		158 Torr·l/s
Number of Pumping Ports		8
Number of Cryosorption Pumps (for on-line regeneration)		8 (16)
Pumping Speed of Each Cryosorption Pump		3.3×10^5 l/s
Pumping Speed of Secondary Pumps ;		
Turbomolecular Pump for Auxiliary System		3.2×10^3 l/s
Mechanical Booster Pump for Recovery System		32 l/s
Rotary Pump for Rough Pumping System		790 l/s
Fuel Gas Refine System (Permeation System through Pd-Alloy Membrane)		
Number of Separators		12
Dimension of Separator		360 mmϕ x 1300 mmL
Effective Surface Area of Each Separator		820 cm^2
Operating Pressures :	upstream	∿ 1 Kg/cm^2
	downstream	< 1 Torr
Operating Temperature		420 °c
Isotope Separation System (Permeation System through Pd-Alloy Membrane)		
Number of Separators ;	1st Cascade	47
	2nd Cascade	46
Dimension of Separator ;	1st Cascade	140 mmϕ x 1.6 m^H
	2nd Cascade	170 mmϕ x 1.6 m^H
Effective Surface Area of Each Separator ;		
	1st Cascade	2541 cm^2
	2nd Cascade	21617 cm^2
Operating Pressure ;	High Pressure Side	∿ 6 Kg/cm^2
	Low Pressure Side	∿ 1 Kg/cm^2
Operating Temperature		420 °c

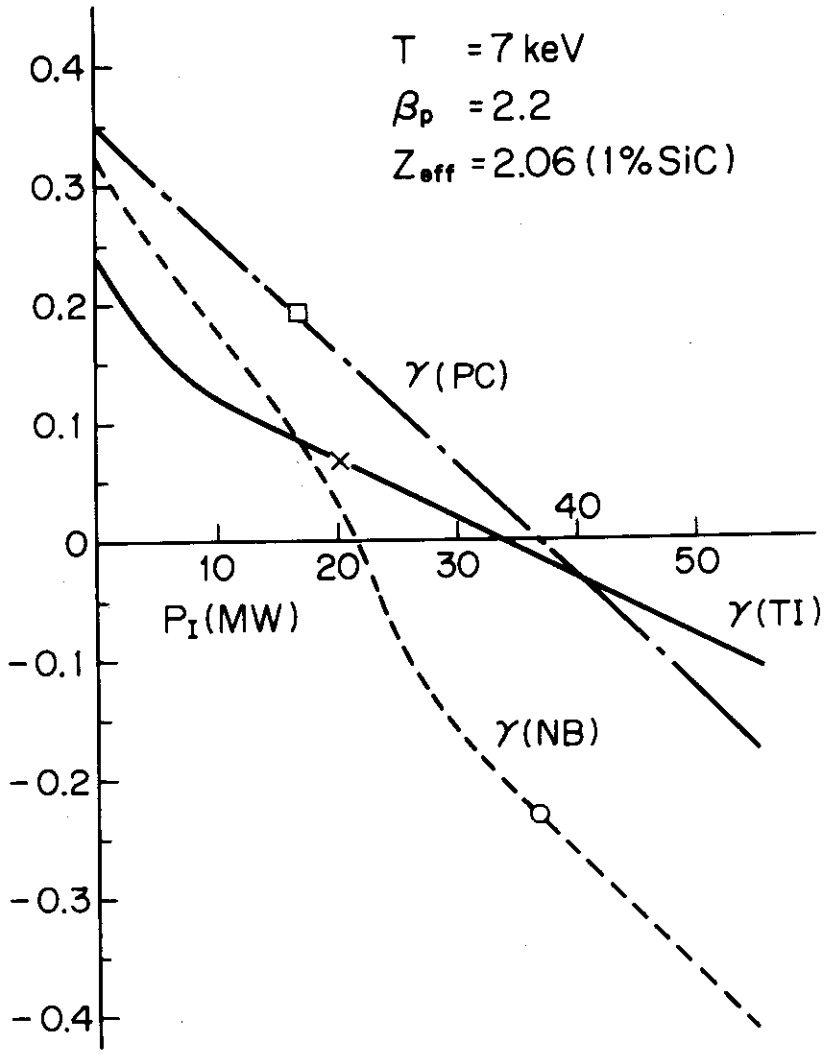

Fig.VII.3-1 Growth rates versus injection power for various scaling laws

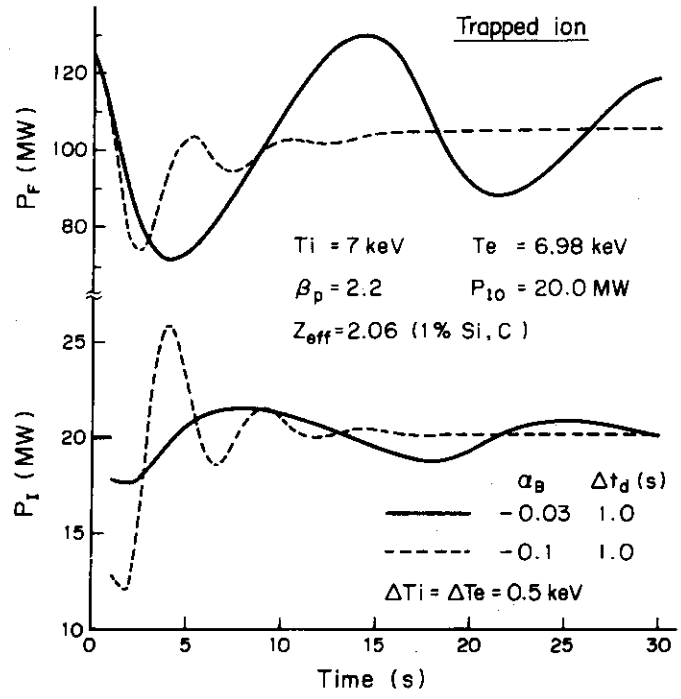

Fig.VII.3-2 Fusion power and injection power transients initiated by a 0.5 keV temperature perturbation for feedback stabilitization by injection power: trapped ion instability scaling.

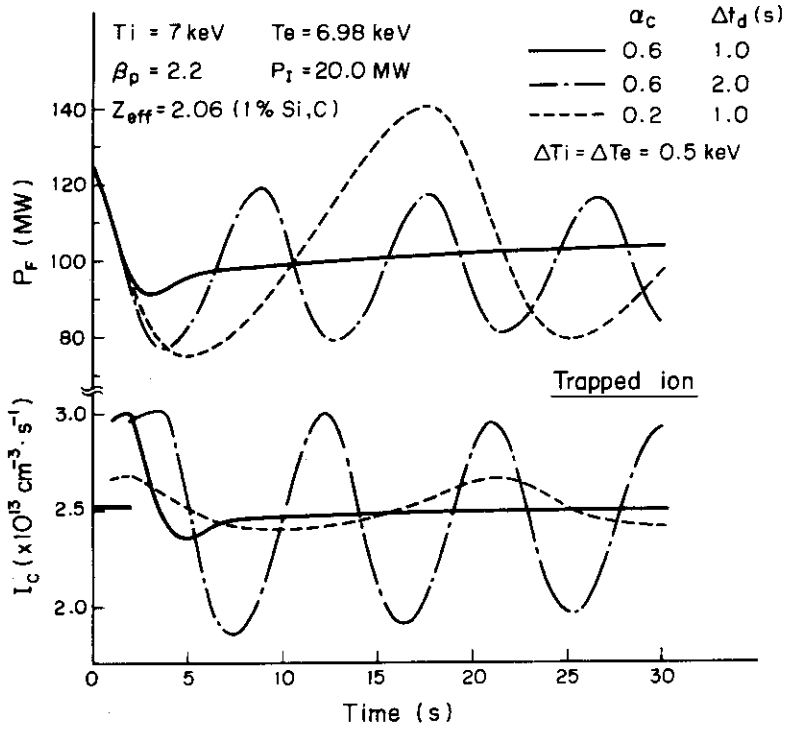

Fig.VII.3-3 Fusion power and injection power transients initiated by a 0.5 keV temperature perturbation for feedback stabilization by fueling: trapped ion instability scaling

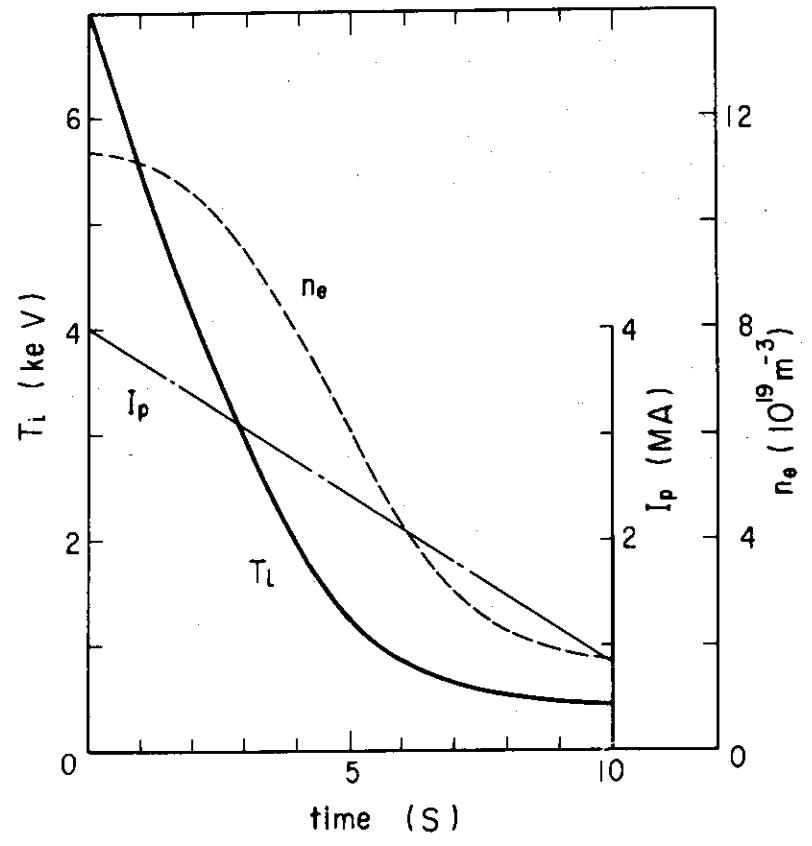

Fig.VII.3-4 Changes of ion temperature T_i, electron density n_e and plasma current I_p during the first stage in shut down process.

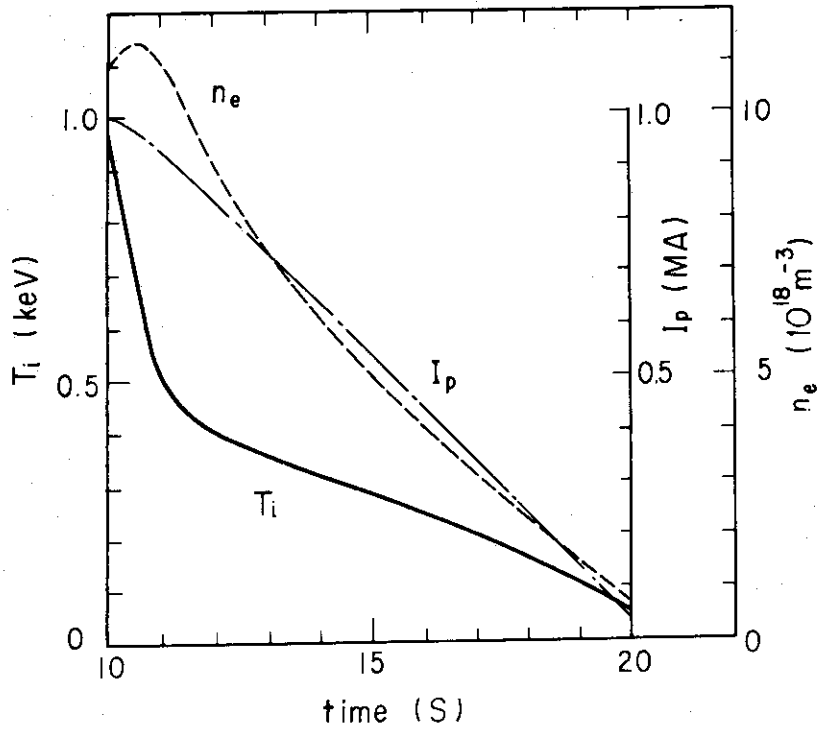

Fig.VII.3-5 Changes of ion temperature T_i, electron density n_e and plasma current I_p during the latter stage in shut down process.

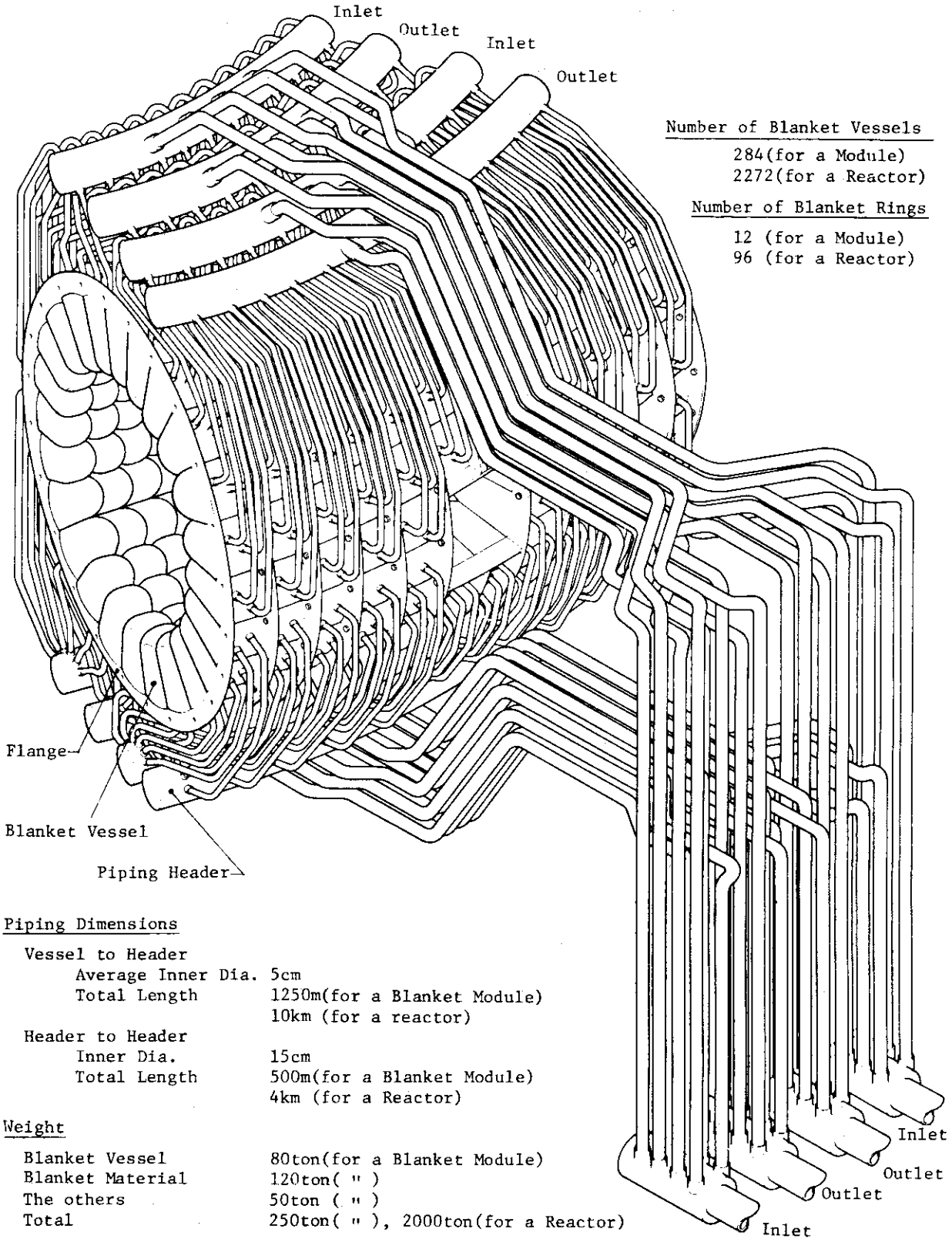

Piping Dimensions

Vessel to Header	
Average Inner Dia.	5cm
Total Length	1250m(for a Blanket Module)
	10km (for a reactor)
Header to Header	
Inner Dia.	15cm
Total Length	500m(for a Blanket Module)
	4km (for a Reactor)

Weight

Blanket Vessel	80ton(for a Blanket Module)
Blanket Material	120ton(")
The others	50ton (")
Total	250ton("), 2000ton(for a Reactor)

Fig.VII.3-6 Blanket module

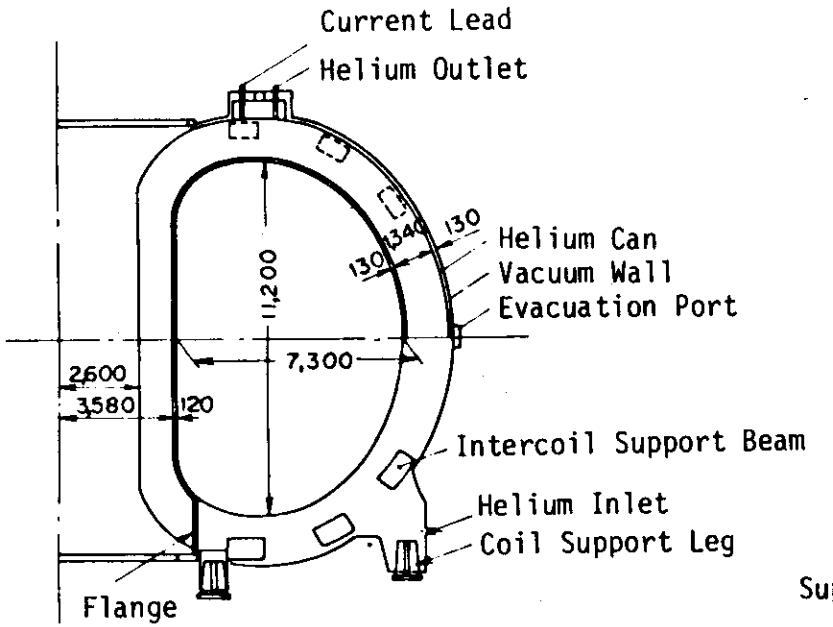

(a) Side View of TF Coil

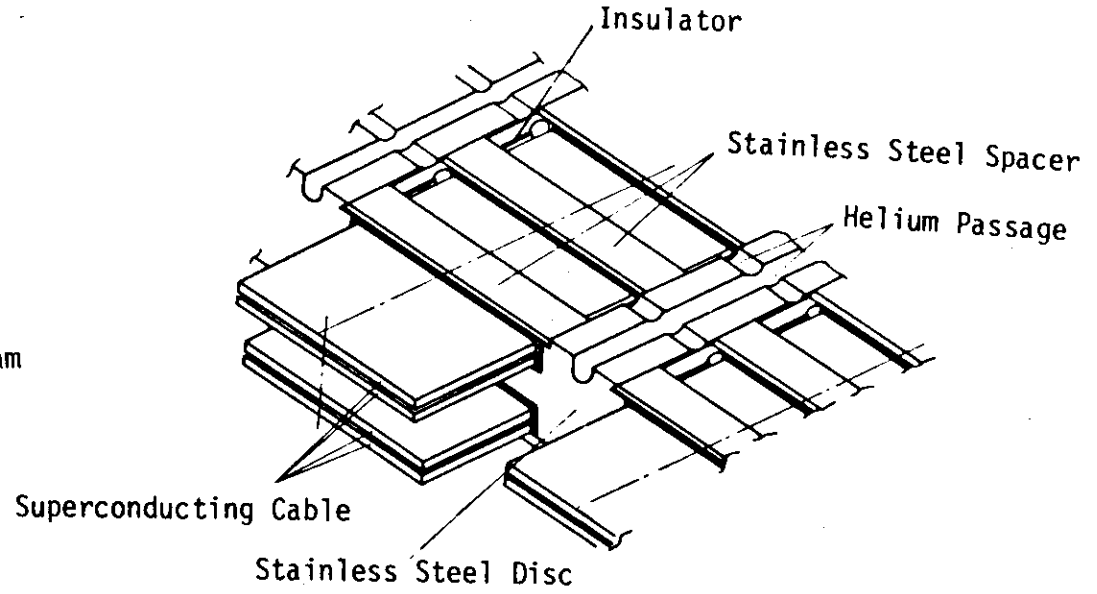

(b) Superconducting Cable and Stainless Steel Disc

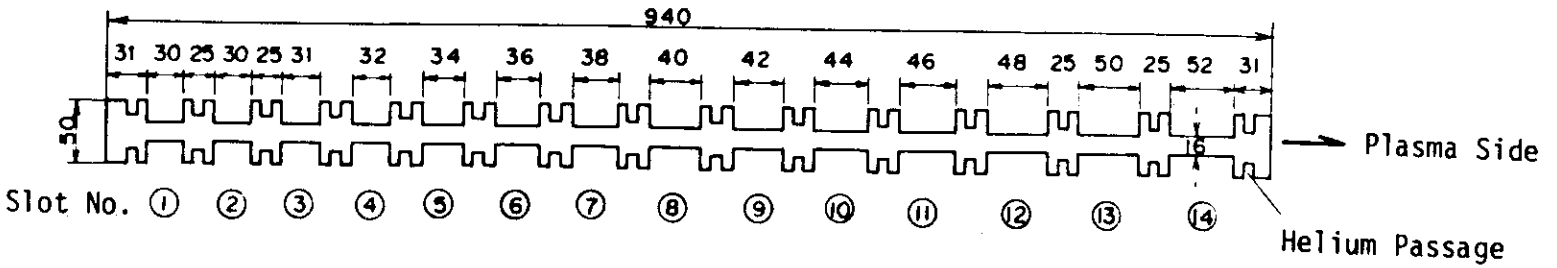

(c) Cross Section of Stainless Steel Disc

Fig.VII.3-7 Toroidal field magnet

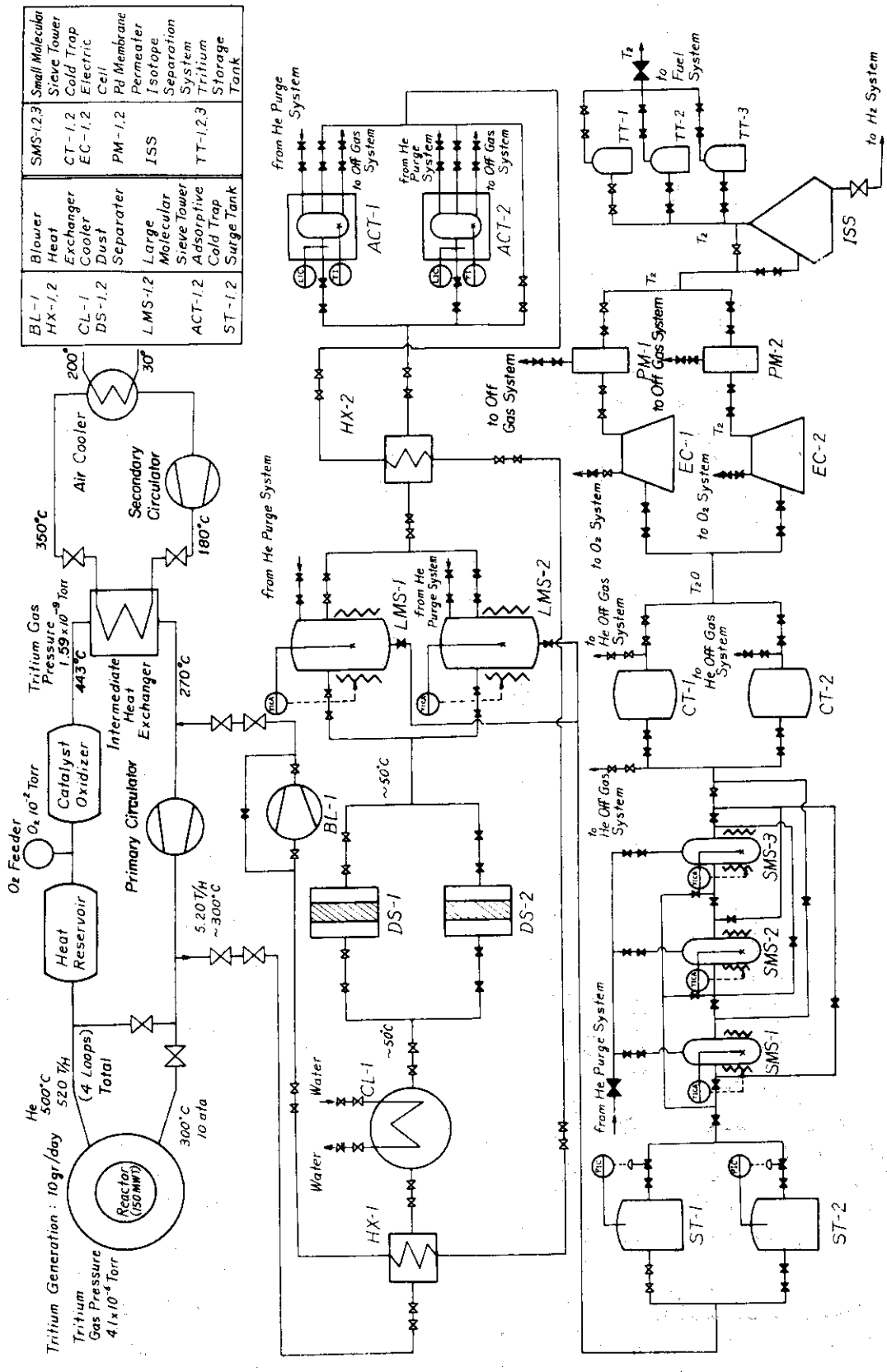

Fig.VII.3-8 Blanket cooling and tritium recovery system

4. Design Related Studies

4.1 Effects of neutron streaming through injection prots on neutronic characteristics of a fusion reactor[16]

Neutron streaming through injection ports has been studied for the fusion reactor designed in JAERI. Such streaming influences the neutronic characteristics of a fusion reactor. In placement of the injection ports of a diameter 140 cm in the designed blanket, reduction of the tritium breeding ratio is about 2 %. Neutron flux of energy over 0.1 MeV is highly peaked in the vicinity of the injection port. Further effects of neutron streaming through injection ports are studied such as radiation heating and damage in the superconducting magnets and induced activity of the injector components and coolant pipings.

4.2 Neutronics design of fusion reactors and application of blanket neutronics experiment to the design[17]

A series of blanket neutronics experiments has been carried out to examine validity of the nuclear data and calculation methods used in neutronics design of the fusion reactors. The measured fission-rate distributions in the four types of spherical blanket assemblies consisting of lithium and/or graphite and/or natural uranium are analyzed. The effects of uncertainty of the nuclear data, processing procedure of the multi-group cross sections, and approximations in neutron transport calculations upon the calculated fission-rates are investigated. The discrepancy between the calculated and measured values of fission-rates is caused mainly by neglecting the anisotropy of secondary neutrons from inelastic and (n,2n) reactions in the multigroup cross section calculation.

The results of the analysis are applied to the neutronics design of the fusion reactors to evaluate the effect of the results upon the blanket nuclear characteristics. In consequence, the substitution of the reflector material, graphite by stainless steel is recommended. It is also pointed out that the present shielding design for the superconducting magnets may be insufficient and increased attenuation may be necessary.

5. Design Study of a Power Reactor[18]

Design of a demonstration power reactor (2000 MW_t) is continued to supply the feedback informations to the design of the experimental reactor

(JXFR). The design includes the whole reactor system and detailed design studies for the repair and maintenance scheme of the reactor and for the reactor cooling system have recently been completed.

6. Safety Analysis

The following items on the safety of JXFR have been investigated;

1) The chemical form and inventory of tritium,
2) Measures to prevent tritium leakage,
3) Radiation dose rates in the reactor room and in environment,
4) Variation of induced activity with time,
5) Evaluation of hypothetical accidents.

These investigations are closely linked with the reactor design itself and are becoming more detailed as the design progresses. So far, JXFR is evaluated to be a highly safe facility. Accident analyses for the major components and subsystems are under way, and overall safety evaluation including that for the personnel is in progress.

References

(1) Sako, K., et al.: Proc. of IAEA Conf. on Plasma Physics and Controlled Nuclear Fusion Research, Berchtesgaden, 1976, IAEA-CN-35/I3-1.

(2) Fusion Reactor System Laboratory, JAERI-M 6670 (1976).

(3) Tone, T., et al.: Proc. 2nd Topical Meeting on the Technology of Controlled Nuclear Fusion, Richland, 1976, Vol.III,975 (CONF-760935-P3, 1977).

(4) Tone, T. and Yamato, H.: "Preliminary study on power balance in the plasma of an experimental fusion reactor" (in Japanese), JAERI-M 6453 (1976).

(5) Kadomtsev, B.B. and Poqutse, O.P.: Nuclear Fusion 11 (1971) 67.

(6) Sinnis, J. et al.: Phys. Rev. Lett. 30 (1972) 1214.

(7) Yoshikawa, S. and Christofilos, N.C.: Proc. 4th Conf. on Plasma Physics and Controlled Nuclear Fusion Research, Madison, 1971, Vol. II, 357 (IAEA, Vienna, 1972).

(8) Dean, S.O., et al.: WASH-1295 (1974).

(9) Ohta, M., et al.: Proc. 4th Conf. on Plasma Physics and Controlled Nuclear Fusion Research, Madison, 1971, Vol.III, 423 (IAEA, Vienna, 1972).

(10) Iida, H., et al.: JAERI-M 6639 (1976) (in Japanese).

(11) Seki, Y., et al.: JAERI-M 6540 (1976) (in Japanese).

(12) Idem: JAERI-M 6783 (1976).

(13) Ide, T., et al.: JAERI-M 6672 (1976) (in Japanese).

(14) Fusion Reactor System Lab., JAERI-M 6921 (1977) (in Japanese).

(15) Ioki, K., et al.: Proc. of Second Topical Meeting on the Technology of Controlled Nuclear Fusion, Richland, 1976, Vol.IV,1273 (CONF-760935-P4, 1977).

(16) Ide, T., et al.: Proceedings of 2nd Topical Meeting on the Technology of Controlled Nuclear Fusion, Richland, 1976, Vol.II.395 (CONF-760935-P2, 1977).

(17) Seki, Y.: JAERI-M 6726 (1976) (in Japanese).

(18) Sako, K., et al.: Proceedings of 2nd Topical Meeting on the Technology of Controlled Nuclear Fusion, Richland, 1976, Vol.II, 607 (CONF-760935-P2, 1977).

VIII. DEVELOPMENT OF A LARGE TOKAMAK ----- JT-60

1. Introduction

If the previous year 1975 is regarded as that of a significant step forward in the JT-60 Program marking the initiation of the detailed (pre-construction) design and engineering development, the year 1976 is then to be remembered as a year of even greater significance in that construction is approved by the government for substantial part of JT-60.

During the year the detailed (pre-construction) design was continued by a cooperative work of five industrial groups and was completed in November 1976. The engineering development of major components was carried out by those groups separately, one firm for the development of one component. All the engineering development contracts were completed by March 1977. Based on the evaluation of those works the specifications of JT-60 Machine was written up to issue a request for quote to industry.

The review of the JT-60 Program has been made by JT-60 Committee of Nuclear Fusion Board of Atomic Energy Commission. An interim report was issued in February 1977, and a final report is expected in summer 1977 which comprises the riview of both JT-60 and JT-4 Programs.

2. Outline of JT-60 Design

The year of 1976 is characterized for JT-60 as the final preparatory year for construction of JT-60.

The detailed design of JT-60 was carried out spending the later half of 1975 and the whole 1976. Office of JT-60 prepared the specifications of JT-60 in February, 1976.[1] It was accomplished on the basis of the results of the preliminary design in 1974 and many research and development programs. JAERI was cooperated by five industries, Sumitomo, Toshiba, Hitachi, Fuji and Mitsubishi under the contract about the detailed design.

In design studies, the essential components for the tokamak machine were deeply examined to obtain sufficient informations to prepare specifications for construction of JT-60 machine. Another purpose of the detailed design was the system design covering all necessary components other than the tokamak machine such as the electric power station or the secondary cooling system to recognize various problems for JT-60 as a whole system. They are, for examples, intercorrelation or confilict between components of JT-60 system, influence on the design by limiting

conditions from the electric line system or analysis of non-normal conditions of JT-60 system. The system design also covered common problems to the whole system such as the earth network or investigation of operation conditions. These informations provided by the detailed design are also very useful for the new site plan.

As the design work was performed, some conflicts were detected. One of them is a geometrical conflict between the poloidal field coils and the reinforcing rib or the supporting rod of the vacuum vessel. Each of them is necessitated for the vacuum vessel to stand the strong force by the induced suddle electric current along it thick-ring at plasma quenching. Therefore, some specifications were changed from the oritinal ones. Toroidal field strength at the plasma axis was reduced to 45 kG from 50 kG. The plasma minor radius was also reduced to 0.95 m from 1.0 m. The pulse duration shortened to five seconds from ten seconds to reduce the temperature rise of poloidal field coils. The results of the detailed design are described in the detailed design report.[2]

The block diagram of JT-60 is shown in Fig. VIII.2-1. In Table VIII.2-1, the main characteristics of JT-60 are summarized and in Fig. VIII.2-2, the tokamak machine of JT-60 is illustrated. The tentative building alignment of JT-60 is shown in Fig. VIII.2-3. The both machines of JT-60 and JT-4(Non-circular Tokamak) will share motor-generators.

Many research and development programs were performed to obtain the reliable informations and data to construct JT-60 with the cooperation by five companies under the contract. All of them were successfully accomplished by the end of FY 1976. Table VIII.2-2 shows items of the R & D program.

The first four of the machine-related contracts are of a large scale and in general proceeded systematically from development of materials and critical components to scaled models, then to a full-scale mode. Emphasis was placed on testing those models as well as establishing the methods of design analysis, processes of fabrication, and methods of in-process testing and quality control. The last six contracts were intended for studies of specific research subjects or development of specific items.

Power supply-related research and development programs are all associated with the poloidal field power supply. For the vacuum circuit breaker approach, a current interruption test at the world record of 130 kA were successfully performed. The development of poloidal field

power supply using a thyrister breaker was performed at lower current levels and was focussed one the tests of circuitries in which current rating of thyristers could in effect be raised significantly over continuous current ratings. An extensive study on the control of plasma position and shape was also carried out.

Results of R & D programs were immediately reflected to the detailed design through the component design studies performed in R & D programs.

References

(1) Office of JT-60: Specifications for Detailed Design of JT-60, Internal memo, 1976 (in Japanese).

(2) Office of JT-60; Detailed Design of JT-60, Internal memo, 1977 (in Japanese).

Table VIII.2-1 Main characteristics of JT-60

1.	Main Parameters		
	Plasma major radius	3	m
	Plasma minor radius, without acting magnetic limiter	0.95	m
	with acting magnetic limiter	0.85	m
	Toroidal field strength	45	kG
	Plasma current, without acting magnetic limiter	2.6	MA
	with acting magnetic limiter	2.1	MA
	Flat top durating	5	sec.
	Maximum injection power	22	MW
2.	Operation		
	Shots, at full coil currents	5×10^4	
	at 50 % coil currents	1.5×10^5	
	pulse discharge cleaning	1×10^5	
	Shot interval at full coil current discharge	10	min.

Table VIII.2-2 "Machine"-related research & development contracts

Items	Company	Completion	Milestones
Toroidal Coils	Hitachi	Feb. 1977	A 1/1 pancake 1/5 coils A 1/1 3-T coil
Poloidal Coils	Toshiba	Feb. 1977	A 1/1 block 1/2 coils A 1/1 Mag.Lin. connecting coil section sections
Vacuum Chamber	Hitachi	Feb. 1977	A 1/1 30-Deg 1/5 sectors sector
Movable Limiter	Sumitomo	Dec. 1976	A 1/1 model
Transient Surface Heating Study	Mitsubishi	Feb. 1977	To 1 kW/cm on Wall Materials and Honeycomb Plates
Study on Joint of Ring & Bellows	Sumitomo	Sept. 1977	Stress analysis & model tests on Joints of Vac. Cham.
Low-Z Materials	Hitachi	Dec. 1976	Analysis and test
Honeycombs & C	Hitachi	Dec. 1976	Fabrication study
Outgas & Sputt.	ULVAC	Dec. 1976	Test on Wall Materials
Study on Joints of Pol. Coil	Hitachi	Dec. 1976	Stress analysis & tests on Poloidal Coil Joints

"Power Supply" & "Control" - related research and development

Items	Company	Completion	Milestones
Pol Field Power Supply (Vacuum Circuit Breaker)	Toshiba	Feb. 1977	1/2 current test, 1/50 & 1/1000 circuit models
Pol Field Power Supply (Thyrister Circuit Breaker)	Hitachi	Feb. 1977	1/20 current test, 1/1000 circuit model
Feed-back Control of Plasma Position & Shape	Toshiba	Nov. 1976	Analysis and computer simulation on Feed-back control of equilibrium
Protection CCT. for Pol. Field Power Supply	Fuji Electr.	Dec. 1976	Analysis of transients in Pol. coils & Power supply & Protection

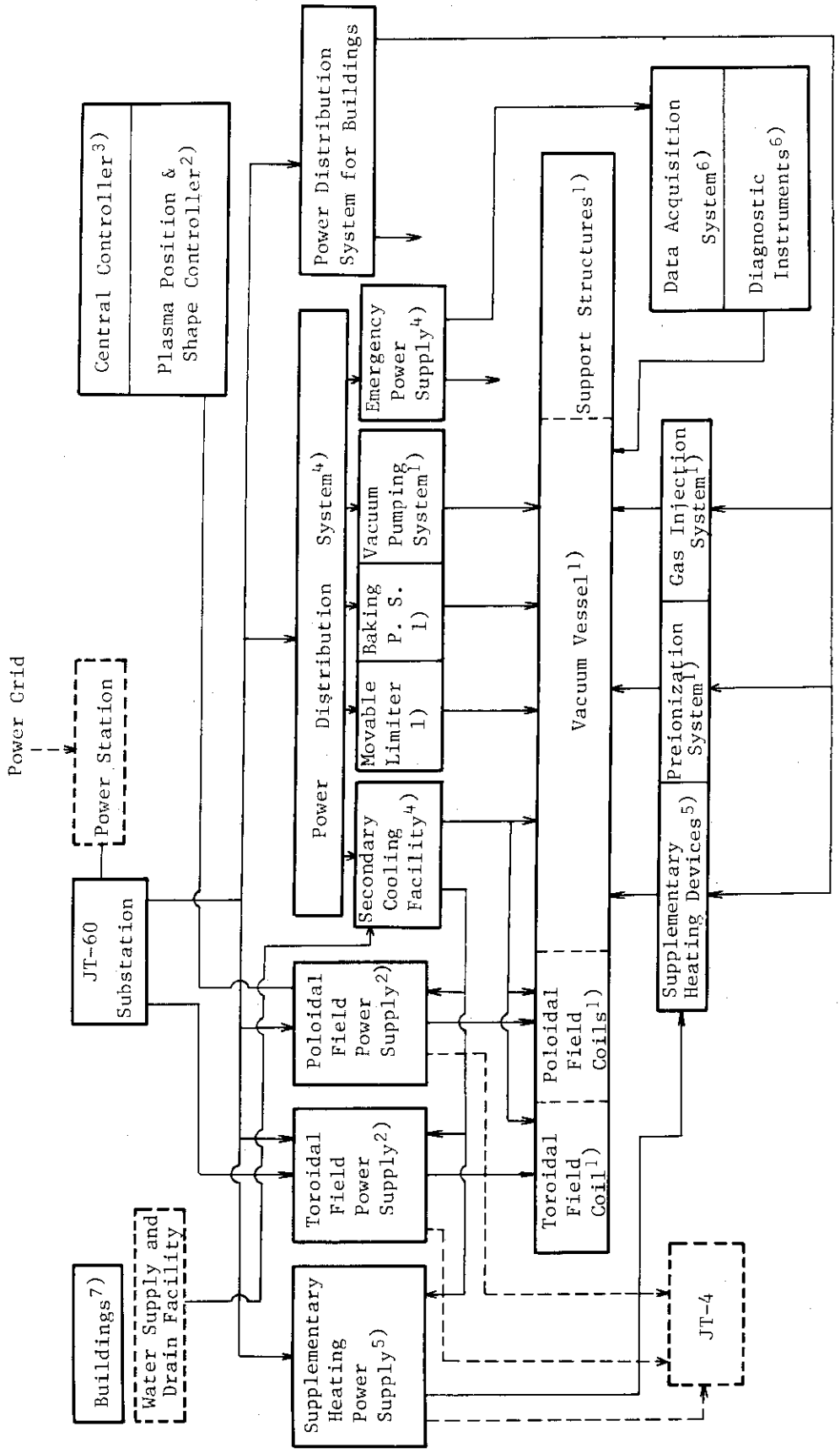

1) Machine
2) Power Supplies
3) Control
4) Auxiliary Facilities
5) Supplementary Heating System
6) Diagnostic and Data Acquisition System
7) Buildings

Classification:

Fig.VIII.2-1 Functional Block Diagram of JT-60

1 Vacuum vessel
2 Liner
3 Fixed limiter
4 Magnetic limiter plate
5 Toroidal field coil
6 Poloidal field coil other than magnetic limiter coil
7 Magnetic limiter coil
8 Supporting structure
9 Vacuum pumping system
10 Neutral beam injector
11 Movable limiter

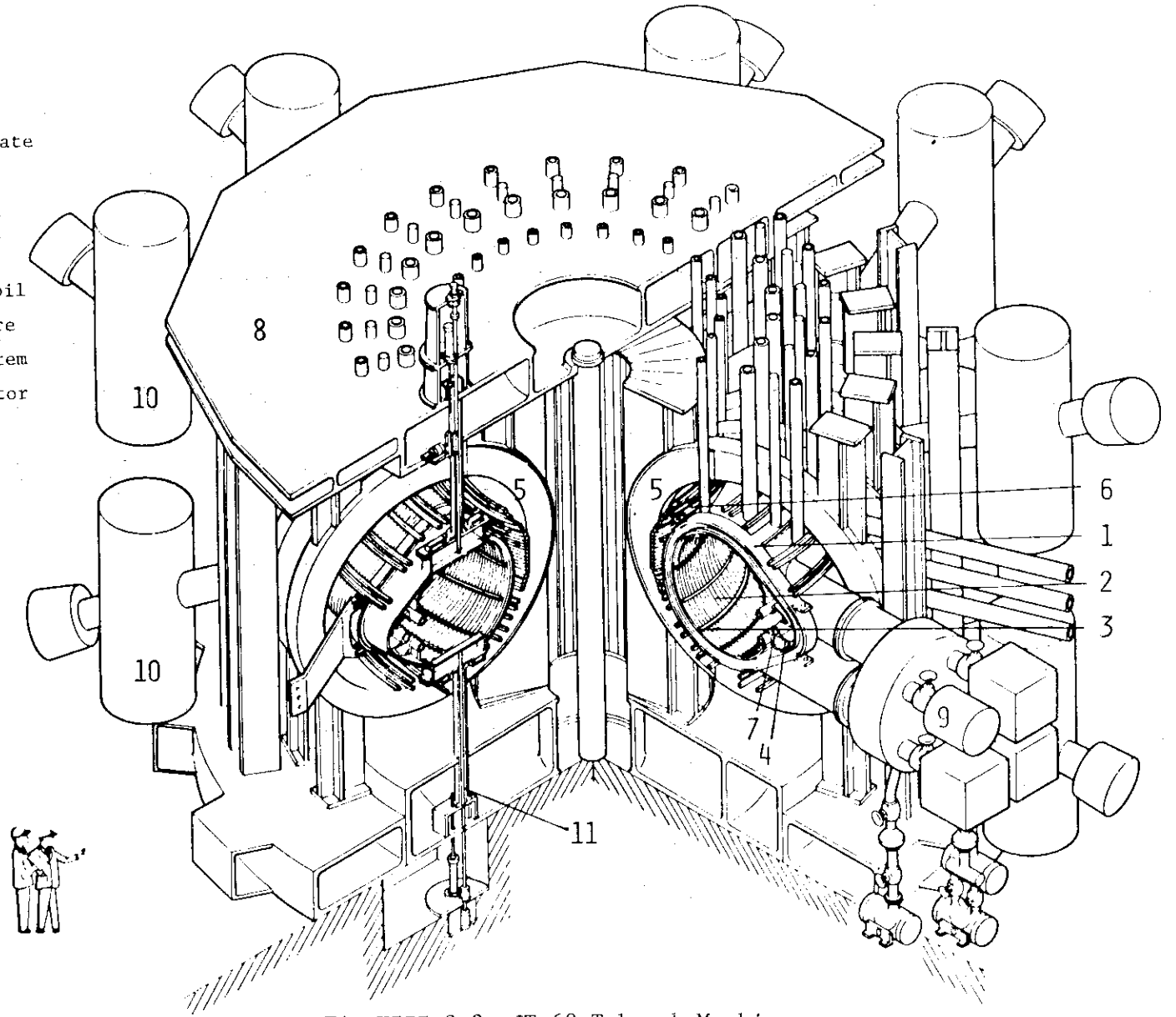

Fig.VIII.2-2 JT-60 Tokamak Machine

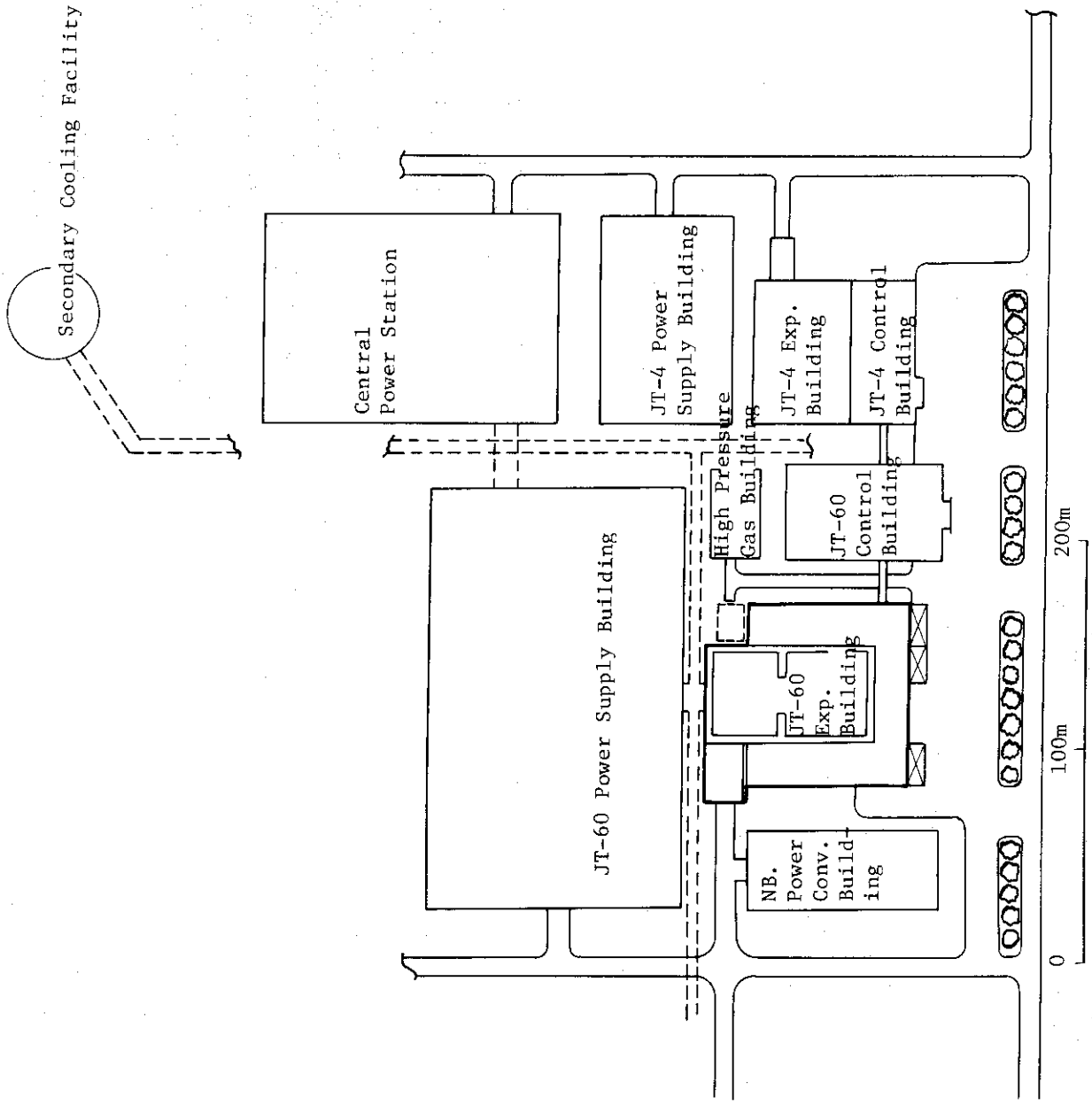

Fig.VIII.2-3 Site plan of JT-60 and JT-4

3. Design of Machine

3.1 Review of machine design

3.1.1 System design

JT-60 machine is composes of a vacuum vessel, toroidal field coils, poloidal field coils, support structures, a primary cooling system, movable limiters, a vacuum pumping system, a plasma monitor system, a gas supply system, and a preionized system. The latter four systems are described in Section 5 and 6.

The design conditions have been frozen by settling the conflict between the requirement of plasma physics and the present engineering technique. The results of the development of each component carried out from fiscal 1976 to fiscal 1977 have been partially taken into the present design. Main design conditions are as follows. (a) Total operation cycles of 3×10^5 and rated operation cycles of 5×10^4 are required for the machine life. (b) The total exposure, the maximum exposure intensity per shot, and the maximum energy of X-rays due to runaway electrons are 2×10^8R, 10^5R, and 10 MeV, respectively. (c) Typical plasma current of 2.7 MA decreases to zero in at least 50 msec. (d) The negative spike of plasmas induces the one-turn voltage of 3 kV with the pulse length of 100 $\sim$ 400 μsec. (e) The magnitude of the earthquake does not exceed 0.3 G.

The design has taken into account the assembly/disassembly, the matching between the components, the earthquake proof, the transportation from industries to the construction site, the environmental assessment, the reliability, faults and their interlocks, tests, and inspections during and after construction, and so on.

3.1.2 Vacuum vessel and its auxiliary components

Specifications of the vacuum vessel and its auxiliary components are shown in Table VIII.3.1-1 and Table VIII.3.1-2, respectively.

1) Vacuum vessel

Fig. VIII.3.1-1 show a cross-sectional view of the vacuum vessel. The material is Inconel 625. Electric resistance of a torus should be higher than 1.3 mΩ. The helium leak rate, the outgassing-rate and the ultimate vacuum pressure are lower than 5×10^{-7} torrℓ/sec, 10^{-11} torrℓ/sec cm^2 and 10^{-8} torr, respectively. The baking temperature will be above 500°C

Table VIII.3.1-1 Specifications of vacuum vessel

Structure	U-shaped Bellows and Thick Rings
Cross Section	Ref. Fig. VIII.3.1-1
Materials	Inconel 625 Stainless steel (port only)
Magnetic Permeability	<1.02
Electric Resistance	>1.3 mΩ
Allowable He Leak Rate	$<5 \times 10^{-7}$ torrℓ/sec
Expected Outgassing-rate	$<1 \times 10^{-11}$ torrℓ/sec cm^2
Expected Ultimate Vacuum	$<10^{-8}$ torr
Baking Temperature	
Vacuum Chamber	500°C
Ports	250°C
Vacuum Seal	
Vacuum Chamber	Welding
Ports	Metal Seal
Earthquake Proof	0.3 G

Table VIII.3.1-2 Specifications of liner, fixed limiter and magnetic limiter plate

Material	Molybdenum
Cross Section	Ref. Fig. VIII.3.1-1
Thickness	
Liner	5 mm
Collector Plate	20 mm
Baking Temperature	200 ∿ 500°C
Expected Outgassing Rate	$<10^{-11}$ torrℓ/sec cm^2
Earthquake Proof	0.3 G

for the vacuum vessel and 250°C for the ports. The vacuum vessel is composed of U-shaped bellows and thick rings. The vacuum vessel is supported at the thick rings by bars extended from a support structure. The vessel is heated by nonmagnetic electric heaters and cooled by water pipes wound around it.

A vacuum vessel is loaded by centripetal forces both toward the major axis and toward the minor axis due to the atmospheric pressure. The centripetal force toward the major axis is about 300 ton and that toward the minor axis is over 1500 tons. The electromagnetic force produced by the interaction of the loop current (0.4 MA) with the poloidal field and by that of saddle current at the thick ring with the toroidal field are less than 0.5 Kg/cm^2 and 5 Kg/cm^2, respectively. The maximum stress caused by the above forces and thermal expansion is about 32 Kg/mm^2 when the hight, pitch and thickness of the bellows are 70 mm, 20 mm and 2.5 mm, respectively.

Moreover, another stress is added to the above at the connection with the thick ring. This local stress is caused by the difference of radial deflection between the bellows and the thick ring. In order to decrease this deflection, the thick ring is vertically supported by supporting rods which restrict the deflection caused by the electromagnetic force due to saddle current and do not restrict the thermal expansion.

2) Liner

Rectangular liners are attached to the inner surfaces of the vacuum vessel. Liner material is molybdenum. Molybdenum is considered a good material for a liner because of the high melting temperature and low sputtering yields. The baking temperature is 500°C and the outgassing rate is expected less than 10^{-11} torrℓ/sec·cm^2. The thickness, width and length of the liner are about 5 mm, 80 mm and less than 400 mm, respectively. The longest liners overhanging the bellows have slits to decrease the electromagnetic force. The temperature of the liners around the magnetic limiter rises up to about 700°C. The shape of the liner surface will be selected from flat or honeycomb.

3) Fixed limiters

Axisymmetric fixed limiters are placed on the inner surfaces of the vacuum vessel as shown in Fig. VIII.3.1-1. Their material, baking tempera-

ture and outgassing-rate are the same as those of the liner. The maximum temperature of the fixed limiter will be about 2,200°C under the severest condition with heat load of 22 MW × 10 sec. The limiter has slots on its surface to decrease thermal stress. And the surface of the limiter is treated by electro-polishing.

4) Magnetic limiter plates

Magnetic limiter plates are positioned on the outer side of the vessel. Fig. VIII.3.1-2 shows the schematic view of the magnetic limiter plates. The material, baking temperature and outgassing-rate are the same as those of the liner. Cooling is done by N_2 gas. In normal operation, the heat load is about 500 W/cm^2 × 2 cm^2 width. The maximum surface temperature rise is 430°C. The maximum thermal stress is 5.6 kg/mm^2 (compression). The mechanical stresses due to the electromagnetic forces are small enough to disregard. The design effort is made to reducing the heat load of the magnetic limiter plate that the intersection of a separatrix line and the plate is fluctuated over the length 10 cm during a discharge by superposing the current of small amplitude and a frequency of 5 Hz on the quassisteady current of the magnetic limiter coil. The surface damage due to runaway electron bombardment is under consideration.

3.1.3 Toroidal field coil

The toroidal field (TF) coil system consists of 18 coil blocks with a circular shape which is shaved at the center side of the torus. The coil bore is 3.88 m and its outside diameter is 5.64 m. 18 coil blocks equally spaced at a major radius of 3.32 m will maintain the field ripple to less than 0.3 % in the plasma region. This arrangement of TF coils provides access to the vacuum vessel for neutral beam injections, diagnostic instrumentations and vacuum lines. It also provides a structural assembly which resists the torque imposed by interaction with the poloidal field.

The coils will be operated in pulse mode with a DC current of 52.1 KA which is ramped up to the desired flat top value, held for 5 seconds and then gradually decreased. In this mode of operation, the TF coil system will produce the required magnetic field of 45 KG at the plasma center of 3.0 m.

Detailed specifications for the TF coil system are listed in Table VIII.3.1-3.

Table VIII.3.1-3 Toroidal Field Coil Specifications

Number of coil	18	
Coil current	52.1	KA
Total turn	1296	turn
Coil major radius	3.32	m
Coil inside radius	1.94	m
Coil outside radius	2.86	m
Field at plasma center	45	KG
Maximum field in coil	98	KG
I^2R	390	MW
$1/2\ LI^2$	2.85	GJ
Equivalent square wave pulse length	38	sec
Total energy consumption per pulse	8.66	GJ
Coil inductance L	2.1	H
Coil resistance R	84	mΩ
Coil time constant L/R	25	sec
Maximum current density	26.8	A/mm^2
Forcing voltage	7.5	KV
Flat top voltage	4.4	KV

One coil block consists of two pancake coils is surrounded by metallic outer case. The two pancakes are connected in series to provide 72 turns for each coil block. There are two parallel cooling circuits per turn. Coolant enters the coil and makes two turns and then exits the outlet manifold. Thickness of turns is designed to make temperature rises uniform in the conductors at the smallest cross section where both the current density and stress are the highest. It becomes clear after studing the results of the numerical analysis and the experiment using 1/2.5 size linear model that the maximum temperature rise attains to 70°C at the smallest cross section.

The conductor of coils is fabricated from two kinds of copper materials. One, which is used in the half turn of the center column side, is 0.2 % Ag-OFC (Oxygen Free Copper) of 40 % cold working ratio and the other, which is used in the other half turn, is OFC of 20 % cold rolled. These conductors are connected by brazing at the top and bottom region where the tensile stress is not so high. Each turn is insulated by a layer of 1 mm thick F-stage insulation composed of epoxy resin semicurred polyamid paper and glass fiber non-woven sheet. This layer is inserted between the turns during winding process. After winding the pancake, these turns of conductors are molded by curing impregnated epoxy resin of

the layer insulation to make hard block of conductors. The pancake is wrapped with additional layer of 10 mm thick F-stage ground insulation composed of epoxy preimpregnated mica tape and epoxy glass tape as a reinforced matrix.

The ideal toroidal field would be produced by a current sheet in shape of a torus generated as a surface of revolution with a circle as the generatrix. However the growth of an irregular field cannot be avoided in the design because of access for various ports, a group of 18 individual and discrete coils, and tolerance of manufacturing and positioning. Three different computer codes were used in order to estimate the distribution of the magnetic field in detail. To provide a 45 KG field in the plasma center, a total of 67.5 MAT is required. The maximum field occurs at the inner radius of the copper in the horizontal symmetry plane and has the value of 98 KG. The percent ripple and the stray field are expected to be less than 0.3 % and 30 G in the plasma region, respectively. The stray field is caused by the leads and the return winding. In order to keep the error field less than 30 G, a tolerance of manufacturing and positioning must be restrained within a few millimeters.

The TF coils must withstand magnetic forces produced by the toroidal and poloidal field and thermal expansion. Magnetic forces consist of centering force of 100,000 tons, radial force of 270,000 tons and torque of 26,000 tons-meter. The stress analysis which takes into account these forces and thermal expansion has been carried out numerically by means of finite element method. The maximum stress intensity of 18 $\sim$ 22 kg/mm^2 is produced in the conductor at the smallest cross section of coils. This value is lower than 0.2 % yield strength of about 30 kg/mm^2 and fatigue strength of 28 kg/mm^2 at 50,000 cycles for 40% cold rolled copper containing 0.2 % silver.

Each TF coil is provided with instruments for monitoring the running state and protecting against abnormal states.

3.1.4 Poloidal field coils

The poloidal field coil (PF coil) assembly is classified into two groups, one consists of ohmic heating coil (OH coil), vertical field coil, quadrupole field coil and horizontal field coil, which are located inside the toroidal field coil bore and outside the vacuum vessel as well, and the other magnetic limiter coil inside the vacuum vessel.

Each turn of these coils must be provided with demountable mechanical

joints from the assembling point of view. This is one of the most important requirements for the design of PF coils.

The specifications of PF coils are shown in Table VIII.3.1-4.

Table VIII.3.1-4 Poloidal field coils specifications

Parameter		OH	V	Q	H	M
Ampere turns (MAT)		±5.5	±1.8	±0.5	±0.13	±0.75
Total turns		60	64	40	12	16
Max. current (kA)		91.7	57.3	21.7	25	94.4
I^2R (MW)		29.3	37.5	1.7	8.8	22.6
1/2LI (MJ)		35.3	18.7	0.1	1.1	4.1
Time const. (sec)		2.4	8.8	0.4	0.3	0.4
Max. current density (A/mm^2)		18.9	27.5	16.4	20.0	27.7
Equivalent square wave pulse length (sec)		7.3	5.8	6.8	7.0	5.6
Working voltage (kV)	ground	<30(AC peak)	<25	<10	<5	<5
	turn-to turn	<1.5(AC peak)	<1.5	<1.5	<1.5	<1.5
Others		$\Delta\phi \sim$ 2.5 v.s	n=0.3∿0.7 B_Z=3.3kG $n=-\frac{R}{B_Z}\frac{\partial B_Z}{\partial R}$	B_Z=±250G at R=R_O±0.5 m	B_H∿200G	

Conductors of the PF coils are made of 0.2 % silver bearing copper. The cooling water pipe is soldered in the groove at one edge of each conductor. The OH coil will be subjected to relatively high normal operating voltage of 25 kV (peak value), then each turn is wrapped with a layer of 5 mm thick F-stage ground insulation of mica-epoxy material. Taking account of the high temperature baking and the hot wall operation, the magnetic limiter coil can be heated nearly up to a temperature of 500°C. In order to adjust the difference of thermal expansion between the can and the coil, a special sliding mechanism is adopted inside the can. Each PF coil block will be subjected to high electromagnetic forces. Considering the assembling procedure of the whole machine, it was determined to provide 18 stainless steel columns between the toroidal field coil blocks which support the PF coil support frames. Moreover, in order to get longer creepage distance between the mechanical joints of conductor

at high potential and the stainless support frames at ground potential, at least three blocks of support frame should be made of special type of FRP.

Comprehensive analytical works were carried out to get sufficient design data for the PF coils. As a result of thermal analysis, the maximum temperatures at the normal part and at the mechanical joint are 70°C and 86°C, respectively, assuming the inlet water temperature of 42°C. The hoop stress due to the electromagnetic force is approximately 3 kg/mm^2 in the OH coil. Considering the bending moment, somewhat higher stress will appear in the coil conductors. The maximum stress in the stainless steel support structure is 12 kg/mm^2. It is found from the result of surge voltage analysis that the maximum turn- to-turn voltage due to the plasma abnormal discharge is approximately 1000 V, whereas the maximum voltage during the normal operation is approximately 500 V. The stray field produced by the OH coil current should be less than 100 G in the plasma region.

3.1.5 Primary cooling system

The primary cooling system of JT-60 is divided into two separated groups - the field coil (TF coils and PF coils) cooling system and the vacuum vessel cooling system. Each system is composed of various components such as pumps, heat exchangers, ion exchangers, filters, a storage tank, valves and pipings.

The average power dissipated in each component is as follows; (a) 16.0 MW in the TF coils, (b) 5.0 MW in the PF coils and (c) 2.0 MW in the vacuum vessel. The energy in each component is carried by the primary coolant and transfered to the secondary coolant and then released in the air at the cooling towers. The coil cooling system is designed to be able to remove the energy dissipated in the field coils by the machine pulse within 600 seconds interval following each pulse.

Since the cooling system provides an electrical path to ground from the conductors of the various coils, it is required that the cooling water is extremely pure, and of high electric resistivity. The resistivity should be at least 10^5 Ω-cm. It is also necessary to provide the cooling system with a clean up subsystem capability for purifying the initial water charge and subsequent makeup water as well as maintaining the high water quality.

This cooling system is provided an adequate capacity to allow for

the operating system without a performance penalty when components of the system are down for maintenance. Therefore, the components such as primary pumps, heat exchangers are in a parallel hook up. The specifications for the cooling system are listed in Table VIII.3.1-5.

3.1.6 Support structure

Support structure consists of upper and lower support structures, a center column, support columns and support arms of vacuum vessel, support arms of toroidal field coils and poloidal field coils and connecting arms as shown in Fig. VIII.3.1-3. Support structure must have enough strength to endure the weight about 4,500 tons, several types of electromagnetic forces and earthquake etc.

Upper and lower support structures are separated into 10 parts to reduce the eddy current, respectively. Major-radial spring constants of the center column are distributed in the axial direction to decrease the stresses on the toroidal field coils. Connecting arms connect the upper support structure and the building, and support the twisting moment of the toroidal field coils. The detail of support structure is to be determined.

3.1.7 Fast movable limiter

A pair of the fast-acting movable limiters are to be installed in the vacuum vessel of JT-60 to suppress skin current in the plasma column. They should travel across the vacuum vessel over a stroke of about 1 m in 0.1 sec in the build-up phase of the plasma current. Each movable limiter system consists of the drive system, a vacuum seal, a bearing usable at high temperature in a vacuum, a molybdenum rail limiter head and its auxiliary members. For the drive is used a hydraulic mechanism with servovalves to control the oil flow. For the vacuum seal are welded Inconel 718 bellows supported by pantographs. For the bearing is adopted a self-lubricant material. The limiter head strengthened by a SUS 304 support is cooled by air flowing through the support during 10 min.

Table VIII.3.1-5 Cooling system specifications

		the field coil system	the vacuum vessel system
Total removal energy	MW	21	2
Total water flow rate	m^3/hr	2800	230
Maximum system pressure	kg/cm^2G	16	12
Number of pump		4	2
Number of heat exchanger		5	1
Max. outlet temperature from heat exchanger	°C	42	
Resistivity of coolant	Ω-cm	10^5	
pH of coolant		5∿9	

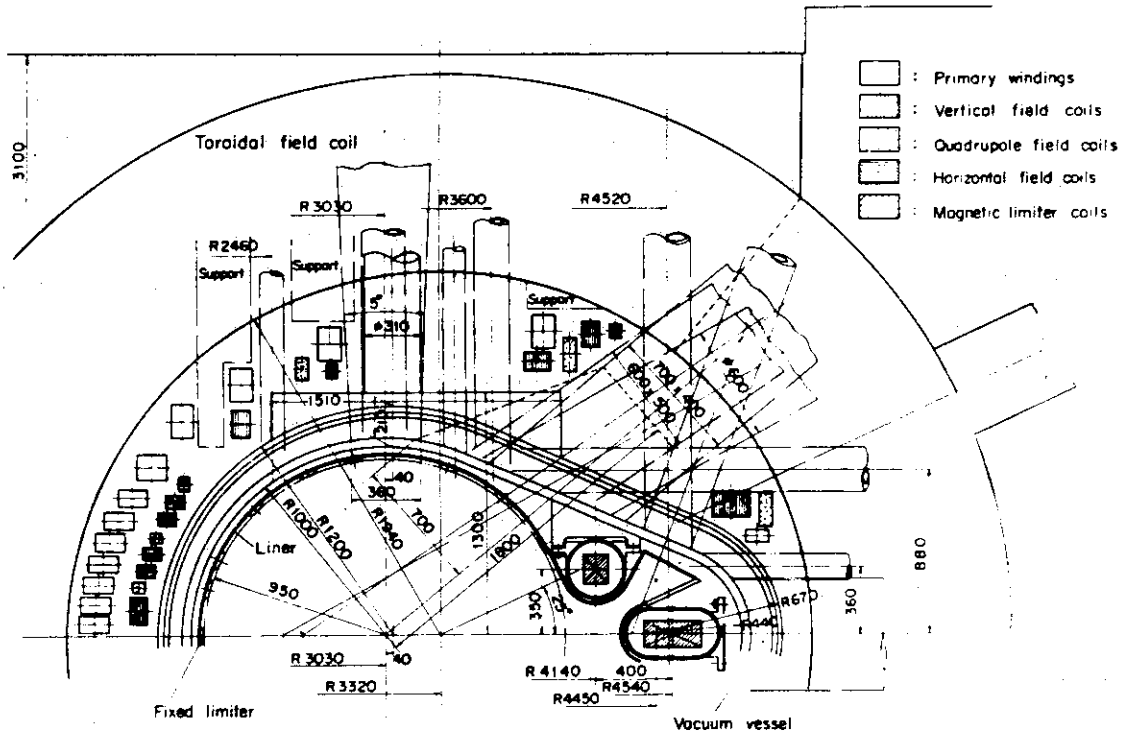

Fig. VIII.3.1-1 Cross sectional view of a vacuum vessel

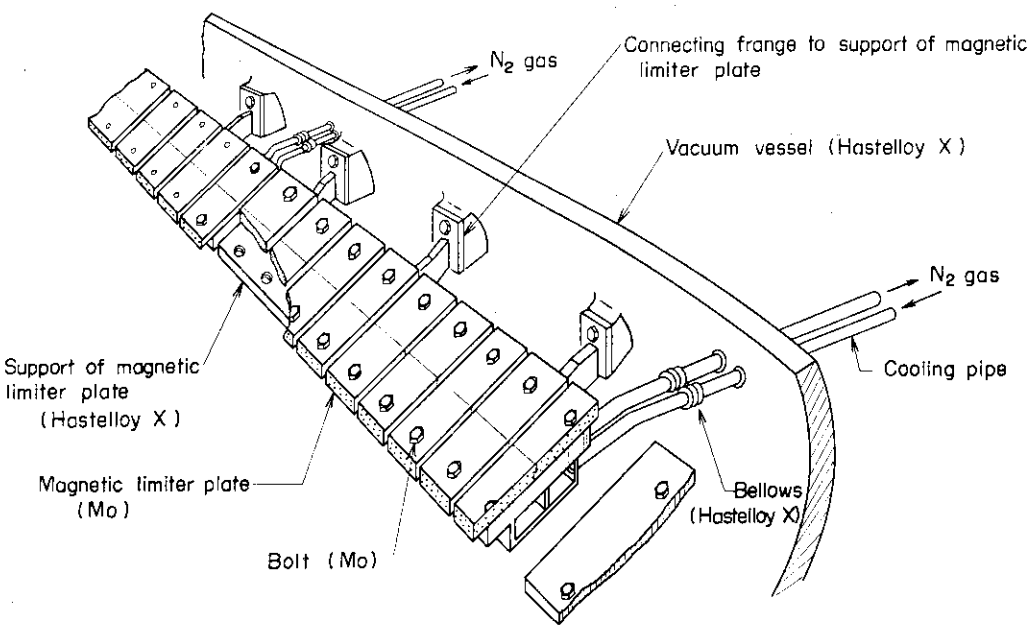

Fig. VIII.3.1-2 Components of magnetic limiter plates

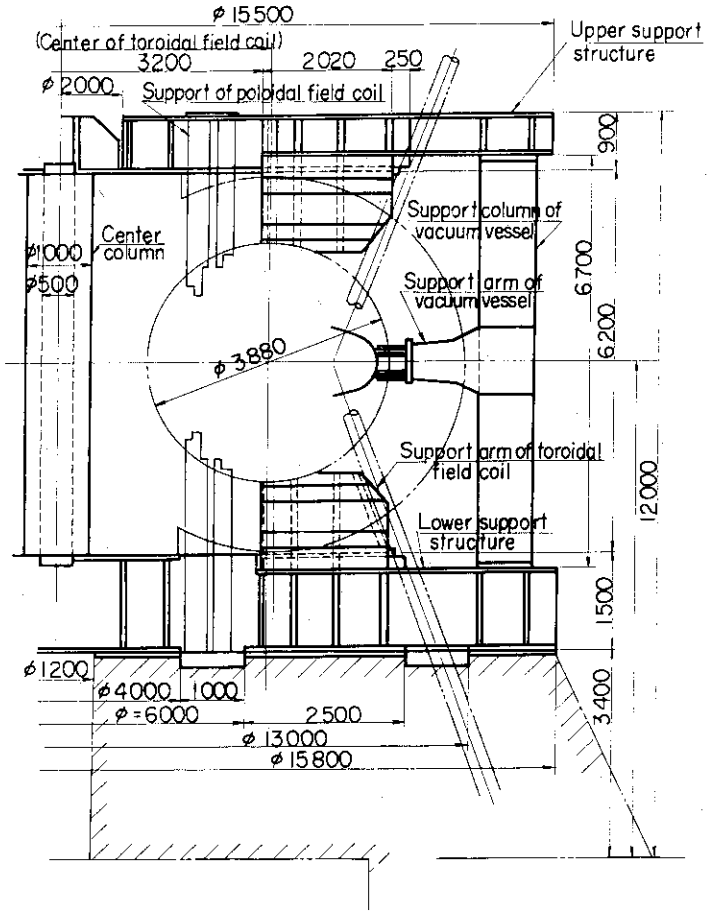

Fig. VIII.3.1-3 Support structure

3.2 Development of components

3.2.1 Vacuum vessel

(a) Selection of the vacuum vessel material

In order to select the vacuum vessel material from several candidates such as Inconel 625, Hastelloy-X, Inconel X-750, SUS304L and so on, various examinations have been carried out on physical, mechanical, electrical, and vacuum properties, feasibility to manufacture, weldability and formability.

As the results of the examinations Inconel 625 and Hastelloy-X were selected for the final candidates of material.

(b) Mechanical tests of Inconel 625 and Hastelloy-X

Mechanical properties of Inconel 625 and Hastelloy-X were examined through the following test items (1) ∿ (5).

Two kinds of specimens, welded joints and parent metals, were tested under different conditions of a room temperature and a baking temperature of 550°C.

Test items are as follows.

(1) The tension test

(2) The fatigue test under the completely reversed stress

(3) The tensile creep test

The results of the test items (1), (2) and (3) are shown in Table VIII.3.2-1, VIII.3.2-2 and VIII.3.2-3, respectively.

(4) The bending fatigue test of the multiple repeated stress in three stress levels

The specimens used in the present tests have the same structure as the connection between the thick ring and the bellows of the vacuum vessel.

The load and its repetition cycle simulate the electromagnetic forces, thermal loads and vacuum pressure under the operation of JT-60, that is, the stress of each specimen was changed from 31 kg/mm^2 to 51 kg/mm^2 under the multipule repeated stress of 10^7 cycle.

No change was found in all specimens.

(5) The bending fatigue test of the long duration heating material

Inconel 625 and Hastelloy-X become brittle when they are heated in the range 600°C to 1000°C for a long period.

The fatigue limit obtained in item (5) was higher than or equal

to that obtained in item (2).

(c) Development of the method for analyzing stress, strain, buckling, vibration and temperature distribution of the vacuum vessel

Developed was a computer code to analyze stress and strain of bellows with a non-circuler cross section and a thick ring with diagnostic ports, in which the bellows was replaced with the orthotropic plates having the same rigidity as the bellows.

Experiments were carried out using three one-fifth and a full scale models of JT-60 vacuum vessel to examine the applicability of the code.

Experimental results showed a good agreement with computed ones.

In order to analyze the temperature distribution, thermal tests were performed using a full scale partial model of JT-60 vacuum vessel.

Experimental results were in sufficient accord with the calculated ones.

(d) Development of the method to manufacture bellows with a non-circular cross section

The thickness, the pitch and the height of the U-shaped bellows were decided to be 2.5 mm, 20 mm and 70 mm, respectively.

Horizontal and vertical inside dimensions of the bellows are 3100 mm and 2300 mm, respectively.

Six full scale and twelve one fifth models of U-shaped bellows made of Inconel 625 and Hastelloy-X were manufactured for trial using hydraulic press and jacks and all of them satisfied the required specifications sufficiently.

Present R & D has made clear the manufacturing technique of U-shaped bellows.

The upper limit of the number and height of bellow with 2 mm thick seem to be 9 and 80 mm, respectively from the technique viewpoint.

(e) Development of welding method of connection between thick ring and bellows

Several kinds of connection structure were tested with respect to welding work, mechanical strength, fatigue and vacuum tightness.

The results show that these connection structure are satisfactorily applicable to the vacuum vessel of JT-60.

(f) Fabrication of connection of the vacuum vessel for the assembling and disassembling

The connection has sufficient mechanical strength by bolts and vacuum tightness by weld.

Two types of connection structure shown in Fig. VIII.3.2-1 are proposed.

(g) Final test using a full scale sectorial model of the vacuum vessel

The items and results of the test are as follows.

(1) Measurements of stress, deformation and temperature distribution under the external water pressure

Experimental results of the vacuum vessel were in sufficient accord with calculated ones and the maximum stress was approximately 14 kg/mm^2 under the pressure of 1 kg/cm^2.

No failure was found under the pressure up to 5 kg/cm^2.

(2) Helium leak test

Experimental results are shown in Table VIII.3.2-4.

(3) Measurement of outgassing-rate for the model of the vacuum vessel (including molybdenum liner)

The results of the measurement are shown in Table VIII.3.2-5.

(4) Ultimate vacuum test

Experimental results of ultimate vacuum these are shown in Table VIII.3.2-6.

(5) Measurement of stress distribution of the bellows under the thermal expansion of the thick ring due to heating

It was shown from the test results that thermal expansion of the thick ring during baking produced the maximum stress of approximately 33 kg/mm^2 at the top of the bellow next to the thick ring and this stress was beyond the allowable one.

Therefore the dimension of the bellows of the vacuum vessel of JT-60 are to be changed as follows; the height H = 80 mm, the plate thcikness t = 2 mm (in this design the maximum stress of the bellows is approximately σ = 10 kg/mm^2).

(6) Measurement of stress under the loads simulating the electromagnetic force due to saddle current

The maximum stress of approximately σ = 10 kg/mm^2 is observed at the top of the bellows next to the thick ring.

(7) The temperature controllability test of the vacuum vessel

The temperature distribution in the vacuum vessel during bake out was uniform in the range of 500°C ± 50°C except diagnostic ports.

(h) Electron beam irradiation test of a magnetic limiter plate

When magnetic limiter coils are energized during a discharge, plasma which diffuse out from a plasma boundary move along a separatrix line and hit a magnetic limiter plate. Engineering problems of the magnetic limiter plate are thermal shock, thermal fatigue, electromagnetic forces at a plasma disruption, evaporation, sputtering and outgassing at higher temperature. We have done the heat cycle tests by electron beam impact to evaluate the applicability of Molybdenum, Pyrolitic Graphite and Silicon Carbide coated onto graphite to JT-60 magnetic limiter plate. The test conditions are as follows: the heat flux ($350w/cm^2$ - $1000w/cm^2$), the irradiated region (2 cm width), the number of repetitions (10 - 320), the beam duration (10 sec). The thickness of specimen is 2 cm for Mo, SiC and 3 cm for PyG. Mechanical strengths, deflections and hardnesses have been measured and the microstructure of the surface has been examined before and after the heat cycle, and the evaporation and surface of the specimen were observed during the electron beam impact. The results of the mechanical tests are shown in Table VIII.3.2-7. The experimental results indicated that there was no change in Mo and PyG surfaces irradiated thermally, but in case of Silicon Carbide coated onto graphite many microcracks and partial exfoilation of coating were found in the irradiated surface. Mo seemed to be the most favourable material for the magnetic limiter plate.

(i) Electron beam irradiation tests of the multi-hole and multi-groove structure plates

When the multi-hole and multi-groove structure plates are heated by plasma particles and radiation, thermal stress and thermal fatigue seem to be more serious problems than in case of smooth plate. To evaluate the applicability of the multi-hole and multi-groove structure plate, we have done the same heat cycle tests as electron beam irradiation test of a magnetic limiter plate. The test conditions are shown in Table VIII.3.2-8. A mechanical strength has been measured and the microstructure of the surface has been examined before and after the heat cycle. The experimental results indicated that there was no change. The mechanical strength such

as tensile strength seemed to decrease because of the notch effect. The recrystallization was observed in the microstructure near the surface. The application of the multi-hole and multi-groove structure, depends on the result of further detailed tests concerning the mechanical fatigue limit, vacuum properties, the plasma interaction and so on.

(j) Fabrications of multi-hole and multi-groove structures

Honey-comb wall design has been proposed as a simple design effort of reducing the number of sputtered particles which enter the plasma. We have developed the fabrication of multi-hole and multi-groove structures on the molybdenum plate. Circular and square multi-hole structures were fabricated by the drilling amd the electronic spark machining, respectively. On the other hand, two types of multi-groove structures, perpendicular and inclined grooves, were fabricated by milling. The dimensions of the multi-hole and the multi-groove made as a trial are shown in Fig. III-3.2-2. It is found from the fabrication that it takes a few hundred hr/m^2 to fabricate a circular multi-hole structure and mult-groove structure and a few thousand hr/m^2 to fabricate a square multi-hole structure. However a square multi-hole structure is superior to the other structures from the viewpoint of the reduction of the effective sputtering yield. If we will adapt a square multi-hole structure, the fabrication time should be shortened.

(k) Development of low-Z materials

Development studies have been carried out aiming at the application of low-Z materials to the liner or the magnetic limiter plate of JT-60.

Coating of low-Z material on refractory metal

The materials and the coating methods are summed up in Tab. VIII.3.2-9. Present investigations show that the coating of graphite and silicon carbide (SiC) on a refractory metal such as Inconel 625 and Hastelloy X seems to be very difficult because of its lower melting temperature compared with the coating temperature. CVD coating of SiC was tried on Hastelloy X substrate having the intermediate layer of Nb/Mo/W and W. As the result, coating was not successful because a large amount of free Si and C deposited on the intermediate layer together with SiC below the melting temperature of Hastelloy X.

Trial porduction of the liner and the magnetic limiter plate made from the low-Z material

Trial productions were carried out of a full scale models of the liner and the magnetic limiter plate made from the low-Z materials, i.e. pyloritic graphite (P.G.) and SiC-coated graphite. And in order to provide the data for the judgement whether they were applicable to JT-60 from the engineering point of view, the following performance tests were carried out.

engineering design and test of the joint of the liner and the magnetic limiter plate to the vacuum vessel, measurement of the thermal resistance and vibration test

The results of the performance tests showed that the liner and the magnetic limiter plate made from the low-Z material are sufficiently applicable to JT-60. On the other hand, application of P.G. to the liner of JT-60 seems very difficult at present because there is a limit and inaccuracy to the dimension of P.G. material.

3.2.2 Toroidal field Coils

(1) Development of conductor materials

Pure copper is not adequate as the conductor materials of the toroidal field coils because the maximum stress intensity of the toroidal field coils become about 23 kg/mm^2 at the temperature of 120°C.

Two conductor materials are selected from eight materials through various tests. One is 0.2% Ag-OFC alloy reduced by 40% for the center pole side, and the other is OFC of 20% reduction for the opposite side. The mechanical properties of these materials are shown in Table VIII.3.2-10.

(2) Development of connecting technique of the winding

The available conductor length is limited from the capacity of a smelting equipment. Two kinds of the conductors above mentioned must be connected at the top and the bottom of each winding, where the stress is expected to be lower. Brazing is chosen as the method of connecting the conductors. Two couples of work coils are excited with a high frequency power supply of 700 Hz, 450 kW, and heat the conductor between them by induction. The properties of the specimen are shown in Table VIII.3.2-11, and are nearly the same as those of an annealed OFC.

The effective brazed area exceeds 70% of the total area, This proves a good quality of brazing.

(3) Development of electrical insulation

Although the forcing voltage of the toroidal field coils is less than 7.5 kV, the mechanical compressive stress in the insulation will exceed 16 kg/mm^2 and the temperature will rise to about 120°C.

As the result of the R & D, the folloiwng insulation systems are chosen. The layer insulation of 1 mm thick is made of a polyamid paper and non-woven glass fibers which are pre-pregnated with an epoxy resin. The ground insulation of 10 mm thick is composed of a main insulation layer of mica and a protection layer of fiber glass, which are also pre-pregnated with the same resin. Each coils unit is insulated individually from the earth. After composing the winding, curing of the resin is carried out by heating the coil unit up to 130°C.

The properties of those insulation systems are as follows:

1) These insulation systems have excellent electrical strength and long voltage endurance life.
2) They are superior in its mechanical properties, particularly in fatigue characteristics.
3) These thermal properties are excellent as proven by the heat cycle test, which also confirm their reliabilities under operating conditions.

(4) Development of manufacturing technique of coils

A full scale three turn model coil which has the wedge shaped conductors with cooling channels, brazing, and insulation has been manufactured to establish the fabrication techniques. The manufacturing process of the coil has been established through the R & D. The results of the mechanical and the electrical tests using this coil are summarized in Table VIII.3.2-12. The destructive test was carried out by loading a hoop force mechanically. The ground insulation was broken at about three times of the operating load of actual machine, but the conductor had no damage.

(5) Establishment of cooling method and thermal analysis

Each winding of the coil has water cooling channels in the conductors. Each channels is along the winding, and is taken out from the conductor side. The thickness of the conductors is decided so that a uniform temperature distribution can be attained at the narrowest section of the coil unit. Temperature distribution in the conductors, temperature of cooling water, and pressure drop in the cooling channel were measured using a

1/2.5 scale straight conductor model with the similar shaped wedge section of the practical coil. A two dimensional code has been developed to calculate the temperature distribution in the coils along the length and across width as a function of time. This code was examined in detail using the 1/2.5 scale straight model coil and compared with the experimental results. For example the typical result is shown in Fig. VIII.3.2-3. Close agreement between observed and calculated values has been obtained in any case.

(6) Development of support structure of the coils and the stress analysis method

Major forces applied to the toroidal field coils are the electromagnetic force produced by an interaction with the toroidal field itself, and the twisting moment owing to an interaction with the poloidal field.

The supporting of the toroidal field coils against these forces are as follows.

1) The centripetal force is supported with a center column.
2) The conductors stand the compression by themselves.
3) The coil blocks is supported free from temperature rise.
4) The twisting force is transferred to the building through the external support structures which are connected to the upper and lower support structure with wedges placed between coil blocks.

The 1/5 scale model coil was to examine the deflection and the stress under loads. The loading was made by oil jacks to simulate electromagnetic forces. The stress analysis was carried out numerically by the finite element method. The highest stress intensity in the conductor was predicted to be 23 kg/mm^2 at the narrowest part of the coil. The measured stress distribution is shown in Fig. VIII.3.2-4. Fatigue test using 1/5 scale coil was carried out under the operating load of actual machine. The values of stress and deflection in the coil indicated no significant difference before and after the fatigue tests. The insulator had a sufficient strength after fatigue test. The numerical stress analysis method has been established by the comparison with above experiment.

(7) Manufacture of a full scale pancake coil

A full scale pancake coil which has the wedge shaped conductors with cooling channels, brazing, insulators surrounded with the metal case has

been fabricated. The manufacturing and fablicating process has been established through the R & D. The fabricated coil is shown in Photo VIII.3.2-1. Examinations of the mechanical and thermal properties of this coil were carried out. The performance is satisfactory and the manufacturing and fabricating techniques are applicable to JT-60 toroidal field coils.

3.2.3 Poloidal field coils

(1) Development of mechanical joint

Each poloidal field coil must be provided with at least one mechanical joint for assembling and disassembling. In addition, the space available for assembly is extremely limited, and this makes the assembly very difficult on site. In order to design the optimum mechanical joint, an experimental study of many different types of mechanical joint was performed. As a result of these investigation one joint was selected to be used for the JT-60 machine, and mechanical and electrical tests were performed.

Tensile tests were performed by using a 1/2.5 scale joint model and a full scale joint model. Rather high compressive strains were observed under the tensile loads. These compressive strains indicate the presence of high bending moments. After the confirmation of the presence of bending moment, the specimen was broken to have the information of stress margine. In the full scale model, failure occurred under a load of 78 ton. This load corresponds to a tensile stress of 10.8 kg/mm^2 at the normal conductor apart from the mechanical joint. Both a 1/2.5 scale and a full scale models were tested under cyclic load of 5 Hz. The fatigue tests were done under pull-relax-pull loads. These tests using the 1/2.5 scale model were performed at both room temperature and 100°C. On the full scale models, these tests were performed at room temperature. The fatigue strength decreased a little with the increase of temperature. The small scale model, which was subjected to a nominal stress of 5.1 kg/mm^2 at a temperature of 100°C, failed after 21,000 cycles of loading.

Temperature rise test of the mechanical joints was performed with thermal load 80 % higher than the operating load of actual machine. The current density and equivalent square wave pulse length in the test were 13.7 A/mm^2 and 15.3 sec, respectively. The maximum temperature rise at the joint was 22°C. Close agreement between observed and calculated values was obtained.

To have the information of tolerable alignment, the assembly procedure

has been done using a full scale mechanical joint. This procedure shows that the tolerable alignment in length, width and height are 1 mm, 5 mm and 2 mm, respectively. T his mechanical joint has excellent performances in connection with assembling flexibility.

(2) Development of insulation

Since the ohmic heating coil will be exposed to relatively high normal operational voltage of approximately 25 kV (peak value), the insulation to ground, especially at the mechanical joint part, is a serious problem. At the normal part apart from the mechanical joints, the insulation to ground is designed to be wrapped with 5 mm thick mica-epoxy insulation material. Mainly to confirm the manufacturing process, vacuum-pressure-impregnation system and resin-rich insulation system were studied. It becomes clear that the resin-rich insulation system is adopted for Poloidal Field coil insulation. This insulation system has satisfied the most strict requirements.

At the mechanical joints, various kinds of insulating operations were tried to develop reasonable insulation system even with rather poor accessibility for the insulation treatment handling on site. A series of insulation test results shows that this insulation system withstands the test voltage AC 38 kV (r.m.s) satisfactorily. However further efforts must be made to get higher insulation reliability.

(3) Development of welding procedure

Each conductor must be provided with several welding joints. MIG welding (Metal Inert Gas Arc Welding) without any preheating is selected to join the conductor of 38 mm thick. The reliability of these joints was investigated using the welded test specimens of 18 mm and 38 mm thick. Welding current, voltage and speed for use with this procedure are 850-1100 A, 35 V and 260-310 mm/min, respectively. Shielding gas of approximately 50 % helium and 50 % argon is recommended. The contents of investigation are macro each test, hardness test, resistivity test, tensile test, creep test and fatigue test. The welded joints show good properties in various tests. For example, tensile strength is about 18 kg/mm^2 and 0.2 % yield strength is about 6 kg/mm^2. And the welded joints pass without failure through 50,000 cycles at 15 kg/mm^2.

(4) Establishment of cooling method

In order to obtain information regarding the temperature rise of Poloidal Field coils, cooling experiment was performed with a 1/2 scale transformer coil with one turn. The experiment has been performed with thermal load 50 % higher than the operating load of actual machine. The experimental results under the condition of water velocity of 2 m/s and a pulse interval of 2.5 min. show that the maximum temperature rises up to 85°C after 10 shots in the mechanically jointed part and 55°C after 3-4 shots in the conductor apart from the joint, although the temperature rises per shot are same in both parts. The maximum temperature in the jointed part depends on the pulse interval and not on the water velocity.

(5) Manufacture of a full scale transformer coil

A full scale transformer coil with two turns was made in order to establish the fabrication method and to carry out a series of experiments. Each turn has the inner diameter of 2.84 m, the outer diameter of 3.24 m and the thickness of 48 mm. 38 jacks are mounted inside the coil. This coil was tested under static and dynamic loads simulating the electromagnetic force by oil jacks. After the stress distributions of this coil were measured under static loads, this coil were tested under a cyclic oil pressure from 0 to 125 kg/cm^2. This load corresponds to a nominal tensile stress of 5.2 kg/mm^2 in the conductor apart from the joint. No signs of failure were observed through 50,000 cycles of loading.

(6) Characteristics of sliding device of the magnetic limiter coil

The magnetic limiter coils are encased by the nonmagnetic cans. To reduce the thermal stress due to the difference of thermal expansions between the can and the magnetic limiter coil, a special sliding device is needed. The characteristics of the sliding device under vertical forces was investigated. The test rig was the straight coil of about 1.4 m long. This coil simulates the actual coil structure. Both vertical and horizontal forces were loaded to the model coil by oil jacks, when the temperature of can are room temperature and about 500°C. The test results for both temperatures almost agreed. The model coil, which was subjected to a vertical load of 10 tons, began to slide at a horizontal load of 80 kg and above.

(7) Manufacture of a full scale magnetic limiter coil

A full scale magnetic limiter coil of 90° section was made in order to

establish the fabrication method and to perform the thermal insulating test. This coil is composed of 4 turns of insulated conductors, vacuum-tight can, sliding and support structures, cooling system and thermal insulation with ceramic plate and fiber. The temperature measurements of these components have been made with no current flow of the conductor after the surface temperature of can was raised up to about 500°C by the heater wound on outer surfaces of the can. The water velocity range was covered up to 3 m/s. The results indicated that the temperature of the most outside electrical insulating material in the non-supporting region was about 40°C, whereas that in the supporting region in the range 80°C to 100°C. The temperature distribution appeared independent on water velocity.

3.2.4 Fast movable limiter

Various engineering problems are involved in constructing a fast movable limiter because the design specifications outlined above exceed the present technology. A full-scale movable limiter, therefore, was designed, constructed and then put to mechanical, electrical and vacuum-technological tests.

The model features a hydraulic drive mechanism with servovalves to control the oil flow. A special vacuum seal allowing a movement at high speeds was developed. It consists of welded bellows jointed together and connected to a pantagraph at the joints. It allows uniform expansion of each bellows at high speeds. Molybdenum disulphide with 20 % tantalum is chosen as the most suitable bearing material after conducting tests on various bearing materials.

The overall test of the model showed that its specifications were met with satisfactory reliability and reproducibility. Furthermore, the endurance test demonstrated that it functioned reliably over 50,000 times of operation. Fig. VIII.3.2-5 shows the full scale model.

Table VIII.3.2-1 Results of tensile strength of welded joint

	U.T.S. kg/mm^2		0.2 % Y.S. kg/mm^2		Elongation %	
	R.T.	550 °C	R.T.	550 °C	R.T.	550 °C
Inconel 625	88	67	52	36	32	22
Hastelloy-X	79	59	45	26	47	35

U.T.S. : Ultimate tensile strength

0.2%Y.S. : 0.2% Yield strength

R.T. : Room temperature

Table VIII.3.2-2 Bending fatigue test (at 550°C)

	Fatigue limit kg/mm^2	
	Parent metal	Welded joint
Inconel 625	28	26
Hastelloy-X	30	26

Table VIII.3.2-3 Tensile creep test (at 550°C, 5×10^4)

	Creep strength kg/mm^2	
	Parent metal	Welded joint
Inconel 625	58	50
Hastelloy-X	29.3	28

Table VIII.3.2-4 Helium leak rates

Condition of vacuum vessel	Helium leak rates (Torr·ℓ/sec)
Before bake out	1.29×10^{-9}
After bake out	2.8×10^{-8}
After reassembling	7.0×10^{-9}
Specification	1×10^{-8}

Table VIII.3.2-5 Outgassing-rate

Condition	Outgassing-rate (Torr.ℓ/sec.cm^2)
Before bake out	1.27×10^{-11}
During bake out	1.28×10^{-7}
After bake out	3.08×10^{-13}
Specification (at R.T.)	1×10^{-11}

Table VIII.3.2-6 Ultimate vacuum

Condition	Ultimate vacuum (Torr)
Before bake out	5×10^{-7}
During bake out	1.3×10^{-4}
After bake out (at 49 hr)	6×10^{-9}
Specification (at R.T.)	1×10^{-8}

Table VIII.3.2-7 The result of mechanical strength test before and after the heat cycle

Material	Item \ Test condition	Before test		After test	
		R.T	500°C	R.T	500°C
Molybdenum	Elongation (%)	14.9±9.1	29.6±9.0	49.4±2.0	37.7±9.4
	Tensile strength (kg/mm^2)	53.5±2.1	26.6±2.3	52.3±1.6	24.5±3.0
	0.2% yield strength (kg/mm^2)	46.3±2.6	24.6±1.5	40.7±3.7	19.4±6.0
	Vickers hardness (kg/mm^2)	273	—	224	—
Pyrolitic-graphite	Tensile strength (kg/mm^2)	5.9±0.9	—	5.9±1.0	—
Silicon-carbide coated onto graphite	Deflection strength (kg/mm^2)	1.8±0.5	—	1.7±0.1	—

R.T. : Room temperature

Table VIII.3.2-8 The conditions of electron beam irradiation test of the multi-hole and multi-groove structure

	Multi-hole structure	Multi-groove structure
Heat flux (w/cm^2)	100	350
Irradiated region (cm)	3	2
Incidnet beam angle (degree)	90	30,50,70
Heating period (sec)	15	10
Number of repetitions	500	500

Table VIII.3.2-9 Materials and coating methods of low-Z materials

Substrate material	Hastelloy X or Inconel 625 (>1 mm thick)
Coating material	graphite or silicon carbide (>100 μ thick)
Intermediate layer material	any material whose permeability is less than 1.02
Coating methods	lining, plasma splay, physical vapor deposition, chemical vapor deposition, activated reactive evaporation

Table VIII.3.2-10 Mechanical properties of conductor materials

Characteristics	Unit	OFC (20% reduction)	0.2% Ag-OFC (40% reduction)
Tensile strength	Kg/mm^2	31.9	40.7
0.2% proof stress	Kg/mm^2	28.4	38.0
Elongation	%	3.7	2.8
Hardness	Hv	103.3	121.2
Electrical conductivity	%IACS	101.1	99.2
Creep rate	R/h	15.5×10^{-5}	3.0×10^{-5}
Fatigue strength	Kg/mm^2	14.-	14.4

Table VIII.3.2-11 Characteristics of brazed specimen

Test specimens / Characteristics \ Test temp.		Joint portion	Heat affected zone	
			OFC (Red.20%)	0.2Ag OFC(Red.40%)
Tensile strength (kg/mm^2)	R.T.	20.2	21.4	21.4
	150°C	16.4	—	—
0.2% proof stress (kg/mm^2)	R.T.	3.7	4.1	4.3
	150°C	3.25	—	—
Elongation (%)	R.T.	40.1	61.0	60.3
	150°C	36.7	—	—
Electrical conductivity (IACS%)	R.T.	97.9	99.65	100.2
	150°C	65.7	—	—
Creep rupture tension and time	150°C	12 kg/mm^2, 95 h	—	—
	200°C	8 kg/mm^2, 91 h	—	—
Tensile strength of full size joint models	R.T.	19.4, 20.8 (kg/mm^2)	—	—

Table VIII.3.2-12 The results of the mechanical and electrical test

Item	Unit	Measured value	Calculated value
Electrical test			
Resistance	Ω	1.448×10^{-4}	1.42×10^{-4}
Inductance	H	1.12×10^{-4}	1.13×10^{-4}
Layer insulation test (test voltage 25 v/turn)		Good	
Ground insulation test (test voltage 14 kV to ground)		Good	
Mechanical test			
Stress by loading oil jacks	kg/mm^2	6.9	7.4
Stress by temperature rise	kg/mm^2	2.7	1.5
Destructive test			
Breaking stress (when the ground insulation breaked)	kg/mm^2	29	

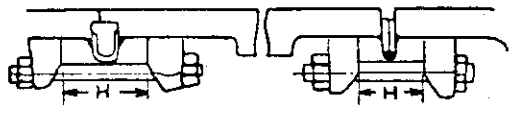

U-ring type Lip type

Fig. VIII.3.2-1 The connection structure

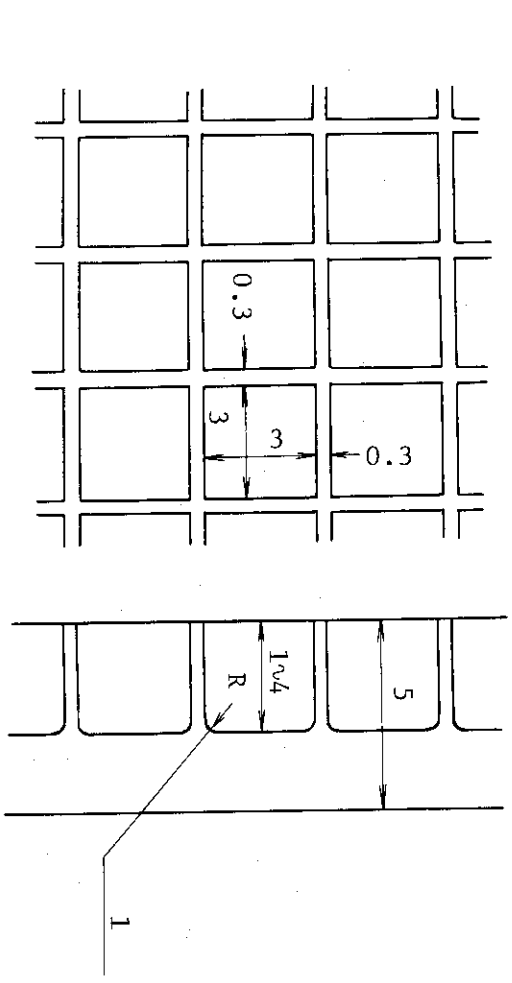

(a) Square multi-hole

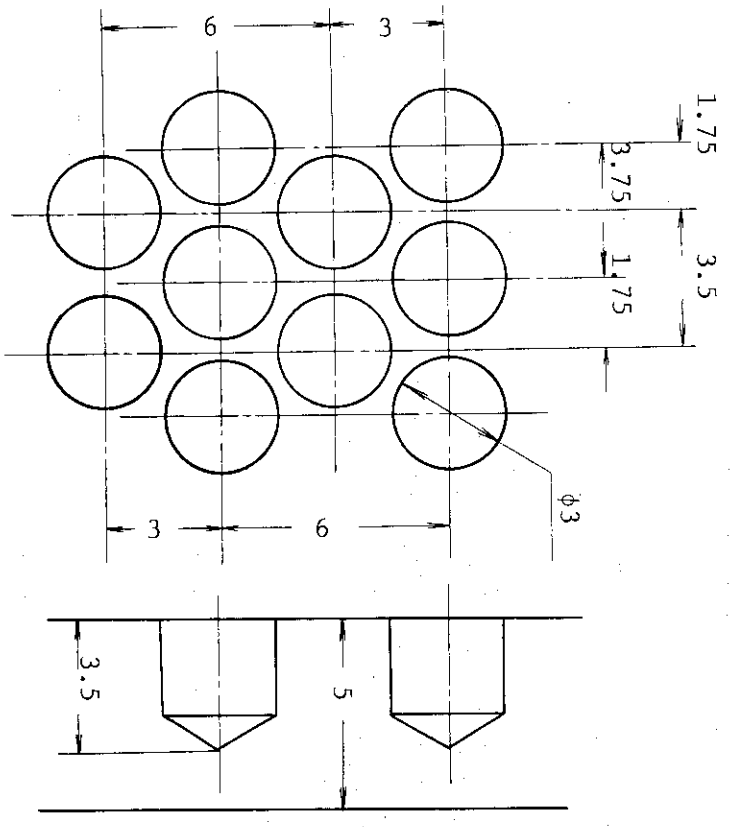

(b) Circular multi-hole

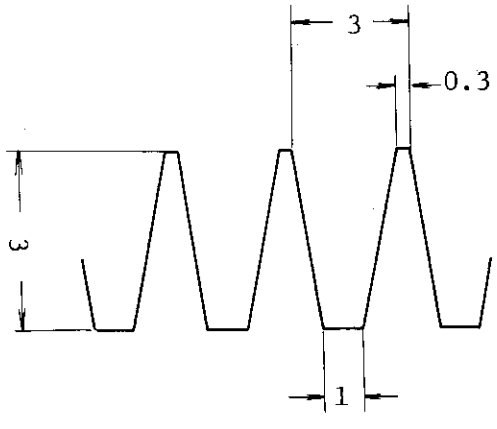

(c) Inclined multi-groove

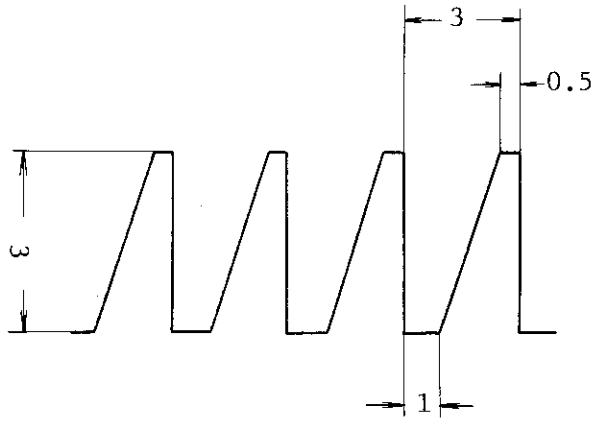

(d) Perpendicular multi-groove

Fig. III.3.2-2 The dimension of the multi-hole and multi-groove made as a trial

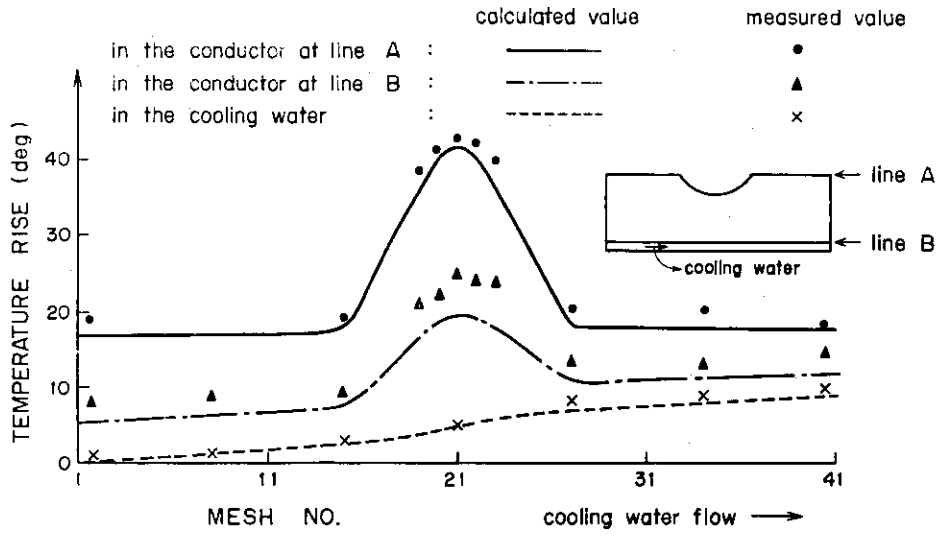

Temperature distribution along the cooling flow line

Fig. VIII.3.2-3 Comparison between measured and calculated temperature distributions using 1/2.5 scale straight model coil

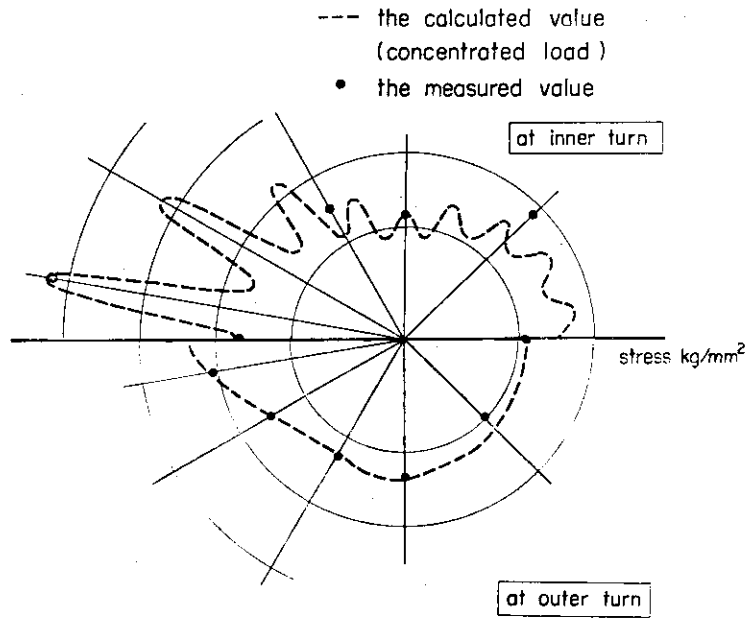

test condition
oil pressure : 700 kg/mm²
electric current : none
cooling water : none

Stress Distribution of 1/5 Coil at the Mechanical Load Test

Fig. VIII.3.2-4 Comparison between measured and calculated stress distributions using 1/5 scale model coil

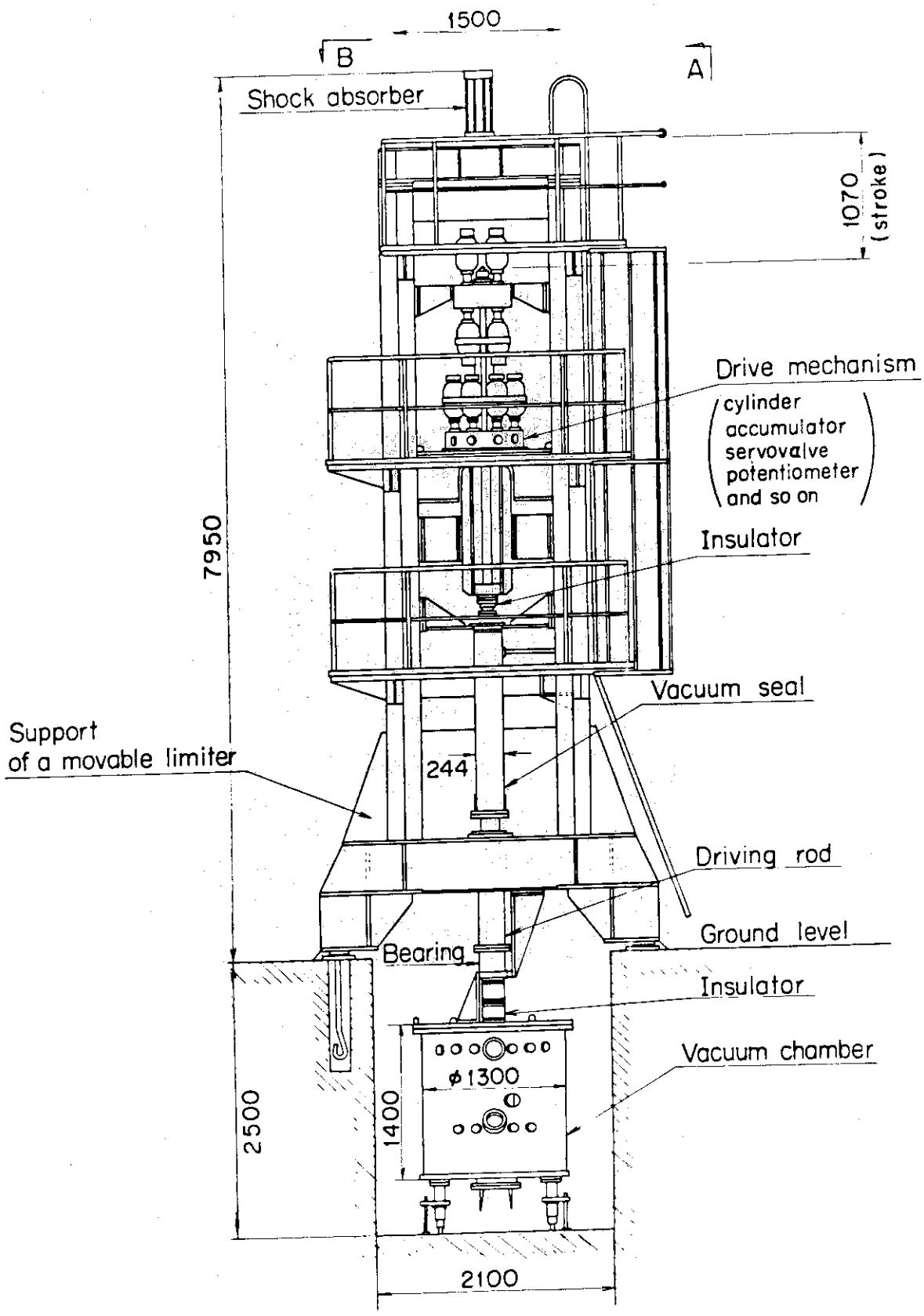

Fig. VIII.3.2-5 Front view of full-scale fast movable limiter

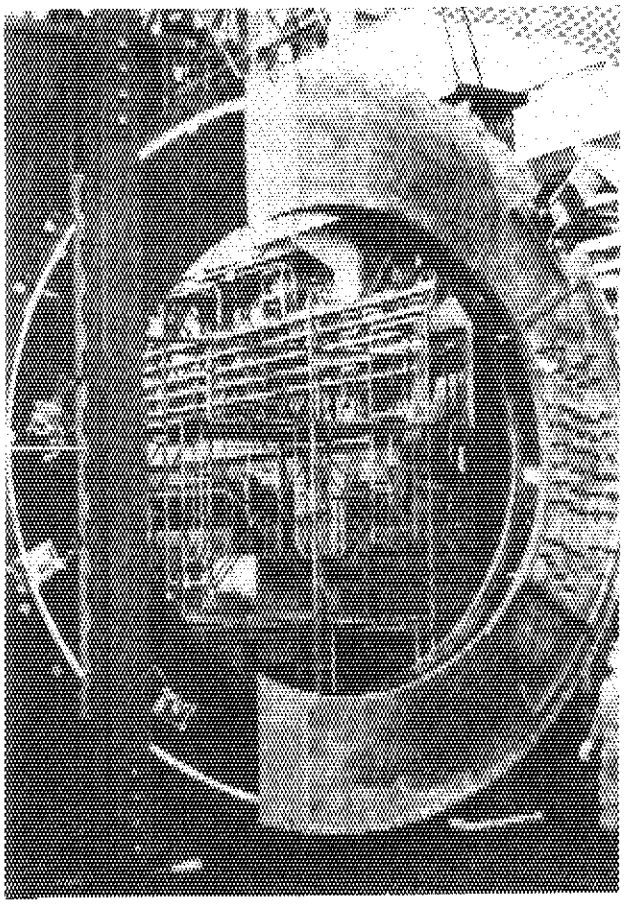

Photo VIII.3.2-1 View of the fabricated full scale pancake coil

4. Design of Power Supplies

4.1 Review of power supply design

4.1.1 Toroidal field power supply

Pulsed large electric power is required for exciting the JT-60 toroidal field coil system. The toroidal field power supply is designed for this purpose. This power supply consists of the following two lines:

(1) the line which feeds the electric power directly from the power network (power line),

(2) the line which feeds the electric power generated by a motor-generator-flywheel set (MG line).

Both lines are connected electrically through the rectifier equipment at the D.C. circuit.

The power line is designed to receive as much power as possible within the allowable disturbances to the power network, aiming to reduce the capacity of the MG set. Then the peak load of 160 MW is permitted to receive. The load of the power line is dropped to zero after the end of the flat-top, by a stepwise interruption of the A.C. power.

The MG line has the generator capacity 198 MVA and the generator energy 3.32 GJ. A vertical-shaft MG set is chosen because it is easy to manufacture and install the flywheel. This equipment employs diodes in the rectifier system. Hence the control of voltage and current is performed by the MG field control.

4.1.2 Poloidal field power supply with vacuum circuit breakers

The detailed design of the poloidal field power supply was completed in November 1976. Since the design of the high voltage circuitry of the ohmic heating system depends on the feature of DC dircuit breakers used, two types of design of the poloidal field power supply, namely, one with vacuum circuit breakers and the other with thyristor circuit breakers, have been made.

The poloidal field coils of JT-60 consist of five coils, namely, the ohmic heating coil, the vertical field coil, the horizontal field coil, the quadrupole field coil and the magnetic limiter coil. Each coil is separately powered and controlled by independent thyristor banks to meet the various operation requirements. A motor-driven generator with flywheel is used for the power source, because pulsed power is required to operate

these coils. Since the poloidal field coils are closely related to plasma behaviors, circuit analyses including plasma characteristics are necessary to determine the ratings of equipments. Considerations for construction and operation costs and protection methods against possible faults were also the major efforts in the detailed design.

(1) The power supply system

The power for each coil is supplied from a motor-driven generator with flywheel through thyristor banks which are controlled according to pre-programmed and also feedback control signals from the plasma position and shape control system. The generator capacity is dependent of both peak load requirements and power factors. On the basis of power consumption analysis and improvement of power factors by separation of thyristor banks, the maximum capacity has been settled as 400 MVA. Design of both types of generator (a vertical-shaft and a horizontal-shaft) was made. The utilized stored energy is 1300 MJ and is stored in the flywheel for the horizontal-shaft generator. For the vertical-shaft generator, no flywheel is used.

(2) The ohmic heating coil circuit

Circuit design of the ohmic heating system has been made using vacuum circuit breakers. Major characteristics of the JT-60 ohmic heating system are to make a multi-stage build up of the plasma current (up to three stages) by a set of inductive energy storage coils to swing the flux of the ohmic heating coil bi-directionally. The design value of the maximum interruption current is 92 kA with the peak voltage across the ohmic heating coil of 25 kV.

(3) The vertical field coil circuit

For excitation of the vertical field coil, two methods are studied comparatively; an inductive energy storage method as in the ohmic heating circuit and a use of a high power thyristor-controlled DC supply. Both methods are found to be competent from the economical point of view. Presently we have not made a choice yet, because it also depends on the mode of operation of both the magnetic limiter and the quadrupole field coils. The choice will be made based on the evaluation of technical performance of the plasma maintaining and magnetic limiter systems and experimental flexibility.

4.1.3 Poloidal field power supply with thyristor circuit breakers

The outline of the design is almost the same as that is described in 4.1.2.

A detailed design of thyristor circuit breakers has been made on the basis of the results of the research and development program of thyristor circuit breakers. A variety of designs of the ohmic heating circuit are possible using thyristor circuit breakers owing to high speed characteristics and high interruption time precision of thyristor elements. Many such designs have been made primarily to reduce the number of thyristor elements used in the circuit. For example, a "series-parallel circuit" is capable of exciting the plasma current in three steps by using each of the two circuit breakers twice in the current build up time of 0.1 sec. Evaluation of these circuits has been made by taking the results of tests by scaled models into consideration.

The design value of the generator capacity is about 600 MVA. This is considerably larger than that described in 4.1.2. Careful evaluation of these two values has been made to settle the final specification value, and presently it may be said that the estimation of the above design value was made on the basis of somewhat conservative considerations. But further study is still needed to determine detailed modes of operation sequences and performance flexibility of the poloidal field system, especially an evaluation of performance flexibility of the power supply for the plasma maintaining field system (the vertical field, etc.) is crucial to settle the final specification.

4.1.4 Power supply for supplementary heating systems

Both neutral beam injection (NBI) and radio-frequency wave heating (RF) are planned as supplementary heating techniques in JT-60. Because the power and the operation requirements of both heating systems are different each other, a design is prepared for separate sets of motor-driven generators with flywheel.

The generator for BNI is required to keep its output voltage through the flushing mode (18 pulses per operation) to the injection mode (1 pulse per operation). From the power requirement of the injector system, the generator capacity is designed 165 MVA (maximum peak capability) and the generating electric energy is 2.46 GJ. A high-speed horizontal-shaft generator is chosen because the generator for NBI needs a quick voltage response: the time constant of the field winding must be as small as

possible.

The generator for RF is required to control its output voltage to meet the load requirement. A horizontal-shaft generator is also chosen from the same reason as for NBI. The generator capacity is designed as 98 MVA (maximum) and the generating energy is 1.26 GJ.

4.2 Development of high current circuit breakers

4.2.1 Development of vacuum circuit breakers and related engineering studies

In JT-60 a DC circuit breaker used for the switching of the ohmic heating power supply should have an interruption ability of 92 kA at recovery voltage of 25 kV. In order to obtain such interruption ability, we have tested a vacuum circuit breaker and a commutating capacitor system. In the system the main current is forcibly made to zero by means of reverse discharge current from the capacitor. Since such a high capability vacuum circuit breaker to interrupt a high current of 92 kA at a high recovery voltage of 25 kV by a single pole has not been developed yet, it is necessary to limit the interruption current to a few tens of kA par one pole. This is also requisite condition for life and reliability of the breaker system. A two-year research and development program to develop a DC circuit breaker for JT-60 was completed in February 1977. The followings are the major items and results of the R and D for vacuum circuit breakers.

(1) Development of vacuum bottles

For this vacuum circuit breaker we have developed new type electrodes which utilize an axial magnetic field to stabilize vacuum arc. The new type electrode has shown a very low and stable arc voltage characteristics even after a few thousands cycles of interruption operations. By this characteristics a long electrical life of vacuum bottle has been achieved.

(2) Development of trigger gaps

A trigger gap in the commutation circuit is also a very important component in the DC circuit breaker system. The gap should have a long life and reliability as required for the vacuum bottle. Careful design has been made for the development and the life and reliability tests have been carried out on a complete set of trigger gaps.

(3) Life test

A life test of vacuum bottles has been carried out by a synthetic test circuit composed of a large capacitor bank. The duty for a bottle is made exactly equal to that in the actual circuit of JT-60. An opening mechanism, trigger gaps for the commutating circuit and other components

such as a saturable reactor, a current equating resistor and a commutating reactor were systematically developed. During the life test to study the ability of the bottle, large number of bottles were made and tested.

(4) Development of parallel operation technique of vacuum circuit breakers

As this vacuum circuit breaker is specially designed for this purpose, the arc current-voltage characteristic is very stable and the arc voltage is low. Major problem for the parallel operation will thus be the jitter of the opening time of each breaker. At the worst case, the maximum difference of the opening time of 4 msec among the branches should be expected. We have tested the current sharing for two paralleled vacuum circuit breakers where a slowly rotating short circuit generator was used to get a quasi-direct current. Almost two hundreds interruption tests with two paralleled breakers at various current level were successfully carried out without observing unbalanced current sharing.

(5) Full scale interruption test

A full scale interruption test for JT-60 was performed at the end of 1976. The purpose of this test is to demonstrate the capability of the vacuum circuit breaker for JT-60. Comparison of the experimental results with the computer simulation results was made. A short circuit generator is operated with a reduced velocity at 10 Hz, and feeds the current to test circuit breakers. They are operated at the current peak and arcs are established in breakers. After several msec, the trigger gap is operated and the commutating current produces a current zero in breakers, and thus the current is interrupted. The rate of rise of recovery voltage after interruption and the voltage across the test breaker were carefully made to be equivalent to that of the actual breaker of JT-60; because a rather large inductance exists in the generator circuit, a DC voltage was sequentially applied as a restriking voltage from the capacitor of the voltage source. Total of 79 times of interruption tests, which include 32 times operations at the rated value of 80 kA at 25 kV and the final test of the maximum of the test facility of 130 kA at 44 kV were made and all were successfully performed. Through the development described briefly here, it may be said that the interruption technique of high DC current with high recovery voltage by vacuum circuit breakers is feasible for JT-60.

4.2.2 Development of thyristor circuit breakers and related engineering studies

Developmental studies of feasibility of thyristor circuit breakers to the ohmic heating system of JT-60 have been made as a two-year research and development program for JT-60. Two kinds of tests have been performed; one is a DC interruption test and the other is a simulation test of the ohmic heating power supply circuits.

(1) DC interruption test

The circuit used for the test and its parameters are shown in Fig. VIII.4.2-1 and Table VIII.4.2-1. Figure VIII.4.2-2 is an oscillogram obtained from a typical interruption test. Interrupted current is 6.17 kA and recovery voltage which is induced across the ohmic heating coil is 12.3 kV. Figure VIII.4.2-3 shows voltage distribution in the thyristor elements of the breaker. The results show that the voltage distribution among five series thyristors is uniform.

(2) Simulation test of the ohmic heating power supply circuits

Many ways of modification of the basic circuit for the ohmic heating system are possible owing to the characteristics of high speed control of thyristor breakers. Figures VIII.4.2-4 and 5 show two examples of the circuits ("parallel" and "series-parallel"), the performance of them was tested with simulation models. Both circuits are capable of three-stage plasma current excitation, that is, they have two inductive energy storages L_2 and L_3 in addition to the ohmic heating coil L_F. Figure VIII.4.2-6 is a typical oscillogram of the performance of the "parallel" circuit where an equivalent plasma resistance changes with time sequentially and the mutual inductances of the relevant coils are simulated with a co-axial cylindrical coil model.

On the basis of these R and D tests, thyristor circuit breakers for the ohmic heating power supply of JT-60 are designed. The specification is shown in Table VIII.4.2-2.

Table VIII.4.2-1 Parameters of interruption test circuit

Element	Rating
L_{sw1}	165 ∿ 251 μH
C_{sw1}	210 μF
T_{sw1}	10S × 2P
T_{sw2}	5S × 4P
R_1	0.5 ∿ 2.5 Ω
L_F	84 mH, 42 mΩ

Table VIII.4.2-2 Specification of thyristor circuit breakers for JT-60

	1st		2nd		3rd	
Interrupting Current	92 kA		92 kA		64 kA	
Restriking Voltage	25 kV		25 kV		25 kV	
Thyristor Switch	Main	Aux	Main	Aux	Main	Aux
Rated Current	92 kA	110 kA	92 kA	110 kA	64 kA	77 kA
Rated Voltage	30 kV	40 kV	30 kV	40 kV	30 kV	40 kV
Thyristor	CF05V	CA02	CF05V	CA02	CF05V	CA02
Parallel	36	24	36	24	24	16
Series	30	20	30	20	30	20
Commutation Capacitor	1200 μF		1200 μF		760 μF	
Charging Voltage	25 kV		25 kV		25 kV	
Inductance	60 μH		60 μH		80 μH	

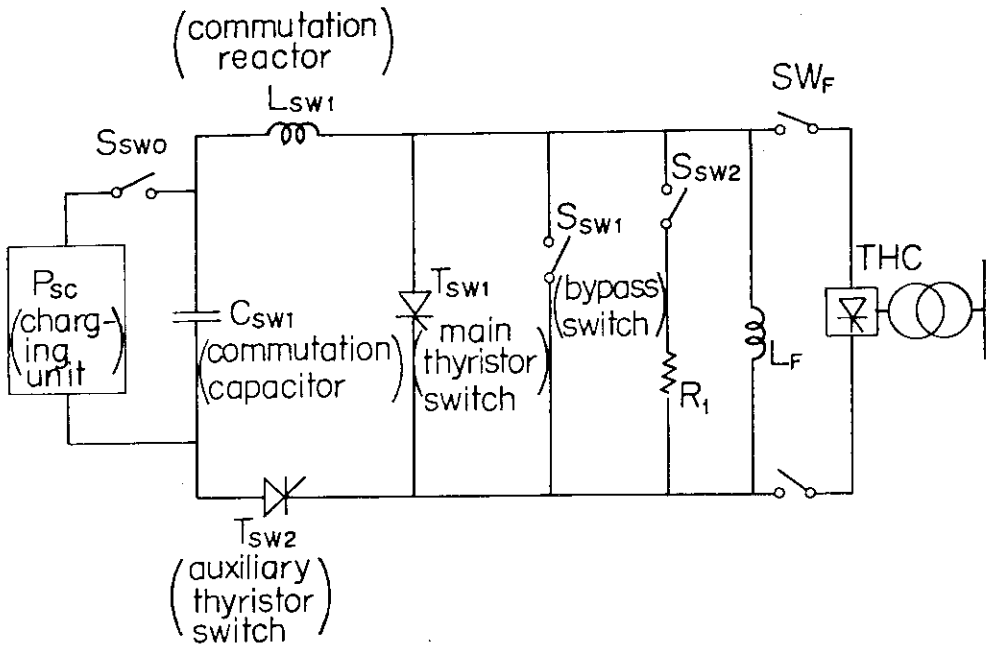

Basic circuit for thyristor circuit breaker

Fig.VIII.4.2-1 Basic circuit for thyristor circuit breaker

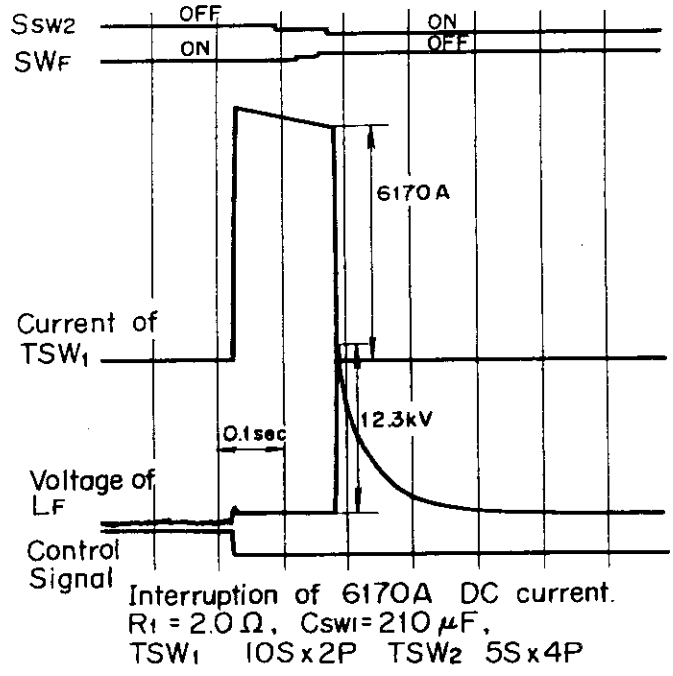

Fig.VIII.4.2-2 Typical oscillogram of interruption test

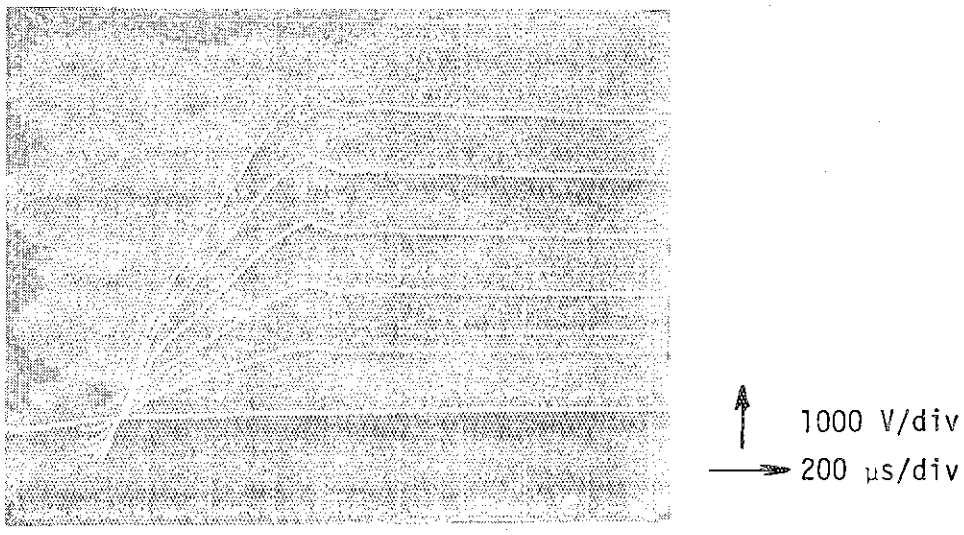

Fig.VIII.4.2-3 Voltage distribution of T_{sw1} thyristor. (Interruption of 3000A DC current. $R_1 = 1.5\Omega$, $C_{sw1} = 180\mu F$, 4500V)

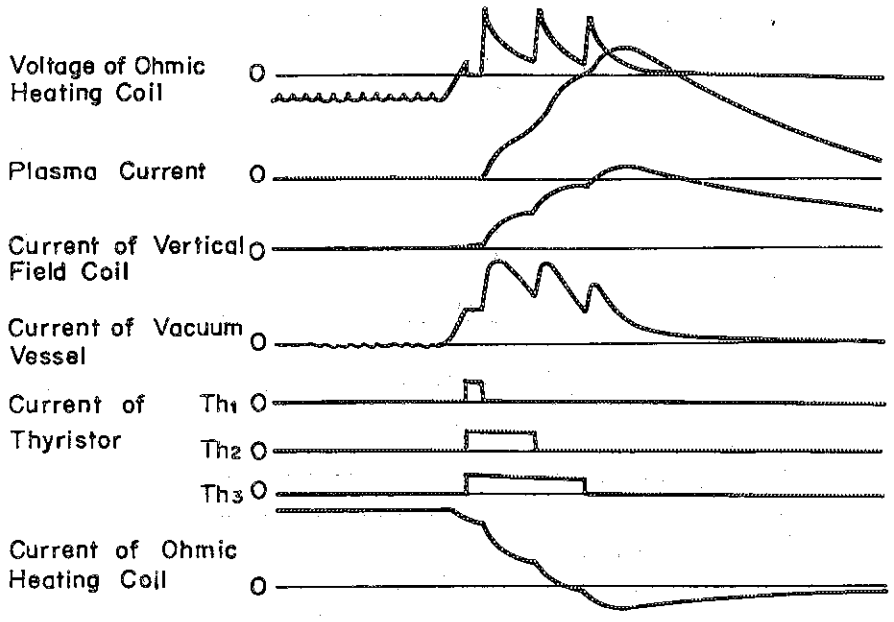

Fig.VIII.4.2-6 Typical oscillogram of performance of parallel type circuit

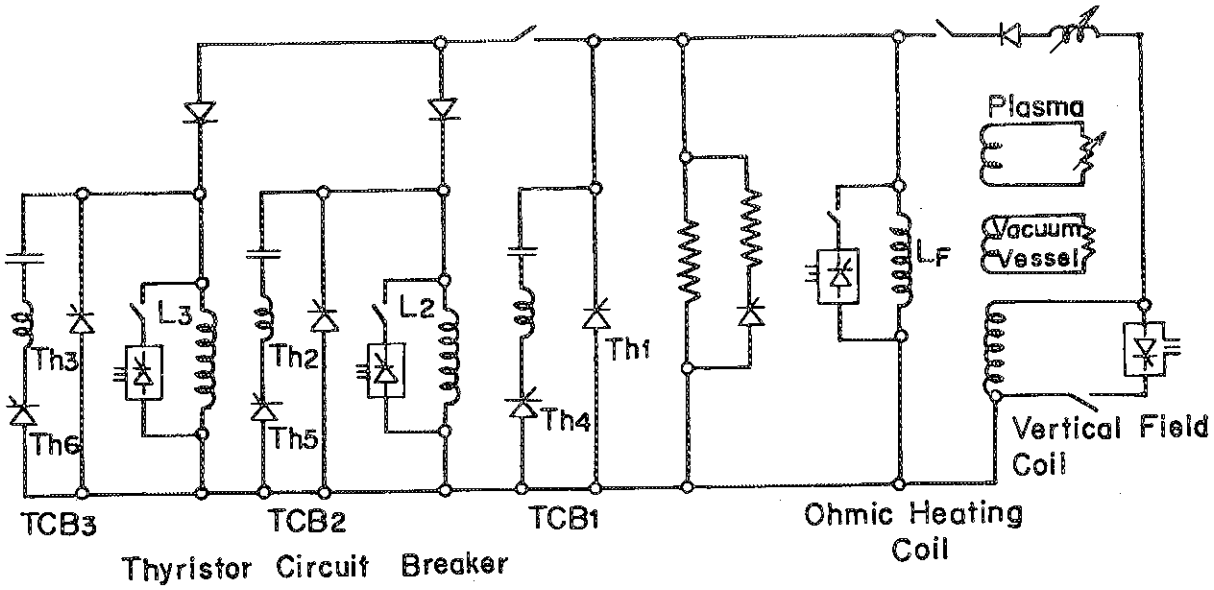

Fig.VIII.4.2-4 Ohmic heating coil circuit with thyristor breakers (parallel type circuit)

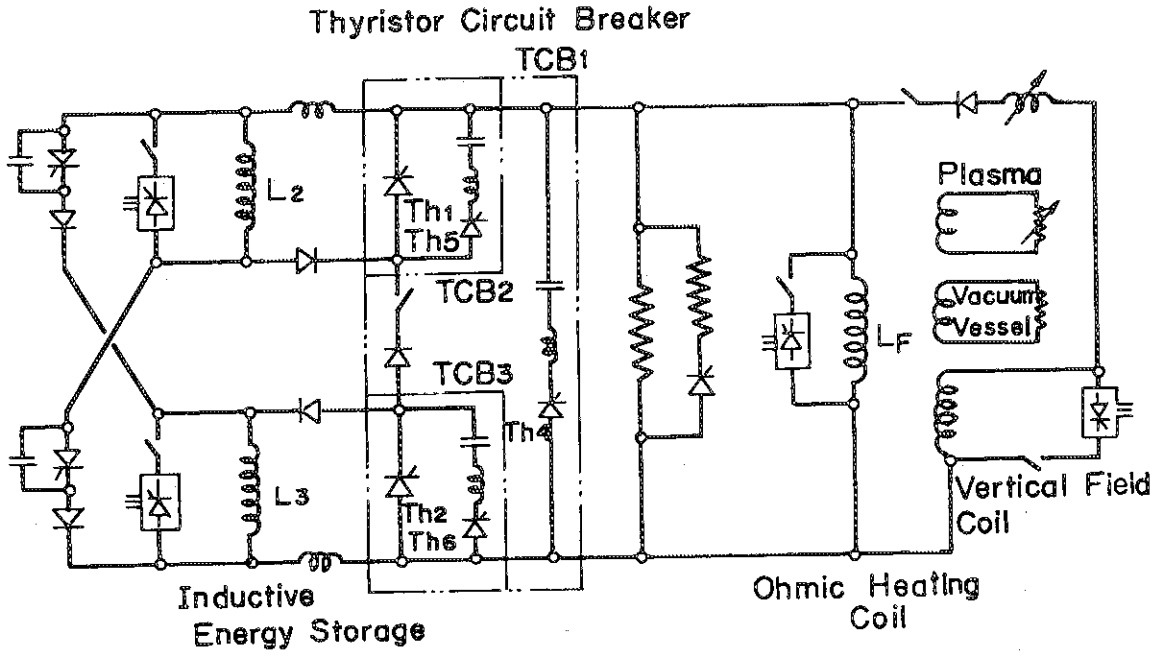

Fig.VIII.4.2-5 Ohmic heating coil circuit with thyristor breakers (series-parallel type circuit)

4.3 Studies related to the design of power supplies

4.3.1 Analysis of high frequency transient voltage oscillations in the poloidal field coils

High frequency transient voltages in the poloidal field coils were calculated to see the characteristics of transient voltage oscillations in the coils and to provide a protection system against possible overvoltages. Such overvoltages may be induced in the system of poloidal field coils by various external voltage surges, e.g., plasma spikes and/or transient voltages associated with the interruption of the ohmic heating circuit.

A calculation was made with a simplified distributed constant circuit model of the poloidal field coils. It is found that a stepwise voltage impulse applied to the coils induces significantly large voltage oscillations in them, while the plasma spikes have relatively small influence on them owing to the presence of the vacuum vessel. It is also shown that a simple CR series circuit connected across the coil is effective to suppress the development of higher harmonic components of these oscillations.

This work was done in cooperation with Fuji Electric Co., Ltd. as one of the items of the research and development program for JT-60.

4.3.2 Three-dimensional analysis of eddy currents

Two-dimensional analysis of eddy currents in the copper parts of the toroidal field coils was made previously to estimate the effect of the eddy currents on one-turn voltages induced by the ohmic heating coil[1].

More general studies by three-dimensional treatment of the problem have been made to make a detailed estimation of the effect of the eddy currents on both one-turn voltages and plasma control fields produced by a variety of poloidal field coils of JT-60. An integral equation which represents eddy currents by means of vector potentials was derived. Fourier-Bessel expansion method is applied to solve the equation. Numerical calculation is now under way.

4.3.3 Design of inductive energy storage coils[2]

In the ohmic heating system of JT-60, a multi-stage inductive energy storage (I.E.S.) system has been designed to reduce the capacity of circuit breakers and the initial stored energy to build up the plasma current.[3][4] Concerning the I.E.S. system, the required weight of conductors of the I.E.S. coils is of prime importance from the engineering

point of view, since in JT-60 the total initial energy in the I.E.S. coils is estimated about 100 MJ and the time constant of each coils is relatively long (∿10 seconds).

With the intention of minimizing the weight of conductors of the I.E.S. coils which is capable of storing a given amount of inductive energy with a given time constant, a basic design study of the effect of geometry of the coil on the optimum weight has been made.

In case of I.E.S. coil of the solenoid type with a rectangular cross section, it is shown that the optimum shape which gives the minimum weight is the square cross section with the side of 0.54R, where R is the mean radius of the coil. Figure VIII.4.3-1 shows how the weight of conductors of the solenoid type coil varies with its shape of cross section, where the time constant of the coil is assumed 10 seconds. The minimum weight occurs when ε is 1.00 and k is 0.27, and is about 60 tons, where ε determines the shape of the coil cross section and is defined as b(height)/a(width), and k as a/2R.

4.3.4 Circuit analysis of poloidal field power supply

In order to analyze the JT-60's poloidal field power supply where faults analysis or protection circuit analysis are very important, we have prepared a processor of network analysis program. This processor program operates as a man-machine communication on the graphic console which is aided by the computer; the circuit to be analyzed are written down with the light pen on a remote time-sharing graphic console, and the computer checks up the design of the circuit and then establishes the circuit equations.

4.3.5 Computer design of trigger gap shapes

Gap switches in the commutating circuit are very important components in the DC circuit breaker. For the JT-60 vacuum circuit breaker system, air-gap switches with a trigger electrode are planned. To design the shape of the gap electrodes, a numerical method has been developed. The basis of the method is to use a finite element method. The gap shapes are determined by means of an interation method. Electrode contours are optimized so as to make the electric field on the surface as uniform as possible.

A simplified flow chart is as follows:

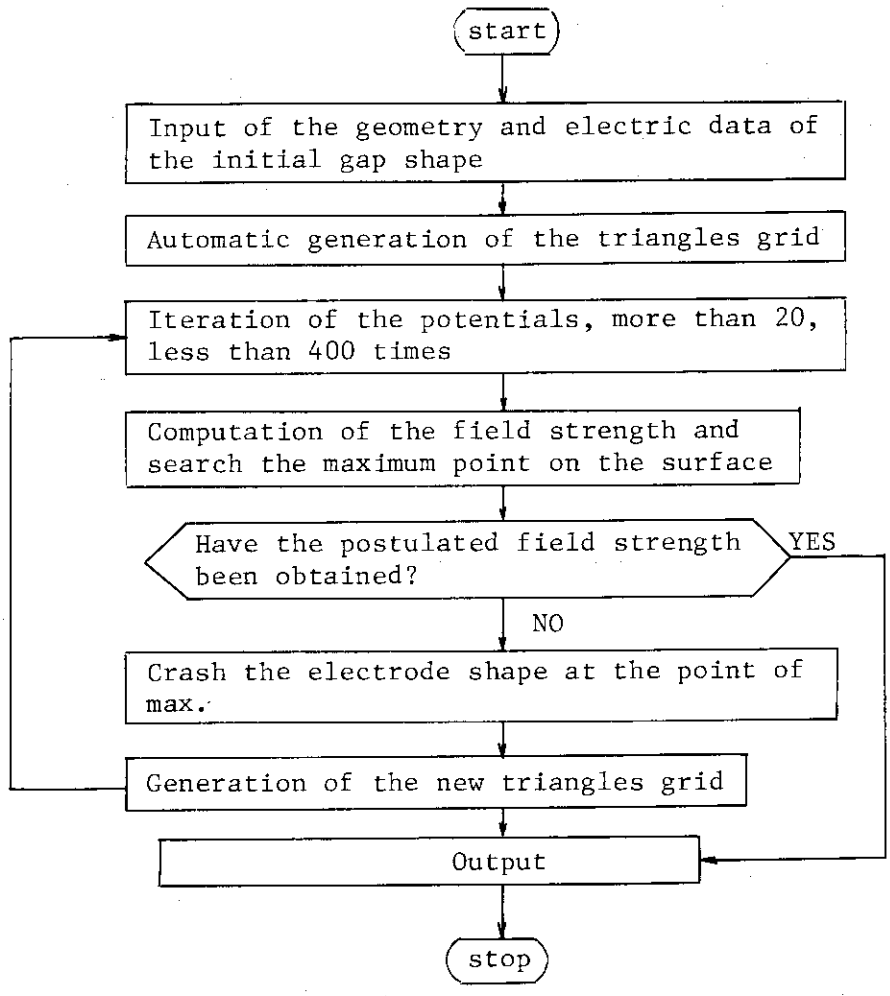

By this optimization technique, some examples were calculated. Figure VIII.4.3-2 shows an obtained gap shape and its equipotential surfaces. A gap with this shape was manufactued by way of trial by numerically controlled machine and the voltage test has been made (4.2.1).

4.3.6 Some considerations on multi-stage inductive energy storage system[4]

In large tokamaks, inductive energy storage (I.E.S.) systems have been applied to the ohmic heating power supply.

In JT-60, a multi-staged build up of the plasma current by subsequent use of inductive energy is planned, and some basic problems concerning the use of an inductive energy have been studied.

Firstly, the efficiency of energy transfer between two inductors has been discussed. Since the plasma can be considered as inductive in the build-up phase of the plasma current, the concept of transfer efficiency between two inductors can be used as a basis for determining the design and the operation parameters of the multi-staged ohmic heating power supply for JT-60.

The relation between the initial stored energy and the interruption capacity required to build up the specified magnitude of plasma current has also been studied. Figure VIII.4.3-3 shows operation characteristics of the JT-60 ohmic heating system at plasma current of 3 MA. Preliminary results show that a reciprocal relationship exists between the initial stored energy and the capacity of circuit breakers. This may imply that an optimization with respect to the cost of I.E.S. coils and the cost of the circuit breakers is necessary to fix the design and operation of the ohmic heating system.

4.3.7 Design of vertical field excitation circuit[5]

To hold the plasma in an equilibrium position during plasma current build-up, it is necessary to make a fast control of the vertical field. The design requirement is to produce rapidly increasing vertical field with an accuracy of ±5 per cent around the proper field strength required to center the plasma in the vacuum vessel.

Two basic circuits for the vertical field power system have been proposed and studied. The first one is a "power supply type" which consists of only a DC power supply or a thyristor converter and is connected to the vertical field coil. The second one is a "hybrid type" which consists of an inductive energy storage system and a DC power supply system. It is found that the power supply type requires a high voltage of about 15 kV if the rate of rise of the plasma current is about 100 MA/sec, and because of this it is economically unattractive. On the other hand, the hybrid type can afford to supply voltages from an inductive energy system and the maximum voltage of a DC power supply can be designed considerably lower; a reference design value is 4 kV. Thus the power supply for the vertical field excitation system depends largely on the rate of the plasma current build-up. Further study and evaluation of the initial phase of the plasma current build-up will be needed to determine the specification of the vertical field power supply system.

4.3.8 Studies of interaction between the poloidal field coils and the plasma

A computer code to study transient phenomena in the poloidal field coil circuits in the presence of induced currents on the vacuum vessel was previously developed[6]. Studies of an early phase of discharge of JT-60 have been continued to determine the necessary voltage for the vertical

field power supply, since the maximum voltage of the vertical field power supply is to be determined from the required voltage to hold the plasma in the initial phase of the plasma current build-up. Plasma conditions at very early time of discharge were determined from the study of breakdown processes as described in 7.2.2.

The necessary vertical field which gives the plasma an equilibrium at the major radius R in the initial phase of interest can be calculated from a well-known equation under the condition of $\beta_p << 1$ and $l_i = 0.5$ (flat profile of the plasma current). The vertical field which will be produced at R is calculated using the code mentioned above. Figure VIII.4.3-4 shows a time evolution of the necessary vertical field and the "actual" vertical field at the major radius R calculated by the actual coil system including the transient currents on the vacuum vessel. The required voltages for the power supply are also shown in the figure. It is also shown that the actual vertical field must be positively biased initially to a very small value of 50 gauss to realize a successful breakdown condition. From these considerations it may be said that the maximum voltage of the vertical field power supply should be larger than 7.5 kV to ensure the positional control of plasma in the initial phase of discharge.

References

(1) Tani, K. et al.: JAERI-M 5999 (February, 1975) (in Japanese).
(2) Yoshida, H. et al.: to be submitted for publication to JAERI-M Report.
(3) Tani, K. et al.: JAERI-M 6467 (March, 1976) (in Japanese).
(4) Shimada, R. et al.: to be submitted for publication to JAERI-memo.
(5) Yabuno, K. et al.: to be submitted for publication to JAERI-M Report.
(6) Shimada, R. et al.: JAERI-M 6469 (March, 1976) (in Japanese).

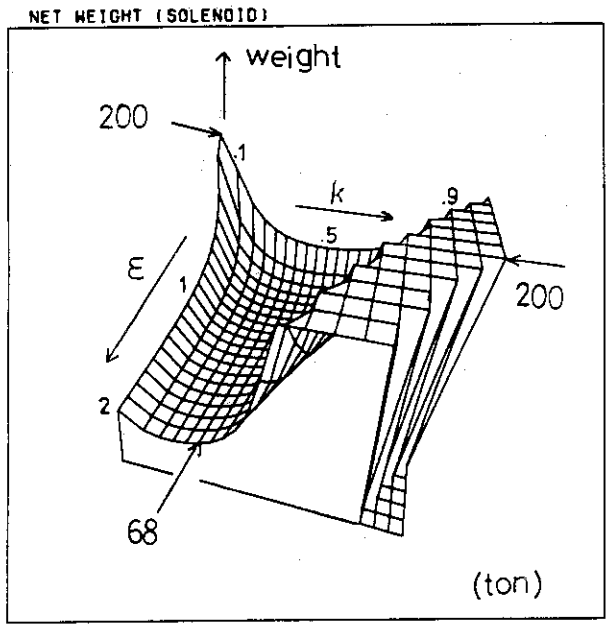

Fig.VIII.4.3-1 Dependence of weight of conductors of solenoid type coil on its shape

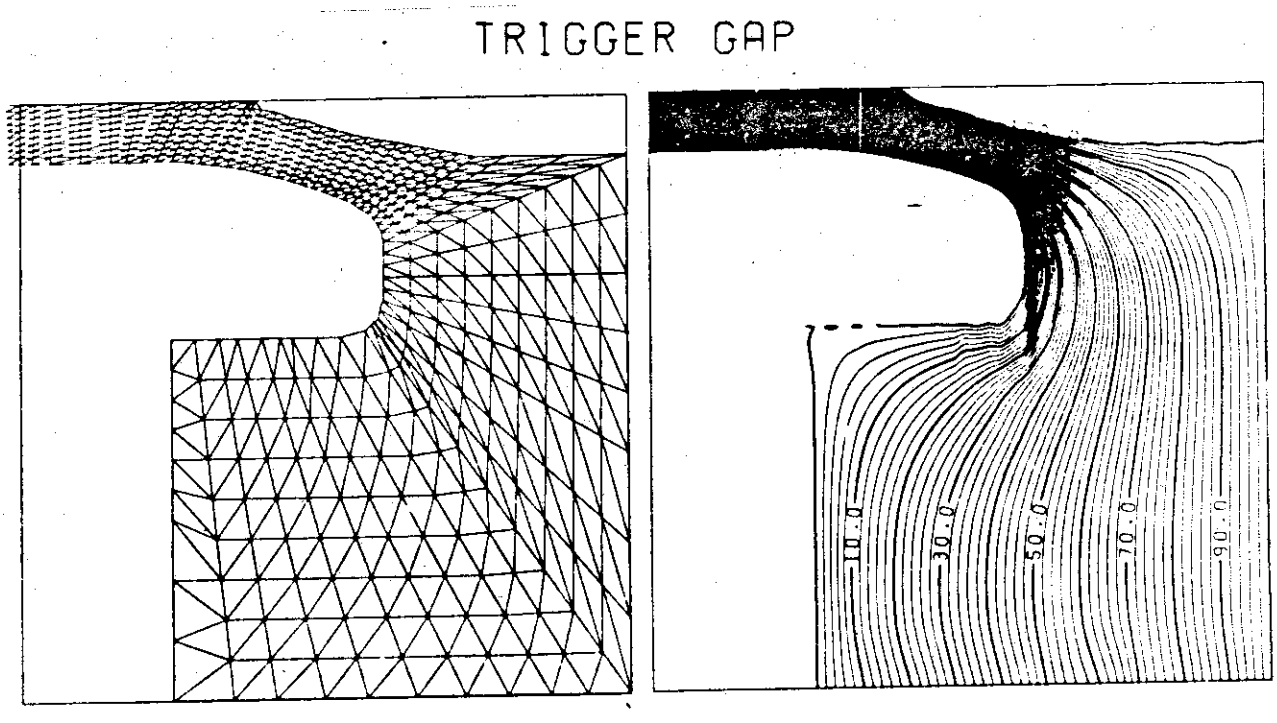

FINITE ELEMENT EQUIPOTENTIAL SURFACE

Fig.VIII.4.3-2 Shape of gap electrode and equi-potential surfaces

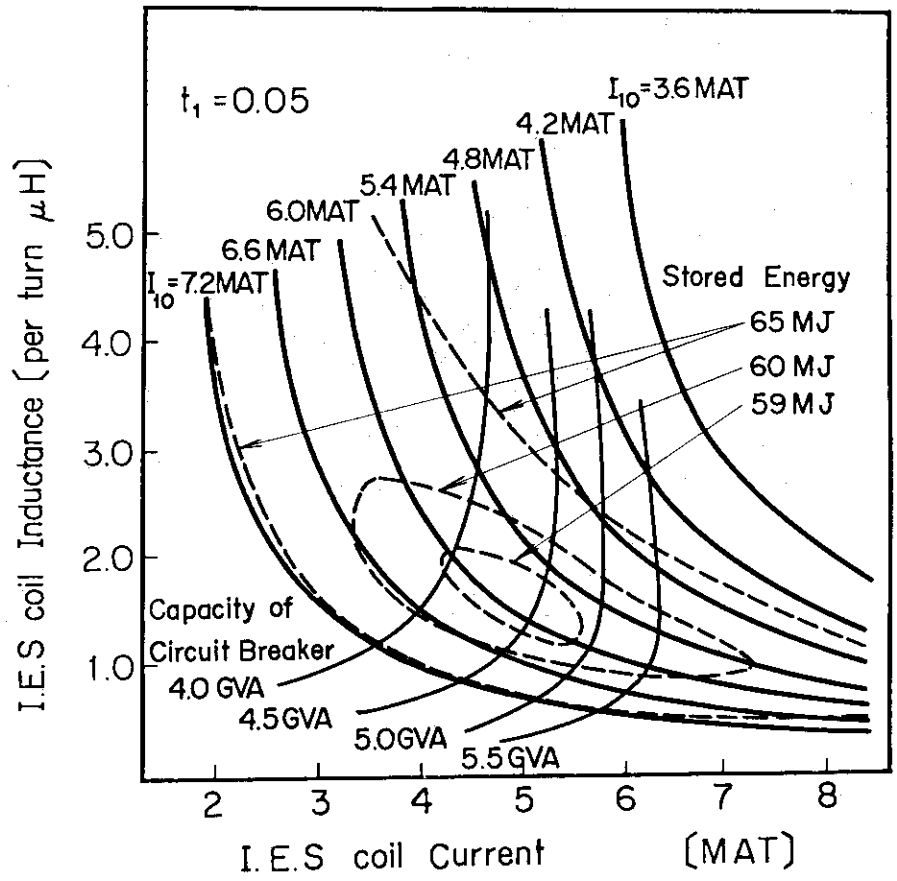

Fig.VIII.4.3-3 Operation characteristics of ohmic heating system

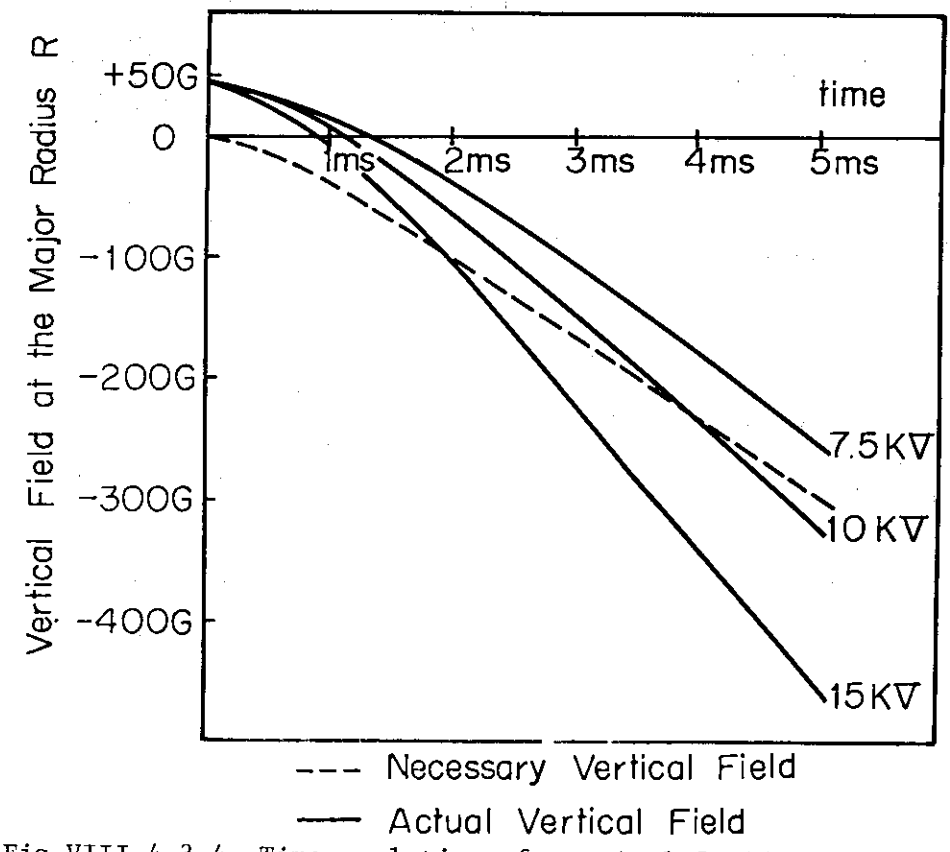

Fig.VIII.4.3-4 Time evolution of vertical fields at an early time of discharge

5. Design of Control and Diagnostic System

5.1 Review of control system design

5.1.1 System design

(a) Design requirements and solutions

The control system has to ensure efficient use of JT-60 device. To attain this role, some requirements are imposed on the control system and respective solutions are taken into design consideration as shown in Fig. VIII.5.1-1.

The requirements are large data capacity, plasma controllability, flexibility, reliability, maintainability, future expansibility and easy handling by a small number of operators. The first requirement is partly due to bigness of JT-60. Moreover, because JT-60 is a developmental machine, a principle is established to extract the maximum amount of data. The quantity of data to be handled then becomes inevitably large. The second requirement means an ability to control the physical characteristics of the plasma directly. Though in a conventional plasma device, an intention to control the plasma characteristics has been weak, it is explicit in JT-60; the control objects include plasma position and shape, plasma current and its distribution, plasma density, and so on. The third requirement, flexibility, must be also characteristic to an experimental device such as JT-60, but the rest are common in plant control systems.

The solutions are computerization, centralization, redundancy, standardization and equipment of an on-line large computer. They are mostly multi-purposed as shown in Fig. VIII.5.1-1. Computerization achieves the operational flexibility easily as well as the ability to handle large amount of data.

Centralization of functions ensures operatability by a small number of operators. Data including physical ones are also centralized to enable the direct control of plasma characteristics. The physical data are used also in the protection of the machine triggering interlocks; for example, insufficient plasma current can tell the failure of the discharge to enable the control system to make counterplans.

Concept of redundancy is introduced to improve reliability. The computers are backed up by hard-wired circuits. Some part of the control system have excessive ability; for example, throughput capability of the plasma data processing shall be compatible with future implementation of direct digital control (DDC).

To ensure the maintainability the number of different models of the computers shall be minimized and standards, such as JIS (Japanese Industrial Standards), JEM (Standards of Japanese Electromachinery Manufactures Association), ISO, CAMAC, etc. shall be adopted.

The control system is equipped with a large computer which is one of the means to enable the control of the physical characteristics of the plasma; it has a capability to compute the control parameters to achieve the desired plasma characteristics during the time interval between two successive shots.

(b) Design procedure

First, a principle is given that the control system has a hierarchical structure: The lower level controls the facility directly and its design is committed to the vendor of the facility, while the higher level controls the lower one.

Based on design of facilities and experiment project, analyses are made which lead to the final design. The routine is given in Fig. VIII.5.1-2, where the subsystems finally designed are shown at the bottom.

(c) Structure of the control system

The control system has a hierarchical structure shown in Fig. VIII.5.1-3. The high level computer at the top of the hierarchy is a large computer to compute the control parameters such as time variations of coil currents during the time interval between shots. It is also used to carry out simulation calculations which take into account the fresh data transferred from the plasma data processor. Coupling between the high level computer and lower level elements is rather loose so that the control system can work without the high level computer.

Below the high level computer the system divides into two branches: one for the device control and the other for plasma data handling.

The control branch is constituted by two levels: central controller and facility controllers. The central controller has several minicomputer CPU's backed up by hard-wired circuits. Its function includes central control, timing, monitoring, safety and protection and man-machine communication. The facility controllers have their respective object facilities: coils, electrical power supplies, auxiliary heating systems, baking system, etc.. Some facility controllers are equipped with mini- or micro-computers; they includes plasma position and shape controller,

baking system controller, electric power supply controller, etc.. Control for local testing and maintenance can be accomplished in the facility controllers independently of the central controller.

The plasma data handling branch also has two levels: plasma data processor and plasma data collectors. The plasma data collectors are based on mini- or micro-computers. They have their respective diagnostic instruments. They are capable of carrying out primary data processing and control of the diagnostic instruments. At present we cannot tell details of the plasma data collectors. Their objective diagnostic are given in Table VIII.5.2-1. The plasma data processor compares the data taken by different diagnostics: for example, electron temperatures based on Thomson scattering and X-ray pulse height analysis. It also calculates secondary plasma parameters which are functions of two or more primary plasma parameters: for example, Z_{eff} value as a function of one-turn voltage, plasma current, ion density, electron density and impurity density.

As shown in Fig. VIII.5.1-3, there are short cuts between two branches, which enables the use of physical data in the control branch and also the use of control data in the processing of physical data. Some physical data, which are easily processed and necessary for the control, and transferred directly from the diagnostic instruments to the central controller. Some data are edited by the plasma data processor and then transferred to the central controller. Note that, the plasma handling branch has the ability of real-time transfer during the discharge even in the case of editing and transferring. These data are itemized in the following section.

A brief discription on the control room design is given in the following. The control building has two main rooms; one for consoles and panels and the other for computers. Each occupies about same area, $\sim$500 m^2. The two rooms are shown in Fig. VIII.5.1-4.

The former room, control room, has master control console connected with the man-machine communication subsystem of the central controller, facility controllers and display panels. Several CPU's of mini-computers of central controllers and plasma data processor together with a large high level computer are placed in the computer room.

Facility controllers have their local stations in the machine building. The CPU's used in the plasma data collectros are situated not in the control building but in small rooms around the machine together with their respective diagnostic instruments. The CPU's have a function to accept

data from plasma data processor and to display them for those in the rooms, besides the original function to collect their own data. The data to be accepted include those concerned with the operating conditions which are sent from the central controller via the plasma data processor.

(d) Central controller

The functional block diagram of the central controller is shown in Fig. VIII.5.1-5, which consists of computerized and hard-wired systems. The computerized system shown in Fig. VIII.5.1-6 is of six subsystems: five functional and one back-up. The subsystems share one global memory. In such a configuration, the data generated within the computerized system are available anywhere in the system. An additional advantage is that, because the functions are distributed, most fault conditions bring into the system performance not total failure but general moderate degradation. One example of the computer for the central controller is HIDIC 80, which features 0.24 μsec cycle time, 2.4∿4.9 μsec floating point arithmetic time and can share one global memory by up to 16 CPU's. Constitution of the CUP's and peripherals are given in Fig. VIII.5.1-6. The hard-wired circuits have functions of safety and protection.

(e) High level control

The control system has a large computer comparable to IBM 370/148 at the top of the hierarchy which performs the high level control: to calculate the control parameters to realize the specified plasma parameters during the time interval between two successive shots.

Some correlations between the control parameters and the plasma parameters are given in Fig. VIII.5.1-7. As is clear in the figure, any plasma parameters are functions of several variables. T his is one of reasons why overall control is required at the top of the control hierarchy.

The calculation aiming the control in the high level computer is of two stages; the first is analysis of the system which is of the controller and the control object, and the second is calculation of the control parameters. Besides the above functions, the computer has another function to predict the plasma parameters under the control parameters manually specified. This is to verify the calculation aiming the control.

Two methods are proposed for the first stage of the calculation, the analysis of the system. One is modification of physical simulations which have been carried out in off-line large computers. Assumptions introduced

in the simulations hitherto will be substituted for fresh experimental results in our system so that the physical model adopted in the simulation can be refined shot by shot.

The other is to regard the system as a large black box whose inputs are control parameters and outputs are physical parameters. Here the physical models are forgotten. This is a technique based on the error-correcting training procedure in learning machines. We expect the latter method is useful to realize such a requirement as to obtain the control parameters which maximize the product of $n\tau$ and T.

In the second stage of calculation of the control parameters, the optimal control theory is applied.

A detailed scenario is made for the program control of plasma position and shape. The control strategies of other plasma parameters are rather conceptual in the present design stage.

5.1.2 Plasma position and shape control

The plasma position and shape control is attained by two complementary means: program control and feedback control. The program control is settled either by operators or by the high level computer, while the feedback control is performed by its own facility controller, which is described here.

The feedback controller has a computer (or computers) and phase-controlled thyristors. We have three coils as actuators: vertical, horizontal and quadrupole field coils to control horizontal position, vertical position and ellipticity of the plasma cross section, respectively. Some physics-oriented analyses have been made to grasp the characteristics of the control object; they include tokamak circuit analysis, eddy current analysis using finite element method and eddy current measurement using a model apparatus. Brief descriptions are given below under these headings. The rest of this section includes descriptions on plasma position and shape detection, feedback control law.

(a) Tokamak circuit analysis[1]

The control of the plasma position and shape requires the description of a tokamak system in terms of electrical circuit theory or automatic control theory. A concept of tokamak circuit is developed for this purpose. Fortunately, a tokamak is nothing but a transformer with a secondary circuit of a plasma so that the plasma behavior can be readily described

by equivalent circuit equations according to this concept. In the equations, magnetic interactions among a plasma and tokamak components are expressed by inductances, which are derived from flux functions based on the MHD theory.

A computer code to solve the equations is developed which can simulate the time variations of plasma position, cross section and currents in the plasma column and tokamak components taking account of the performance of the feedback control system.

The treatment is an extension of those used in the analysis of feedback control systems of CLEO[2] and JIPP T-II[3]. However, ours does not remain within the limit of linear treatment so that it can carry out the simulation through all phases of the discharge: current build-up, flat-top and shut-down phases.

(b) Eddy current analysis

Eddy currents are induced on the tokamak components responding to the field of the poloidal coils and plasma motion, which modifies the field in the plasma region, so their analysis is important in the plasma position and shape control. Because of complex shapes of the components, for example the vacuum vessel is of heavy rings and bellows, the liner is of many rectangular plates, and so on, three dimensional finite element method is adopted in the analysis.

Here the system of coils, vacuum vessel, liner and plasma is divided into finite elements, and vector and scalar potentials are obtained in each element. The element in the poloidal cross section are shown in Fig. VIII.5.1-8. As is shown in the figure, shapes of some components is simplified to make the analysis easy. In spite of these simplifications, dimension and half width of the global matrix are about 8500 and 550, respectively, which we believe are one of the largest ever treated by digital computers.

Magnetic field distributions are obtained as a function of frequency of the coil currents and plasma motion by the analysis. The obtained results are useful in electro-magnetic force estimation applied on the components as well as in their original purpose, plasma position and shape control.

A more analytical method than the finite element methods is also applied in the study of the time behavior of the eddy current[4],[5]. The procedure is as follows: Scalar potentials of the magnetic field are

introduced inside and outside of tokamak components. They are expanded in modified bessel and triangular functions. Relations between coefficients of the expansion are derived under the continuity condition on the component. Imposing restrictions on the current distribution by the shape of the component, we obtain a matrix equation between the coefficients. The matrix equation can be solved with a computer as an eigenvalue problem. The time behavior of the eddy current on the component can be expressed by the eigenfunctions.

(c) Eddy current measurement using a model apparatus

To verify the analysis on the eddy current, measurement of magnetic field due to the eddy current is carried out using a model apparatus of JT-60. The model has dimensions 1/13 of the real machine in length. It has following components: toroidal coils, vacuum vessel, air-core transformer coil, vertical field coil and plasma simulator. The shape of the components are simplified so as to make crosscheck with the calculations easy.

The plasma simulator is a poloidal coil inside the vacuum vessel, whose current distribution is expressed by cosine function; time variation of plasma position is then substituted for that of coil current. Sinusoidal current is applied either on the vertical coil or on the plasma simulator and induced magnetic field is measured as a function of the current frequency.

(d) Plasma position and shape detection

Conventional position detection using pair of magnetic probes inner and outer region of a toroidal plasma cannot be used in JT-60 because of the magnetic limiter coil situating in the outer region on the horizontal symmetry plane. Instead of this method, we employ at least a dozen of probes measuring not only tangential but also normal components of the poloidal magnetic field (see Fig. VIII.5.1-9), decompose their signals into Fourier components, and then obtain horizontal position, vertical position and ellipticity as functions of the Fourier components. The method is a refinement of that proposed by Zakharov and Shaftanov[6]. Details of our method is described elsewhere[7],[8],[9].

(e) Control law

Recent development of mini-computers enables us to implement the

control law based on the optimal, or modern control theory in the realtime feedback controller. In this method the system is described by a set of linear differential equations and a performance index function is introduced. The feedback is applied so as to minimize (or maximize) the performance index. Real-time solution of matrix Riccati equation is required of the controller to obtain the feedback quantities.

The method has a few advantages: First, capacity limitations of the power supplies of the coils can be taken into consideration. Second, interference between coils can also be taken into consideration; because of their own setting errors and induced eddy currents in other components, the poloidal coils generate error fields in the plasma region, which can be cancelled out by this method. We cannot count out, however, some risks in the implementation. First, the state of the control object must be linearized. Second, examination is necessary on the stability of the system and influence of disturbances. Third, this will be the first trial and we fear vaguely the optimal control theory is smart but impractical.

In spite of these risks, the trial seems still fruitful. Our controller shall have the ability to carry out the modern control law as well as the conventional control law.

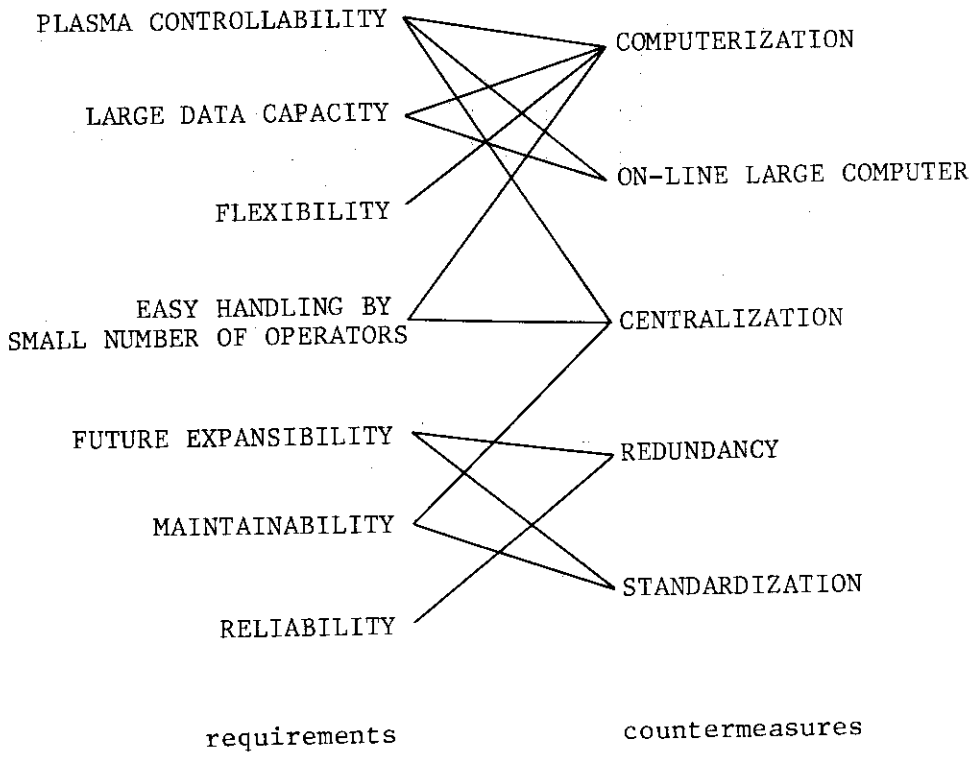

Fig.VIII.5.1-1 Design requirements and their solutions

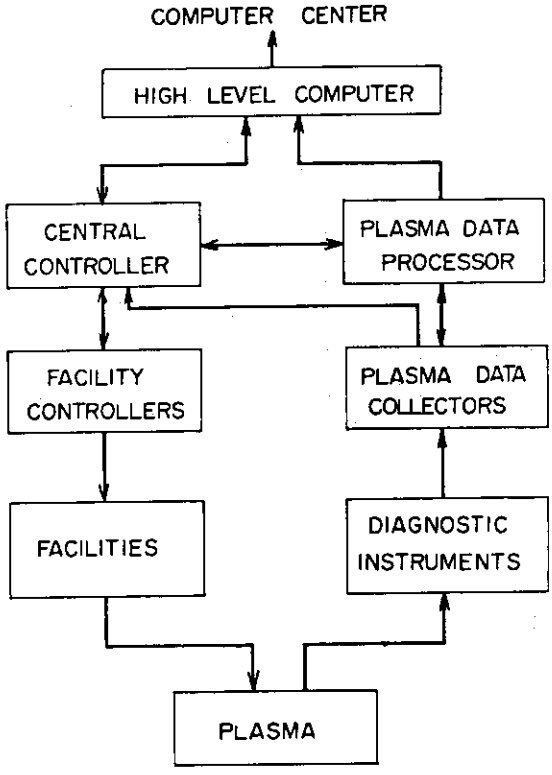

Fig.VIII.5.1-3 Structure of the control system

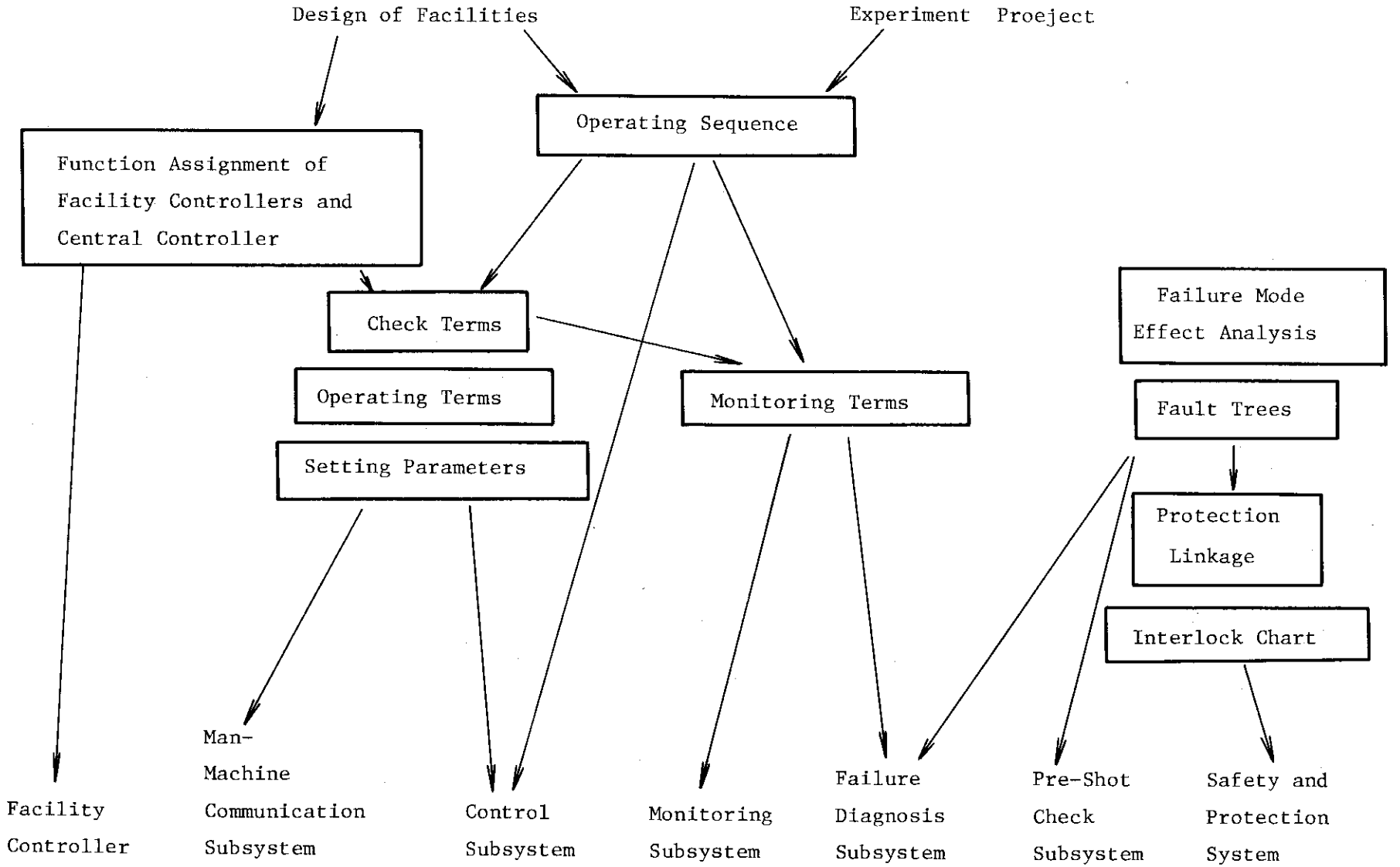

Fig.VIII.5.1-2 Design procedure

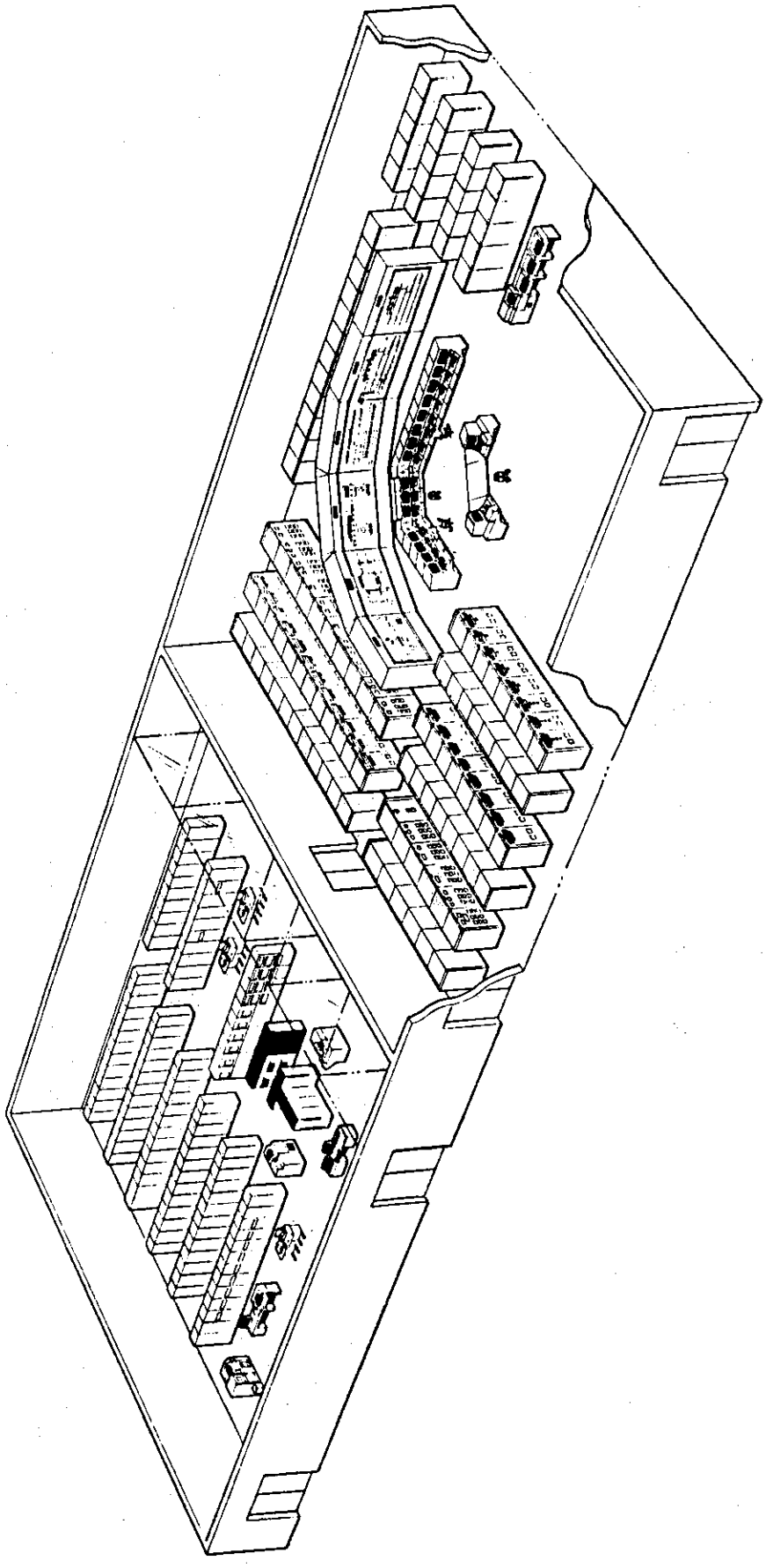

Fig.VIII.5.1-4 Control rooms

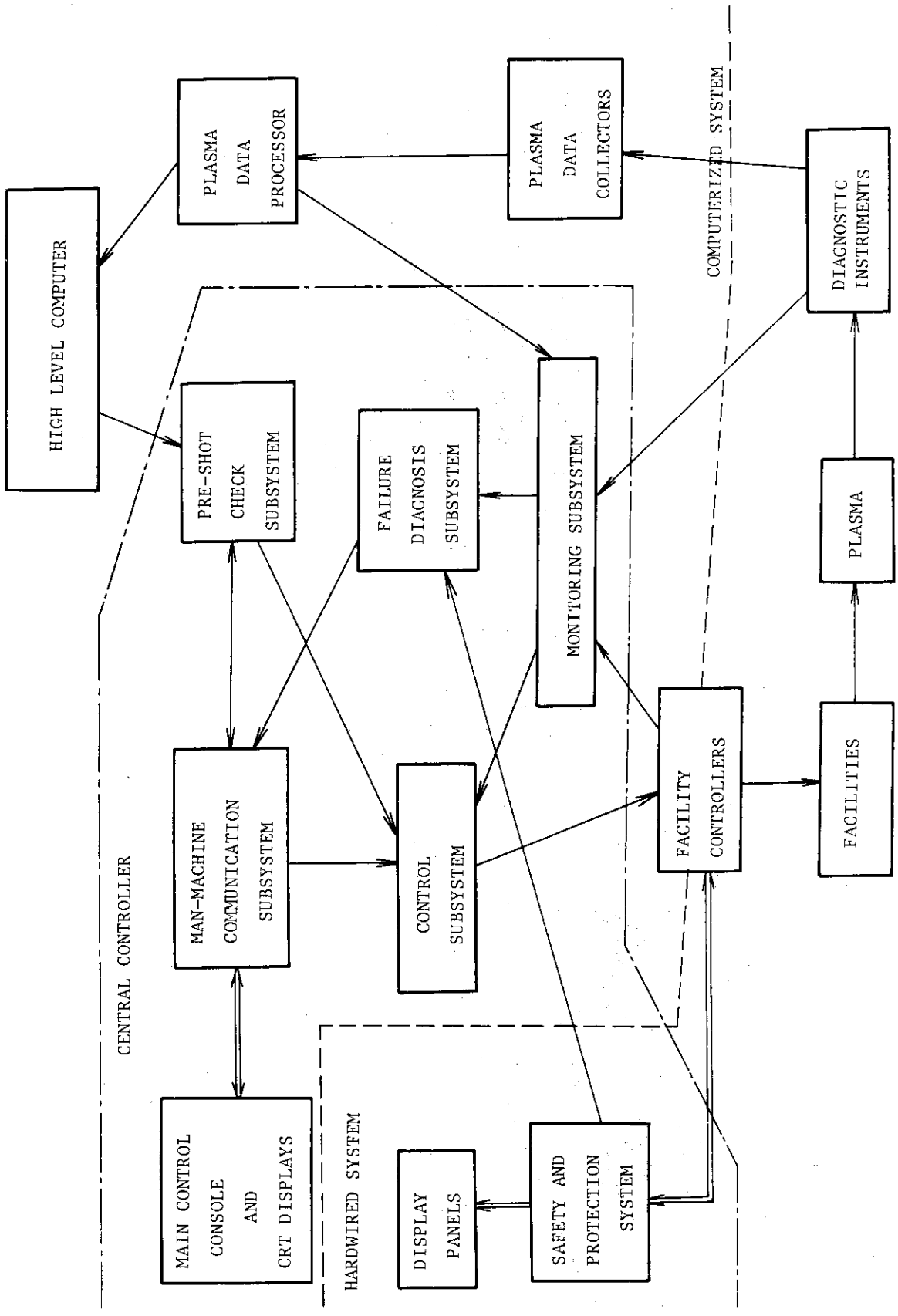

Fig.VIII.5.1-5 Functional block diagram of the central controller

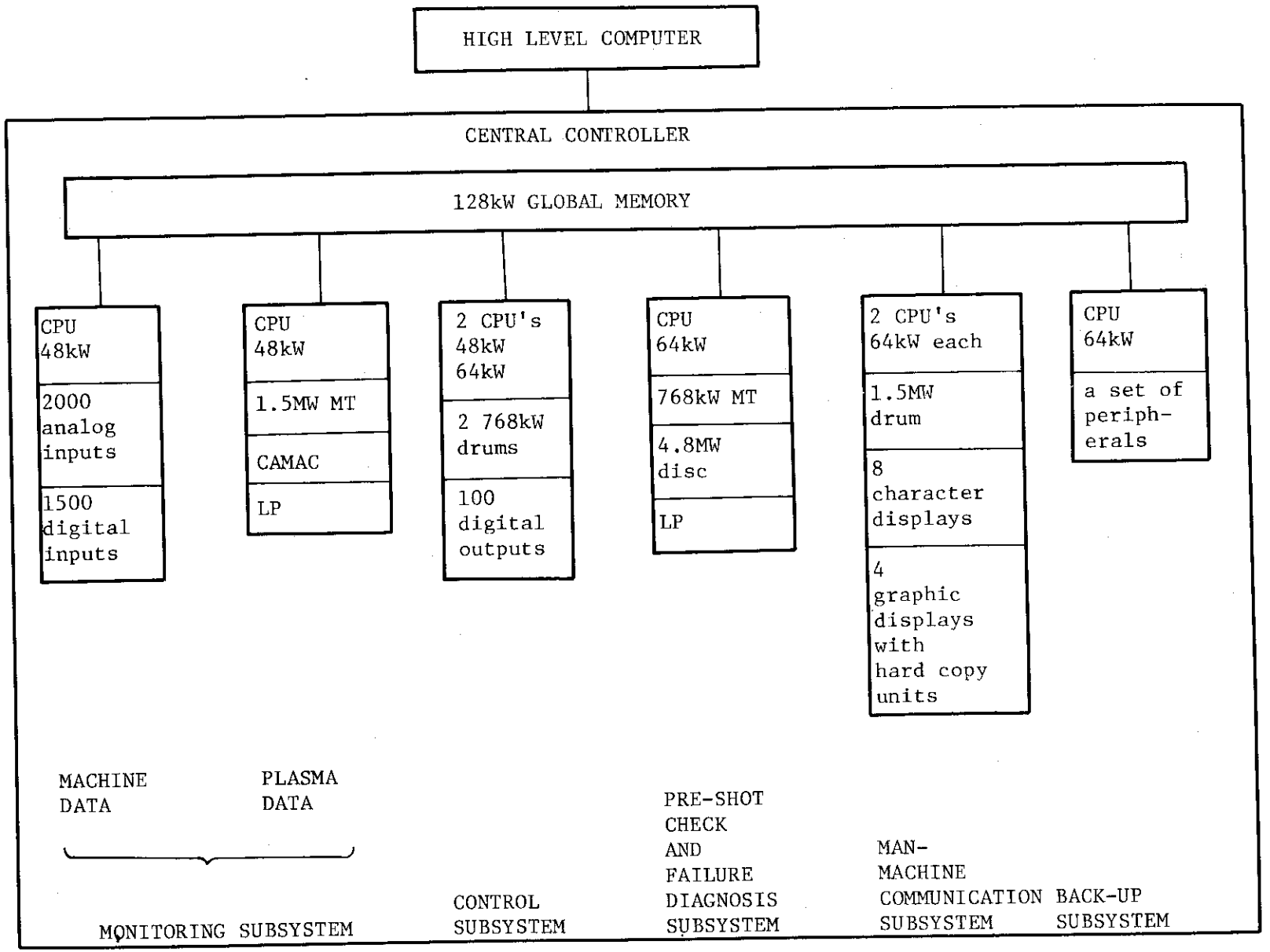

Fig.VIII.5.1-6 Computerized system

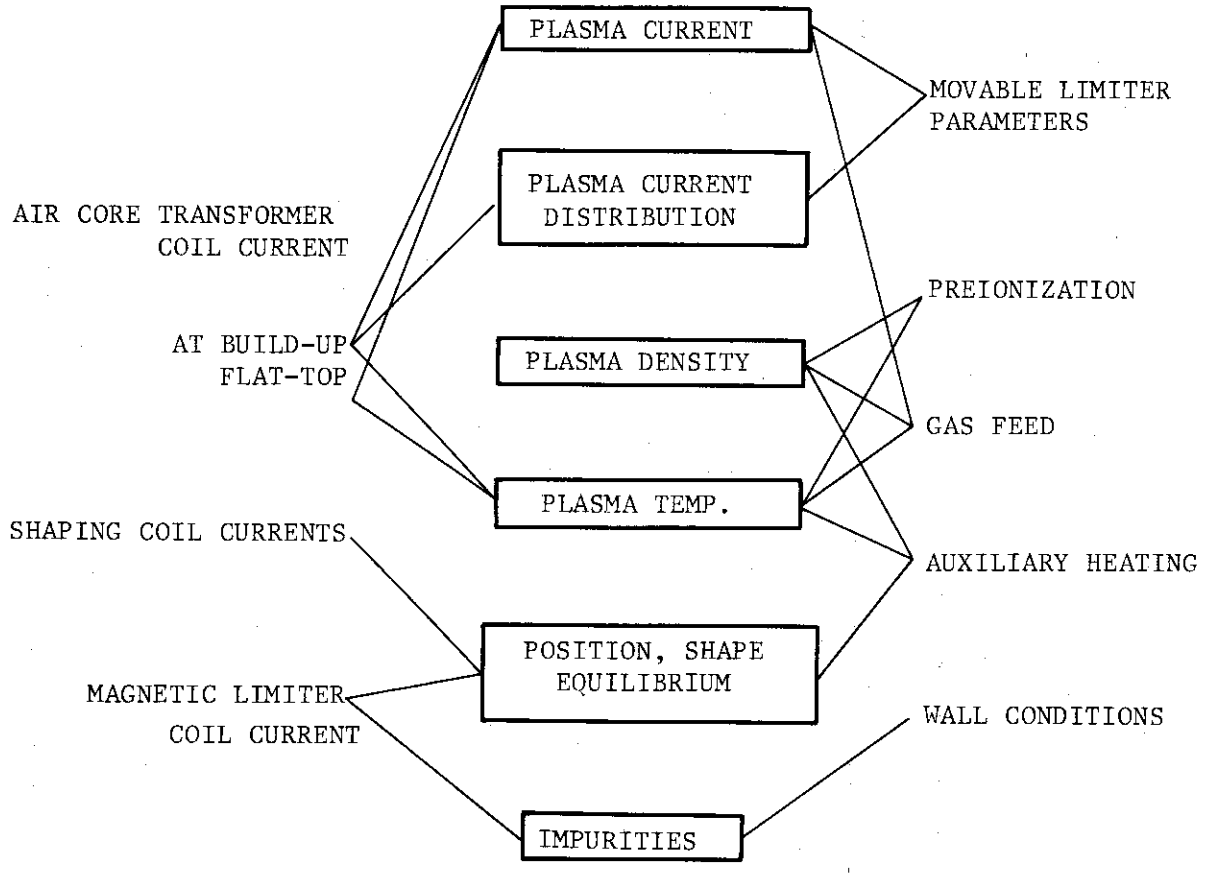

Fig.VIII.5.1-7 Correlations between control parameters and plasma parameters

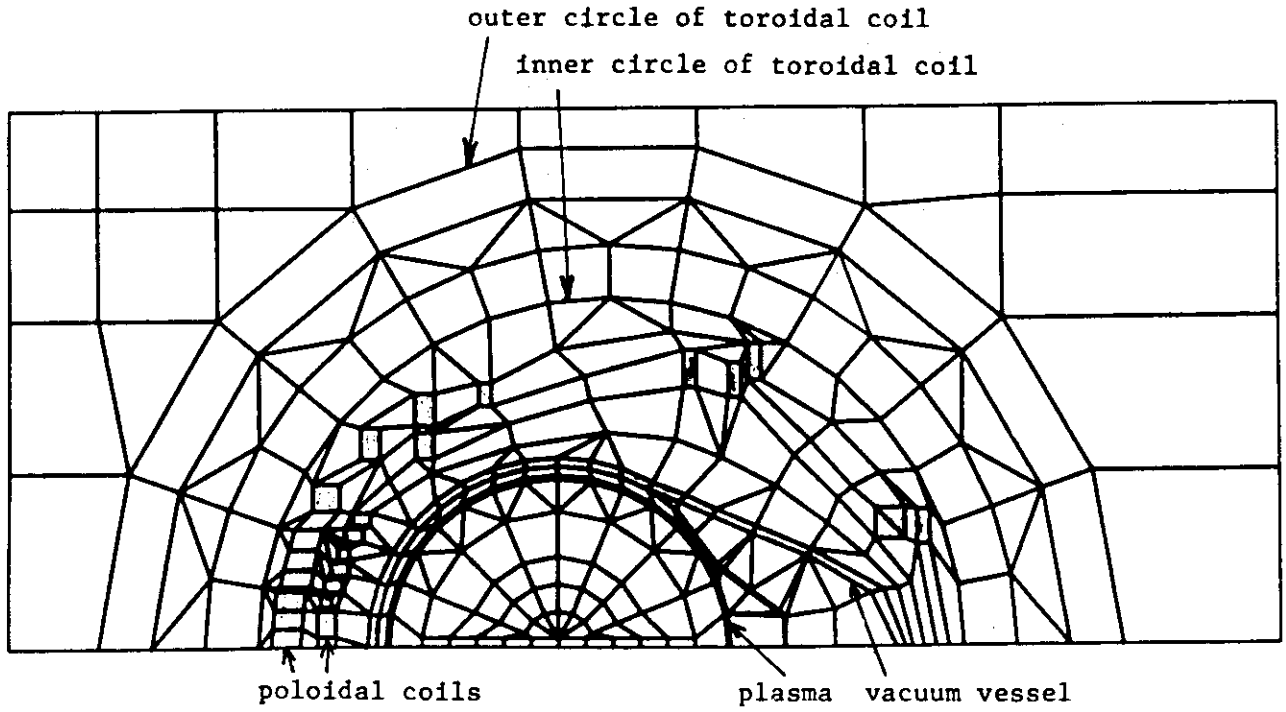

Fig.VIII.5.1-8 Finite elements for the eddy current analysis

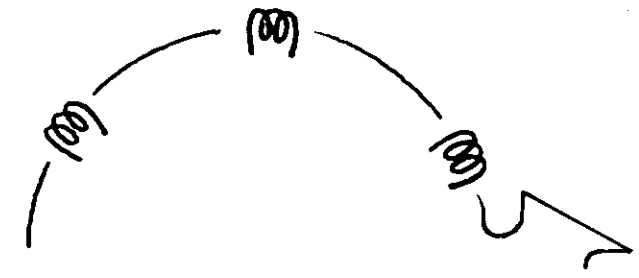

(a)

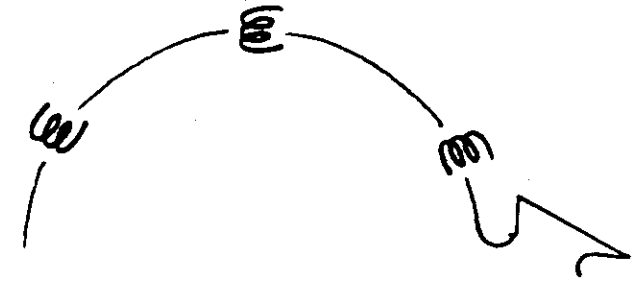

(b)

Fig.VIII.5.1-9 Magnetic probe signals for plasma position and shape detection, (a) Tangential poloidal field measurement, (b) Normal poloidal field measurement.

5.2 Planning of Diagnostic System

Emphasis has to be placed on diagnostics in the JT-60 program. This is not only because of their usual role of making measurements of plasma parameters for the understanding of plasma behaviers, but also due to the bearing they have on the plasma and the device control and especially on the safeguard of the device.

5.2.1 Requirements in diagnostic planning for JT-60

Basic requirements in the diagnostic planning for JT-60 are as follows:

(a) Multiple measurements for each plasma parameter.
Crosschecking of plasma parameters by multiple diagnostic methods is needed to raise the reliability of measurements.

(b) Efficient use of each discharge.
All parameters required should be obtained in one discharge as many as possible. This requirement will enhance the efficiency and progress of experiments. For example, basic diagnostic equipments should be consolidated as a diagnostic system capable of temporarily and spatially resolved measurement.

(c) Capable data acquisition system.
A data acquisition system should be provided to acquire and process the output from diagnostic sensors. An efficient usage of a data acquisition system is required in the on-line plasma control and should expedite step-by-step progress of experiments.

(d) Reliable diagnostic equipments.
Since a wide range of diagnostics should be employed it is necessary to make each diagnostic equipment highly reliable. Especially sensors for the plasma control system must be made highly reliable.

(e) Systematic development of advanced diagnostic methods.
The plasma parameters to be measured in JT-60 are extended to a wider range than those established in the past. New diagnostic methods have to be developed and tested.

5.2.2 Proposed diagnostic plan

A list of the proposed diagnostics with an abbreviated statement of their purpose is given in Table VIII.5.2-1.

In the standard diagnostic methods, submillimeter-wave interferometers, multipulse laser scattering equipments, super grazing incidence

monochrometers, and a high-counting-rate X-ray pulse height analysis system should hold high priority. In the new diagnostic methods the development of a FIR laser scattering system and the wall surface analysis system should be started at an early stage.

5.2.3 Arrays of diagnostic ports

A layout of diagnostics is shown in Fig. VIII.5.2-1.

(a) Horizontal access ports

Since the magnetic limiter will be set at the outer region of the vacuum vessel on the horizontal symmetry plane, there remains an access to the plsma along horizontal lines of sight only in the upper or lower edge regions of the plasma.

(b) Vertical access ports

There must be an access to the plasma along vertical lines of sight. The planar arrays of 2 or 3 elliptic tubes will be set at 4 sections of the vacuum vessel and can be used as vertical access ports of 6 to 8 chords. Other many planar arrays will have 3 vertical lines of sight around the torus.

(c) Oblique access ports

There is an access to the plasma along oblique lines of sight. The corresponding oblique access ports should be large so that the plasma can be viewed over a wide solid angle. Each port can be shared among heating systems, evacuating systems, or diagnostic equipments. It is desirable to have as many large oblique access ports as possible, so as to maximize access to the plasma.

5.2.4 Notes

Some of the problems associated with diagnostics are described below.

(a) Pumping

It is desirable to have a gate valve for each diagnostic equipment to be connected to the vacuum vessel in vacuum. Tests on the tightness and durability of all-metal gate valves should be made and the optimum baking temperature of the valves should be determined. The connections between the vessel and the vacuum diagnostic equipments have a reasonably large surface area. Care has to be taken to keep the outgas from the surfaces to a tolerable rate.

(b) Electrical safety breaks

There must be a provision for electrical insualtions between the diagnostic equipments and the diagnostic ports or between the diag nostic equipments and the ground. This is necessary to protect personnel and the diagnostic equipments from high voltages that may appear on the vacuum vessel by the plasma or as a result of device malfunction.

(c) Alignment mechanisms of vertical access ports

The vertical access ports will be extended above the device to beyond the poloidal and toroidal field coils and below the device to the basement. The arrays above and below the vessel must line up, so that the plasma can be viewed through from the top and the basement. Therefore alignment mechanisms by which we will be able to adjust setting errors and thermal displacements of the ports must be employed to the vertical access ports.

(d) Limitation of the space available to diagnostic equipments

The space around the machine is occupied by apparatas with high priority, such as neutral beam injectors and vacuum pumps. Care should be taken to leave as much space for diagnostics as practical and also to design the machine support structures to suit the diagnostics equipments.

(e) Radiation shielding

Diagnostic equipments must be shielded against hard X-rays which will be mainly produced at the magnetic limiter and limiter regions by runaway electrons and neutrons which will be produced from γ-n reactions.

(f) Magnetic shielding

Diagnostic equipments should be shielded against stray magnetic fields, as required to permit satisfactory operation. In turn, such magnetic shielding must not affect the field back at the plasma significantly. Expected maximum intensities of stray magnetic fields at the distance of 7 and 15 meters from the major axis of the device on the equatorial plane are about 500 and 30 gausses, respectively. In the vertical direction, its intensities at the distance of 7 and 15 meters from the minor axis are about 700 and 140 gausses, respectively. These values are much larger than in the present-day devices.

Table VIII.5.2-1 Proposed JT-60 diagnostic system

I. Standard Diagnostic Methods	
Diagnostic Name	Brief Description of Purpose
1. Electro-magnetic method	
1-1) One-turn Loops	Loop volts
1-2) Rogowski Coils	Plasma current (Total ohmic current)
1-3) Magnetic Probe Coils	Plasma position and shape, gross fluctuations
1-4) Diamagnetic Loops or Rogowski Coils for Toroidal Coil Current	Plasma pressure
2. Interferometry	
2-1) 4 mm μ-wave Interferometers	Electron density of initial breakdown and magnetic limiter plasmas
2-2) 2 mm μ-wave Interferometers Multichannel	Electron density in outer regions of plasma
2-3) Submillimeter-wave Interferometers HCN or CH_3OH laser, multichannel	Radial and temporal behavior of electron density
3. Thomson Scattering	
3-1) Ruby Laser Scattering Equipment Low stray light optical system	Spatial variation of electron temperature and density
3-2) Multipulse Laser Scattering Equipments Multipulse Nd or ruby laser	Spatial variation of electron temperature and density at several times
4. Spectroscopy	
4-1) FIR Spectrometers	Synchrotron radiation
4-2) Visible Spectrometers	Hydrogen atom density and impurity content close to plasma surface
4-3) V.U.V. Spectrometers Normal and Grazing incidence monochrometers	Impurity content, power radiated, ion temperature close to plasma surface
4-4) Ultra-soft X-ray Spectrometers Super grazing incidence and crystal monochrometers	Impurity content, power radiated, ion temperature

(part 1)

Diagnostic Name	Brief Description of Purpose
5. X-ray	
5-1) X-ray Pulse Height Analysis Semiconductor detector, high counting rate electronic circuits	Electron temperature, electron velocity distribution, impurity concentration
5-2) Soft X-ray Detectors SSD or PIN detectors	Internal plasma fluctuations, hot plasma column
5-3) Hard X-ray Detectors NaI or plastic scintillators	Runaway electron effects
6. Neutron	
6-1) Neutron Spectrometer H_e^3 spectrometer	Ion temperature
6-2) Neutron Counters B^{10} counters or activation detectors	Neutron flux
7. Neutral Particle Analysis	
7-1) Charge Exchange Neutral Particle Analysers	Ion temperature in outer region of plasma
7-2) High Energy Neutral Particle Detectors SSD detectors	Ion temperature, beam thermalization
8. Boundary Layer Analysis	
8-1) Thermal Flux Detectors Bolometers, thermocouples, IR TV	Total power loss to limiter or wall
8-2) Neutral Gas Analysers Fast ion gauges, mass analyser	
8-3) Plasma Position Detectors Fiber arrays, visible TV	

(part 2)

II. New Diagnostic Methods	
Diagnostic Name	Brief Description of Purpose
9. FIR Laser Scattering CH_3F or D_2O laser	Spatial variation of ion temperature and Z_{eff}
10. Resonance Scattering High power tunable laser	Spatial variation of impurity content
11. Current Density Distribution One of following methods : Heavy ion beam, H beam (counter injection), α-particle, Zeeman splitting, laser scattering, second harmonic-wave generation	Current density distribution, $B_p(r)$, $q(r)$
12. Fluctuation Analysis 12-1) Fluctuation CO_2 laser and μ-wave scattering 12-2) Potential Tl beam	Spatial variation of fluctuations Spatial variation of plasma potential
13. Wall Surface Analysis Auger electron spectroscopy, secondary ion mass analyser, X-ray micro-analyser	Examine wall surface effects

(part 3)

DIAGNOSTIC NAME	SECTION NO.
1. INTERFEROMETRY	
1-1. 4 mm μ-WAVE INTERFEROMETER	①
1-2. 2 mm μ-WAVE INTERFEROMETER	⑦,⑧,⑯,⑰
1-3. SUB-mm-WAVE INTERFEROMETER	⑧,⑰
2. THOMSON SCATTERING	
2-1. RUBY LASER SCATTERING	⑱
2-2. MULTI-PULSE LASER SCATTERING	⑱
3. SPECTROSCOPY	
3-1. FIR SPECTROMETER	③,⑫
3-2. VISIBLE SPECTROMETER	①,⑦,⑫,⑱,⑱
3-3. V.U.V. SPECTROMETER	②,④,⑤,⑤,⑪,⑬,⑭
3-4. ULTRA-SOFT X-RAY SPECTROMETER	③,⑤,⑩,⑭
4. X-RAY	
4-1. X-RAY PULSE HEIGHT ANALYSIS	⑤,⑨,⑭,⑱
4-2. SOFT X-RAY DETECTOR	⑤
4-3. HARD X-RAY DETECTOR	④,⑦,⑬,⑯
5. NEUTRON	
5-1. NEUTRON SPECTROMETER	①
5-2. NEUTRON COUNTER	⑥
6. NEUTRAL PARTICLE	
6-1. CHARGE EXCHANGE NEUTRAL PARTICLE ANALYSER	②,④,⑩,⑪,⑮,⑮
6-2. HIGH ENERGY NEUTRAL PARTICLE DETECTOR (SSD)	⑨,⑮
7. BOUNDARY LAYER ANALYSIS	
7-1. THERMAL FLUX DETECTOR	⑮
7-2. NEUTRAL GAS ANALYSER	⑤
7-3. PLASMA POSITION DETECTOR	⑨
8. COLLECTIVE SCATTERING (FIR LASER SCATTERING)	⑨
9. RESONANCE SCATTERING	⑥
10. WALL SURFACE ANALYSIS	
10-1. AUGER ELECTRON ANALYSER	⑯
10-2. SECONDARY ION MASS ANALYSER	
10-3. X-RAY MICRO-ANALYSER	⑬

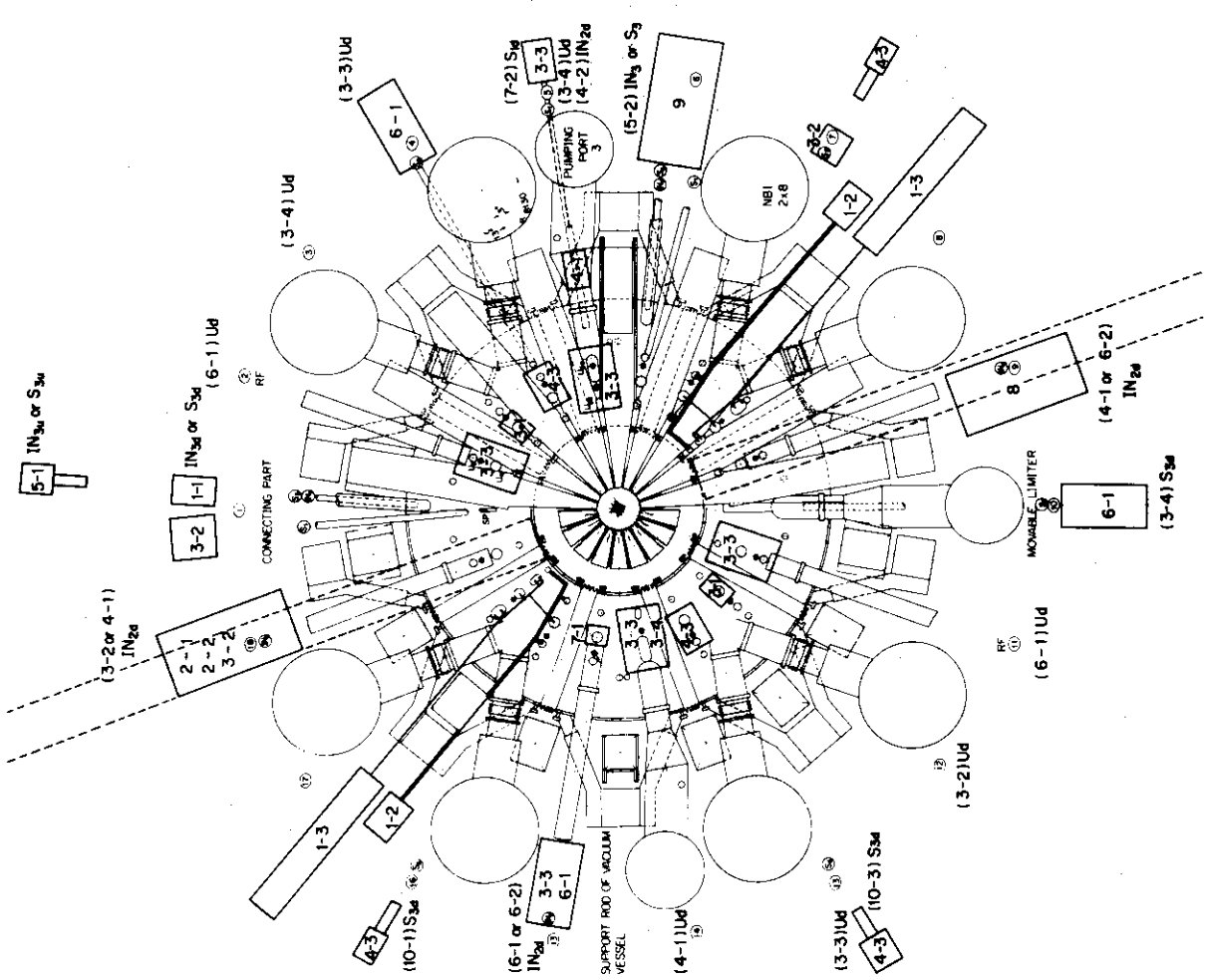

Fig.VIII.5.2-1 Conceptual layout of diagnostics

6. Design of Auxiliary Systems

6.1 Review of auxiliary system design

In the year 1976-7 the design of vacuum pumping system, secondary cooling system, and power distribution system were made by industry as part of the detailed design of JT-60. The design studies of gas supply and preionization systems were also made.

6.1.1 Vacuum pumping system

The vacuum pumping system of JT-60 is to provide ultrahigh vacuum in the vacuum vessel and help produce clean surfaces at the first wall (limiters and liners). It also should have a pumping capability large enough to evacuate the vacuum vessel in an interval between discharges.

The system consists of the following major subsystems:

Pump subsystem (main pumps, auxiliary pumps, roughing pumps, supplementary pumps, and maintenance pumps),
Compressor subsystem,
Cooling subsystem,
Liquid nitrogen supply subsystem,
Nitrogen gas inlet subsystem, and
Control and measure-ent subsystems.

The main pumps are turbomolecular pumps and have a net total pumping speed of 20,000 ℓ/sec (N_2). The vacuum pumping system consists of two identical sets each connected to a pumping port of vacuum vessel. The diagram of one of those sets is shown in Fig. VIII.6.1-1.

6.1.2 Secondary cooling system

The secondary cooling system is to remove and dissipate heat generated in each system of JT-60 transferred through its heat exchanger. Major components of the system are a cooling tower, water pumps and pipes, and water processing units.

The design was made under the following conditions; maximum wet thermometer temperature 26.5°C, maximum temperature of supply water 30°C, and maximum allowable water supply 150 m^3/hr. Some of the characteristic values of the system is summarized below:

Total circulation of water	15,300 m^3/hr
Inlet temperature at exchanger	35°C
Outlet temperature at exchanger	39°C

Cycle number	8.5
Total water supply	121 m^3/hr
Average heat removed	5.2×10^7 kcal/hr

6.1.3 Power distribution system

The power distribution system receives electric power from the central power station and distributes the power directly to the toroidal and the poloidal field coil power supply and through power distribution subsystems to the vacuum pumping, secondary cooling, and other systems and to the buildings. The distributed power is as follows:

1. Toroidal field coil power supply:
   - to motor-generator 30 MVA
   - to the coil directly 180 MVA
2. Poloidal field coil power supply:
   - to motor-generator 30 MVA
3. Supplementary heating power supply:
   - to motor-generator 30 MVA
4. Operation distribution subsystem: 15 MVA
5. Building distribution subsystem: 12.5 MVA

6.1.4 Gas supply system

The system serves for the purpose of injecting gases (H_2, He, Ne, O_2 and Ar) into the vacuum vessel. It can be classified into four supply subsystems, one continuous and three pulsed. The latter three are respectively for initial filling of the vessel, for density control and for terminating discharges.

Specifications of the system is summarized below:

1. Continuous gas supply subsystem
   - Vacuum vessel pressure for discharges 1×10^{-5}-5×10^{-4} torr.
   - Vacuum vessel pressure for the oxidation-reduction process 1×10^{-4}-1 torr.for H_2 and O_2
2. Pulsed gas supply subsystem for initial filling
   - Vacuum vessel pressure for discharges 5×10^{-5}-5×10^{-4} torr.
   - Maximum supply rate 1.3×10^4 torr.ℓ/sec
3. Pulsed gas supply subsystem for density control
   - Supply rate 0.5-80 torr.ℓ/sec
   - Control response time 10 msec

4. Pulsed gas supply subsystem for terminating discharges

Supply	10-800 torr.ℓ
Supply rate	5,000 torr.ℓ/sec

6.1.5 Preionization system

The system aims at producing a weakly-ionized plsma in a gas filled in the vacuum vessel before the initiation of a discharge.

Three types of preionization methods are considered. They are those using an electron gun, a J × B plasma gun, and a radio frequency power supply.

References

(1) Suzuki, Y., Ogata, A., Ninomiya, H., Aikawa, H. and Noda, N., JAERI-M 6531 (1976).

(2) Hugill, J. and Gibson, A., Nuclear Fusion 14 (1974) 611.

(3) Ogata, A., Ph. D. dissertation, Tokyo Univ. (1975), Fujiwara, M., Ito, S., Matsuoka, K., Matsuura, K., Miyamoto, K. and Ogata, A., Japan. J. Appl. Phys. 14 (1975) 675.

(4) Kameari, A., Aikawa, H., Ninomiya, H. and Suzuki, Y., JAERI-M 6468 (1976).

(5) Kameari, A., Ninomiya, H. and Suzuki, Y., JAERI M 6953 (1977).

(6) Zakharov, L.E. and Shafranov, V.D., Sov. Phys. Tech. Phys. 18 (1973) 151.

(7) Aikawa, H., Ogata, A. and Suzuki, Y., Japan. J. Appl. Phys. 15 (1976) 2031.

(8) Ogata, A., Aikawa, H. and Suzuki, Y., Japan. J. Appl. Phys. 16 (1977) 185.

(9) Aikawa, H., Ogata, A. and Suzuki, Y., JAERI M 6931 (1977).

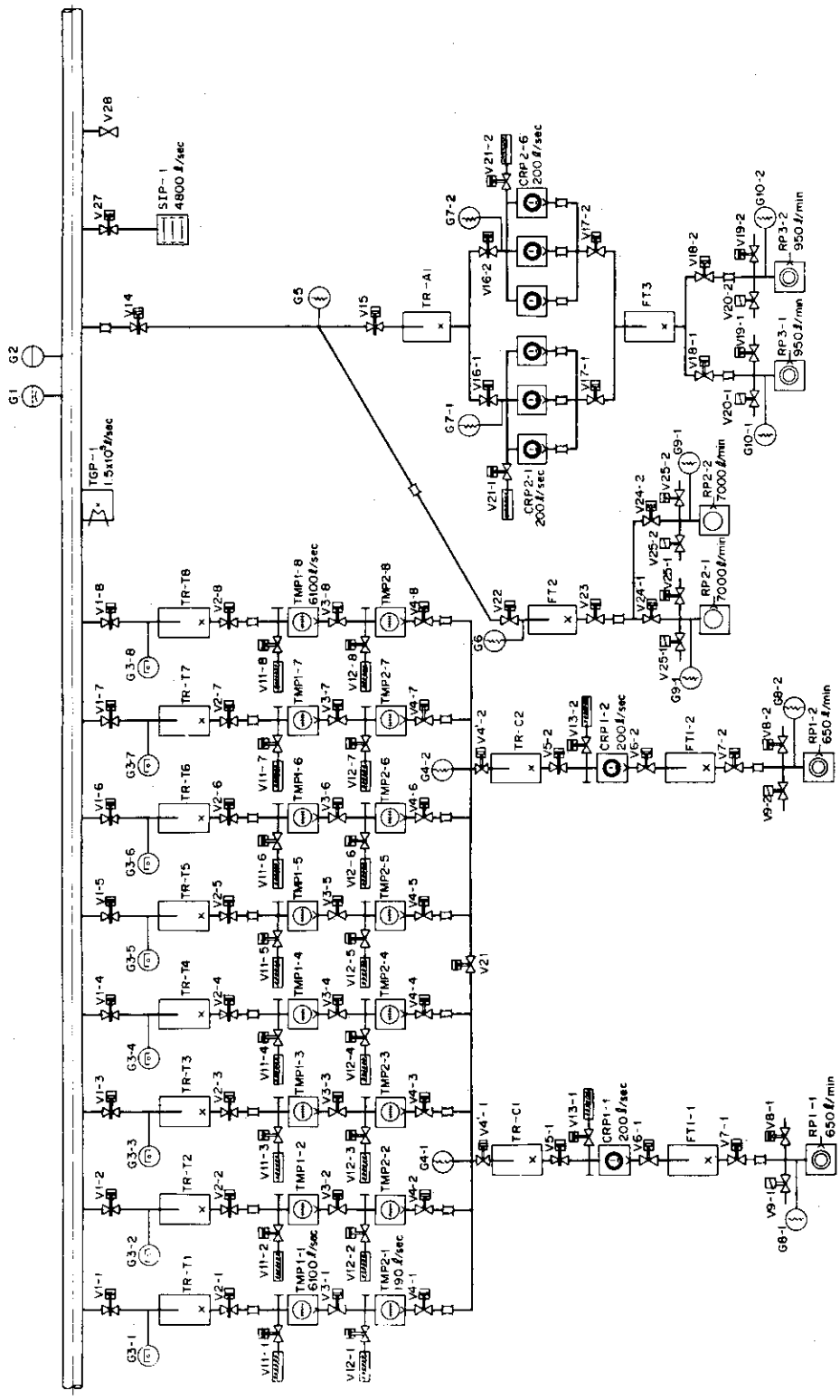

Fig. VIII.6-1 Diagram of one of two sets of vacuum pumping system

7. Studies on Plasma Physics and Elementary Processes Relevant to JT-60 Program

7.1 Studies related to magnetohydrodynamics behaviors

7.1.1 Plasma equilibrium during the current build-up with dynamic magnetic limiter[1]

At present we have no diagnostic tools to measure a plasma current profile directly in the tokamak experiments. However, various tokamak simulations, as well as informations on internal inductance of plasma, present the fact that a skin current profile may be formed at the current-rise phase of a discharge, and that it grows a central core profile in the steady state. This behavior has a few disadvantages in the tokamak operations that a kink instability can be excited, and joule heating at the periphery of plasma leads to a large amount of energy loss, which results in the excessive thermal loading to limiters.

To avoid these difficulties, two methods are applicable, both of which are based on the idea of expanding a plasma radius dynamically in proportion to the plasma current in the start-up phase: One method is a use of a movable high speed limiter, the other is a use of a dynamic magnetic limiter. Here, the latter has been studied which suppresses a skin current distribution during a current-rise phase of a discharge in a large tokamak JT-60. An octupole field is adopted to obtain a series of the equilibrium configurations in each stages of the increasing plasma current by free-boundary MHD equilibrium calculation.

The configurations in case of $q > 1$ are always stable against positional, ideal local, and convective instabilities. However, periphery of the plasma column suffers from the resistive instability even if $q > 1$. The length of the unstable layers is predicted to be approximately $10 \sim 14$ cm at the outside and $4 \sim 6$ cm at the inside of the poloidal cross section.

While the resistive instability can be excited in case of an ordinary circular plasma when $q < 1$ because of uneffectiveness of a shear field, separatrix line at the outer surface of poloidal cross section, in our case, makes a situation harder.

7.1.2 Positional instabilities in a Tokamak with a magnetic limiter[2]

Recently, non-circular cross section tokamaks have been studied as a promising approach in fusion devices because of the possible attainment of a high β plasma in them. Such fusion devices in the reactor stage are

designed to have external conductors for positional control of a plasma instead of a conventional copper shell since a longer discharge duration is expected. Moreover a magnetic limiter (or a divertor) is considered to be needed in recent tokamaks in order to reduce impurity particles in a plasma. Positional instabilities of the plasma confined in these magnetic configurations, i.e., vertical displacement and horizontal expansion, become a significant problem.

The stability conditions for these positional instabilities in circular cross section tokamaks have been discussed by Yoshikawa by using the approximation of large aspect ratio R/a where R and a are the major and the minor radius of the plasma, respectively. He has given the stability criteria $0 < n < 3/2$ where n is the so called n-index $(-R/B_Z \cdot \partial B_Z/\partial R)$ of the vertical field. The lower limit $n > 0$ for vertical displacement of non-circular plasma has been also obtained numerically by Okabayashi and Sheffield, and Lackner and Macmahon independently.

The stability conditions of a plasma with respect to its rigid vertical displacement and horizontal expansion are numerically studied for a tokamak with magnetic limiters. The stability regions are discussed in terms of the decay index n of the equilibrating vertical field at the center of the plasma cross section. The plasma is stable up to $n = 2.32$ for the horizontal expansion even when a magnetic limiter is located in the outer side of the plasma cross section. For the vertical displacement, the plasma is stable even if $n = -1.16$ when magnetic limiters exist in the upper and lower sides of the plasma cross section. These results indicate that the uniformly displaced plasma is stabilized by the existence of the auxiliary coils, because the current flowing in the coils makes the curvature of the magnetic field lines convex to the plasma.

7.1.3 Computer code for determination of poloidal field coil positions[3],[4]

A computing code using a graphic display is developed for positioning various poloidal coils (transformer, vertical field, quadrupole field and horizontal field coils) in the large tokamak JT-60. It enables us to determine the optimum positions despite the constraints such as the interference between coils and the forbidden regions occupied by measuring ports, neutral beam injectors, vacuum system, etc..

In detailed design of large Tokamak JT-60, standard positions of the poloidal coils (transformer, vertical field, quadrupole field, and horizontal field) have been determined by this code POPOCO GRADIS using a

graphic dispaly . It is possible to suppress the stray field due to a current flowing through the transformer coils below 26 G at plasma periphery. However, it becomes as high as 150 G when the position of each transformer coil has a setting error of 2 cm in random directions.

The other control fields can be held within 5 % of the objective functions.

7.2 Studies related to partial and energy balances

7.2.1 Breakdown processes of toroidal discharges

In toroidal geometry, it seems little has been known about breakdown processes of electrical discharges[5]. To determine the maximum voltage of the poloidal field power supplies, especially of the ohmic heating power supply, knowledge about the breakdown phase of discharge is necessary.

The problem here is how electrons increase in number and are lost in the breakdown phase of toroidal discharges. If the electrons are collisional enough to be described by the α-ionization processes, electron avalanche occurs depending on the rate of multiplication of electrons by the α-effect and the rate of loss caused by the toroidal drift of electrons out towards the wall of the vacuum vessel.

At the initial phase of discharge, it is necessary to take into account the electromagnetic coupling between the plasma and the poloidal field coils and the vacuum vessel. It should be noted that the vacuum vessel carries a larger part of currents at this phase than plasma and these currents produce an error field in the plasma region which influences the growth of the plasma current.

To study the initial phase of discharge of JT-60, the following equation is used to model the plasma circuit:

$$L_p\dot{I}_p + R_pI_p + \Sigma M\dot{I} = 0.$$

The electric field which the electrons in the plasma feel is due to the resistive voltage and is not the inductive one. To calculate the breakdown process of discharge, it is important to consider the effect of the currents induced in the vacuum vessel on the growth of the plasma current as described above. Based on this consideration, a ring model computer code was developed to study the transient electric currents and magnetic fields in the system of poloidal field coils of JT-60 at the initial phase of plasma current build-up. This computer code is available to analyze the transient phenomena of all the related poloidal field coils including the vacuum vessel of JT-60. Figure VIII.7.2-1 shows an example of obtained results of the time evolution of electron density N_e and plasma resistance, where the calculation does not include the electron loss processes and it was made till the ionization rate of 0.15 was reached.

7.2.2 Effect of minor-radius expansion in the current build-up phase[6]

To avoid a strong skin effect in the current density which may appear in the current rising-phase in a large tokamak, JT-60 has been designed to be operated with a fast movable limiter and a magnetic limiter to make a minor-radius expansion of the plasma during current build-up.

A plasma simulation code was developed to study the current build-up process with a minor-radius expansion of the plasma in JT-60. Plasma simulation is made with a model which represents well overall plasma behavior of the present-day tokamaks. The external electric circuit is taken into consideration in the calculation. A calculation with typical parameters of JT-60 shows a weak skin distribution in the current density and the electron temperature, if the minor radius of the plasma is increased with build-up of the plasma current.

7.2.3 Impurity analysis

Estimation of the permissible level of impurity concentration in JT-60 has been performed from the standpoint of related energy losses due to light or heavy impurities such as carbon, oxygen an iron[7]. Our considerations were on the basis of a following simple model. On the assumption of a cylindrical plasma, a set of MHD equations for the stationary impurity ion densities, taking into account the empirical diffusion across the magnetic field and ionization-recombination process (including dielectronic recombination), is given as

$$-1/r\cdot d(r\Gamma_k)/dr + n_e(\alpha_{k-1}n_{k-1}-\alpha_k n_k) - n_e(\beta_{k-1}n_k-\beta_k n_{k+1}) = 0$$

where $\Gamma_k = -(1+q^2)\rho_k{}^2\nu_k[\gamma_d\cdot dn_k/dr - \gamma_w(k-1)(1/n_i\cdot dn_i/dr - 1/2T_i\cdot dT_i/dr)n_k]$

$k = 2,3 \ldots, M$

Numerical results, total energy losses including ionization, excitation and bremsstrahlung per unit volume are empirically expressed as following

$$P_t = 3.2\times10^{-4}(\bar{n}_e/10^{20})^2 c_z(\%)A^2 \quad (MW/m^3)$$

Input power of supplementary heating is estimated to be about $0.1 \sim 0.5$ MW/m^3, therefore permissible level $c_z\%(=N_z/N_e\times10^2)$ of impurities should

be evaluated. Provided that $p_t \leq 0.1$ MW/m^3, $\bar{n}_e = 5\times10^{19}$/m^3, in JT-60 they are

C ; 9 % O ; 5 % Fe ; 0.4 %

where $\bar{n}_e$, N_e and N_Z denote the average electron density, total number density of electron and total number density of impurities respectively. In JT-60, first wall is planned to be made of molybdenum, therefore we must estimate the permissible level of molybdenum concentration. From above empirical extrapolation, its value will be estimated to be of the order of 0.1 %. But, for more detailed estimation and impurity analysis of experimental data in JT-60, it is necessary that impurity code of molybdenum is accomplished. Similar estimation for molybdenum to light impurities is now in progress. It includes many open problems such as atomic structures, transition probabilities, oscillator strengths and their identifications with the experiments. As one of the investigations of molybdenum, we study a general formula of the dielectronic recombination process in order to evaluate the ionization balance including impurity transport across the magnetic field, neglecting density effect in tokamak plasma. The results for most probable resonance transition is as following[8]

$$\alpha_{di}(n\ell,n'\ell') = \frac{h^3}{2(2\pi mkT)^{3/2}} \sum_{n''} \sum_{\ell''} \frac{\omega(n'\ell')2(2\ell''+1)}{\omega(n\ell)} \exp\left(-\frac{E_{ex}+z^2 I_H/n''^2}{T}\right) \times \frac{A_r(n'\ell' \to n\ell)A_a(n'\ell';n''\ell'' \to n\ell;E_e\ell_e)}{A_r(n'\ell' \to n\ell) + A_a(n'\ell';n''\ell'' \to n\ell;E_e\ell_e)}$$

Numerical results for oxygen, carbon are agree well with the results from Bergess's formula[9]

$$\alpha_{Burg} = 2.4\times10^{-9}\, A(x)\, B(z)\, f \exp(-\tilde{E}/T)\, T^{-3/2}$$

$$A(x) = x^{1/2}(1+0.105x+0.015x^2)^{-1} \qquad x > 0.05$$

$$B(z) = z^{1/2}(z+1)^{5/2}(z+13.4)^{-1/2} \qquad z \leqq 20$$

$$x = E_{ex}/(z+1)I_H$$

$$\tilde{E}/T = E_{ex}/\{1+0.015z^3(z+1)^{-2}\}/T \qquad \tilde{E}/T \leqq 5.0$$

which is available for only light impurities ($z \leqq 20$).

Atomic structure calculation will be performed by means of the Dirac-Hartree-Fock method[10] or Pauli approximation for the elements of moderate atomic number.

7.2.4 Studies of neatral beam injection heating

Quasi-perpendicular neutral beam injection is planned in JT-60 to attain sufficient beam penetration into the plasma. The injection angles are set at 90 ± 20 degrees with respect to the magnetic axis and ±36 degrees with respect to the median plane. The preferable parameters of the plasma before injection are chosen so that $\bar{n}_e Z_{eff} \sim 8\times10^{13}$ cm^{-3} for the hydrogen beam at 75 keV. When $\bar{n}_e Z_{eff} << 8\times10^{13}$ cm^{-3} the beam power deposits near the plasma edge. Then the energy loss is enhanced as well as the fast ions born near the edge impact more likely the wall and/or the limiter. On the other hand for $\bar{n}_e Z_{eff} << 8\times10^{13}$ cm^{-3}, a large amount of the beam atoms bombard directly the wall without being ionized. The beam power 20 MW may sustain the plasma beta at $\beta_p = 1$ in case where the energy confinement time $\tau_E \sim 0.3$ sec.

The loss and the slowing-down processes of the fast ions born in the plasma have been studied in a Monte-Carlo simulation code. The loss of the fast ions having banana orbits does not exceed a few percents of the injected atoms in a device such as JT-60. In the meanwhile the energy loss owing to the charge-exchange process increases beyond ten percents of the injected beam power when the neutral atom density is more than 3×10^3 cm^{-3} near the plasma edge. The escaping atoms have energies in the range 1-10 keV where the sputtering yield is maximum for the molybdenum wall. Hence the control of the neutral atom density in the plasma is important to achieve the successful injection heating in JT-60.

During the slowing-down stage of the fast ions the energy spectrum of the fast ions becomes broad with increasing the electron temperature of the base plasma. This result implies that the beam energy transferred to the plasma ions increases as the electron temperature becomes high. For typical parameters of JT-60, $\bar{n}_e = 3\times10^{13}$ cm^{-3} and $Z_{eff} = 3$, the beam energy is delivered equally to the electrons and the ions when $kT_e \sim 4$ keV.

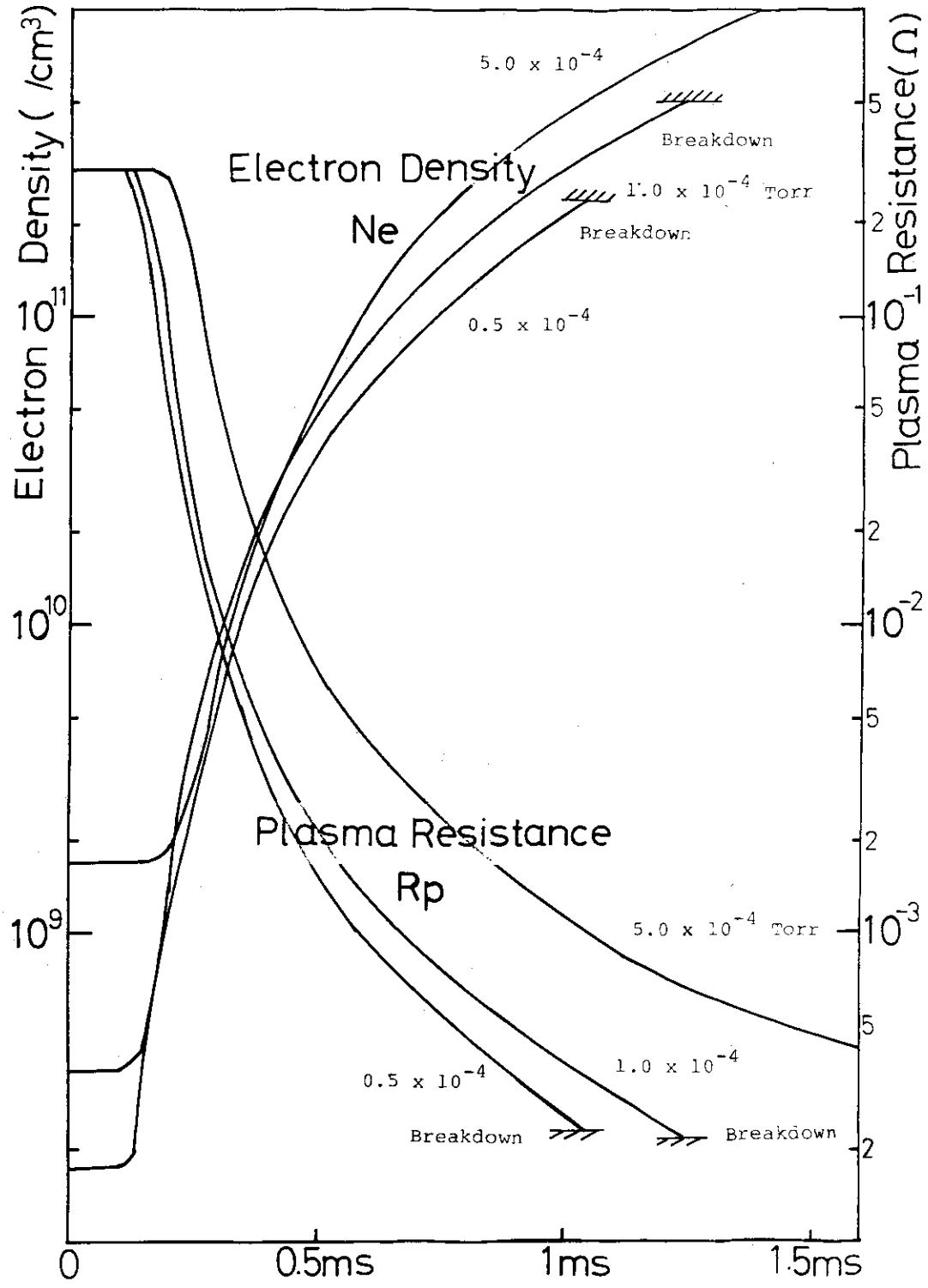

Fig. VIII.7.2-1 This evolution of electron density and plasma resistance at breakdown phase of discharge

7.3 Experimental studies of surface-related problems[11]

As the countermeasures to contamination by light impurities such as oxygen and carbon in tokamak devices, especially in future large ones, the following experiments were performed to study cleaning methods of the first wall.

7.3.1 Outgassing rates of first wall materials

A high vacuum is necessary to reduce the initial adsorbed gases on the wall surface before the final treatment such as a discharge cleaning, and to prevent the large amount of ambient gases from adsorption during the intervals of discharges. Baking is a one of the potential method to attain a high vacuum, but there exist few available data as to the outgassing rates in a UHV region except for stainless steel especially as to those after baking at high temperature. We have been studied for two years as to the outgassing rates of some wall materials including low-Z materials by a bakeout of 500°C.

Those at room temperature of 304 stainless steel, stainless steel YUS-170, Inconel 625, Hastelloy-X and molybdenum were reduced to 6.7×10^{-10}, 8.8×10^{-11}, 7.3×10^{-11}, 3.6×10^{-11} and 5.1×10^{-11} $Pa.\ell.s^{-1}.cm^{-2}$ after they were baked for 50, 50, 200, 50 and 100 hours, respectively, as shown in Table VIII.7.3-1. Those of pyrolitic graphite and silicon carbide coated onto graphite by chemical vapour deposition are 1.2×10^{-9} and 8.0×10^{-8} $Pa.\ell.s^{-1}.cm^{-2}$ after they were baked for 50 hours. These characteristics are shown in Figs. VIII.7.3-1 and 2. Pyrolitic graphite is one of the potential materials.

7.3.2 Cleaning of molybdenum surfaces by chemical treatment

In order to remove carbon and oxygen from molybdenum surface, 0.1 torr oxygen and 1 torr hydrogen gases were supplied alternately at a surface temperature of 350, 425 and 500°C, and the surface composition was observed by AES. Depth profiles of the atomic composition in the molybdenum surface layers were also measured by Auger/sputter techniques after the treatments.

The samples were cleaned by heating up to 1800°C in vacuum till the fraction of carbon and oxygen on the surface was reduced to a few ten atomic percent (a/o), and the thickness of the contaminated layers by more than 10 a/o carbon and a few atomic percent oxygen was about 1000 Å.

After this thermal cleaning, the samples were exposed to air for a few hours. By chemical treatment at 500°C, the final fraction of surface impurities was less than 10 a/o, while at 350°C and 425°C such effect was not observed. These results are shown in Figs. VIII.7.3-3 and 4.

7.3.3 Surface damage due to energetic ion bombardment

A part of energetic neutral beam for supplementary heating penetrates the plasma and hits the first wall. This process is considered to be one of the potential source of the plasma contamination. Recently, anomalous sputtering yeild was reported[12], i.e. sputtering yeild of the blistered surface exceeded by one order or more in comparison with that of no blistered surface, and also it had strong dependence on the surface temperature. The experiments were performed to study the surface errosion under the pulsed hydrogen ion beam bombardment.

Pulsed ion beam irradiated polycrystalline molybdenum surfaces at the energy of 25 keV with the dose rate of 30 mA/cm^2 for 100 msec with the duty cycle of 9 %. The total doses amounted to 20 C/cm^2. The target temperature ranged from room temperature to 500°C. The radiation damage was observed by scanning electron microscope (SEM) and microstylus techniques.

Our results are expressed as the following.

I) Blistering did not take place at the temperature exceeding 150°C within the total dose of 20 C/cm^2. One can explain this in consideration of the gas release due to high diffusivity in molybdenum. This is qualitatively consistent with the result by Varbeek and Eckstain[13].

II) A new type of surface damage "Grain Ejection" was found especially near the temperature of 200°C[14]. This is quite different from blistering, because its damage size was about grain one of 20 μm ∿ 30 μm. Grain ejection had strong dependence with the target temperature, i.e. it took place at very narrow temperature range of 200 ± 50°C. One can explain qualitatively the temperature dependence of grain ejection in consideration of hydrogen diffusion in molybdenum.

Maintaining the first wall to be 500°C in JT-60 is considered to be powerful method against surface errosions such as blistering and grain ejection.

References

(1) Ninomiya, H., Kameari, A. and Suzuki, Y.: JAERI-M 6656 (1976).

(2) Ninomiya, H., Suzuki, Y. and Kameari, A.: Japan. J. Appl. Phys. 15 (1976) 2201.

(3) Kameari, A., Ninomiya, H., Aikawa, H. and Suzuki, Y.: JAERI-M 6324 (1975).

(4) Aikawa, H., Ninomiya, H., Kameari, A. and Suzuki, Y.: JAERI-M 6552 (1976).

(5) Papoular, R.: EUR-CEA-FC-769 (1975)

(6) Kobayashi, T*., Tazima, T., Tani, K., and Tamura, S.: The effect of plasma minor-radius expansion in the current build-up phase of a large tokamak, JAERI-M 7014, (March, 1977), 23 pp. (in Japanese), (* on leave from Atomic Energy Research Laboratory, Hitachi, Ltd.).

(7) Tazima, T., Nakamura, Y., and Inoue, K.: Nuclear Fusion, 17 (1977) 419.

(8) Nakamura, Y., Kasai, S., and Tazima, T.: JAERI-M 7019 (1977).

(9) Burgess, A.: Astrophys. J. 141 1558 (1964).

(10) Grant, I.P.: Adv. Phys. 19 747 (1970).

(11) Tazima, T., Gomay, Y.: Proc. Int. Symp. Plsma Wall Interaction (Jülich, 1976) 559~571.

(12) Kimura, T., Okuda, S., Kobayashi, J. and Akimune, H.: submitted to J.J.A.P.

(13) Varbeek, J. and Eckstein, W.: Applications of Ion Beams to Metals, ed S.T. Picraux, E.P. ErNisse, F.L. Vook (Plenum Press 1974).

(14) Nakamura, Y., Shibata, T. and Tanaka, M.: to be published in J. Nucl. Mats.

Table VIII.7.3-1 Outgassing rates of SS-304L, YUS-170, Inconel-625, Hastelloy-X, Molybdenum, Pyrolytic graphite and SiC coated onto graphite. [$Pa.l.s^{-1}.cm^{-2}$]

		Before bake-out				During bake-out				After bake-out			
		Time from starting pumping (hour)				Time after the temperature reaches 500°C (hour)				Time after the heater is turned off (hour)			
		1	5	10	20	1	5	10	50	1	5	10	20
Stainless steel SS-304L	Total	2.9E-6*4	5.3E-7	2.7E-7	1.3E-7	3.5E-5	7.6E-6	4.0E-6	2.3E-7	9.0E-9	2.5E-9	1.3E-9	6.7E-10
	m/e= 2(H_2)	1.9E-7	5.6E-8	2.9E-8	1.7E-8	2.5E-5	6.5E-6	2.7E-6	1.9E-7	8.5E-9	2.0E-9	9.3E-10	-
	18(H_2O)	1.5E-6	2.4E-7	1.3E-7	7.6E-8	3.9E-7	-	-	-	1.7E-10	-	-	-
	28(CO)	1.5E-7	3.6E-8	1.5E-8	1.1E-8	9.2E-6	7.3E-7	2.3E-7	3.9E-8	1.5E-10	3.4E-11	-	-
Stainless steel YUS-170	Total	5.2E-7	3.1E-8	1.3E-8	4.1E-9	3.7E-7	1.1E-7	5.7E-8	1.7E-8	3.4E-9*2	(4.0E-10)	(2.0E-10)	(8.6E-11)
	m/e= 2(H_2)	8.4E-8	3.2E-9	1.6E-9	3.8E-10	5.7E-8	2.5E-8	2.3E-8	4.3E-9	3.1E-9*2	-	-	-
	18(H_2O)	1.7E-8	1.3E-8	2.3E-9	2.0E-9	1.0E-8	1.3E-9	-	-	-	-	-	-
	28(CO)	2.7E-8	2.9E-9	1.3E-9	5.6E-10	2.3E-7	4.9E-8	2.7E-8	4.9E-9	1.3E-11*2	-	-	-
Inconel-625	Total	9.3E-6	1.3E-6	6.4E-7	2.6E-7	-	-	5.2E-6	2.4E-7	3.3E-10	1.4E-10	1.1E-10	7.3E-11
	m/e= 2(H_2)	9.0E-7	1.7E-7	1.2E-7	9.0E-8	-	-	4.1E-6	5.7E-8	1.7E-10	6.7E-11	6.9E-11	5.3E-11
	18(H_2O)	2.1E-6	4.5E-7	2.2E-7	1.6E-7	-	-	-	-	-	-	-	-
	28(CO)	7.7E-7	2.1E-7	1.3E-7	1.0E-7	-	-	8.3E-7	1.7E-7	6.0E-12	4.1E-12	3.4E-12	2.9E-12
Hastelloy-X	Total	1.7E-6	1.3E-7	6.7E-8	3.3E-8	-	1.6E-6	9.6E-7	2.0E-7	(3.7E-10)	(3.6E-11)	-	-
	m/e= 2(H_2)	2.8E-7	1.9E-8	1.0E-8	5.3E-9	-	2.0E-7	6.9E-8	2.4E-8	(2.3E-10)	(1.1E-11)	-	-
	16(CH_4)	5.1E-8	5.1E-9	2.8E-9	1.5E-9	-	-	-	-	(1.7E-11)	-	-	-
	18(H_2O)	7.3E-7	5.3E-8	2.7E-8	1.1E-8	-	3.6E-8	-	-	-	-	-	-
	28(CO)	8.0E-8	6.7E-9	3.7E-9	2.1E-9	-	1.2E-6	6.0E-7	1.3E-7	(1.1E-11)	(6.7E-12)	-	-
Molybdenum	Total	1.1E-5	1.6E-7	3.2E-8	4.7E-9	2.5E-6	6.3E-7	4.0E-7	1.6E-7	1.7E-10	9.3E-11	6.9E-11	5.1E-11
	m/e= 2(H_2)	1.1E-6	1.3E-8	4.0E-9	5.3E-10	6.2E-7	1.6E-7	8.0E-8	2.0E-8	9.3E-11	4.4E-11	2.7E-11	1.5E-11
	18(H_2O)	4.0E-6	7.6E-8	1.3E-8	1.9E-9	5.2E-7	1.3E-7	8.0E-8	1.7E-8	1.7E-12	9.3E-13	8.0E-13	8.0E-13
	28(CO)	8.0E-7	1.2E-8	3.1E-9	3.3E-10	7.7E-7	1.7E-7	1.3E-7	7.3E-8	3.2E-11*3	2.5E-11*3	2.7E-11*3	2.7E-11*3
	44(CO_2)	3.6E-7	2.9E-9	6.7E-10	-	-	-	-	-	-	1.6E-12	1.1E-12	7.7E-13
Pyrolytic graphite	Total	1.1E-6	1.3E-7	5.3E-8	2.0E-8	1.1E-5	4.7E-6	2.6E-6	1.0E-6	(1.2E-9)	(1.6E-10)	(1.3E-10)	(1.3E-10)
	m/e= 2(H_2)	2.4E-7	1.7E-8	7.3E-9	3.7E-9	1.5E-6	1.8E-7	1.0E-7	4.0E-8	(8.6E-10)	(1.3E-10)	(1.0E-10)	(8.0E-11)
	16(CH_4)	-	-	-	-	-	-	-	-	(6.0E-11)	(4.7E-12)	(2.7E-12)	(2.0E-12)
	18(H_2O)	4.8E-7	6.4E-8	2.5E-8	9.3E-9	6.9E-7	6.7E-8	-	-	-	-	-	-
	28(CO)	1.0E-7	1.1E-8	4.7E-9	1.9E-9	7.3E-6	3.3E-6	2.0E-6	7.3E-7	(3.3E-11)	(8.0E-12)	(5.6E-12)	(2.7E-12)
SiC coated onto graphite	Total	1.5E-5*1	3.6E-6	1.3E-6	4.3E-7	2.4E-5	5.2E-6	3.5E-6	-	-	-	-	-
	m/e= 2(H_2)	4.8E-6*1	8.0E-7	4.0E-7	1.5E-7	1.5E-5	4.8E-6	1.9E-6	-	-	-	-	-
	16(CH_4)	4.5E-7*1	6.7E-8	-	-	-	-	-	-	-	-	-	-
	18(H_2O)	2.7E-6*1	4.0E-7	1.6E-7	3.7E-8	-	-	-	-	-	-	-	-
	28(CO)	2.3E-6*1	8.0E-7	2.7E-7	1.3E-7	2.3E-6	5.3E-7	1.5E-7	-	-	-	-	-

*1: The outgassing rates at 2 hours from starting pumping.
*2: The outgassing rates at 0.35 hours after the heater is turned off.
*3: Nitrogen is a dominant gas in this stage.
*4: The expression 2.9E-6 shows 2.9 x 10^{-6}.

The outgassing rates shown in brackets are estiamted by assuming P_{H_2O} in Eq.3.

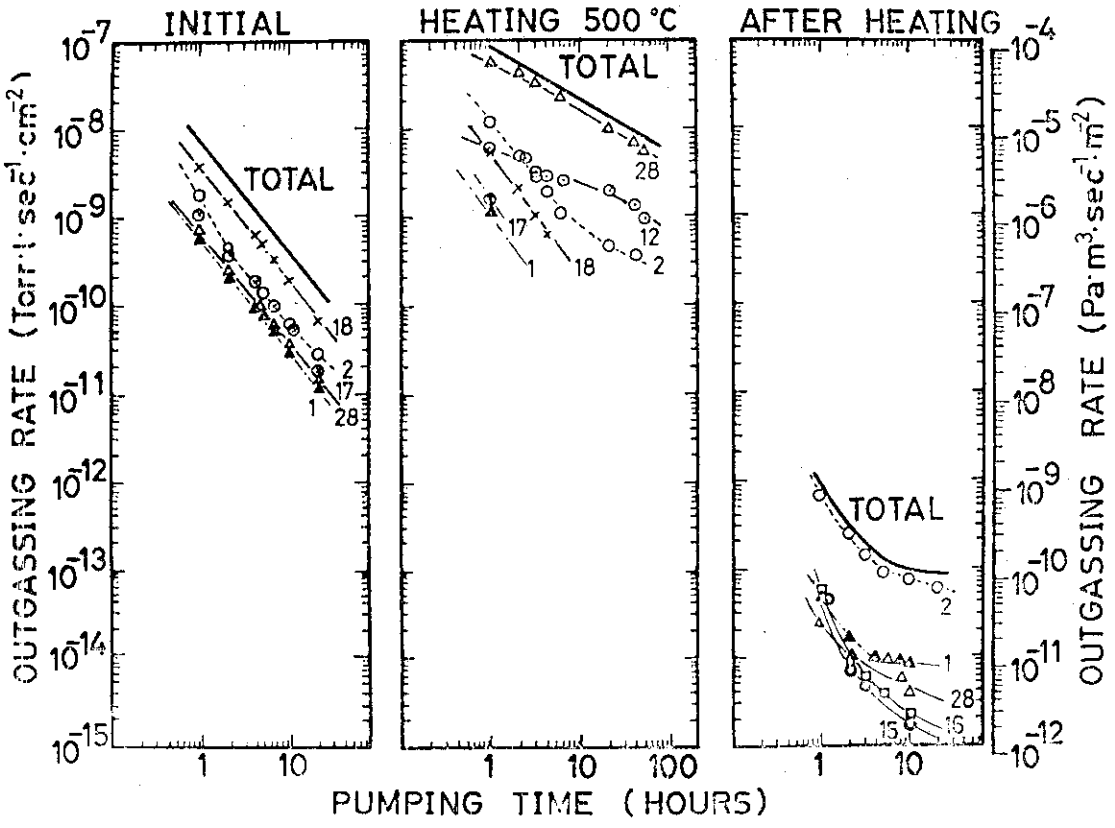

Fig. VIII.7.3-1 The outgassing rate of pyrolitic graphite

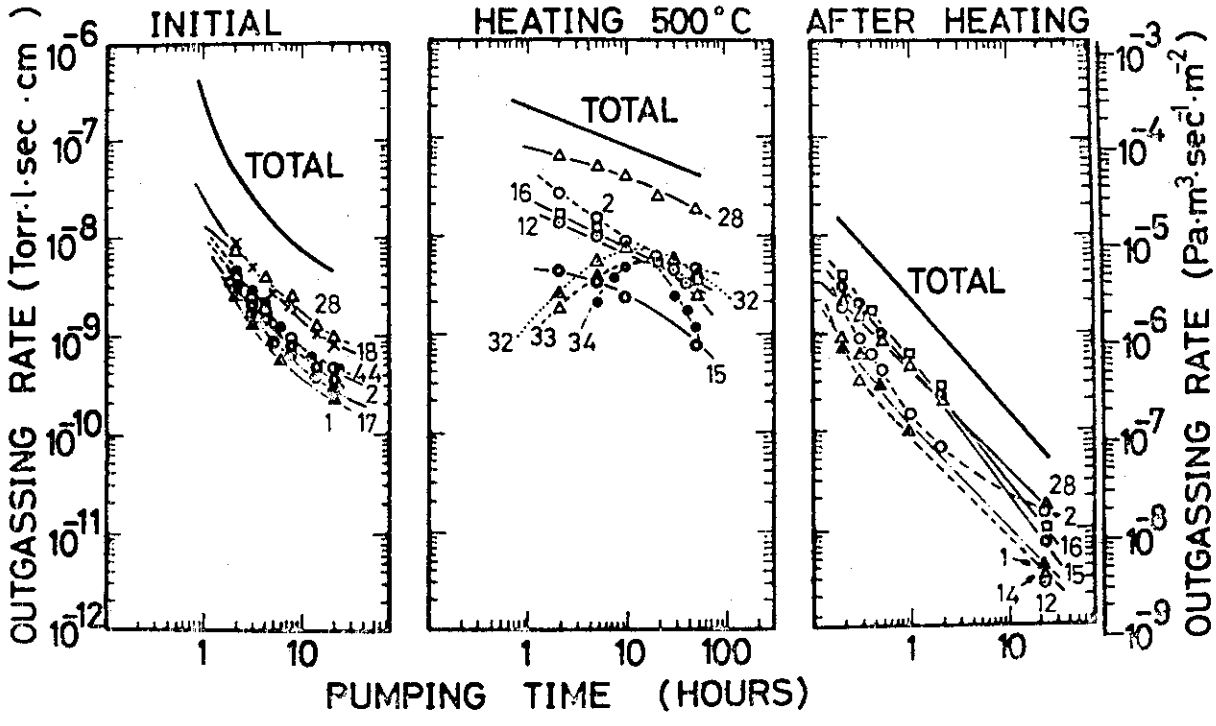

Fig. VIII.7.3-2 The outgassing rate of silicon carbide

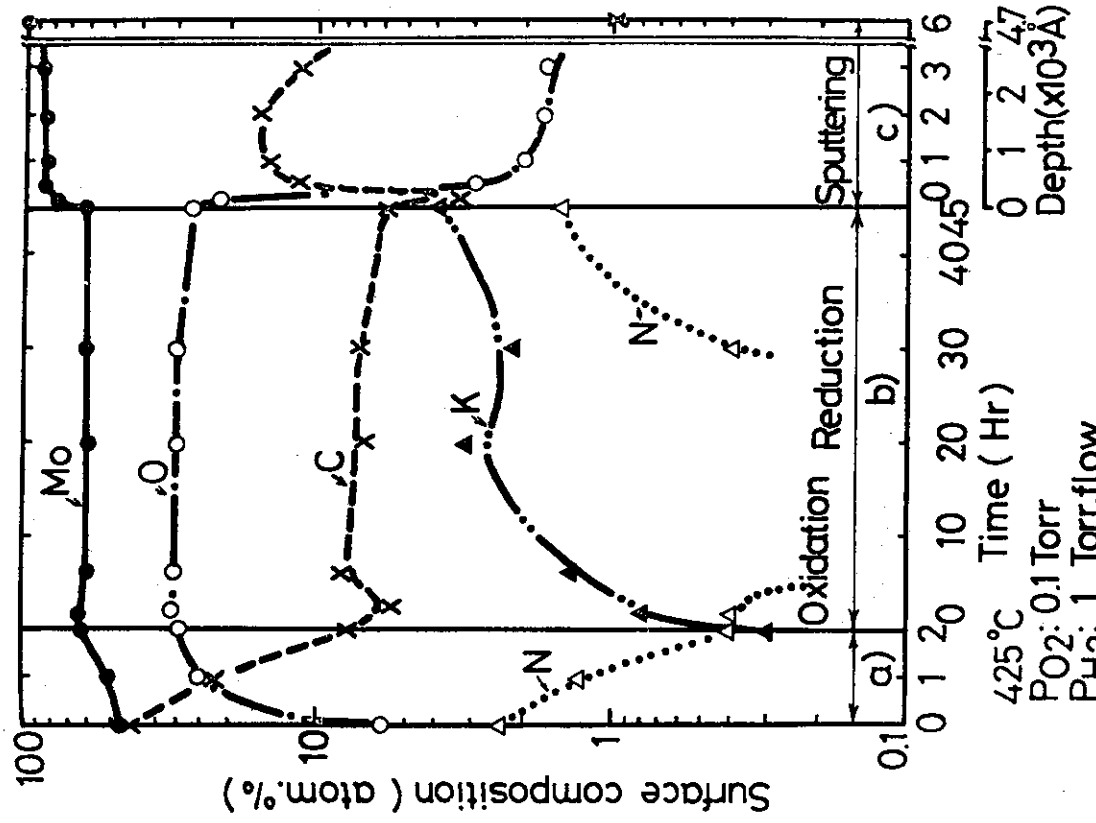

Fig. VIII.7.3-4 Chemical treatment on the molybdenum surface at 425°C

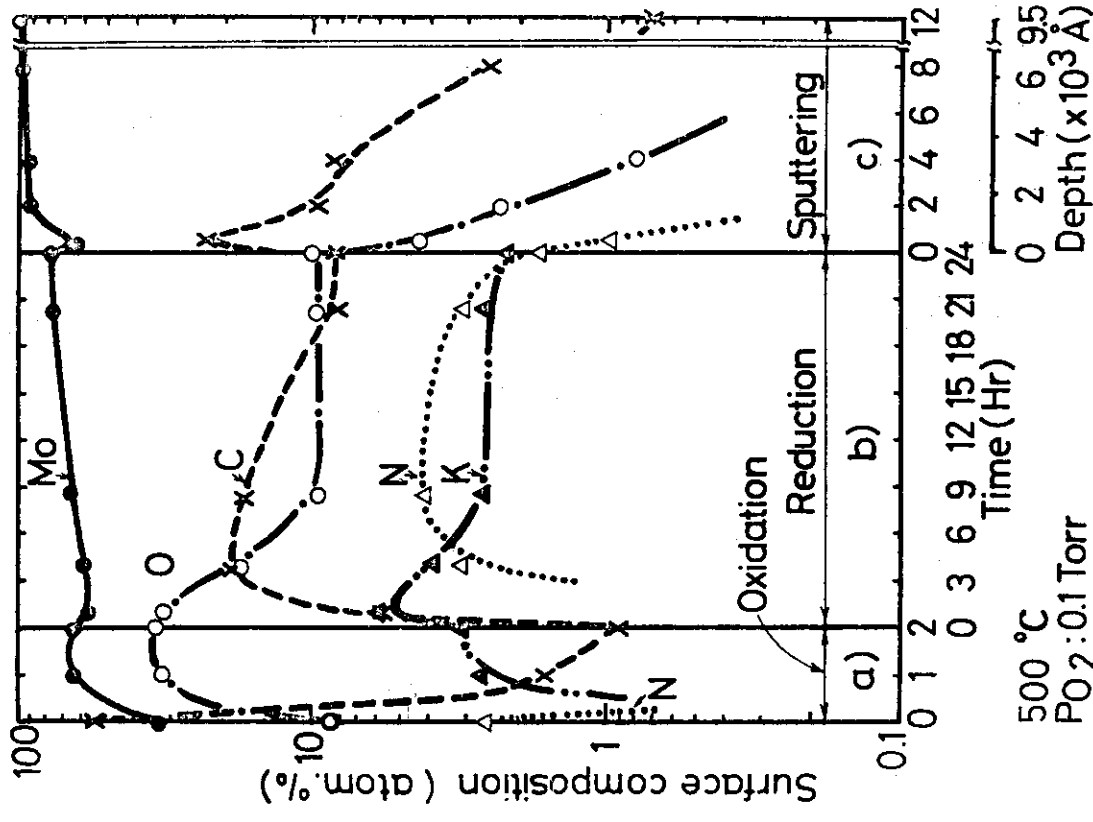

Fig. VIII.7.3-3 , Chemical treatment on the molybdenum surface at 500°C

IX. DEVELOPMENT OF A NONCIRCULAR TOKAMAK ---- JT-4

1. Introduction

JT-4 is a tokamak device under design with elongated plasma cross section and axisymmetric divertors. The basic purpose of JT-4 is to obtain experimental informations to attain higher efficiency of future large tokamaks or reactors. The purposes and design of JT-4 are examined at an official committee (The Nuclear Fusion Council) and will be approved in 1977. The device is expected to be operational at the end of 1981, the same time as JT-60.

2. Purposes and Schedule

JT-4 is a tokamak device with a plasma column of non-circular cross section and axisymmetric divertors. One of the equilibrium calculation results and the bird's eye view of JT-4 are shown in Fig. IX.2-1 and IX.2-2. The objectives of JT-4 program are to experimentally investigate 1) the effect of non-circular plasma cross section on attaining higher beta values and 2) the effect of divertor on reducing impurity contents and on controlling plasma density.

The experimental results on above objectives are essential to design efficient and low cost tokamak devices or reactors. To make these studies extraporatable to larger devices, high temperature plasmas are required for JT-4. Plasma temperature of more than 1 keV is set as one of the requirements. The additional heating by neutral beam injection with 50 keV and 6 MW will be applied to get plasma beta value of 0.05.

The main parameters of JT-4 are shown in Table IX.2-1.

Following the preliminary design of JT-4[1],[2] in FY 1975, the engineering studies and the tests of critical components were carried out in FY 1976, and the detailed design will be done in FY 1977. The final design which is almost the first stage of the construction is planned in FY 1978, and the construction is expected to start in FY 1979.

Table IX.2-1 JT-4 main parameters

Major Radius	0.45 m
Minor Cross Section Half Width	
Vertical (b)	0.68 m
Horizontal (a)	0.4 - 0.45 m
Ellipticity (b/a)	1.0 - 1.7
Toroidal Field	30 kG
Flattop	2 sec
Maximum Plasma Current	1.0 MA
NBI Heating Power	6 MW

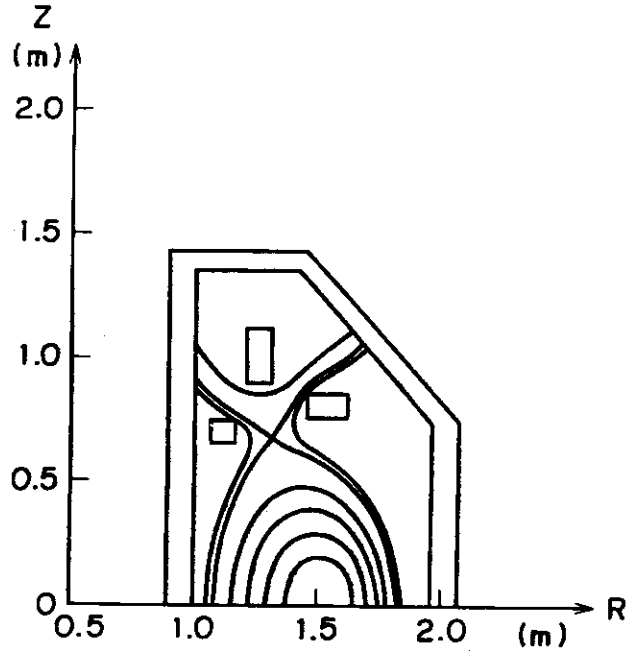

Fig.IX.2-1 Plasma equilibrium configuration of JT-4

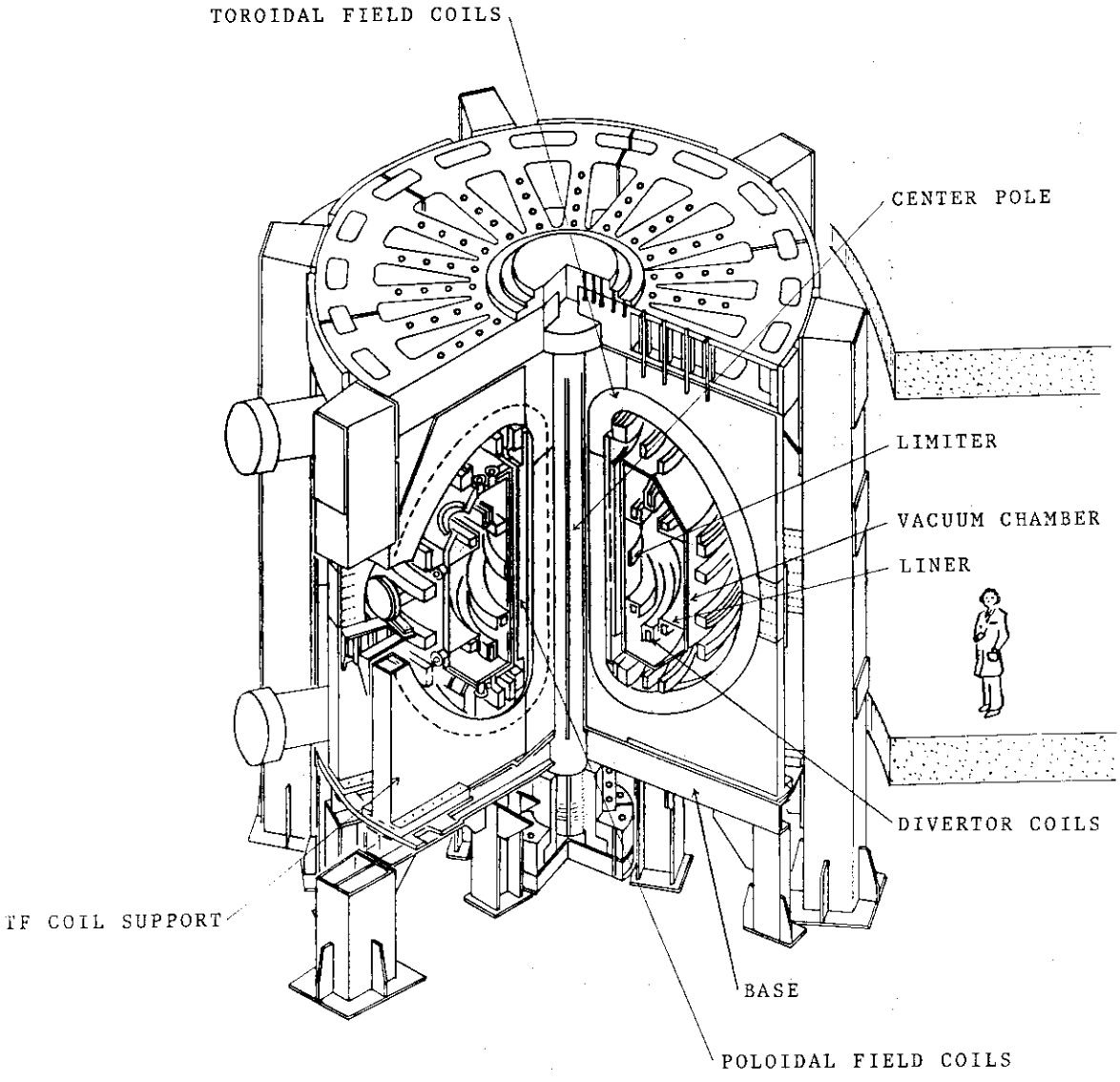

Fig.IX.2-2 Bird's eye view of JT-4

3. Design of JT-4

3.1 Development of noncircular welded bellows

In the JT-4 preliminary design, thin welded bellows with a noncircular cross-section was adopted from viewpoints of high one-turn electrical resistance around the torus, mechanical strength and limited spece for the bellows. The bellows section has a double vacuum structure and the bellows is only required to keep a high vacuum.

In order to overcome engineering difficulties, a noncircular welded bellows was examined again and the scaled models were made to test several properties.

The one-turn electrical resistance around the torus is kept more than 2 mΩ with two bellows sections. An equivalent pressure load of 1.2 kg/cm^2 is applied to the bellows in case of the emergency condition of the ASME Code. On account of mechanical, electrical and fabricating properties. Hastelloy X is preferable which belongs to a super alloy of nickel base. The thickness, the pitch and the span are decided to be 0.6 mm, 3.4 mm and 46 mm, respectively. The number of convolutions is 44 for one of the bellows sections. (Fig. IX.3.1-1) Spacers are put in 13 positions and spacers with a support in 6 positions in the cross-section.

Stress of the bellows were analyzed by a zoom-up method. Displacement were calculated by a simplified method and results were used in a detailed analysis of 2 convolutions from the end of the bellows, using a 3-dimensional FEM. The thermal stress was studied with a direct analysis method on 6 convolutions from the end of the bellows. A buckling was investigated by a simplified model. These results were evaluated according to the ASME Code and satisfied requirements except a thermal stress with baking temperature of 400°C. Temperature gradients along a bellows produced by the temperature difference between the vacuum chamber and the liner were limited to 4 °C/cm.

With respect to vacuum properties, the outgassing rate must be less than 10^{-12} torr·ℓ/s·cm^2 and it will be possible by appropriate surface treatments. A hydrogen penetration rate through 500°C bellows is estimated to be over 10^{-5} torr·ℓ/s in case of the pressure of 0.1 torr in the outer vacuum region, which can be reduced.

Scaled models of bellows section were made to establish the fabrication techniques. One model was a piece of bellows sections made of SUS 304 with a full scale of the thickness, the pitch and the span and the

cross-section was one third of a full scale. The other was a partial model made of Hastelloy X with a full scale. The former was put to several tests. In manufacturing of bellows TIG welding was applied and sufficient attention was paid to vacuum properties.

Several tests were carried out about the fabrication: accuracy of sizes, non-destructive inspections, cleanliness test, He leak test and pressure test. Results were in general satisfactory. A measurement of electrical resistance of a bellows agreed to the calculation.

Displacements and stresses of the bellows model were measured and compared with the numerical analysis. In one of the tests an end of the bellows section was fixed and one-dimensional load was imposed on the other end. The measured displacements and stresses roughly agreed with the calculated values. An external pressure load test in a high pressure water tank was also carried out.

3.2 Development of TF coil joint

JT-4 has splittable toroidal field (TF) coils instead of splittable poloidal field (PF) coils. It is because the available work space between the TF coils and the vacuum chamber is small and there are a number of PF coils which would have to be connected in a small space with high insulation voltage if the TF coils were not splittable.

The design points of the TF coil joint are the strong electromagnetic force, the thermal stress, the cooling, the insulation and the assembly. In the preliminary design of FY 1975, two kinds of design are proposed. One is to connect the copper conductors tightly and keep the other part free to avoid thermal compression stress. The other is to support all the electromagnetic force by casing and keep the joint part free except electric contact. In FY 1976, the former case was studied experimentally. At first one of joint structure was selected out of five kinds of candidate structures after tensile fatigue test using half scaled specimens. The structure was further improved and was put to the final tensile fatigue test, electric contact resistance test, stress distribution measurement, and current flow test. The final structure is shown in Fig. IX.3.2-1 and the tolerable stress of the conductor (applied tensile force divided by cross section at B in Fig. IX.3.2-1) is shown in Fig. IX.3.2-2. When the outer major radius of inner straight part of TF coil is 70 cm, the maximum stress of conductor at B is about 5.5 kg/mm^2 with space factor

of 0.7. It is shown in Fig. IX.3.2-2 that the joint structure selected here can work up to 2×10^5 times of full rating operation, and the design requirement of 1×10^5 times is satisfied.

The contact resistance of the half scaled joint model is 0.3 μΩ and increases up to 0.5 μΩ after 5×10^5 cycles of fatigue test, which is less than 40 % of the resistance of copper of the joint part. The partial test of strength of bolts and copper nuts was carried out to determine the shape of bolts and the fastening torque. The assembly test in a small inner space was also carried out with full scale wooden model shown in Photo. IX.3.2-1. The free joint structure was also studied and a kind of spring contactor plate was tested.

The TF coil will be designed again using those results obtained in FY 1975 and 1976, and the final design is expected to be fixed in FY 1977. The parameters of JT-4 TF coils at the preliminary design are shown in Table IX.3.2-1.

3.3 Experiments on in-situ coating of molybdenum

In the JT-4 preliminary design, Mo liner was used because of its low sputtering ratio and high melting point. In the design study of 1976, a composite wall consisting of a suitable coating on a substrate was chosen to avoid the difficulties in fabrication of Mo liner. An in-situ cleaning of the first wall is desirable because of the gas adsoption. For these reasons an in-situ coating of Mo was proposed and preliminary experiments were carried out.

Two physical vapor deposition (PVD) processes were applied. One method was a vacuum deposition with an electron-beam heated vapor source and with the substrate biased negatively up to 3 kV. Several standard specimens were made in this process. The other was a normal vacuum deposition with a resistively heated Mo wire sublimator. This method is suitable for the in-situ coating, but some improvements are necessary to increase the deposition rate and the life. Substrates were Hastelloy X and their temperature were varied between 200°C and 840°C. Several tests were followed to evaluate coated samples about the film adhesion, the impurity content, the film thickness distribution, the gas desorption, and so on.

Observations with the microscope and the scanning electron microscope (SEM) revealed that the thick film of about 10 μm lost a metallic luster and cracked in some cases. The thin film of 0.1 - 1 μm had a metallic luster and an amorphous structure. Following experiments were done

with thin film samples. Several hundreds of heat cycles between 45°C and 500°C were applied to samples and no change was observed. Atomic composition was measured by the Auger electron spectroscopy (AES). Mo contents were generally 85 - 97 a/o and residual components were mainly carbon and oxigen. The surface and sometimes the interface were contaminated with carbon and oxigen. The thickness distribution of coated samples made by the normal vacuum deposition was measured in a solid angle 2π and nearly uniform. The effects of the baking on outgassing rates were studied with a cylindrical test samples coated with Mo. The baking temperature was 500°C. Outgassing rates were similar to that of the substrate (Hastelloy X).

3.4 Experiments on titanium sublimation pumps[3]

For the divertor pumps in JT-4, high pumping speed and large capacity are required. Initially two alternative concepts are proposed: Volume getter pumps based on a Zr/Al alloy and Ti sublimation pumps. For the latter a small pump with the simple structure was made to investigate the pumping properties. A geometrical area of 470 cm^2 is coated with Ti. The temperature of pumping panels can be controlled at -196°C, room temperature and 150°C. Measurements of pumping properties are made for pure H_2, N_2, CO_2 and O_2 gases, respectively, and for hydrogen gas with small quantity of CO_2 or O_2 or N_2 as an impurity.

It is shown in Fig. IX.3.4-1 that the pumping speed depends not only on the sticking probability but also on the diffusion of gas particles inwards the Ti film so that more than one monolayer of Ti is necessary to attain maximum pumping speed. The sticking probabilities obtained for various gases are shown in Table IX.3.4-1. The maximum pumping speed of 650 ℓ/s for molecular H_2 gas corresponds to the sticking probability of 0.03. The initial pumping speed just after Ti flash is larger with the panels at the low temperature than at the high temperature. The quantities of the absorbed gas with the panel at the low temperature, however, are smaller than that at the high temperature because the sticking probabilities and the diffusion coefficients of the Ti film depend oppositely on the temperature of the panels.

For hydrogen gas with the impurity component of N_2 or CO_2 or O_2 gas, pumping speeds do not depnd on the species or quantity of the mixed gas with impurity content of between 0.02 and 2 %.

Table IX.3.2-1 Toroidal field coil parameters (Preliminary Design)

Toroidal Field (R = 1.4 m)	30	kG
Ampere Turns	21	MAT
Number of Coils	18	
Turns per Coil	10	
Length of a Turn	∿10	m
Area of Cross Section at Center	8250	cm^2
Average Current Density at Center (with space factor : 0.75)	33	A/cm^2
Resistance (75°C without Feeder Bars)	8	m
Inductance	45	mH
Time Constant	5.5	sec
Stored Energy	306	MJ
Flattop Current	117	kA
Flattop Voltage	957	V
Flattop Power	112	MW
Voltage between Turns	5.3	V
Rise Time (Fsorcing 160%)	5.4	sec
Equivalent Square Wave Width	7.3	sec

Table IX.3.4-1 Pumping speeds and sticking probabilities

	H_2	N_2	O_2	CO_2
Pumping speed (ℓ/s)	650	90	420	310
Sticking probability	0.031	0.016	0.081	0.070

Assuming the Maxwell distributions of velosities for gas particles.

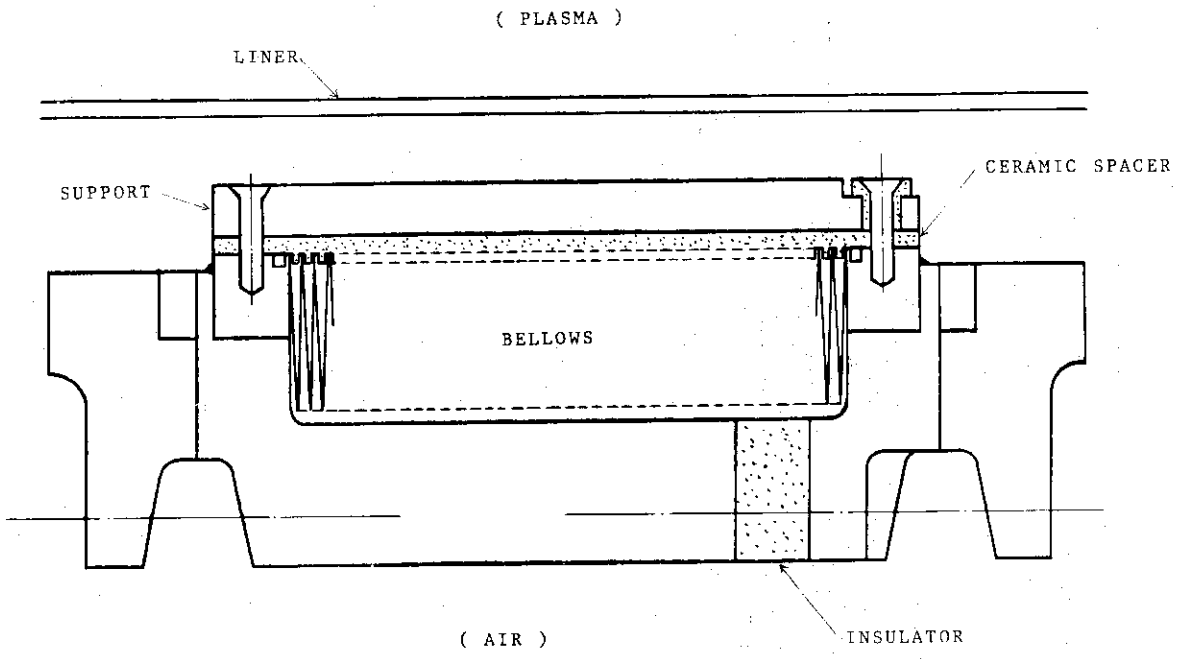

Fig.IX.3.1-1 Bellows section of vacuum chamber

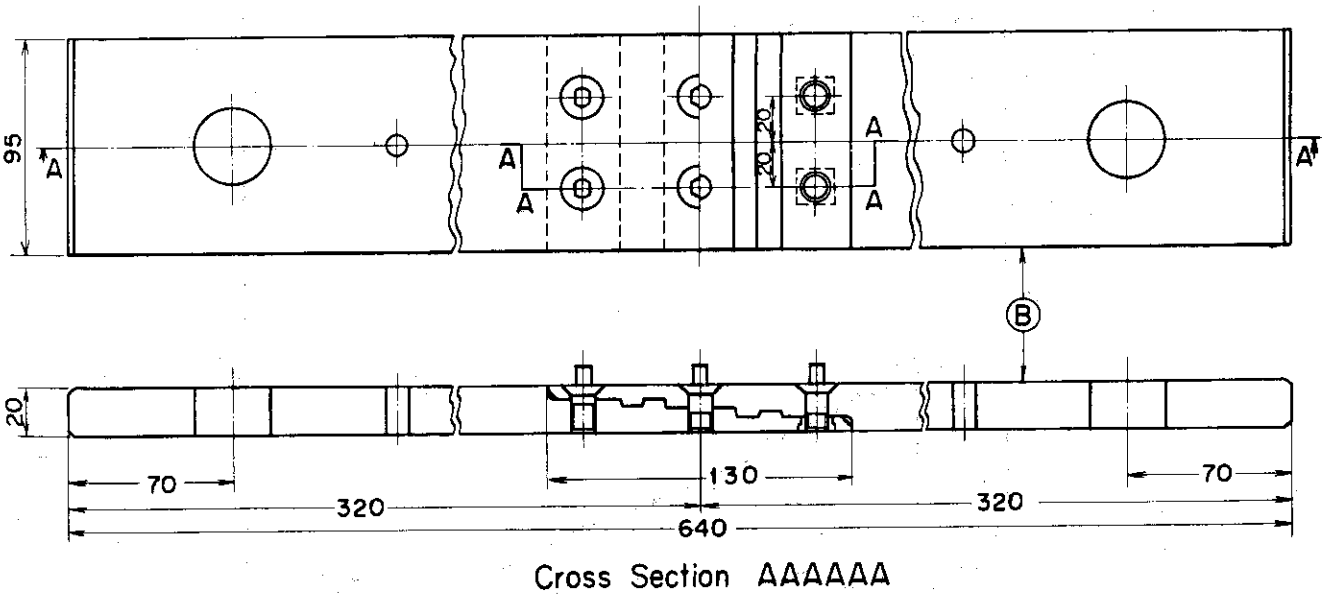

Fig.IX.3.2-1 Test model of TF coil joint

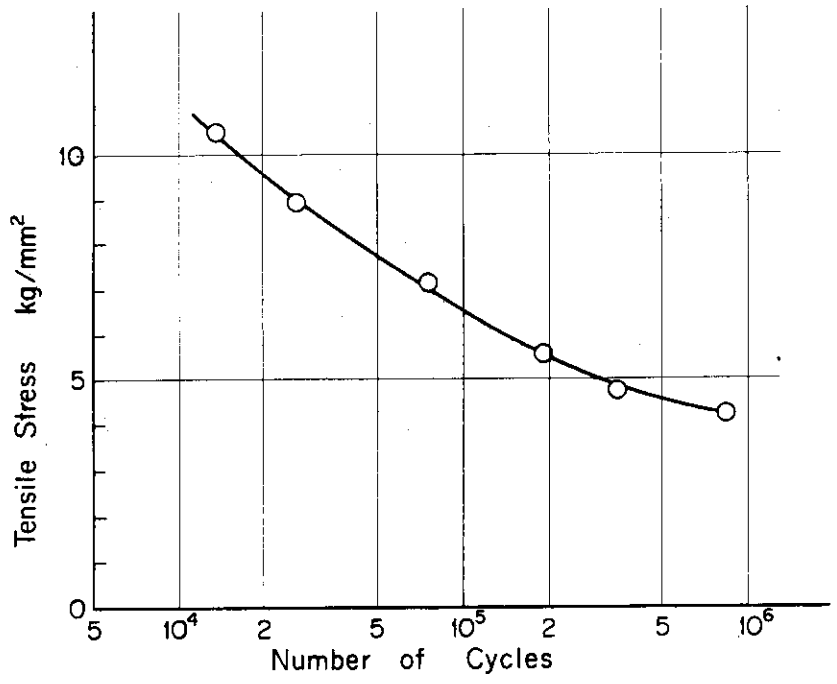

Fig.IX.3.2-2 Tensile fatigue test data of TF coil joint

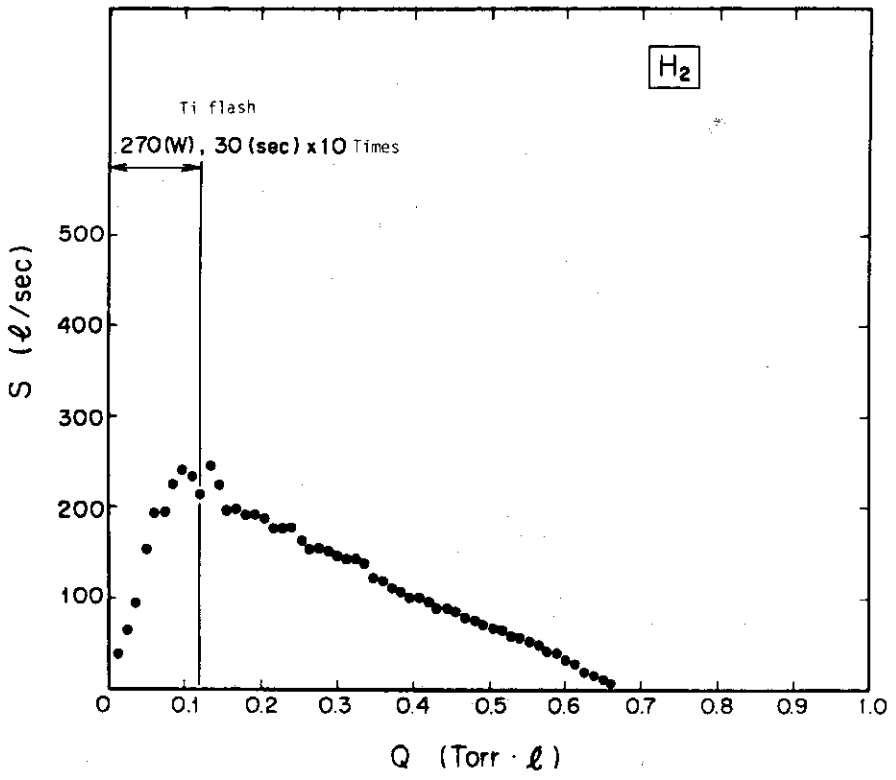

Fig.IX.3.4-1 Pumping speed for the molecular hydrogen gas. The first ten points show the dependence of the pumping speed on the thickness of Ti film. The folloiwng points show the relation between the pumping speed and the accumulated quantities of absorbed gas.

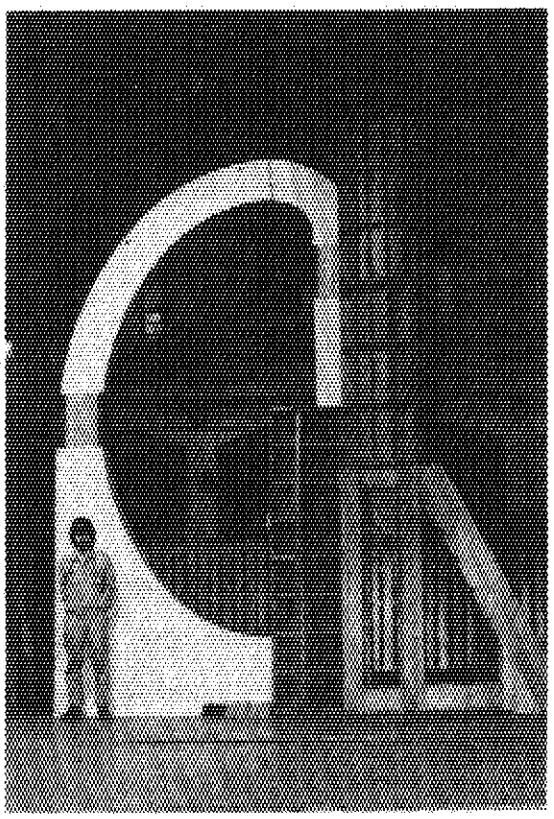

Photo IX.3.2-1 Full scale wooden model of TF coil

3.5 Design study of poloidal field system

1) Basic concepts of poloidal field system

The poloidal magnetic field in the plasma is produced and controlled by two independent coil systems, the primary coils of a current transformer (OH-coil) and the equilibrium-field coils (EF-coils). The OH-coil produces a time-varying magnetic flux linking the plasma. The electric field by this flux variation initiates and maintains the toroidal discharge current required for plasma confinement and ohmic heating. The EF-coils control the magnetic configuration of the discharge, that is the plasma shape and position. The EF-coil system consists of six species of poloidal coil;

i) divertor coil (D-coil)
ii) shaping coil (S-coil)
iii) vertical field coil (V-coil)
iv) quadrupole field coil (Q-coil)
v) position control coil (C-coil)
vi) horizontal field coil (H-coil)

The electrical decoupling between the OH-coil and each EF-coil is necessary to maintain the condition that the EF-coil currents are proportional to the plasma current. The decoupling is performed by setting the ampere-terns of each EF-coil to zero. A general view of the coil positions is shown in Fig. IX.3.5-1.

In 1976, a detailed design of poloidal field system including its power supply was made on the basis of the preliminary engineering design made in 1975.

2) OH-coil system

The design of the OH-coil requires a configuration of current-carrying conductors suitably placed so as to induce the desired electric field in the plasma region. Basic physics design requirements for the OH-coil under $I_p = 1$ MA operation are : (i) a total magnetic flux variation of 5 V-sec, (ii) a minimum one-turn voltage of 300 V at the beginning of the plasma discharge, and (iii) a maximum magnetic error field in the plasma region of less than 50 G.

Within these constraints, the design of the system has been optimized to minimize the space requirements and resistive power for the coil system. The positions of the OH-coil were determined by using the SIMPLEX

code[4] developed in JT-60 project. At full volt-second capability, total ampere-turns in the OH-coil are about 9.0 MAT, with a typical resistive power dissipation of about 50 MW.

3) EF-coil system

The external magnetic field required for the toroidal equilibrium is characterized in terms of two quantities, the strength of its vertical component and the index of curvature, (B_V, n). In JT-4, this equilibrium field (B_V, n) is applied by three EF-coils, namely S-, V- and Q-coil. S-coil induces the dominant portion of the equilibrium field by preprograming control of its current and/or changing its connection. V- and Q-coil produce the small field (δB_V, δn) by feedback control of those currents. By varying the flux values of these three coils and the D-coil, either circular, elliptical or D-shaped configuration can be achieved. For $q_{limiter}$ = 3.0, typical plasma current is about 0.55 MA for a circular discharge, 1.1 MA for a 1.7 : 1 ellipse at B_t = 3.0 T.

Axisymmetric mode involving overall vertical displacement of plasma column is the most troublesome for a elliptic discharge. C-coil is set in order to suppress this mode by a feedback control or a passive-coil connection.

The number, spacing and resistance of the EF-coils are determined by a combination of physics and engineering conditions, including (i) a maximum EF-coil center-to-vacuum chamber spacing to insure adequate plasma shaping ability and stability, (ii) adequate plasma access for neutral beam injections and diagnostics, and (iii) EF-coil current densities, thermal and mechanical stresses compatible with convectional hollow-conductor-cooling copper coil technology. A typical total resistive power dissipation in the EF-coils are about 60 MW. This power is supplied from a single set of motor-flywheel-generator for JT-60 project through the thyristor rectifier system.

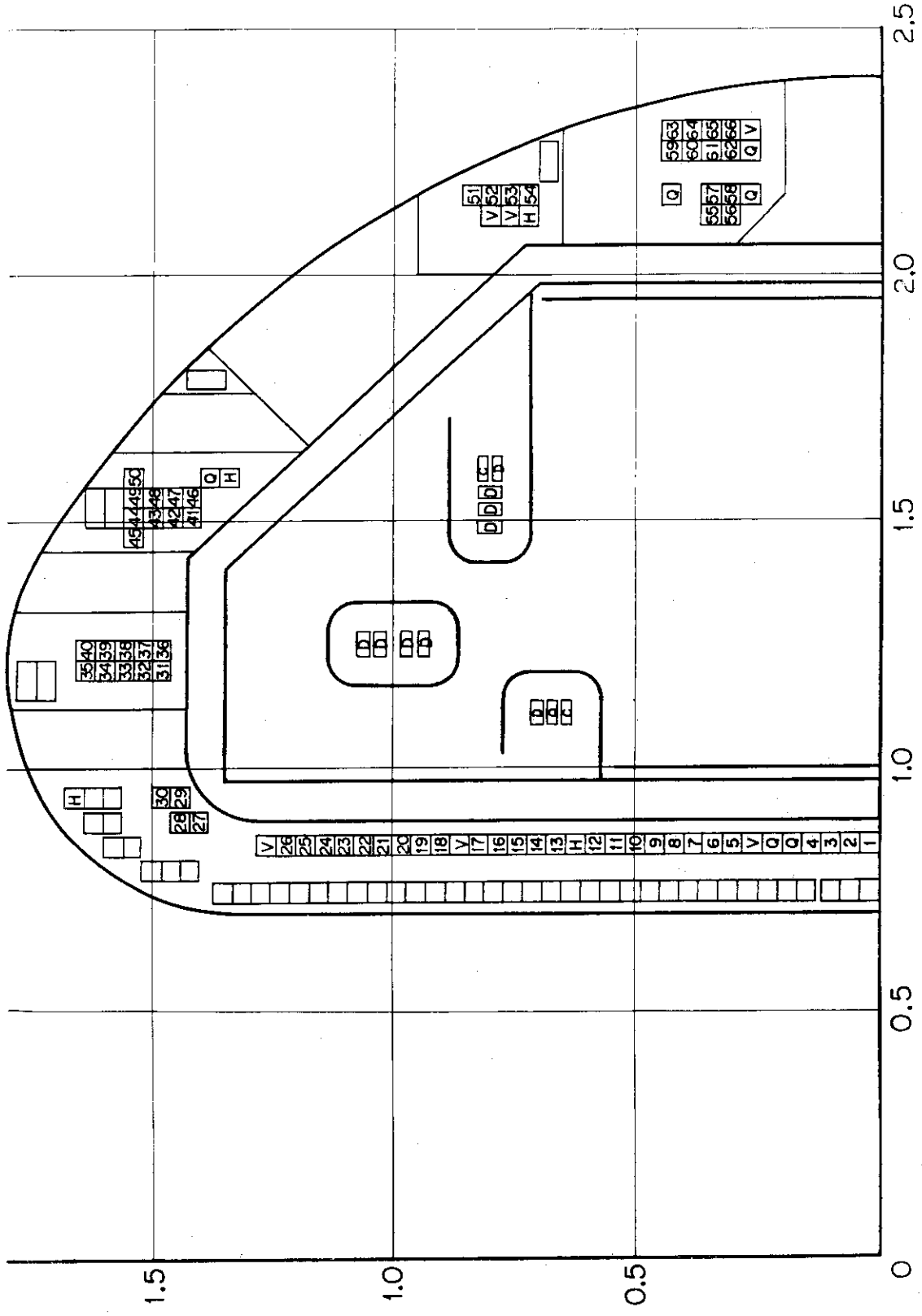

Fig. IX. 3.5-1 Position of PF Coils

4. Plasma Physical Studies Relevant to JT-4 Program

4.1 Study on the positional instability of JT-4 plasma[5]

The JT-4 plasma with elongated cross section is positionally unstable against the axisymmetric vertical displacement. When the plasma column moves, the eddy currents are induced in the conductors such as the vacuum chamber around the plasma. The eddy currents in the conductors are effective to stabilize the positional instability. It is called the shell effect. It is easy to calculate the shell effects of coils, but it is not easy to obtain the shell effects of the vacuum chamber because the distribution of the induced current is also to be calculated.

The numerical method is developed to calculate the shell effects of the vacuum vessel by replacing it with many ring coils which are shown in Fig. IX.4.1-1 so that the vessel can be regarded as a set of equivalent lumped circuits. The movement of the plasma column is represented by a pair of coils flowing a dipole current. The Fig. IX.4.1-2 shows the shell effects of the vacuum chamber and the stabilizer conducting plates. The stability condition of the positional instability cerived from an analysis[6] including the shell effect is $n + n_s > 0$ where n is the index of curvature of the equilibrium field and n_s is that of the field lines produced by the induced current in the shell (vacuum chamber). The stabilizer plates shown in Fig. IX.4.1-2 (b), (c) and (d) are effective for the stabilization of the positional instability of JT-4 plasmas.

The numerical calculation results for a vacuum chamber with a circular cross section and a large aspect ratio were compared with the analytic results for a cylindrical vessel as an assessment of the numerical calculation method presented here.

4.2 Behavior of particles near the separatrix magnetic surface[7]

The drift surfaces of plasma particles are nearly on the magnetic surfaces, except small radial deviation depending on their velocities. In a tokamak with poloidal divertors as JT-4, some particles go to the divertor chamber and are captured, which would be trapped particles if there is no divertor. Namely, there is additional loss region in the velocity space which directly affects the transport phenomena of the main plasma. The "loss region" of the boundary plasma particles on the velocity space is investigated by analytic and numerical methods. One of the

results is shown in Fig. IX.4.2-1 (b), where $K = R_s/R_s$, $A = R_a/R_s$, $\Omega_p = qB_p/m$. The loss region depends on the function $\Delta \cdot \Omega_p$, and the corresponding width of the layer of the loss region in real space is of the order of the ion poloidal gyroradius.

4.3 Destruction of magnetic surfaces in a divertor region attributed to a discrete structure of magnetic coil[8]

A divertor region or a scrape-off layer is usually regarded as a consequence of particle's diffusion. On the other hand, it is well known that perturbations of magnetic fields often destroy equilibrium magnetic surfaces. It's destruction of magnetic surfaces occurs on the basis of overlapping of adjacent magnetic islands.

In this work, we consider a divertor region which is formed by a plasma current, a divertor current and a uniform magnetic field in the same direction. Effects of the descrete of magnetic coils are then taken account of. Analysis is based on "Stochasticity", and a spread of the divertor region or the scrape-off layer is calculated in terms of a magnetic ripple.

In an unperturbed system, equations for the magnetic lines of force are given and action-angle variables are introduced. Perturbations arising from the descrete structure of magnetic coils act as external forces on the equations for the magnetic lines of force, and resonate with the rotational transform of the unperturbed magnetic field in certain circumstances. The condition for this resonance is obtained and formation of magnetic islands around each resonance is studied. Finally, the stochastic condition is studied and the stochastic layer is calculated.

If the temperature becomes higher or the scale of an installation becomes larger, the destruction of magnetic surfaces near the separatrix region may play an important role in the scrape-off layers.

References

(1) JT-4 Group: JT-4 Program, JAERI-M 6666, (August, 1976), 265 pp, (in Japanese).

(2) Kitsunezaki, A., Seki, S., Saito, R., Matsuda, T., Yokomizo, H. and Yoshikawa, M.: JT-4 Program, Proc. of International Symposium on Plasma Wall Interaction, (Permagon Press, 1977).

(3) Yokomizo, H., Seki, S., Kitsunezaki, A., Matsuda, T. and Saito, R.: Shell Effects of Vacuum Vessel for the Positional Instability, JAERI-M 6693, (September, 1976), 37 pp, (in Japanese).

(4) Kobayashi, T., Tani, K., Takeda, T., Kobayashi, T., Shimada, R., Tamura, S. and Yoshida, Y.: Optimum Design of the Poloidal Field Coils of a Large Fusion Device, JAERI-M 6451, (February, 1976), 62 pp, (in Japanese).

(5) Yokomizo, H., Kitsunezaki, A., Matsuda, T., Saito, R. and Seki, S.: Experiment of Ti Sublimation Pump for JT-4 Divertor, Internal memo (July, 1977), 22 pp, (in Japanese).

(6) Fukuyama, A.*, Seki, S., Momota, H.* and Itatani, R.*: Positional Instabilities in a Tokamak with a Resistive Shell, JJAP 14 (1975) 871.

(7) Saito, R., Seki, S., Kitsunezaki, A., Matsuda, T. and Yokomizo, H.: Behavior of Plasma Ions near the Separatrix in a Tokamak with a Poloidal Divertor, JAERI-M 6727, (October, 1976), 31 pp, (in Japanese).

(8) Tomita, Y.*, Seki, S. and Momota, H.*: Destruction of Magnetic Surfaces in a Divertor Region Attributed to a Discrete Structure of Magnetic Coils, J. Phys. Soc. Japan 42 (1977) 687.

(* Univ. of Kyoto)

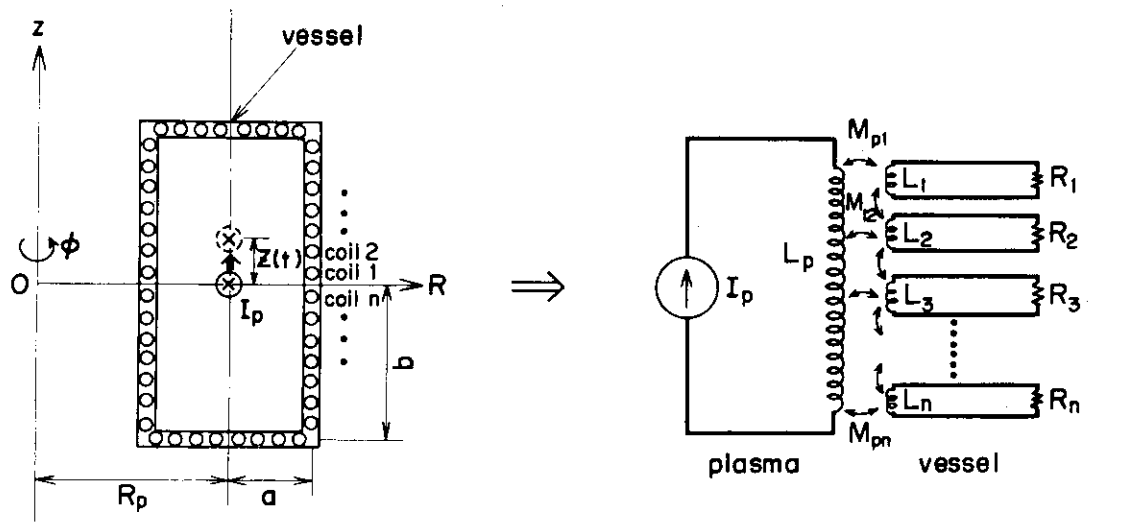

(a) Division to Many Rings (b) Equivalent Lumped Circuit

Fig.IX.4.1-1 Equivalent ring coils of vacuum chamber

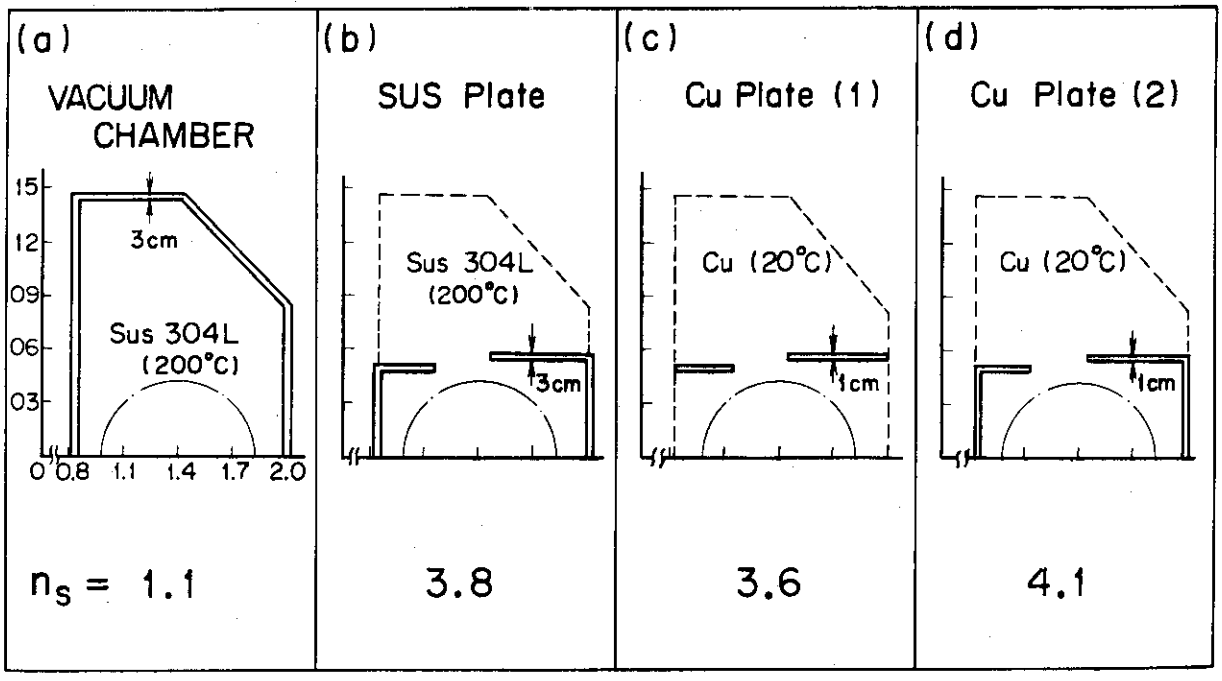

Fig.IX.4.1-2 Shell effects of vacuum chamber and stabilizer plates

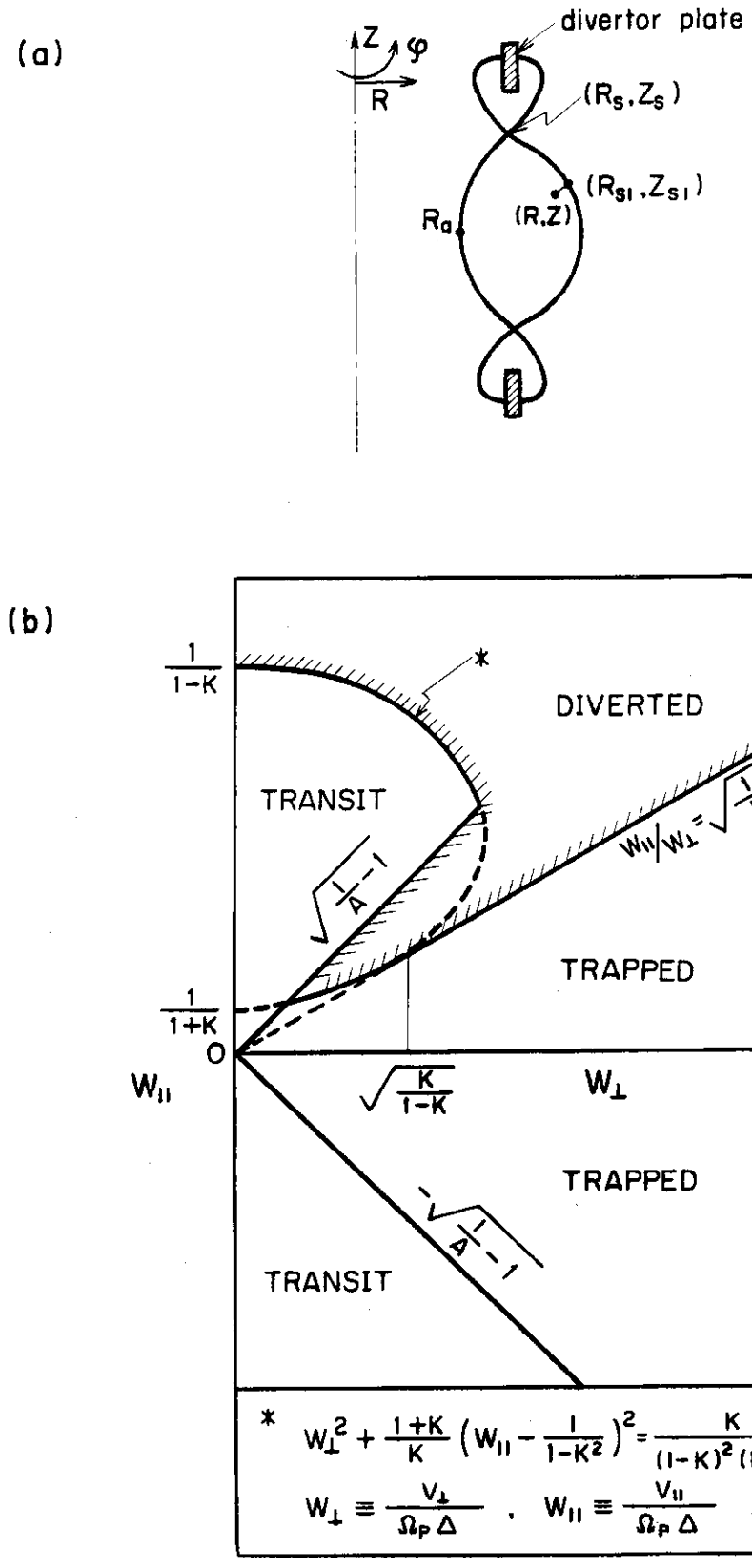

Fig.IX.4.2-1 Behavior of particles near the separatrix magnetic surface

APPENDIXES

A1. Publication List

A1.1 List of JAERI-M Report

1) Kurita, G. and Amano*, T.: "Two dimensional simulation of the mhd stability (1)", JAERI-M 6474 (1976).
(* Osaka University)

2) Suzuki, Y., Ogata, A., Ninomiya, H., Kameari, A.*, Aikawa, H. and Noda, N.**: "Tokamak circuit", JAERI-M 6531 (April, 1976).
(* On leave from Mitsubishi Atomic Power Industries Inc.
** On leave from Institute of Plasma Physics, Nagoya Univ., Nagoya)

3) Seki, Y., et al.: "Evaluation of shielding design for superconducting magnets (II)" JAERI-M 6540 (1976) (in Japanese).

4) Aikawa, H., Ninomiya, H., Kameari, A.* and Suzuki, Y.: "Standard positions of the poloidal coils in large Tokamak JT-60", JAERI-M 6552 (April, 1976).
(* On leave from Mitsubishi Atomic Power Industries Inc.)

5) Takashima, T., Yamamoto, M., Nakamura, H., Ohkubo, M., Ohta, M., Maeda, H.*, Minaguchi, T.*, Mori, H.*, Okamura, H.*, Uchida, T.* and Yamada, T.*: "Design of the movable limiters for JT-60", JAERI-M 6572, (May, 1976) (in Japanese).
(* Sumitomo Heavy Industries, Ltd.)

6) Tazima, T., Inoue, K. and Nakamura*, Y.: "Density Distributions of Impurities and Related Energy Losses in Tokamak Plasmas", JAERI-M 6606, (June 1976).
(* On leave from Sumitomo Heavy Industries, Ltd.)

7) Iida, H., et al.: "Induced activity and dose rates in the JAERI experimental fusion reactor (JXFR)", JAERI-M 6639, (1976). (in Japanese).

8) Shimada, R., Tani, K., Tamura, S., Kobayashi, T.*, Kobayashi, T.** and Yoshida, Y.***: "Some engineering problems in D.C. circuit breakers", JAERI-M 6646, (August, 1976) (in Japanese).
(* On leave from Hitachi, Ltd., ** On leave from Fuji Electric Co., Ltd., *** Scholarshio fellow, Tohoku University).

9) Gomay*, Y., Tazima, T., Fujisawa, N., Suzuki, N. and Konosima, S.: "The Study of Discharge Cleaning in the JFT-2 Tokamak with Surface Observation by AES", JAERI-M 6647, (July 1976).
(* On leave from Tokyo Shibaura Electric Co., Ltd.)

10) Ninomiya, H., Kameari, A.* and Suzuki, Y.: "Current build-up with dynamic magnetic limiter", MAERI-M 6656 (July, 1976).
(* On leave from Mitsubishi Atomic Power Industries Inc.)

11) Kitsunezaki, A., Seki, S., Saito, R.*, Matsuda, T., Yokomizo, H.** and Yoshikawa, M.: "JT-4 program", JAERI-M 6666, (August, 1976). (in Japanese).
(* On leave from Mitsubishi Electric Co., Ltd., ** The University of Tokyo).

12) Fusion Reactor System Laboratory: "Preliminary design of an experimental fusion reactor (Interim Report)", JAERI-M 6670, (1976), (in Japanese).

13) Ide, T., et al.: "Calculation of the neutron radiation damage in D-T fusion reactor materials", JAERI-M 6672, (1976) (in Japanese).

14) Yokomizo, H.*, Seki, S., Kitsunezaki, A., Matsuda, T. and Saito, R.**: "Shell effects of vacuum vessel for the positional instability", JAERI-M 6693, (September, 1976) (in Japanese).
(* The University of Tokyo, ** on leave from Mitsubishi Electric Co., Ltd.).

15) Maeno, M., et al.: "A fast ionization gauge for neutral pressure measurement in the vicinity of the JFT-2 plasma", JAERI-M 6712 (1976) (in Japanese).

16) Seki, Y.: "Neutronics design of fusion reactors and applications of blanket neutronics experiment to the design", JAERI-M 6726, (1976) (in Japanese).

17) Saito, R.*, Seki, S., Kitsunezaki, A., Matsuda, T. and Yokomizo, H.**: "Behavior of plasma ions near the separatrix in a tokamak with a poloidal divertor", JAERI-M 6727, (October, 1976) (in Japanese).
(* On leave from Mitsubishi Electric Co., Ltd., ** The University of Tokyo).

18) Takashima, T., Morishita, O.*, Yamamoto, M., Shimizu, M., Ohta, M., Okamura, H.** and Minaguchi, T.**: "Design and characteristics of

the drive mechanism for movable limiters of JT-60 (I)", JAERI-M 6733, (September, 1976) (in Japanese).
(* On leave from Sumitomo Heavy Industries, Ltd., ** Sumitomo Heavy Industries, Ltd.).

19) Seki, S., Maeda, H., Kitsunezaki, A. and Saito, R.*: "Numerical code SPHEX for free boundary MHD equilibrium with Legendre expansion method", JAERI-M 6734, (October, 1976) (in Japanese).
(* On leave from Mitsubishi Electric Co. Ltd.).

20) Ohara, Y.: "Simulation code for beam trajectories in an ion source "IONORB"", JAERI-M 6757, (October, 1976) (in Japanese).

21) Maeno, M., Matsuzaki, Y. and Fuzisawa, N.: "A delay circuit for constant current operation of JFT-2", JAERI-M 6762, (October 1976) (in Japanese).

22) Tanaka, S. and Shibata, T.: "Pulsed gas feed to the ion source", JAERI-M 6778, (November, 1976) (in Japanese).

23) Seki, Y., et al.: "Evaluation of shielding design for superconducting magnets (III), JAERI-M 6783, (1976) (in Japanese).

24) Ohara, Y.: "Numerical simulation for design of a two stage acceleration system in a high power ion source", JAERI-M 6813, (November, 1976).

25) Morishita, O.*, Takatsu, H., Takashima, T., Yamamoto, M., Ohta, M., Yoshii, A.** and Suzuki, M.**: "Stress analysis of the bellows and its connection with a thick ring of the vacuum vessel", JAERI-M 6822, (November, 1976) (in Japanese).
(* On leave from Sumitomo Heavy Industries, Ltd., ** Sumitomo Heavy Industries, Ltd.)

26) Nishimura*, H. and Shimamoto, S.: "Two-dimensional stress analysis computer code for element coil test by finite element method", JAERI-M 6865 (1977) (in Japanese).
(* On leave from Hitachi, Ltd.)

27) Imai, T., Nagashima, T. and Azumi, M.: "Numerical studies of lower hybrid wave propagation in JFT-2", JAERI-M 6902, (Feburary, 1977) (in Japanese).

28) Fusion Reactor System Laboratory: "Design study of superconducting

troidal fuel magnet for tokamak fusion power reactor", JAERI-M 6921 (1977) (in Japanese).

29) Aikawa, H., Ogata, A. and Suzuki, Y.: "Detection of the position and cross-section of a Tokamak plasma with magnetic probes, JAERI-M 6931 (January, 1977).

30) Kameari, A.*, Ninomiya, H. and Suzuki, Y.: "Eddy currents induced on the torus with non-uniform resistances", JAERI-M 6953 (January, 1977).
(* On leave from Mitsubishi Atomic Power Industries Inc.)

31) Momota, H.*, Fukuyama, A.*, Azumi, M., Okamoto, M. and Takizuka, T.: "Theoretical investigations of lower hybrid resonance heating in a tokamak", JAERI-M 6964 (1976).
(* Kyoto University)

32) Tuda, T.: "Temperature gradient effect on impurity ion transport", JAERI-M 6965 (1977) (in Japanese).

33) Shibata, T., Itoh, T., Shirakata, H. and Sugawara, T.*: "Composition of neutral beam for heating JFT-2 plasma", JAERI-M 6990, (February, 1977) (in Japanese).
(* On leave from Tokyo Shibaura Electric Co., Ltd.)

34) Nakamura, H., Ninomiya, H., Shimizu, M. and Ohta, M.: "Heat analysis of the magnetic limiter plate for JT-60", JAERI-M 7013, (February, 1977) (in Japanese).

35) Kobayashi, T.*, Tazima, T., Tani, K. and Tamura, S.: "Effect of plasma minor-radius expansion in the current build-up phase of a large tokamak", JAERI-M 7014, (February, 1977) (in Japanese).
(* On leave from Hitachi, Ltd.)

36) Nakamura*, Y., Kasai, S. and Tazima, T.: "Dielectronic Recombination of Carbon, Oxygen and Iron in Low-density and High-temperature Plasmas", JAERI-M 7019, (February 1977) (in Japanese).
(* On leave from Sumitomo Heavy Industires, Ltd.)

37) Sugawara, T., et al.: "JFT-2 Tokamak neutral injector and preliminary results of additional heating experiment", JAERI-M 7043, (April, 1977).

38) Sugihara, M. and Ogasawara, M.*: "Nonlinear saturation of dissipative trapped ion instability and anomalous transport", JAERI-M 7050, (1977).
(* Keio University)

A1.2 List of Papers Published in Journals

1) Aikawa, H., Ogata, A. and Suzuki, Y.: "Derivation of plasma displacement in a Tokamak from magnetic probe signals", Japan. J. Appl. Phys. 15 (1976) 2031.

2) Ninomiya, Y., Suzuki, Y. and Kameari, A.*: "Positional instabilities of a plasma in a Tokamak with a magnetic limiter", Japan. J. Appl. Phys. 15 (1976) 2201.
(* On leave from Mitsubishi Atomic Power Industries Inc.)

3) Maeda, H., et al.: "Plasma behavior near a separatrix magnetic surface in the JFT-2a Tokamak", Nucl. Fusion 16 (1976) 148.

4) Shimomura, Y., et al.: "Plasma behavior with a separatrix magnetic surface in JFT-2a tokamak", Phys. Fluids 19 (1976) 1635.

5) Hamada, Y.*, Suzuki, Y., Ohasa, K.**, Fujiwara, M.** and Miyamoto, K.**: "Study of helical plasma equilibria", Plasma Physics 18 (1976) 889.
(* Faculty of Science, Kyoto University, ** Institute of Plasma Physics, Nagoya University)

6) Shoji, T.: "Plasma equilibrium in axisymmetric hybrid systems", Nuclear Fusion 16 (1976) 829.

7) Fukuyama, A.*, Momota, H.*, Itatani, R.* and Takizuka, T.: "Stochastic acceleration by an electrostatic wave near ion cyclotron harmonics", Phys. Rev. Letters 38 (1977) 701, see also Sect. 4.1.
(* Kyoto University)

8) Porkolab, M.*, Bernabei, S.*, Hooke, W.M.*, Mothley, R.W.* and Nagashima, T.: "Observation of parametric instabilities in lower hybrid radio frequency heating of tokamaks", Phys. Rev. Letters, 38 (1977) 230.
(* Princeton University)

9) Ogata, A., Aikawa, H. and Suzuki, Y.: "Accuracy of plasma displacement measurement in a Tokamak using magnetic probes", Japan. J. Appl. Phys. 16 (1977) 185.

10) Takeuchi, H., Funahashi, A., Takahashi, K., Shirakata, H. and Yano, S.: "A 10-channel neutral particle energy analyzer for measurements of ion temperatures on Tokamak plasmas", Japan. J. Appl. Phys. 16 (1977) 139.

11) Yatsui, K.*, Imai, T. and Furumi, M.*: "Cross field-current-driven electrostatic instabilities in an inhomogeneous plasma", J. Phys. Soc. Japan, 42 (1977) 652.
(* Osaka University)

12) Tomita, Y.*, Seki, S. and Momota, H.*: "Destruction of magnetic surfaces in a divertor region attributed to a discrete structure of magnetic coils", J. Phys. Soc. Japan 42 (1977) 687.
(* Kyoto University)

13) Amano, T.* and Okamoto, M.: "Numerical investigation of the time evolution of impurity concentration in a Tokamak", J. Phys. Soc. Japan 42 (1977) 1019.
(* Osaka University)

14) Kasai, S., et al.: "Determination of electron temperatures during initial phases of Tokamak discharges by an improved time-history method of spectral lines", J. Phys. Soc. of Japan 43 (1977) 310.

A1.3 List of Papers Published in Conference Proceedings

1) Shirakata, H., Itoh, T., Kondoh, U.*, Matsuda, S., Ohara, Y., Ohga, T., Shibata, T., Sugawara, T.** and Tanaka, S.: "The ion source development for neutral injection heating at JAERI", 3rd International Meeting on Theoretical and Experimental Aspects of Heating of Toroidal Plasmas, Grenoble, France, 1976, Vol. I. 33.
(* On leave from Nissin Electric Co. Ltd., ** on leave from Tokyo Shibaura Electric Co. Ltd.)

2) Shirakata, H.: "Additional heating in the Japanese tokamak JT-60, 3rd International Meeting on Theoretical and Experimental Aspects of Heating of Toroidal Plasmas, Grenoble, France, 1976, Vol.II, p.219.

3) Tone, T., et al.: "Some considerations on a plasma in the JAERI experimental fusion reactor", Proc. of the 2nd Topical Meeting on the Technology of Controlled Nuclear Fusion, Richland, 1976, Vol.I, 975 (CONF-760935-P3).

4) Ioki, K.*, et al.: "Superconducting toroidal field magnet for a Tokamak fusion reactor", ibid, Vol.IV, 1273.
(* On leave from Mitsubishi Atomic Power Industries Co.)

5) Sako, K., et al.: "Conseptual design of the JAERI demonstration fusion reactor", ibid, Vol.II, 607.

6) Ide, T.*, et al.: "Effects of neutron streaming through injection ports on neutronic characteristics of a fusion reactor", ibid, Vol.II, 395.
(* On leave from Sumitomo Heavy Industries Co.)

7) Maekawa, H. and Seki, Y.: "Fission rate distributions in lithium and hybrid fusion blanket assemblies", ibid, Vol.III, 883.

8) Maeda, H., et al.: "DIVA Divertor and JFT-2 confinement experiments", Proc. of the 6th IAEA Conf. on Plasma Physics and Controlled Nuclear Fusion Research, Berchtesgaden, 1976, Vol.II, 289.

9) Sako, K., et al.: "Preliminary design of a Tokamak experimental fusion reactor", ibid, Vol.III, 239.

10) Maeda, H., et al.: "Plasma wall interaction in DIVA", Proc. Int. Symp. on Plasma Wall Interaction, Jülich, Germany, (1976) 537.

11) Tazima, T., and Gomay, Y.*: "Experimental Studies on the Methods of Surface Cleaning for Tokamak Devices", International Simposium on Plasma-Wall-Interaction (Jülich 1976) 559.
(* On leave from Tokyo Shibaura Electric Co., Ltd.)

12) Kitsunezaki, A., Seki, S., Saito, R.*, Matsuda, T., Yokomizo, H.** and Yoshikawa, M.: "JT-4 program", Proceedings of the International Symposium on Plasma Wall Interaction, (Jülich, 1976), 697 pp.
(* On leave from Mitsubishi Electric Co. Ltd., ** University of Tokyo)

13) Suzuki, Y.: "Review of the work on plasma-wall interaction in Tokamak plasma confinement at JAERI", Proc. of the Intl. Symp. on Plasma Wall Interaction (Jülich, 1976).

14) Sone K. , et al.: "Sputtering yields for 0.1-6 keV protons incident onto molybdenum and graphite targets", Proc. Intern. Symp. Plasma Wall Interaction (Jülich, 1976) p.323.

A2. Personnel of the Division

A2.1 Number of the staff of the Division

	FY 1976	FY 1977
Regular staff*1	102	121
Staff on loan	24	22*2
Guest scientist	4	6*3
Scholarship fellow	20	30

*1 Including scientists, technicians, and secretaries.

*2 Six from Tokyo Shibaura Electric Co., Ltd.
Four from Hitachi Ltd.
Two from Mitsubishi Atomic Power Industries Inc.
Two from Sumitomo Heavy Industries, Ltd.
Two from Mitsubishi Electric Co.
One from Mitsubishi Heavy Industries, Ltd.
One from Fuji Electric Co., Ltd.
One from Sumitomo Electric Industries, Ltd.
One from Nissin Electric Co., Ltd.
One from Kawasaki Heavy Industries, Ltd.
One from Oki Electric Industry Co., Ltd.

*3 Three from the University of Tokyo
Two from Nihon University
One from Ochanomizu University

A2.2 List of Scientific Staffs and Officers during FY 1976

(A) Division of Thermonuclear Fusion Research

MORI, Sigeru (Head)
OBATA, Yukio (Deputy Head)
AKAMA, Kouzou (Administrative Manager)

Plasma Theory Laboratory

AZUMI, Masafumi
KURITA, Genichi**1
OKAMOTO, Masao
SUGIHARA, Masayoshi**2
TAKEDA, Tatsuoki
TAKIZUKA, Tomonori
TANAKA, Masatoshi (Chief)
TSUNEMATSU, Toshihide
TUDA, Takasi

Experimental Plasma Physics Laboratory

TANAKA, Masatoshi (Chief)

* JFT-2

FUJISAWA, Noboru
HIRAYAMA, Toshio
KONOSHIMA, Shigeru
MAENO, Masaki
SHIMADA, Michiya
SUZUKI, Norio
YAMAMOTO, Takumi**3

* JFT-2a

KIMURA, Haruyuki
MAEDA, Hikosuke
NAGAMI, Masayuki
ODAJIMA, Kazuo
SENGOKU, Seio**4
SHIMOMURA, Yasuo

UEDA, Noriaki*5
YAMAMOTO, Shin

* Diagnostics

FUNAHASHI, Akimasa
KASAI, Satoshi
KAWAKAMI, Tomohide
KUMAGAI, Katsuaki
SHOJI, Teruaki
SUGIE, Tatsuo
TAKAHASHI, Koki
TAKEUCHI, Hiroshi
YAMAUCHI, Toshihiko

Facility Operation and Engineering Section

ANNO, Katsuto
ARAI, Takashi
HASEGAWA, Kouichi
HIRATSUKA, Hajime
ISAKA, Masayoshi
KAZAWA, Minoru
KODAMA, Kouzou
KUNIEDA, Shunsuke (Deputy Chief)
MATUZAKI, Yoshimi
SHIBATA, Takatoshi
SHIINA, Tomio
SUNAOSHI, Hidenori
TANI, Takashi
TOKUTAKE, Toshikuni
TOYOSHIMA, Noboru
YOKOKURA, Kenji

Plasma Heating Laboratory

SHIRAKATA, Hirofumi (Chief)

* Neutral Beam Injection Heating

AKIBA, Mitsunori**5

ARAKAWA, Yoshihiro**6
HORIIKE, Hiroshi**7
ITOH, Takao
KAWAI, Mikito
KONDOH, Umeo *7
MATSUDA, Shinzaburo
OHARA, Yoshihiro
OHGA, Tokumichi
SHIBATA, Takemasa
SUGAWARA, Tohru*1
TANAKA, Shigeru

* Radiofrequency Heating
IMAI, Tsuyoshi
NAGASHIMA, Takashi

Plasma Engineering Laboratory

MORI, Sigeru (Chief)

* Surface Phenomena
ABE, Tetsuya**8
MURAKAMI, Yoshio
OBARA, Kenziro
OHTSUKA, Hidewo
SAIDO, Masahiro
SHIRAISHI, Kensuke
SONE, Kazuho
YAMADA, Rayji

* Superconducting Magnet
ANDO, Toshinari
NAKAYAMA, Yoshinaga*1
NISHIMURA, Hidetomo*3
HOSODA, Yoshikado*2
SATOW, Takashi*4
SHIMAMOTO, Susumu

Fusion Reactor System Laboratory

ASAMI, Naoto*5
IDE, Takahiro*2
IIDA, Hiromasa
IOKI, Kimihiro*5
MAKI, Koichi*3
SAKO, Kiyoshi (Chief)
SEKI, Yasushi
SUZUKI, Tatsushi*9
TONE, Tatsuzo
YAMAMOTO, Takashi*9
YAMATO, Harumi*1

(B) Division of Large Tokamak Development

MORI, Sigeru (Head)
ISO, Yasuhiko (Deputy Head)
SAITO, Jo (Administrative Manager)

Large Tokamak Development Laboratory

YOSHIKAWA, Masaji (Chief)

* Planning and Coordination

GOMAY, Yoshio*1
HIRAOKA, Toru
NAKAMURA, Yoshiharu*2
TAZIMA, Teruhiko

* Machine Design and Development

ANDO, Toshiro
KASAWAKI, Kozou
MIKI, Nobuharu*1
MORISHITA, Osamu*2
NAKAMURA, Hiroo
NISHIO, Satoshi
OHKUBU, Minoru
OHTA, Mitsuru
SAIGO, Tsugumoto*3
SHIMIZU, Masatsugu
TAKASHIMA, Tetsuo
TAKATSU, Hideyuki
YAMAMOTO, Masahiro

* Power Supplies Design and Development

KISHIMOTO, Hiroshi
KOBAYASHI, Tomofumi*3
OHTSUKA, Michio*3
SHIMADA, Ryuichi
TAMAGAWA, Toru*1
TAMURA, Sanae
TANI, Keiji

YABUNO, Kohei*3
YOSHIDA, Hidetoshi

* Control/Diagnostics Design and Development
AIKAWA, Hiroshi
ITAGAKI, Tokiyoshi
KAMEARI, Akihisa*5
KOIKE, Yukio*6
MATOBA, Tohru
NINOMIYA, Hiromasa
OGATA, Atsushi
SUZUKI, Yasuo
TAKANO, Ichiro*1

* JT-4 GROUP
KITSUNEZAKI, Akio
SEKI, Shogo
YOKOMIZO, Hideaki
MATSUDA, Toshiaki
SAITO, Ryuta*4

(C)

Office of Fusion Program
TANIGUCHI, Sukenobu (Administrative Manager)
INOUE, Kenji
TAKEDA, Takashi

Guest Scientists
IWATA, Giichi (Ochanomizu University)
KAWAKAMI, Ichiro (Nihon University)
TUZI, Yutaka (The University of Tokyo)
YASUKOCHI, Ko (Nihon University)

On leave from

*1 Tokyo Shibaura Electric Co., Ltd.
*2 Sumitomo Heavy Industries Ltd.
*3 Hitachi Ltd.
*4 Mitsubishi Electric Co.
*5 Mitsubishi Atomic Power Industries Inc.
*6 Oki Electric Industry Co., Ltd.
*7 Nissin Electric Co., Ltd.
*8 Kawasaki Heavy Industries Ltd.
*9 Fuji Electric Co., Ltd.

Scholarshop fellows

**1 Osaka University
**2 Keio University
**3 Nagoya University
**4 Tokai University
**5 Tokyo Institute of Technology
**7 The University of Tokyo
**8 Hokkaido University

A3. Budget of the Division

(unit: millon yen)

	FY*1 1976	FY*1 1977
Scientific program	3,531.4	7,335.8*2
(excluding staff & administrative cost)	(11,491.6)	(16,516.2*3)
Building	345.6	

*1 From April to March

*2 Including cashing of the financial obligation for FY 1977

*3 The total financial obligation from FY 1977 to FY 1980 for the construction of part of the components of JT-60 and for the development of plasma heating systems.

ERRATA

Page	Line	As printed	To read
(5)	↑2	interative	iterative
(10)	↑10	damage energetic	damage due to energetic
(13)	↑14	新しい遂次	新しい逐次
(15)	↓6	結晶粒子放出	結晶粒放出
(16)	↓17	3次元電源解析	3次元渦電流解析
3	↓14	$\Delta\psi=0$	$\nabla\psi=0$
17	↑4	inerative	iterative
21	↓11	, $<\Delta\rho>$ etc.	, $<\Delta^*\rho>$ etc.
116	Interchange the contents of Table IV.2.1-1 and Table IV.2.4-1 on page 129 with the captions unchanged.		
150	↓11	beam[17].	beam[7].
213	↑16	manifold.	manifold except the outer few layers.
	↑7	rolled.	working ratio.
215	↓20	$\Delta\phi$ ∿2.5 v.s	$\Delta\phi$ ∿25 v.s
	↑10	Taking	Taking into
227	↓14	The supporting	The supporting methods
229	↓3	T his	This
	↑5	each	etch
331	↓10	, Yoshiharu	, Yukiharu

In A1.2 List of Papers Published in Journals on pages 322∿323, the following papers should be added.

Toi, K. and Takeda, T.: "Optimum design of control coils in a Tokamak device by nonlinear optimization", J.J.A.P. 16 No.2 (1977) 325.

Takeda, T.: "Numerical method for solution of the integral equation of the first kind - Applications to analysis of plasma density profile", J. Computational Phys. 21 No.3 (1976) 305.